Aeroradiometric Measurements in the Framework of the Swiss ARM25 and International AGC25 Exercises

Alberto Stabilini, László Varga, Federico Geser, Cristina Poretti, Fabian Hauenstein, Stéphane Maillard, Adrian Hess, Benno Bucher, Ladislaus Rybach, Erwan Manach, Romain Vidal, Vincent Faure, Alexandra Muhr, Christopher Strobl, Tönjes Koschine, Birgit Seiler, Michael Thomas, Carsten Panek, Claudia Bender, Torsten Fiolka, Fahmi Rouatbi, Lubomír Gryc, Jan Helebrant, Marek Helebrant, Martina Nováková, Marcel Ohera, Aneta Bendiková, Ondřej Kareš, Jiří Komárek, Petr Menhart, Matěj Trš, Olga Andzelika Olechnovic, Dominykas Sinkevicius, Valdemaras Milinkevicius, Adomas Seputis, Julius Ziliukas, Mindaugas Kersys, Mindaugas Stravinskas, Audrius Vaicekauskas, Gintaras Jankunas, Rolandas Volskis, Dora Chiang, Jonathan Conde, Michael Reed, Simon Karlsson, Julien Spruytte, Malgorzata Kasprzak, Gerald Scharding, Sabine Mayer

PSI-Report No. 26-02
2026
ISSN 3042-6391

DOI: https://doi.org/10.55402/psi:84944

PSI

Aeroradiometric Measurements in the Framework of the Swiss ARM25 and International AGC25 Exercises

Alberto Stabilini[1], László Varga[1], Federico Geser[1], Cristina Poretti[2], Fabian Hauenstein[3], Stéphane Maillard[4], Adrian Hess[2], Benno Bucher[5], Ladislaus Rybach[6], Erwan Manach[7], Romain Vidal[7], Vincent Faure[7], Alexandra Muhr[8], Christopher Strobl[8], Tönjes Koschine[9], Birgit Seiler[8], Michael Thomas[8], Carsten Panek[8], Claudia Bender[10], Torsten Fiolka[10], Fahmi Rouatbi[10], Lubomír Gryc[11], Jan Helebrant[11], Marek Helebrant[11], Martina Nováková[11], Marcel Ohera[11], Aneta Bendiková[12], Ondřej Kareš[12], Jiří Komárek[12], Petr Menhart[12], Matěj Trš[12], Olga Andzelika Olechnovic[13], Dominykas Sinkevicius[13], Valdemaras Milinkevicius[13], Adomas Seputis[13], Julius Ziliukas[13], Mindaugas Kersys[14], Mindaugas Stravinskas[14], Audrius Vaicekauskas[14], Gintaras Jankunas[14], Rolandas Volskis[14], Dora Chiang[15], Jonathan Conde[15], Michael Reed[15], Simon Karlsson[16], Julien Spruytte[17], Malgorzata Kasprzak[1], Gerald Scharding[2], Sabine Mayer[1]

[1]Department of Radiation Safety and Security, Paul Scherrer Institute (PSI), 5232 Villigen PSI, Switzerland
[2]National Emergency Operations Centre (NEOC), 3003 Bern, Switzerland
[3]Spiez Laboratory, 3700 Spiez, Switzerland
[4]NBC-EOD Centre of Excellence (Nuclear Biological Chemical defense and Explosive Ordnance Disposal), 3700 Spiez, Switzerland
[5]Swiss Federal Nuclear Safety Inspectorate (ENSI), 5201 Brugg, Switzerland
[6]Institute of Geophysics, Swiss Federal Institute of Technology Zürich (ETHZ), 8092 Zürich, Switzerland
[7]French Nuclear Safety and Radiation Protection Authority (ASNR), France
[8]Federal Office for Radiation Protection (BfS), Neuherberg, Germany
[9]Federal Office for Radiation Protection (BfS), Berlin, Germany
[10]Fraunhofer Institute for Communication, Information Processing and Ergonomics (FKIE), Germany
[11]National Radiation Protection Institute (SÚRO), Bartoškova 1450/28, 140 00 Prague, Czech Republic
[12]314th CBRN Monitoring Centre of the Czech Army, Czech Republic
[13]Radiation Protection Centre (RSC), Lithuania
[14]State Border Guard Service under the Ministry of the Interior of the Republic of Lithuania (SBGS), Lithuania
[15]National Nuclear Security Administration Office of Nuclear Incident Policy and Cooperation (NNSA NIPC NA-81), USA
[16]Swedish Radiation Safety Authority (SSM), Sweden
[17]Mirion Technologies (MGPI) SAS, 174 Route d'Eyguières, FR 13113 Lamanon, France

DOI: https://doi.org/10.55402/psi:84944

PSI-Report No. 26-02
2026
ISSN 3042-6391

PSI


NATIONAL EMERGENCY OPERATIONS CENTRE
AGC25
AIRBORNE
RADIOMETRICS
2025
SWITZERLAND
CH | DE | FR | CZ | LT

Abstract

This document reports on the aeroradiometry measurement exercises conducted in Switzerland in 2025. Measurements were performed between the 27th of May 2025 and the 6th of June 2025 and were structured into two campaigns.

The first campaign, ARM25, comprised routine airborne gamma-spectrometry surveys over Swiss nuclear facilities located in Mühleberg and Gösgen. These surveys were carried out on behalf of the Swiss Federal Nuclear Safety Inspectorate (ENSI) in the vicinity of the Gösgen nuclear power plant and the Mühleberg plant, currently in decommission. Outside the operational areas, no radioactivity exceeding natural background levels was detected. No deviations were observed compared with results from previous years.

The second campaign consisted of a week long international exercise, AGC25, hosted in Switzerland and coordinated by the Swiss expert group for airborne gamma spectrometry (FAR). Airborne gamma-spectrometry measurements using helicopters and drones were performed by national teams from Switzerland, Germany, France, the Czech Republic and Lithuania. Ground-based measurements were performed by the Swedish observer team in coordination with the exercise organisers. Switzerland contributed to the helicopter surveys with two teams, respectively managed by the National Emergency Operations Centre (NEOC) and the Nuclear, Biological, Chemical Defence and Explosive Ordnance Disposal Centre of Excellence (NBC-EOD). For the first time, an international exercise included source search operations using drones, in addition to helicopters. The exercise demonstrated successful multinational coordination, efficient implementation of composite mapping techniques, and effective localisation, identification and quantification of radionuclide sources.

Overall, the campaign strengthened operational readiness, enhanced interoperability with partner nations, and confirmed the high level of training and technical capability among the personnel involved in aeroradiometry.

Contents

List of Figures

List of Tables

Chapter 1

Introduction

This document reports on the aeroradiometry measurement exercises, which have taken place in Switzerland in 2025. Measurements were performed between 27th May 2025 and 6th June 2025 and structured into two campaigns.

1.1 Swiss Aeroradiometric Measurements 2025 (ARM25)

The first campaign (ARM25) comprised routine airborne gamma-spectrometry surveys over Swiss nuclear facilities located in Mühleberg and Gösgen. These surveys were carried out on behalf of the Swiss Federal Nuclear Safety Inspectorate (ENSI) in the vicinity of the Gösgen nuclear power plant and the Mühleberg nuclear power plant, which is currently being decommissioned.

1.2 International Airborne Gamma Spectrometry Campaign 2025 (AGC25)

The second campaign consisted of an international exercise (AGC25) hosted in Switzerland and coordinated by the Swiss expert group of airborne gamma spectrometry (FAR). The purpose of the exercise was to strengthen international cooperation between national airborne radiation monitoring units.

Since the participating teams rely on different measuring equipment, analysis software, and calibration standards, it is essential to verify that their systems can work together, that measurement methods are compatible, and that the results are comparable. Activities of this type require continuous training and benchmark measurements under reference radiological conditions, as well as practice in coordinating logistics between multiple monitoring groups and helicopter crews. When foreign teams take part, special emphasis must be placed on ensuring that both the joint measurement tasks and the flight operations are managed safely and efficiently. A key aspect of the exercise was the exchange of data. The ERS 2.0 data format was successfully used to share measurement data and results.

The international campaign was planned over six days, including the teams' arrivals on the 1st June. Each group was assigned five missions to be completed within four working days, followed by the analysis of collected data and a presentation of initial findings on Friday, 6th June 2025. The teams were later given additional time to refine their evaluations, with the finalised results compiled in this report, which also outlines the individual assignments and summarises the overall outcomes.

Chapter 2

Organisation of the AGC25

2.1 Why organising an international exercise?

The purpose of these exercises is to promote, maintain and further develop mutual cooperation among national airborne radiological monitoring teams across Europe. This cooperation is driven by two main objectives. Firstly, it allows teams to compare equipment, measurement strategies, and techniques, ensuring that results are consistent and comparable. This not only validates the methodologies employed but also enables the wider community to benefit from the expertise and innovations developed by individual groups. Secondly, these exercises provide an opportunity to train the coordination of multiple international teams. In the event of a radiological accident on European territory, it is likely to assume that cross-border assistance will be required from neighbouring states.

Since 2007, Switzerland has regularly taken part in international exercises together with its neighbouring countries. In Switzerland, the National Emergency Operations Centre (NEOC) is responsible for the deployment and coordination of the national sampling and measurement organisation. It collects the data and information required to assess the radiological situation, evaluates these, and ensures the timely and appropriate communication with the competent federal and cantonal authorities, as well as the notification of the International Atomic Energy Agency (IAEA) and of the neighbouring countries. Should international assistance be required to conduct radiological measurements on Swiss territory, for example following a radiological incident, the NEOC would be responsible for integrating these external measurement assets into the existing national sampling and measurement organisation and for coordinating their activities.

In a real event, a crucial point in the initial phase is to enable international teams to become operational within a short time and to work seamlessly in accordance with the emergency management processes of a given country. Given that airborne monitoring teams operate different measurement systems, use different data evaluation software and algorithms and apply different calibration procedures, ensuring interoperability, validating methodologies and guaranteeing the reproducibility of the results are essential. Another important goal is the quick and reliable exchange of data among all partners.

Regular joint training is indispensable to achieve these objectives. As a Swiss saying goes “in Krise Köpfe kennen” (“in a crisis, knowing the right people is crucial”) remains one of the most effective ways to ensure efficient and effective cooperation, especially in an emergency situation.

2.2 Key steps in the organisation of the AGC25

International airborne gamma campaigns are complex, multi-layered operations that demand careful long-term planning, extensive coordination, and clear communication among all participating

institutions. The AGC25 exercise conducted in Switzerland provides a relevant example of the organisational effort required to effectively integrate foreign teams into the national sampling and measurement organisation. This section summarises the essential steps, processes, and considerations necessary to plan, prepare, and execute an international radiological exercise of comparable scale.

2.2.1 Strategic planning and initial coordination 24 - 18 months before

The organisation of an international exercise, such as the AGC25, ought to begin almost two years in advance. Early steps include identifying suitable dates that align with the availability of key partners of the hosting nation, e.g. the Air Force for helicopter support and ground base locations. Securing the budget at this stage is essential to ensure that the exercise can be carried out without later constraints. Once these preparatory elements are in place, an official announcement is sent to potentially interested foreign partner organisations. This is followed by a preliminary survey to assess interest, confirm participation, and gather initial preferences regarding dates and proposed activities. For the first time, the inclusion of drone-based measurements was proposed as part of the AGC25 exercise.

In parallel, the Exercise Coordination Team shall be established. In the case of the AGC25, this multidisciplinary body (Figure 2.1) comprised representatives from the NEOC, aeroradiometry experts from the Paul Scherrer Institute and other national organisations, the Swiss Air Force, military staff, regulatory authorities, logistics, IT support, and radiation protection experts. The early involvement of regulatory authorities is particularly important, as it significantly facilitates approval processes in the later stages of the planning phase.

Figure 2.1: Exercise Coordination Team of AGC25.

2.2.2 Coordination with national partners and early logistics 18 - 12 months before

Once the coordination structure has been established, the following step is to develop a proposal for the exercise plan. This includes outlining potential mission scenarios, defining preliminary objectives, identifying the required resources and specifying the information required for an effective mission planning. If additional resources or personnel are needed from partner institutions (for

example, for the supervision of radioactive sources) official requests may be submitted during this phase.

At the same time, early logistical preparations should also commence. These include reserving suitable rooms and facilities, as well as liaising with accommodation providers to secure group rates and confirm bookings in advance.

2.2.3 Participant data collection and mission design 12 - 6 months before

To enable precise planning, participants were provided with a detailed questionnaire. The information collected included helicopter specifications (e.g. dimensions, fuel type, endurance), drone characteristics, team composition (number of members), supported data formats, and any specific requirement needed, such as liquid nitrogen or specialised equipment. Participants were also asked to indicate preferred dates for the international Kick-Off Meeting.

The guiding principle for mission design was to develop a set of realistic and varied scenarios that would provide meaningful learning opportunities. These scenarios were intended to be sufficiently challenging, while avoiding unnecessary complexity that could cause operational difficulties or frustration to participants. For AGC25, five helicopter missions and two drone missions were planned. These covered a range of tasks, including reference measurements, background measurements, composite mapping, source searches, and less common operational scenarios. Each team was expected to conduct 8–10 hours of measurement flights over four days (including transfer time), depending on the aircraft endurance.

Since Switzerland has relatively few areas with significant levels of natural or man-made radioactivity, it was decided to deploy sealed radioactive sources for three of the five missions, which took place on different days. Based on the information upon the teams' systems gathered via questionnaire and on the experience of the exercise management team, suitable sources were initially selected in terms of radionuclide and activity, and subsequently evaluated considering their availability and applicability conditions.

In parallel, requests for cooperation were submitted to military training areas considered suitable for the placement of radioactive sources during the exercise.

2.2.4 Regulatory preparation, radiation safety and mission finalisation 6 - 2 months before

As the exercise approached, planning became increasingly detailed and refined. A virtual Kick-Off Meeting on 16th January 2025 with all international participants provided an overview of the exercise structure, mission concepts, daily routines, airbase logistics, evaluation methods, and media plans.

Once the responses from the military training areas had been received and evaluated, the locations for the placement of the radioactive sources were finalised. On-site inspections were conducted to confirm feasibility, safety, and accessibility, supported by photographic documentation. On this basis, detailed source deployment concepts were developed for all missions involving radioactive sources. These concepts included justification for the use of the selected radioactive sources, dose assessments, defined safety measures, and the preparation of a comprehensive radiation protection plan. The resulting documentation was submitted to the competent regulatory authorities to obtain the necessary approvals.

Particular attention was required for the use of a high-activity ^{75}Se source. As this type of source is normally used for weld inspections, its employment outside the usual scope required special authorisation from the regulatory authority. To support this request, PSI conducted simulations and calculations to determine the necessary shielding configuration that would guarantee the safety

of the personnel handling the source, including the thickness and height of the shielding well. Subsequently, in the presence of the regulatory authority, the entire setup was tested in the field, and the dose rate values that had previously only been calculated and simulated were verified through measurements.

At the same time, communication material for the media was prepared, schedules for each team were developed, and translation of official documents were organised. A cloud-based sharing environment was established to support information exchange, before, during and after the exercise.

2.2.5 Final preparations and pre-exercise activities 2 months to a few days before

During the final two months, the operational planning was completed and all key documents were finalised (Figure 2.2). Mission task sheets were prepared for each flight, providing detailed instructions, flight parameters, restricted areas, coordinates, schedules, and mapping references. At the same time, comprehensive daily programmes were established for each participating team. In the final weeks, remaining administrative matters were addressed, including access to and movement within the military training areas through participant lists and access authorisations, as well as arrangements for meals and refreshments.

Logistical arrangements were also concluded. These included the transport of radioactive sources, the provision of reliable internet connectivity at the bases, final reservations for social events, and completion of customs clearance procedures for foreign teams transporting specialised equipment by car, an aspect of particular relevance for the drone teams.

A communication plan was implemented, comprising an emergency telephone line and a dedicated Signal chat group, procedures for aircraft arrival and landing, and a coordinated press release. In addition, the police and local authorities of the interested regions were informed about the exercise.

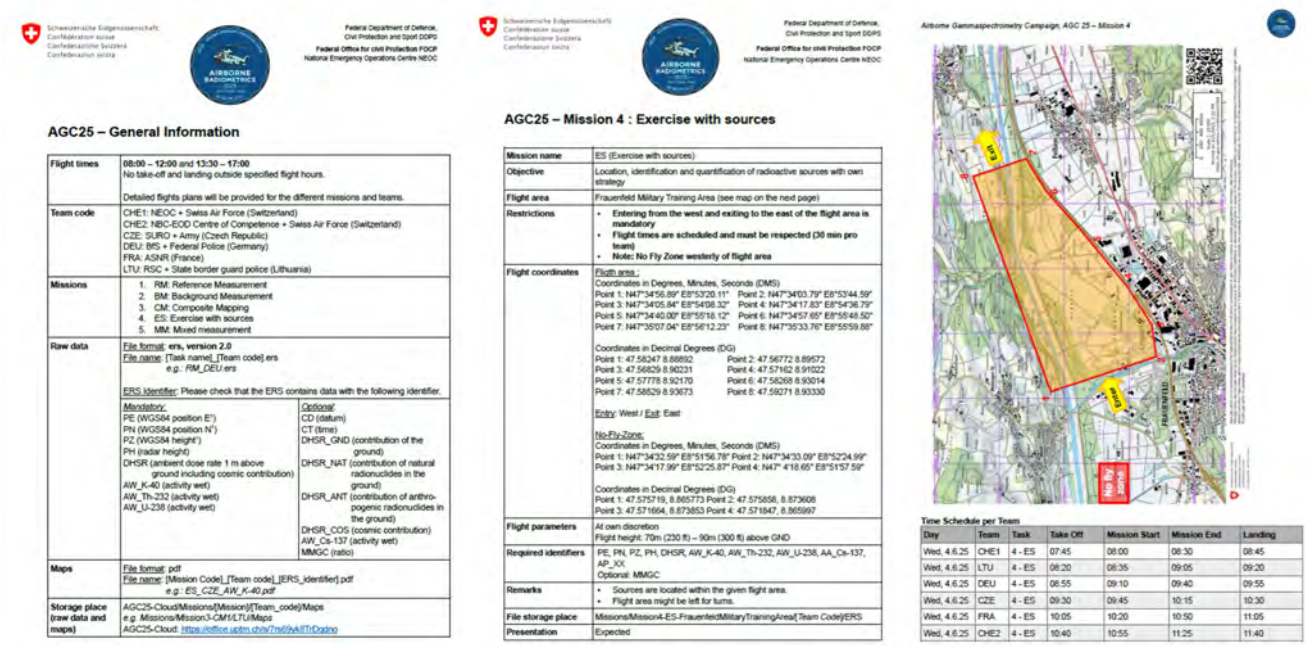

AGC25 – General Information

Flight times	08:00 – 12:00 and 13:30 – 17:00 No take-off and landing outside specified flight hours. Detailed flights plans will be provided for the different missions and teams.
Team code	CHE1: NEOC + Swiss Air Force (Switzerland) CHE2: NBC-EOD Centre of Competence + Swiss Air Force (Switzerland) CZE: SURO + Army (Czech Republic) DEU: BfS + Federal Police (Germany) FRA: ASNR (France) LTU: RSC + State border guard police (Lithuania)
Missions	1. RM: Reference Measurement 2. BM: Background Measurement 3. CM: Composite Mapping 4. ES: Exercise with sources 5. MM: Mixed measurement
Raw data	File format: ers, version 2.0 File name: [Task name]_[Team code].ers e.g.: RM_DEU.ers ERS Identifier: Please check that the ERS contains data with the following identifier. Mandatory: PE (WGS84 position E°) PN (WGS84 position N°) PZ (WGS84 height') PH (radar height) DHSR (ambient dose rate 1 m above ground including cosmic contribution) AW_K-40 (activity wet) AW_Th-232 (activity wet) AW_U-238 (activity wet) Optional: CD (datum) CT (time) DHSR_GND (contribution of the ground) DHSR_NAT (contribution of natural radionuclides in the ground) DHSR_ANT (contribution of anthropogenic radionuclides in the ground) DHSR_COS (cosmic contribution) AW_Cs-137 (activity wet) MMGC (ratio)
Maps	File format: pdf File name: [Mission Code]_[Team code]_[ERS_identifier].pdf e.g.: ES_CZE_AW_K-40.pdf
Storage place (raw data and maps)	AGC25-Cloud/Missions/[Mission]/[Team_code]/Maps e.g. Missions/Mission3-CM/LTU/Maps AGC25-Cloud: https://office.uclm.ch/s/7ni0jAxlTrDqdno

AGC25 – Mission 4 : Exercise with sources

Mission name	ES (Exercise with sources)
Objective	Location, identification and quantification of radioactive sources with own strategy
Flight area	Frauenfeld Military Training Area (see map on the next page)
Restrictions	• Entering from the west and exiting to the east of the flight area is mandatory • Flight times are scheduled and must be respected (30 min pro team) • Note: No Fly Zone westerly of flight area
Flight coordinates	Flight area : Coordinates in Degrees, Minutes, Seconds (DMS) Point 1: N47°34'56.89" E8°53'20.11" Point 2: N47°34'03.79" E8°53'44.59" Point 3: N47°34'05.84" E8°54'08.32" Point 4: N47°34'17.83" E8°54'36.79" Point 5: N47°34'40.00" E8°55'16.12" Point 6: N47°34'57.65" E8°55'48.50" Point 7: N47°35'07.04" E8°56'12.23" Point 8: N47°35'33.76" E8°55'59.88" Coordinates in Decimal Degrees (DG) Point 1: 47.58247 8.88892 Point 2: 47.56772 8.89572 Point 3: 47.56829 8.90231 Point 4: 47.57162 8.91022 Point 5: 47.57778 8.92170 Point 6: 47.58268 8.93014 Point 7: 47.58529 8.93673 Point 8: 47.59271 8.93330 Entry: West / Exit: East No-Fly-Zone: Coordinates in Degrees, Minutes, Seconds (DMS) Point 1: N47°34'32.59" E8°51'56.78" Point 2: N47°34'33.09" E8°52'24.99" Point 3: N47°34'17.99" E8°52'25.87" Point 4: N47° 4'18.65" E8°51'57.59" Coordinates in Decimal Degrees (DG) Point 1: 47.575719, 8.865773 Point 2: 47.575858, 8.873608 Point 3: 47.571664, 8.873853 Point 4: 47.571847, 8.865997
Flight parameters	At own discretion Flight height: 70m (230 ft) – 90m (300 ft) above GND
Required identifiers	PE, PN, PZ, PH, DHSR, AW_K-40, AW_Th-232, AW_U-238, AA_Cs-137, AP_XX Optional: MMGC
Remarks	• Sources are located within the given flight area. • Flight area might be left for turns.
File storage place	Missions/Mission4-ES-Frauenfeld/MilitaryTrainingArea/[Team Code]/ERS
Presentation	Expected

Airborne Gammaspectrometry Campaign, AGC 25 – Mission 4

Time Schedule per Team

Day	Team	Task	Take Off	Mission Start	Mission End	Landing
Wed, 4.6.25	CHE1	4 - ES	07:45	08:00	08:30	08:45
Wed, 4.6.25	LTU	4 - ES	08:20	08:35	09:05	09:20
Wed, 4.6.25	DEU	4 - ES	08:55	09:10	09:40	09:55
Wed, 4.6.25	CZE	4 - ES	09:30	09:45	10:15	10:30
Wed, 4.6.25	FRA	4 - ES	10:05	10:20	10:50	11:05
Wed, 4.6.25	CHE2	4 - ES	10:40	10:55	11:25	11:40

Figure 2.2: Example of documents prepared for AGC25.

2.3 AGC25 facts

2.3.1 Participants

The exercise took place from the 1st to the 6th June 2025. A total of seven nations participated, deploying six helicopters (two of them Swiss), five drones, and one ground-based team capable of performing measurements both from vehicles and on foot. In total, approximately 140 people were involved in the exercise, including personnel responsible for source supervision and transport. Around 100 participants were based in Dübendorf.

2.3.2 Airbase

The main operating base was the military airfield LSDM in Dübendorf (Figure 2.3), which had already hosted the international campaigns in 2007 and 2017. The site was selected primarily for its good accessibility from France and Germany and its proximity to Zurich International Airport. An apron area, equipped with a large tent, was arranged and reserved for the four foreign helicopters, providing sufficient space for the aircrafts from France, Germany, and Lithuania. The larger Czech helicopter was to be accommodated in a hangar only if required.

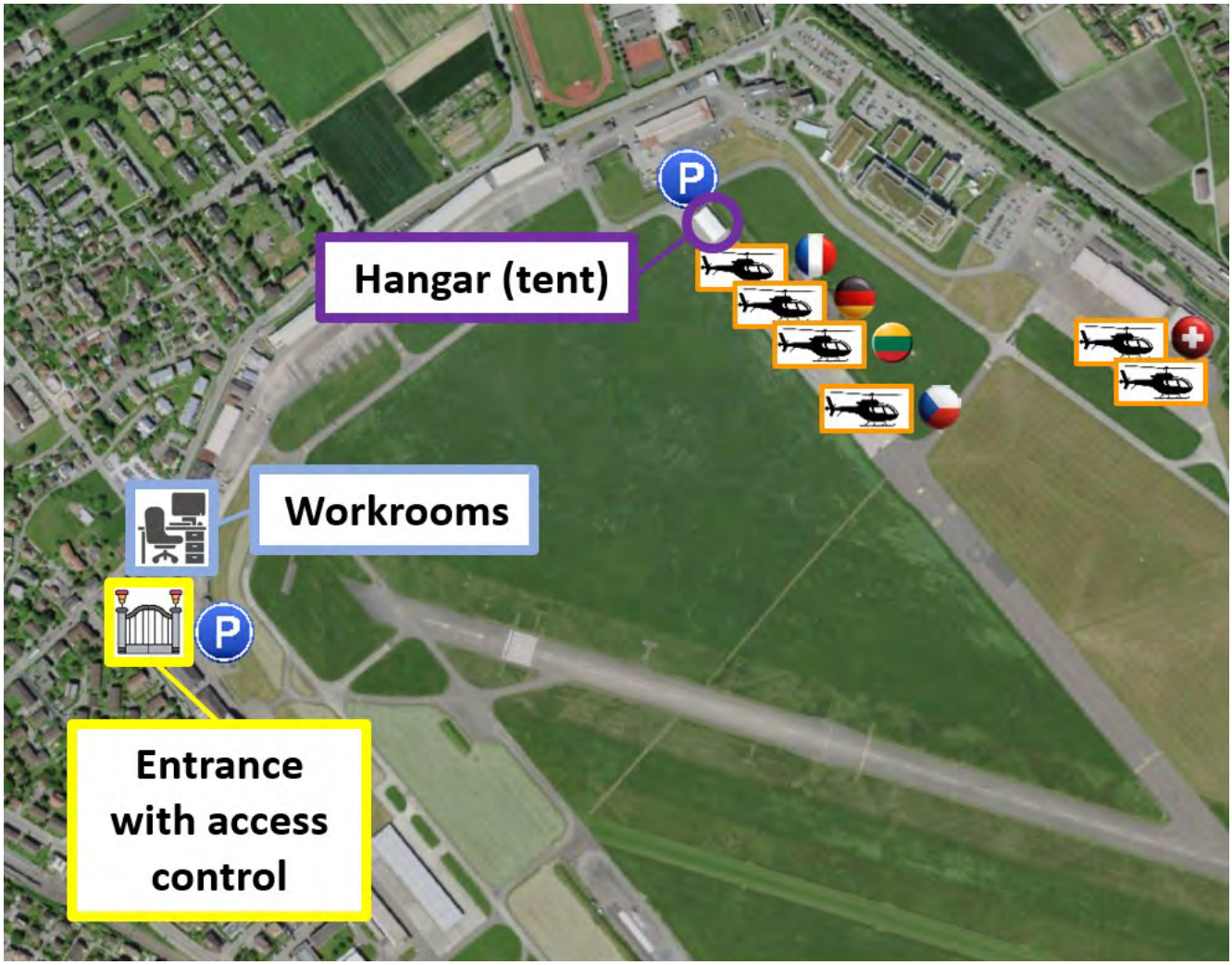

Figure 2.3: Location of the main facilities available at the AGC25 Airbase (LSDM).

2.3.3 Workrooms

Four rooms were available for the exercise activities. Owing to the large number of participants (approximately 100 persons attended the initial briefing on Sunday, 1st June), the two largest rooms were used for the briefing, one of them equipped with video transmission. Following the briefing, one of the rooms was made available to the teams, while the other was rearranged to host the press conference on the morning of 2nd June. After the press conference, the room was converted into a social area, equipped with coffee machines and facilities for refreshments. On Friday, for the final debriefing of the exercise, the setup as on Sunday afternoon was restored, with two rooms, one of them equipped with video transmission.

2.3.4 Missions

All five missions were successfully completed by all helicopter teams. Only one mission, the composite mapping flight on 3rd June 2025, had to be planned twice. On Monday, the Swiss team led the planning for the mission scheduled for Tuesday, with all teams participating. Due to adverse weather conditions, the plan had to be adapted on Tuesday morning within just two hours. During the mission, five helicopter teams flew for 2 - 3 hours on Tuesday afternoon instead of the originally planned 4 - 6 hours. The flight plan included a common reference line that all teams had to fly before entering the survey area. In addition, a common entry from the south and exit to the north of the measurement area were defined in order to improve flight safety. Further details are provided in section 7 and section 8 of this report. All five drone teams successfully completed their two assigned missions. In addition, the Swedish team carried out, with the authorisation of the exercise coordination team, several independent measurements, both within the designated mission areas and at other locations across Switzerland.

2.3.5 Accommodation

Accommodation for all foreign participants was arranged in Oerlikon, approximately 15 minutes from the LSDM airbase. As communicated during the kick-off, each team had to organise its own meals (except the ones explicitly provided) and transport between the hotel and the airbase, while transport within the airbase area to the hangars was provided by the organisers.

2.3.6 Wi-Fi and data sharing

Throughout the exercise, a reliable Wi-Fi network was available. A cloud-based storage platform was used for the exchange of documents and data. After each mission, and at the latest by the following day, each team was asked to upload the files containing the measurements and the preliminary results in the required data format to the designated directories. This process, including the handling of preliminary data, worked well.

2.3.7 Communication during the exercise

Following the main briefing on Sunday, short daily briefings were held in the mornings, mainly among the pilots, focusing on weather conditions and mission-specific details.

In addition, for the first time, daily debriefings in the evening were organised involving both the exercise management and the participants. These sessions provided a review of the day's activities (mission execution, issues encountered, availability of results) and aimed to ensure transparency, facilitate feedback, and support continuous improvement.

As in AGC24 in the Czech Republic [1], the open-source encrypted messaging service Signal was used for communication among all participants. The NEOC created a dedicated chat group and invited the team leaders, who in turn added their respective team members. The group was used for operational updates, organisational information, as well as messages from and to individual aircraft. The publicly available ADS-B Exchange platform (https://globe.adsbexchange.com) was used for live tracking of participating aircraft. The tool was useful for coordinating the work with the personnel on the field, who was responsible for the deployment of the radioactive sources.

2.3.8 Media

Several Swiss media outlets attended the exercise. Many journalists took the opportunity to view the monitoring systems up close, conduct interviews, and observe and film the take-off of two helicopters. Coverage included multiple articles in print and online media, as well as two television reports broadcast on the national Italian- and French-language channels.

2.4 Lessons learned and challenges ahead

The key lessons learned during the organisation of the AC25 exercise highlight the importance of:

1. Regular exercises as a fundamental element to continuously improve performance and operational efficiency.

2. Clearly defined rules from the outset, in particular regarding data formats, naming conventions, and standards for information exchange, in order to ensure consistency and to avoid delays at later stages regarding data source, handling and versioning. The adoption of the ERS 2.0 format for airborne radiometric measurements already provides a solid starting point.

3. Allocating sufficient time for mutual exchange, enabling participants to gain a common understanding of others measurement strategies, detection systems, and analytical procedures.

4. Strong, well-coordinated, and goal-oriented support teams are needed to effectively manage unexpected challenges. Despite thorough preparation, international exercises- as well as real accidents- inevitably face operational constraints. Changes in weather conditions, helicopter availability, and unforeseen technical issues may require rapid adaptation and replanning.

5. Media activities play a significant role in ensuring public acceptance and transparency, and therefore deserve appropriate attention and integration in the exercises.

One of the challenges for the future will be the integration of aerial measured data into the IAEA platform (IRMIS), which would allow countries worldwide to rapidly access to measurements results in the event of an emergency.

Chapter 3

AGC25 participants

3.1 Teams

Teams from five countries participated to the international exercise AGC25. A short description of the teams and how they are embedded in their national emergency response organisation is provided in the following sections.

3.1.1 Czech Republic (Team CZE)

The Czech airborne team is classified under the National Radiation Protection Institute (SÚRO), which is a public research institution engaged in professional activities in the field of population protection against ionising radiation. SÚRO was established by the decision of the chairman of the State Office for Nuclear Safety (SÚJB). Details about the organization can be found at https://www.suro.cz/cz.

The activities of the Czech airborne team are carried out within the framework of the Czech radiation monitoring network, in cooperation with specialists from the Czech Armed Forces (AČR), who operate their own Army Radiation Monitoring Network (ARMS). Both teams conduct joint exercises within the Czech Republic as well as international exercises, and they operate the Mi-17 army transport helicopter for their missions.

3.1.2 France (Team FRA)

The ASNR, the French Nuclear Safety and Radiation Protection Authority, has, since the 1st of January 2025, integrated the missions and activities of the ASN (Nuclear Safety Authority) and the IRSN (Radioprotection and Nuclear Safety Institute), in accordance with the law of the 21st of May 2024 on the organisation of nuclear safety and radiation protection governance, to address the challenge of revitalising the nuclear industry.

Among ASNR's responsibilities is the regular radiological monitoring of the national environment. As a technical expert in radiological and nuclear risks, ASNR also plays an active role within the French emergency management system.

To complement existing static monitoring capabilities, such as the Teleray remote sensing network, mobile in-situ measurement systems have been acquired and incorporated into the overall monitoring toolbox since 2010. These systems, based on gamma-ray detectors of varying sizes, provide geolocated measurements every second. They can be deployed in backpacks, vehicles, or a range of aerial platforms, including aeroplanes, helicopters, and drones.

These mobile systems are employed for environmental surveys during peacetime and form part of ASNR's mobile unit, which is dedicated to characterising environmental contamination in the

event of a nuclear incident. They are regularly used during national nuclear emergency exercises and operated by trained personnel.

3.1.3 Germany (Team DEU)

The German Federal Office for Radiation Protection (Bundesamt für Strahlenschutz, BfS) is responsible for monitoring gamma radiation using specialised airborne measurement systems. To carry out this mission, BfS collaborates closely with the German Federal Police, whose aircraft can be equipped with BfS measurement systems. This approach allows rapid, large-scale assessment of environmental radioactivity, providing a critical tool for nuclear emergency management in the event of accidental releases of radioactive material from nuclear installations. BfS currently operates four such airborne measurement systems across Germany.

Within BfS, the Federation's competences in radiation protection are centralised, and the organisation undertakes a broad spectrum of tasks in nuclear accident management and environmental radioactivity monitoring. These include airborne mapping of gamma ambient dose equivalent rates and artificial radionuclides following radiological incidents, as well as mapping naturally occurring and anthropogenic radionuclides distributed in the environment. BfS is subordinated to the Federal Ministry for the Environment, Nature Conservation, Nuclear Safety and Consumer Protection.

The Federal Police Flight Service (Bundespolizei Flugdienst, BPOLFLD) constitutes the aviation arm of the German Federal Police. It operates six flying squadrons stationed across Germany and provides aviation support to Federal Police bureaus and other national and international public agencies, including BfS. BPOLFLD performs a wide range of operations on a daily basis, often maintaining 24/7 readiness, and is subordinated to the Federal Ministry of the Interior and Community.

3.1.4 Lithuania & USA (Team LTU)

In accordance with the National Plan for the Protection of the Population in the Event of a Nuclear Emergency, aerial radiation surveys in Lithuania are coordinated and operated at the state level by the Radiation Protection Centre (RSC) and the State Border Guard Service (SBGS) under the Ministry of the Interior. If necessary, the Lithuanian Air Force (LAF) can also be involved. The gamma-spectrometric equipment is provided, installed, and operated by RSC, while the aircraft and trained aircrew are supplied by SBGS. Installation of new aerial radiation survey equipment at SBGS is currently in progress.

In 2024, Lithuania signed an agreement with the U.S. National Nuclear Security Administration Office of Nuclear Incident Policy and Cooperation (NNSA NIPC NA-81) to enhance national capabilities and competencies in emergency preparedness and response to nuclear or radiological incidents. This cooperation includes internal training, participation in international exercises, and technical support. During AGC25, the Lithuania–USA measurement team comprised specialists from RSC, SBGS, and NNSA NIPC NA-81.

The Radiation Protection Centre (RSC) is the regulatory authority for radiation protection in Lithuania. It is responsible for overseeing public and environmental exposure, regulating practices involving ionising radiation sources, and contributing to national radiation protection policy. RSC implements regulatory control, conducts radiological monitoring, assesses public, occupational, and accidental exposures, provides personal dosimetry, performs radiological investigations, and manages radiological emergencies, including mitigation of their consequences. Its duties also include operating an early radiation warning system, conducting aerial and ground radiation surveys, performing radiological consequence assessments, and providing data-driven recommendations to the government for protective measures.

The Aviation Board (AB) within SBGS operates 24/7 and provides the aircraft and aircrew for aerial radiation reconnaissance in cooperation with RSC. At the national level, SBGS, together with

RSC and the Fire and Rescue Department, implements aerial and ground radiation surveys, sample analysis, measurement, and transmission of survey data. SBGS's core responsibilities include state border protection, search and rescue operations, air support for law enforcement agencies, airborne radiometry, and participation in Frontex operations.

The U.S. NNSA Office of Nuclear Incident Policy and Cooperation (NIPC NA-81) develop policy and provides capacity-building emergency preparedness training to counter and respond to radiological and nuclear incidents, accidents, and terror threats, shares knowledge of nuclear and radiological threats with federal, state, local, and international partners by conducting training, international exercises, information exchanges, counter nuclear smuggling scenario-based policy discussions, and delivers radiological medical training for foreign first responders and partners. NIPC carries out domestic and international capacity-building programs and assists in developing nuclear incident response policy in the United States and with international partners, provides nuclear and radiological technical support to U.S. and foreign partners for major public events and emergencies, international nuclear and radiological incident modelling capabilities, long-term equipment loans to foreign partners, offers subject matter expertise to develop international guidance and standards with the International Atomic Energy Agency (IAEA), and coordinates with the IAEA's Incident and Emergency Centre for international radiological or nuclear incident response.

3.1.5 Switzerland (Teams CHE1 & CHE2)

In Switzerland, two organisations are involved in aeroradiometric measurements: the National Emergency Operations Centre (NEOC), responsible for civil emergencies, including incidents with a radiological component, and the NBC-EOD Centre of Excellence (Nuclear, Biological and Chemical Defence and Explosive Ordnance Disposal), which conducts measurement tasks of a military nature and, in a subsidiary role, also supports civil operations. The NEOC is the Swiss federal centre of expertise for exceptional events in the Federal Office of Civil Protection (FOCP). It is operational on a 24 hours a day basis and is the first point of contact for the partners of civil protection. It operates a national reporting and situation centre. In the field of radioactivity, it has the competence to order that immediate measures be taken to protect the population. For this purpose it assesses the radiological situation and deploys the sampling and measurement organisation if necessary. The NBC-EOD Centre of Excellence is the specialist body of the Swiss Armed Forces for all issues relating to nuclear, biological and chemical threats, ordnance disposal and demining. The NBC task force can be backed up by other militia units if necessary.

Swiss airborne gamma-ray spectrometry measurements started in 1986 as research program at the Institute of Geophysics of the Swiss Federal Institute of Technology Zurich (ETHZ) [2]. In 1994 airborne gamma-ray spectrometry was included into the Emergency Organization Radioactivity (EOR), under the direction of the NEOC. In 2018, the ARM measuring system used by NEOC in past exercises was replaced with the RLL (Radiometrie Land-Luft) system owned by the Swiss armed forces. Since then, the deployment of the airborne gamma-spectrometric system is organised by the National Emergency Operations Centre (NEOC) and the NBC-EOD Centre of Excellence. NEOC and NBC-EOD are also responsible for the recruitment and training of the measurement teams (in the case of NEOC, including militia members of the NEOC military staff) as well as for ensuring the operational readiness of the systems. Aerial operations are coordinated and performed by the Swiss Air Force with Super Puma helicopters. The maintenance of the RLL systems is performed by the manufacturer according to a service agreement with the Swiss Armed Forces. Four identical gamma-spectrometric pieces of equipment are stationed in pairs at the military airfields of Dübendorf and Payerne and can be fully operative and airborne within four hours. Responsibility for scientific support and development of the aeroradiometric measurement passed from the Institute of Geophysics of ETHZ to the Radiation Metrology Section of the Paul Scherrer Institute (PSI) in 2003, in cooperation with ENSI (Swiss Federal Nuclear Safety Inspectorate).

General scientific coordination and planning of the annual measuring flights is provided by the Expert Group for Airborne Gamma Spectrometry (FAR), which consists of experts from all Swiss institutions concerned with aeroradiometry. FAR, formerly a working group of the Swiss Federal Commission for NBC protection (ComNBC), was re-organized as an expert group of the NEOC in 2008. Additional information can be found at https://far.ensi.ch/.

The Swiss team participated to the AGC25 international exercise with two helicopters and teams: CHE1, coordinated by the NEOC with the support of the NEOC military staff, and CHE2, coordinated by the NBC-EOD. Specialists from the measurement equipment and software supplier, Mirion, were integrated into the CHE2 team, with the objective of facilitating the exchange of information on operational procedures and practices, and to foster the continued development of the equipment.

Regarding drones, responsibility lies with the emergency response teams of Spiez Laboratory (EEVBS). Spiez Laboratory is Switzerland's federal centre of expertise for protection against nuclear, biological and chemical (NBC) hazards and is part of the Federal Office for Civil Protection. Its responsibilities include the analysis and assessment of hazardous substances, support to authorities and emergency responders during NBC incidents, the conduct of research, training and laboratory analyses, as well as participation in international arms control and disarmament agreements. The EEVBS serves as the operational deployment unit of Spiez Laboratory. It comprises specialised teams for nuclear, biological, and chemical hazards, capable of rapid intervention during incidents and providing expert technical support to emergency responders.

3.2 Helicopter-borne measuring systems

3.2.1 Team CZE

The Czech team for airborne emergency monitoring employs Mi-17 helicopters (NATO code HIP-H) operated by the Czech Armed Forces. This Soviet-designed helicopter type (Figure 3.1), in service since 1975 as a transport aircraft, provides ample space inside the cabin and versatility for monitoring tasks. With a cargo cabin measuring $5.34\,\mathrm{m} \times 2.32\,\mathrm{m} \times 1.8\,\mathrm{m}$ (L×W×H), a practical ceiling of up to $4500\,\mathrm{m}$ (approximately $13\,300\,\mathrm{ft}$), and a maximum range of $930\,\mathrm{km}$, the Mi-17 offers an excellent opportunity to accommodate numerous measuring instruments and up to eight operators on board, effectively serving as a flying laboratory.

Figure 3.1: MI-17 Helicopter of the Czech army during take-off.

In terms of hardware and software for airborne monitoring, significant changes have taken place since the ARM17 exercise in 2017 (Appendix A). The Czech team tested and helped design practical features of the newly developed Rad-Patrol2 airborne gamma spectrometer, produced by NUVIA a.s. .

The Czech team deployed the Rad-Patrol2 airborne gamma-ray spectrometric system (Figure 3.2) during AGC25. Developed by NUVIA a.s. and owned by SÚRO, the instrument was installed on board the Mi-17 and used during the AGC25 exercise in Switzerland. Following testing and parameter adjustments in the Czech Republic, the spectrometer was operated under real conditions for the first time during this exercise. The system consists of four units, each containing a NaI(Tl) crystal with dimensions of $4'' \times 4'' \times 16''$ ($4\,\mathrm{L}$). It is equipped with all necessary electronics and supplementary components, including a GPS receiver, radar altimeter, and a newly developed pilot guidance unit. Fully independent of on-board systems, the spectrometer can be easily installed in a wide range of aircraft as cargo. The gamma-ray spectrometer operates across an energy range of

approximately $35\,\mathrm{keV}$ to $3\,\mathrm{MeV}$, typically in 1024 channels, and additionally records cosmic photons with energies above $3\,\mathrm{MeV}$. Upon start-up, the system automatically adjusts to maintain energy calibration, eliminating the need for radioactive calibration sources before or during flight. It also calculates dead time and corrects counts accordingly. Data can be wirelessly transmitted to a ground station for rapid processing. Spectra, GPS positions, altitude, and other relevant parameters are recorded every second in a PEI binary file, enabling subsequent data review and post-processing.

The Czech Team also had an AIRIS airborne gamma-ray spectrometric system (Figure 3.3) installed on board the Mi-17 during AGC25. Owned by the Czech army and developed by Pico Envirotec Inc. in Toronto, Canada, AIRIS is the most recent version of the older IRIS system previously described in the ARM17 report, and is comparable to the IRIS spectrometer owned by SÚRO. During the AGC25 exercise, AIRIS was employed to determine the activities of point sources, since not all response functions of the selected man-made point sources had yet been calculated for Rad-Patrol2.

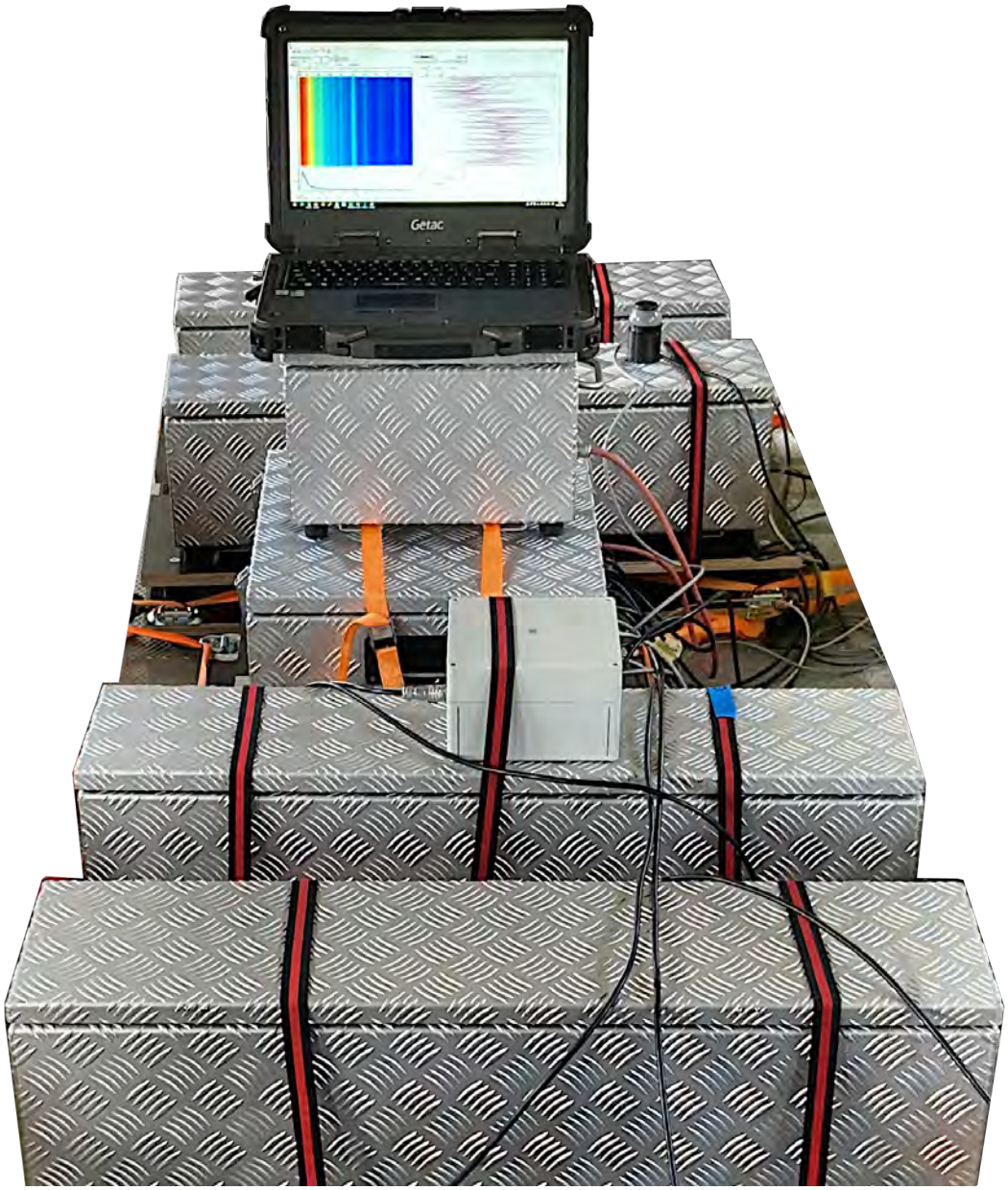

Figure 3.2: Rad-Patrol2 spectrometer used by the Czech Team.

Figure 3.3: AIRIS spectrometer used by the Czech Team.

3.2.2 Team FRA

For standard helicopter surveys, ASNR uses a chartered AS350 helicopter (Figure 3.4), equipped with two externally mounted metallic gridded baskets, each accommodating two individual detection units. For studies or exercises, a four-year contract with a private helicopter company provides ASNR a ready access to aircraft for surveys. The contractor for AGC25, Hélicoptères de France, undertakes a wide range of aerial operations, including scientific flights such as LiDAR campaigns. In the event of an emergency, ASNR could also utilise aircraft from the army or civil security services.

Figure 3.4: French ULYSSE system installed on EUROCOPTER AS 350 B2 used during AGC25 viewed from the right side.

The ASNR aerial measuring system, known as *ULYSSE*, is composed of modular components that can be easily integrated into a variety of carriers. It is based on the SpirMobile suite and devices provided by Mirion, a Franco-American company specialising in radiation detection, protection, and measurement.

Each detection unit (Figure 3.5) is composed of a ruggedized IP65 box containing a thallium-doped sodium iodide (NaI(Tl)) crystal, a photomultiplier tube with multi-channel analyser, and a Geiger-Müller tube. The crystal measures $4'' \times 4'' \times 16''$ ($4\,\mathrm{L}$), and the box dimensions are $24\,\mathrm{cm} \times 24\,\mathrm{cm} \times 84\,\mathrm{cm}$. The standard aerial measuring system (AMS) configuration employs four detector units, providing a total detection volume of $16\,\mathrm{L}$. Each unit connects to an acquisition laptop via ruggedized USB cables and is powered through the same connection. A fast digital analyser is associated with each detector, continuously acquiring 1024-channel elementary spectra, sampled by the acquisition server every second.

The elementary spectrum is first stabilised by fitting the energy–channel relationship using a dedicated algorithm that identifies natural radionuclide peaks (^{40}K, ^{238}U, ^{232}Th). The spectrum is then scaled and linearised to provide the energy–channel conversion of $3\,\mathrm{keV}$ per channel.

Figure 3.5: Left: IP65 box containing the $4\,\mathrm{L}$ NaI-detector of the ULYSSE system. Right: view of the detector components inside the IP65 box.

Measurement positioning is performed using an external GPS device connected to the acquisition server, typically via Bluetooth, with a refresh rate of $10\,\mathrm{Hz}$. The height above ground is calculated from the GPS altitude above sea level, corrected using terrain elevation provided by an embedded digital elevation model (DEM). The standard DEM for AMS is the $90\,\mathrm{m}$ resolution SRTM model.

On-board, real-time mapping, visualisation, and analysis are performed using Mirion's dedicated software installed on the acquisition laptop (Figure 3.6). Two ASNR specialists aboard the aircraft share the tasks of monitoring, verification, control, and communication with the ground team. One laptop serves as the main acquisition server, while the other functions as a client. The software interface can be configured in various ways for each operator. Flight plans are provided to the pilot in GPX or KML format for integration into the aircraft's navigation system.

ASNR has developed specific scripts that transmit acquired measurement data to its databases in real time via a 4G connection. This allows back-office personnel to monitor missions and perform analyses during or immediately after flights.

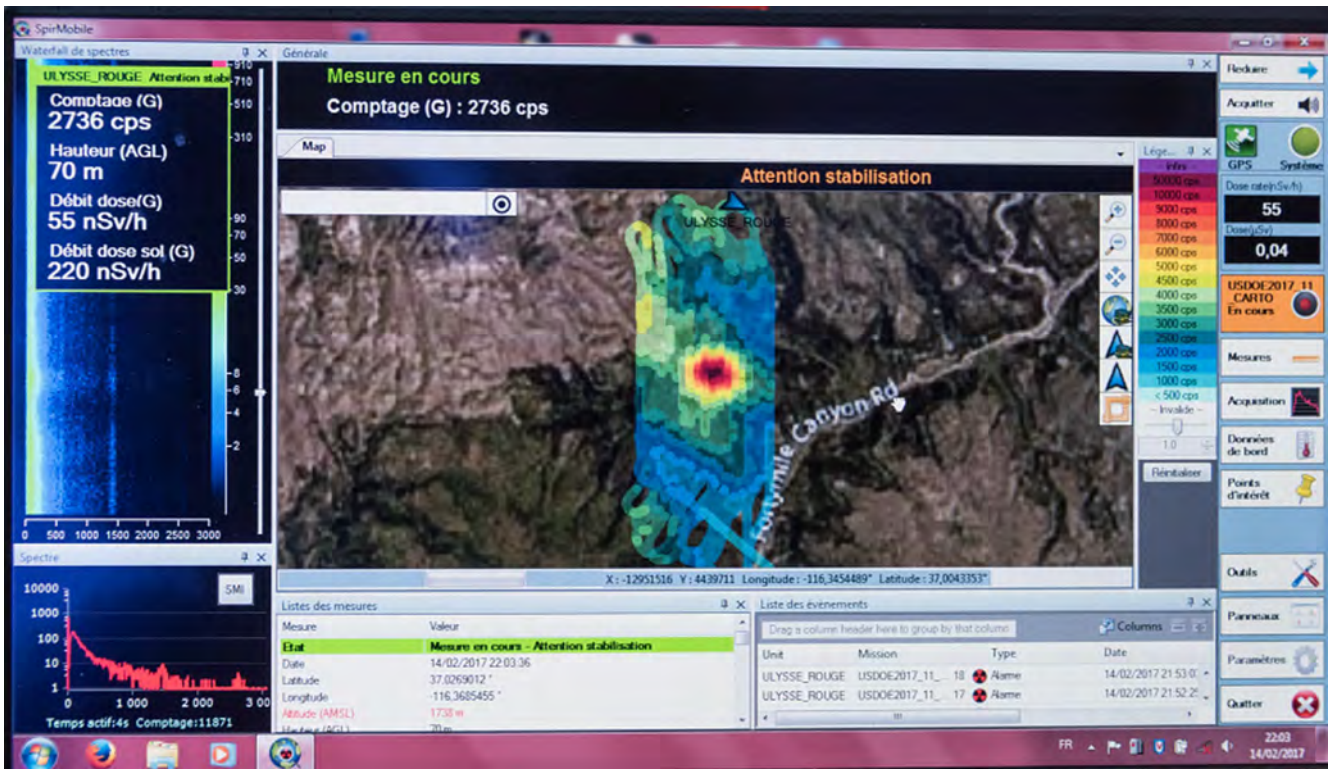

Figure 3.6: Screenshot of the French ULYSSE system during a measuring flight.

3.2.3 Team DEU

The German Federal Office for Radiation Protection (Bundesamt für Strahlenschutz, BfS) has the mission of detecting gamma radiation using special airborne measuring systems to determine the ambient gamma dose rate at a height of one meter, as well as the activity and activity concentration of certain radionuclides in and on the ground. In order to fulfil this task, BfS cooperates with the German Federal Police. Specifically, EC135 helicopters (Figure 3.7) can be equipped with BfS' measurement systems. This measurement method allows for a fast and large-scale assessment of environmental radioactivity. This offers an important tool for nuclear emergency management in case of accidental releases of radioactive material from a nuclear installation. Four of these measurement systems are available at BfS in Germany.

Figure 3.7: German Federal Police type EC135 helicopter used for airborne gamma-spectrometric measurements.

The measuring systems (see Figure 3.8) consist of four high efficiency NaI(Tl) scintillation detectors (total volume $16\,\mathrm{L}$) and one high-resolution HPGe semiconductor detector. The high efficiency of the NaI(Tl)-detectors allows the detection of a radionuclide distribution at a high spatial resolution using integration times of one or two seconds. Data measured with the HPGe-detector usually has to be integrated over a longer period of time due to the lower efficiency of that type of detector. However, the high energy resolution of the HPGe-detector allows to unambiguously identify the individual radionuclides. The measurement data recorded with these detectors are pulse-height spectra, which assign counting pulses or rates to the measured photon or gamma energy. To obtain reliable values for the individual radionuclides' activities or for the gamma dose rate from the measured data, several processing steps and corrections must be performed in post-processing.

For data acquisition as well as post-processing BfS utilizes in-house-developed software. For calculations that include the full-energy photo-peak or the pulses contained therein, the so-called window method is used. This method involves placing energy windows around the photon energy of natural or artificial radionuclides to be analysed. These windows have an upper and a lower limit as well as an average energy value corresponding to the photo-peak energy. Within this defined window, all pulses are assigned to the photon energy under consideration. This ensures that spectral analysis can be performed even with low counting statistics and without a clear peak shape in the pulse height spectrum. The counting pulses obtained by the window method must also be subjected to a background correction, a (flight) altitude correction and the so-called stripping, in which the pulse components originating from other radionuclides and photon energies are subtracted from the photo-peak under consideration. Therefore, the measurement systems have been characterised and calibrated carefully.

BfS' measurement systems are calibrated according to the procedure used for the calibration of in-situ gamma-spectrometers. The detector response and the angular dependency as a function of energy are determined using point sources. The attenuation of the gamma-rays due to the helicopter components is taken into account. The unscattered photon flux depending on the distribution of radionuclides in soil and the position of the detector for the given altitude is calculated. The calibration is confirmed by measurements over areas with a known content of natural and artificial radionuclides.

Figure 3.8: Airborne measurement system of the German Federal Office for Radiation Protection mounted in a German Federal Police type EC135 helicopter.

3.2.4 Team LTU

Airborne gamma spectrometry measurements are conducted using helicopters provided by SBGS. In 2025, Lithuania enhanced its airborne capabilities by assigning two new helicopters (H145/BK117 D-3, Figure 3.9) to perform airborne radiological survey missions alongside their other duties, whose main characteristics are summarised in Table 3.1. Future helicopters will be equipped with specialised gamma detector systems that can be easily installed or removed, fully integrated with the aircraft's power supply, navigation system, fuel level sensors, and other onboard systems.

Table 3.1: Helicopter specifications of the Lithuanian team.

Helicopter type	H145 / BK117 D-3
Maximum airspeed	$140\,\mathrm{kt}$ $(280\,\mathrm{km\,h^{-1}})$
Maximum recommended load	$600\,\mathrm{kg}$
Maximum flight endurance	$2.5\,\mathrm{h}$
Flight crew	2 pilots, 2 equipment operators
Optimum flight altitude	$300\,\mathrm{ft}$ $(100\,\mathrm{m})$
Measurement flight speed	$50 - 65\,\mathrm{kt}$ $(100 - 130\,\mathrm{km\,h^{-1}})$

Figure 3.9: Lithuanian aircraft H145, used during AGC25

The equipment for manned aerial gamma spectrometry system consists of four thallium-doped sodium iodide (NaI(Tl)) scintillation detectors $2'' \times 4'' \times 16''$, $2\,\mathrm{L}$ each; Radiation Solutions, RSX1) illustrated in Figure 3.10, providing a total detector volume of $8\,\mathrm{L}$ and integrated into a single data stream. Spectral data are acquired at $1\,\mathrm{Hz}$ and binned into 1024 channels, each $3\,\mathrm{keV}$ wide, covering

energies up to $3072\,\mathrm{keV}$. The summed spectra from all detectors are transmitted via the controller unit (Radiation Solutions RS-605), which interfaces the external detectors with the host computer. Configuration of data export, acquisition, and interpretation is managed through the RadAssist graphical user interface (Radiation Solutions) installed on the host computer. This interface enables full operational control of the system, including real-time monitoring and recording of spectral data. When multiple detectors are connected, the system provides both summed spectra and individual detector spectra. Two host computers are used: one for system control and data acquisition, and a second for real-time data evaluation and telemetry to storage systems and remote operators. A GPS module integrated into the controller provides positioning information and altitude corrections are applied using a digital elevation model (DEM, SRTM90). The system is powered by a portable power station (Jackery Explorer 500), illustrated in Figure 3.11. For redundancy, a backup kit consisting of two $4\,\mathrm{L}$ NaI(Tl) detectors, an additional Geiger–Müller counter, and a neutron detector are included.

Figure 3.10: Detector package of the Lithuanian aerial measurement system (RSX1, $2\,\mathrm{L}$ NaI(Tl) scintillation detectors).

Figure 3.11: Installation of the Lithuanian aerial measurement system in the H145 helicopter.

3.2.5 Teams CHE1 & CHE2

Swiss airborne radiometry measurements are conducted using an Aerospatiale AS 332 Super Puma helicopter (TH 06) of the Swiss Air Forces (Figure 3.12). This helicopter has excellent navigation properties and allows emergency operations during bad weather conditions and night time.

Figure 3.12: Aerospatiale AS 332 Super Puma helicopter (TH 06) of the Swiss Air Forces.

The measuring system RLL (Radiometrie Land-Luft) consists of a radiation detector featuring four NaI(Tl) scintillation crystals having a total volume of $16.8\,\mathrm{L}$ with their associated photo-multipliers and multichannel analysers (MCA) for low level measurements, and one Geiger-Müller tube and associated electronics for high dose-rate measurements (Figure 3.13). The spectroscopic measuring chain provides a linear energy calibration of the MCA up to $3.072\,\mathrm{MeV}$ divided into 1024 channels. NaI detectors, Geiger-Müller tube and associated acquisition chain are installed in an aluminium case with thermal insulation foam. The detection container is mounted in the cargo bay below the centre of the helicopter (Figure 3.14). The RLL system registers position, air pressure, air temperature and radar altitude data provided by the helicopter via the internal ARINC bus. Figure 3.15 shows the complete system packaged for storage.

Figure 3.13: RLL Detector: 4 NaI(Tl) scintillation crystals, total volume of $16.8\,\mathrm{L}$.

The equipment control, data acquisition and storage are performed with a rugged computer working as a data server. Two additional redundant rugged client computers are used as operator interface for real-time evaluation, data mapping and communication. All computers are installed in an equipment rack, including an additional battery as power supply back-up. Both operators can manage the system with their associated client computer, display, keyboard and trackball. The additional third central display on the operators' console is mirrored on a screen in the cockpit, located between the pilots, and is used for information exchange with the pilots and general radiological situation awareness (Figure 3.16). System settings may vary slightly between military and civilian missions. For military operations, detection and identification capabilities are typically enhanced by enabling a running average over five one-second measurement cycles, providing an improved sensitivity at the expense of a marginally reduced geo-localisation. Table 3.2 summarises the specifications of the RLL system.

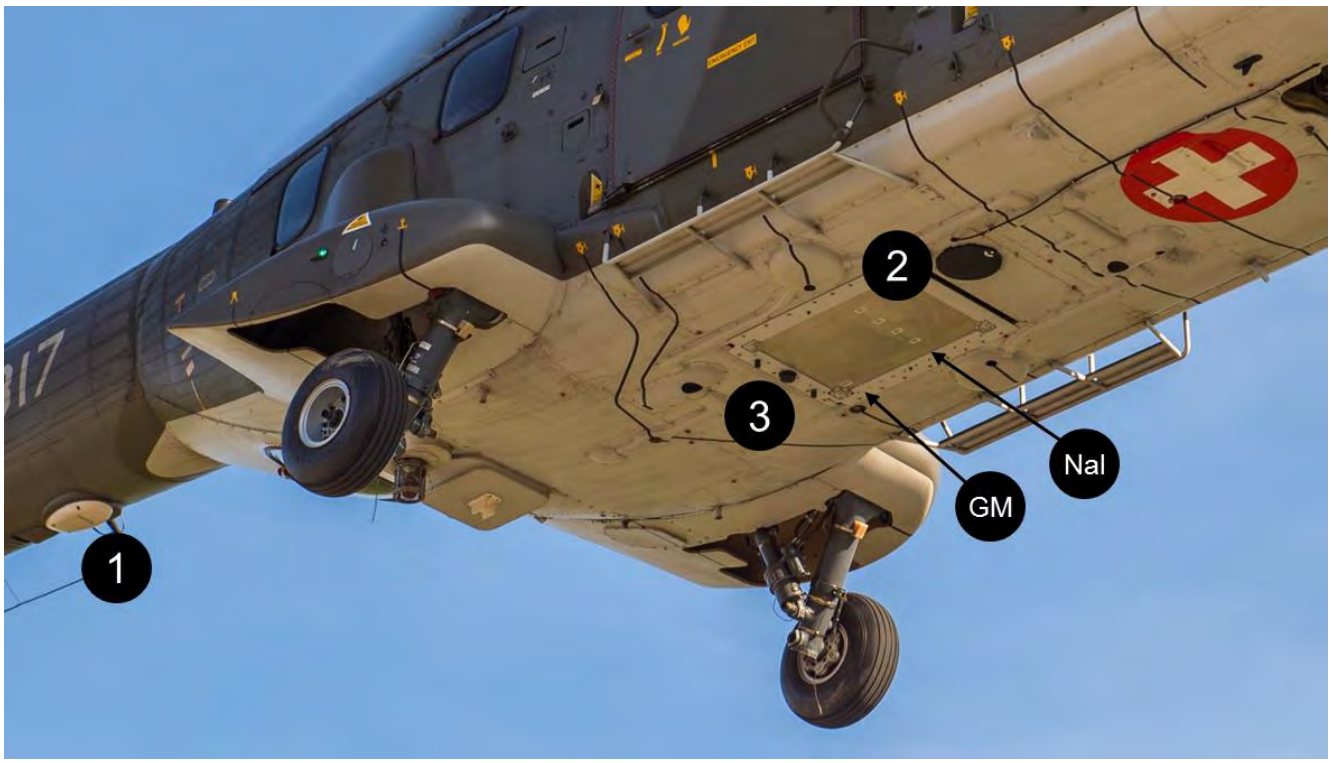

Figure 3.14: RLL detector mounted in the cargo bay of a Super Puma helicopter. 1. Radar altimeter. 2. Detection container marked with detector reference points. 3. UMTS antenna for data upload.

Figure 3.15: Components of the RLL system. 1. Lifting platform for the installation of the detection container. 2. Floor plates and accessories case. 3. Monitors and operator console. 4. Detection container. 5. Operator seats and equipment rack.

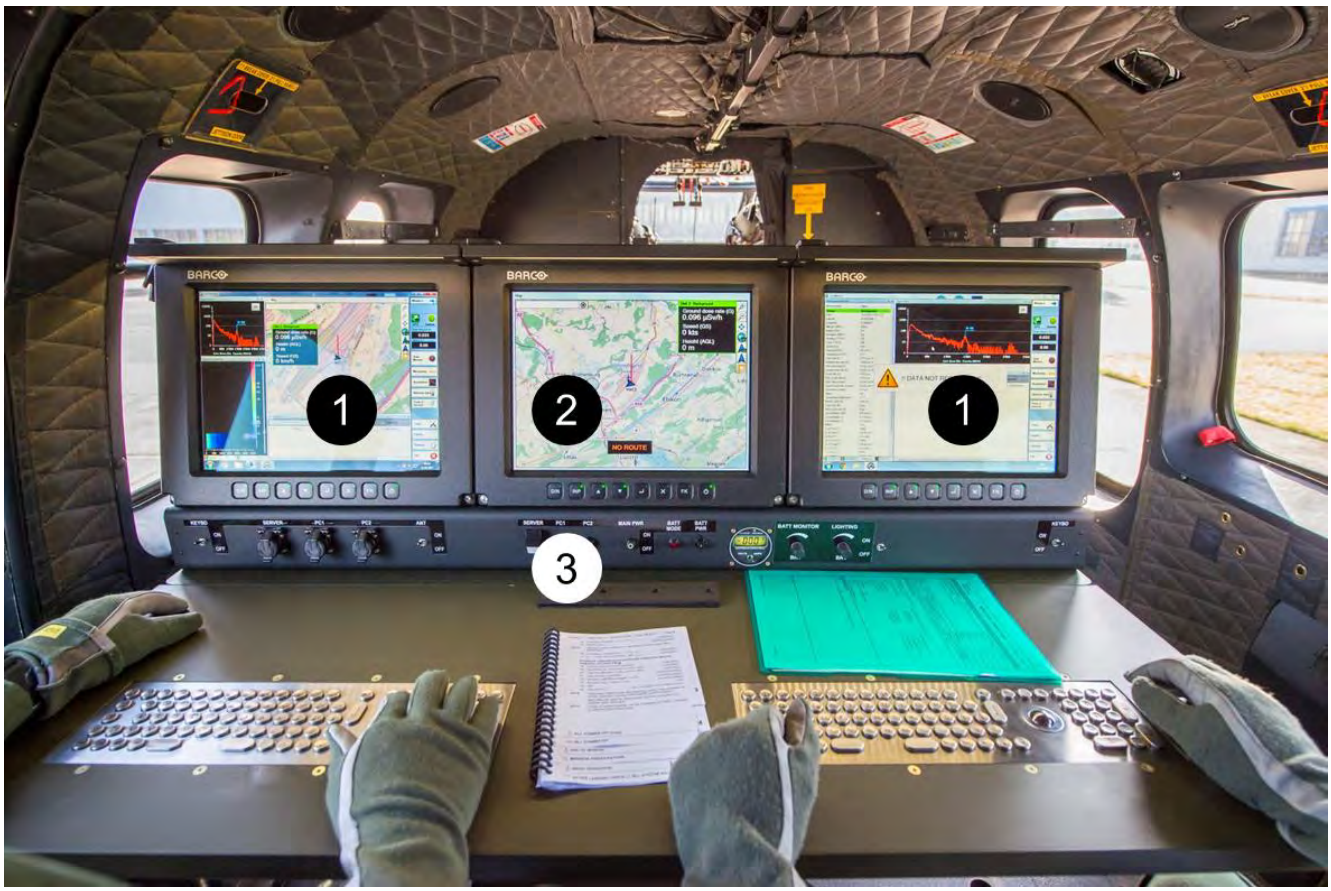

Figure 3.16: Operator console of the RLL system. 1. Displays of the client computers. 2. Common display (mirrored in the cockpit). 3. Control panel with switches for power, lighting and communication and USB ports for file exchange.

Table 3.2: Specifications of RLL system used by CHE1 and CHE2 Teams.

Detection systems	$4 \times 4\,\mathrm{L}$ NaI(Tl) detector 1 Geiger-Müller detector for high range dose rate
Sample time	$1\,\mathrm{s}$ sampling $5\,\mathrm{s}$ moving average for identification
Energy range	$30 - 3000\,\mathrm{keV}$
Spectrometer	1024 channels
Method of evaluation	Real time identification Calculation/extrapolation on ground, resp. $1\,\mathrm{m}$ above ground
Positioning system	Military GPS (Civilian GPS as backup)
Altimetry system	Radar (GPS as backup)
Computer	1 server for data acquisition 2 client computers as user interface

3.3 Drone measuring systems

3.3.1 Team CZE

The Robodrone Kingfisher by Robodrone Industries s.r.o. (Czech Republic) is a versatile UAV designed for professional applications (Figure 3.17). Powered by six electric motors with carbon propellers, it can reach speeds of up to $45\,\mathrm{km\,h^{-1}}$ and carry loads of up to $5\,\mathrm{kg}$, with a maximum take-off weight of $10\,\mathrm{kg}$. Depending on the payload, the Kingfisher offers a flight time of up to $45\,\mathrm{min}$. Pilots operate the drone using the JETI DS-16 RC control unit, which also allows for telemetry monitoring via a $2.4\,\mathrm{GHz}$ Duplex wireless system. For mission planning and advanced control, the UAV is supported by a custom-built portable PC running Ubuntu GNU/Linux and Robodrone GroundControl software.

Figure 3.17: CZE Robodrone Kingfisher UAV and the base station and *DRONES G* by NUVIATech Instruments modular gamma spectroscopy system.

The drone is equipped with a *DRONES G* by NUVIATech Instruments modular gamma spectroscopy system. The module, shown in Figure 3.17, consists of a NaI(Tl) $2'' \times 2''$ $(0.1\,\mathrm{L})$ gamma spectroscopy probe and a high-dose-level detector equipped with two energy-compensated GM tubes. Time and position data are synchronized with GPS. Real-time gamma dose rate measurement is based on recalculation from the spectrum. Accumulation time is selectable by the user, starting from $1\,\mathrm{s}$. The module offers internal data storage in the main unit as well as wireless real-time data transfer to the control unit (laptop) using the Dronic software application. The *DRONES G* system specification are summarised in Table 3.3.

Table 3.3: Specification of the *DRONES G* gamma spectroscopy system

Dose Rate Range	$50\,\mathrm{nGy} - 100\,\mathrm{mGy\,h^{-1}}$
Energy Range	$50\,\mathrm{keV} - 3\,\mathrm{MeV}$
Resolution	$< 7\,\%$ on ^{137}Cs at $662\,\mathrm{keV}$
Weight (total)	max. $4.5\,\mathrm{kg}$
Power	$3\times$ LiPol, $11.1\,\mathrm{V}$ DC / $5100\,\mathrm{mA\,h}$

3.3.2 Team FRA

The system consists of an Innovadrone Surveyor and a SpirExplorer system from Mirion.
The Innovadrone Surveyor is a Quadricopter-drone with a maximum take-off mass of $8\,\mathrm{kg}$ with a payload capacity of $3.5\,\mathrm{kg}$. The drone itself weighs $6.3\,\mathrm{kg}$ overall. It features a CUAV X7 flight controller, dual u-blox F9P RTK GNSS modules, and redundant Inertial Measurement Units (IMU) for stable and accurate autonomous flight. Powered by a $16\,\mathrm{A\,h}$ Li-ion battery, it achieves up to $68\,\mathrm{min}$ flight time without payload and around $40\,\mathrm{min}$ with full configuration. Flight plans are prepared using the ArduPilot Mission Planner software, allowing for automated execution of missions. The Mission Planner software and GETAC laptop ground station enable real-time telemetry and mission control over a $2.4\,\mathrm{GHz}$ link. The Mirion SpirExplorer detector integrates a NaI(Tl) $1.3'' \times 2''$ ($0.04\,\mathrm{L}$) crystal for gamma spectrometry measurement over $30\,\mathrm{keV} - 3\,\mathrm{MeV}$ and two GM (mid and high range) tubes for dose-rate. The detector is powered by the drone and records data at $0.5\,\mathrm{s}$ intervals with 1024-channel spectroscopy. Measurements are streamed in real time, linked to geolocation data from the drone's GPS modules. Real-time mapping, visualisation, and analysis are performed using the dedicated Mirion software installed on the acquisition laptop at the ground station.

Figure 3.18: The French drone system

3.3.3 Team DEU

The "HUGIγN" payload was designed and built at the Fraunhofer FKIE within a project for the Bundeswehr Research Institute for Protective Technologies and CBRN chemical, biological, radiological, nuclear Protection (WIS Wehrwissenschaftliches Institut für Schutztechnologien – ABC-Schutz).

Figure 3.19: The "HUGIγN" system in flight.

The task was to develop a system for the automatic reconnaissance of radioactive isotopes. This includes the detection, localisation and identification of the isotopes. The key system is an Innoriid Innospec gamma spectrometer with the following specification:

Table 3.4: Specification of the Innoriid Innospec gamma spectrometer

Size	$76\,\mathrm{mm} \times 25.4\,\mathrm{mm}$ $(0.04\,\mathrm{L})$
Energy Range	$15\,\mathrm{keV} - 3\,\mathrm{MeV}$
Sensitivity	$> 2500\,\mathrm{cps}/(\mathrm{Sv}/\mathrm{h})$
Dose Rate Range	0.01–$200\,\mathrm{Sv\,h^{-1}}$ with a NaI scintillator, further up with a GM tube

The spectrometer is connected to small form factor PC Intel NUC-8BEK for data recording, processing, fusion and transferring to the ground control station. Other components of the payload are two cameras, a XSens MTI-G-710 GPS/INS unit and communication link using a mobile network

adaptor or long-range Wi-Fi. The cameras are a Ximea electrooptical camera with $2.3\,\mathrm{Megapixel}$ and a passive FLIR thermal camera with $0.3\,\mathrm{Megapixel}$, both are used for documenting the area beneath the payload, a video stream for the operator and detection and localisation of objects using machine learning. The GPS/INS unit delivers the current position and orientation of the payload. The software is implemented using the Robot Operating System (ROS) for the communication between the sensors, the platform and the ground control station. The payload also has its own power supply to be independent from the drone platform.

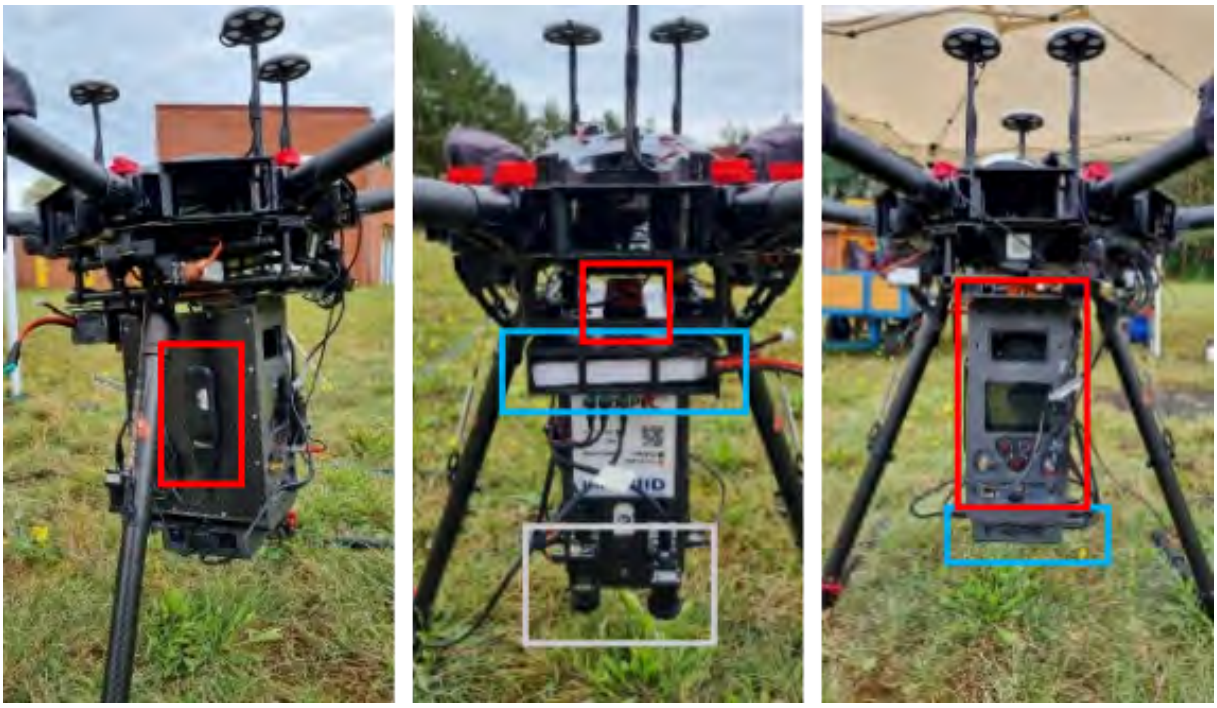

Figure 3.20: (left) mobile network communication; (middle) GPS/INS unit (red), power supply (blue), camera sensors (white); (right) Innospec spectrometer (red), PC (blue)

For the operator on the ground any Laptop or PC with a communication link to the payload can be used to host the software for the ground control station. The ground control station provides user interface for the operator and feature an overview over all relevant flight data. The current state and sensor data of the drone is displayed together with livestreams from the camera. The map highlighting the dose rate, the position of the drone and planned flight path is displayed. If a significant deviation from the background radiation has been found, the estimated position is displayed next to an image of the associated area. As all the data is recorded on the drone, possible breaks in the communication do not interrupt the system, the ground control station will be updated as soon as the link is re-established. Also, all the data is logged for after flight documentation and can be processed further, should the need arise. The drone is a commercially available DJI Matrice 600 Pro. It features a maximum take-off weight of $12\,\mathrm{kg}$ and up to $45\,\mathrm{min}$ of flight time ($20\,\mathrm{min}$ with the payload). The drone is capable of automatic flight using waypoints, and, as the payload can send flight commands directly to the drone, the operator is only needed for a manual take-over during emergencies and does not have to control the system manually. As the payload is independent of the platforms' power supply and communication, the payload can be adapted for other platforms quickly.

3.3.4 Team LTU

For the AGC 2025 campaign, the drone measurement system consisted of a DJI Matrice 350 RTK drone equipped with a Medusa Radiometrics MS-100 detector. The Matrice 350 RTK is an

industrial drone designed for autonomous missions and high-precision aerial surveys. It features RTK GNSS positioning, an autopilot system, and UGCS SkyHub integration, providing precise navigation, autopilot control, and power/data management for payloads. Each battery pack allows approximately $20\,\mathrm{min}$ of flight, and three battery sets provide up to one hour of continuous operation. An external power source enables full recharge of batteries in approximately $40\,\mathrm{min}$, allowing rapid turnaround for extended missions.

The Medusa MS-100 is a compact gamma spectrometer adapted from ground in-situ measurement instruments. It consists of a $2'' \times 2''$ CsI $(0.1\,\mathrm{L})$ scintillator, capable of measuring ^{40}K, ^{238}U, ^{232}Th, and Cs isotopes with real-time spectral and dose-rate monitoring. Dose rate can also be viewed in $\mathrm{Gy\,s^{-1}}$, although it is not currently streamed or saved to local projects. The detector's power, data communication, and integration with the drone autopilot are managed through the UGCS SkyHub interface. Ground clearance is obtained from the onboard GPS and an additional radar altimeter mounted at the front of the drone. The system also includes sensors for temperature, pressure and humidity, which can be used for altitude and environmental correction during post-processing in GAMMAN software. Flight missions are planned in UGCS on a dedicated laptop and uploaded to the DJI remote controller in DJI JSON or KML/KMZ format.

Data from the detector can be accessed via any device with Wi-Fi and a web browser using the mDOS interface. This web-based interface allows real-time visualisation of spectra, monitoring, saving, exporting, and preliminary analysis of measurement data. Standard spectra of ^{40}K, ^{238}U, ^{232}Th, and ^{137}Cs are displayed scaled by their calculated concentrations, with a typical integration time of $1\,\mathrm{s}$. Users can create or download projects, inspect logged data, and modify device settings directly through the interface.

Ambient dose equivalent rate can be calculated in GAMMAN software and is expressed in $\mathrm{pSv\,h^{-1}}$. Currently, data projection onto the ground surface is not supported – all values are calculated at the detector's flight altitude. This limitation has been reported to both the manufacturer and GAMMAN developers. The system also includes an API for live data streaming to iAVID software, enabling simultaneous monitoring and analysis by multiple users across different platforms.

Figure 3.21: The Lithuanian drone system

3.3.5 Team CHE

The entire system consists of an Acecore Noa and a Drones-G measurement system from Nuvia. The Acecore NOA is a heavy-lift hexacopter drone designed for demanding industrial and survey missions. It features a carbon-fibre frame, six motors, and high-precision GNSS navigation for autonomous flight. The drone supports a maximum payload of $\sim 20\,\mathrm{kg}$ and achieves up to $35\,\mathrm{min}$ flight time, depending on the payload. Onboard sensors record GPS, temperature, pressure and humidity, while redundant systems ensure safe operation in challenging environments. Flight plans are programmed via the drone's Ardupilot Mission Planner, supporting grid surveys, waypoints, and automated missions. Telemetry allows continuous monitoring of spectra, dose rates, and environmental parameters during flight. Mounted beneath the drone is the Nuvia Drones-G radiation measurement system, integrating a NaI(Tl) $3'' \times 3''$ $(0.35\,\mathrm{L})$ scintillator and GM tubes for gamma spectroscopy and dose-rate detection from $\sim 50\,\mathrm{keV}$ to $3\,\mathrm{MeV}$. The system streams real-time spectral and dose-rate data, linked with geolocation for mapping and analysis. The software for this is called Dronic.

Figure 3.22: The Swiss drone system

Chapter 4

Data Evaluation

Each of the six teams participating in AGC25 evaluated the raw data acquired during the missions using the algorithms and software described in this chapter. Each team submitted preliminary results during the international campaign and final results by September 2025 for each mission.

4.1 Team CZE

Between 2017 and 2020, a new evaluation program, AGAMA, was developed in cooperation with the Czech company NUVIA a.s. . A key development within the Czech team has been the evaluation of airborne measurement data. The AGAMA software package is employed for survey (flight plan) preparation, data browsing, post-processing, and visualisation on georeferenced maps. In addition to providing a sophisticated computational environment, this program incorporates numerous enhancements compared to the earlier PRAGA4 program, which was used during the ARM17 and AGC19 campaigns. The most important features of the software, including a description of the data processing workflow, are summarised in the following sections. More detailed information lies beyond the scope of this report; references to other reports or relevant publications are provided where appropriate.

The AGAMA program operates on 64-bit Windows 7 or higher. Its primary focus is on emergency monitoring in the event of a radiation incident and aerial monitoring of strong radiation sources. However, it is also applicable in geophysical studies for determining activity concentrations of naturally occurring radionuclides. In future versions, data processing is expected to incorporate correction for radon in the air, based on Monte Carlo simulations.

This version of AGAMA supports data processing from NaI(Tl) detectors with dimensions of $16'' \times 4'' \times 4''$, smaller scintillation detectors such as NaI(Tl) $3'' \times 3''$ (or $2'' \times 2''$), small $CeBr_3$ and plastic detectors, as well as semiconductor HPGe detectors. Default processing parameters in AGAMA were derived from test flights conducted between 2017 and 2022, using both measurements from the IRIS airborne spectrometer (manufactured by Pico Envirotec, Inc., Ontario, Canada) and Monte Carlo simulations.

Since 2023, the new Rad-Patrol2 spectrometer has been tested to determine all necessary parameters. This spectrometer was first deployed operationally at AGC25, in parallel with the AIRIS spectrometer operated by specialists from the Czech Army, mounted on the Mi-17 helicopter.

The AGAMA program facilitates the preparation of flight plans, display and processing of airborne spectrometry data, and visualisation of the processed data on georeferenced OpenStreetMap layers. Users can create, save, and modify projects, performing partial operations such as energy calibration, subtraction of aircraft background and cosmic radiation contributions, calculation of activity concentrations of natural radionuclides and surface activities, determination of air dose rates on the helicopter board and at $1\,\mathrm{m}$ above ground, and calculation of minimum detectable

activities. AGAMA employs a range of computational methods to calculate these quantities and support decision-making in both emergency and routine monitoring scenarios.

Input Data Formats

Both the IRIS/AIRIS and Rad-Patrol2 spectrometers are capable of opening the standard PEI binary data files, originally designed by Pico Envirotec Inc., Toronto, Canada, and subsequently adopted and modified by NUVIA a.s.. Each PEI file consists of a header, containing the file description, and a data Section. All information is recorded in one-second intervals, including spectra, GPS positions, flight heights, and other relevant parameters. PEI files can be stored in either compressed or uncompressed formats. In addition, data files in ERS 1.0 and ERS 2.0 formats can also be readily opened and created within the AGAMA software package.

Flight Preparation

The AGAMA software allows the creation of arbitrary polygons, survey lines, tie lines, waypoints, and special lines, with the capability to continuously modify them on georeferenced online or offline maps. It also supports the generation of spiral-shaped survey patterns, with variable spacing between the spiral lines. The software can calculate the length of individual survey and tie lines, as well as determine the total length of the flight path within a polygon. This functionality enables operators to estimate the total flight time and plan schedules efficiently during emergency operations.

Examples of individual flight plans are illustrated in Figure 4.1, showing a polygon (Mission 5) with a special line highlighted in orange. Figure 4.2 depicts a spiral with a spacing of $200\,\mathrm{m}$, a smoothness of 14 points, and a total of 140 points, along with 36 waypoints indicated by white points.

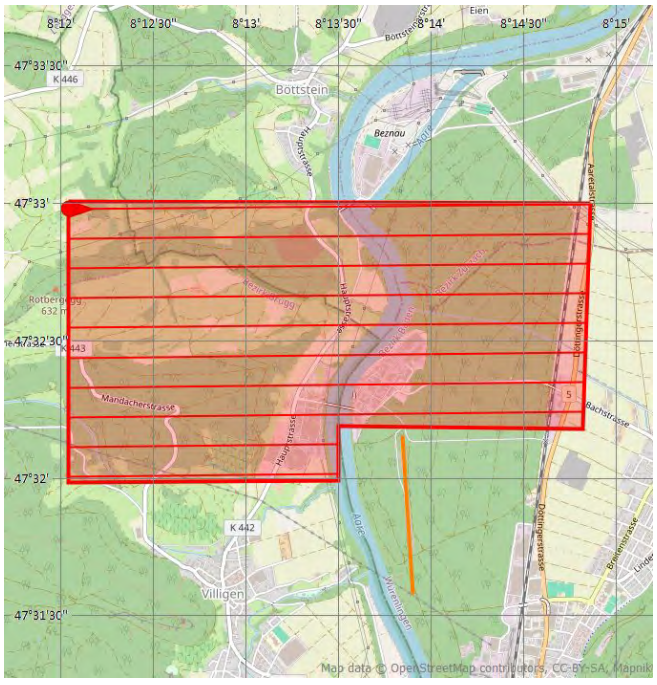

Figure 4.1: Flight plan preparation in AGAMA: Polygon (Mission 5) with a special line (orange).

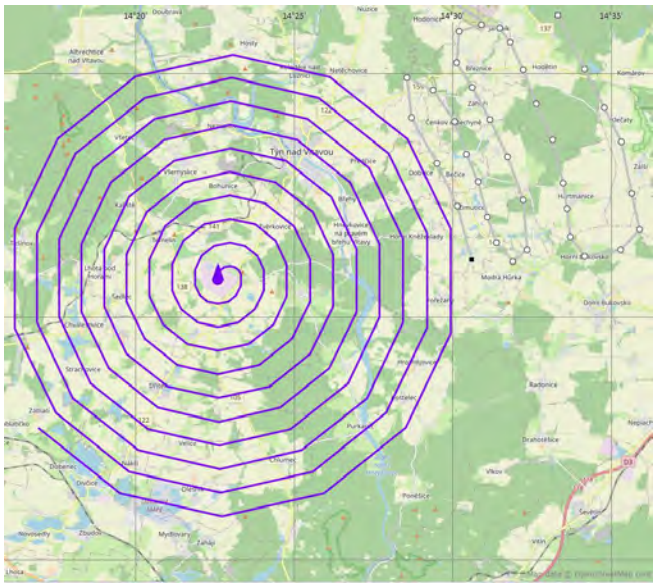

Figure 4.2: Flight plan preparation in AGAMA: Spiral survey pattern with 200 m spacing, smoothness of 14 points, total of 140 points, and 36 waypoints (white).

Helicopter background and cosmic spectra calculation

The aircraft background and cosmic gamma-rays contribute to the measured gamma spectrum onboard the aircraft. The following procedure has been used for decades in geophysical airborne surveys. The aircraft and cosmic background contributions in spectral windows have been estimated as follows:

$$CR_{BKG} = CR_{B,Heli} + S_c\, CR_{Cos} \tag{4.1.0.1}$$

where CR_{BKG} is the combined aircraft (in this case, helicopter) background and cosmic gamma-ray contribution in each spectral window, $CR_{B,Heli}$ is the helicopter background in each spectral window, CR_{Cos} is the cosmic channel count rate, and S_c is the cosmic stripping factor for the spectral window. Acquiring spectra over a wide and deep water reservoir eliminates the contribution from the terrestrial environment. However, since no such suitable water areas exist in the Czech Republic, alternative methods were sought to remove this effect. Based on Monte Carlo simulations, it was found that the terrestrial contribution is negligible at altitudes above $1500\,\mathrm{m}$ above ground level.

The above Equation was applied to the full spectrum, channel by channel. A relatively simple method based on the non-negative least squares (NN-LSQ) approach was proposed. This method assumes that spectra are recorded at two or more altitude levels ranging from $1900\,\mathrm{m}$ to $2900\,\mathrm{m}$ above sea level, where the terrestrial component is fully eliminated. At least 300 one-second spectra are required to achieve reliable results. Two further assumptions are necessary: (i) a basis for the primary components (full energy peaks) must be available, i.e., the expected peaks in the helicopter background (Figure 4.3) and the secondary continuous component (Compton scattering, Figure 4.4), and (ii) radon must be absent. Using a number of such data sets for the Mi-17 helicopter, the NN-LSQ procedure was applied, yielding very good results.

The Mi-17 helicopter background spectrum and the gamma cosmic contribution for 1 cps in the cosmic channel (the last channel in the spectrum), determined from the data of Mission 2 at three altitudes ($1200\,\mathrm{m}$, $1800\,\mathrm{m}$, and $2400\,\mathrm{m}$ above water level), are shown later in this report (see Section 8.3). The mathematical procedure is described in detail in [3].

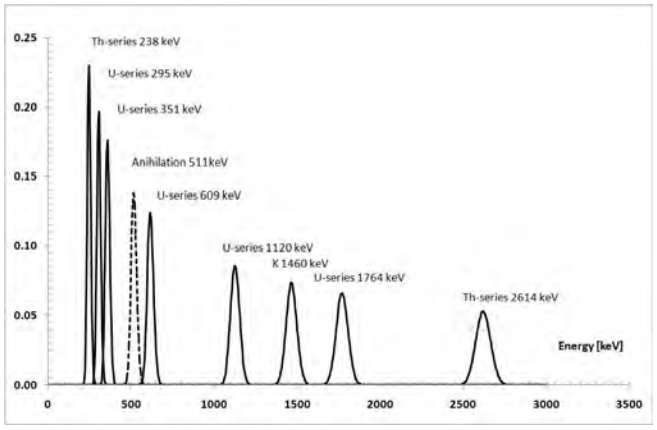

Figure 4.3: Basis for primary component (full energy peaks) – Expected peaks in background helicopter peaks for algorithm.

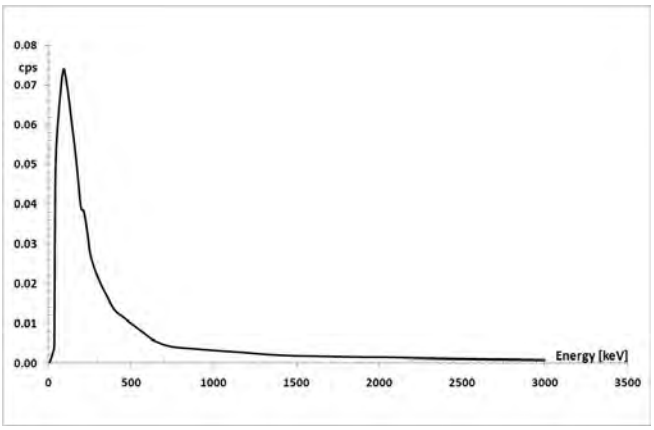

Figure 4.4: Secondary component (Compton scattering).

Activity estimate

The AGAMA software package calculates activities in two ways. The first method is the *window method*, which is based on the procedure described in IAEA recommendations, additionally including the calculation of ^{137}Cs activity per unit surface. This method is applicable for radiation monitoring

during normal radiation situations to estimate the activity concentrations of natural radionuclides ^{40}K, ^{238}U, and ^{232}Th in $\mathrm{Bq\,kg^{-1}}$, and activities per unit surface of ^{137}Cs in $\mathrm{Bq\,m^{-2}}$.

The second method is based on the *least squares (LSQ)*, using response functions of selected nuclides. This method is now considered for data processing in both normal radiation situations (activity concentrations of natural radionuclides and activity per unit surface of ^{137}Cs) and emergency monitoring (^{131}I, ^{137}Cs, ^{134}Cs) with large $16'' \times 4'' \times 4''$ NaI(Tl) detectors in the late phase of an emergency situation. It is also capable of estimating activities of point sources and "small hot spots" for selected nuclides. The response functions are selected based on the qualitative analysis of the spectra.

Additionally, air dose (kerma) rates can be calculated from the activities obtained by the extended window method (large-volume NaI(Tl) detectors) and from full spectra for all detectors connected to the Rad-Patrol2 control unit.

At present, the Rad-Patrol2 control unit is capable of processing data from HPGe detectors, and AGAMA can calculate the air dose rate in $\mathrm{nGy\,h^{-1}}$. It is also being prepared for processing surface activities of man-made nuclides. The original method for estimating the surface activities of selected man-made nuclides in the energy range from $200\,\mathrm{keV}$ to $2000\,\mathrm{keV}$ is described in [4].

Extended window (ROI) method Based on IAEA recommendations, the method extends the standard window technique to four elements (^{40}K, ^{238}U, ^{232}Th, and ^{137}Cs) using a combination of Monte Carlo simulation and experimental calibration. Six additional stripping parameters and three sensitivities are defined and calculated for ^{137}Cs.

The standard calculation method is extended to a 4×4 matrix including ^{137}Cs parameters, leading to the introduction of six new stripping factors, δ (K→Cs), ϵ (U→Cs), and τ (Th→Cs), with the other three stripping factors, i.e., the contributions of ^{137}Cs to the K, U, and Th windows, set to d(Cs→K)$= e$(Cs→U)$= t$(Cs→Th) $= 0$. A summary of the stripping factor is reported in Table 4.1. The stripping factors and sensitivities for ^{137}Cs were calculated from simulated spectra for calibration pads and converted to an infinite surface, based on the definition of stripping factors as the ratio of counts between individual windows.

The net count rates of a given nuclide in individual windows, assuming $b = g = d = e = t = 0$, are given by:

$$n_{Th,Th} = \frac{n_{Th} - a\ n_U}{1 - a\ \alpha} \tag{4.1.0.2}$$

$$n_{U,U} = \frac{n_U - \alpha\ n_{Th}}{1 - a\ \alpha} \tag{4.1.0.3}$$

$$n_{K,K} = n_K - \gamma\ n_{U,U} - \beta\ n_{Th,Th} \tag{4.1.0.4}$$

$$n_{Cs,Cs} = n_{Cs} - \delta\ n_K - (\epsilon - \gamma\ \delta)\ n_{U,U} - (\tau - \delta\ \beta)\ n_{Th,Th} \tag{4.1.0.5}$$

where $n_{i,i}$ are the net count rates of nuclides in individual windows ($i, i = K, K;\ U, U;\ Th, Th;$ Cs, Cs), and n_i is the gross count rate in the energy window corrected for background (see Table 4.2). All calculated values are given in SI units. Originally, for the IRIS/AIRIS spectrometer, the stripping factors for natural radionuclides were adopted from IAEA recommendations [5], while the ^{137}Cs stripping factors were calculated for a "surface calibration pad" using Monte Carlo simulation (MCNP 6.1 transport code).

Table 4.1: Stripping factors for large-volume $16'' \times 4'' \times 4''$ NaI(Tl) detectors.

Stripping factor	Base value	Increment per m	Equation	Reference
α	0.254	0.00049	$0.254 + 0.00049\ H$	IAEA
β	0.386	0.00065	$0.386 + 0.00065\ H$	IAEA
γ	0.760	0.00069	$0.760 + 0.00069\ H$	IAEA
a	0.05	0	0.05	IAEA
τ	1.188	-0.000538	$1.188 - 0.000538\ H$	Simulations
ϵ	2.155	-0.00164	$2.155 - 0.00164\ H$	Simulations
δ	0.272	0.000683	$0.272 + 0.000683\ H$	Simulations

Table 4.2: Mi-17 helicopter background count rates and cosmic gamma contribution per 1 count in cosmic channel.

Window	Lower threshold [keV]	Upper threshold [keV]	Helicopter BKG [cps]	Cosmic [cps/1count]
^{137}Cs	618	705	14.0	0.0957
^{40}K	1370	1570	9.8	0.0662
U-series	1660	1860	4.9	0.0543
Th-series	2410	2810	0.4	0.0579

The background count rates in individual windows were taken from the full Mi-17 helicopter background spectrum and the gamma cosmic contribution (see Section 8.3). Net count rates at flight height H are then converted to a reference height $H_{\text{ref}} = 100\,\mathrm{m}$:

$$n_{i,i(\text{cor})} = n_{i,i}\ e^{-\mu_i\ (H_{\text{ref}} - H)} \tag{4.1.0.6}$$

where μ_i is the window attenuation coefficient (per metre), $n_{i,i}$ is the observed count rate at flight height H, and $n_{i,i(\text{cor})}$ is the corrected count rate at H_{ref}.

Attenuation factors μ_i and Sensitivities $S_{K,K}, S_{U,U}, S_{Th,Th}, S_{Cs,Cs}$ were determined by hovering over reference areas in the Czech Republic and are summarised in Table 4.3. Activity concentrations are calculated as:

$$A_{Cs} = \frac{n_{Cs,Cs(\text{cor})}}{S_{Cs,Cs}} \tag{4.1.0.7}$$

$$A_K = \frac{n_{K,K(\text{cor})}}{S_{K,K}} \tag{4.1.0.8}$$

$$A_U = \frac{n_{U,U(\text{cor})}}{S_{U,U}} \tag{4.1.0.9}$$

$$A_{Th} = \frac{n_{Th,Th(\text{cor})}}{S_{Th,Th}} \tag{4.1.0.10}$$

The activity concentrations of natural nuclides A_K, A_U, A_{Th} are reported in $\mathrm{Bq\,kg^{-1}}$, and the surface activity A_{Cs} of ^{137}Cs is in $\mathrm{kBq\,m^{-2}}$. The exponential distribution of ^{137}Cs with $\alpha/\rho = 0.206\ \mathrm{cm^2\,g^{-1}}$ (also used in LSQ and NN-LSQ methods) is applied [6]. For the distribution defined in [7] ($\beta = 9.5\ \mathrm{g\,cm^{-2}}$), a conversion factor of 2 should be applied.

Table 4.3: Attenuation coefficients and sensitivities for individual windows of the extended window method at $100\,\mathrm{m}$ flight altitude for IRIS/AIRIS spectrometers.

Attenuation coefficient [m^{-1}]	Sensitivity	Unit
$\mu_{\mathrm{K}} = -0.0095$	$S_{\mathrm{K,K}} = 0.178$	$\mathrm{cps\,Bq^{-1}\,kg}$
$\mu_{\mathrm{U}} = -0.0082$	$S_{\mathrm{U,U}} = 0.379$	$\mathrm{cps\,Bq^{-1}\,kg}$
$\mu_{\mathrm{Th}} = -0.0074$	$S_{\mathrm{Th,Th}} = 0.768$	$\mathrm{cps\,Bq^{-1}\,kg}$
$\mu_{\mathrm{Cs}} = -0.0112$	$S_{\mathrm{Cs,Cs}} = 5.8$	$\mathrm{cps\,kBq^{-1}\,m^2}$

The above parameters are valid only to the IRIS/AIRIS spectrometer, which was also installed on the Mi-17 helicopter during AGC25. The same parameters for the Rad-Patrol2 spectrometer have been determined and are currently under validation. Using the available response functions for Rad-Patrol2, all required parameters and constants were recalculated. Initial tests indicate that the newly calculated constants yield better agreement between the extended window and NN-LSQ methods and in-situ ground measurements. The IRIS/AIRIS parameters for the extended window method will additionally be recalculated on the basis of the response functions. After detailed verification, this method will be submitted for publication in a peer-reviewed journal.

Least square (LSQ) method The LSQ method is based on response functions calculated using Monte Carlo simulations. For the Rad-Patrol2 spectrometer, a complete set of response functions is currently available for ^{40}K, ^{238}U, and ^{232}Th (homogeneously distributed), as well as for ^{137}Cs with an exponential distribution. Response functions for ^{134}Cs and ^{131}I (surface distribution), as well as for various point sources, are currently being calculated.

The LSQ method operates using response functions corresponding to unit activity. For clarity, the principle of the LSQ method is illustrated using a summary spectrum in Figures 4.5a and 4.5e, acquired by Rad-Patrol2 on five survey lines over the Thun Military Training Area (Mission 1). The mathematical approach is described in detail in [8].

The response functions for ^{40}K, for the U series, and for the Th series in $\mathrm{cps\,Bq^{-1}\,kg^{-1}}$ are shown in Figures 4.5 b – 4.5 d. The LSQ method searches for the best fit of a combination of the relevant response functions. Figure 4.5e shows an example of the best fit for the summary spectrum acquired along the five survey lines. In this Figure, the yellow line represents the summary spectrum over the polygon at the Thun Military Training Area, the light blue line is the background-corrected spectrum, and the black line is the simulated fitted spectrum, constructed from response functions corresponding to $192\,\mathrm{Bq\,kg^{-1}}$ of ^{40}K, $16\,\mathrm{Bq\,kg^{-1}}$ of U series, and $12\,\mathrm{Bq\,kg^{-1}}$ of Th series.

This LSQ principle is applied within the AGAMA software to each one-second spectrum recorded during airborne measurements. The LSQ method can be further adjusted to physical measurements by considering non-negative least squares (NN-LSQ), whose only difference with LSQ being that all negative activity values obtained in the solution are mathematically set to zero.

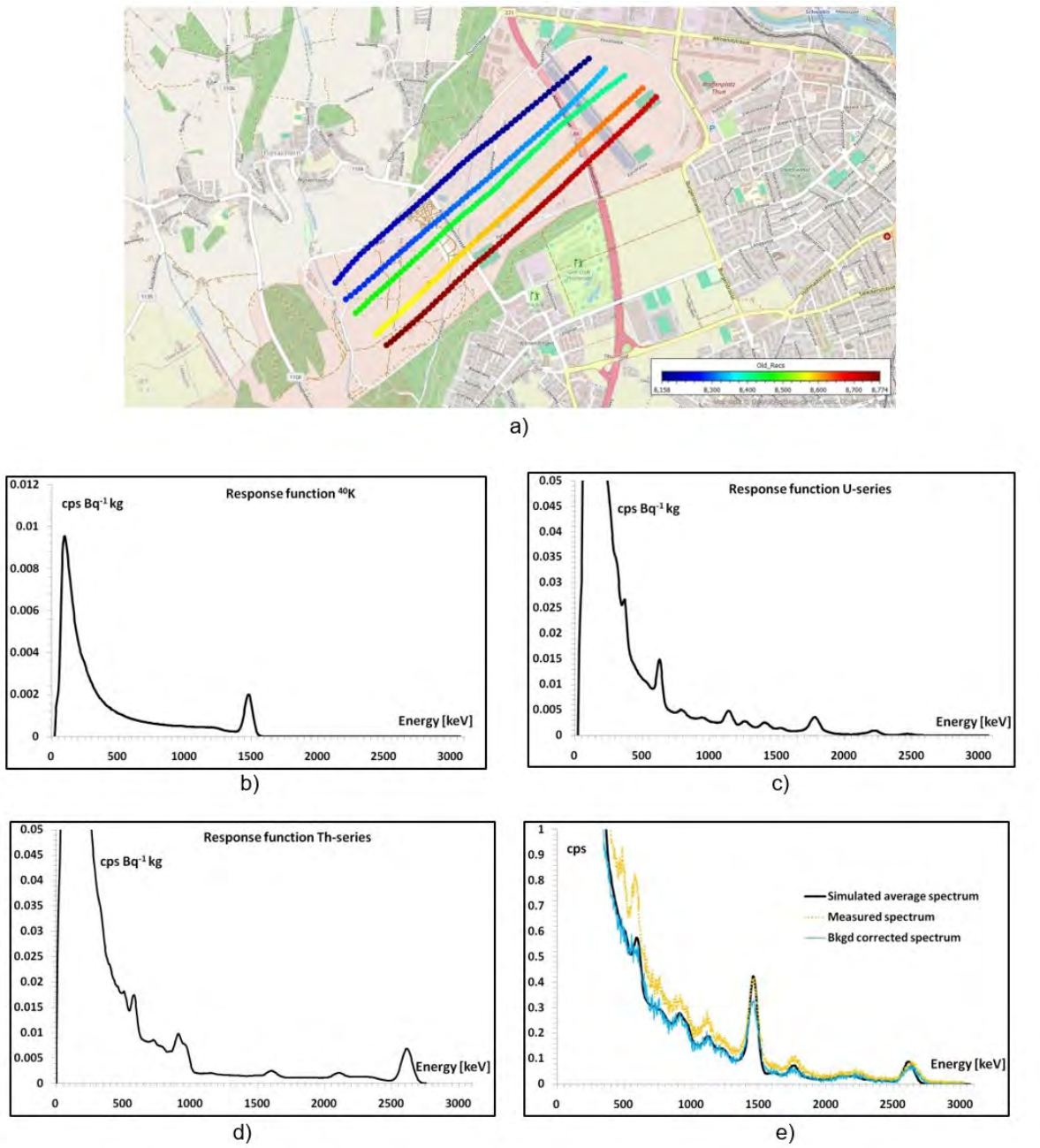

Figure 4.5: a) Selected 5 lines, Mission 1, Thun Military Training Area. b) Response function of ^{40}K. c) Response Function of U-series. d) Response function of Th-series. e) Summary spectrum acquired on 5 lines (yellow), background corrected spectrum (blue) and spectrum obtained by superimposing simulated response functions (black).

The MMGC ratio is sensitive to the presence of man-made radionuclide that typically emit photons in the lower energy range. An increase in the MMGC ratio indicates the likely presence of anthropogenic radioactivity in the measured spectrum:

$$MMGC\ Ratio = \frac{\sum_{E=35\,\mathrm{keV}}^{1400\,\mathrm{keV}} n(E)}{\sum_{E=1400\,\mathrm{keV}}^{3000\,\mathrm{keV}} n(E)} \tag{4.1.0.11}$$

where $n(E)$ denotes the counts in individual channels and E is the energy in keV.

Dose rate calculations from activities and full spectrum

The AGAMA software package always calculates the air dose rate from the ground (ADR_GND) in $\mathrm{nGy\,h^{-1}}$. It is always assumed that the electron equilibrium is fulfilled and the air kerma rate is equal to air dose rate.

Air dose rate calculated from activities The air dose rate from the ground (ADR_GND) can be calculated from activities determined using the extended window method, provided the spectrum contains only natural radionuclides and ^{137}Cs. This Equation is valid only if K, U, Th, and ^{137}Cs are present and are the sole contributors to the dose rate. Under this assumption, the dose rate at 1 m above the ground can be calculated as:

$$ADR\_GND_{1m} = A_{\mathsf{Cs}}\ 1.05 + A_{\mathsf{K}}\ 0.0417 + A_{\mathsf{U}}\ 0.462 + A_{\mathsf{Th}}\ 0.604 \tag{4.1.0.12}$$

where A_{Cs} is the surface activity, exponentially distributed, in $\mathrm{kBq\,m^{-2}}$, and A_{K}, A_{U}, and A_{Th} are the activity concentrations in $\mathrm{Bq\,kg^{-1}}$. The coefficients are taken from ICRU Report 53 [7].

Air dose rate calculated from full spectrum ADR_GND is computed from the full energy spectrum ($35\,\mathrm{keV}$ to $3\,\mathrm{MeV}$) and refers to the local ADR_GND onboard the helicopter (commonly denoted as ADR_GND_{loc}). Air dose rates derived from the total count rate depend on both the energy and type of the gamma radiation source. Consequently, the calculation of the air dose rate is based on the principle of the relative absorbed dose rate, which represents the energy absorbed in the detector (the so-called power-spectrum). This approach was initially developed for small, symmetrical NaI(Tl) detectors, plastic scintillators, and HPGe detectors [9]. Calculating the air dose rate according to the power-spectrum principle requires calibration of the detectors using well-defined air dose rates. Calibration can be performed either experimentally with radiation sources or via Monte Carlo simulations. Both approaches were employed to calibrate the detectors of the IRIS/AIRIS and Rad-Patrol2 airborne spectrometers. Since a multichannel analyser is always employed, the following relationship can be applied:

$$AE = \frac{\sum_{k=i}^{n} E_j\ N(E_j)}{t} \tag{4.1.0.13}$$

where AE is the relative absorbed energy rate in $\mathrm{MeV\,s^{-1}}$, t is the live (real) time in s, i is the initial channel number, and n is the final channel number. $N(E_j)$ represents the number of counts with energy E_j in the interval E_j to $E_j + dE_j$ recorded during the acquisition time t. The AE value is obtained from the energy-calibrated spectrum. The ADR_GND_{loc} in the air volume corresponding to the detector volume can then be expressed using a k^{th} degree polynomial relationship:

$$ADR\_GND_{loc} = \sum_{k=1}^{n} A_k\ (AE)^{k-1}\ \sim\ A_1 + A_2\ AE + A_3\ (AE)^2 + A_4\ (AE)^3 \tag{4.1.0.14}$$

where A_k are calibration constants. Both spectrometers (IRIS/AIRIS and Rad-Patrol2) were calibrated using both measurements with reference sources and Monte Carlo simulation.

Unlike small, symmetrical detectors, large-volume NaI(Tl) detectors require determination of their angular dependence. Since the detectors are mounted inside the helicopter, the attenuation factor must also be considered. For the IRIS/AIRIS spectrometer, the angular dependence is illustrated in Figure 4.6 and the calibration Equation is:

$$ADR\_GND_{loc} = -0.3589 + 0.02391\ AE\ k + 0.0000000572361\ k^2\ AE^2 \tag{4.1.0.15}$$

where AE is the relative absorbed dose rate in $\mathrm{MeV\,s^{-1}}$, and k is a factor accounting for attenuation and angular dependence, i.e., $k = k_{ang}\ k_{att} = 1.7$. This Equation is valid for energies from $35\,\mathrm{keV}$ to $3\,\mathrm{MeV}$ and air dose rates from $6\,\mathrm{nGy\,h^{-1}}$ to $120\,\mathrm{nGy\,h^{-1}}$.

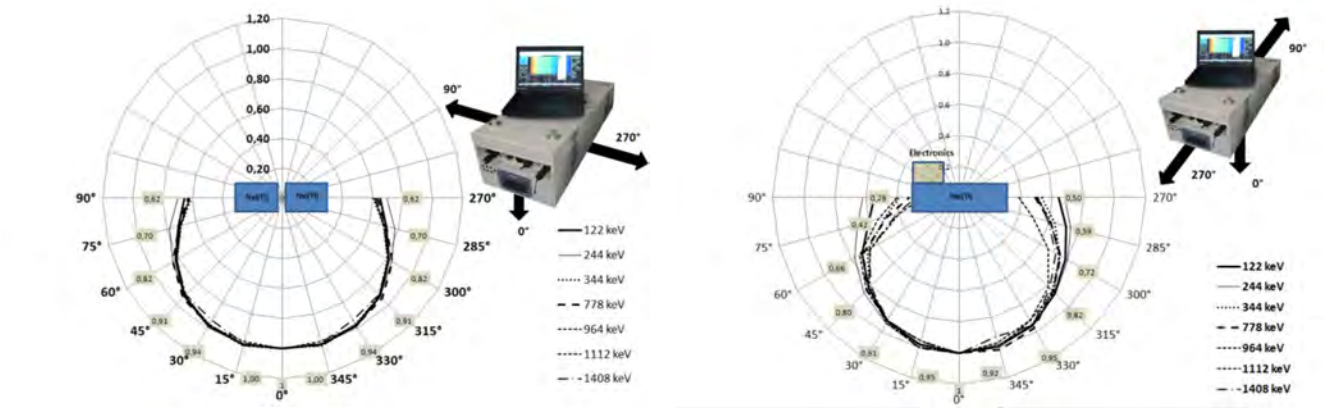

Figure 4.6: Angular dependence k_{ang} of IRIS/AIRIS gamma-ray spectrometer.

For the Rad-Patrol2 spectrometer, the calibration Equation is:

$$ADR\_GND_{loc} = 0.068372 + 0.04736\ k\ AE - 3.53469\,10^{-7}\ k^2\ AE^2 \tag{4.1.0.16}$$

where AE is the relative absorbed energy rate in $\mathrm{MeV\,s^{-1}}$, and $k = k_{ang}\ k_{att} = 1.7$. This Equation is valid for energies from $35\,\mathrm{keV}$ to $3\,\mathrm{MeV}$ and air dose rates from $10\,\mathrm{nGy\,h^{-1}}$ to $170\,\mathrm{nGy\,h^{-1}}$.

For emergency monitoring, these Equations can be slightly modified for higher air dose rates; however, they were not used in AGC25 and are therefore not presented here. While the Rad-Patrol2 covers a range of air dose rates approximately four times lower than that of IRIS, it can correct for dead time, unlike IRIS.

ADR_GND_{loc} is the air dose rate on the helicopter board. After subtracting the background and the cosmic contribution, to convert ADR_GND_{loc} to ADR_GND_{1m} (air dose rate $1\,\mathrm{m}$ above ground), the following relation was derived from extensive experimental measurements and verified using Monte Carlo simulations. For emergency situations, alternative relationships can be established depending on the ratios of man-made nuclides ^{137}Cs, ^{134}Cs, and ^{131}I present on contaminated surfaces, which are beyond the scope of the present report.

$$ADR\_GND_{1m} = \frac{ADR\_GND_{loc}}{1.006\ e^{-0.008\ H}}\ [\mathrm{nGy\,h^{-1}}] \tag{4.1.0.17}$$

where H is the flight ground clearance in metres. This exponential function may be approximated by a polynomial one, with both approaches yielding equivalent results up to a flight height of $250\,\mathrm{m}$ above ground:

$$ADR\_GND_{1m} = \frac{ADR\_GND_{loc}}{1.0022 - 0.0073749\ H + 2.139\,10^{-5}\ H^2 - 2.2052\,10^{-8}\ H^3}\ [\mathrm{nGy\,h^{-1}}] \tag{4.1.0.18}$$

Recalculation to ground ambient dose equivalent rate To convert from ADR_GND_{1m} to ambient dose equivalent rate from the ground (DHSR_GND), the following formula is applied:

$$DHSR\_GND[\mathrm{\mu Sv\,h^{-1}}] = ADR\_GND_{1m}[\mathrm{nGy\,h^{-1}}]\ 0.0012\,[\mathrm{\mu Sv\,nGy^{-1}}] \tag{4.1.0.19}$$

Cosmic dose rate calculation as a function of altitude above sea level. The DHSR_COS caused by the contribution of cosmic radiation of all components (not only the contribution of gamma radiation in the range up to $3\,\mathrm{MeV}$) has been calculated so far according to the following Equation:

$$DHSR\_COS = 32\ 2^{(0.001\ h)/1.5}\ [\mu\mathrm{Sv\,h^{-1}}] \tag{4.1.0.20}$$

where h is the height above sea level in km. Then, total ambient dose equivalent rate is given by the formula:

$$DHSR = DHSR\_GND + DHSR\_COS\ [\mu\mathrm{Sv\,h^{-1}}] \tag{4.1.0.21}$$

MDA calculation Minimum detectable activities (MDA) are calculated for all activity concentrations of natural radionuclides, surface activities of man-made nuclides, and activities of point sources. Two approaches are implemented in AGAMA:

Currie's method [10] – This approach considers only the statistics of detected counts, neglecting uncertainties associated with other parameters in the calculation. Both the minimum significant activity (MSA) and the minimum detectable activity (MDA) are computed for each one-second spectrum using the following Equations based on Poisson statistics:

$$MSA = 2.33\ \sqrt{\mu_B}\ K \tag{4.1.0.22}$$

$$MDA = (2.71 + 4.65\sqrt{\mu_B})\ \ K \tag{4.1.0.23}$$

where μ_B is the background count for one second spectrum and K is the conversion factor from counts to activities.

ISO/IEC 11929:2010 recommendation – This approach accounts for additional quantities incorporated into the conversion factor K. Currently, AGAMA considers only the uncertainty in the flight altitude as measured by the radar altimeter. Selected estimates of MDA are provided in Table 4.4.

Table 4.4: Estimate of MDA for 4×4 litre NaI(Tl) detectors at $100\,\mathrm{m}$ flight height, following ISO 11929.

	MDA (ISO)	Point sources	MDA (ISO)
$^{40}\mathrm{K}$	$\sim 120 - 150\,\mathrm{Bq\,kg^{-1}}$	$^{60}\mathrm{Co}$	$\sim 50 - 70\,\mathrm{MBq}$
U-series	$\sim 10 - 20\,\mathrm{Bq\,kg^{-1}}$	$^{137}\mathrm{Cs}$	$\sim 100\,\mathrm{MBq}$
Th-series	$\sim 5 - 15\,\mathrm{Bq\,kg^{-1}}$	$^{131}\mathrm{I}$	$\sim 40 - 50\,\mathrm{MBq}$
$^{137}\mathrm{Cs}$	$\sim 5 - 7\,\mathrm{kBq\,m^{-2}}$		

Data browsing and import AGAMA enables the display of charts for all input and output channels. Data can be saved in multiple formats, including PEI binary files, .csv files, ERS 1.0 or ERS 2.0 files, and KML/KMZ files. The software also allows visualisation of data on open-source maps and the export of the displayed maps as .jpg, .png, or other image formats. In addition, AGAMA supports data transfer to other mapping software, such as MapInfo or the open-source QGIS, which is now used for post-processing all output data.

Maps AGAMA provides rapid visualisation of survey results directly on maps. An example of an AGAMA map from Mission 5 is shown in Figure 4.7. Figure 4.8 presents three flight lines over Lake Thun from Mission 2, at altitudes of $90\,\mathrm{m}$, $180\,\mathrm{m}$, and $300\,\mathrm{m}$, exported as a KML/KMZ file.

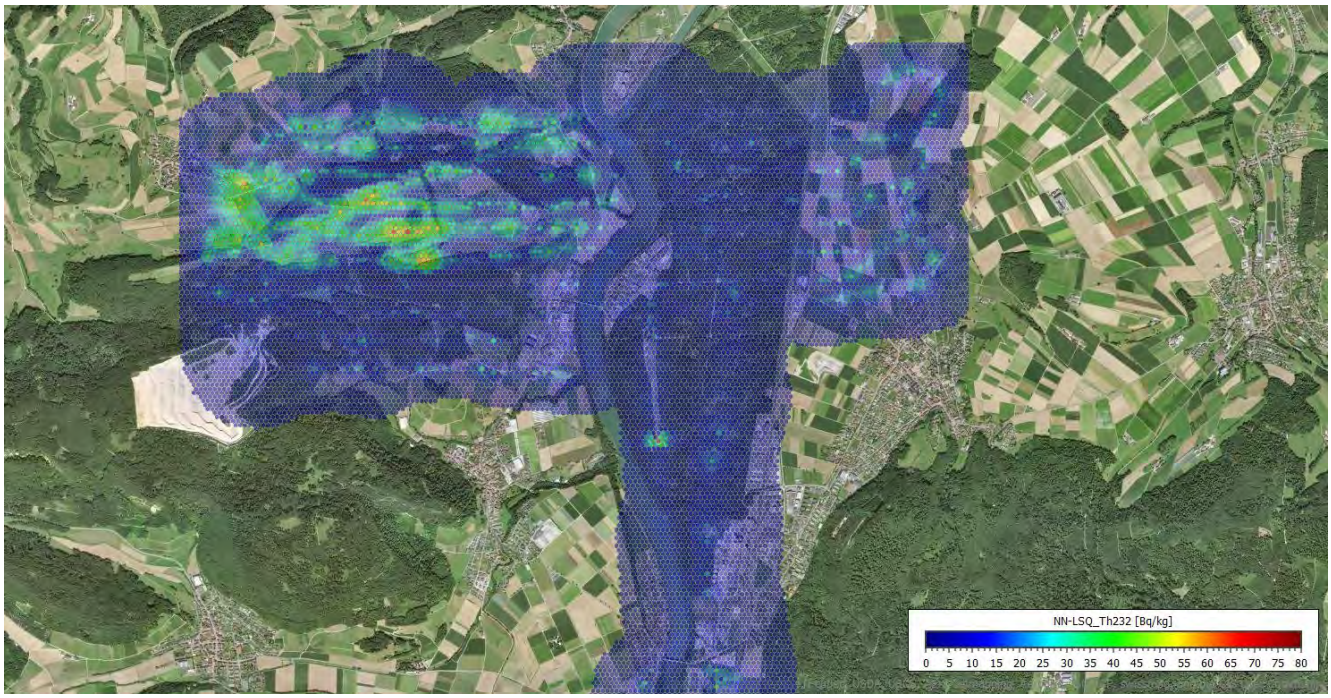

Figure 4.7: Example of a map: Activity concentrations of ^{232}Th in Mission 5.

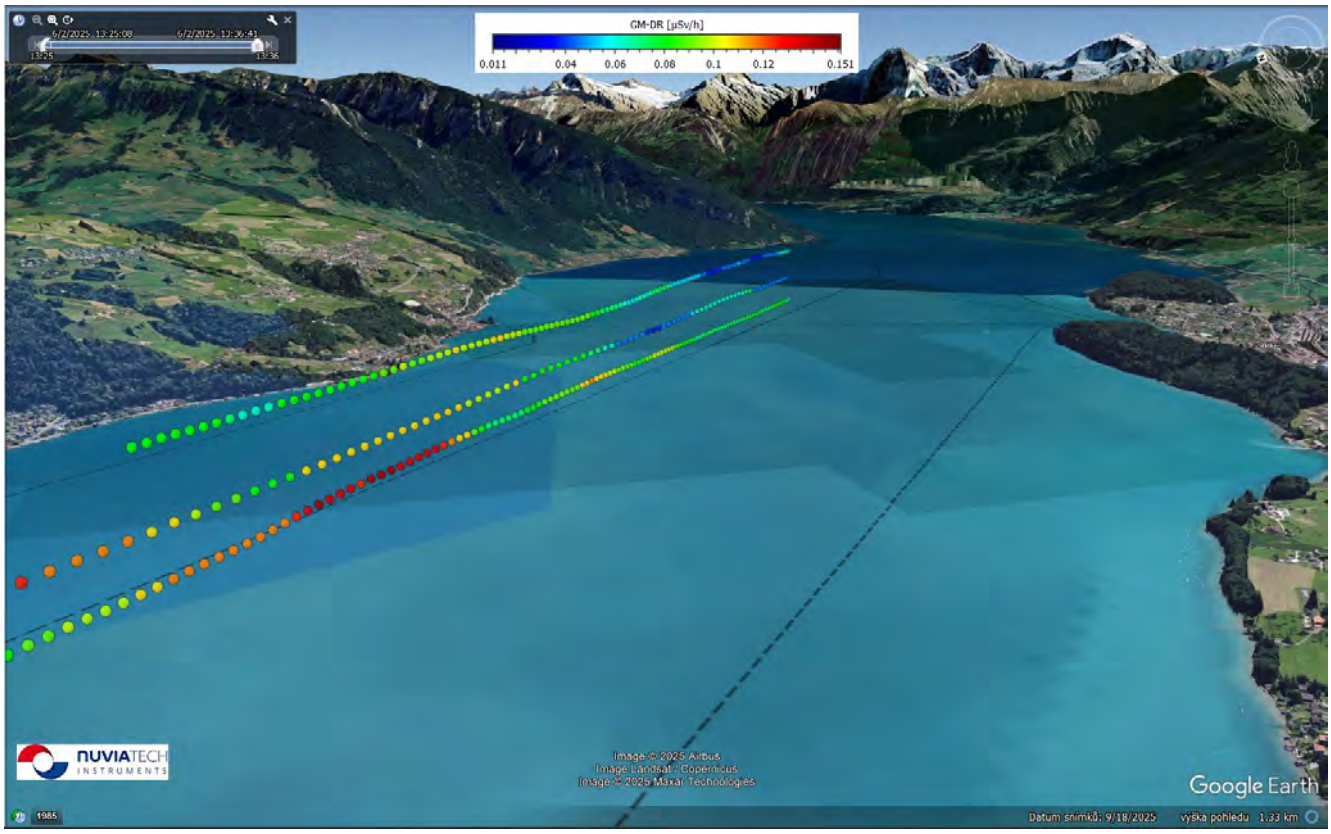

Figure 4.8: Example of KML/KMZ file from AGAMA over Lake Thun (Mission 2; heights of $90\,\mathrm{m}$, $180\,\mathrm{m}$ and $300\,\mathrm{m}$).

4.2 Team FRA

ASNR has chosen to integrate Mirion's acquisition data into its spectroscopic analysis framework, sketched in Figure 4.9. Scripts were developed to query the Mirion database (hosted on the acquisition laptop) in real time during flights and to transmit the data via FTP to the ASNR database over a 4G communication link. The database is based on LINSSI, a generic database for gamma-ray spectrometry developed through an international collaboration between Health Canada (HC), Aalto University School of Science, and the Radiation and Nuclear Safety Authority (STUK). LINSSI also provides web-based data visualisation tools, which have been adapted to meet ASNR's requirements.

One of the key advantages of this strategy is that back-office operators are able to monitor missions and perform analyses already during the flight or immediately after its completion, without delay.

Post-processing and data extraction can be performed directly from the ASNR database via dedicated web interfaces, enabling integration or further analysis in software such as ArcGIS (spatial analysis), Kartotrak (geostatistics), and InterWinner (spectral analysis).

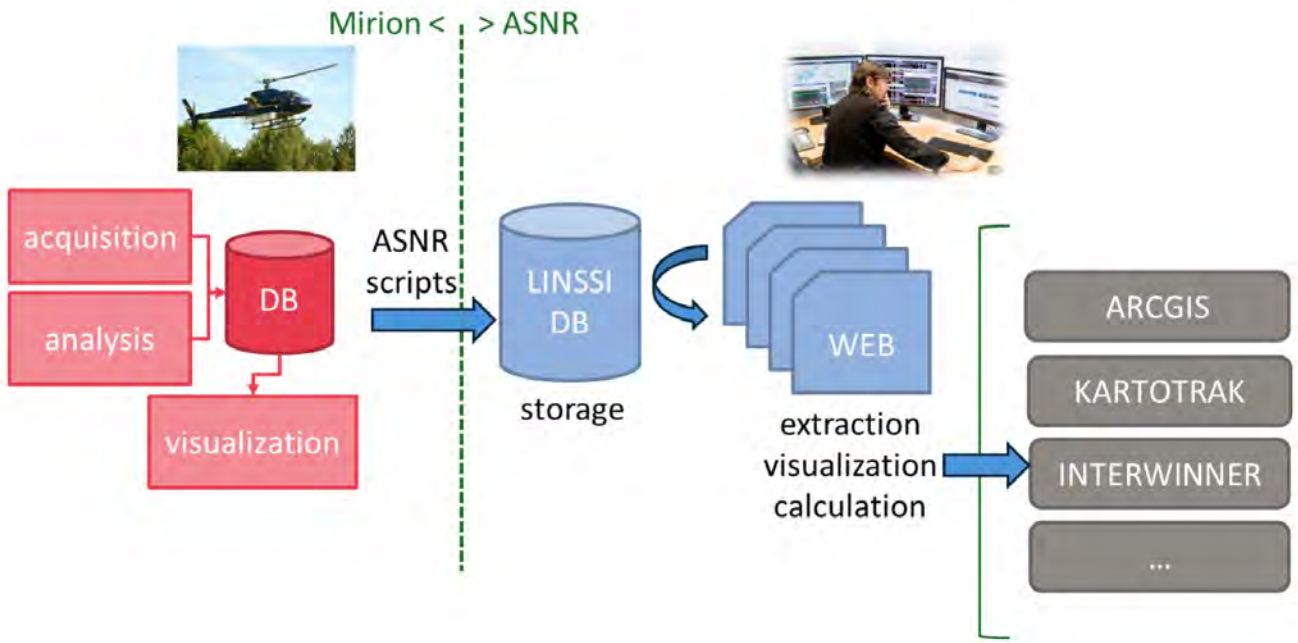

Figure 4.9: Scheme of ASNR processing suite.

Ambient dose equivalent rate 1 m above the ground

The evaluation of the gamma dose rate at $1\,\mathrm{m}$ above ground from aerial measurements can be performed either using the total spectral count rate (Eq. 4.2.0.24) or the local dose rate calculated with the standard weighted-windows method (Eq. 4.2.0.25). An exponential function, parametrised by an attenuation coefficient, is used to describe the altitude dependence of both the count rate and the local dose rate.

$$DR^{\mathrm{gnd}}_{1\,\mathrm{m}} = \alpha_{\mathrm{conv}} \left(N^{\mathrm{tot}}_{h} - N^{\mathrm{bckgnd}}_{h} \right) e^{\mu_N h} \tag{4.2.0.24}$$

$$DR^{\mathrm{gnd}}_{1\,\mathrm{m}} = \left(DR^{\mathrm{local}}_{h} - DR^{\mathrm{bckgnd}}_{h} \right) e^{\mu_{DR} h} \tag{4.2.0.25}$$

where h is the ground clearance, and N^{bckgnd}_{h} and DR^{bckgnd}_{h} denote, respectively, the count rate and

dose rate at the flight altitude that cannot be attributed to radiation originating from the ground (i.e. cosmic radiation, intrinsic background, radon progeny). The parameter α_{conv} converts count rate into dose rate.

Standard ASNR values for μ_N, μ_{DR}, and α_{conv} were determined during the Lake Mohave spiral experiment conducted as part of the joint ASNR–US DOE survey at the Nevada National Security Site (2017), whose results are summarised in Figure 4.10. The obtained ASNR values are $0.006\,\mathrm{m}^{-1}$, $0.0063\,\mathrm{m}^{-1}$, and $0.005\,92\,\mathrm{nSv\,h^{-1}\,cps^{-1}}$, respectively.

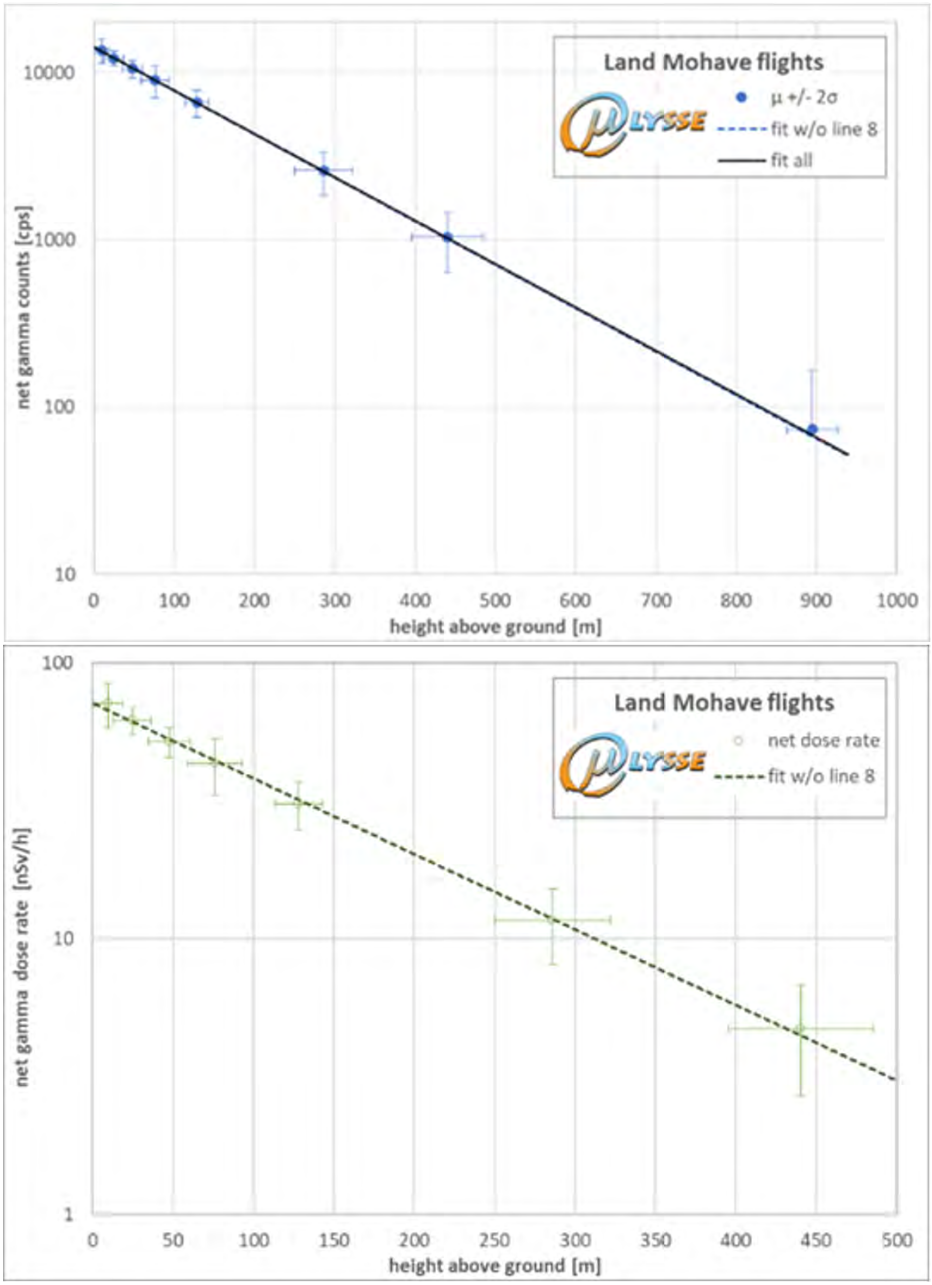

Figure 4.10: Net count rate and ambient dose equivalent rate vs. ground clearance. Spiral experiment at lake Mohave, joint survey with US-DOE (2017).

The set of coefficients used for the calculation of the local gamma dose rate using the weighted-windows method has been determined by Mirion, for a photon fluence normal to the $(40 \times 10)\,\mathrm{cm}^2$ face of the $4\,\mathrm{L}$ NaI unit. The ambient dose equivalent rate is then estimated applying a factor of 1.4, experimentally determined by ASNR, to the local gamma dose rate.

It should be noted that a single exponential dependence with altitude may not be suitable in situations involving ground contamination following an accident. In such cases, an exponential dependence would still be applied, but only for correcting the count rates or local ambient dose equivalent rates to the reference survey altitude (h_{ref}). The exponential parameters and conversion coefficients would then be determined from *in situ* ground measurements and flights at different ground clearances close to h_{ref}.

$$DR_{1\,\mathrm{m}}^{\mathrm{gnd}} = \alpha_{\mathrm{conv}}^{h_{\mathrm{ref}}} \left(N_h^{\mathrm{tot}} - N_h^{\mathrm{bckgnd}} \right) e^{\,\mu_N (h - h_{\mathrm{ref}})} \tag{4.2.0.26}$$

$$DR_{1\,\mathrm{m}}^{\mathrm{gnd}} = \beta_{\mathrm{conv}}^{h_{\mathrm{ref}}} \left(DR_h^{\mathrm{local}} - DR_h^{\mathrm{bckgnd}} \right) e^{\,\mu_{DR} (h - h_{ref})} \tag{4.2.0.27}$$

The cosmic contribution to the ambient dose equivalent rate, calculated using the following expression from Butterweck et al. (2018) (Appendix A), can then be added to the contribution from the ground:

$$DR_{1\,\mathrm{m}}^{\mathrm{COSM}} = 37\, e^{\,0.38\, z} \tag{4.2.0.28}$$

where z is the terrain altitude above sea level in km.

Activity concentration in the soil of ^{40}K, ^{238}U and ^{232}Th

The evaluation of the telluric ^{40}K, ^{238}U and ^{232}Th activity concentrations in the soil from aerial measurements follows the standard IAEA windows method [11]. The general expression relating ground concentrations to the count rates in the three spectral windows is given by:

$$\begin{pmatrix} n_K \\ n_U \\ n_{\mathrm{Th}} \end{pmatrix} = \begin{pmatrix} S_{K,K} & S_{K,U} & S_{K,\mathrm{Th}} \\ S_{U,K} & S_{U,U} & S_{U,\mathrm{Th}} \\ S_{\mathrm{Th},K} & S_{\mathrm{Th},U} & S_{\mathrm{Th,Th}} \end{pmatrix} \begin{pmatrix} c_K \\ c_U \\ c_{\mathrm{Th}} \end{pmatrix} \tag{4.2.0.29}$$

where $c_{\mathrm{K}}, c_{\mathrm{U}}$, and c_{Th} are the ground concentrations of ^{40}K, ^{238}U and ^{232}Th respectively, and $n_{\mathrm{K}}, n_{\mathrm{U}}$, and n_{Th} the count rates in the corresponding windows, after subtraction of the non-terrestrial background contribution. Parametrised expressions for the sensitivity coefficients $S_{i,j}$ as a function of ground clearance h were determined by Mirion via Monte Carlo simulations, in the form:

$$S_{i,j} = \left(a_{i,j}\, h^4 + b_{i,j}\, h^3 + c_{i,j}\, h^2 + d_{i,j}\, h + e_{i,j} h^0 \right)^{-1} \tag{4.2.0.30}$$

The inverted matrix $[\mathbf{S}]^{-1}$ provides the solution for $c_{\mathrm{K}}, c_{\mathrm{U}}$, and c_{Th} from the measured count rates $n_{\mathrm{K}}, n_{\mathrm{U}}$, and n_{Th}, which forms the basis of the calculations performed by the Mirion software. ASNR's post-processing of aerial measurements data is based on the $S_{i,j}$ coefficients provided by Mirion; however, it avoids explicit matrix inversion by using the relationships expressed through the stripping coefficients, as illustrated in Figure 4.11 and formalised in the following equations.

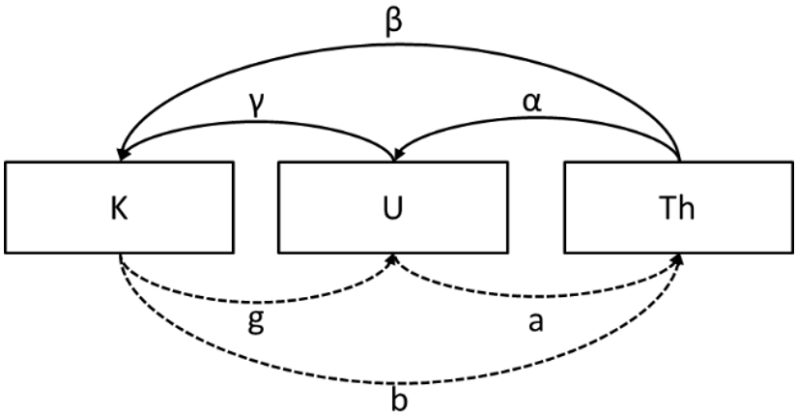

Figure 4.11: ^{40}K, ^{238}U and ^{232}Th stripping coefficients schematic representation.

$$n_{\mathrm{K}} = n_{\mathrm{K,K}} + \gamma\, n_{\mathrm{U,U}} + \beta\, n_{\mathrm{Th,Th}} \tag{4.2.0.31}$$

$$n_{\mathrm{U}} = g\, n_{\mathrm{K,K}} + n_{\mathrm{U,U}} + \alpha\, n_{\mathrm{Th,Th}} \tag{4.2.0.32}$$

$$n_{\mathrm{Th}} = b\, n_{\mathrm{K,K}} + a\, n_{\mathrm{U,U}} + n_{\mathrm{Th,Th}} \tag{4.2.0.33}$$

where, for instance, $\mathrm{n_{K,K}}$ is the count rate in the K window due to the K source. One can find that:

$$\begin{aligned} \alpha &= \frac{S_{U,\mathrm{Th}}}{S_{\mathrm{Th,Th}}} \qquad \beta = \frac{S_{K,\mathrm{Th}}}{S_{\mathrm{Th,Th}}} \qquad \gamma = \frac{S_{K,U}}{S_{U,U}} \\ a &= \frac{S_{\mathrm{Th},U}}{S_{U,U}} \qquad b = \frac{S_{\mathrm{Th},K}}{S_{K,K}} \qquad g = \frac{S_{U,K}}{S_{K,K}} \end{aligned} \tag{4.2.0.34}$$

With the assumption that b and g are negligible, the "net" count rates can be evaluated from measurements by:

$$n_{\mathrm{Th,Th}} = \frac{n_{\mathrm{Th}} - a\, n_U}{1 - a\alpha}\,, \qquad n_{U,U} = \frac{n_U - \alpha\, n_{\mathrm{Th}}}{1 - a\alpha}\,, \qquad n_{K,K} = n_K - \beta\, n_{\mathrm{Th,Th}} - \gamma\, n_{U,U} \tag{4.2.0.35}$$

and finally, the ground concentrations by:

$$c_K = \frac{n_{K,K}}{S_{K,K}}\,, \qquad c_U = \frac{n_{U,U}}{S_{U,U}}\,, \qquad c_{\mathrm{Th}} = \frac{n_{\mathrm{Th,Th}}}{S_{\mathrm{Th,Th}}} \tag{4.2.0.36}$$

with the sensitivities and stripping coefficients being calculated for each $1\,\mathrm{s}$ measurement using the formulas described previously (see Figure 4.12).

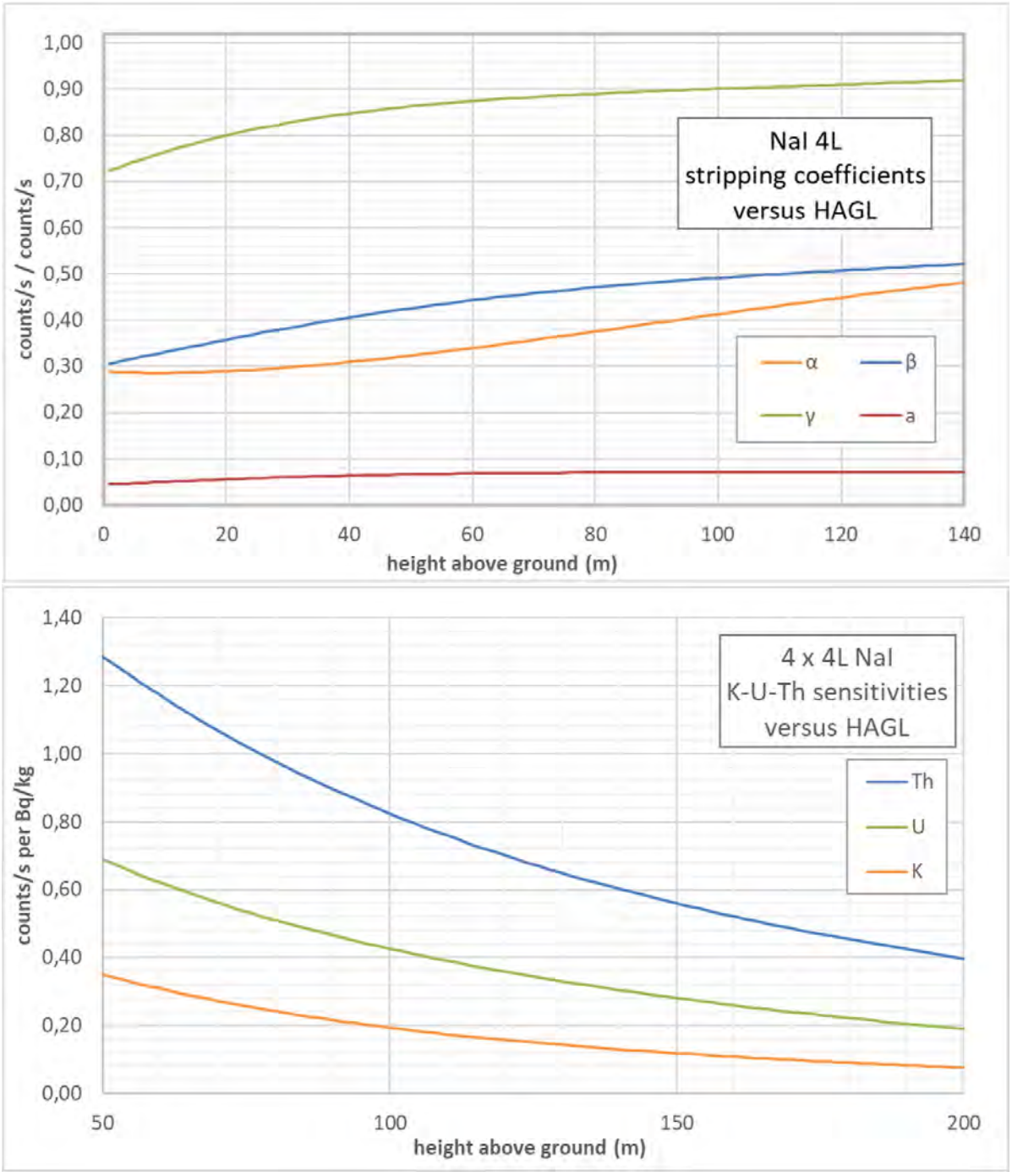

Figure 4.12: Stripping coefficients (upper panel) and sensitivity for KUTh (lower panel) vs. height above ground for ASNR AMS.

Note that the soil model used by Mirion in their Monte Carlo simulations is a *dry soil, standard terrestrial basalt*, with a density of $2.4\,\mathrm{g\,cm^{-3}}$, and without water. For in-situ measurements, ASNR typically uses *soil number 3* as defined in [7], which contains $10\,\%$ water and has a density of $1.6\,\mathrm{g\,cm^{-3}}$. It can be shown that the attenuation properties of the two soil types are not significantly different.

Background assessment

The elimination of non-terrestrial background contributions is mandatory before calculating ^{40}K, ^{238}U and ^{232}Th activity concentrations or the ambient dose equivalent rate, for example. The most reliable

method for estimating background is to conduct a flight over a water body near the survey area; however, this is often not feasible.

Analysis of various ASNR flights over water bodies (mainly during intercomparison exercises) indicates that the background can vary over a wide range, as shown in the top panel of Figure 8.65. This high sensitivity can be attributed to the design of the ASNR aerial measurement system, which employs four individual units mounted in external baskets, exposing all four faces to atmospheric radon progeny.

Cross-plots between count rates from different windows or the local dose rate exhibit linear correlations (see Figure 8.66). These correlations were used to generate a table of background parameters for radon conditions ranging from low to high (Table 4.5).

From a practical standpoint, the optimal set of coefficients is that which provides consistent evaluations of ground activity concentrations at different altitudes during a hovering flight over a reference location in the survey area, supplemented by *in situ* ground measurements where available.

Table 4.5: Background coefficients sets

DHSR [nSv/h]	Total counts	^{40}K	^{238}U	^{232}Th
5.2	695	11.9	6.3	$5-6$
5.9	765	13.1	8.2	$5-6$
6.5	836	14.4	10.1	$5-6$
7.2	907	15.6	12.1	$5-6$
7.8	977	16.8	14.0	$5-6$
8.5	1048	18.1	15.9	$5-6$
9.1	1118	19.3	17.8	$5-6$
9.8	1189	20.5	19.7	$5-6$
10.4	1259	21.8	21.6	$5-6$
11.1	1330	23.0	23.5	$5-6$
11.7	1400	24.2	25.4	$5-6$
12.4	1471	25.5	27.3	$5-6$
13.0	1542	26.7	29.2	$5-6$
13.7	1612	27.9	31.2	$5-6$
14.3	1683	29.2	33.1	$5-6$
15.0	1753	30.4	35.0	$5-6$
15.6	1824	31.6	36.9	$5-6$
16.3	1894	32.9	38.8	$5-6$
16.9	1965	34.1	40.7	$5-6$
17.6	2035	35.3	42.6	$5-6$
18.2	2106	36.6	44.5	$5-6$
18.9	2176	37.8	46.4	$5-6$

Sources detection and quantification

The Mirion software suite provides an algorithm called SIA for radionuclide identification and quantification, specifically designed for Homeland Security applications in accordance with the ANSI N42.38 standard [12] and IEC 62484 standard [13]. This algorithm has been optimised to provide rapid decisions even with low-quality spectra resulting from short acquisition times. It operates by

analysing numerous regions of interest (over 70 ROIs), accounting for an interference matrix, and applying a partial deconvolution process.

The SIA algorithm can handle multi-isotope sources (set to identify up to four isotopes simultaneously along with background) and provides, for each known isotope, a confidence level and a quantification expressed in counts per second. This quantification can be converted into activities for either surface contamination ($\mathrm{Bq\,m^{-2}}$) or a point source (Bq), using specific Mirion formulas and parameters.

ASNR also provides tools for the detection and quantification of artificial radioactivity from acquisition data, including the MMGC ratio method, various window-based metrics, and peak deconvolution algorithms (InterWinner).

Monte Carlo simulations (using Penelope) were performed to evaluate the three-dimensional response of the NaI elementary units to direct photon flux, as illustrated in Figure 4.13.

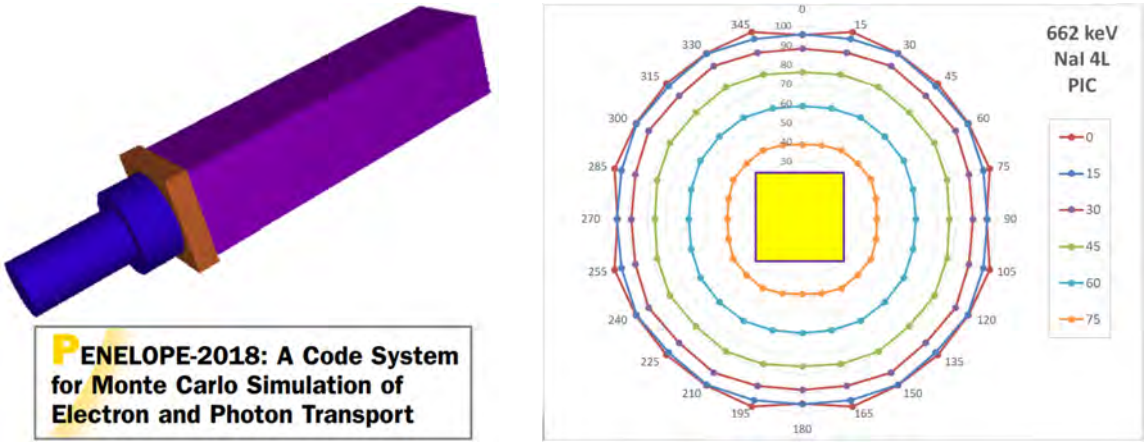

Figure 4.13: 3D Monte-Carlo simulation of $4\,\mathrm{L}$ NaI unit response to photon flux.

A transport code has been developed to reproduce aerial measurements of point sources. It is based on standard photon transport theory for photon flux and the three-dimensional response obtained from Monte Carlo simulations. This tool can be used for source search tasks to determine the location and activity of a source by optimising its position on a grid (see Figure 4.14) so as to best reproduce the acquired data (see Figure 4.15).

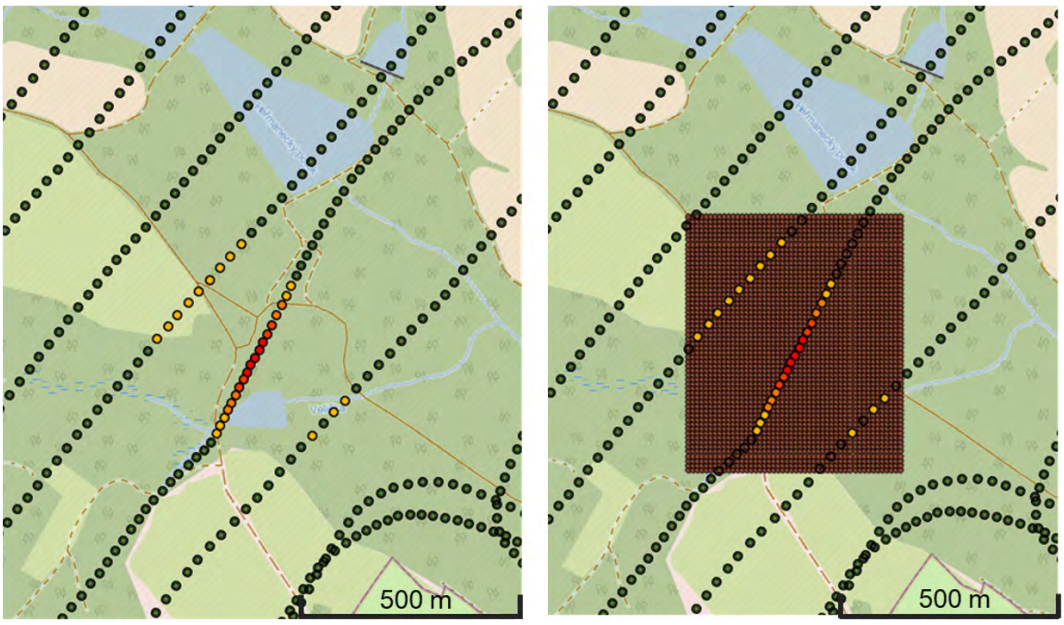

Figure 4.14: Measurement points and grid for source location optimisation.

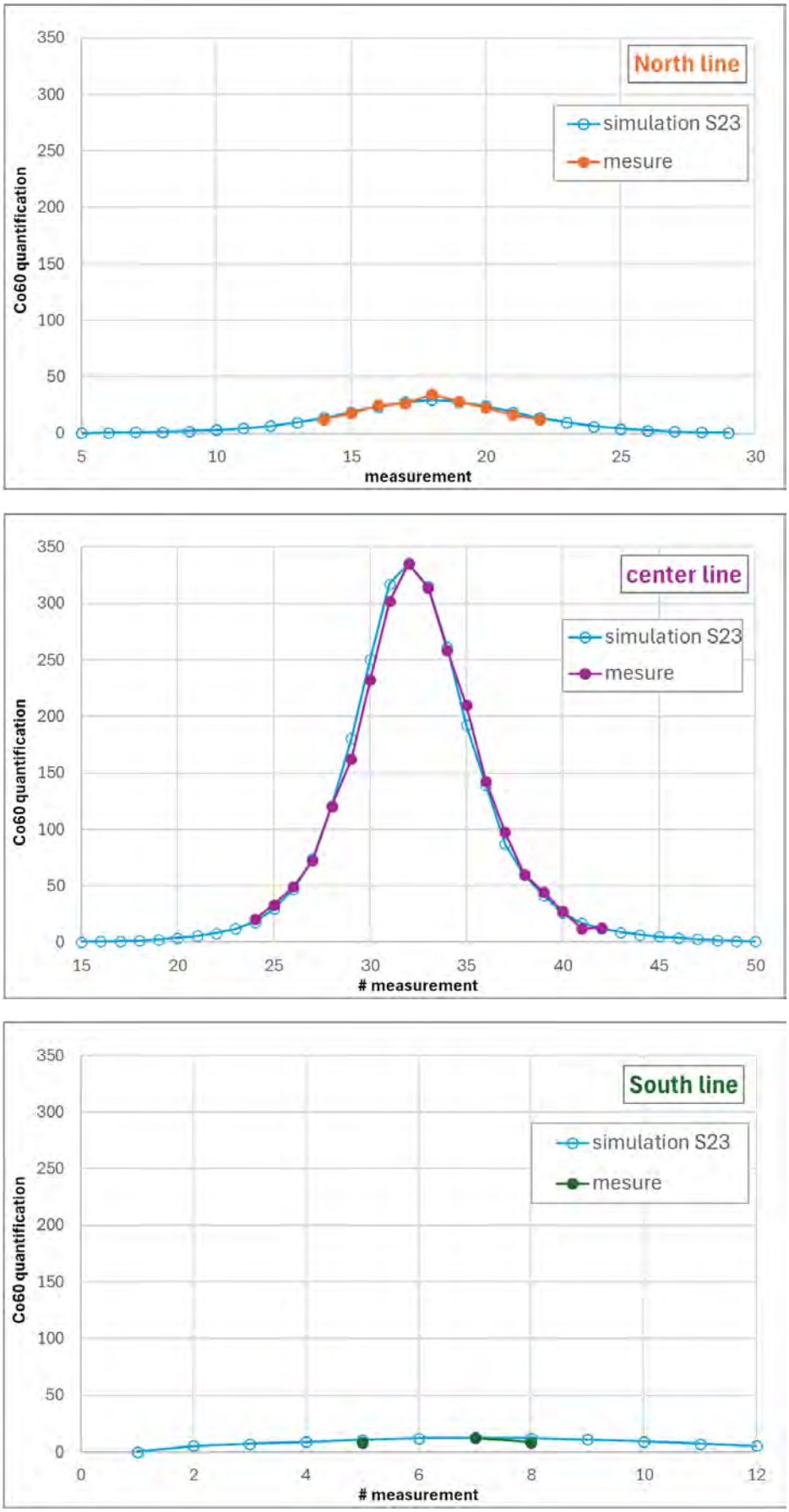

Figure 4.15: Measurement reproduction using direct photon transport code and ASNR AMS 3D response to photon flux (AGC24 Mission 3, source search).

4.3 Team DEU

For both data acquisition and post-processing, BfS utilises in-house developed software.

Data acquisition

During the flight, energy spectra are measured simultaneously with all employed detector types (HPGe, NaI(Tl), dose rate meters, etc.) using BfS's data acquisition software, CFS (Control Flight Server). Spectra, ambient dose equivalent rates, specific activities, and detector parameters are displayed directly on the operator's screen via the graphical user interface of PISA (Programmable Interface for Spectrometry Applications), enabling online monitoring of measured radionuclide activities. In addition, the helicopter's position is continuously tracked via GPS to accurately geolocate the radionuclide measurements, and the flight altitude is recorded using a radar altimeter.

After landing, the ambient dose equivalent rate, the specific activities of natural radionuclides (^{40}K, ^{238}U, and ^{232}Th), and the surface contamination due to artificial radionuclides (e.g. ^{137}Cs) are calculated from the NaI(Tl) or HPGe spectra at each point along the flight path. Within approximately 20 minutes, the radiological situation along the flight trajectory can be visualised on digital maps, allowing regions of low or elevated concentrations of natural and artificial radionuclides to be easily identified.

Post-processing

For post-processing, BfS uses its software *Rohflug*. In calculations that include the full-energy photo-peak of NaI(Tl) spectra or the pulses contained therein, the so-called window method is used. This method involves setting energy windows around the photon emission energies of natural and artificial radionuclides to be analysed. Each window is defined by an upper and lower limit, as well as an average energy corresponding to the photo-peak energy. All pulses falling within the defined window are assigned to the corresponding photon energy. This approach ensures that spectral analysis can be performed even with low counting statistics and without a clearly defined peak in the pulse height spectrum. The radionuclides evaluated using this method as standard are ^{40}K, ^{238}U, ^{232}Th, ^{137}Cs, and ^{60}Co.

The counting pulses obtained using the window method need to be adjusted by the background correction, the flight altitude correction, and the so-called stripping procedure, in which contributions from other radionuclides and photon energies are subtracted from the window of interest. In fact, due to scattering processes in the air, the ground, and the detector itself, photons originating from radionuclides with higher energies can also contribute counts in lower-energy windows. To obtain the net count rate in each energy window, these contributions must be removed by applying the stripping procedure to each NaI(Tl) spectrum. The stripping coefficient matrix, shown in Table 4.6, is determined from measurements on a set of calibration pads that were produced mixing potassium, uranium, and thorium in a predetermined concentration. The stripping matrix for the German measurement systems is scheduled to be updated in the coming years.

Table 4.6: Matrix of stripping coefficients.

	^{137}Cs	^{40}K	^{238}U	^{232}Th
^{232}Th	0.000	0.000	0.090	–
^{238}U	0.000	0.000	–	0.330
^{40}K	0.000	–	0.990	0.570
^{137}Cs	–	0.570	2.660	1.680

For the calculation of specific activities, a height correction is performed, in which the values at the actual flight altitude for each measurement point are being normalised to a reference altitude. Then specific activities are estimated applying experimentally determined calibration factors described in Schütz et al. [14].

For the calculation of ambient gamma dose rates from the measurement data, the net counts in the total count window (250 keV – 3000 keV), once adjusted to the reference altitude, are being multiplied with a corresponding conversion coefficient described in ICRP 74 [15].

For the evaluation of the HPGe-spectra, a program especially adapted to low counting statistics is used. It identifies the total absorption peaks of the individual radionuclides and calculates their net count rate.

4.4 Team LTU

All aerial data acquisition, ground-level adjustment, and radioactive source identification were conducted online (excluding quantification of detected radioactive sources) during the mission using the commercially available software iAVID. iAVID is a software framework with associated modules for real-time acquisition, visualization, and analysis of radiation data from aerial and mobile detection systems. It supports mission planning, data collection from multiple sensors, visualization and analysis of incoming or uploaded radiological data, processing of georeferenced spectral data into quantitative radiation levels, and data transmission to cloud services for remote monitoring and adjudication by users. Post-processing correction of results was required because the reference measurements at the Mission 1 site were conducted only on the final day of AGC2025. The source identification windows in iAVID are shown in Figure 4.16. Quantification of identified sources during Mission 5 and Mission 3 was performed using InterSpec (Sandia Labs), an open-source application for the analysis of spectral nuclear radiation data using a peak-based methodology. The relative efficiency curve for the $2 \times 4 \times 16$ NaI log($932\,\%$) available in the InterSpec database was applied for spectral analysis and estimation of source activity (see Figure 4.17).

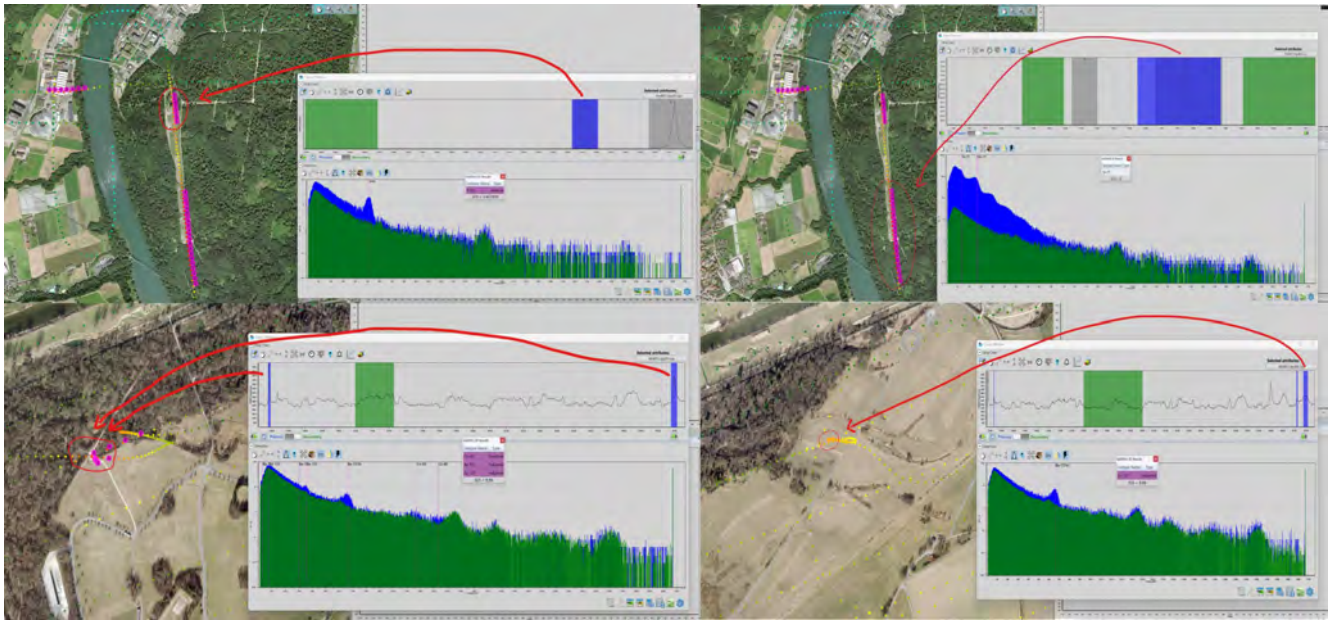

Figure 4.16: Examples of online source identifications in iAVID software.

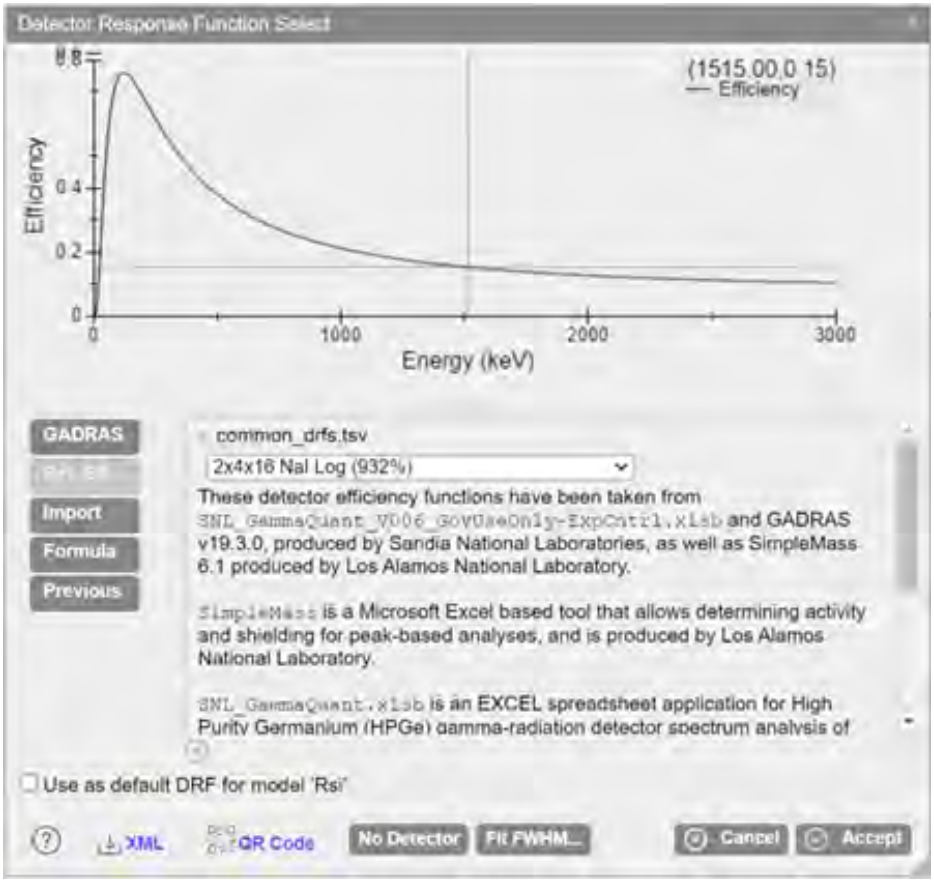

Figure 4.17: Screenshot of InterSpec efficiency curve used for radioactive source quantification.

For the naturally occurring radioactive material (NORM) mapping on the ground from aerial measurements the one window method and the Gaussian extraction approach was applied (fitting a Gaussian function to the primary photo-peaks of interest: potassium (K), natural uranium (U) natural thorium (Th) to extract counts above the continuum in each of those windows.

Preparation of the system for selected NORM mapping was done in accordance with spiral flight procedure described by P. Wasiolek [16]. The height attenuation coefficient per NORM element was determined empirically from an altitude spiral flight pattern, when single circuit flight pattern involved flying over the land at a fixed altitude, followed by flying over the water at the same altitude.

Conversion coefficients for NORM were adjusted based on the activity concentration [$\mathrm{Bq\,kg^{-1}}$] in-situ and dose rate [$\mathrm{nSv/h}$] ground measurements at Mission 1 Thun Military Area provided during AGC2025 in post-processing. It was not possible to adjust a system for searching point ^{137}Cs and a ^{60}Co sources based on provided by AGC 2025 in-situ measurements, because it was not possible to fly over located sources. Thus, the detection and quantification of artificial point source was done based on calibration coefficients obtained in the preparation phase, implementing flights over ^{137}Cs ($450\,\mathrm{MBq}$) source at different altitude and angels. Comparison of initial and adjusted conversion coefficients are provided in Table 4.7. The background subtraction and extrapolation to the ground was done based on adjusted Beer–Lambert law:

$$\mathrm{f_{e,cal}} = \alpha\,(\mathrm{f_e} - \mathrm{f_{e,0}})\; e^{\beta(\mathrm{z}-\mathrm{z_0})} \tag{4.4.0.37}$$

where,

$\mathrm{f_{e,cal}}$ – is the pointwise calibrated value for the appropriate element at ground level
α – conversion coefficient ($\mathrm{nSv\,h^{-1}}$ or $\mathrm{Bq\,kg^{-1}}$ per count)
$\mathrm{f_e}$ – is the pointwise detector measurement value (in cps) for the appropriate energy region at the aircraft height

$f_{e,0}$ – is the mean background value (in cps) for the appropriate energy region at the aircraft height
β – the energy dependent height attenuation coefficient in m^{-1}
z – the height above ground in m
z_0 – reference altitude to which the calibrated conversion correction is applied (typically 1 m above ground level (AGL))

Table 4.7: Ground calculation coefficients.

Quantity	Units	Energy window [keV]			α [value per cps]		β [m^{-1}]
		Left	Right	Centroid	Host	Corrected based on AGC25 in-situ	
DHSR	$\mu\mathrm{Sv\,h^{-1}}$	–	–	–	$3.306\ 10^{-5}$	$7.6245\ 10^{-5}$	0.0059
AW_K-40	$\mathrm{Bq\,kg^{-1}}$	1338	1578	1461	0.00024	4.4938	0.0082
AW_U-238	$\mathrm{Bq\,kg^{-1}}$	1671	1869	1764	0.15	1.0502	0.0084
AW_Th-232	$\mathrm{Bq\,kg^{-1}}$	2469	2793	2614	0.36	1.1613	0.0066
AA_Cs-137	$\mathrm{Bq\,m^{-2}}$	600	620	661	1.61	0.1951	0.013

4.5 Team CHE1 & CHE2

4.5.1 The Swiss Airborne Gamma-Spectrometry (AGS_CH) Software

Since 2000, the software MGS32 developed by the Research Group for Geothermics and Radiometry of the Institute of Geophysics of the Swiss Federal Institute of Technology Zurich (ETHZ) (Bucher, 2001) [17] had been used. The proprietary software for data evaluation provided by the manufacturer of the RLL system, in use since 2017, was tested sufficient for supplying data to support decisions in radiological emergencies (Appendix A). Thus, with the introduction of the RLL system, a new evaluation software, named AGS_CH, was published. AGS_CH is restricted to off-line evaluation following measurement and complements the proprietary RLL software by focusing on the investigation of scientific aspects and by providing a testbed for new algorithms for the evaluation of airborne gamma spectrometry data.

AGS_CH, was written in Visual Basic under the .net environment, using Microsoft Forms. The use of an additional mapping tool from a third party vendor was rejected to reduce dependencies of the code. The possibility of XAML-Islands in Microsoft Forms allowed to include a sufficient mapping functionality for a fast overview of results. Necessary geographic transformations and projections are programmed directly into the code. The results are exported in plain text formats readable by Geographic Information Systems (GIS), which are used for the production of final maps for publishing. Starting with the exercise of this year, the software AGS_CH is used to produce the data presented in the PSI reports without further indication. Results derived with a different evaluation software are flagged accordingly in the text.

The AGS_CH software follows the evaluation algorithm described in Schwarz (1991) [2, 18], based on the "window-method". The impulses in eight photon energy windows of each spectrum are summed for further evaluation (Table 4.8). The right hand column of Table 4.8 notes the energy of the relevant photon emission. The “total” energy window sums counts for photon energies between $401\,\mathrm{keV}$ and $2997\,\mathrm{keV}$.

Three energy windows are associated with natural radionuclides. The “potassium” window measures photon emissions of ^{40}K at $1461\,\mathrm{keV}$. The determination of the activities of uranium and thorium utilises high energy emissions of the decay products ^{214}Bi and ^{208}Tl to minimise absorption losses in the air between the ground and the detector.

Four energy windows are employed for the determination of artificial radioactivity. Those at $662\,\mathrm{keV}$ and $1250\,\mathrm{keV}$ measure the emissions of ^{137}Cs and ^{60}Co, respectively. The remaining two MMGC (Man Made Gross Count) energy windows measure in the photon energy interval $401\,\mathrm{keV}$ to $1400\,\mathrm{keV}$ (MMGC1) radiation from artificial and natural radionuclides and in the photon energy interval $1400\,\mathrm{keV}$ to $2997\,\mathrm{keV}$ (MMGC2) mainly natural radionuclides. The ratio of the count rates in these energy windows can be used for the search of artificial radioactive sources.

Additional to the acquired spectra, a special channel is dedicated for the measurement of photon energies between $2900\,\mathrm{keV}$ and $3500\,\mathrm{keV}$. This channel is used to determine the fraction of the measured counts in the spectra, which are correlated to cosmic radiation. Simplifying, this channel (measured separately from the spectrum) is called the cosmic window.

Table 4.8: Energy windows for data evaluation with AGS_CH (CHE1 & CHE2).

Window	Lower energy limit [keV]	Upper energy limit [keV]	Full energy peak [keV]
Total	400	2997	–
Potassium (^{40}K)	1369	1558	1461
Uranium (^{214}Bi)	1664	1853	1765
Thorium (^{208}Tl)	2407	2797	2615
Caesium (^{137}Cs)	600	720	662
Cobalt (^{60}Co)	1100	1400	1173, 1332
MMGC1	400	1400	–
MMGC2	1400	3000	–
Cosmic	2900	3500	–

The photons registered in the detector origin from several different sources. Goal of the measurement is the determination of the part of the signal, which is correlated to radionuclides in the soil. The signal has to be reduced in respect to other sources of photon radiation, which therefore have to be identified and quantified. Additionally, the measuring signal is dependent on several influencing parameters, which may vary during a measuring flight. For optimum quality of the derived results, the influence of these parameters has to be corrected. The steps for data processing are described in the following sections in detail. Corrections are applied either in the energy windows described above or for each channel of the spectrum separately.

Dead time correction

During the processing of an impulse, the detector and spectrometer are blocked from registering further impulses. This effect reduces the number of counted impulses at high count rates. The dead time of the spectrometer is measured directly and can be utilised for the according correction.

$$CR_{corr,t} = CR_{raw} \frac{t_{meas}}{t_{meas} - t_{dead}} \tag{4.5.1.0.38}$$

with:

$CR_{corr,t}$: Deadtime corrected count rate [cps]
CR_{raw}: Measured count rate [cps]
t_{meas}: Measuring time of the spectrometer [s]
t_{dead}: Time during which the spectrometer was blocked [s]

Detector background and cosmic radiation

The detector measures photons which originate from the detector itself and the surrounding helicopter. Both components are assumed constant for a specific combination of detector and helicopter. To this background is added a second component generated by cosmic radiation. The primary cosmic radiation consists of $87\,\%$ protons, of $12\,\%$ alpha particles and of $1\,\%$ heavy nuclei. Photons are generated during interaction of the primary cosmic radiation with the atmosphere. The effect of these photons on the measuring signal is dependent on elevation, air pressure and latitude. A linear relationship between the count rate produced by cosmic radiation in any channel of the

spectrum and the count rate in the cosmic window was found experimentally. Thus, the count rate in the cosmic window can be used for the direct correction in other energy windows. The correction for background and cosmic radiation can be formulated as

$$CR_{corr,B} = CR_{corr,t} - (CR_B + S_c CR_c) \tag{4.5.1.0.39}$$

with:

$CR_{corr,B}$: Background corrected count rate [cps]
CR_B: Background count rate of detector and helicopter [cps]
CR_c: Count rate in cosmic window [cps]
S_c: Cosmic correction factor [-]

The two constants, CR_B and S_c, are determined from ascents over large water bodies. Owing to the absorption of radiation by water, terrestrial radiation is largely suppressed, allowing direct measurement of the term $CR_B + S_c CR_c$ for each energy window. The background is independent of flight altitude, whereas the contribution of cosmic radiation increases with altitude. These two effects can therefore be disentangled through linear regression of the measured count rates. As discussed in Butterweck et al. (2021) (Appendix A), the small size of the cosmic energy window introduces relatively large statistical uncertainties in the cosmic count rate. For this reason, a methodology based on Deming regression [19] for estimating CR_B and S_c has been proposed and has been in use since 2020.

The background and cosmic correction of the Swiss AGS_CH system is based on a series of altitude profile measurements acquired in previous years over Swiss lakes, supplemented by the most recent results from background measurements over Lake Thun during Mission 2 (see Section 8.3.1). Table 4.9 summarises the slopes of the Deming regression derived from these measurements, together with the average slope adopted as the estimator for the cosmic correction. Using this average slope, the intercepts of the linear model for cosmic correction can be calculated, representing the constant background of the measuring system. Table 4.10 presents the backgrounds based on the average slopes reported in Table 4.9. Since the estimated cosmic background is the outcome of a process involving averaging, negative values may arise when values lie particularly close to zero. As noted in previous reports (Appendix A), airborne radon and its progeny may influence this methodology. Results should therefore be carefully inspected and excluded in cases of large deviations relative to others.

The background and slope used for the data evaluation of the current exercise are stored under the identifiers ISWB_winname and ISWC_winname in the header Section of all ERS 2.0 files (see Section C) generated for AGC25 data evaluation.

Table 4.9: Determination of the average slope for cosmic correction (S_c) from seven altitude profiles with sufficient altitude range.

	Slope of cosmic correction [–]						
Energy Window	Total	^{40}K	^{238}U	^{232}Th	^{137}Cs	^{60}Co	SDI
Lake Constance 2023c	4.11	0.23	0.13	0.30	0.17	0.36	3.15
Lake Geneva 2018c	5.20	0.28	0.21	0.29	0.45	0.60	3.96
Lake Neuchâtel 2019c	5.48	0.31	0.23	0.26	0.60	0.66	4.09
Lake Neuchâtel 2021c	5.68	0.33	0.23	0.29	0.57	0.72	4.28
Lake Neuchâtel 2021m	6.32	0.35	0.27	0.30	0.75	0.76	4.70
Lake Thun A 2022c	6.32	0.48	0.30	0.33	0.91	1.09	4.66
Lake Thun B 2022c	7.17	0.41	0.32	0.31	0.92	0.80	5.21
Lake Thun CHE1 2025	4.93	0.28	0.22	0.24	0.50	0.57	3.70
Lake Thun CHE2 2025	4.10	0.18	0.13	0.10	0.32	0.37	3.09
Lake Zug 2017c	5.96	0.31	0.25	0.29	0.69	0.70	4.51
Average	5.53	0.32	0.23	0.27	0.59	0.66	4.14
Standard deviation	0.98	0.09	0.06	0.07	0.24	0.21	0.68

Table 4.10: Determination of the background count rate (CR_B) using the average slope of cosmic stripping from Table 4.9.

	Background count rate [cps]						
Energy Window	Total	^{40}K	^{238}U	^{232}Th	^{137}Cs	^{60}Co	SDI
Lake Constance 2023c	124	8	6	0.3	20	12	85
Lake Geneva 2018c	147	10	7	0.3	23	15	101
Lake Neuchâtel 2016c	129	7	6	1.2	21	10	88
Lake Neuchâtel 2019c	104	8	5	−1.0	16	10	70
Lake Neuchâtel 2021c	121	8	5	0.0	18	11	84
Lake Neuchâtel 2021m	145	9	7	0.4	23	14	98
Lake Neuchâtel 2022m	111	7	6	−0.8	19	10	74
North Sea 2018c	34	4	0	−0.1	5	1	22
Lake Thun A 2020c	73	6	3	−0.4	11	6	48
Lake Thun B 2020c	73	5	3	−0.4	11	6	48
Lake Thun A 2022c	134	9	6	−0.1	22	13	91
Lake Thun B 2022c	157	9	8	0.6	25	15	109
Lake Thun CHE1 2025	80	6	4	−0.3	13	7	53
Lake Thun CHE2 2025	77	5	4	−1.4	13	7	50
Lake Zug 2017c	56	5	2	−0.2	8	3	38

Energy resolution and Compton scattering

Several factors may cause a photon emitted by a radionuclide on or in the ground to be registered in an energy window associated with a different radionuclide:

- Photons emitted from the soil may undergo Compton scattering in the soil itself, in vegetation, in buildings, in the air between the surface and the helicopter, and even within the detector. The associated energy loss can lead to the photon being registered in a lower-energy window.
- The relatively poor energy resolution of a NaI(Tl) detector, compared with modern solid-state detectors, increases the likelihood that photons with energies close to the boundaries of a window are incorrectly recorded in an adjacent energy window.
- The parent radionuclides ^{238}U and ^{232}Th produce complete decay chains, emitting photons across the entire energy spectrum.

The influence of these effects on the signal is determined experimentally. Corrections are then applied to account for unwanted contributions from other nuclides to the signal in a given energy window, using stripping factors. These stripping factors are derived in the laboratory with point sources placed approximately $1\,\mathrm{m}$ from the detector. For the naturally occurring radionuclides ^{40}K, ^{238}U, and ^{232}Th, the laboratory-derived values are further adjusted to represent infinite, homogeneously distributed sources measured at a ground clearance of $100\,\mathrm{m}$, following the methodology described by Schwarz (1991) [2].

Accordingly, the corrected count rate $CR_{corr,B}(i)$ in energy window i is expressed as the sum of contributions from all photon sources j, each weighted by a stripping coefficient fi,j.

$$CR_{corr,B}(i) = \sum_{j=1}^{8} f_{i,j}\, CR_{corr,S}(j) \tag{4.5.1.0.40}$$

with:

$CR_{corr,B}(i)$: Background corrected count rate measured in energy window i [cps]
$CR_{corr,S}(j)$: Background corrected count rate measured in the energy window of source component j [cps]
$f_{i,j}$: Stripping coefficient of component j into energy window i [-]

For the derivation of the contributions of the different photon sources $CR_{corr,S}(j)$ from measured count rates $CR_{corr,B}(i)$, the system of linear Equations has to be solved. The Equation above can be formulated as

$$\overline{CR}_{corr,B} = \overline{\overline{f}}\ \overline{CR}_{corr,S} \tag{4.5.1.0.41}$$

with:

$\overline{CR}_{corr,B}$: Vector of background corrected count rates in the eight energy windows [cps]
$\overline{CR}_{corr,S}$: Vector of background corrected count rates measured in the energy windows of source components [cps]
$\overline{\overline{f}}$: Matrix of stripping coefficients [-]

Matrix $\overline{\overline{f}}$ is then inverted with the help of the LU-decomposition (reduction to two triangular matrices, L(ower) and U(pper)), which yields

$$\overline{CR}_{corr,S} = \overline{\overline{f}}^{-1}\ \overline{CR}_{corr,B} \tag{4.5.1.0.42}$$

with:

$\overline{\overline{f}}^{-1}$: Inverted matrix of stripping coefficients [-]

The stripping coefficients $f_{i,j}$ can be determined with measurements of radioactive point sources near to the detector, which are then corrected for altitude and scattering in soil for the natural radionuclides.

$$f_{i,j} = g_{i,j} + f_{i,j,point} \tag{4.5.1.0.43}$$

with:

$f_{i,j,point}$: Stripping coefficients derived from measurements with point sources [-]
$g_{i,j}$: Correction for altitude and scattering in soil [-]

Table 4.11 gives an overview on the current stripping factors of the four Swiss systems, with the values of detector RLL 004 determined for three of the four NaI crystals, due to quality issues. The stripping factors are stored under the ISWS identifier in the header of the ERS 2.0 data files (Appendix C).

Table 4.11: AGS_CH stripping factors for relevant energy windows of the RLL detectors.

Detector		RLL 001	RLL 002	RLL 003	RLL 004
Year		2020	2024	2022	2021
"from"-window	"to"-window	Stripping factor			
Uranium	Potassium	0.93	0.95	0.98	0.92
Thorium	Potassium	0.48	0.46	0.50	0.47
Cobalt	Potassium	0.07	0.06	0.05	0.04
Thorium	Uranium	0.36	0.33	0.34	0.34
Uranium	Thorium	0.05	0.06	0.06	0.05
Potassium	Caesium	0.45	0.44	0.48	0.37
Uranium	Caesium	3.16	3.21	3.18	2.78
Thorium	Caesium	1.65	1.59	1.64	1.44
Cobalt	Caesium	0.15	0.13	0.13	0.12
Potassium	Cobalt	0.76	0.75	0.79	0.66
Uranium	Cobalt	2.37	2.35	2.32	2.26
Thorium	Cobalt	0.68	0.66	0.63	0.65

Altitude, air pressure, air temperature and atmospheric radioactivity

Normalisation of the measured data to a fixed altitude of $100\,\mathrm{m}$ above ground improves the comparability of the multitude of point measurements along the flight lines. An exponential dependence between photon attenuation and altitude is assumed.

$$CR_{corr,h} = CR_{corr,S}\frac{e^{-\mu_{ref}h_{ref}}}{e^{-\mu h}}; \quad \mu = \mu_{ref}\frac{T_{ref}}{T}\frac{P}{P_{ref}} \tag{4.5.1.0.44}$$

with:

$CR_{corr,h}$: Count rate corrected to reference altitude h_{ref} [cps]
μ_{ref}: Attenuation coefficient at reference conditions [m^{-1}]
μ: Attenuation coefficient at measurement conditions [m^{-1}]
h_{ref}: Reference altitude h_{ref} = $100\,\mathrm{m}$
h: Altitude above ground [m]
T_{ref}: Reference temperature T_{ref} = $273.15\,\mathrm{K}$
T: Air temperature [K]
P_{ref}: Reference pressure P_{ref} = $101\,325\,\mathrm{Pa}$
P: Air Pressure [Pa]

A more complex method, which takes into account topographic effects with the help of the terrain digital elevation model (DEM) can be used. The attenuation coefficients for the respective radiation components are determined with ascents over flat terrain. The measured net counts for different altitudes are fitted to an exponential curve using the least squares method. The so determined attenuation coefficient is extrapolated with the measured values of air temperature and air pressure to the reference conditions. The attenuation coefficients determined and normalised to reference conditions are listed in Table 4.12 together with the uncertainties according to GUM (extension factor $k = 1$).

Table 4.12: Experimentally determined attenuation coefficients.

Component	μ_{ref} [m^{-1}]	$U(\mu_{\mathrm{ref}})$ [m^{-1}]
Total	$6\ 10^{-3}$	$3\ 10^{-4}$
^{40}K	$8\ 10^{-3}$	$2\ 10^{-4}$
Uranium	$5.5\ 10^{-3}$	$3\ 10^{-4}$
Thorium	$6\ 10^{-3}$	$3\ 10^{-4}$
^{137}Cs	$1\ 10^{-2}$	$6\ 10^{-4}$
^{60}Co	$8\ 10^{-3}$	$2\ 10^{-4}$
MMGC1	$6\ 10^{-3}$	$3\ 10^{-4}$
MMGC2	$6.5\ 10^{-3}$	$3\ 10^{-4}$
SDI	$5.3\ 10^{-3}$	$3\ 10^{-4}$

Specific activity calibration

Activity concentrations of radionuclides in soil can be estimated from the normalised measured count rates $CR_{corr,h}$. In the case of natural radionuclides, a homogeneous distribution in soil is assumed, whereas for artificial radionuclides the activity is assumed to be located in a thin layer of topsoil. The calibration factors (table 4.13) are determined by comparing the measured count rates with results from radioanalytical measurement of soil samples and in-situ gamma-spectrometric measurements.

Table 4.13: Experimentally determined calibration factors for activity concentration.

Component	Nuclide	Calibration factor $[\mathrm{Bq\,kg^{-1}\,cps^{-1}}]$
Potassium	^{40}K	6.37
Uranium	^{214}Bi	2.87
Thorium	^{208}Tl	1.42
Caesium	^{137}Cs	1.13

Surface activity calibration

The calibration factor from stripped count rate to surface activity concentration of $201\,\mathrm{Bq\,m^{-2}\,cps^{-1}}$ for ^{137}Cs was derived from the activity concentration per unit mass according to the procedure described in Butterweck et al. (2022) (Appendix A), where an exponential distribution of the radionuclide in the soil with a relaxation mass per unit area $\beta = 9.5\,\mathrm{g\,cm^{-2}}$ was used. The relation between the activity concentration per unit mass at the surface of the soil, in $\mathrm{Bq\,kg^{-1}}$, and total activity per unit surface A_S, in $\mathrm{Bq\,m^{-2}}$, integrated over the complete depth profile is:

$$A_S = A_{m,0}\,\beta \tag{4.5.1.0.45}$$

Ambient dose equivalent rate calibration

The specific activities determined in the previous paragraph are used to calculate the terrestrial ambient dose equivalent rate, $dH^*(10)/dt$, at one metre above ground, arising from both natural and anthropogenic sources. For measurements made using in-situ gamma spectrometry, the air kerma is estimated using the conversion factors listed in ICRU Report 53 [7]. Multiplication by factors of $1.1\,\mathrm{Sv\,Gy^{-1}}$ (for the uranium- and thorium-decay series) or $1.2\,\mathrm{Sv\,Gy^{-1}}$ (for caesium) yields the terrestrial ambient dose equivalent rate, assuming radioactive equilibrium within the decay series (Table 4.14).

Table 4.14: Ambient dose equivalent rate conversion factors.

Nuclide	Conversion factor $[\mathrm{nSv\,h^{-1}\,Bq^{-1}\,kg^{-1}}]$
^{40}K	0.044
^{214}Bi	0.55
^{208}Tl	0.77
^{137}Cs	0.20

The total terrestrial ambient dose equivalent rate is estimated using a second approach, which involves a direct calculation of the ambient dose equivalent rate via the spectrum dose index (SDI) method. This methodology utilises the energy deposited in the detector as a direct measure of the ambient dose equivalent rate, $dH^*(10)/dt$. The dose delivered by a photon is assumed to be proportional to its energy. Thanks to the automatic gain stabilisation of the measuring system using the ^{40}K photon emission, the mapping of channel number to energy interval can be regarded as constant. The SDI is then calculated as the sum of the products of channel number k and net count rate CR_{raw}.

$$SDI = \sum_{k=1}^{n} k\, CR_{raw}(k) \tag{4.5.1.0.46}$$

with:

$CR_{raw}(k)$: Raw count rate in channel k [cps]
SDI: Spectrum dose index [cps]
n: number of channels

In a next step the SDI is corrected for background and cosmic radiation.

$$SDI_{corr} = SDI - SDI_{back} - SDI_{cosmic} \tag{4.5.1.0.47}$$

with:

SDI_{cosmic}: Contribution of cosmic radiation to SDI [cps]
SDI_{back}: Contribution of background to SDI [cps]
SDI_{corr}: Corrected SDI [cps]

The contribution of the background is calculated using a background spectrum of the aircraft and the equipment.

$$SDI_{back} = \sum_{k=1}^{n} k\, CR_{back}(k) \tag{4.5.1.0.48}$$

with:

$CR_{back}(k)$: Raw count rate of the background spectrum in channel k [cps]
SDI_{back}: SDI of the background spectrum [cps]
n: number of channels

The contribution of the cosmic radiation is calculated using the count rate of the cosmic window and the cosmic stripping coefficients of each channel.

$$SDI_{cosmic} = CR_{cosmic} f_{cosmic} = CR_{cosmic} \sum_{k=1}^{n} kS(k) \tag{4.5.1.0.49}$$

with:

SDI_{cosmic}: SDI derived from counts in the cosmic window [cps]
CR_{cosmic}: Raw count rate in the cosmic window [cps]
f_{cosmic}: Bulk stripping factor for the influence of cosmic radiation [-]
$S(k)$: Cosmic stripping coefficient for channel k [-]
n: number of channels

The SDI reduced for background and cosmic radiation is corrected to reference altitude h_{ref} = $100\,\mathrm{m}$.

$$SDI_{alt} = SDI_{corr} e^{\mu_{air}(h - h_{ref})} \tag{4.5.1.0.50}$$

with:

SDI_{alt}: SDI at reference altitude [cps]
μ_{air}: Attenuation coefficient in air [m^{-1}]
h: Flight altitude [m]
h_{ref}: Reference altitude [m]

A comparison to ambient dose equivalent rate measurements at ground level yields directly the calibration factor to the ambient dose equivalent rate $dH^*(10)/dt$.

$$DR_{terr} = \alpha SDI \tag{4.5.1.0.51}$$

with:

DR_{terr}: Terrestrial ambient dose equivalent rate $dH^*(10)/dt$ at 1 m above ground [$\mathrm{nSv\,h^{-1}}$]
α: Calibration factor $\alpha = 5.96\ 10^{-5}$ [$\mathrm{nSv\,h^{-1}\,cps^{-1}}$]

The total ambient dose equivalent rate comprises two components: terrestrial and cosmic ambient dose equivalent rates. The cosmic ambient dose equivalent rate has until last year been determined by accounting for its height dependence, including the contribution from neutron radiation (see Bouville and Lowder, 1988 [20]; UNSCEAR, 2008 [21]):

$$DR_{cosmic} = DR_{neutron} + DR_{charged} = 8.963e^{0.78z} + 32.594e^{0.38z} \tag{4.5.1.0.52}$$

with:

DR_{cosmic}: Cosmic ambient dose equivalent rate $dH^*(10)/dt$ at height z above sea level [$\mathrm{nSv\,h^{-1}}$]
$DR_{neutron}$: Cosmic ambient dose equivalent rate $dH^*(10)/dt$ at height z above sea level originating from neutron radiation [$\mathrm{nSv\,h^{-1}}$]
$DR_{charged}$: Cosmic ambient dose equivalent rate $dH^*(10)/dt$ at height z above sea level originating from charged particles and photons [$\mathrm{nSv\,h^{-1}}$]
z: Height above sea level [km]

The flux and ambient dose equivalent rate of cosmic rays vary significantly with latitude and longitude, and are further modulated by the solar cycle, with variations up to $50\,\%$, as illustrated in Figure 4.18. To account for these effects, a new methodology for estimating the cosmic ambient dose equivalent rate was implemented in AGS_CH, based on the PARMA algorithm developed by the Japanese Research Group for Radiation Transport Analysis [22]. This tool enables the computation of the cosmic ambient dose equivalent rate for a specific location and time, using GPS coordinates of the measurements to determine the local magnetic rigidity and the date to obtain the appropriate solar modulation parameter, thereby accounting for solar activity.

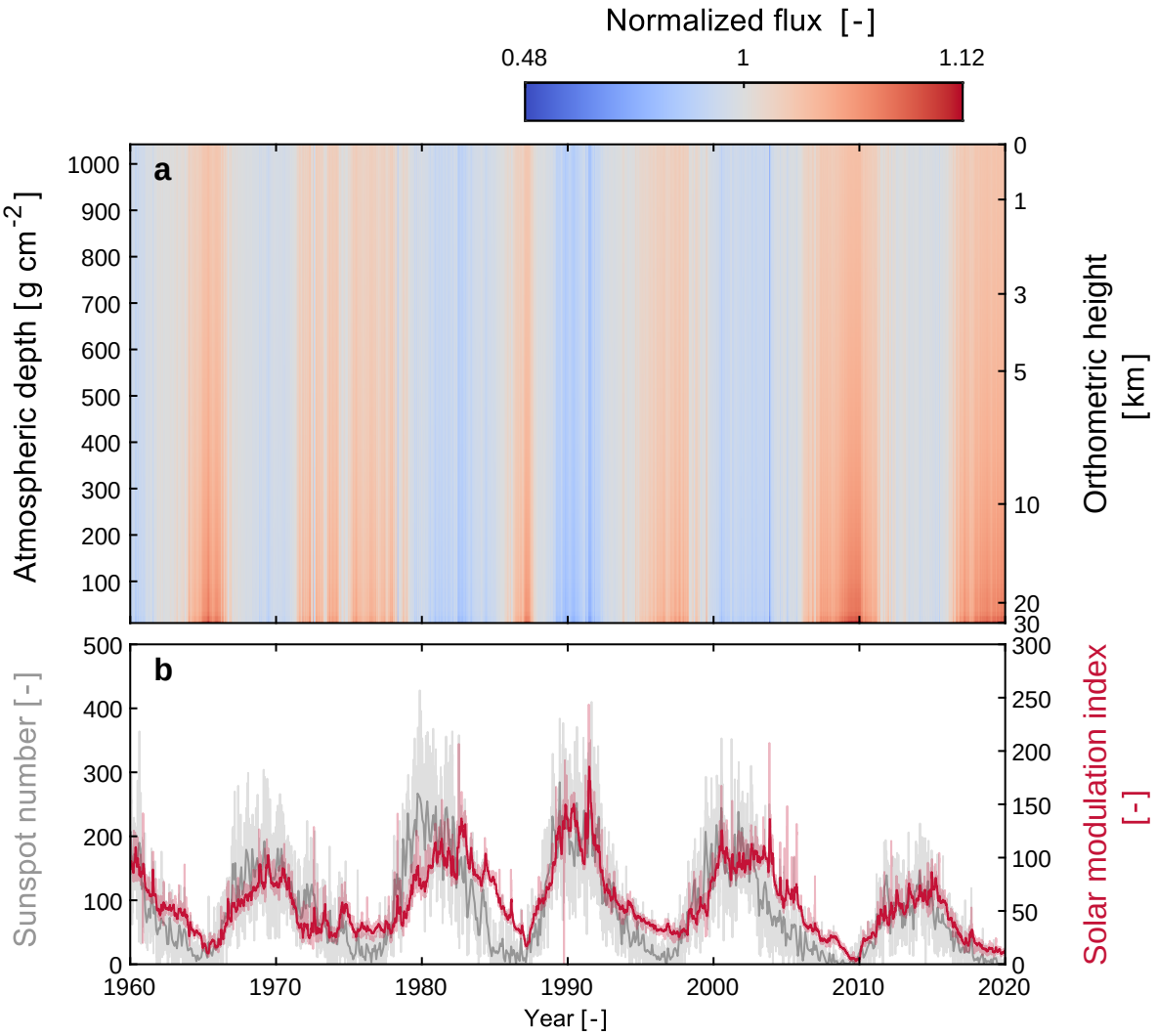

Figure 4.18: Cosmic flux variation with solar modulation index and atmospheric depth, from Breitenmoser [23].

4.5.2 Mirion Software (SPIR)

Signal processing and spectra analysis

Each of the four NaI(Tl) radiation detectors is associated with a 1024 channel spectrometer providing elementary spectra from approximately 0 to $3\,\mathrm{MeV}$. The real accumulation time is 1 second. The first step of the signal processing is the energy stabilisation that corrects the effect of possible temperature changes (despite the excellent thermal insulation of the detection container) and a hypothetical ageing process of the detector assemblies. The stabilisation process uses the ^{40}K peak as reference (other NORM isotopes like ^{226}Ra or ^{232}Th are possible) and produces an offset and a slope for each spectra. Subsequently and based on the linearity characteristics obtained during the initial detector characterisation stored in the spectrometers, the elementary spectra are normalised to spectra without offset and with a fixed gain of $3\,\mathrm{keV}$ per channel. At this stage, the normalised spectra can be summed to build the total channel (other configurations like right and left channel are possible, e.g. in vehicle). The normalised total spectrum is then available for dose rate calculation and further analysis like isotope identification. The further signal processing depends of the situation and required mission type. NBC-EOD Centre of Excellence basically uses a standard configuration for background mapping and source search or an adapted configuration for

contamination mapping. With the standard configuration the software uses a sliding accumulation of the normalised spectra (1 second) over 5 seconds in order to improve the confidence level of the isotope identification process. Some criteria or combination of criteria like increased count rate (full spectra or defined region of interest) or increased dose rate can trigger a longer accumulation in order to identify the detected isotopes (these events are named “detection”). For the mapping of a contaminated area the isotope is assumed to be identified and the operators do not need to be warned with continuous identification results. In this case, the used configuration does not require the sliding of the normalized spectra and does not trigger a longer accumulation. Therefore, only the 1 second spectra are used.

Isotope identification

The used proprietary isotope identification algorithm (SIA IdentPro Identification Algorithm) has been specially optimised in order to provide fast decisions based on spectra with poor statistical features. It is based on the analysis of many regions of interest (over 70 ROIs), taking into account an interference matrix and an additional process by partial deconvolution. This algorithm does not require preliminary peak recognition: it takes into account large statistical fluctuations and does not require a calibrated efficiency. It also takes into account possible shielding and background variation. The algorithm is able to identify up to four isotopes from the isotope groups listed in Table 4.15. Different filters or combination of filters allow discrimination of the alarms displayed and recorded. These filters can be set for example on isotope group, dose rate or count rate.

Table 4.15: Isotope groups used by the SIA algorithm. NORM: Naturally occurring radioactive materials. SNM: Special nuclear materials.

Isotope group	Isotopes
NORM	^{40}K, ^{238}U-series, ^{232}Th-series
Medical	^{18}F, ^{51}Cr, ^{67}Ga, ^{99}Mo, ^{99m}Tc, ^{103}Pd, ^{111}In, ^{123}I, ^{125}I, ^{131}I, ^{132}I, ^{133}I, ^{133}Xe, ^{153}Sm, ^{201}Tl
Industrial	^{22}Na, ^{57}Co, ^{60}Co, ^{106}Ru/Rh, ^{133}Ba, ^{134}Cs, ^{137}Cs, ^{152}Eu, ^{166}Ho, ^{192}Ir, ^{207}Bi, ^{241}Am, Bremsstrahlung, H(n,γ)
SNM	^{233}U, ^{235}U, ^{237}U, ^{238}U, ^{237}Np, ^{239}Pu, ^{241}Pu

Ground ambient dose equivalent rate

The system calculates the ground dose rates according to IAEA’s technical note TECDOC 1363, 2003 [5]. The cosmic dose rate at the flight level, the detector background and the local radon background are subtracted from the actual dose rate at the flight level. The cosmic dose rate at the flight level is converted from the cosmic channel with a conversion factor of $0.002\,203\,\mu\mathrm{Sv\,h^{-1}\,cps^{-1}}$. The intrinsic detector background dose rate is estimated at $2\,\mathrm{nSv\,h^{-1}}$ and the radon dose rate set as $0\,\mathrm{nSv\,h^{-1}}$. The measured altitude above ground is first corrected to standard conditions of air pressure and temperature according to the outside air pressure and temperature provided by the helicopter. The dose rate at flight altitude resulting after subtraction of cosmic, intrinsic and radon dose rate is then extrapolated to ground level ($1\,\mathrm{m}$ above ground) with an exponential correction.

$$DR_{1m} = DR_h e^{-0.0056h} \tag{4.5.2.0.1}$$

with:

DR_{1m}: Terrestrial dose rate at $1\,\mathrm{m}$ above ground [$\mathrm{nSv\,h^{-1}}$]
h: Height of detector above ground [m]
DR_h: Dose rate at flight altitude [$\mathrm{nSv\,h^{-1}}$]

NORM concentration calculation

The activity concentration of naturally occurring radioactive materials (NORM) in the soil is assumed to be constant with depth. The used algorithm is based on a reverse matrix calculation. The matrix coefficients are specific for the different regions of interest (ROI) used for different NORM nuclides and are functions of the altitude above ground and of the attenuation of the vehicle. The matrix coefficients are estimated by Monte Carlo simulations with a uniform soil concentration in an infinite plate of $50\,\mathrm{cm}$ thickness.

Table 4.16: Energy ranges and algorithm parameters. BKGND: Intrinsic background count rate in ROI. Radon: Count rate in ROI due to airborne radon progeny. Cosmic: Count rate in ROI due to cosmic radiation.

NORM	Isotope	Main peak [keV]	Energy range (ROI)	BKGND [cps]	Radon [cps]	Cosmic [cps]
Potassium	^{40}K	$1461\,\mathrm{keV}$	1370 to $1570\,\mathrm{keV}$	2.30	0.00	23
Uranium	^{214}Bi	$1765\,\mathrm{keV}$	1660 to $1860\,\mathrm{keV}$	0.73	0.00	21
Thorium	^{208}Tl	$2614\,\mathrm{keV}$	2410 to $281\,\mathrm{keV}$	0.00	0.00	26

As a first step, the net count rates CR_K, CR_U and CR_{Th} in the NORM energy ranges are calculated by subtracting the intrinsic background count rate, the count rate due to airborne radon progeny and the count rate produced by cosmic radiation. The activity concentrations of the individual NORM components are calculated from a linear combination of all of these net count rates multiplied with stripping correction factors.

$$C_K = CR_K\,a' + CR_U\,b' + CR_{Th}\,c' \tag{4.5.2.0.2}$$

with:

C_K: Activity concentration of Potassium [$\mathrm{Bq\,kg^{-1}}$]
a': Stripping factor associated with potassium energy range and potassium activity concentration. [$\mathrm{Bq\,kg^{-1}\,cps^{-1}}$]
b': Stripping factor associated with uranium energy range and potassium activity concentration. [$\mathrm{Bq\,kg^{-1}\,cps^{-1}}$]
c': Stripping factor associated with thorium energy range and potassium activity concentration. [$\mathrm{Bq\,kg^{-1}\,cps^{-1}}$]

$$C_U = CR_K\,d' + CR_U\,e' + CR_{Th}\,f' \tag{4.5.2.0.3}$$

with:

C_U: Activity concentration of Uranium [$\mathrm{Bq\,kg^{-1}}$]
d': Stripping factor associated with potassium energy range and uranium activity concentration. [$\mathrm{Bq\,kg^{-1}\,cps^{-1}}$]
e': Stripping factor associated with uranium energy range and uranium activity

concentration. [$\mathrm{Bq\,kg^{-1}\,cps^{-1}}$]

f': Stripping factor associated with thorium energy range and uranium activity concentration. [$\mathrm{Bq\,kg^{-1}\,cps^{-1}}$]

$$C_{Th} = CR_K g' + CR_U i' + CR_{Th} k' \tag{4.5.2.0.4}$$

with:

C_{Th}: Activity concentration of Thorium [$\mathrm{Bq\,kg^{-1}}$]

g': Stripping factor associated with potassium energy range and thorium activity concentration. [$\mathrm{Bq\,kg^{-1}\,cps^{-1}}$]

i': Stripping factor associated with uranium energy range and thorium activity concentration. [$\mathrm{Bq\,kg^{-1}\,cps^{-1}}$]

k': Stripping factor associated with thorium energy range and thorium activity concentration. [$\mathrm{Bq\,kg^{-1}\,cps^{-1}}$]

The stripping coefficients can be considered as elements of an inverse matrix $\overline{\overline{A}}^{-1}$ of matrix $\overline{\overline{A}}$.

$$\overline{\overline{A}}^{-1} = \begin{bmatrix} a' & b' & c' \\ d' & e' & f' \\ g' & i' & k' \end{bmatrix}; \overline{\overline{A}} = \begin{bmatrix} a & b & c \\ d & e & f \\ g & i & k \end{bmatrix} \tag{4.5.2.0.5}$$

The coefficients of matrix $\overline{\overline{A}}$ are assumed proportional to a nuclide specific attenuation factor and inverse proportional to a nuclide and detector specific factor and a polynomial in dependence of ground clearance h. The coefficients of the polynomials determined with Monte Carlo calculations are listed in Table 4.17.

$$a = \frac{\rho_{Potassium}}{a_1 h^4 + a_2 h^3 + a_3 h^2 + a_4 h + a_5} \frac{1}{\delta_{Potassium}} \tag{4.5.2.0.6}$$

with:

a: Count rate in potassium energy range due to potassium activity concentration. [$\mathrm{cps/Bqkg}$]

a_1: Polynomial coefficient [$\mathrm{m^{-4}}$]

a_2: Polynomial coefficient [$\mathrm{m^{-3}}$]

a_3: Polynomial coefficient [$\mathrm{m^{-2}}$]

a_4: Polynomial coefficient [$\mathrm{m^{-1}}$]

a_5: Polynomial coefficient [-]

$\rho_{Potassium}$: Attenuation factor for potassium photons [-]

$\delta_{Potassium}$: Detector specific calibration factor for potassium [$\mathrm{Bq\,kg^{-1}\,cps^{-1}}$]

$$b = \frac{\rho_{Potassium}}{b_1 h^4 + b_2 h^3 + b_3 h^2 + b_4 h + b_5} \frac{1}{\delta_{Potassium}} \tag{4.5.2.0.7}$$

with:

b: Count rate in potassium energy range due to uranium activity concentration. [$\mathrm{cps/Bqkg}$]

b_1: Polynomial coefficient [$\mathrm{m^{-4}}$]

b_2: Polynomial coefficient [$\mathrm{m^{-3}}$]

b_3: Polynomial coefficient [$\mathrm{m^{-2}}$]

b_4: Polynomial coefficient [m^{-1}]
b_5: Polynomial coefficient [-]
$\rho_{Potassium}$: Attenuation factor for potassium photons [-]
$\delta_{Potassium}$: Detector specific calibration factor for potassium [$\mathrm{Bq\,kg^{-1}\,cps^{-1}}$]

$$c = \frac{\rho_{Potassium}}{c_1 h^4 + c_2 h^3 + c_3 h^2 + c_4 h + c_5} \frac{1}{\delta_{Potassium}} \tag{4.5.2.0.8}$$

with:

c: Count rate in potassium energy range due to thorium activity concentration. [$\mathrm{cps/Bqkg}$]
c_1: Polynomial coefficient [m^{-4}]
c_2: Polynomial coefficient [m^{-3}]
c_3: Polynomial coefficient [m^{-2}]
c_4: Polynomial coefficient [m^{-1}]
c_5: Polynomial coefficient [-]
$\rho_{Potassium}$: Attenuation factor for potassium photons [-]
$\delta_{Potassium}$: Detector specific calibration factor for potassium [$\mathrm{Bq\,kg^{-1}\,cps^{-1}}$]

$$d = 0 \tag{4.5.2.0.9}$$

with:

d: Count rate in uranium energy range due to potassium activity concentration. [$\mathrm{cps/Bqkg}$]

$$e = \frac{\rho_{Uranium}}{e_1 h^4 + e_2 h^3 + e_3 h^2 + e_4 h + e_5} \frac{1}{\delta_{Uranium}} \tag{4.5.2.0.10}$$

with:

e: Count rate in uranium energy range due to uranium activity concentration. [$\mathrm{cps/Bqkg}$]
e_1: Polynomial coefficient [m^{-4}]
e_2: Polynomial coefficient [m^{-3}]
e_3: Polynomial coefficient [m^{-2}]
e_4: Polynomial coefficient [m^{-1}]
e_5: Polynomial coefficient [-]
$\rho_{Uranium}$: Attenuation factor for uranium photons [-]
$\delta_{Uranium}$: Detector specific calibration factor for uranium [$\mathrm{Bq\,kg^{-1}\,cps^{-1}}$]

$$f = \frac{\rho_{Uranium}}{f_1 h^4 + f_2 h^3 + f_3 h^2 + f_4 h + f_5} \frac{1}{\delta_{Uranium}} \tag{4.5.2.0.11}$$

with:

f: Count rate in uranium energy range due to thorium activity concentration. [$\mathrm{cps/Bqkg}$]
f_1: Polynomial coefficient [m^{-4}]
f_2: Polynomial coefficient [m^{-3}]
f_3: Polynomial coefficient [m^{-2}]

f_4: Polynomial coefficient [m^{-1}]
f_5: Polynomial coefficient [-]
$\rho_{Uranium}$: Attenuation factor for uranium photons [-]
$\delta_{Uranium}$: Detector specific calibration factor for uranium [$\mathrm{Bq\,kg^{-1}\,cps^{-1}}$]

$$g = 0 \tag{4.5.2.0.12}$$

with:

g: Count rate in thorium energy range due to potassium activity concentration. [$\mathrm{cps/Bqkg}$]

$$i = \frac{\rho_{Thorium}}{i_1 h^4 + i_2 h^3 + i_3 h^2 + i_4 h + i_5} \frac{1}{\delta_{Thorium}} \tag{4.5.2.0.13}$$

with:

i: Count rate in thorium energy range due to uranium activity concentration. [$\mathrm{cps/Bqkg}$]
i_1: Polynomial coefficient [m^{-4}]
i_2: Polynomial coefficient [m^{-3}]
i_3: Polynomial coefficient [m^{-2}]
i_4: Polynomial coefficient [m^{-1}]
i_5: Polynomial coefficient [-]
$\rho_{Thorium}$: Attenuation factor for thorium photons [-]
$\delta_{Thorium}$: Detector specific calibration factor for thorium [$\mathrm{Bq\,kg^{-1}\,cps^{-1}}$]

$$k = \frac{\rho_{Thorium}}{k_1 h^4 + k_2 h^3 + k_3 h^2 + k_4 h + k_5} \frac{1}{\delta_{Thorium}} \tag{4.5.2.0.14}$$

with:

k: Count rate in thorium energy range due to thorium activity concentration. [$\mathrm{cps/Bqkg}$]
k_1: Polynomial coefficient [m^{-4}]
k_2: Polynomial coefficient [m^{-3}]
k_3: Polynomial coefficient [m^{-2}]
k_4: Polynomial coefficient [m^{-1}]
k_5: Polynomial coefficient [-]
$\rho_{Thorium}$: Attenuation factor for thorium photons [-]
$\delta_{Thorium}$: Detector specific calibration factor for thorium [$\mathrm{Bq\,kg^{-1}\,cps^{-1}}$]

Table 4.17: Polynomial coefficients determined with Monte Carlo calculations.

	$_1$ [m^{-4}]	$_2$ [m^{-3}]	$_3$ [m^{-2}]	$_4$ [m^{-1}]	$_5$ [$-$]
a	$3.24\,10^{-11}$	$-1.12\,10^{-8}$	$3.84\,10^{-6}$	$1.47\,10^{-4}$	$2.08\,10^{-2}$
b	$1.63\,10^{-10}$	$-4.09\,10^{-8}$	$2.26\,10^{-5}$	$3.02\,10^{-3}$	$3.41\,10^{-1}$
c	$6.00\,10^{-10}$	$-4.12\,10^{-7}$	$1.40\,10^{-4}$	$-2.32\,10^{-3}$	1.61
e	$1.55\,10^{-10}$	$4.59\,10^{-10}$	$1.04\,10^{-5}$	$3.95\,10^{-3}$	$2.45\,10^{-1}$
f	$-6.31\,10^{-10}$	$5.44\,10^{-7}$	$-9.89\,10^{-5}$	$1.71\,10^{-2}$	1.69
i	$2.69\,10^{-9}$	$-1.17\,10^{-6}$	$5.44\,10^{-4}$	$5.81\,10^{-3}$	5.56
k	$2.37\,10^{-10}$	$-9.51\,10^{-8}$	$4.08\,10^{-5}$	$3.69\,10^{-3}$	$4.90\,10^{-1}$

Point source and surface activity calculation

The RLL system calculates activity (point source and surface contamination) based on the results of the identification algorithm (SIA), which calculates the net counts per second for each identified isotope. First, the algorithm corrects the count rate with the attenuation of the vehicle and then converts the attenuated count rate into $\mathrm{Bq\,cm^{-2}}$ or into MBq using a "sensitivity versus altitude" function. For each isotope, the sensitivity as a function of the ground clearance is estimated with Monte Carlo simulations. For the activity estimation of a point source, the algorithm assumes that the helicopter flies directly above the source. For a surface contamination, the used model assumes a uniform contamination on an infinite and flat surface. This method does not require stripping corrections or background corrections, because the identification algorithm already takes into account the interference between nuclides and provides net count rates. Table 4.18 exemplifies the detector factor $F_{Detector}(N)$ for some radionuclides.

$$A(N) = \frac{Q(N)}{Q_{ref}(N)\frac{4}{h^2}e^{-0.129h\mu(N)}}\frac{F_{Detector}(N)}{F_{Attenuation}(N)} \tag{4.5.2.0.15}$$

with:

N: Nuclide
$A(N)$: Activity of a point source of nuclide N [MBq]
$Q(N)$: Quantification for nuclide N provided by the SIA algorithm [-]
h: Ground clearance [m]
Q_{ref}: Nuclide reference quantification [-]
$\mu(N)$: Attenuation coefficient for nuclide N [m^{-1}]
$F_{Detector}(N)$: Detector factor for nuclide N depending on detector configuration [$\mathrm{MBq\,m^{-2}}$]
$F_{Attenuation}(N)$: Attenuation factor for nuclide N including detector shielding [-]

$$CA(N) = \left(c_1h^4 + c_2h^3 + c_3h^2 + c_4h + \frac{1}{Q_{ref}(N)}\right)Q(N)\frac{F_{Detector}(N)}{F_{Attenuation}(N)} \tag{4.5.2.0.16}$$

with:

N: Nuclide
$CA(N)$: Surface activity of nuclide N [$\mathrm{Bq\,m^{-2}}$]
$Q(N)$: Quantification for nuclide N provided by the SIA algorithm [-]
h: Ground clearance [m]
c_1: Polynomial coefficient [m^{-4}]
c_2: Polynomial coefficient [m^{-3}]

c_3: Polynomial coefficient [m^{-2}]
c_4: Polynomial coefficient [m^{-1}]
Q_{ref}: Nuclide reference quantification [-]
$\mu(N)$: Attenuation coefficient for nuclide N [m^{-1}]
$F_{Detector}(N)$: Detector factor for nuclide N depending on detector configuration [$\mathrm{MBq\,m}^{-2}$]
$F_{Attenuation}(N)$: Attenuation factor for nuclide N including detector shielding [-]

Table 4.18: Detector factor $F_{Detector}(N)$ for some radionuclides N.

Nuclide N	$F_{\text{Detector}}(N)$ [$\mathrm{MBq\,m}^{-2}$]
^{40}K	2.16
^{60}Co	2.16
^{131}I	1.36
^{137}Cs	1.60
^{192}Ir	1.36
^{238}U	2.55
^{232}Th	2.46
^{75}Se	1.49

Chapter 5

Data format and Presentation

5.1 Data format ERS 2.0

The data exchange between the participants utilised the European Radiometric and Spectrometry (ERS) format described already in detail (PSI-report 18-04) (Appendix A). The coordinates were reported in the World Geodetic System WGS84 reference system.

5.2 Maps presentation

5.2.1 Gridding algorithm

The gridding of all the ARM25 and the AGC25 results has been performed with the gridding functionality of AGS_CH. The gridding function takes the georeferenced individual measurement results associated with a given quantity (i.e. identifier) and arranges them into a spatial grid for the creation of maps. Depending on the defined cell dimensions, it either assigns values directly to grid cells based on coordinates or iterates through each cell to determine which measurement points fall within its area. To each cell is then assigned the average of all valid individual measurement values. After the initial grid is generated, the function carries out resampling steps: empty cells are filled using the average of neighbouring cells, provided that enough valid neighbours exist. The predefined settings are:

- cell size $125\,\mathrm{m}$
- number of neighbours: 5
- number of resampling iterations: 3

5.2.2 Data presentation

Maps are given in EPSG:2056 – CH1903+ /LV95 coordinates. Concerning the measurements of the ARM25, for all measuring areas, a map of the total dose rate (ambient dose equivalent rate $dH*(10)/dt$ extrapolated to $1\,\mathrm{m}$ above ground) and the flight lines is presented together with a map of the Man-Made-Gross-Count (MMGC) ratio and the one of ^{232}Th activity concentration.

The MMGC-ratio is defined as the quotient between the count rate summed over the energy window (MMGC1), between $400\,\mathrm{keV}$ and $1400\,\mathrm{keV}$, and the count rate summed over the energy window (MMGC2), between $1400\,\mathrm{keV}$ and $3000\,\mathrm{keV}$. As most anthropogenic radionuclides emit

photons below $1400\,\mathrm{keV}$, the ratio will rise due to these additional photons, whereas natural radionuclides are registered in both energy windows, keeping the ratio relatively constant. Although the MMGC-ratio is undoubtedly a useful quantity, it is worth mentioning that it is prone to show artefacts when particularly low counts in the MMGC2 energy window occur due to limited counting statistics. As this can also lead to increased MMGC-ratios, a careful inspection of the MMGC2 counts is required for elevated values. If the dose rate or the MMGC-ratio indicate elevated values, maps of individual radionuclides (like e.g. ^{40}K or ^{137}Cs activity concentrations) are added based on the average photon spectrum over the affected area.

The map of the ^{232}Th activity concentration (activity per wet mass, AW_Th-232) provides information on the quality of the measurements for recurrent sites, as this quantity is expected to remain constant over time.

In the case of large changes of topography in the measured area, a map of the terrestrial dose rate, calculated from the total dose rate deducted by the altitude-dependent cosmic component, is included. In the case of measuring flights aiming at mapping natural radionuclide concentrations, a supplementary map of the ^{40}K activity concentration (activity per wet mass, AW_K-40) may also be presented.

^{238}U activity concentration maps (activity per wet mass, AW_U-238) are presented as needed. These maps are however affected, especially for low ^{238}U concentrations, by the variable concentration of radon and its progeny in the atmosphere at the time of measurement.

Concerning the international exercise AGC25, results and maps are provided according to the requests stated in the mission description (Chapter 7). If needed, these are accompanied by additional ones to address specific aspects of the results.

5.2.3 Colour scale

A discrete colour scale was defined by the Swiss Expert Group for Aeroradiometrics (FAR) in 2019 and is used for all results in this report. The colours and their representation as red, green and blue (RGB) values are listed in Table 5.1 together with the represented ranges of measured values. The unit of ambient dose equivalent rates used is $\mu\mathrm{Sv\,h^{-1}}$, the unit used to store ambient dose equivalent rate values in the ERS 2.0 format (Butterweck et al. (2018), see Appendix A).

Colour	Red	Green	Blue	Dose rate [µSv h^{-1}]	MMGC-ratio	Activity per mass [Bq kg^{-1}] ^{40}K	Activity per mass [Bq kg^{-1}] ^{238}U, ^{232}Th, ^{137}Cs	Activity per area [kBq m^{-2}] ^{137}Cs ($\beta = 9.5\,\mathrm{g\,cm^{-2}}$)
	153	0	153	> 10	> 100	> 10000	> 5000	> 1000
	204	0	102	5 – 10	50 – 100	5000 – 10000	1000 – 5000	200 – 1000
	204	0	0	2 – 5	15 – 50	2000 – 5000	500 – 1000	100 – 200
	255	0	0	0.5 – 2	9 – 15	1500 – 2000	250 – 500	50 – 100
	255	176	51	0.3 – 0.5	8 – 9	1000 – 1500	200 – 250	40 – 50
	255	235	51	0.2 – 0.3	7 – 8	800 – 1000	150 – 200	30 – 40
	230	255	128	0.15 – 0.2	unused	600 – 800	100 – 150	20 – 30
	173	255	153	0.1 – 0.15	unused	400 – 600	75 – 100	15 – 20
	73	255	106	0.08 – 0.1	6 – 7	200 – 400	50 – 75	10 – 15
	102	255	255	0.06 – 0.08	5 – 6	100 – 200	25 – 50	5 – 10
	77	148	255	0.04 – 0.06	unused	50 – 100	12.5 – 25	2.5 – 5
	51	102	179	< 0.04	< 5	< 50	< 12.5	< 2.5

Table 5.1: Quantification of the colour scale.

5.3 Drones

The evaluation and processing of the drone data were carried out without any fixed specifications for visual or analytical presentation. Each team was free to assess the data and conduct the missions according to their own protocols and procedures. Consequently, the parameters presented in the measurement results vary. Some teams displayed the counts per second, while others calculated dose rates at the detector, or at $1\,\mathrm{m}$ above the ground.

Chapter 8.7 therefore presents the evaluations from the individual teams as they were produced and submitted for the compilation of this report.

Chapter 6

Recurrent Swiss aeroradiometry surveys

On the 27th and 28th of May 2025, the Swiss team CHE1 conducted measurements over the Mühleberg (KKM) and Gösgen (KKG) nuclear power plants prior to the international exercise AGC25. Measurements over Swiss nuclear installations are carried out on a biennial basis at the request of the Swiss Federal Nuclear Safety Inspectorate (ENSI). The results of the measurements using the Mirion software (SPIR) are summarised in the report published by the NEOC [24] and available at https://www.naz.ch.

The evaluation parameters used in AGS_CH, modified following the results of the international intercomparison exercises described in Sections 8.2 and 8.3, are documented in Appendix C. The survey of the surroundings of KKM and KKG detected no artificial radionuclides outside the plant premises. Within the KKM site, ^{60}Co was identified, originating from activated components resulting from ongoing dismantling activities. These materials are permitted to remain on site and are closely monitored by the competent authorities.

6.1 Gösgen Nuclear Power Plant (KKG)

The environs of the Gösgen Nuclear Power Plant (KKG) were surveyed on 28th May during ARM25. The survey flight path is shown in Figure 6.1. The ambient dose equivalent rate map (Figure 6.2) indicates variations attributable to a variable concentration of natural radionuclides and attenuation by water bodies. No signal from the pressurised water reactor was detected, as activation products from the primary cooling circuit remain confined within the shielded reactor building. The man-made gross-count (MMGC) ratio, used as an indicator of anthropogenic radionuclides, shows no elevated values within the survey area (Figure 6.3). The activity concentration of ^{232}Th (Figure 6.4) corresponds to expected values for northern Switzerland.

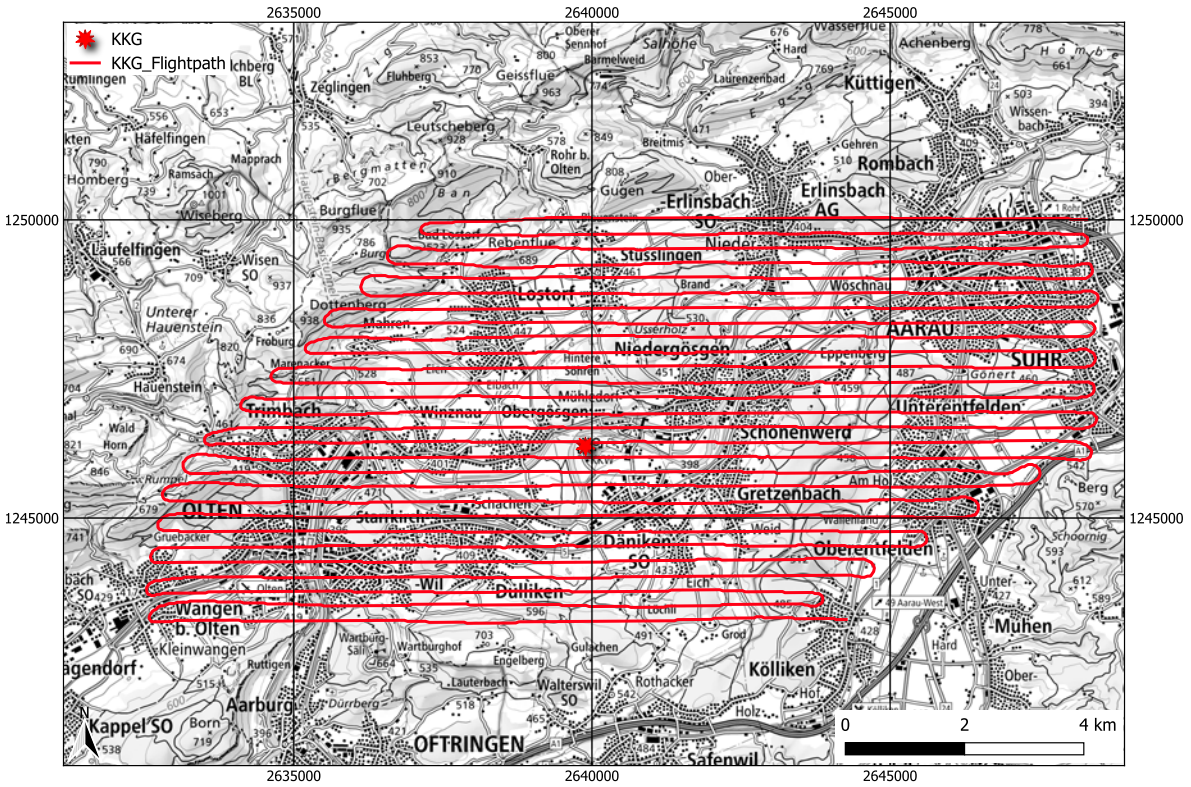

Figure 6.1: Flight path of the survey in the vicinity of KKG. Geodaten©swisstopo.

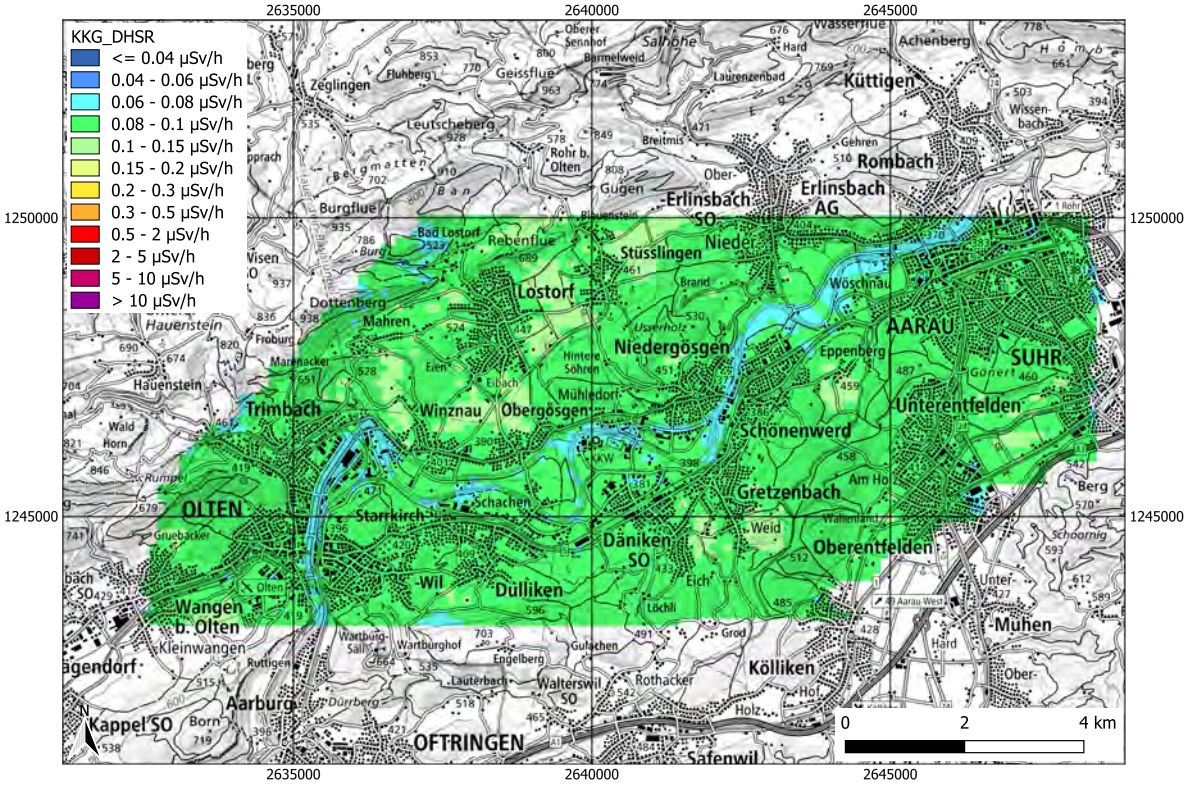

Figure 6.2: Ambient dose equivalent rate in the vicinity of KKG. Geodaten©swisstopo.

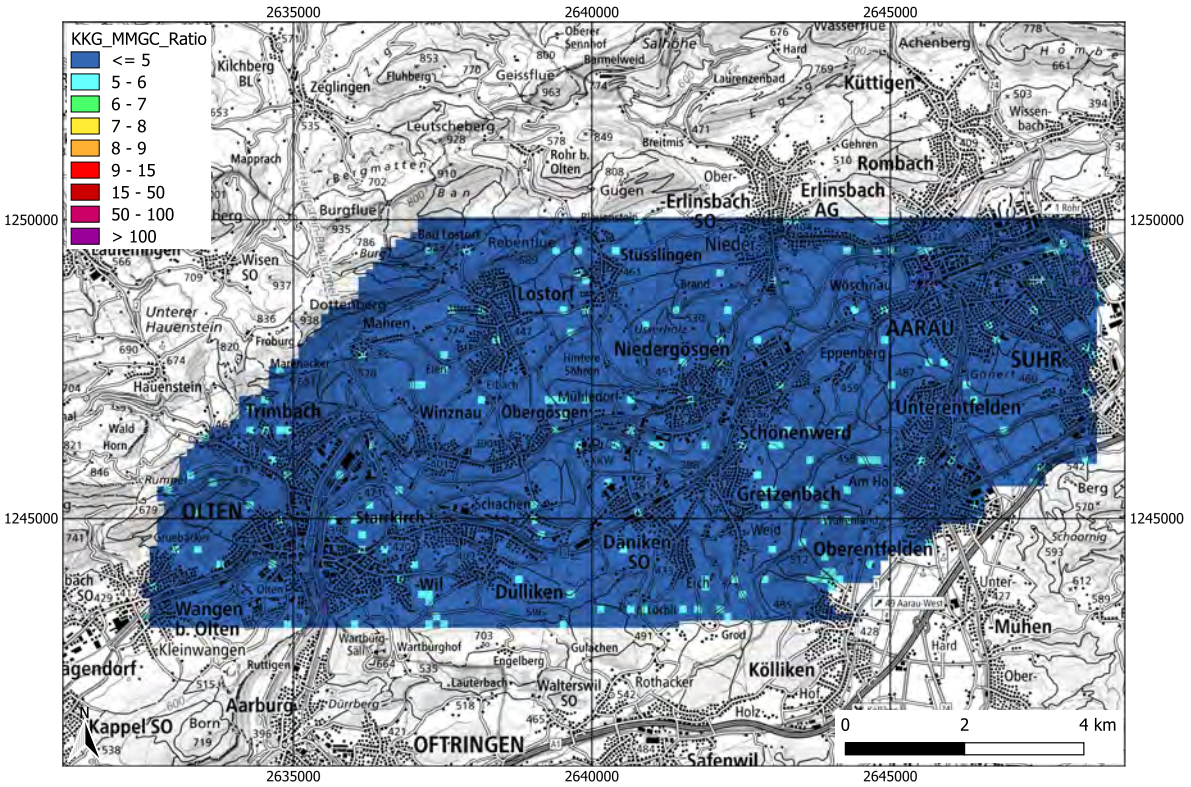

Figure 6.3: MMGC-ratio in the vicinity of KKG. Geodaten©swisstopo.

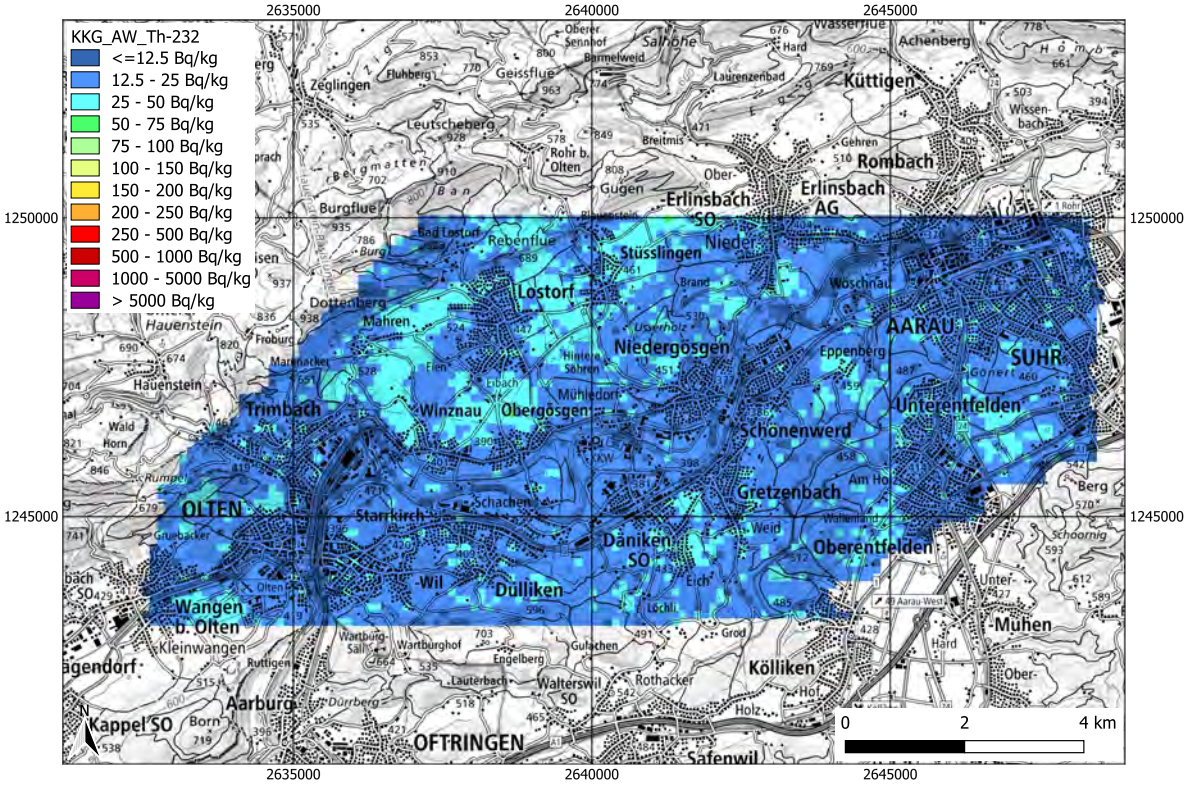

Figure 6.4: ^{232}Th activity concentration in the vicinity of KKG. Geodaten©swisstopo.

6.2 Mühleberg Nuclear Power Plant (KKM)

The Mühleberg Nuclear Power Plant (KKM) has been under decommissioning since 2019. During the dismantling phase, activated material is removed from the shielded reactor building, processed, and stored temporarily on the plant premises. The competent authority (ENSI) is informed of the stored components and continuously monitors compliance with legal dose-rate limits. The temporarily stored radioactive components are clearly detected by the RLL system, as shown by both the dose-rate and MMGC maps (Figures 6.6 and 6.7). In addition to the full-energy peaks of the natural radionuclides ^{40}K, ^{214}Bi, and ^{208}Tl, the spectrum acquired above the plant premises (Figure 6.8) also exhibits the characteristic peaks of ^{60}Co, one of the most common activation products in steel components of nuclear power plants. The ^{232}Th map (Figure 6.9) shows activity concentrations consistent with typical values for northern Switzerland.

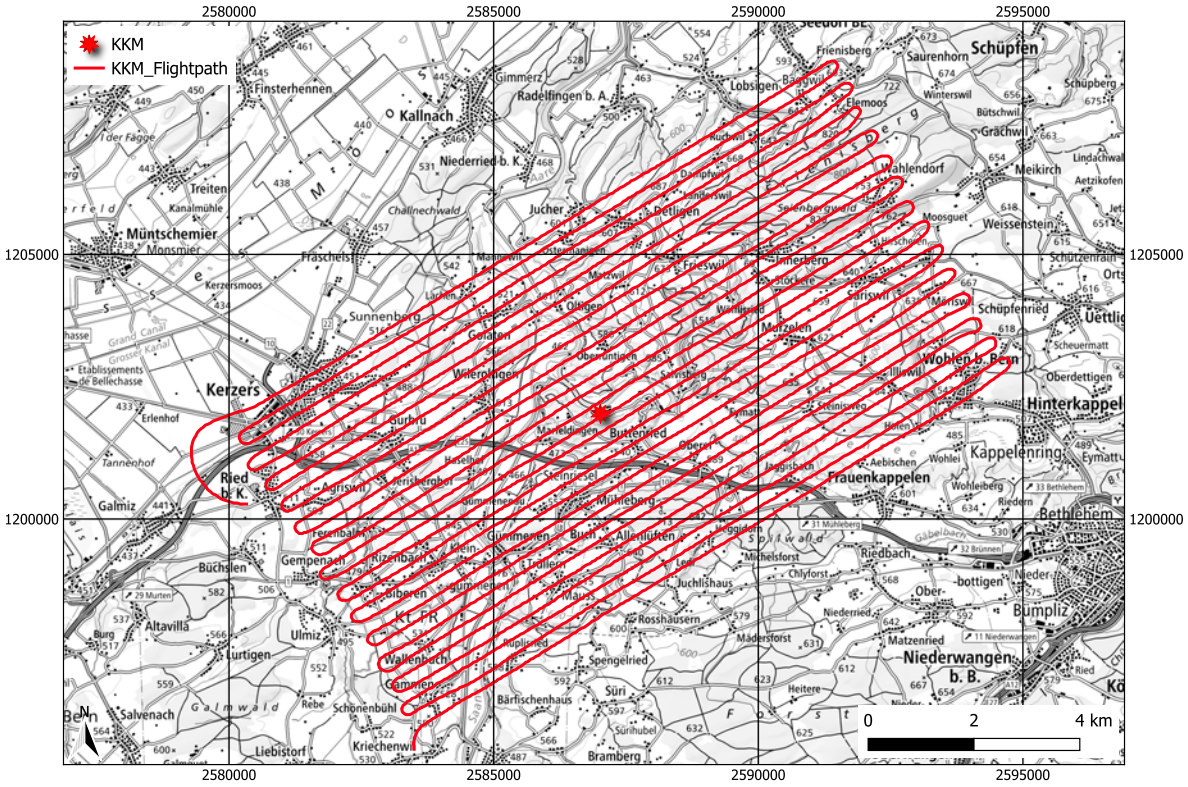

Figure 6.5: Flight path in the vicinity of KKM. Geodaten©swisstopo.

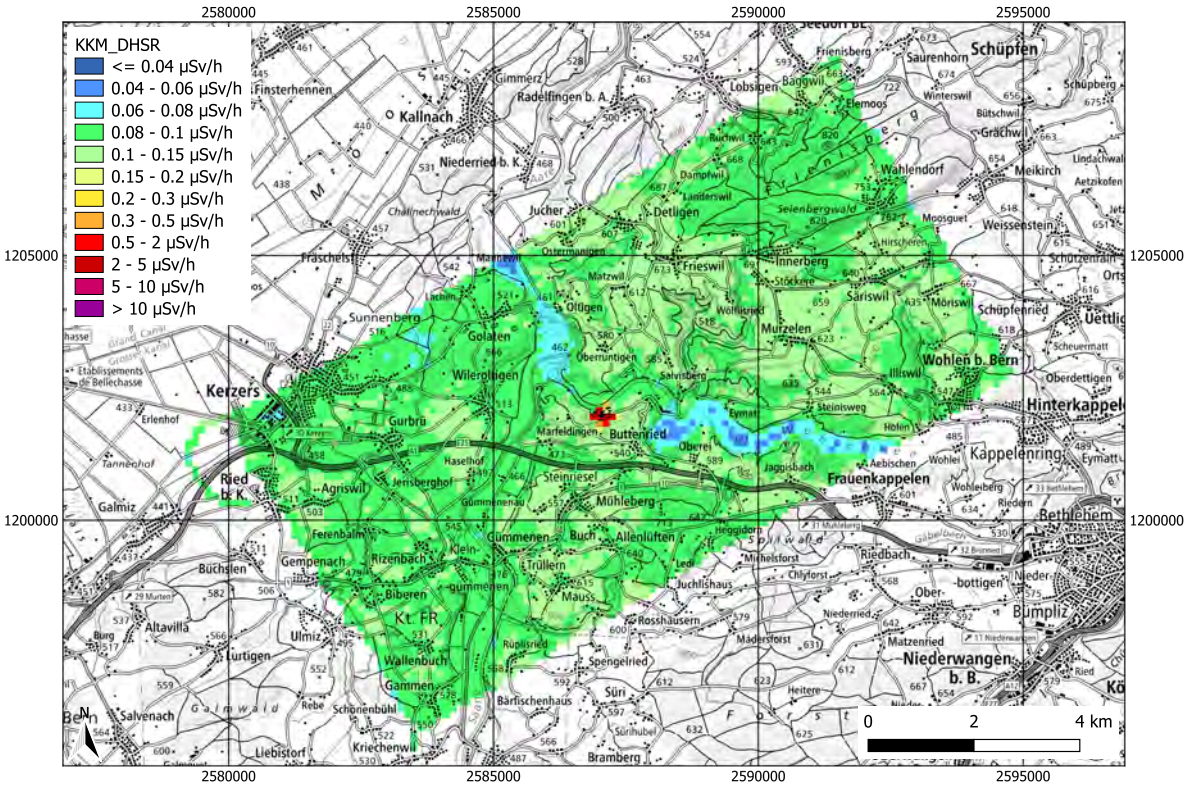

Figure 6.6: Ambient dose equivalent rate in the vicinity of KKM. Geodaten©swisstopo.

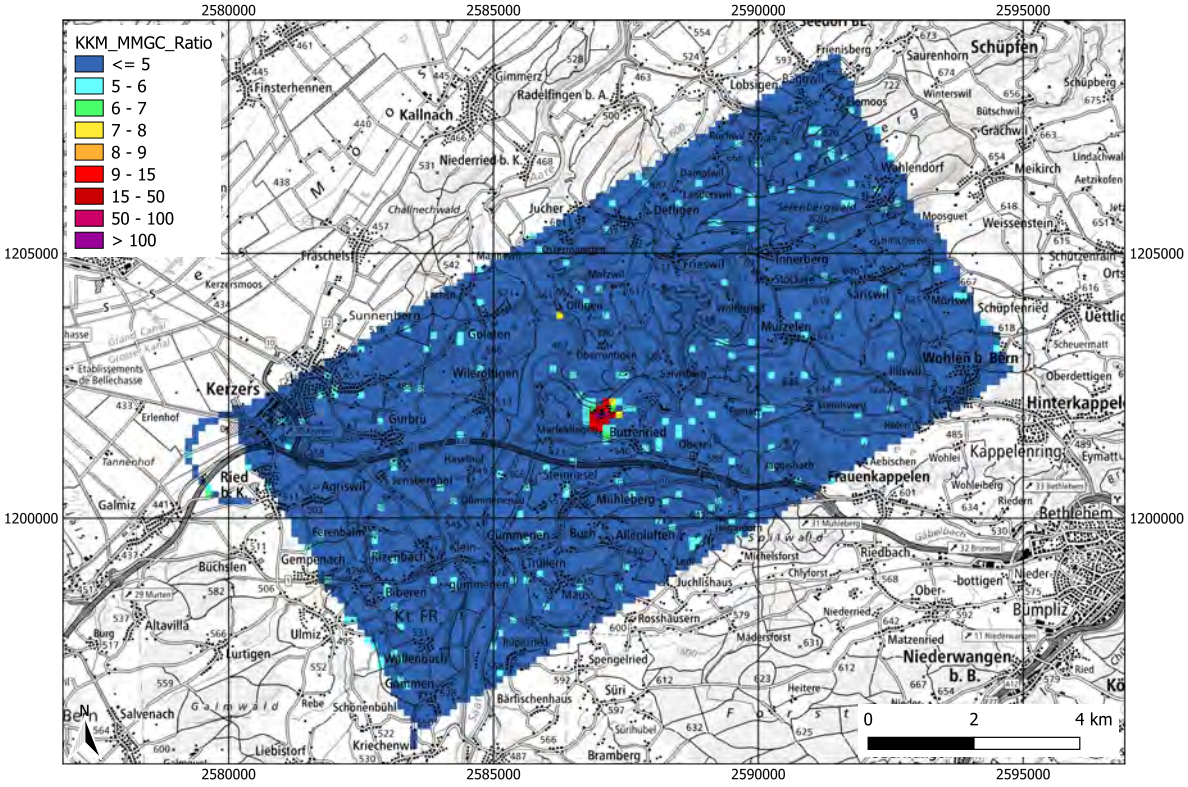

Figure 6.7: MMGC-ratio in the vicinity of KKM. Geodaten©swisstopo.

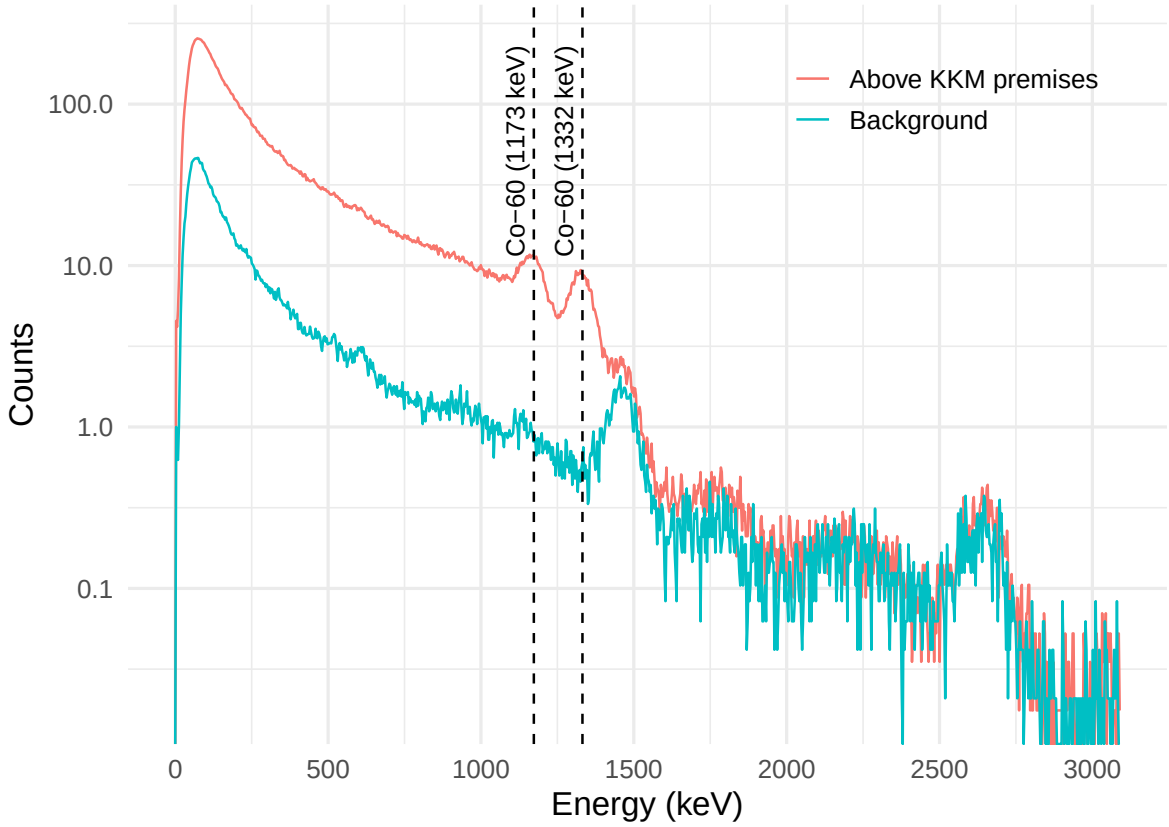

Figure 6.8: Photon spectrum over KKM premises compared to the background.

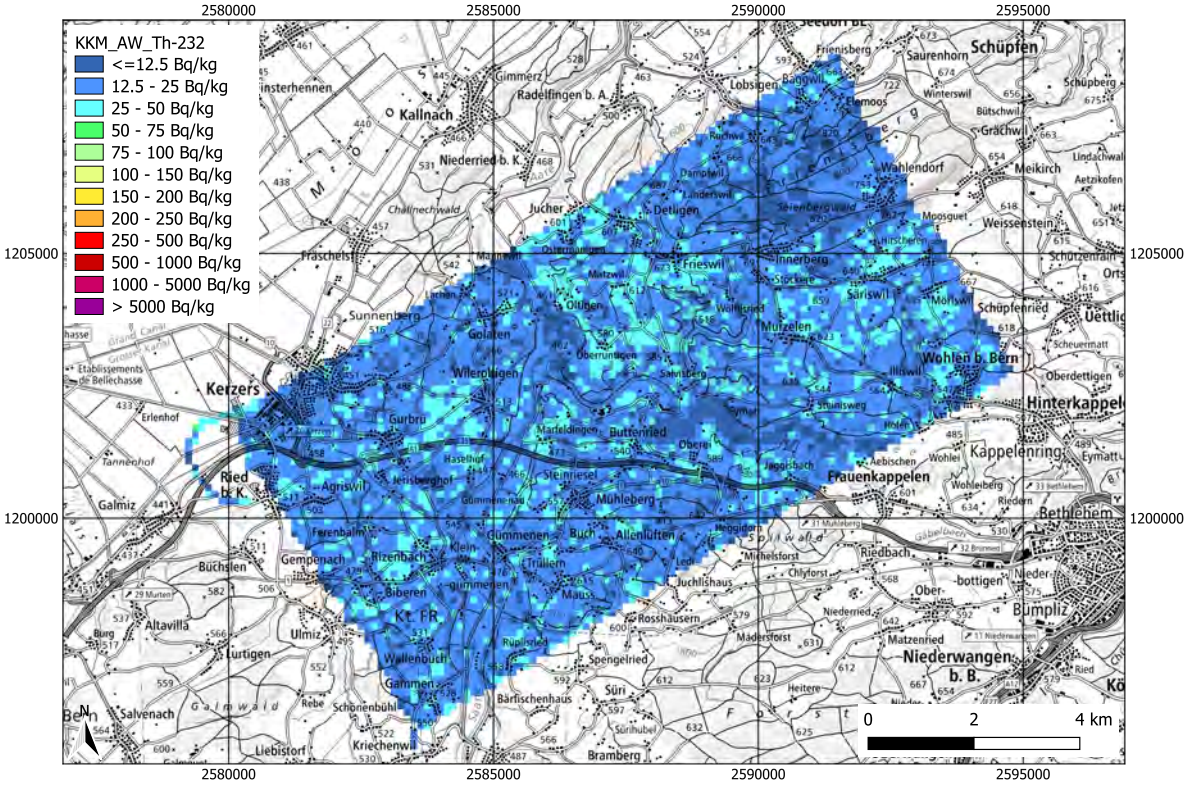

Figure 6.9: ^{232}Th activity concentration in the vicinity of KKM. Geodaten©swisstopo.

Chapter 7

Missions overview in the frame of the AGC25 international exercise

An overview of the exercise locations is provided in Figure 7.1.The military airfield in Dübendorf (LSMD) was chosen as base for flight operations as well as settlement for the rest of the team, including data analysis experts and the organisation team. The farthest areas designated for the exercise were those for missions one and two, located approximately $100\,\mathrm{km}$ from the base.

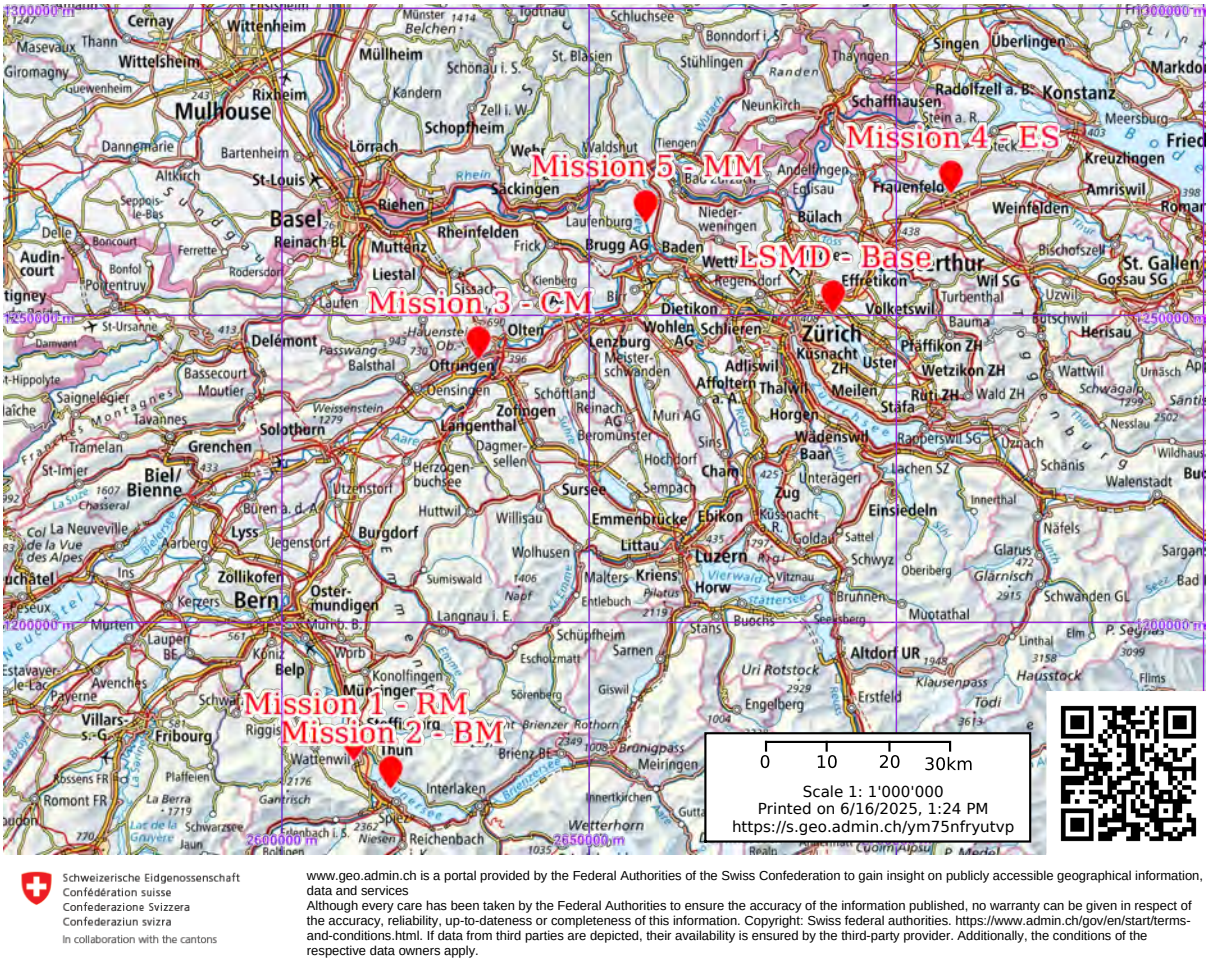

Figure 7.1: Mission locations of the AGC25.

Figure 7.2 outlines the complete schedule for the AGC25 exercise, spanning from Sunday, 1st June to Friday, 6th June 2025. The exercise commenced with a general briefing on Sunday followed by press-related activities and base setup on Monday morning. Operational missions

began on Monday afternoon with Missions 1 and 2 (Reference Measurement - RM and Background Measurement - BM), as well as Mission 5 (Mixed Measurements - MM). The six helicopter teams were equally split over the Missions 1 & 2 and Mission 5. Mission 3 (Composite Mapping - CM) was planned to be carried out on Tuesday, followed by Mission 4 (Exercise with Sources - ES) on the subsequent day, which also included drone-based operations. The remaining sessions for Mission 5 and Missions 1 & 2 were scheduled for Thursday morning. Friday was dedicated to data evaluation, debriefings, final presentations, and the official closure of the exercise. Daily morning briefings with the pilots, end-of-day debriefings, lunch breaks, and logistical preparations were consistently integrated into the programme. The timetable in Figure 7.2 served as a central coordination tool to ensure a coherent and well-paced execution of all AGC25 activities.

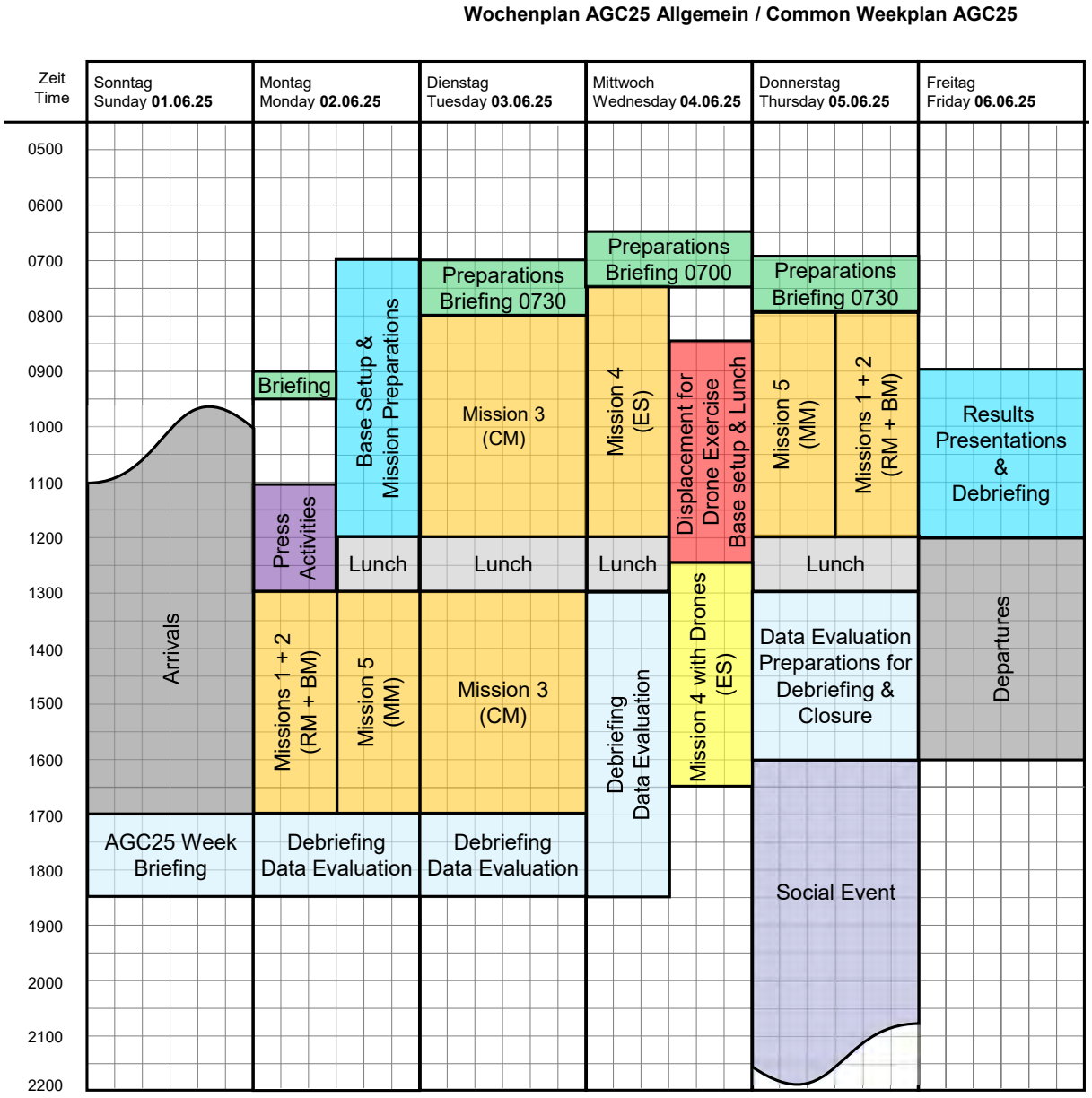

Figure 7.2: General schedule of the AGC25 week.

7.1 Mission 1 – RM – Thun military training area

Mission 1 (RM) was conducted to establish a reference measurement over an area characterised by smooth topography and a natural isotopic distribution. The site, located within the Thun Military Training Area, was thoroughly characterised in 2020 using in-situ gamma spectrometry and ambient dose equivalent rate measurements (PSI Report 21-01, see Appendix A). Figure 7.3 shows the locations of the in-situ measurements, and the corresponding values are reported in Table 7.1. The average over these locations was used as the reference for the ambient dose equivalent rate and radionuclides activity concentrations.

Figure 7.3: Overview of 2020 in-situ measurement at Thun military training ground. ©swisstopo.

The mission consisted of seven parallel flight lines, spaced by $125\,\mathrm{m}$, represented in Figure 7.4, each defined as follows:

Line 1: from $46.74761, 7.57829$ to $46.76044, 7.59893$

Line 2: from $46.74675, 7.57933$ to $46.76072, 7.60183$

Line 3: from $46.74588, 7.58038$ to $46.76037, 7.60370$

Line 4: from $46.74501, 7.58142$ to $46.75989, 7.60538$

Line 5: from $46.74386, 7.58246$ to $46.75910, 7.60653$

Line 6: from $46.74317, 7.58350$ to $46.75808, 7.60734$

Line 7: from $46.74241, 7.58455$ to $46.75696, 7.60798$

Table 7.1: Results of 2020 in-situ measurements at the military training area in Thun.

Point	Dose rate	Activity concentration $[\mathrm{Bq\,kg^{-1}}]$			
	$[\mathrm{nSv\,h^{-1}}]$	^{40}K	^{137}Cs	^{238}U	^{232}Th
1	68 ± 5	102 ± 12	0.8 ± 0.3	13 ± 2	10 ± 2
2	70 ± 6	110 ± 12	0.5 ± 0.2	14 ± 2	12 ± 2
3	67 ± 5	87 ± 10	–	13 ± 2	10 ± 2
4	73 ± 9	181 ± 20	1.7 ± 0.4	17 ± 2	18 ± 3
6	71 ± 5	121 ± 13	0.7 ± 0.7	15 ± 2	11 ± 3
7	79 ± 2	203 ± 29	2.4 ± 0.8	15 ± 3	18 ± 5
8	80 ± 6	211 ± 21	5.5 ± 1.3	17 ± 3	17 ± 3
9	84 ± 6	250 ± 24	6.5 ± 1.4	19 ± 3	24 ± 5
10	85 ± 6	251 ± 23	7.3 ± 1.4	18 ± 3	22 ± 3
11	65 ± 38	117 ± 96	–	11 ± 5	9 ± 6
12	80 ± 47	118 ± 97	–	10 ± 5	9 ± 7
15	85 ± 6	224 ± 23	6.8 ± 1.6	23 ± 4	20 ± 5
16	55 ± 32	80 ± 66	–	16 ± 12	8 ± 6
17	80 ± 6	280 ± 61	2.9 ± 1.2	17 ± 3	24 ± 4
18	80 ± 6	188 ± 41	7.5 ± 2.0	15 ± 3	16 ± 3
19	86 ± 7	201 ± 44	4.7 ± 1.5	15 ± 3	21 ± 4
20	83 ± 7	251 ± 53	6.2 ± 1.6	20 ± 3	24 ± 4
25	71 ± 6	210 ± 45	2.8 ± 0.9	21 ± 3	19 ± 4
27	78 ± 6	175 ± 39	6.6 ± 1.8	18 ± 3	16 ± 3
28	75 ± 6	173 ± 39	3.8 ± 1.3	14 ± 3	15 ± 5
29	88 ± 7	262 ± 57	6.5 ± 1.9	20 ± 4	23 ± 5
30	82 ± 7	247 ± 54	4.7 ± 1.5	18 ± 3	21 ± 6
32	83 ± 7	264 ± 56	7.1 ± 1.8	29 ± 4	21 ± 6
Average	77 ± 8	187 ± 63	4.5 ± 2.4	17 ± 4	17 ± 6

All lines had to be flown at the reference ground clearance of $90\,\mathrm{m}$ ($300\,\mathrm{ft}$). For each team, the total measurement time could not exceed 15 minutes (detailed schedule in Table 7.2). Flight speed was determined at the discretion of each team. Additional survey lines within the designated area were permitted until the 15 minute time limit had elapsed. Upon completion of Mission 1, teams had to proceeded directly to Lake Thun to carry out Mission 2.

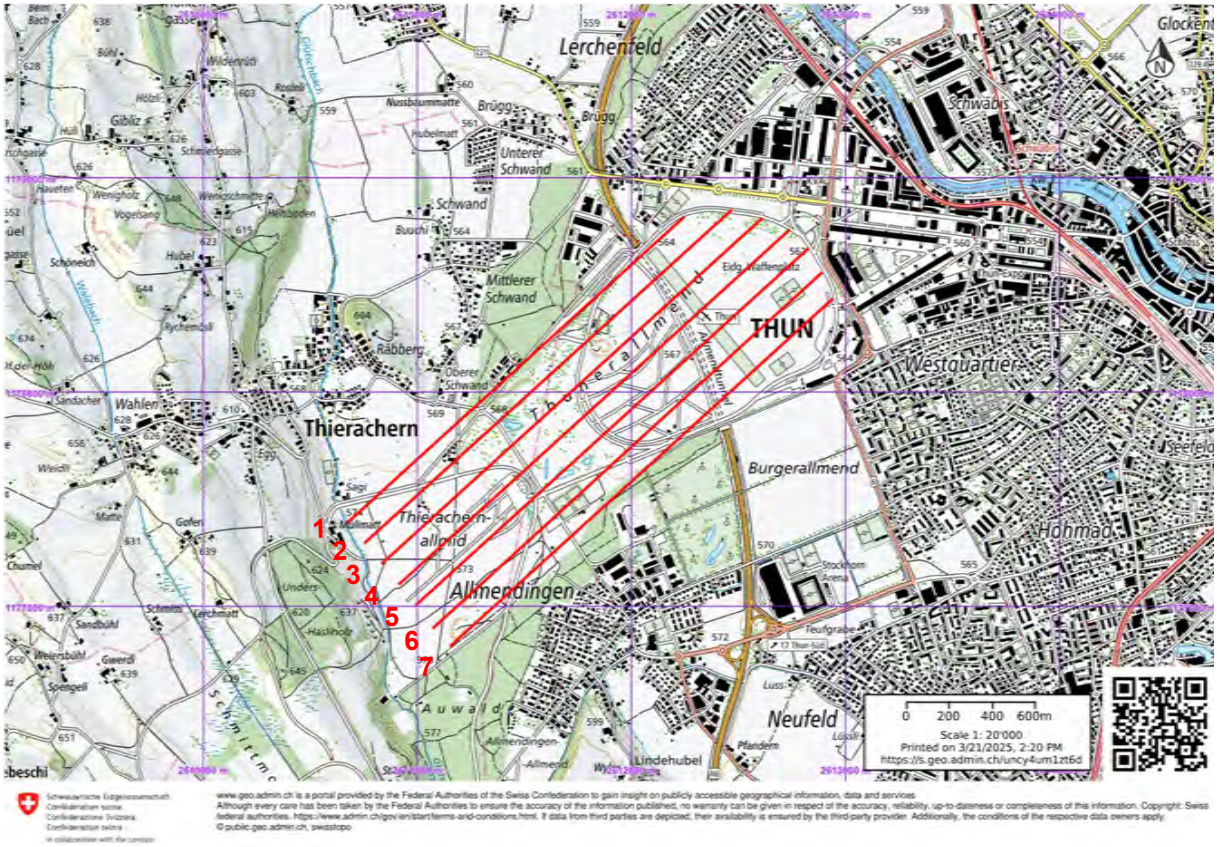

Figure 7.4: Map of Mission 1 – RM at the Thun military training area, with given flight lines.

Table 7.2: Mission 1 schedule.

Day	Team	Mission	Take Off	Mission Start	Mission End	Landing
Mo, 2.6.25	CZE	1 – RM	13:30	14:05	14:20	→ 2 – BM
Mo, 2.6.25	DEU	1 – RM	13:30 (to refuel Belp)	14:40	14:55	→ 2 – BM
Mo, 2.6.25	CHE2	1 – RM	14:40	15:15	15:30	→ 2 – BM
Thu, 5.6.25	CHE1	1 – RM	08:00	08:35	08:50	→ 2 – BM
Thu, 5.6.25	FRA	1 – RM	08:35	09:10	09:25	→ 2 – BM
Thu, 5.6.25	LTU	1 – RM	09:10	09:45	10:00	→ 2 – BM

7.2 Mission 2 – BM – Lake Thun

Mission 2 (BM) involved conducting background radiation measurements over a body of water, specifically Lake Thun. The primary objective of the mission was to obtain data of the helicopters and cosmic radiation background, without the signal of terrestrial radionuclides. The task consisted in a single predefined line (Start: 46.72840, 7.64814, End: 46.68943, 7.71726), over Lake Thun (Figure 7.5), to be flown at increasing ground clearances. The heights above ground level to be covered, in priority order, were as follows: $90\,\mathrm{m}$ ($300\,\mathrm{ft}$), $180\,\mathrm{m}$ ($600\,\mathrm{ft}$), $300\,\mathrm{m}$ ($1000\,\mathrm{ft}$), $600\,\mathrm{m}$ ($2000\,\mathrm{ft}$), $1200\,\mathrm{m}$ ($4000\,\mathrm{ft}$), $1800\,\mathrm{m}$ ($6000\,\mathrm{ft}$), and $2400\,\mathrm{m}$($8000\,\mathrm{ft}$). Priority was given to the altitudes below $300\,\mathrm{m}$. The time allotted to each team for the mission was 30 minutes, with approximately two minutes spent on the line at each flight altitude per pass. The schedule of each team is summarised in Table 7.3.

Figure 7.5: Map of Mission 2 – BM over Lake Thun, with given flight line.

Table 7.3: Mission 2 schedule.

Day	Team	Mission	Take Off	Mission Start	Mission End	Landing
Mo, 2.6.25	CZE	2 – BM	1 – RM →	14:25	14:55	15:30
Mo, 2.6.25	DEU	2 – BM	1 – RM →	15:00	15:30	16:05
Mo, 2.6.25	CHE2	2 – BM	1 – RM →	15:35	16:05	16:40
Thu, 5.6.25	CHE1	2 – BM	1 – RM →	08:55	09:25	10:00
Thu, 5.6.25	FRA	2 – BM	1 – RM →	09:30	10:00	10:35
Thu, 5.6.25	LTU	2 – BM	1 – RM →	10:05	10:35	11:10

7.3 Mission 3 – CM

Mission 3 (CM) focused on a composite mapping exercise conducted collaboratively by all participating teams. The objective was twofold: (1) survey a large area, of approximately $2200\,\mathrm{km}^2$, using coordinated flight operations and comprehensive measurement strategies to produce common radiological maps, (2) locate any radioactive source within the large predefined area. The mission was set in the Central Plateau region of Switzerland, whose map is provided in Figure 7.6. The designated measurement area was defined by five geographical points:

Point 1: $47.38572, 7.50671$

Point 2: $47.02627, 7.75089$

Point 3: $47.23962, 8.35246$

Point 4: $47.50477, 8.16434$

Point 5: $47.50008, 7.83374$

The Mission started with the planning on Monday June 2$^{\text{nd}}$, when a dedicated group including member of all teams and guided by the host nation was tasked with devising the survey strategy and subdividing and assigning areas to each team.

Operational restrictions for this mission included the allocation of two full fuel tanks per team, one for the morning and one for the afternoon session. Refuelling was exclusively foreseen at the LSMD base during the midday break. Ahead of the mission planning, information about the possible presence of radioactive sources in the area, with at least one known source of ^{137}Cs having an activity larger than $350\,\mathrm{MBq}$ was given. Nevertheless, the number, location, nuclide and activity of the radionuclide sources was not disclosed.

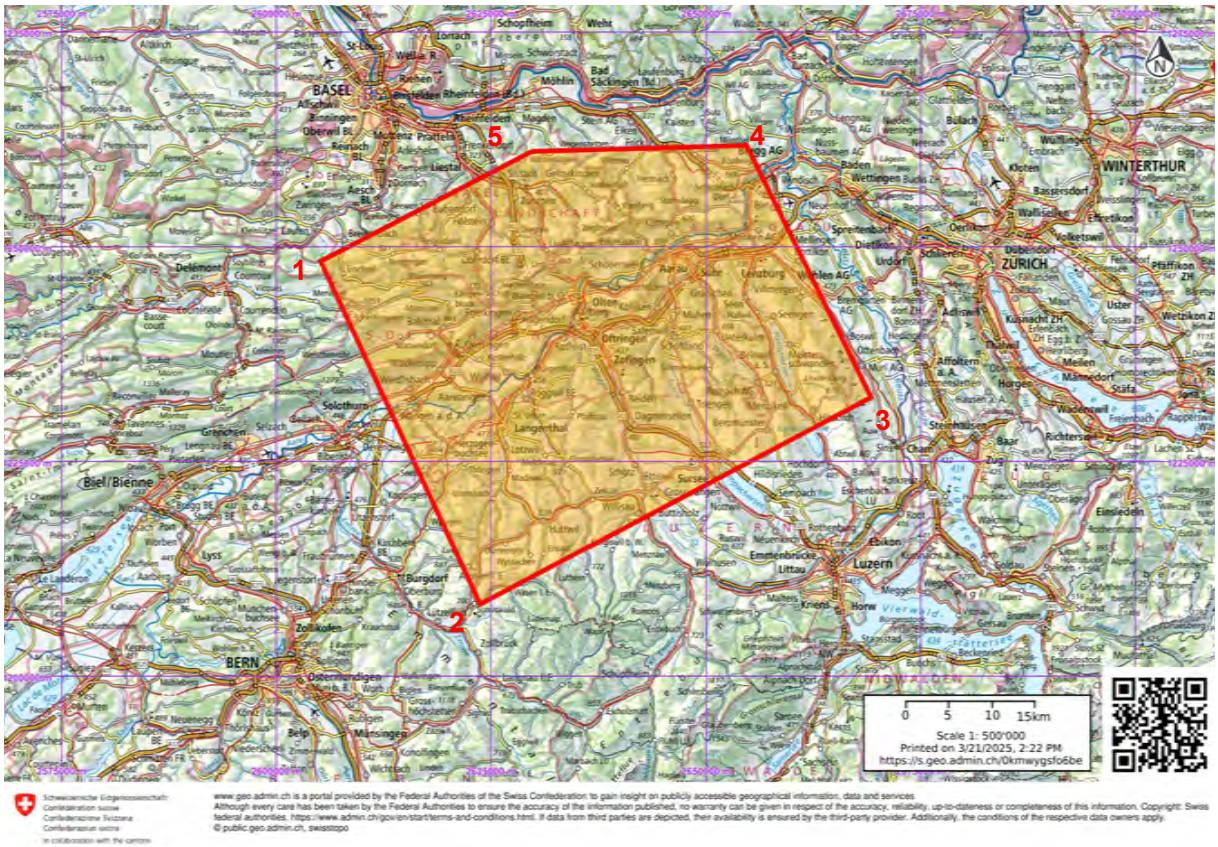

Figure 7.6: Map of Mission 3 – CM in the region: Breitenbach (SO) – Huttwil (BE) – Muri (AG) – Brugg (AG) – Liestal (BL).

Radionuclide sources, summarised in Table 7.4, were deployed in three locations:

At Seebru, six ^{137}Cs sources were positioned, next to one another, on a restricted military site. Their combined activity amounts to $0.4\,\mathrm{GBq}$, representing a low-to-moderate intensity configuration.

At Eichwald, three different radionuclides are co-located within a military area: ^{137}Cs ($0.7\,\mathrm{GBq}$), ^{133}Ba ($0.4\,\mathrm{GBq}$), and ^{60}Co ($0.16\,\mathrm{GBq}$). The total deployed activity on the mission day is approximately $1.26\,\mathrm{GBq}$. This site therefore provided a mixed-isotope detection challenge of moderate activity level.

At Dagmersellen, a single high-activity ^{137}Cs source ($8.5\,\mathrm{GBq}$) was positioned next to a gas depot building located in a publicly accessible woodland area. Owing to its high activity, this source would have constituted the most significant detection signal of the mission, simulating a scenario requiring heightened security considerations. During the exercise, however, the source was not removed from its shielding as originally planned; instead, it remained inside the opened shielding, resulting in a narrowly collimated, upward-directed radiation field.

All sources were transported, handled, and supervised by qualified personnel holding recognised Swiss radiation protection certifications. Oversight was ensured by the NBC-EOD Centre of Excellence, under whose licence the sources are operated. Each site was continuously staffed with redundant monitoring teams, ensuring both operational safety and regulatory compliance.

Table 7.4: Source specifications for Mission 3 at the three deployment sites.

Location	Coordinates & Site	Nuclide & Activity
Seebru	$7.70124\ \ 47.46442$ Military area	$6\times$ ^{137}Cs, $0.067\,\mathrm{GBq}$
Eichwald	$8.09757\ \ 47.46739$ Military area	^{137}Cs, $0.70\,\mathrm{GBq}$ ^{133}Ba, $0.40\,\mathrm{GBq}$ ^{60}Co, $0.16\,\mathrm{GBq}$
Dagmersellen	$7.97804\ \ 47.20367$ Gas depot	^{137}Cs, $8.50\,\mathrm{GBq}$

7.4 Mission 4 – ES – Frauenfeld military training area

Mission 4 (ES) was designed to test the ability of teams to detect, identify, and quantify radioactive sources within a defined area. The exercise took place in the Frauenfeld Military Training Area, depicted in Figure 7.7, with radioactive sources located within the defined perimeter, identified by the following eight corner points:

Point 1: $47.58247, 8.88892$

Point 2: $47.56772, 8.89572$

Point 3: $47.56829, 8.90231$

Point 4: $47.57162, 8.91022$

Point 5: $47.57778, 8.92170$

Point 6: $47.58268, 8.93014$

Point 7: $47.58529, 8.93673$

Point 8: $47.59271, 8.93330$

Although the flight strategy was left free, some operational restrictions were enforced. Each team had to enter the flight area from the west and exit to the east. Additionally, a designated No Fly Zone to the west of the mission area was present. Scheduled flight times were allocated for each team and summarised in Table 7.5, with a maximum duration of 30 minutes per team. The recommended altitude was between 70 and 90 meters above ground level.

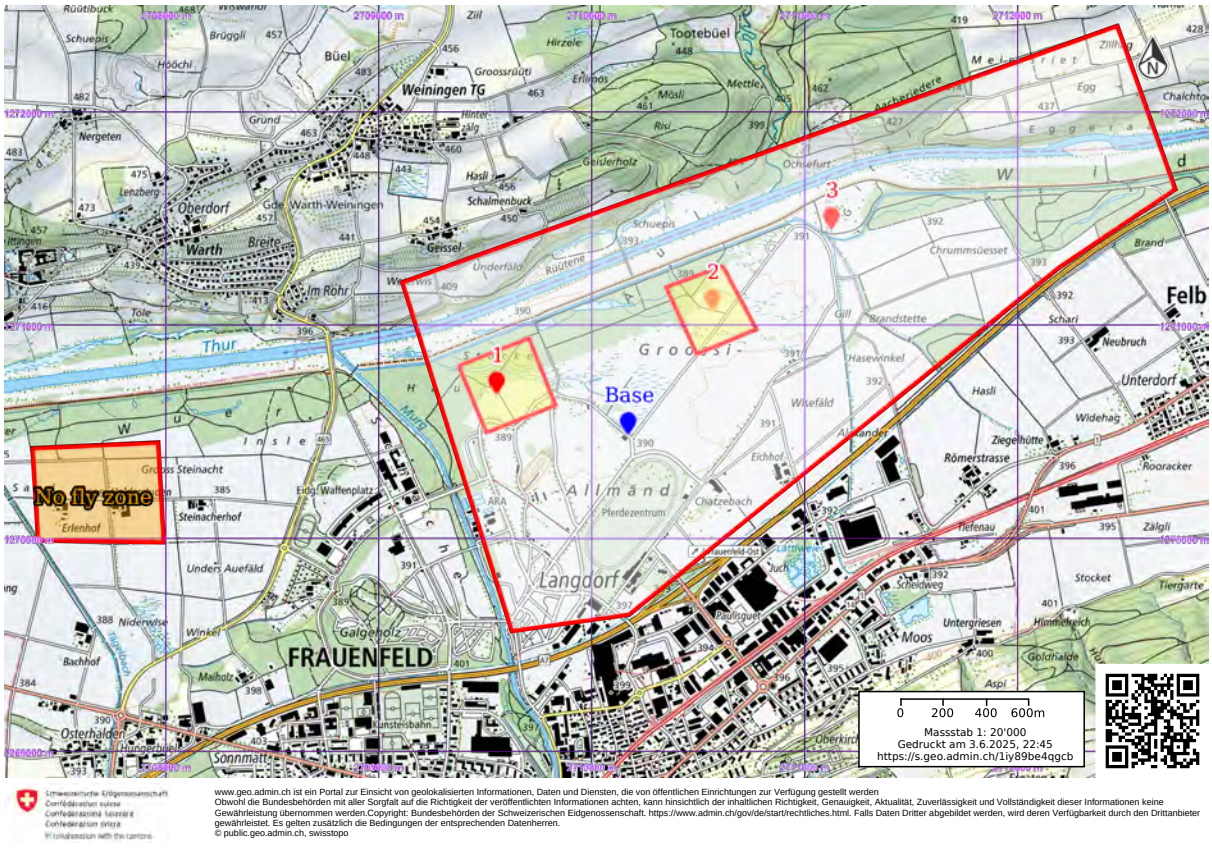

Figure 7.7: Location of radioactive sources in Mission 4.

Table 7.5: Mission 4 schedule.

Day	Team	Task	Take Off	Mission Start	Mission End	Landing
Wed, 4.6.25	CHE1	4 – ES	07:45	08:00	08:30	08:45
Wed, 4.6.25	LTU	4 – ES	08:20	08:35	09:05	09:20
Wed, 4.6.25	DEU	4 – ES	08:55	09:10	09:40	09:55
Wed, 4.6.25	CZE	4 – ES	09:30	09:45	10:15	10:30
Wed, 4.6.25	FRA	4 – ES	10:05	10:20	10:50	11:05
Wed, 4.6.25	CHE2	4 – ES	10:40	10:55	11:25	11:40

Radionuclide sources were placed within the designated areas at three locations (Points 1,2, and 3) illustrated in Figure 7.7. The precise location, radionuclide and activity is summarised in Table 7.6. The ^{137}Cs sources at point 2 were arranged in a line along the path at $10\,\mathrm{m}$ intervals, as shown in Figure 7.8.

Table 7.6: Source specifications for Mission 4 at the three deployment sites.

Location	Coordinates	Nuclide & Activity
Point 1	8.89487 47.57770	^{137}Cs, $0.7\,\mathrm{GBq}$ ^{133}Ba, $0.4\,\mathrm{GBq}$ ^{60}Co, $0.16\,\mathrm{GBq}$
Point 2	8.90843 47.58104	$6\times$ ^{137}Cs, $0.067\,\mathrm{GBq}$
Point 3	8.91595 47.58440	^{241}Am, $1.8\,\mathrm{GBq}$

Figure 7.8: ^{137}Cs sources layout at Point 2 during Mission 4.

7.5 Mission 5 – MM – Paul Scherrer Institute

The objective of Mission 5 (MM) was to conduct detailed measurements over two specific areas of interest. Area A, encompassing most of the Paul Scherrer Institut (PSI), including the high energy accelerators' complex where very short-lived radionuclides are emitted from the stack, and the surrounding region, including Rotbergegg, where naturally elevated activity concentrations of ^{232}Th are present. Area B, covering instead the SwissFEL facility at PSI, where a $2.7\,\mathrm{TBq}$ ^{75}Se source was placed to test the limits of the acquisition systems.

The flight schedule for the mission is summarised in Table 7.7 The mission had to comply with strict operational constraints. Most importantly, the total flight time over Areas A and B combined could not exceed 30 minutes. Additionally, Area B was designated as a No Fly Zone until all operations in Area A were fully completed.

For Area A, the designated flight polygon is defined by the following six points represented in Figure 7.9 :

Point 1: 47.55010, 8.20070

Point 2: 47.53310, 8.20070

Point 3: 47.53320, 8.22500

Point 4: 47.53650, 8.22500

Point 5: 47.53630, 8.24694

Point 6: 47.55000, 8.24760

For Area B, the mission began with a mandatory flight line, starting at (47.535932, 8.230735) and ending at (47.526310, 8.231715), to be flown North to South. After this initial line, additional measurements could be taken within the defined rectangular region, provided the total duration remains within the 30 minute limit. Flight parameters, including flight paths within both areas, were left to the teams' discretion. However, the recommended flight height was 90 meters above ground level.

The $2.7\,\mathrm{TBq}$ ^{75}Se source was housed in an isotope handling device designed for radiographic weld testing. The device features remote control of the source position and a collimator limiting radiation to a $60°$ cone. To shield lateral emissions and ensure personnel safety, a $5\,\mathrm{cm}$ lead shield was installed around the collimator. The source was positioned within the fenced perimeter of the SwissFEL accelerator complex at coordinates PN 47.528907, PE 8.231452. Photographs of the installation, including the handling device and shielding, are shown in Figure 7.10. Simulations and calculations were conducted by the Calibration Laboratory for Ionising Radiation at PSI from the early planning stages of the mission to ensure the safety of personnel handling the source. A few weeks prior to the exercise, the entire setup was tested at the designated location in the presence of the regulatory authority. Transport and positioning and supervision of the source were carried out by a specialised company with qualified personnel holding recognised Swiss radiation protection certifications. In addition, a team of PSI radiation protection officers was present on-site during the two half-days over which the mission took place.

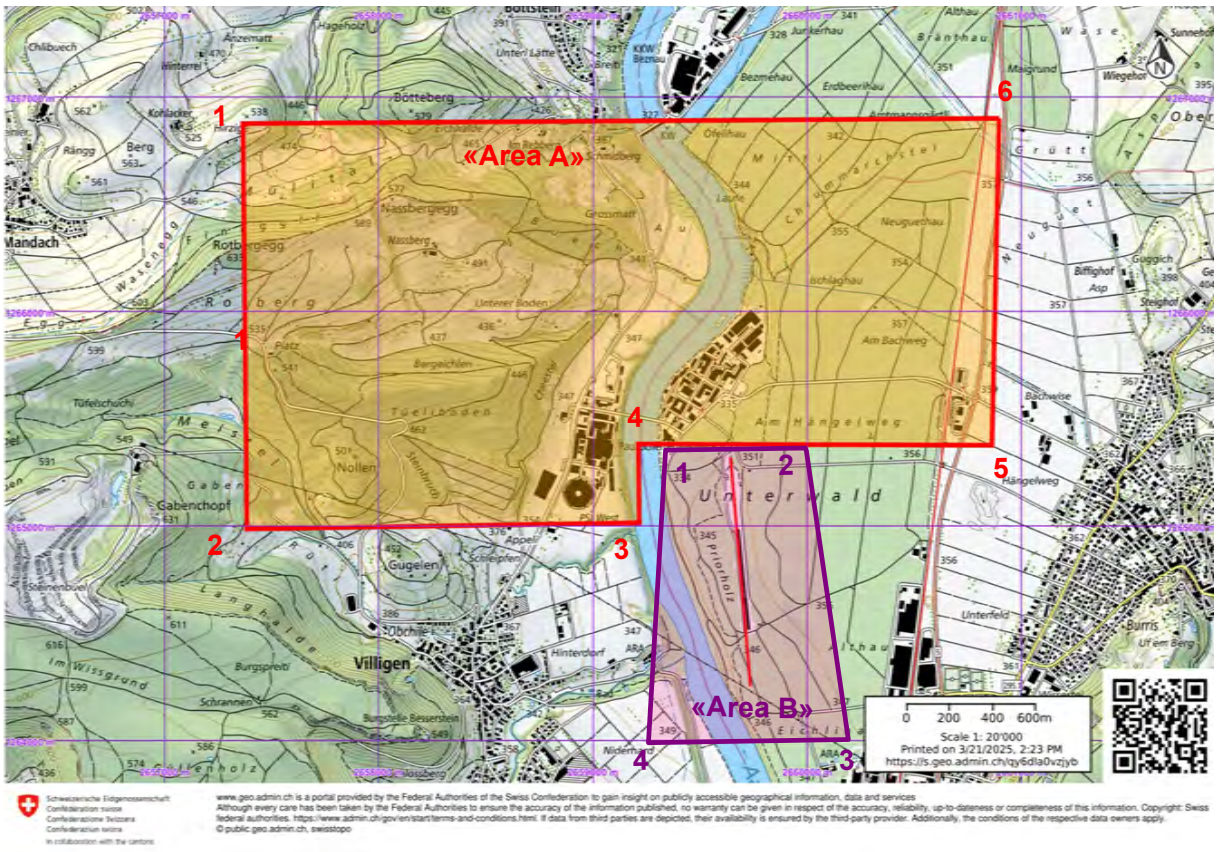

Figure 7.9: Map of Mission 5 – MM over Paul Scherrer Institute.

Table 7.7: Mission 5 schedule.

Day	Team	Task	Take Off	Mission Start	Mission End	Landing
Mo, 2.6.25	CHE1	5 – MM	13:40	14:00	14:30	14:50
Mo, 2.6.25	FRA	5 – MM	14:15	14:35	15:05	15:25
Mo, 2.6.25	LTU	5 – MM	14:50	15:10	15:40	16:00
Thu, 5.6.25	CHE2	5 – MM	08:05	08:25	08:55	09:15
Thu, 5.6.25	DEU	5 – MM	08:40	09:00	09:30	09:50
Thu, 5.6.25	CZE	5 – MM	09:15	09:35	10:05	10:25

Figure 7.10: ^{75}Se source used in Mission 5B: (a) Lead shield. (b) Lead shield at the rear and deployment hose. (c) Collimator inside the lead shield.

7.6 Mission with Drones

The afternoon of Wednesday, 4th June was dedicated to a drone exercise. This drone mission was adapted from Mission 4, which had been conducted with helicopters in the morning (see Section 7.4). The objective of the exercise was to locate, identify, and quantify the radioactive sources. As the entire area allotted to helicopters was too large for the drones to cover, two smaller zones around the radioactive sources were designated, referred to as Area 1 and Area 2 , shown in Figure 7.11. The sources were placed within the perimeter of the two areas, as indicated in Table 7.8.

Each team was allocated 45 minutes to fly and take measurements in each area. Additionally, teams were permitted to begin setting up their equipment 30 minutes before their scheduled time slot.

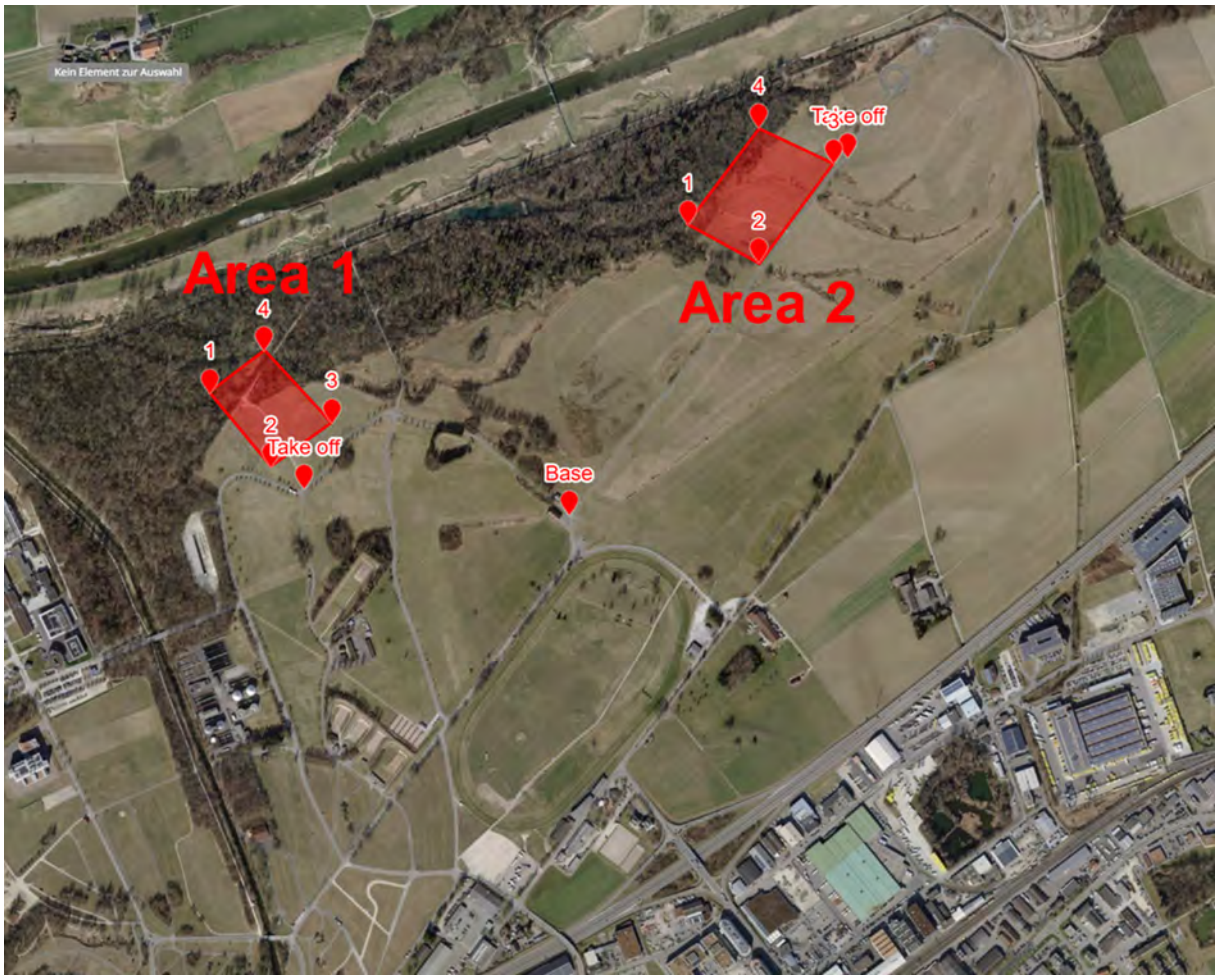

Figure 7.11: Area1 and Area2 used for drone measurements as part of Mission 4.

Table 7.8: The mission locations and the radioactive nuclides used for the Mission with drones.

Area	Coordinates		Sources	Source Number
Area 1	47.34400	8.53402	^{133}Ba, $0.4\,\mathrm{GBq}$	1 (Figure 7.12)
	47.34408	8.53403	^{137}Cs, $0.7\,\mathrm{GBq}$	2 (Figure 7.12)
	47.34415	8.53410	^{60}Co, $0.16\,\mathrm{GBq}$	3 (Figure 7.12)
Area 2	47.34517	8.54303	$6 \times {}^{137}$Cs, $0.067\,\mathrm{GBq}$	$1-6$ (Figure 7.13)
	47.34522	8.54271	^{241}Am, $1.8\,\mathrm{GBq}$	7 (Figure 7.13)

Figure 7.12: A close-up of the radioactive sources' location during Mission with Drones in Area 1.

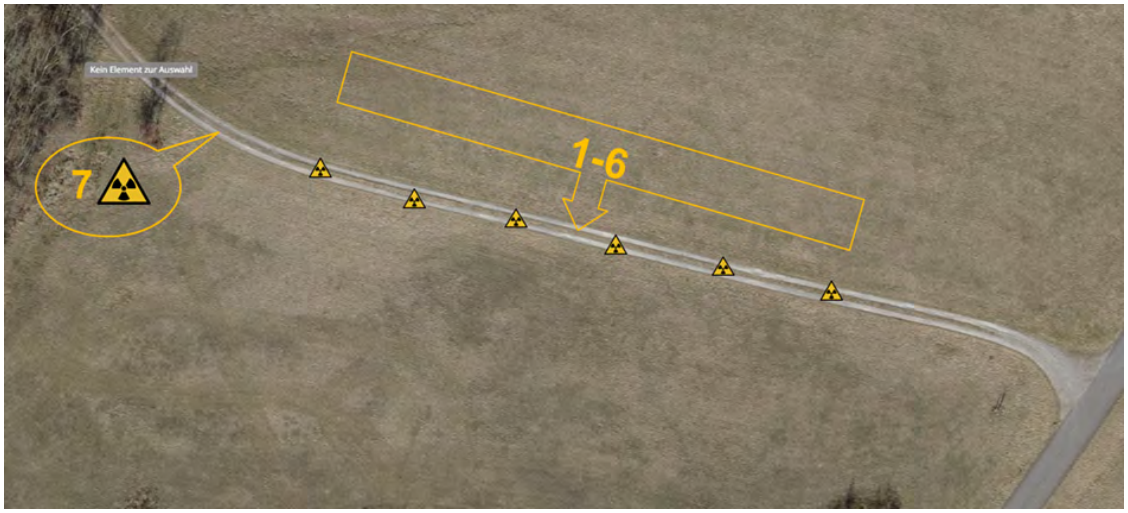

Figure 7.13: A close-up of the radioactive sources' location during Mission with Drones in Area 2.

7.7 Ground-based measurements

The Swedish Radiation Safety Authority (SSM) participated as observers in the AGC25 exercise in Switzerland. Apart from observing aerial measurements, the Swedish team also performed in agreement with the organisers of the AGC25 car-borne and backpack surveys.

The following monitoring tasks were undertaken by the Swedish team during the AGC25 Exercise.

- **Mission i SWE – large scale dose rate survey**
  During the exercise week SSM performed a number of car-borne dose rate surveys.
- **Mission ii SWE – source search Frauenfeld**
  Location, identification and quantification of radioactive sources within two designated areas in the outskirts of Frauenfeld, during the exercise with drones (Section 7.6). Movements were restricted to roads within the areas and in moments when no drones were flying.
- **Mission iii SWE – source search Paul Scherrer Institute**
  Location, identification and quantification of radioactive sources in the vicinity of the Paul Scherrer Institute, during Mission 5 (Section 7.5).

The following equipment was used: a Mona EPR system equipped with a $3" \times 3"$ NaI(Tl) detector and set to an integration time of 5 seconds; an Automess AD6150 with a Scintillator Probe 6150AD-b/E; and a Mirion AccuRad PRD.

Chapter 8

Results of the AGC25 international exercise

Each of the six participating teams – namely CHE1, CHE2, CZE, DEU, FRA, and LTU – submitted the results of an initial, preliminary evaluation within just a few hours following the completion of the measurement phase of the mission. The primary purpose of this rapid evaluation was to provide the teams with an opportunity to practise and refine their skills in quick data processing, as well as in the rapid generation and presentation of results, capabilities that are particularly critical in the context of an emergency response scenario, where timely and accurate information can be essential for decision-making. The raw data acquired by the Swiss teams, CHE1 and CHE2, and analysed using the AGS_CH software, were also processed within the same time frame.

Following the conclusion of the exercise, more thorough evaluations were carried out, and the final results were submitted to the AGC25 organising team no later than the 15$^{\text{th}}$ of September 2025.

8.1 Meteorological conditions during the international exercise

This section details environmental and weather conditions present during the AGC25. Weather parameters, such as air temperature, humidity, air pressure, wind, precipitation, and cloud coverage, relevant for aeroradiometric studies are displayed. The meteorological data utilised in this study is obtained from publicly accessible datasets provided by the Federal Office of Meteorology and Climatology MeteoSwiss [25]. All measurements are derived from ground-based observations featuring a temporal resolution of $10\,\mathrm{min}$.

Table 8.1: The missions and their respective dates presented with the nearest weather station, where meteorological data in $10\,\mathrm{min}$ intervals is available.

Mission	Weather station	Begin	End
Base (LSMD)	Zürich/Affoltern (REH)	01.06.2025 – 09:00	06.06.2025 – 16:00
Mission 1 (RM)	Thun (THU)	02.06.2025 – 13:30	02.06.2025 – 17:00
		05.06.2025 – 08:00	05.06.2025 – 17:00
Mission 2 (BM)		02.06.2025 – 13:30	02.06.2025 – 17:00
		05.06.2025 – 08:00	05.06.2025 – 17:00
Mission 3 (CM)	Egolzwil (EGO)	03.06.2025 – 08:00	03.06.2025 – 17:00
Mission 3 (DEU)		04.06.2025 – 11:30	04.06.2025 – 13:30
Mission 4 (ES)	Aadorf/Tänikon (TAE)	04.06.2025 – 07:30	04.06.2025 – 12:00
Mission 5 (MM)	Würenlingen/PSI (PSI)	02.06.2025 – 13:30	02.06.2025 – 17:00
		05.06.2025 – 08:00	05.06.2025 – 17:00

For each Mission conducted during the campaign, the meteorological conditions are characterised using data obtained from the weather station geographically closest to the respective mission's location. An overview of the missions alongside their associated weather stations is given in Table 8.1.
The environmental parameters considered in this analysis are defined as follows:

- air temperature [$^{\circ}\mathrm{C}$]
- relative humidity [$\%$]
- atmospheric pressure [hPa]
- wind velocity [$\mathrm{m\,s^{-1}}$]
- precipitation [mm]
- global radiation [$\mathrm{W\,m^{-2}}$]

The first three parameters, the air temperature, relative humidity and atmospheric pressure, are standard indicators of weather conditions and in this context, they offer a general overview on the environment present during the missions. Wind velocity is particularly relevant for flight operations, especially when conducting radiometric studies with drones. Precipitation is a critical environmental parameter when conducting radiometric studies as it can induce the process called wet deposition. The phenomenon is known and was studied and reported by Fujinami [26] and by Paatero and Hatakka [27] among others. ^{222}Rn is a radioactive isotope decaying via alpha decay with half life of 3.82 days [28] and is present naturally in the atmosphere. While ^{222}Rn in gas form is not highly soluble in water, its short-lived progeny such as polonium-218, lead-214 or bismuth-214 when attached to aerosols can be removed from the atmosphere by precipitation and deposited on the ground. This leads to an enhancement in ground radioactivity, the gamma-emitting radionuclides (^{218}Po, ^{214}Pb) contained in precipitation produce heterogeneous distribution of localised increases in gamma radiation exposure at ground level. The ^{238}U maps are especially affected by this phenomenon, since radon is a product of the uranium decay chain. The global radiation parameter quantifies the solar irradiation incident upon the ground surface and serves as an inversely proportional quantity for the cloud coverage, with lower radiation levels indicating increased cloud presence.

The meteorological parameters are evaluated for each mission and presented in the associated figures (see Figure 8.1, and Figures 8.2 – 8.9). For Mission 5, data on wind velocity is unavailable as the corresponding meteorological station (PSI) did not report measurements for this parameter (see Figure 8.4, 8.5). The environmental conditions are shown for a time window extending about one hour before the start and one hour after the end of each mission.

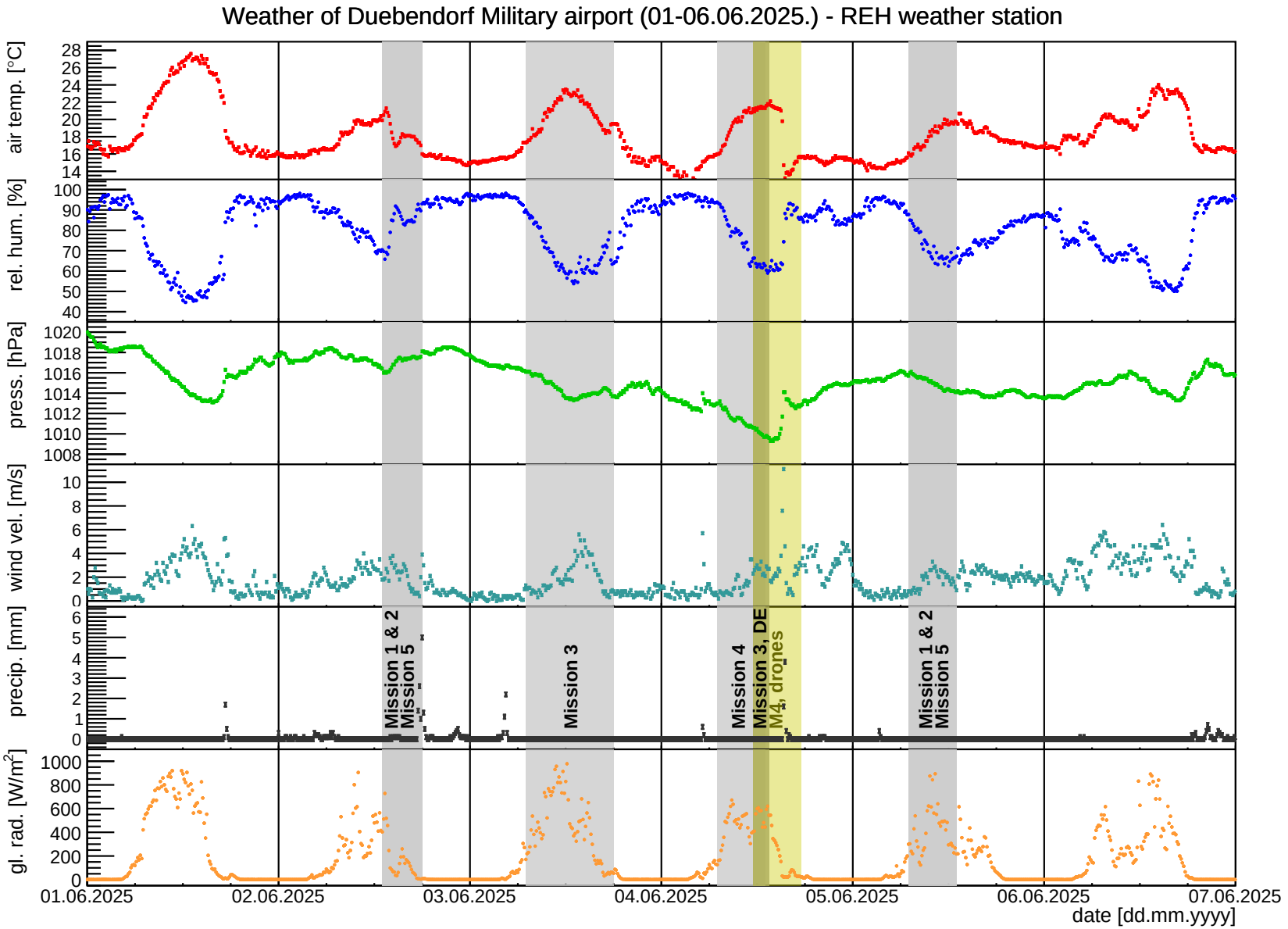

Figure 8.1: A summary of environmental conditions representative for the Dübendorf military airport (base) is shown. The timing of the individual missions is indicated on the figure, however, note that the sites of the missions do not spatially coincide with the location of the base.

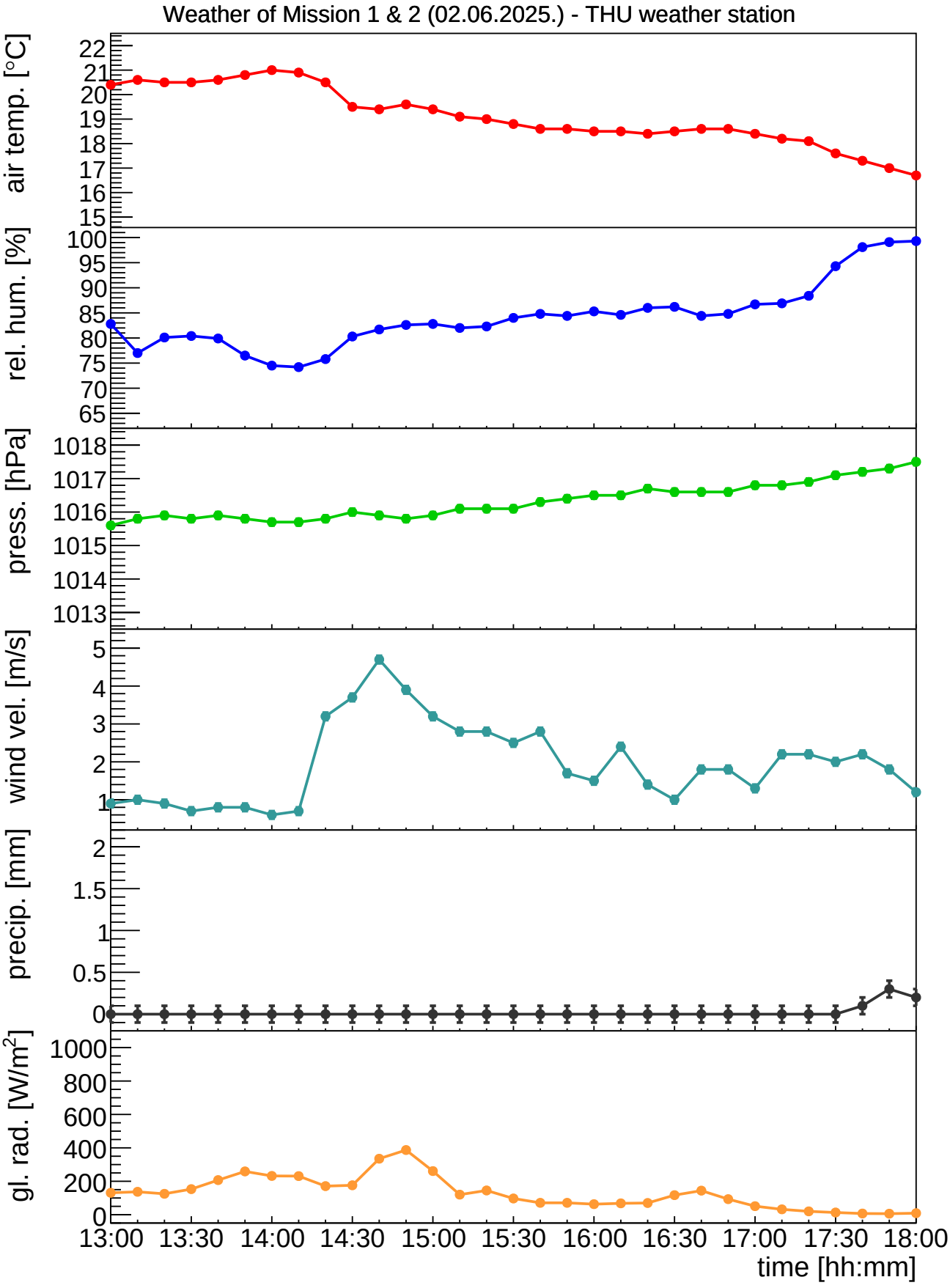

Figure 8.2: Environmental conditions corresponding to Mission 1 & 2, conducted on 02.06.2025.

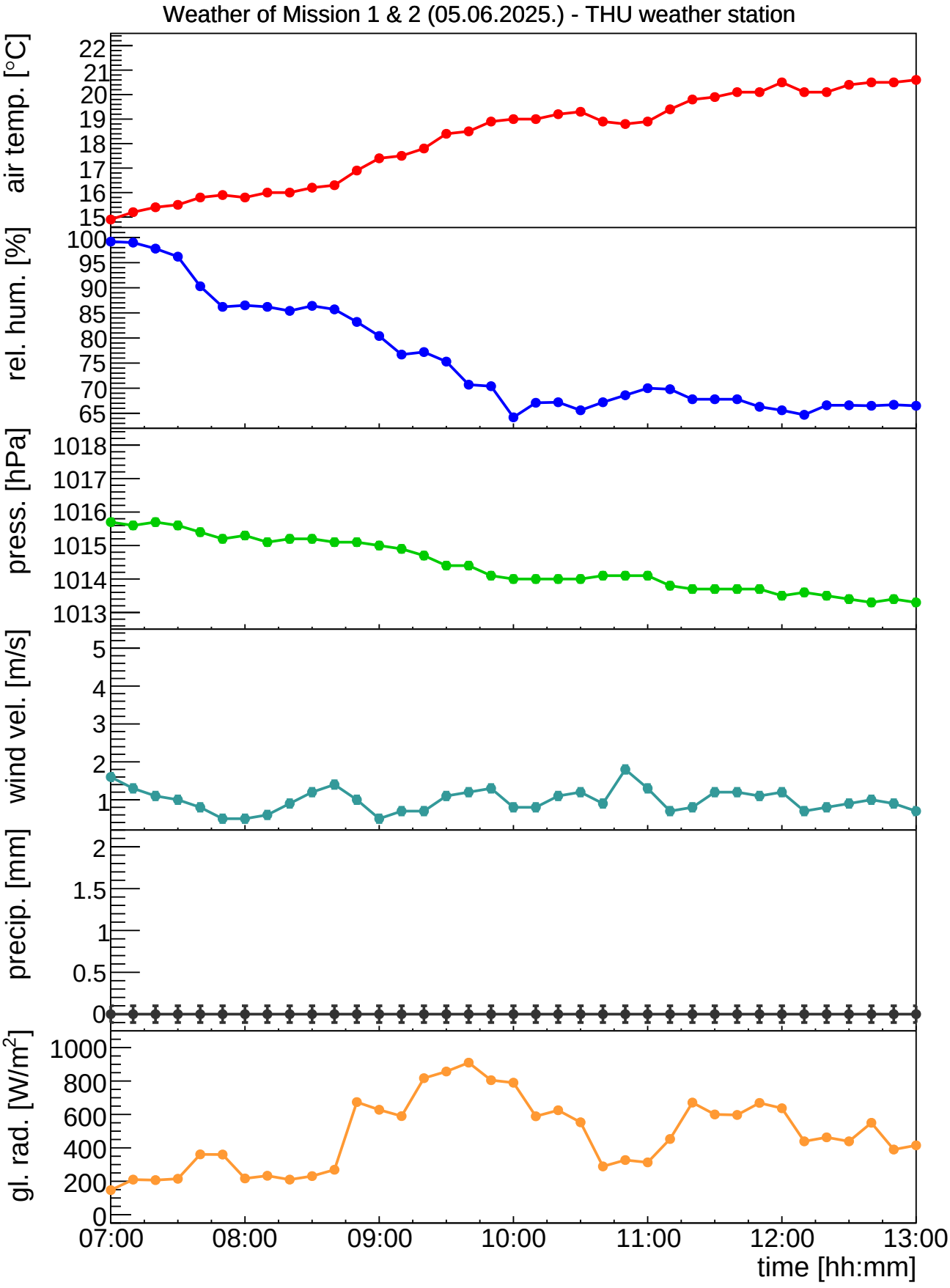

Figure 8.3: Environmental conditions corresponding to Mission 1 & 2, conducted on 05.06.2025.

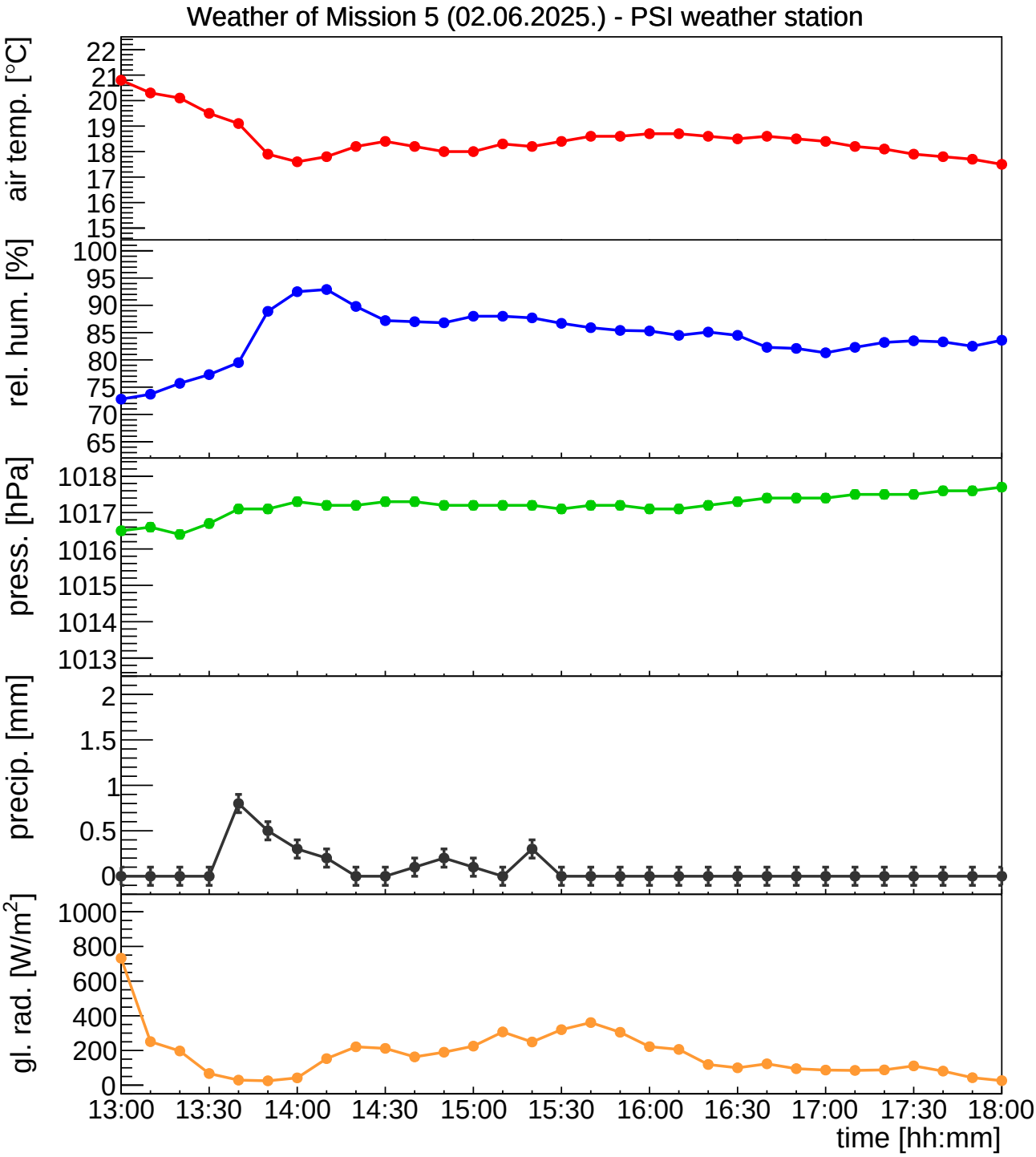

Figure 8.4: Environmental conditions corresponding to Mission 5, conducted on 02.06.2025.

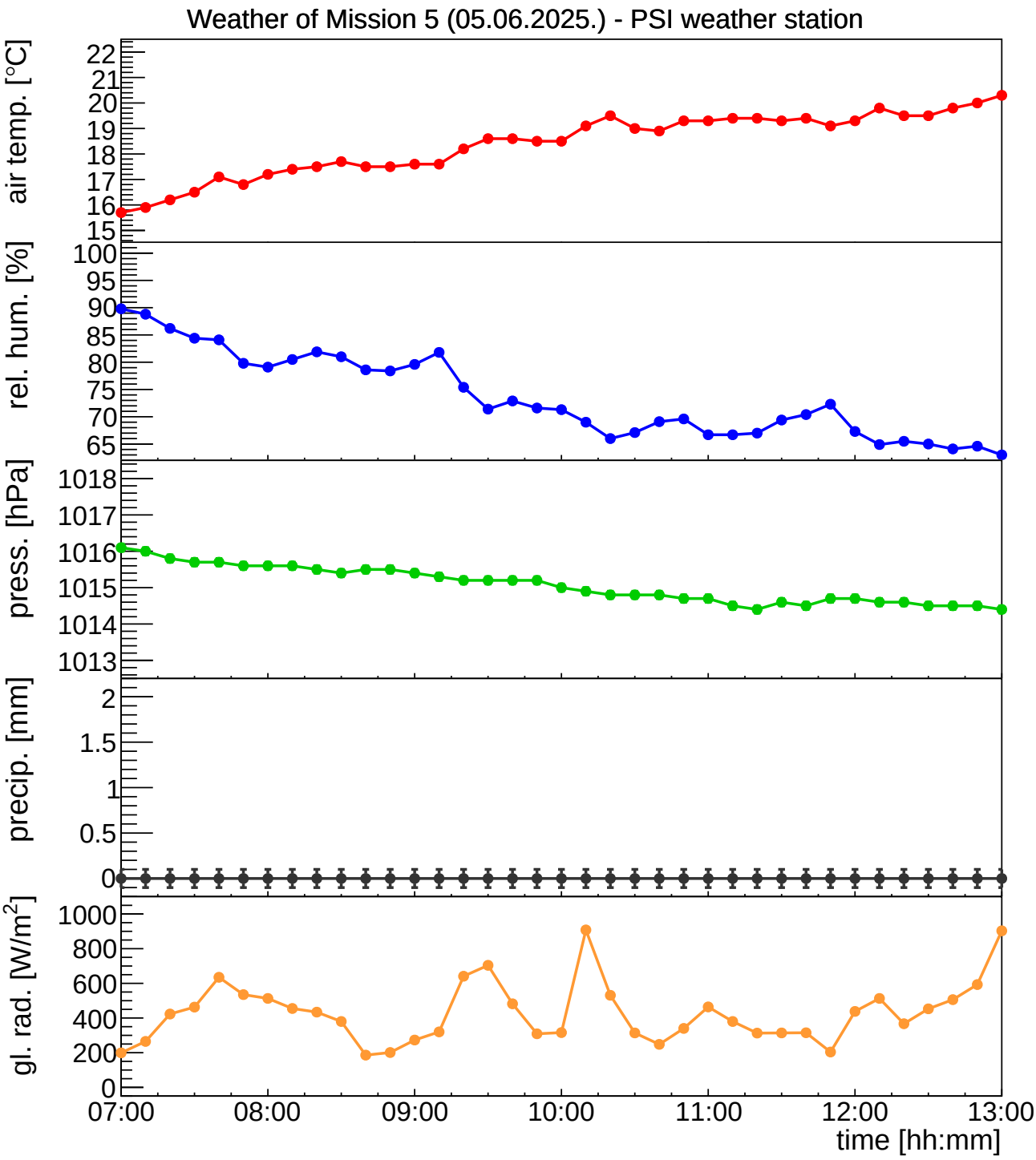

Figure 8.5: Environmental conditions corresponding to Mission 5, conducted on 05.06.2025.

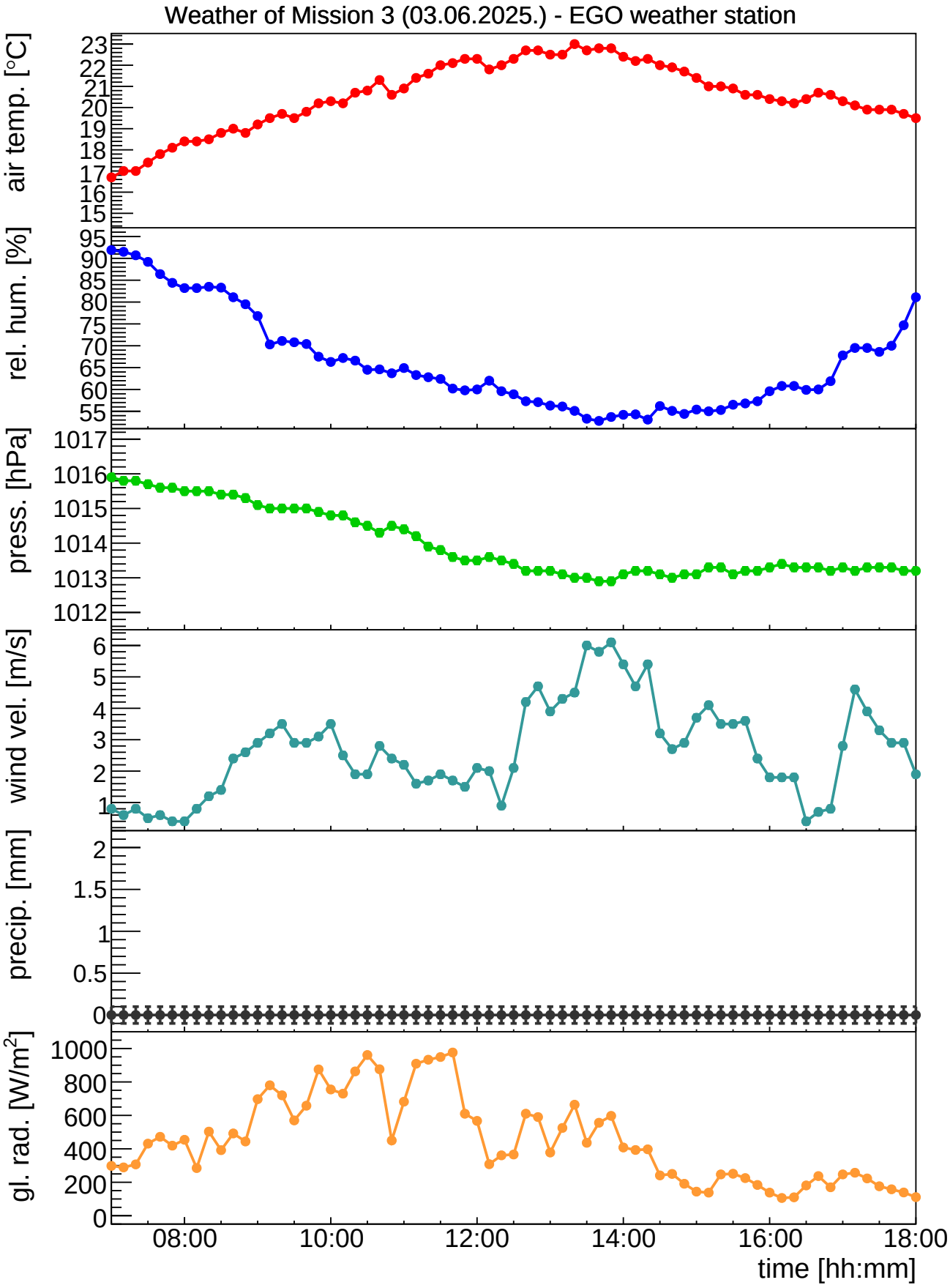

Figure 8.6: Environmental conditions corresponding to Mission 3, conducted on 03.06.2025

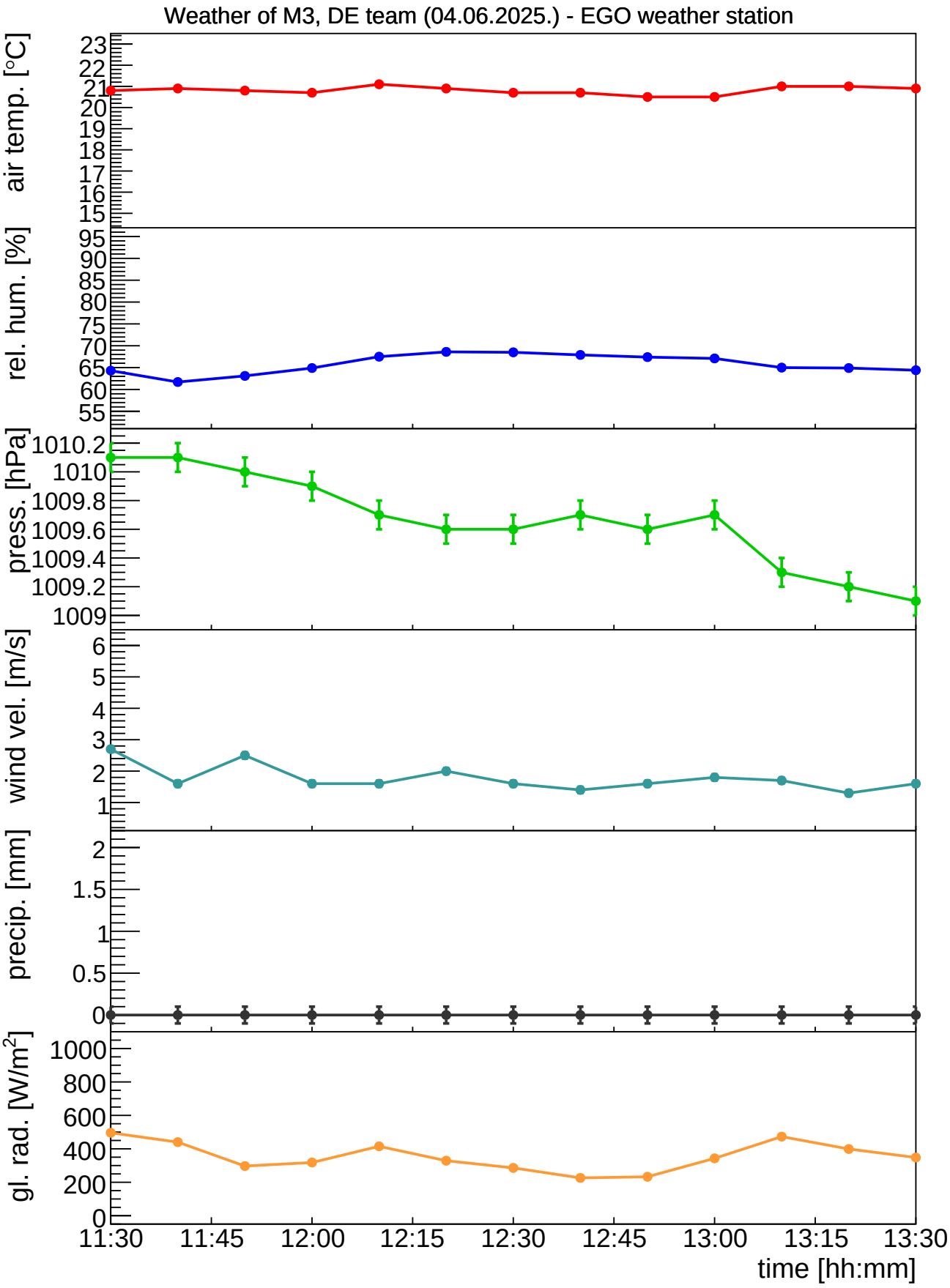

Figure 8.7: Environmental conditions corresponding to Mission 3, conducted on 04.06.2025.

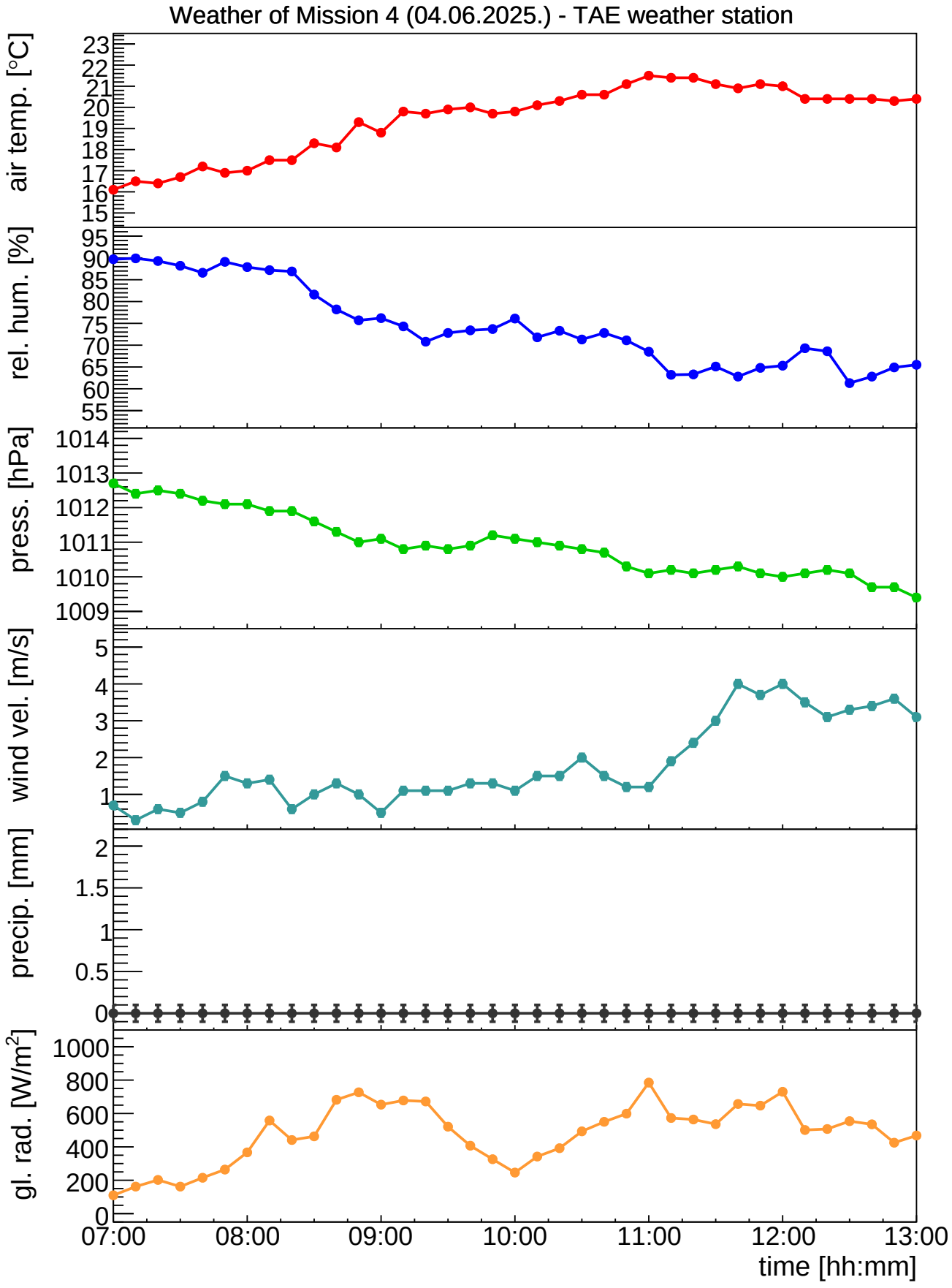

Figure 8.8: Environmental conditions corresponding to Mission 4, conducted on 04.06.2025.

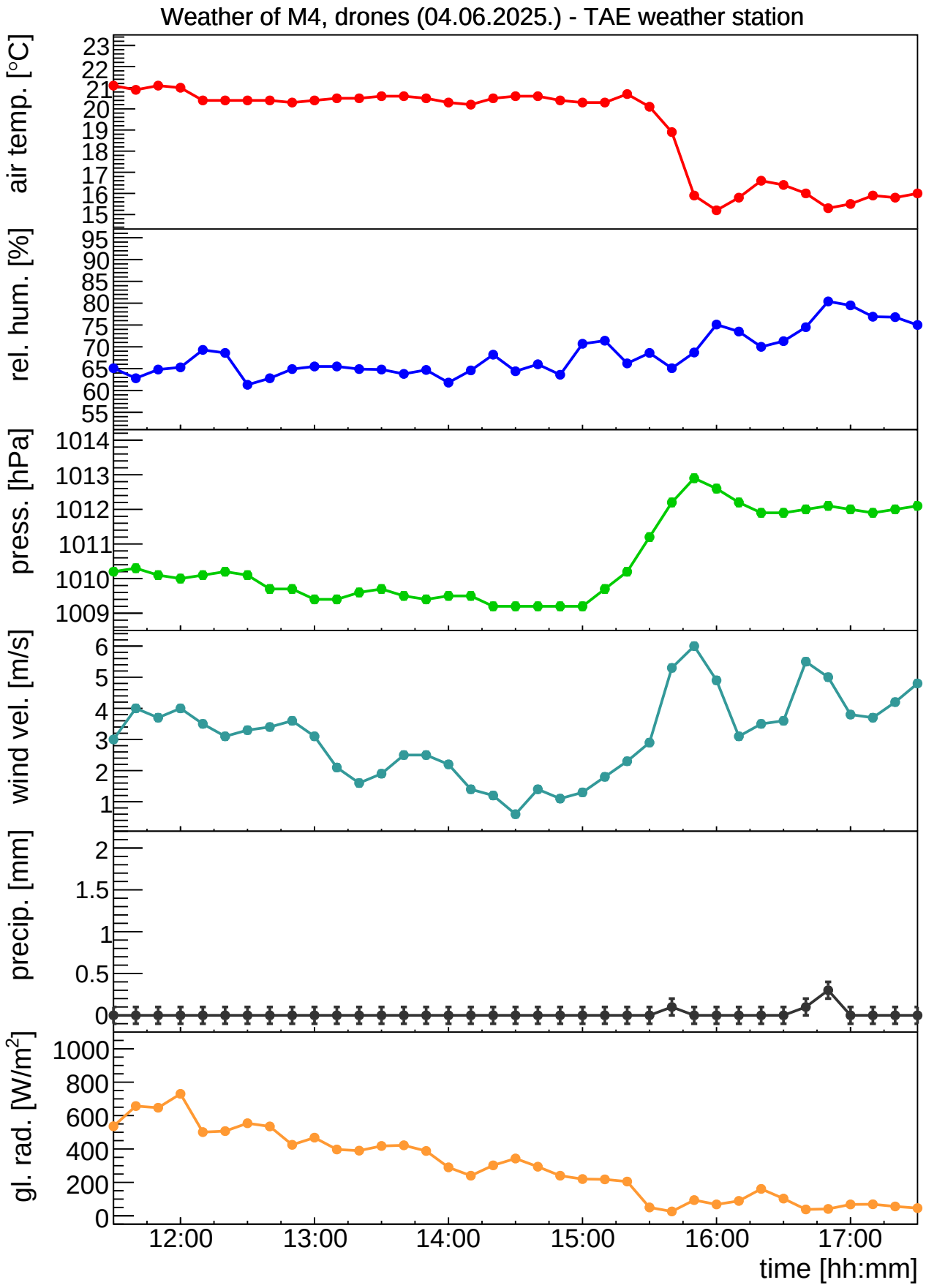

Figure 8.9: Environmental conditions corresponding to Mission 4, conducted on 04.06.2025 using drones.

8.2 Mission 1 – RM – Thun military training area

8.2.1 Comparison

In this section, the preliminary results of Mission 1 are compared to the final results evaluated after the exercise. For the teams CHE1, CHE2, CZE and DEU, no changes were made between the preliminary and final evaluations; therefore, the preliminary results are also considered final.

The preliminary evaluation of the Swiss data using the AGS_CH software used background and cosmic corrections performed in 2024 and a calibration carried out in 2021. The re-evaluation employed updated background and cosmic corrections, derived from the assessment of Mission 2, along with revised calibration factors.

The French team corrected both their preliminary and final results to account for the absence of one detector, as one of the four experienced technical issues during the measurements. The results from Mission 1 were calculated and reported using two different background estimations: one corresponding to a low radon concentration and another reflecting the elevated radon levels observed during Mission 2 (Section 8.3). As weather conditions and environmental data indicated possible higher radon concentrations during Mission 1, the latter estimation was considered more representative of the measurement conditions and was therefore adopted for inter-team and reference-value comparisons.

The LTU team conducted a preliminary evaluation of the data applying correction factors for background extraction, attenuation, and conversion, all of which were determined in 2024 shortly after the measurement system became operational, as described in Section 4.4. The re-evaluation yielded updated background corrections based on the Mission 2 assessment, as well as revised conversion coefficients (see Table 4.7). These new conversion coefficients were derived from system cross-calibration using in-situ measurements from Mission 2 and, therefore, more accurately reflect the site-specific response.

The results are presented per team using box plots. In each box plot, the thick black line represents the median value, while the coloured box denotes the interquartile range, covering the middle $50\,\%$ of the data. The whiskers extend to indicate the overall spread of the measurements, excluding any outlier. It should be noted that the variation shown by the box plots reflects the spatial variability of the measured values across the survey area, rather than the measurement uncertainty.

Figure 8.10 illustrates the ground clearance (PH) maintained by each team while surveying the target area during Mission 1. The prescribed ground clearance of $90\,\mathrm{m}$ above ground level is shown as a red dashed line. Overall, all teams successfully maintained ($\pm 10\,\mathrm{m}$) the assigned ground clearance throughout the survey. Minor differences observed between CHE1 and CHE1_AGS_CH, as well as between CHE2 and CHE2_AGS_CH, which share the same raw data, are attributed to the different methods used to calculate ground clearance. The Mirion software directly employs radar-derived ground clearance values, whereas the AGS_CH software estimates the clearance from corrected altitude data obtained via GPS and barometric measurements, from which the digital elevation model of the surveyed area is subtracted (Butterweck et al., 2021; see Appendix A).

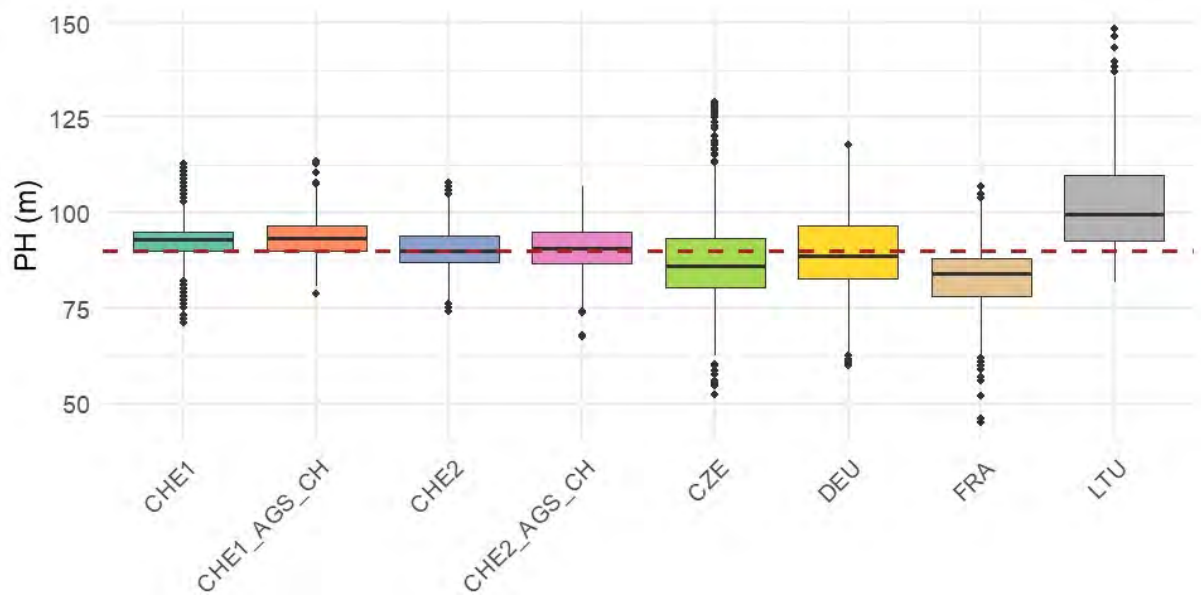

Figure 8.10: Ground clearance (PH) distribution in Mission 1 (RM) of each team. Reference ground clearance $90\,\mathrm{m}$ (red dashed line).

Figure 8.11 displays the preliminary estimation of the ambient dose equivalent rate (DHSR) measured within the reference area of the Thun military training ground, as determined during the exercise. All ambient dose equivalent rates derived from airborne measurements deviate between $-60\,\%$ and $11\,\%$ from the values obtained by ground measurements. The dose rates reported in the preliminary evaluation by the Lithuanian team are significantly lower compared to the results of other teams. Figure 8.12 summarises the final results of the ambient dose equivalent rate after applying updated background corrections and adjusted calibration, where applicable, for each team. The ambient dose equivalent rates evaluated by the Lithuanian team no longer exhibit the discrepancies observed in the preliminary evaluations, agreeing well with the reference. Deviations of the final averaged ambient dose equivalent rate from the reference value range between $-25\,\%$ and $5\,\%$.

In a further evaluation, the CZE team recalculated the ambient dose equivalent rate, estimating the cosmic dose rate with EXPACS, which takes into account the exact date and geographical position. Since it was a preliminary implementation of the method not embedded and validated in AGAMA, it was decided not to include it in the final results. The formulas applied since 2017 differ from the EXPACS model, and since AGAMA does not yet support EXPACS, calculations were based on averages over the measured area. For the given parameters (46.75357 N, 7.59651 E; 3rd June 2025; $674\,\mathrm{m}$ altitude, local effect parameter 0.2), the cosmic dose rate estimated using the previous calculation implemented in AGAMA was $32\,\mathrm{nSv\,h^{-1}}$, while the EXPACS estimate was $46\,\mathrm{nSv\,h^{-1}}$, resulting in a total ambient dose equivalent rate of $73\,\mathrm{nSv\,h^{-1}}$ including the terrestrial contribution. Although this difference is not significant for emergency response due to its relatively small absolute value, future work should aim to standardise the calculation method to ensure consistency and comparability of results among teams.

Figure 8.13 presents the preliminary estimates of the ^{40}K activity concentration (AW_K-40) measured within the defined polygon in the reference area of the Thun military training ground during the exercise. Airborne measurements show deviations ranging from $-35\,\%$ to $70\,\%$ compared to ground-based values. The preliminary results reported by the Lithuanian team display higher ^{40}K activity concentration than those of other teams. Following the application of updated background corrections and calibration adjustments, the final ^{40}K results, summarised in Figure 8.14, show improved consistency and alignment with reference values. The final averaged deviations from the reference are between $-35\,\%$ and $2\,\%$.

The preliminary ^{232}Th activity concentrations (AW_Th-232) estimated, shown in Figure 8.15,

were already fairly consistent with ground measurements, exhibiting only minor discrepancies of $-25\,\%$ to $15\,\%$. All teams reported similar values, and only minor adjustments were made in the final evaluation. Figure 8.16 summarises the final results after corrections in background and calibration. Final deviations lie between $-40\,\%$ and $-2\,\%$.

Airborne measurements of ^{238}U activity concentration (AW_U-238) initially showed moderate deviations from ground-based data, ranging from $-20\,\%$ to $250\,\%$ (Figure 8.17). The Lithuanian team overestimated the activity compared to some other teams. Following background correction and recalibration, the final results (Figure 8.18) show only small adjustments, and all teams' measurements now align more closely with the reference, with final deviations between $-20\,\%$ and $35\,\%$.

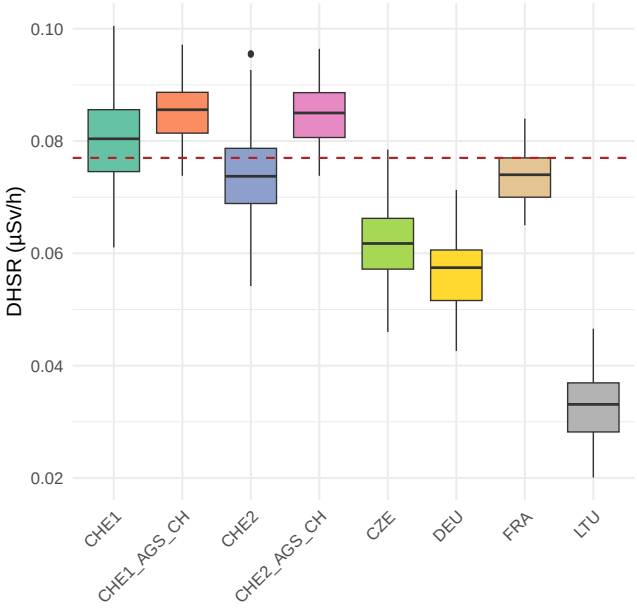

Figure 8.11: Ambient dose equivalent rate distribution (DHSR) measured in Mission 1 (RM) by each team (preliminary analysis). Reference dose rate $77\,\mu\mathrm{Sv\,h^{-1}}$ (red dashed line).

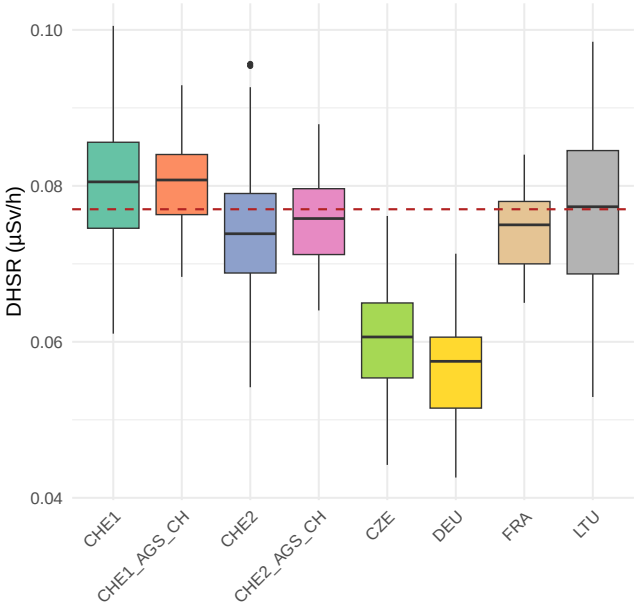

Figure 8.12: Ambient dose equivalent rate distribution (DHSR) measured in Mission 1 (RM) by each team (final analysis). Reference dose rate $77\,\mu\mathrm{Sv\,h^{-1}}$ (red dashed line).

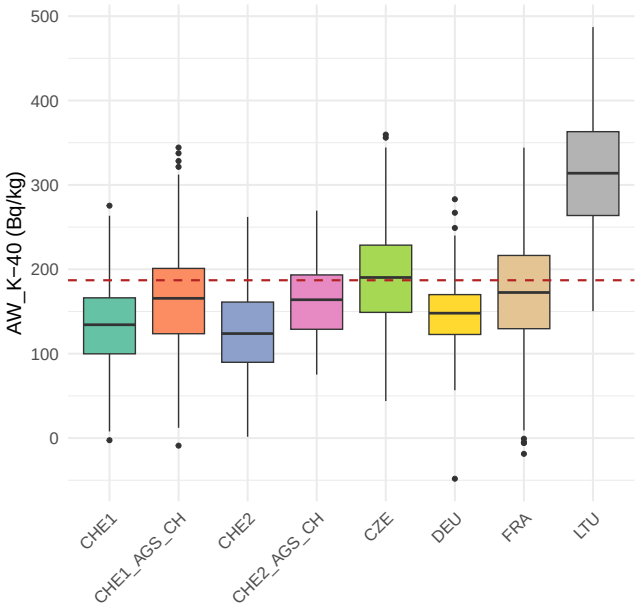

Figure 8.13: Activity concentration distribution of ^{40}K measured in Mission 1 (RM) by each team (preliminary analysis). Reference activity concentration $187\,\mathrm{Bq\,kg^{-1}}$ (red dashed line).

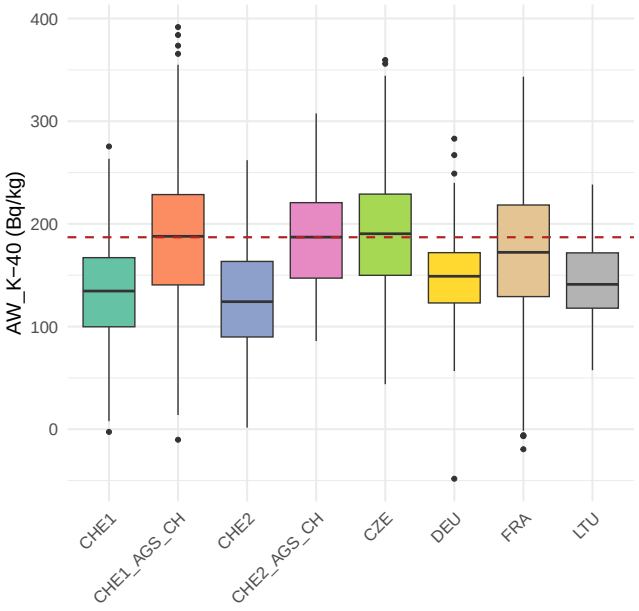

Figure 8.14: Activity concentration distribution of ^{40}K measured in Mission 1 (RM) by each team (final analysis). Reference activity concentration $187\,\mathrm{Bq\,kg^{-1}}$ (red dashed line).

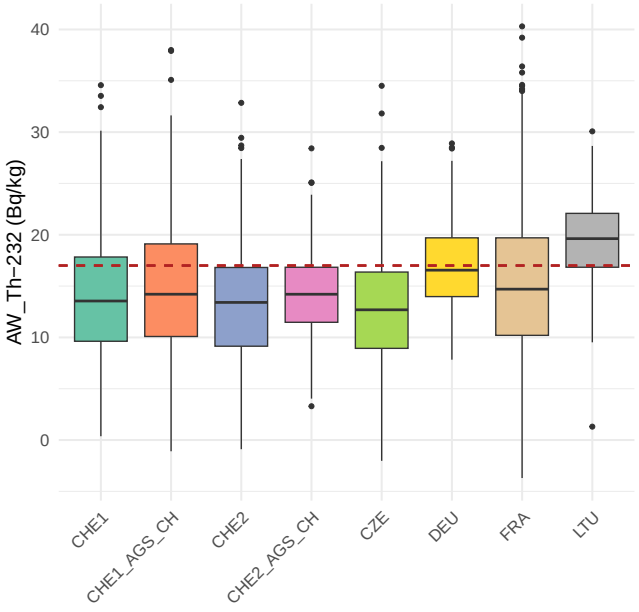

Figure 8.15: Activity concentration distribution of ^{232}Th measured in Mission 1 (RM) by each team (preliminary analysis). Reference activity concentration $17\,\mathrm{Bq\,kg^{-1}}$ (red dashed line).

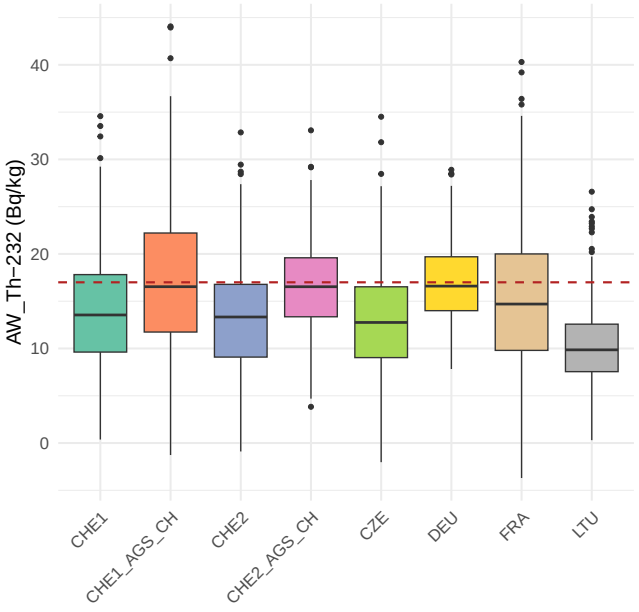

Figure 8.16: Activity concentration distribution of ^{232}Th measured in Mission 1 (RM) by each team (final analysis). Reference activity concentration $17\,\mathrm{Bq\,kg^{-1}}$ (red dashed line).

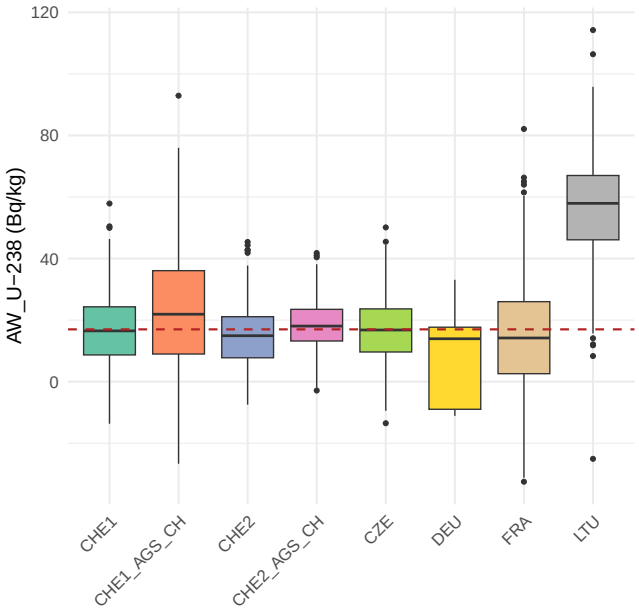

Figure 8.17: Activity concentration distribution of ^{238}U measured in Mission 1 (RM) by each team (preliminary analysis). Reference activity concentration $17\,\mathrm{Bq\,kg^{-1}}$ (red dashed line).

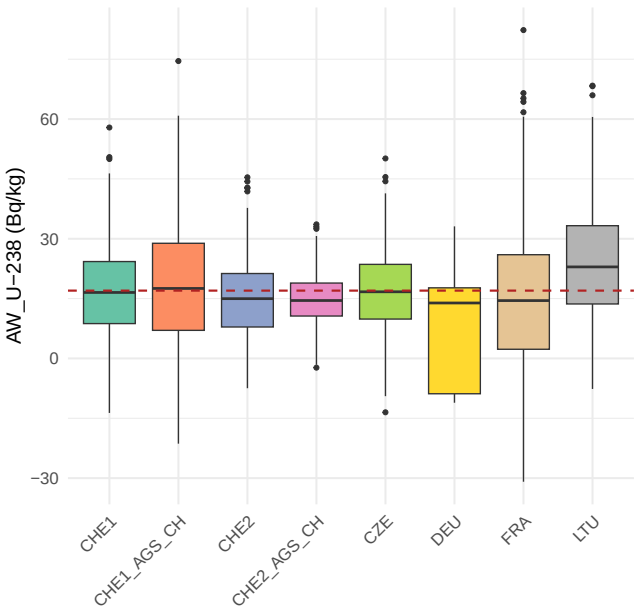

Figure 8.18: Activity concentration distribution of ^{238}U measured in Mission 1 (RM) by each team (final analysis). Reference activity concentration $17\,\mathrm{Bq\,kg^{-1}}$ (red dashed line).

8.2.2 Maps

In this section, the flight paths, the spatial distributions of dose rates and radionuclide activities are presented for the Thun military training area, based on the analysis of the Mission 1 dataset. First, the flight paths taken by each team are illustrated. Then, the total ambient dose equivalent rate distribution (DHSR) measured by each team are introduced. Last, the activity maps are presented for ^{40}K, ^{232}Th, and ^{238}U, respectively.

Flight paths

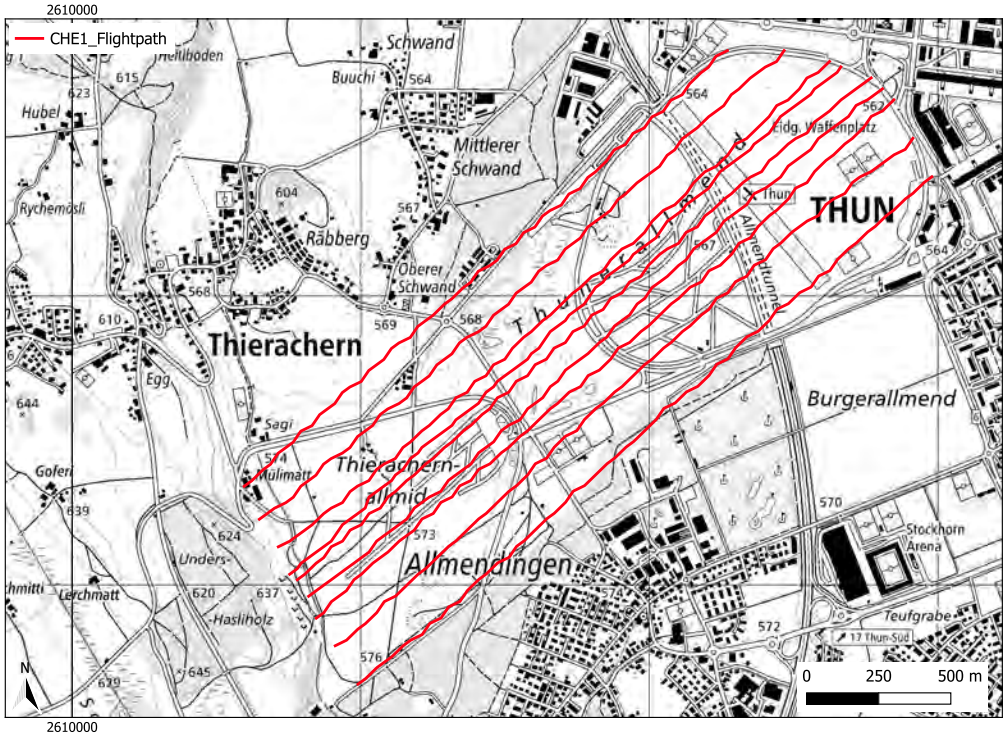

Figure 8.19: The flight path taken at the Mission 1 (RM) area by the CHE1 team. The flight paths are identical for the CHE1 and CHE1_AGS_CH datasets. Geodaten©swisstopo.

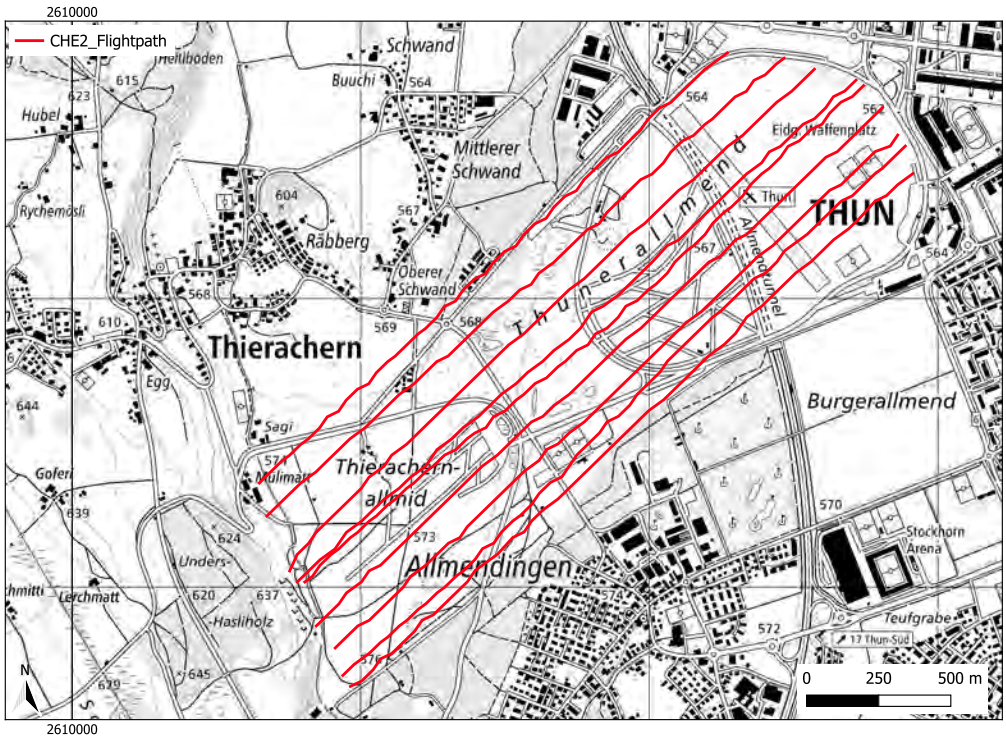

Figure 8.20: The flight path taken at the Mission 1 (RM) area by the CHE2 team. The flight paths are identical for the CHE2 and CHE2_AGS_CH datasets. Geodaten©swisstopo.

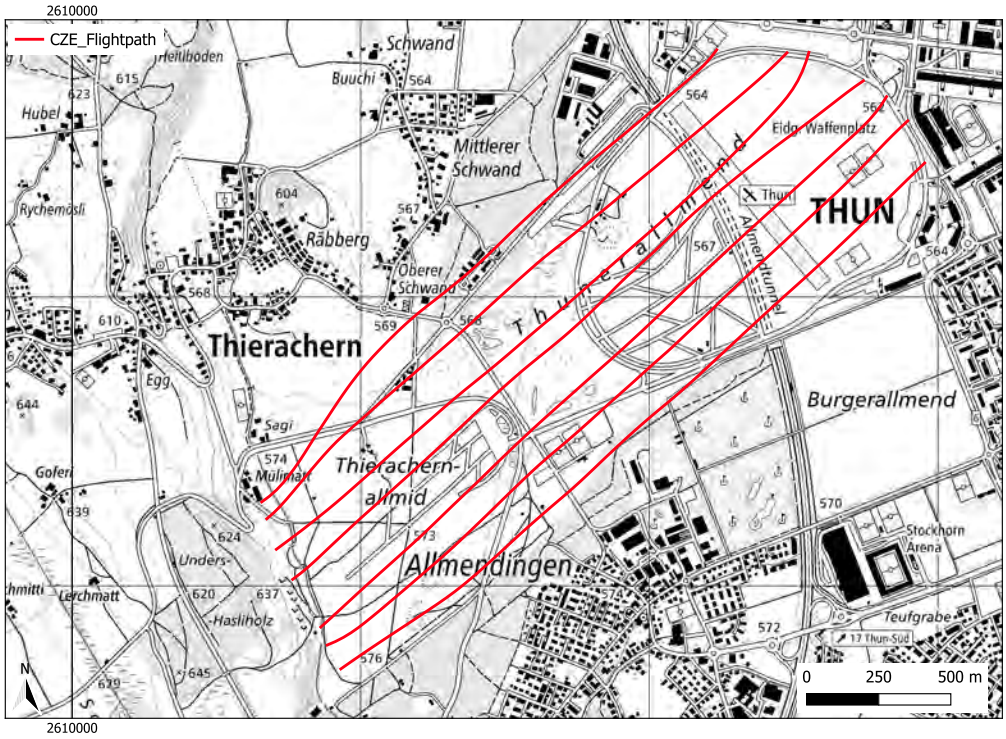

Figure 8.21: The flight path taken at the Mission 1 (RM) area by the CZE team. Geodaten©swisstopo.

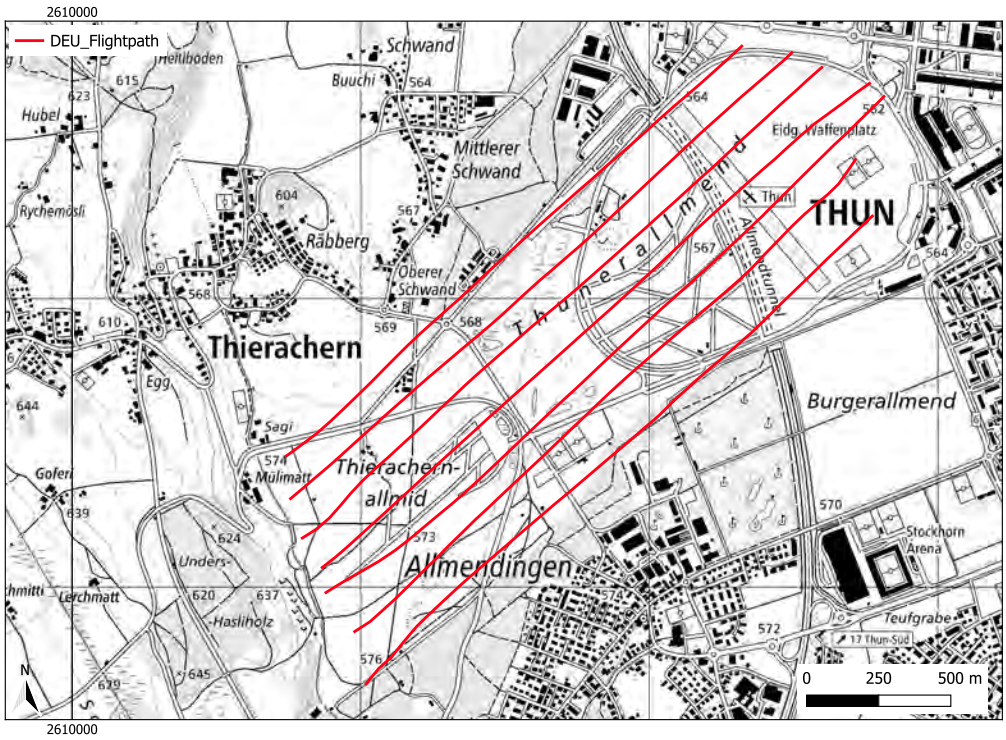

Figure 8.22: The flight path taken at the Mission 1 (RM) area by the DEU team. Geodaten©swisstopo.

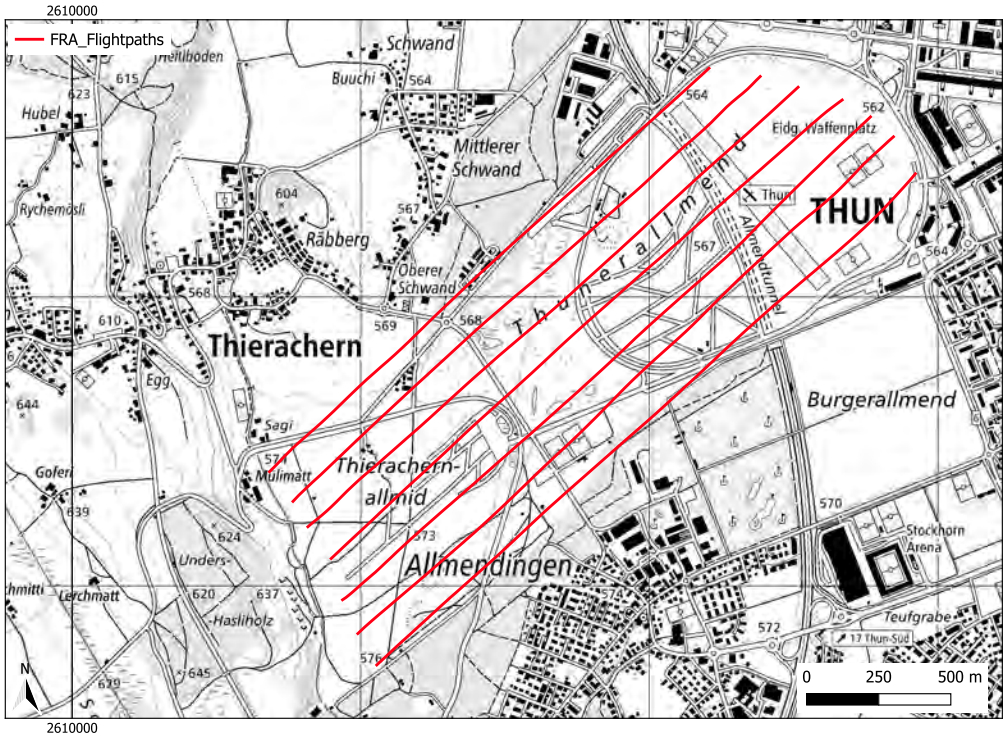

Figure 8.23: The flight path taken at the Mission 1 (RM) area by the FRA team. Geodaten©swisstopo.

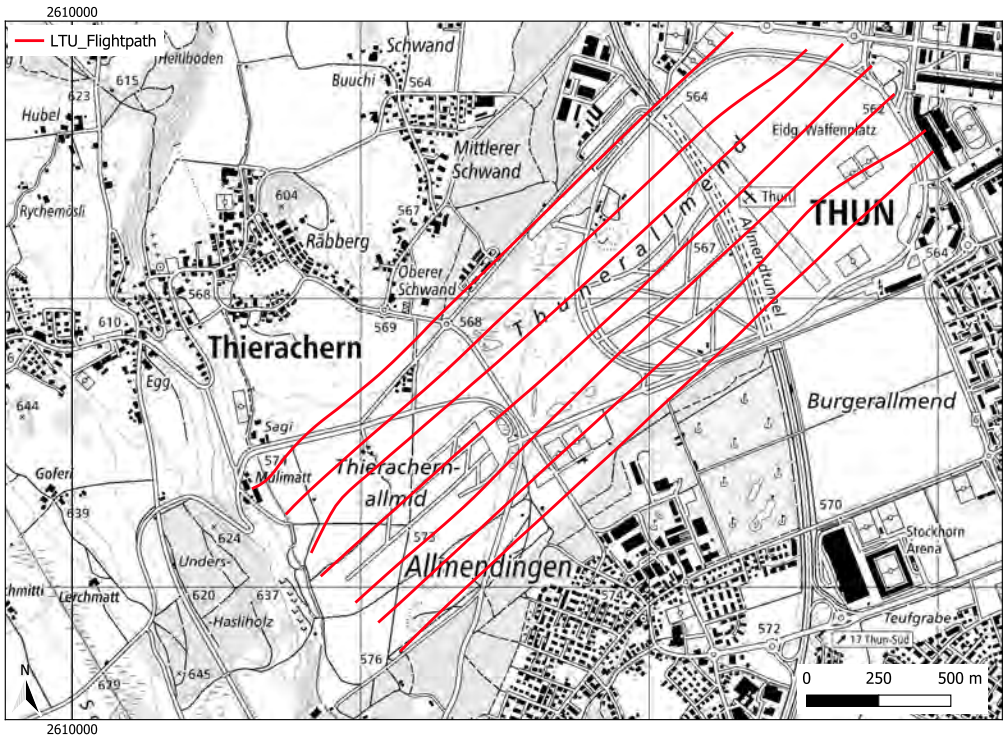

Figure 8.24: The flight path taken at the Mission 1 (RM) area by the LTU team. Geodaten©swisstopo.

Ambient dose equivalent rate

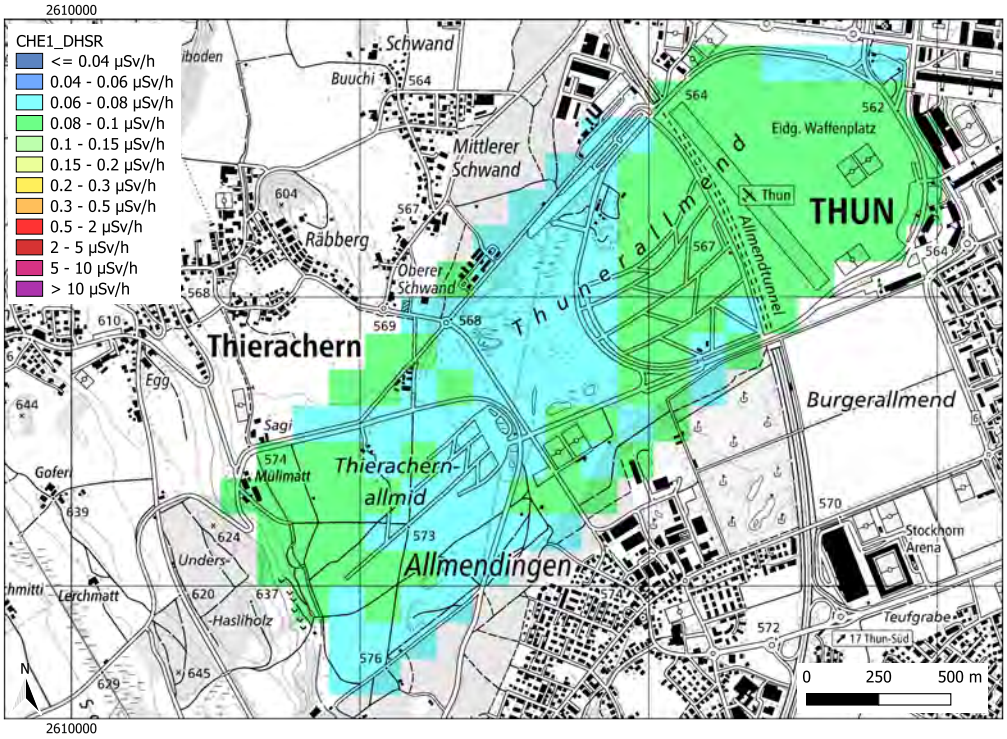

Figure 8.25: Ambient dose equivalent rate distribution (DHSR) measured at the Mission 1 (RM) area by the CHE1 team. Geodaten©swisstopo.

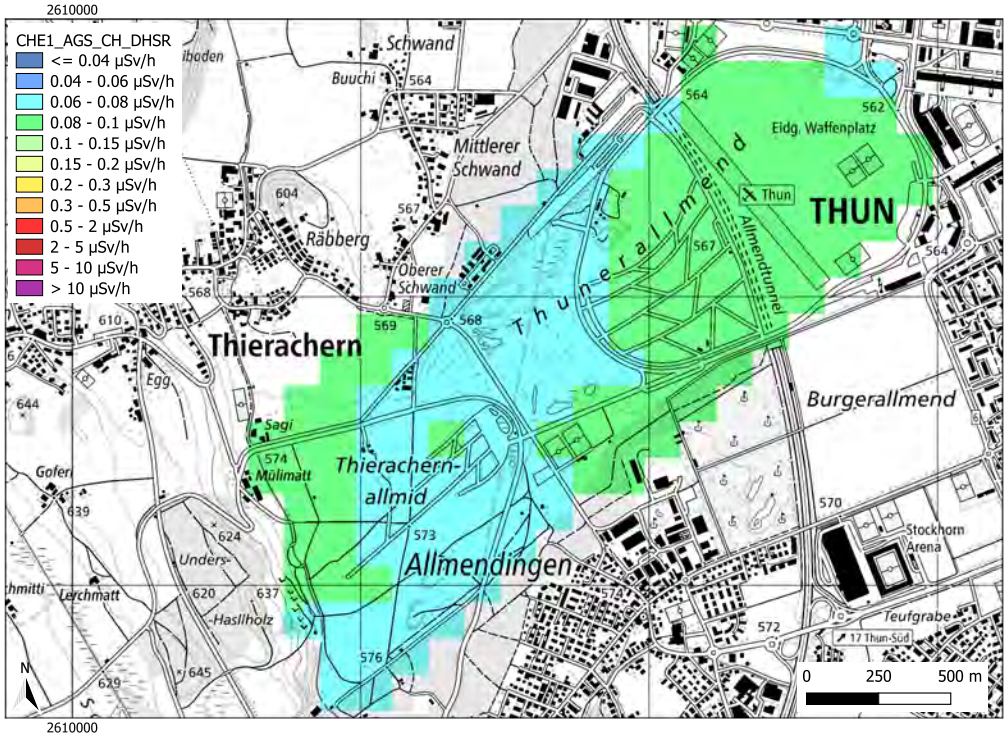

Figure 8.26: Ambient dose equivalent rate distribution (DHSR) measured at the Mission 1 (RM) area by the CHE1 team. Dataset is analysed with AGS_CH. Geodaten©swisstopo.

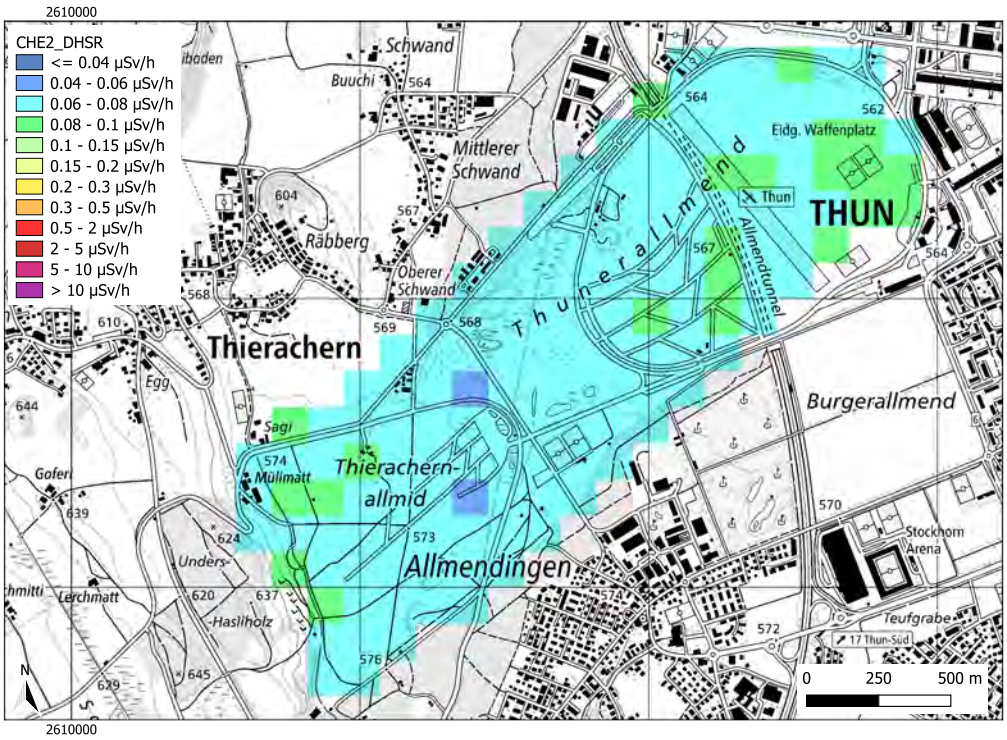

Figure 8.27: Ambient dose equivalent rate distribution (DHSR) measured at the Mission 1 (RM) area by the CHE2 team. Geodaten©swisstopo.

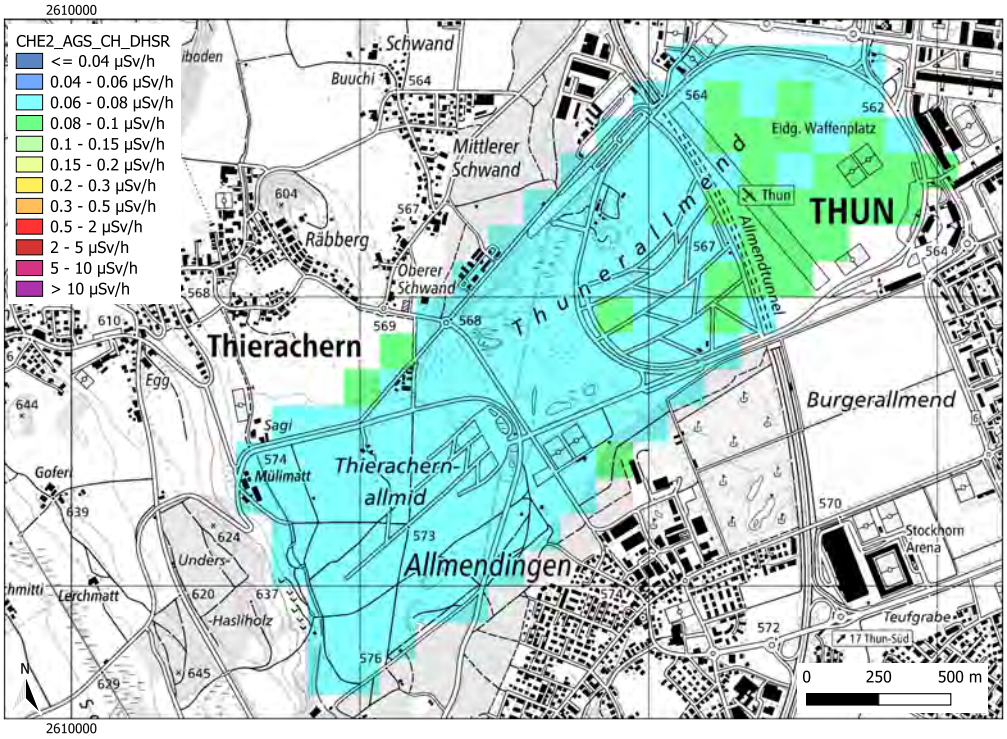

Figure 8.28: Ambient dose equivalent rate distribution (DHSR) measured at the Mission 1 (RM) area by the CHE2 team. Dataset is analysed with AGS_CH. Geodaten©swisstopo.

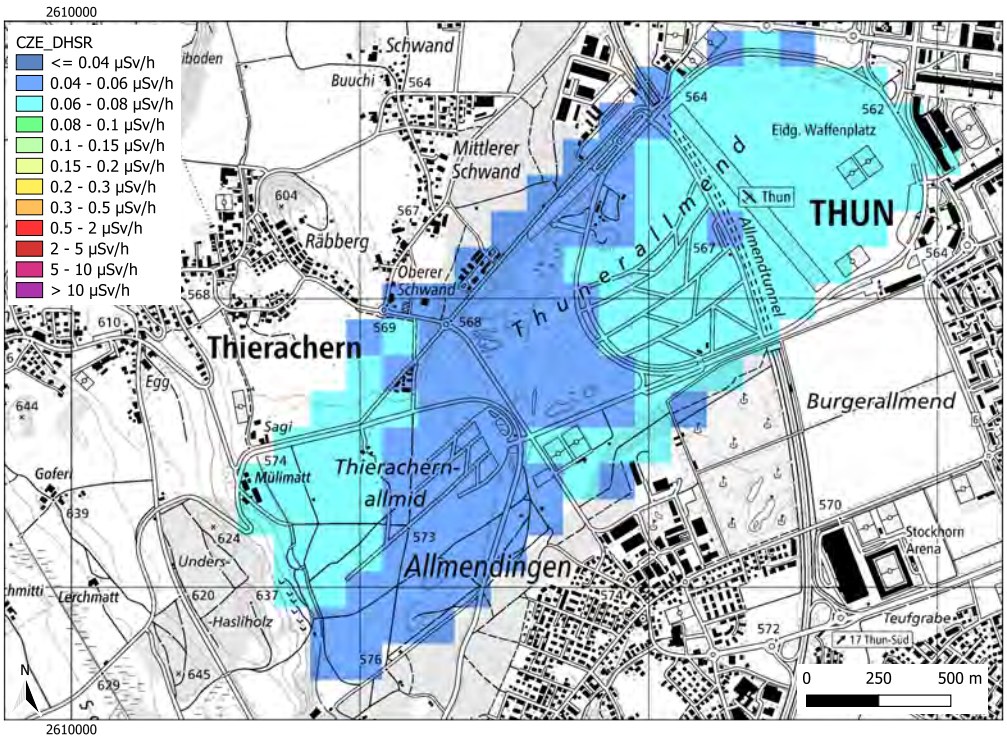

Figure 8.29: Ambient dose equivalent rate distribution (DHSR) measured at the Mission 1 (RM) area by the CZE team. Geodaten©swisstopo.

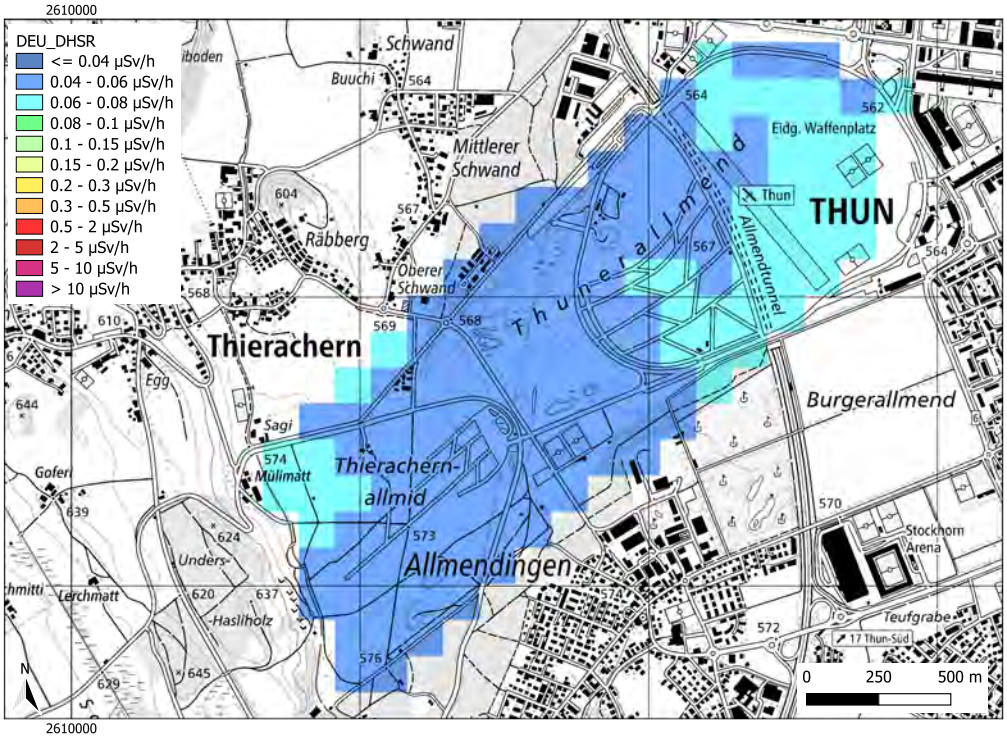

Figure 8.30: Ambient dose equivalent rate distribution (DHSR) measured at the Mission 1 (RM) area by the DEU team. Geodaten©swisstopo.

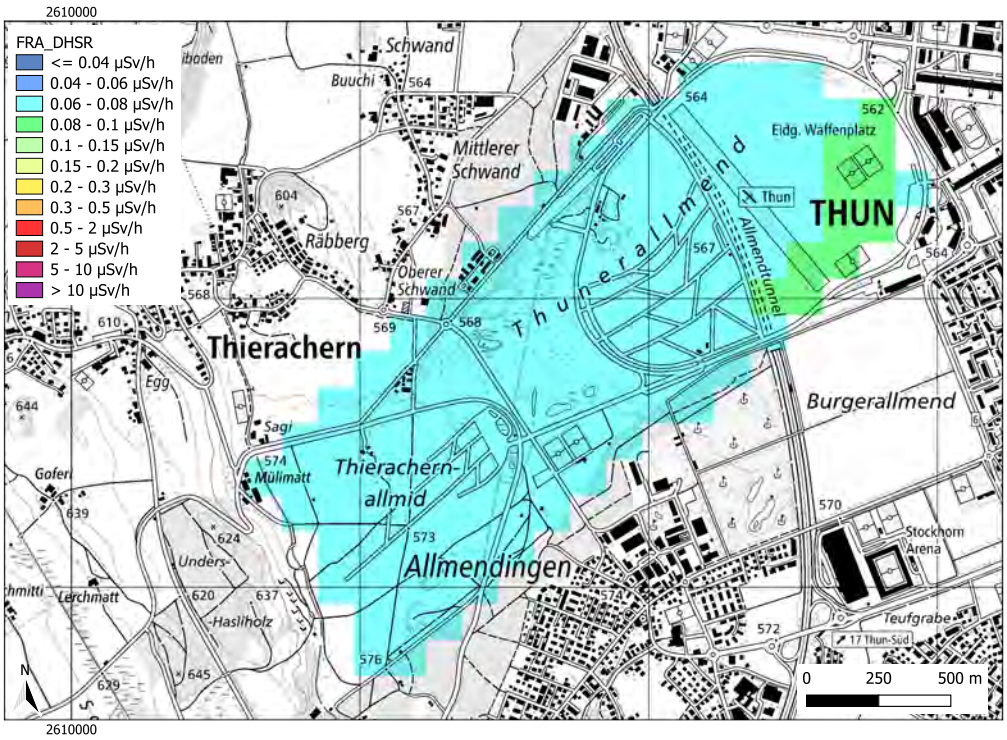

Figure 8.31: Ambient dose equivalent rate distribution (DHSR) measured at the Mission 1 (RM) area by the FRA team. Geodaten©swisstopo.

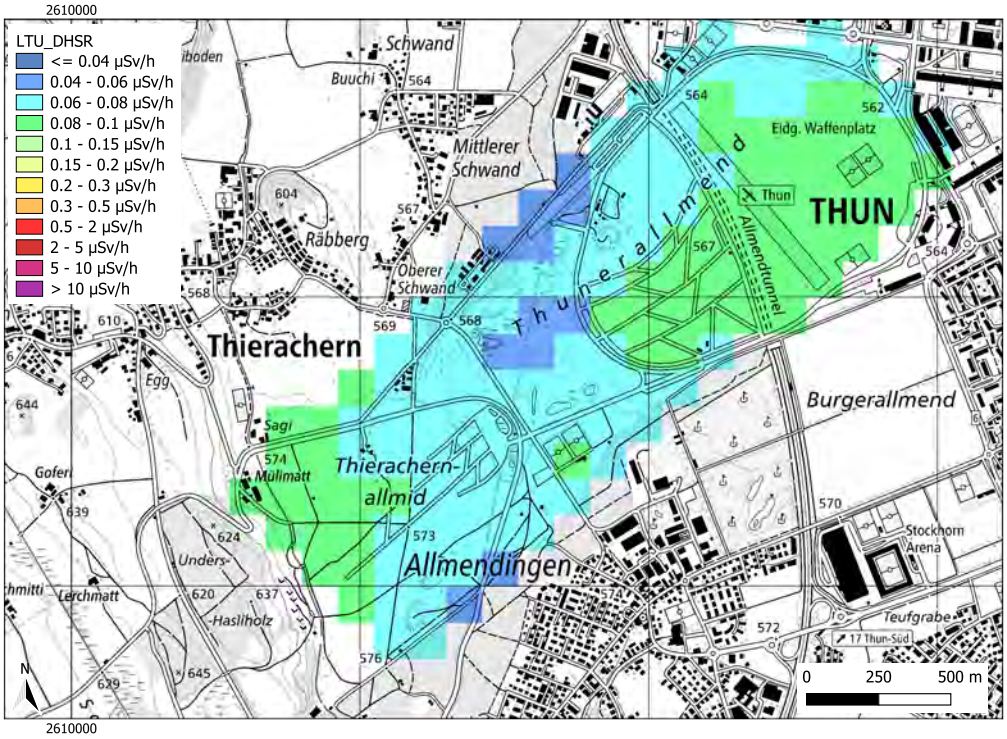

Figure 8.32: Ambient dose equivalent rate distribution (DHSR) measured at the Mission 1 (RM) area by the LTU team. Geodaten©swisstopo.

Activity concentration distribution of ^{232}Th

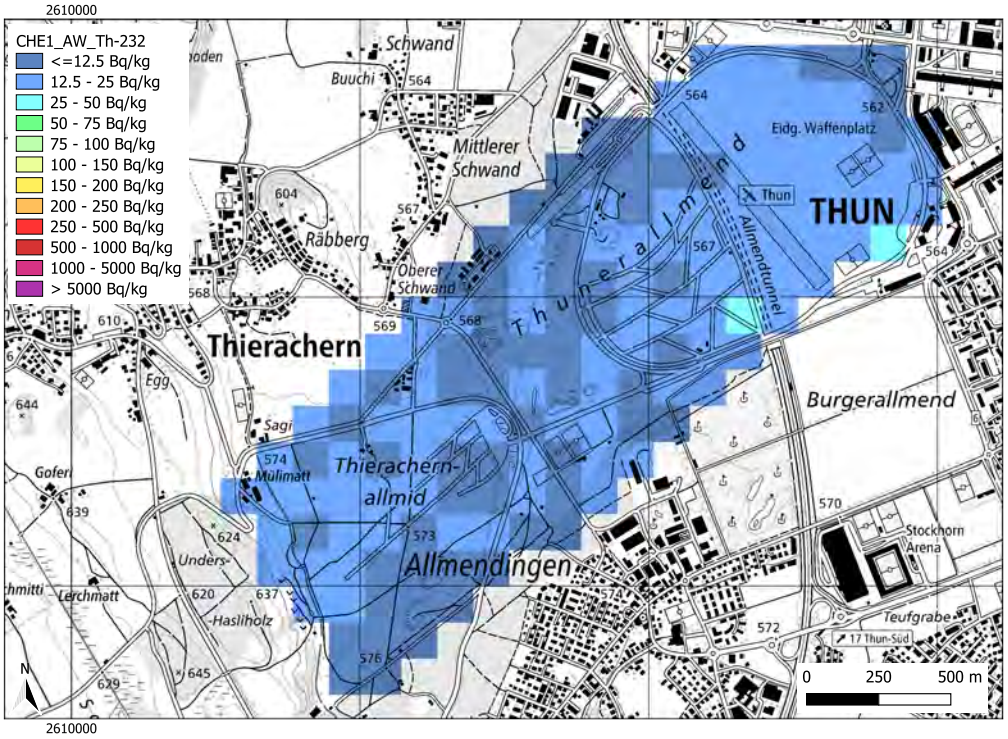

Figure 8.33: Activity concentration of ^{232}Th measured at the Mission 1 (RM) area by the CHE1 team. Geodaten©swisstopo.

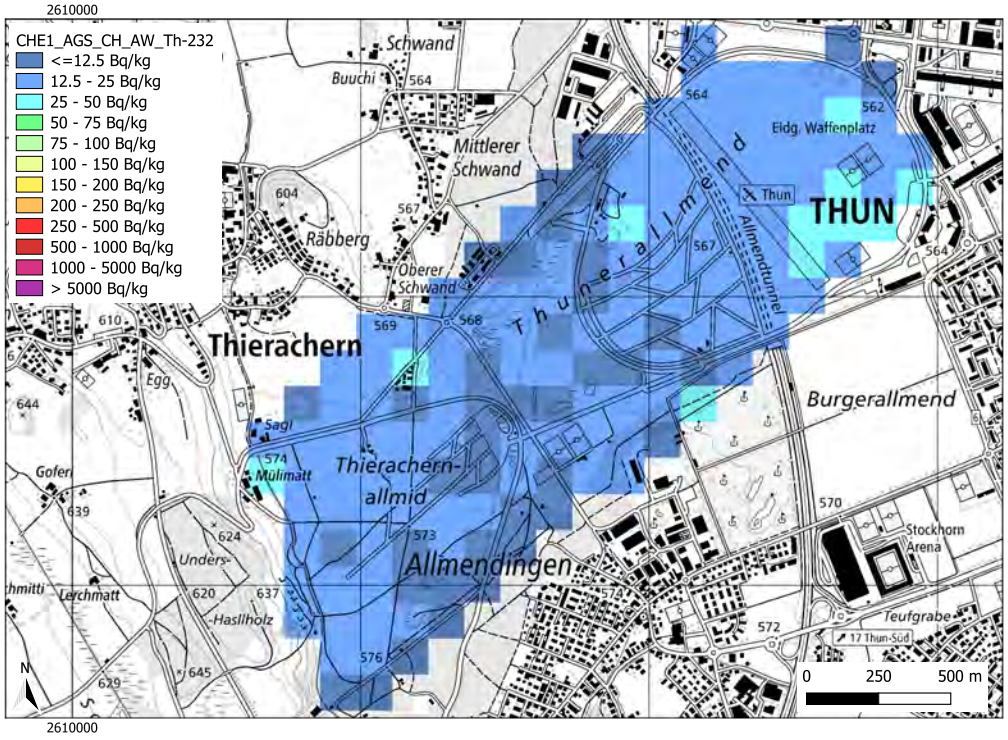

Figure 8.34: Activity concentration of ^{232}Th measured at the Mission 1 (RM) area by the CHE1 team. Dataset is analysed with AGS_CH. Geodaten©swisstopo.

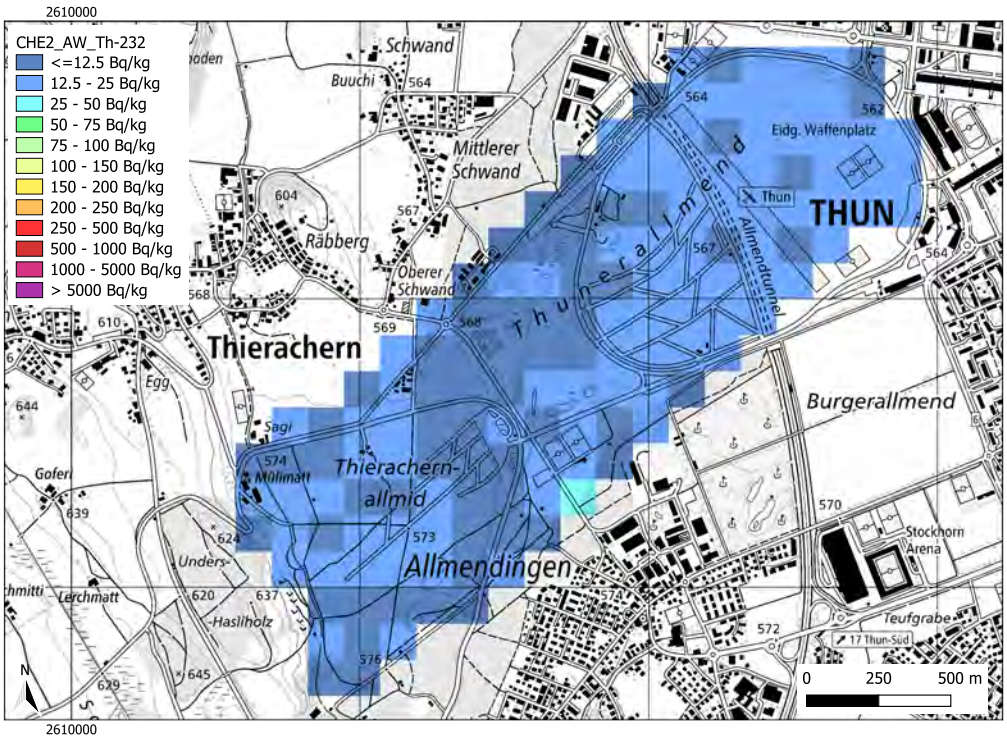

Figure 8.35: Activity concentration of ^{232}Th measured at the Mission 1 (RM) area by the CHE2 team. Geodaten©swisstopo.

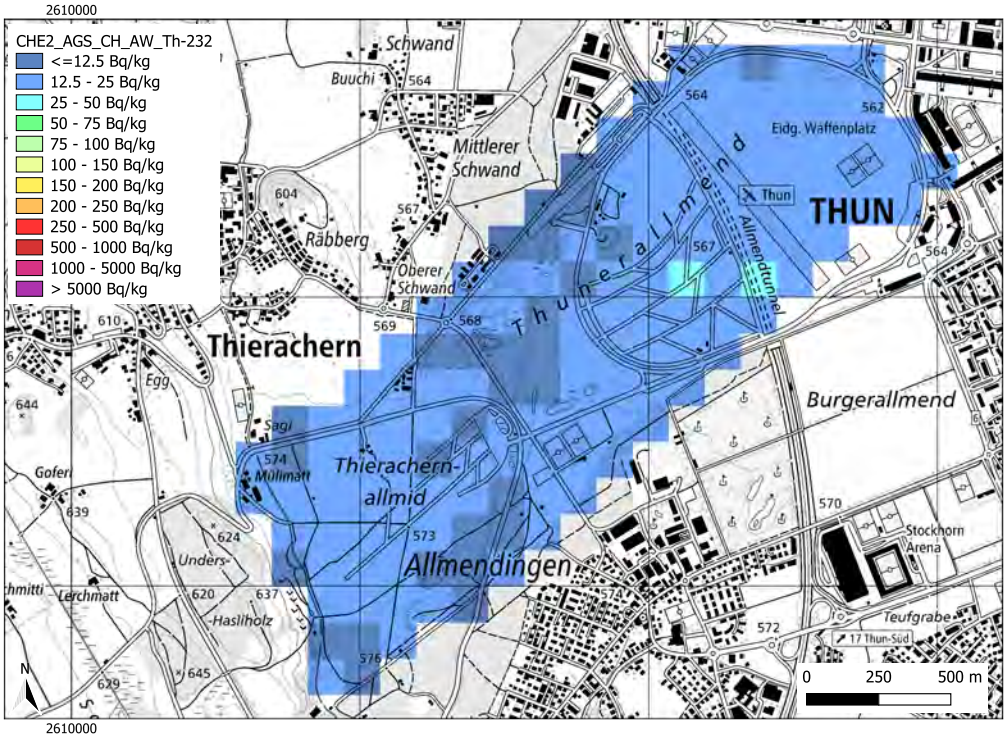

Figure 8.36: Activity concentration of ^{232}Th measured at the Mission 1 (RM) area by the CHE2 team. Dataset is analysed with AGS_CH. Geodaten©swisstopo.

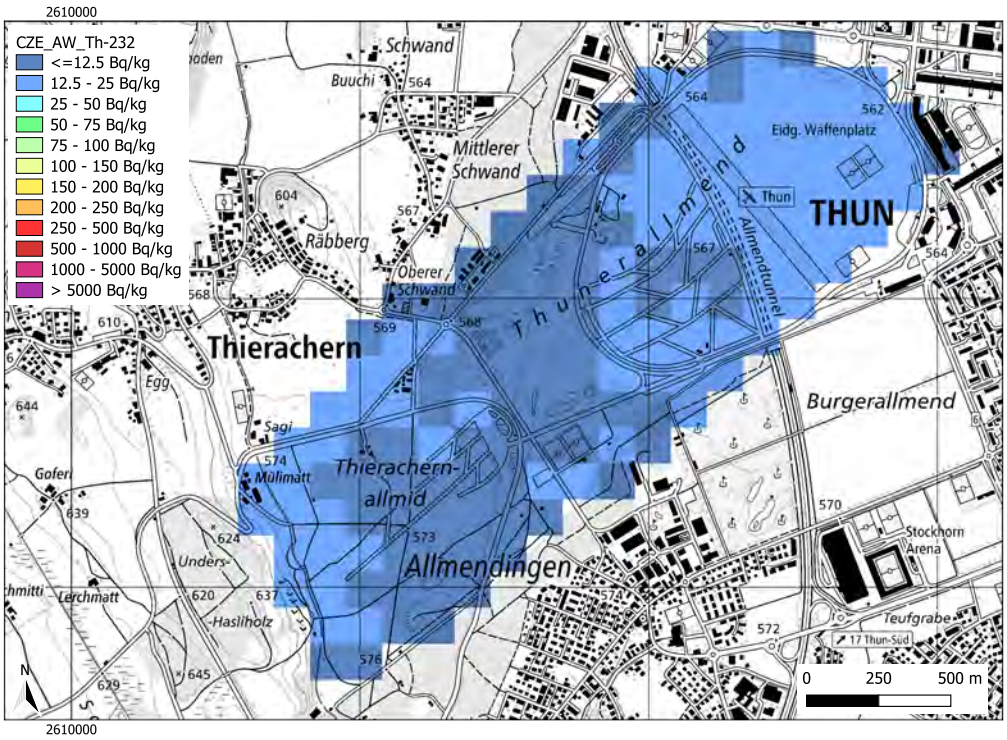

Figure 8.37: Activity concentration of ^{232}Th measured at the Mission 1 (RM) area by the CZE team. Geodaten©swisstopo.

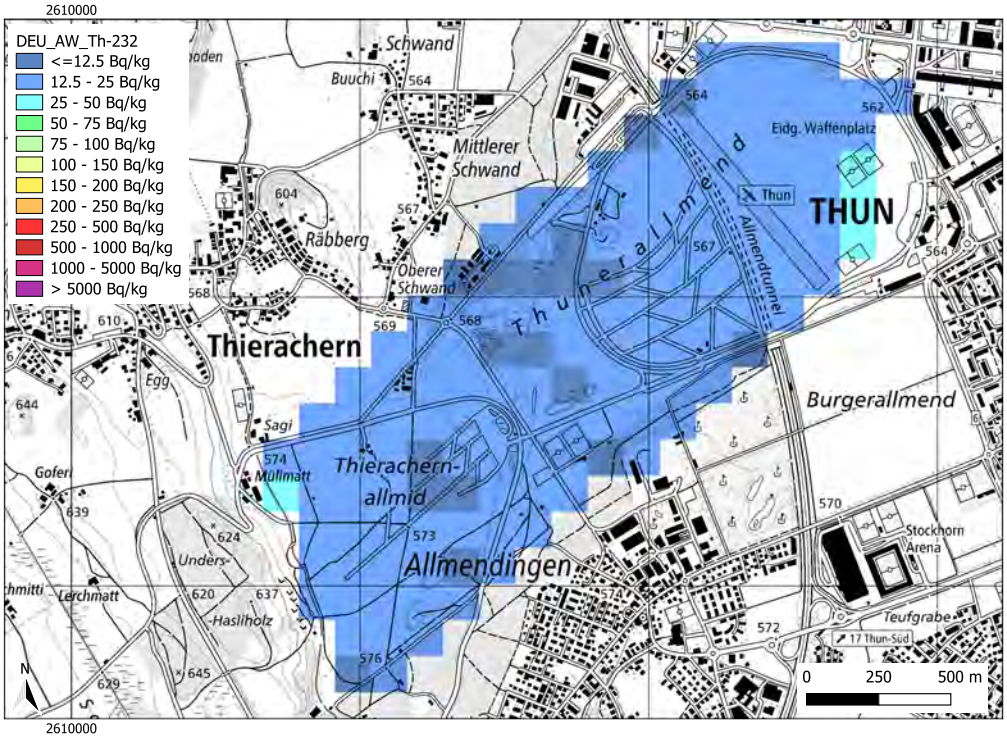

Figure 8.38: Activity concentration of ^{232}Th measured at the Mission 1 (RM) area by the DEU team. Geodaten©swisstopo.

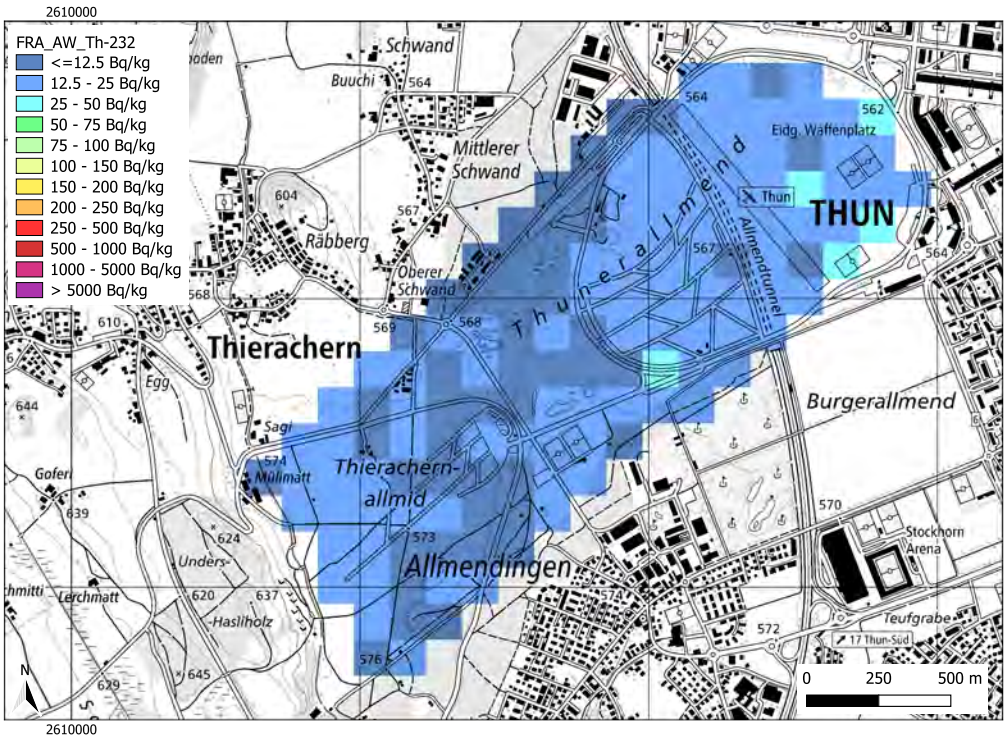

Figure 8.39: Activity concentration of ^{232}Th measured at the Mission 1 (RM) area by the FRA team. Geodaten©swisstopo.

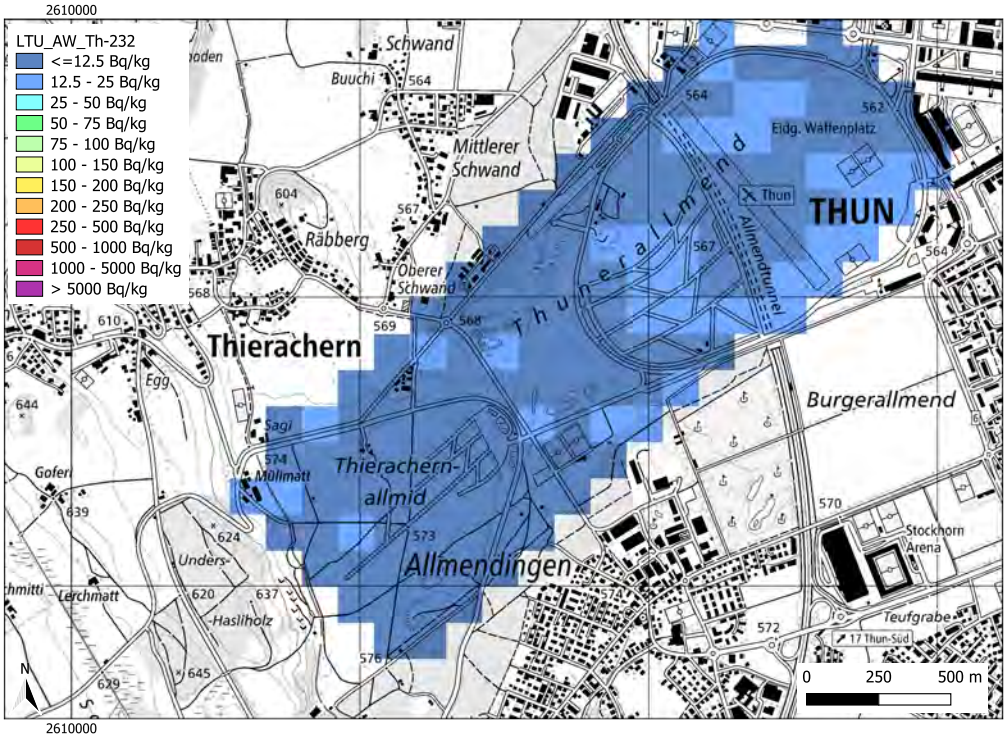

Figure 8.40: Activity concentration of ^{232}Th measured at the Mission 1 (RM) area by the LTU team. Geodaten©swisstopo.

Activity concentration distribution of ^{40}K

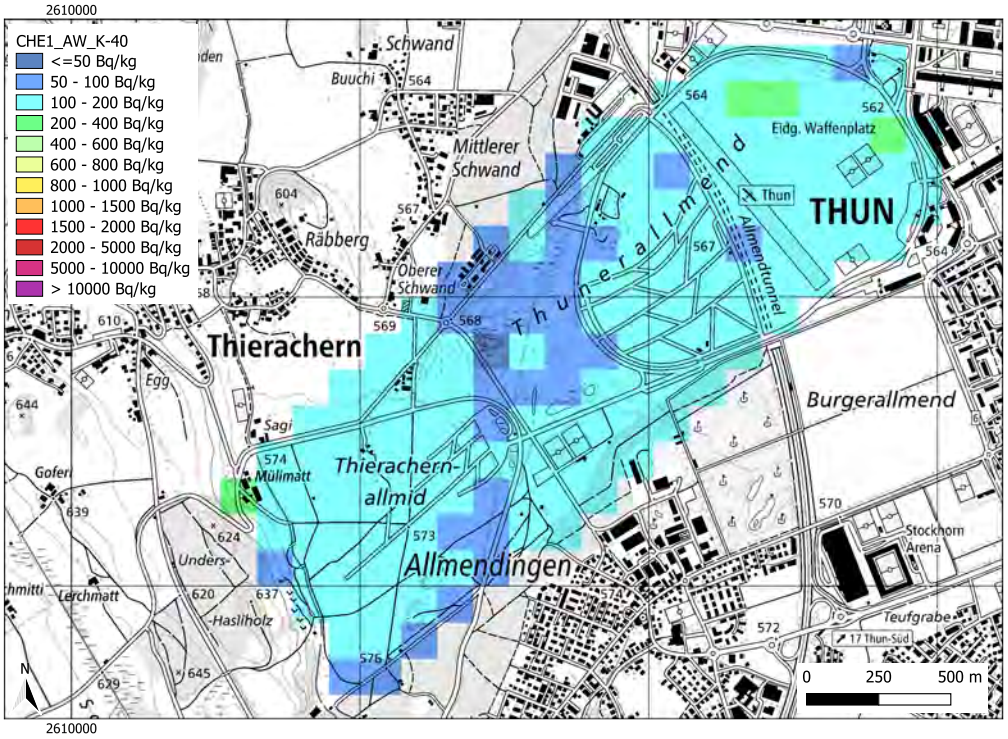

Figure 8.41: Activity concentration of ^{40}K measured at the Mission 1 (RM) area by the CHE1 team. Geodaten©swisstopo.

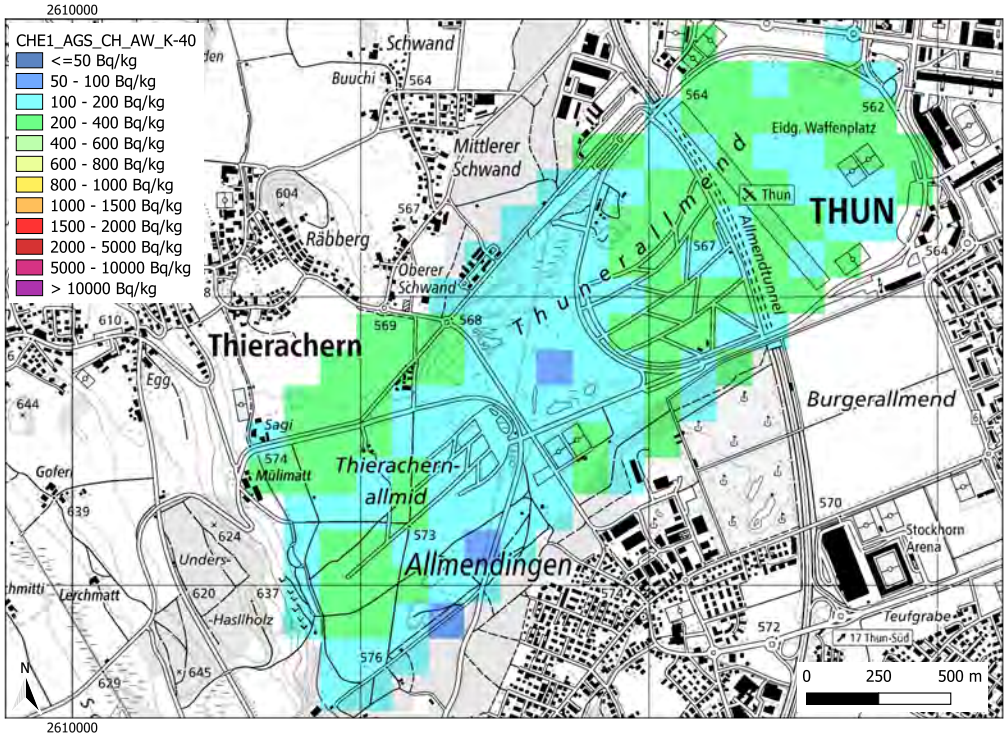

Figure 8.42: Activity concentration of ^{40}K measured at the Mission 1 (RM) area by the CHE1 team. Dataset is analysed with AGS_CH. Geodaten©swisstopo.

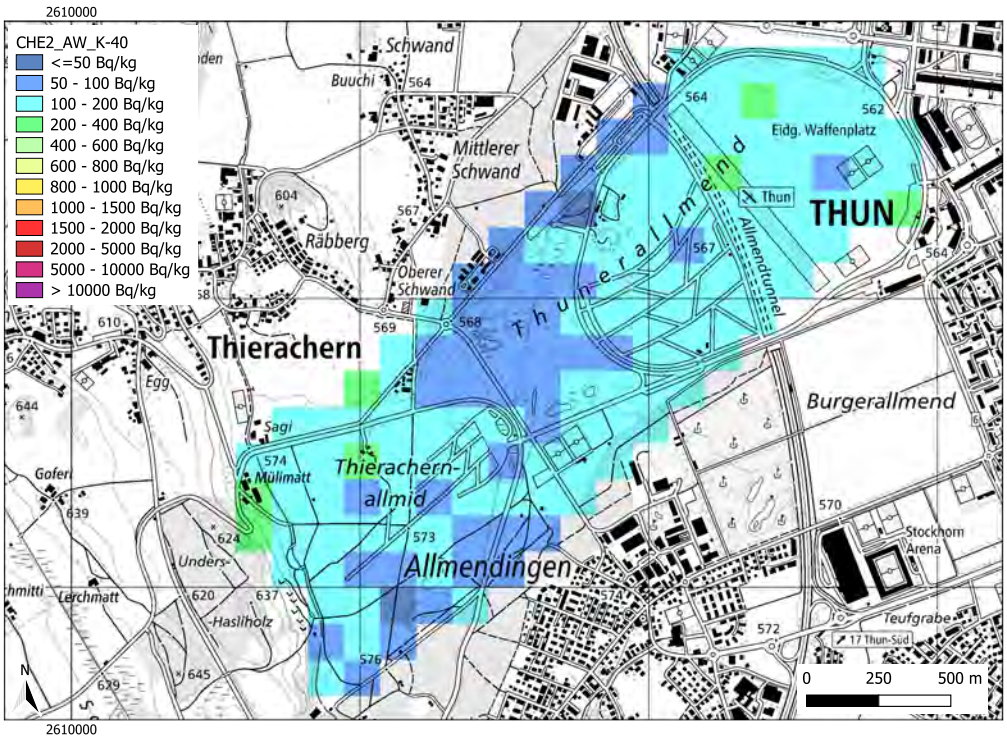

Figure 8.43: Activity concentration of ^{40}K measured at the Mission 1 (RM) area by the CHE2 team. Geodaten©swisstopo.

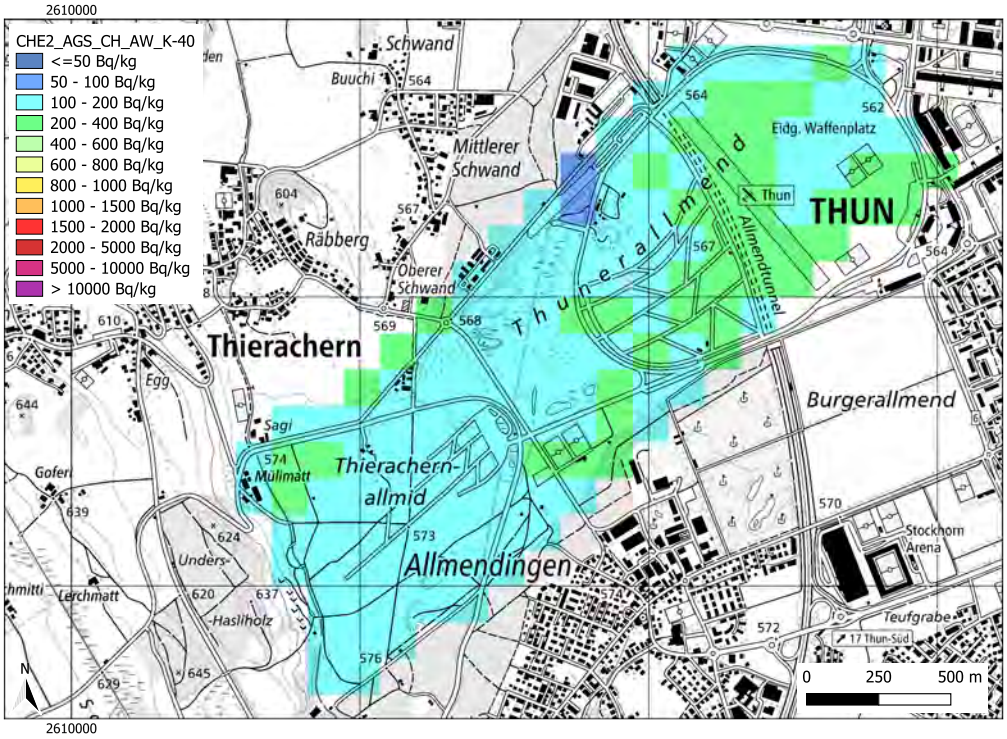

Figure 8.44: Activity concentration of ^{40}K measured at the Mission 1 (RM) area by the CHE2 team. Dataset is analysed with AGS_CH. Geodaten©swisstopo.

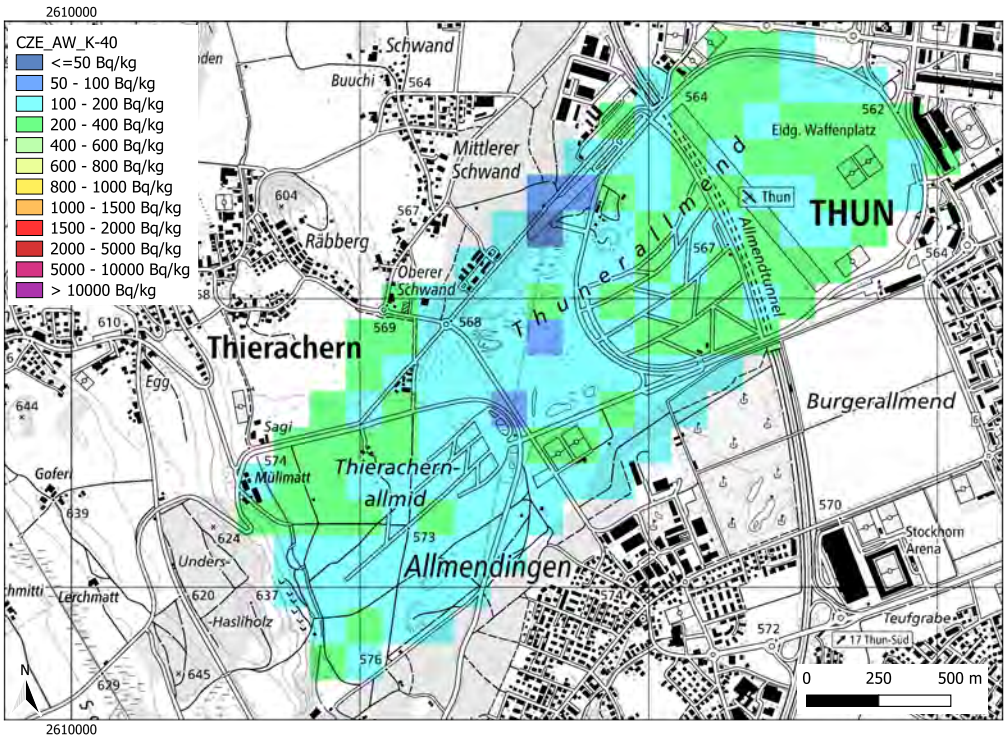

Figure 8.45: Activity concentration of ^{40}K measured at the Mission 1 (RM) area by the CZE team. Geodaten©swisstopo.

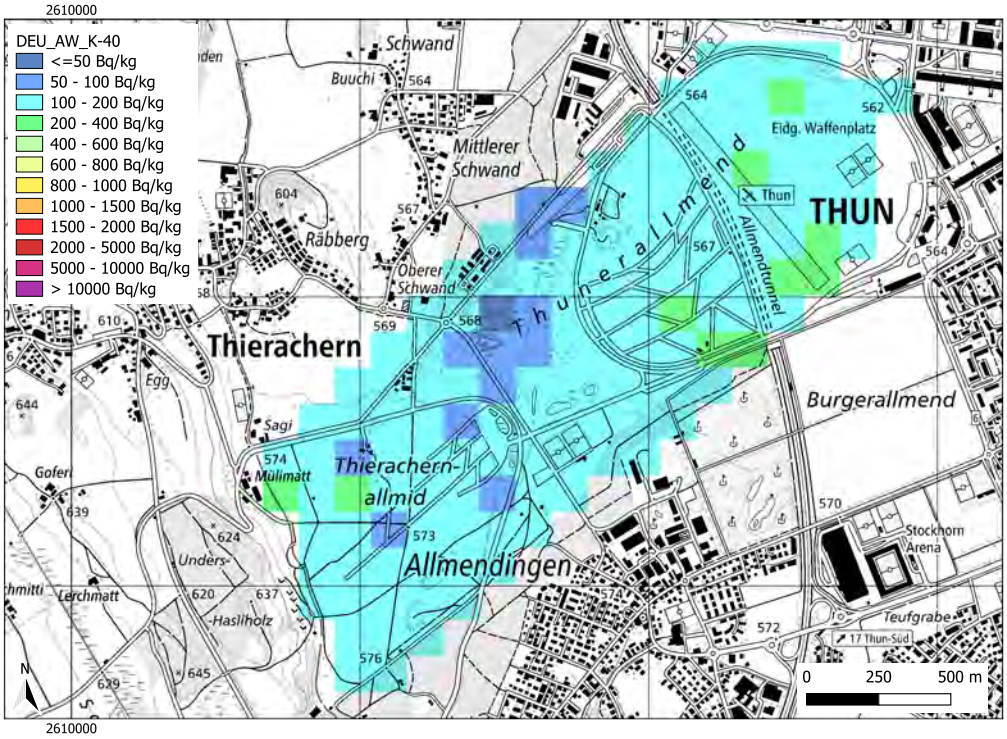

Figure 8.46: Activity concentration of ^{40}K measured at the Mission 1 (RM) area by the DEU team. Geodaten©swisstopo.

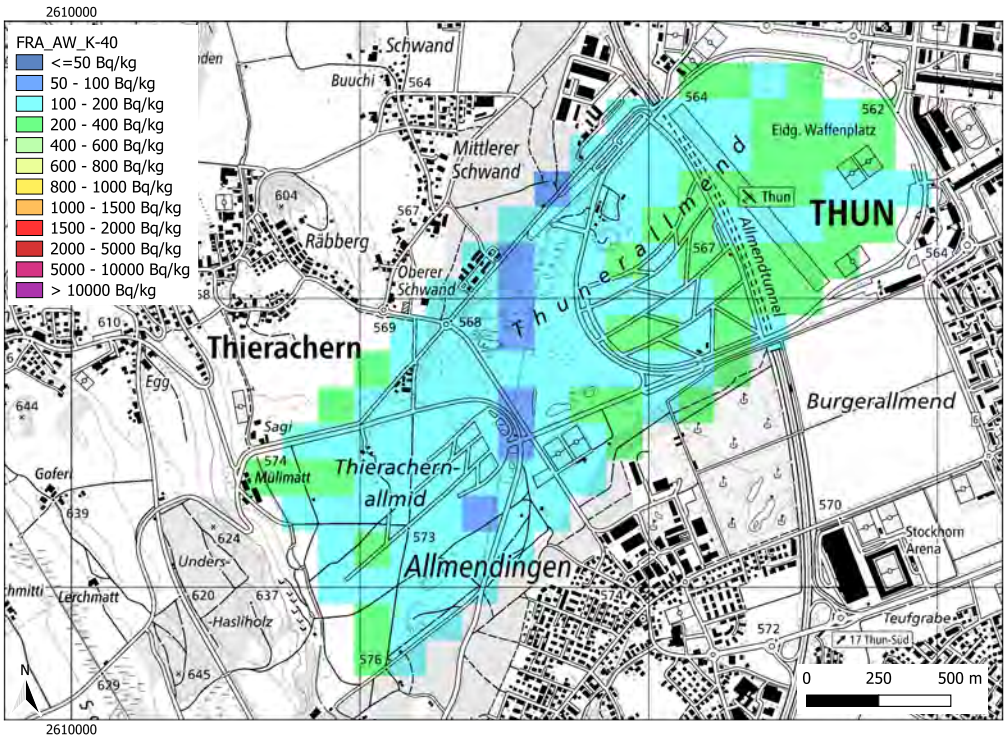

Figure 8.47: Activity concentration of ^{40}K measured at the Mission 1 (RM) area by the FRA team. Geodaten©swisstopo.

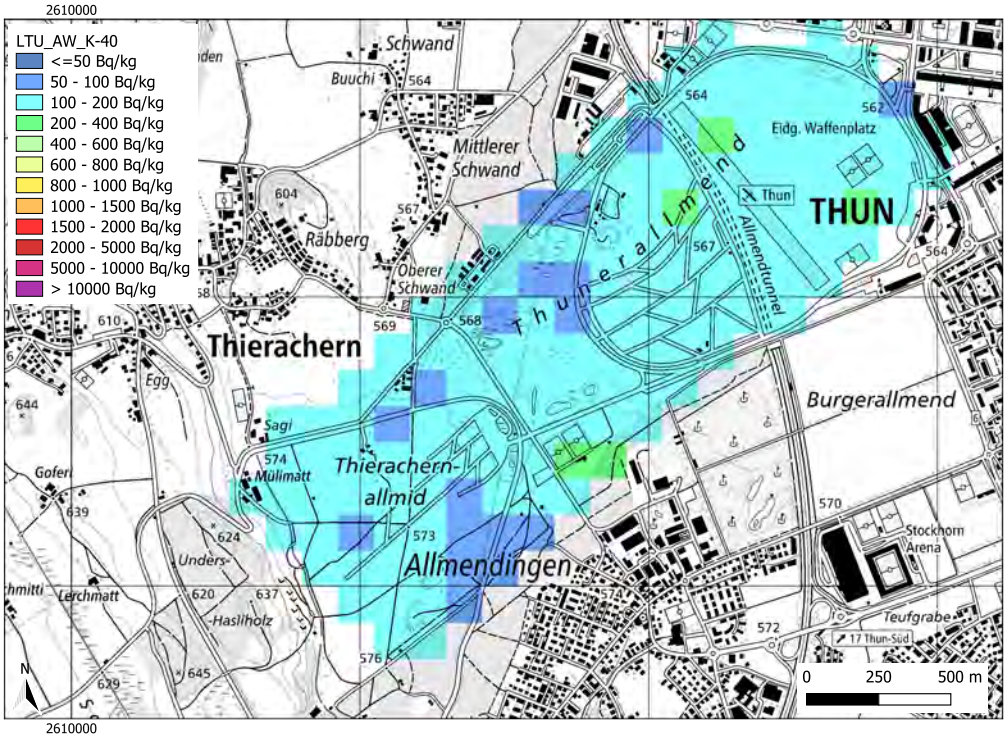

Figure 8.48: Activity concentration of ^{40}K measured at the Mission 1 (RM) area by the LTU team. Geodaten©swisstopo.

Activity concentration distribution of ^{238}U

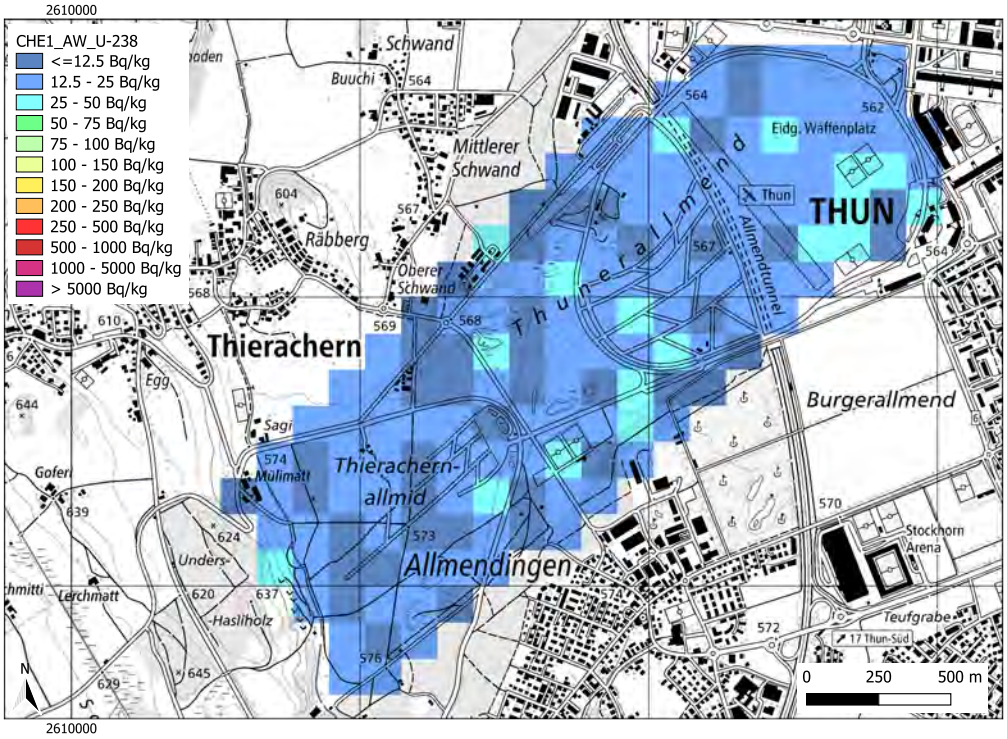

Figure 8.49: Activity concentration of ^{238}U measured at the Mission 1 (RM) area by the CHE1 team. Geodaten©swisstopo.

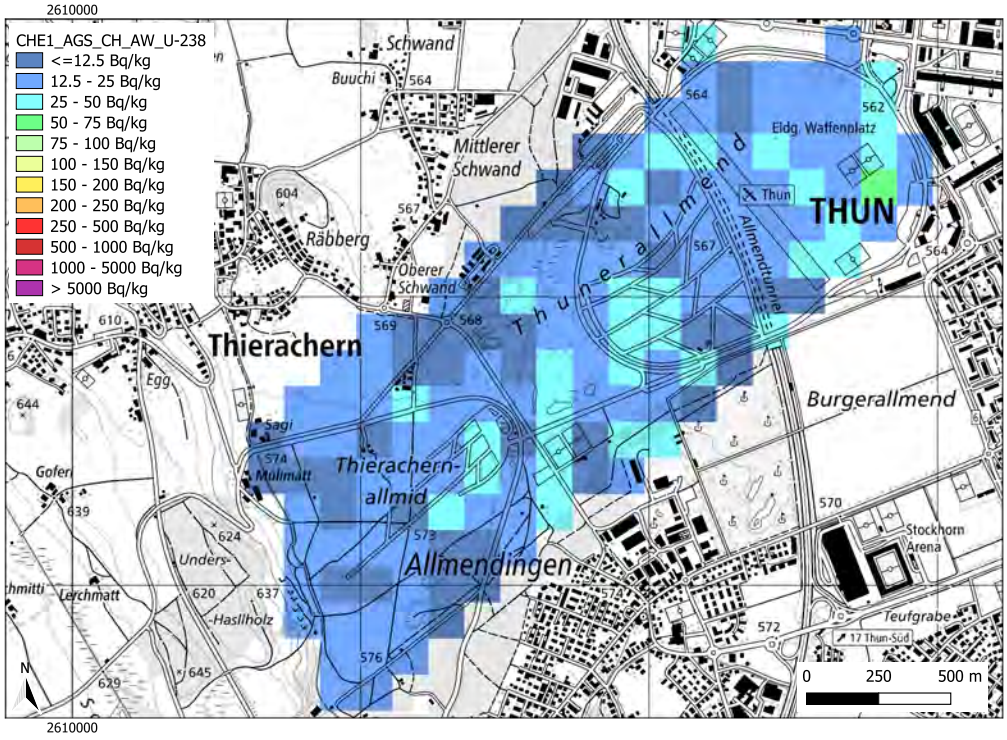

Figure 8.50: Activity concentration of ^{238}U measured at the Mission 1 (RM) area by the CHE1 team. Dataset is analysed with AGS_CH. Geodaten©swisstopo.

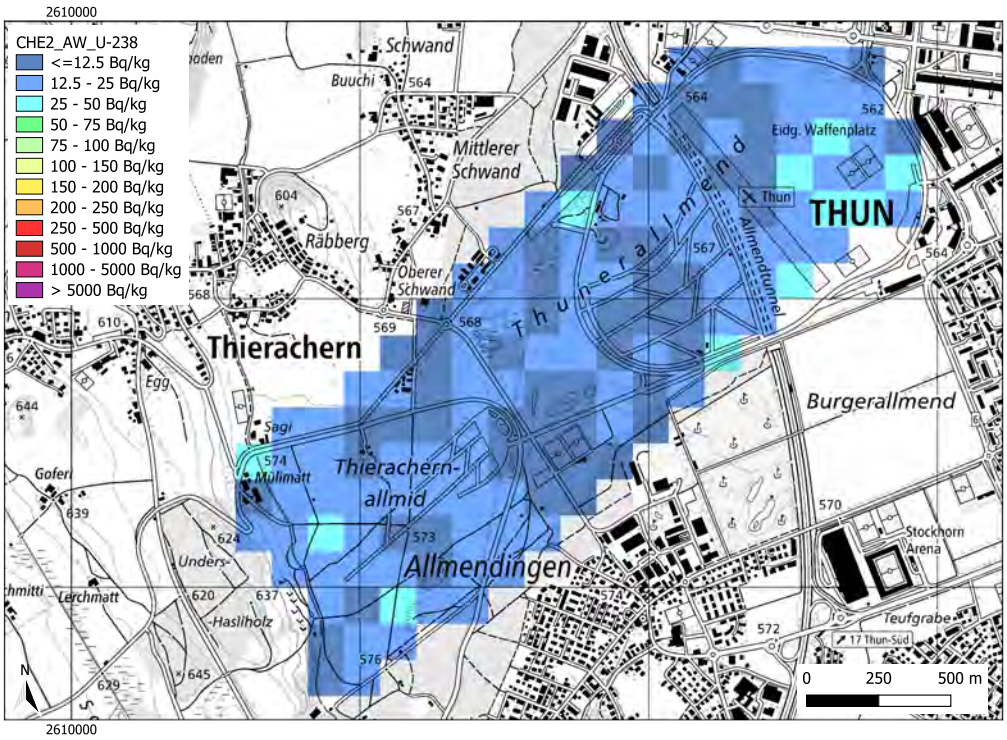

Figure 8.51: Activity concentration of ^{238}U measured at the Mission 1 (RM) area by the CHE2 team. Geodaten©swisstopo.

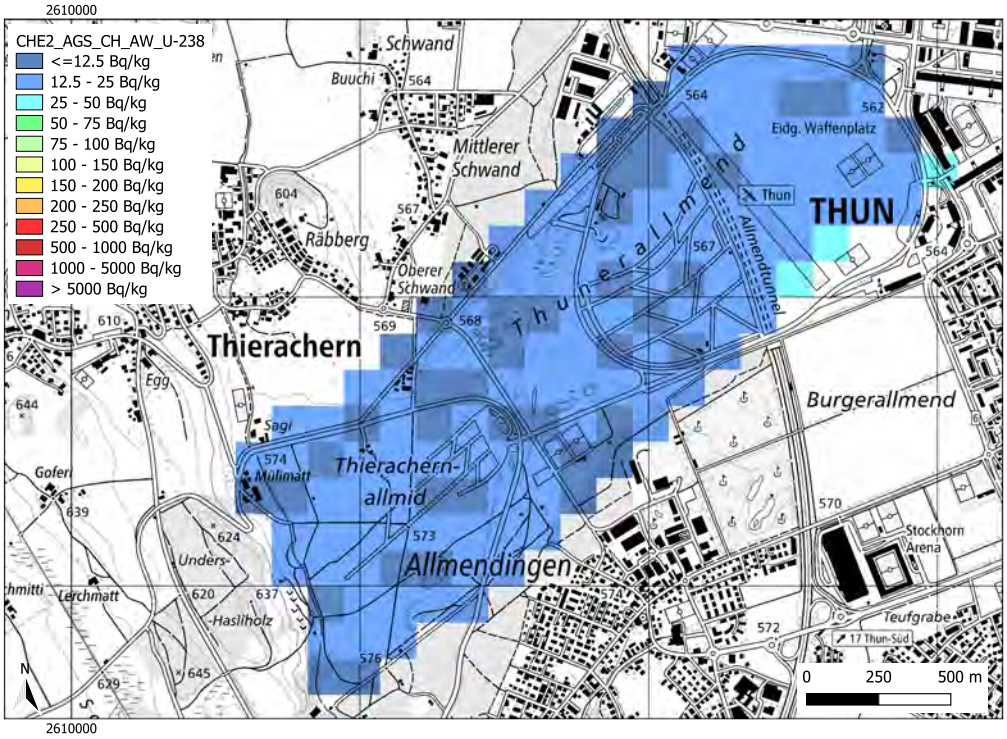

Figure 8.52: Activity concentration of ^{238}U measured at the Mission 1 (RM) area by the CHE2 team. Dataset is analysed with AGS_CH. Geodaten©swisstopo.

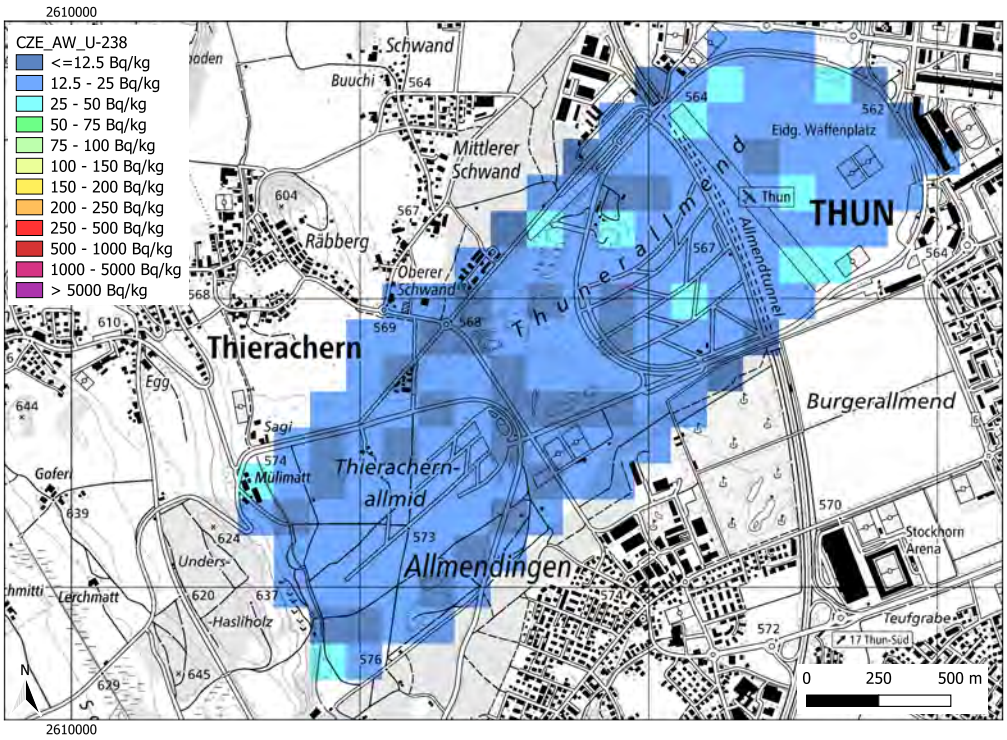

Figure 8.53: Activity concentration of ^{238}U measured at the Mission 1 (RM) area by the CZE team. Geodaten©swisstopo.

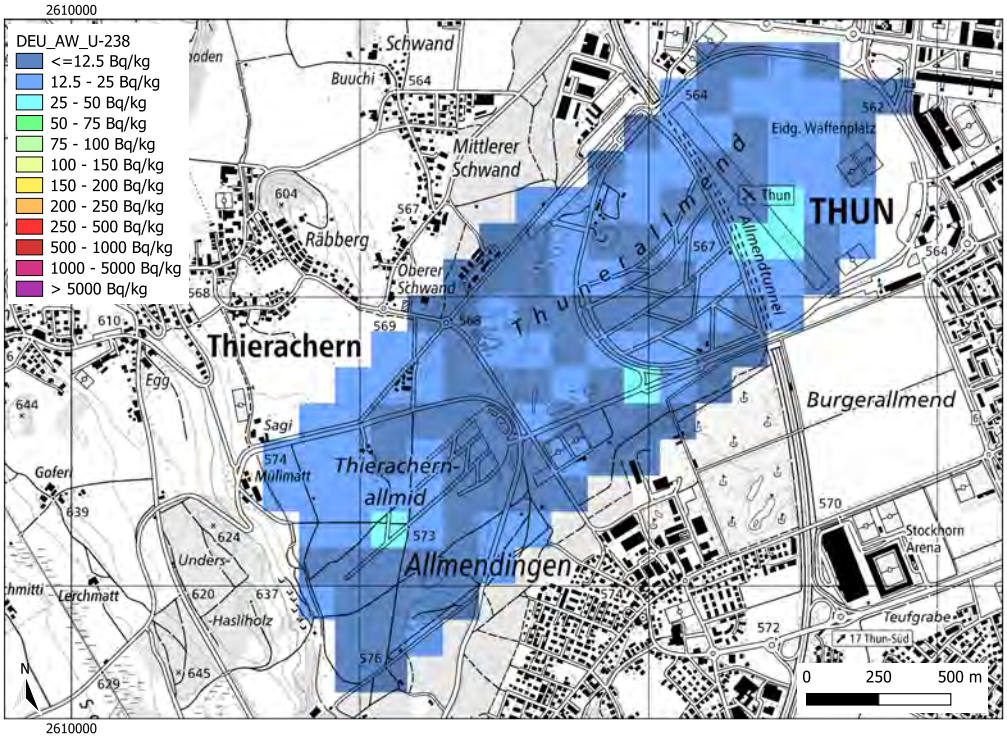

Figure 8.54: Activity concentration of ^{238}U measured at the Mission 1 (RM) area by the DEU team. Geodaten©swisstopo.

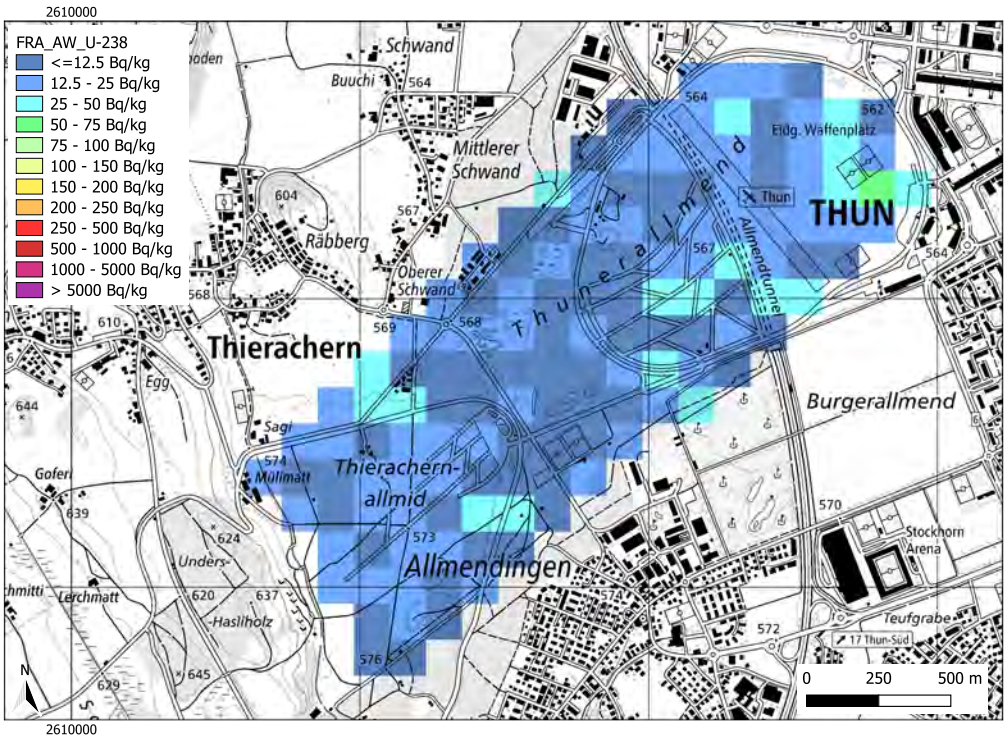

Figure 8.55: Activity concentration of ^{238}U measured at the Mission 1 (RM) area by the FRA team. Geodaten©swisstopo.

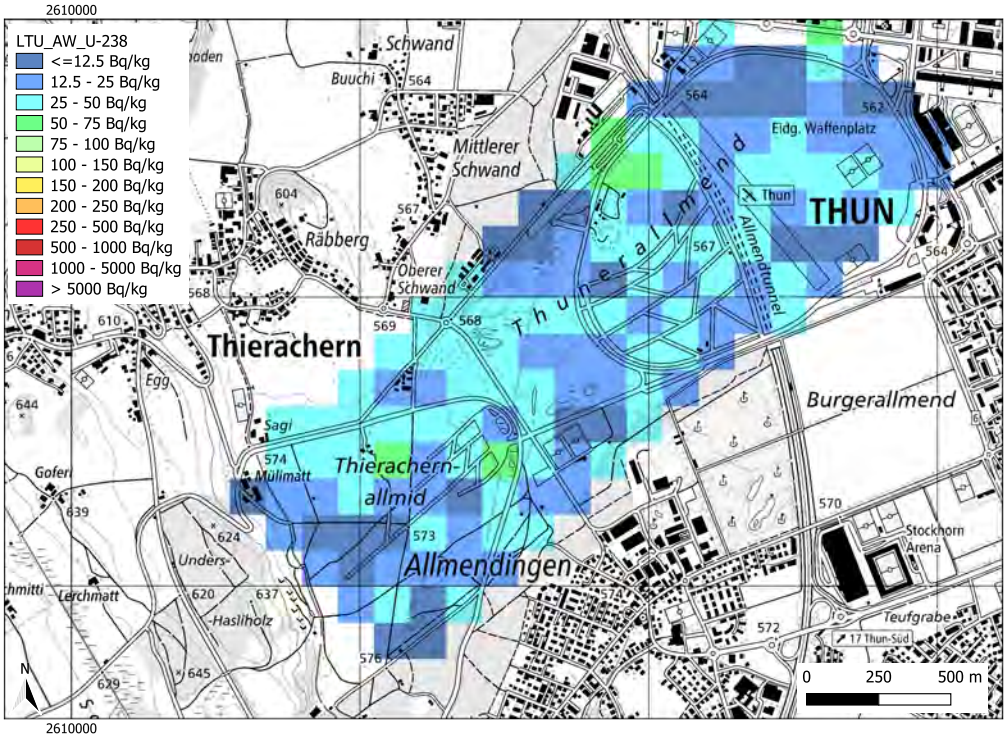

Figure 8.56: Activity concentration of ^{238}U measured at the Mission 1 (RM) area by the LTU team. Geodaten©swisstopo.

8.3 Mission 2 – BM – Lake Thun

8.3.1 CHE1 and CHE2

Measurements were conducted by the Swiss teams CHE1 and CHE2 along flight lines over Lake Thun at seven altitude levels, as shown in Figure 8.57. The measured data and corresponding spectra were averaged over the respective flight lines.

The parameters of the exponential interpolation of cosmic counts *vs.* altitude, from the measurements in 2025, differ only slightly from the current configuration used in the Mirion software of $\#C\_COS = 16.8\, e^{(0.44\, PZ)}$ (Figure 8.58). The influence of such a change remains marginal for measurements taken under nominal conditions (approximately $100\,\mathrm{m}$ above ground level), due to the low fraction of the count rate associated with cosmic radiation. The spectra shown in Figure 8.59, acquired by CHE1, exhibit an increase in count rates across the entire energy spectrum with increasing flight altitude, as well as a more pronounced annihilation peak at $511\,\mathrm{keV}$. Both effects are attributable to the increasing contribution of cosmic radiation.

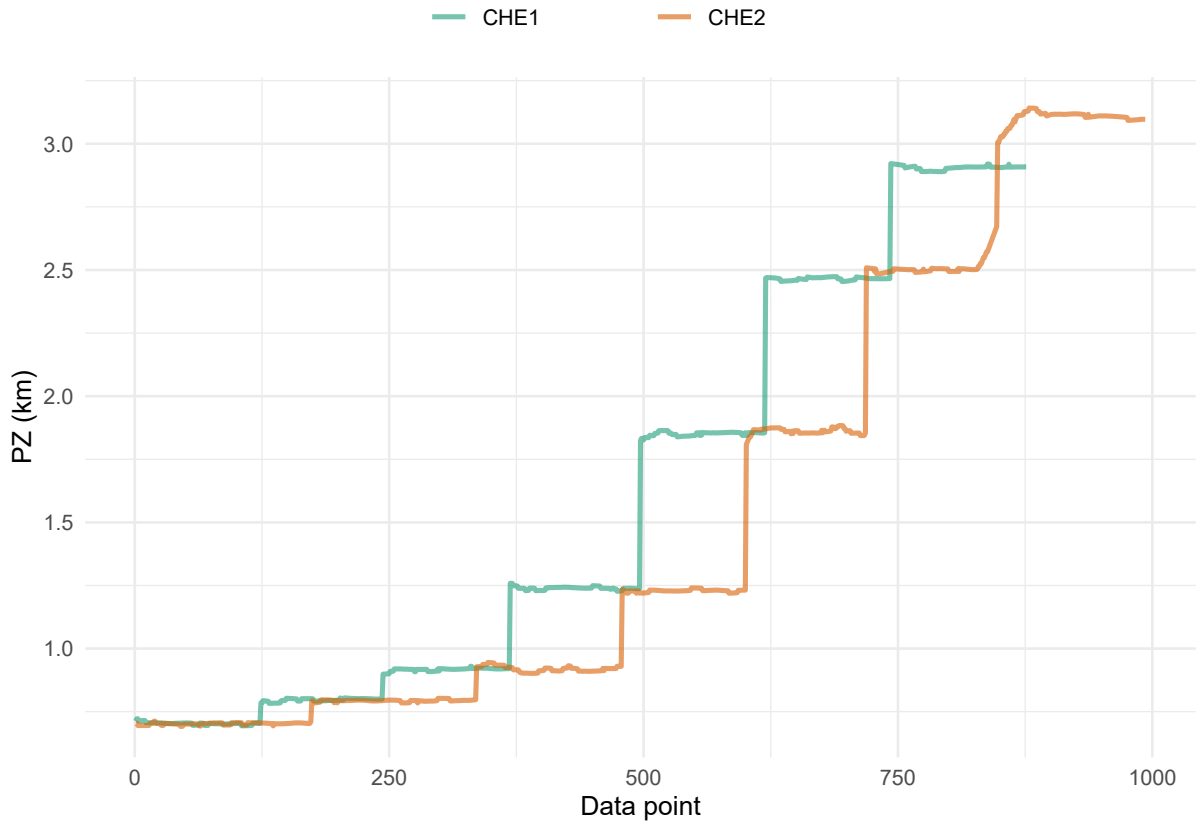

Figure 8.57: Altitude profiles over Lake Thun of teams CHE1 and CHE2.

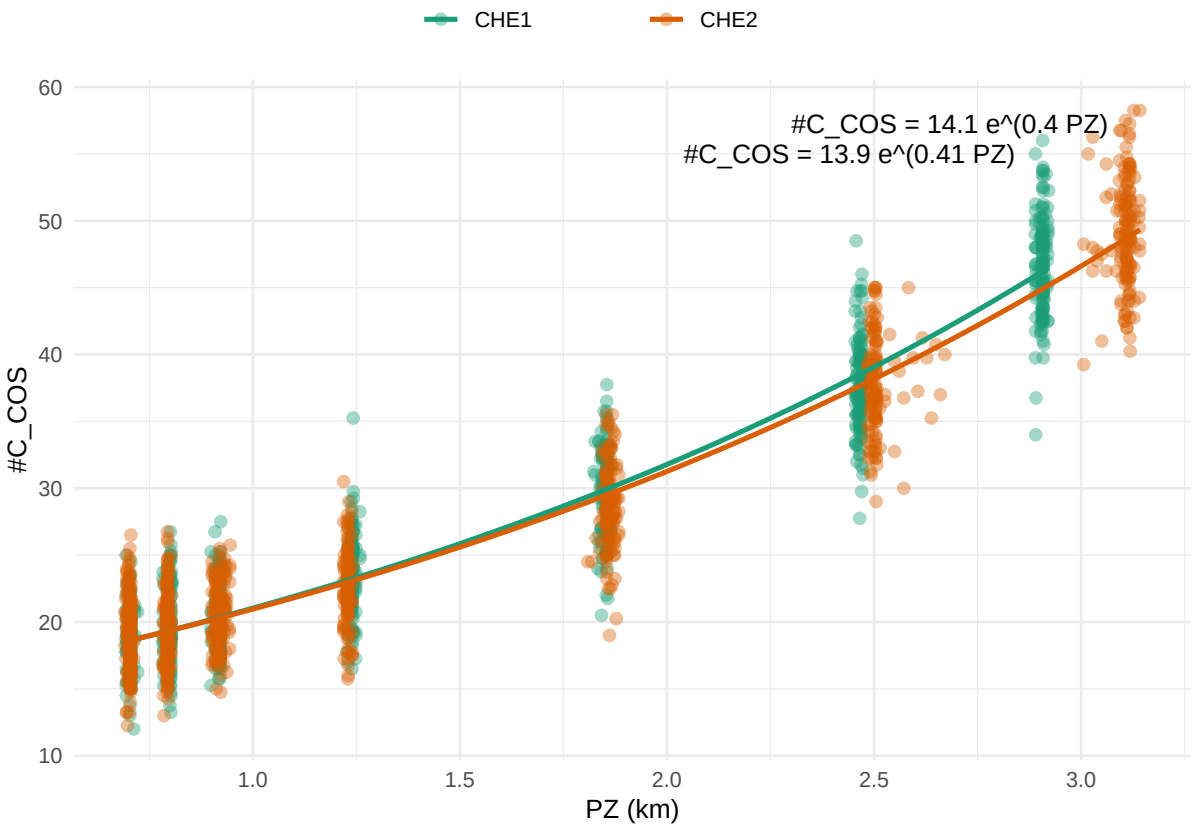

Figure 8.58: Cosmic counts as function of altitude over Lake Thun of teams CHE1 and CHE2.

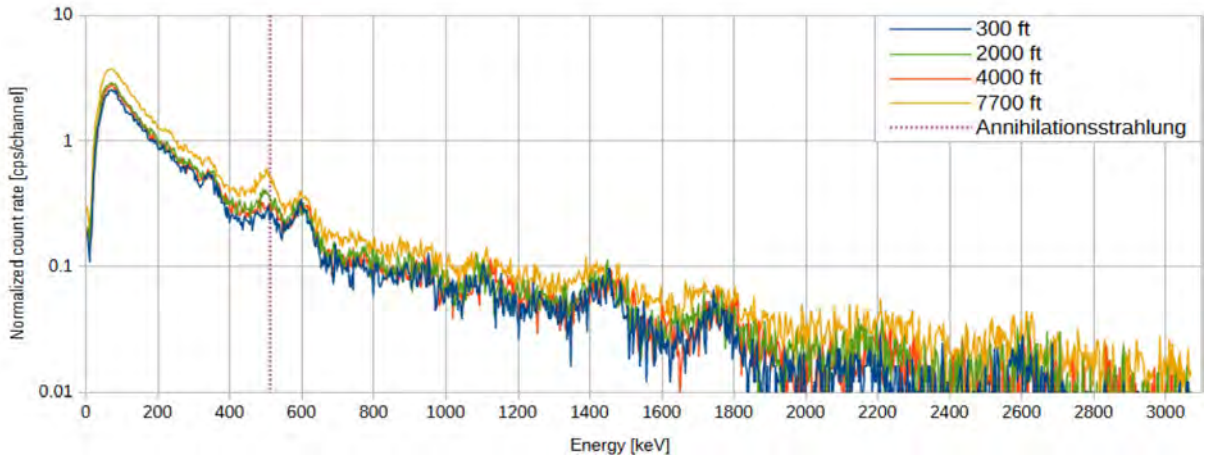

Figure 8.59: Acquired spectra at different altitudes over Lake Thun (team CHE1).

AGS_CH

In AGS_CH, the correction for the influence of cosmic radiation, as well as instrument and helicopter background, is based on the count rate in the cosmic window corresponding to photon energies between $2.9\,\mathrm{MeV}$ and $3.5\,\mathrm{MeV}$. This count rate increases with altitude, as illustrated in Figure 8.58. The correction of cosmic and background contributions for the individual energy windows was performed using the cosmic count rate, as described in Section 4.5.1. The count rate in each energy window above the lake consists of an altitude-dependent component, representing the influence of cosmic radiation, and a constant component arising from natural radionuclides within the detector

and helicopter materials. A linear relationship is thus expected between the count rate in the cosmic window and the count rate in the respective energy window. Figure 8.60 presents an overview of the calculated linear relationships between the count rate in each energy window and the cosmic count rate for the flights of CHE1 and CHE2. The slopes and intercepts derived from the linear regressions for each window were added to Table 4.9 and Table 4.10, which summarise the results of previous flights used for cosmic correction and background estimation, respectively.

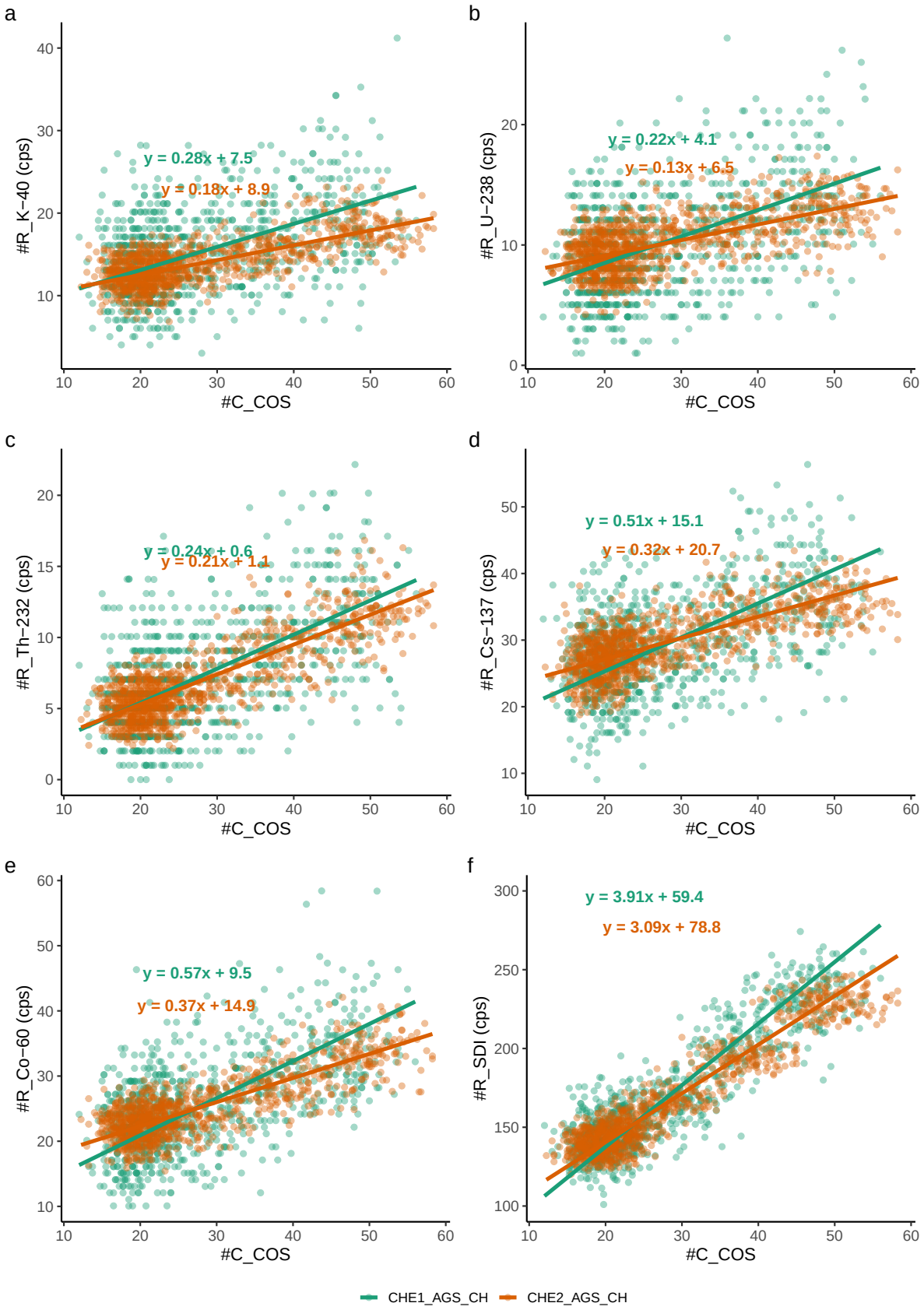

Figure 8.60: Cosmic counts versus window counts (^{40}K, ^{238}U, ^{232}Th, ^{137}Cs, ^{60}Co, SDI) over Lake Thun for teams CHE1 and CHE2. Lines and equations show the Deming regressions used to estimate background and cosmic contributions.

8.3.2 CZE

For Lake Thun, The Czech team used the altitude profile to update the system background and cosmic contribution in the AGAMA software. Data from $1200\,\mathrm{m}$ ($4000\,\mathrm{ft}$), $1800\,\mathrm{m}$ ($6000\,\mathrm{ft}$), and $2400\,\mathrm{m}$ ($8000\,\mathrm{ft}$) were employed to calculate the helicopter background and cosmic gamma contributions using an improved methodology relative to the standard approach [3]. This allowed a direct comparison with the routine method and an evaluation of its suitability for the current dataset. Figure 8.61 presents the cosmic gamma contribution for the Rad-Patrol2 system, while Figure 8.62 shows the helicopter and detector background derived from the altitude profile.

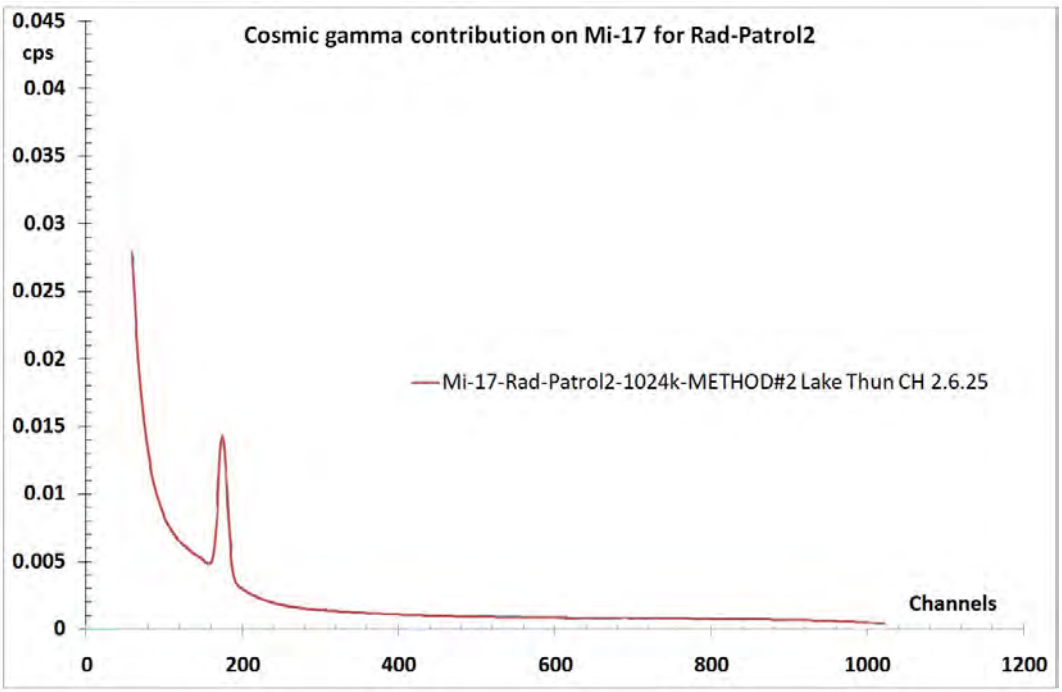

Figure 8.61: Cosmic gamma contribution measured over Lake Thun by team CZE.

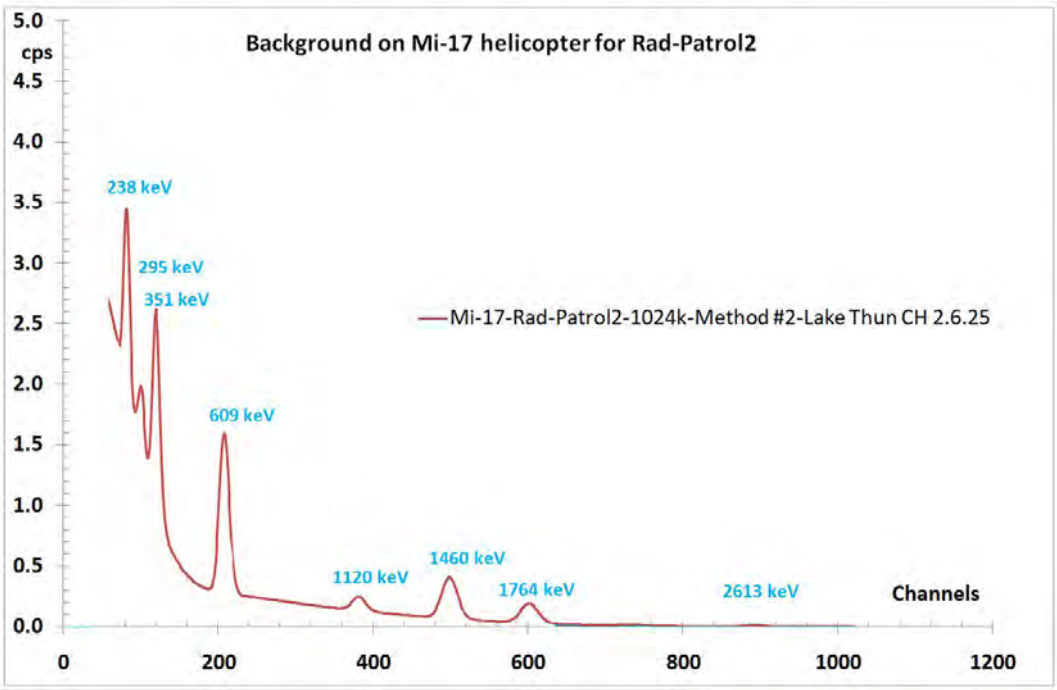

Figure 8.62: Background spectrum derived from the altitude profile over Lake Thun by team CZE.

8.3.3 DEU

To characterise the background contributions arising from the system itself, the helicopter components, personnel, and cosmic radiation for each energy window, flights were conducted over Lake Thun at different altitudes, as illustrated in Figure 8.63.

The German team began at the highest altitude and gradually moved to lower altitudes. This procedure produced a set of measurement data that was subsequently divided according to the different flight altitudes. For each flight altitude, sum spectra were created and analysed according to the predefined energy windows for the following radionuclides: ^{137}Cs, ^{40}K, ^{238}U, and ^{232}Th. The count rates measured above the lake at the standard flight altitude of $90\,\mathrm{m}$ ($300\,\mathrm{ft}$) were then adopted as background counts for all other measurements during the AGC25 campaign.

The background count rate for each energy window resulting of this analysis are summarised in Table 8.2.

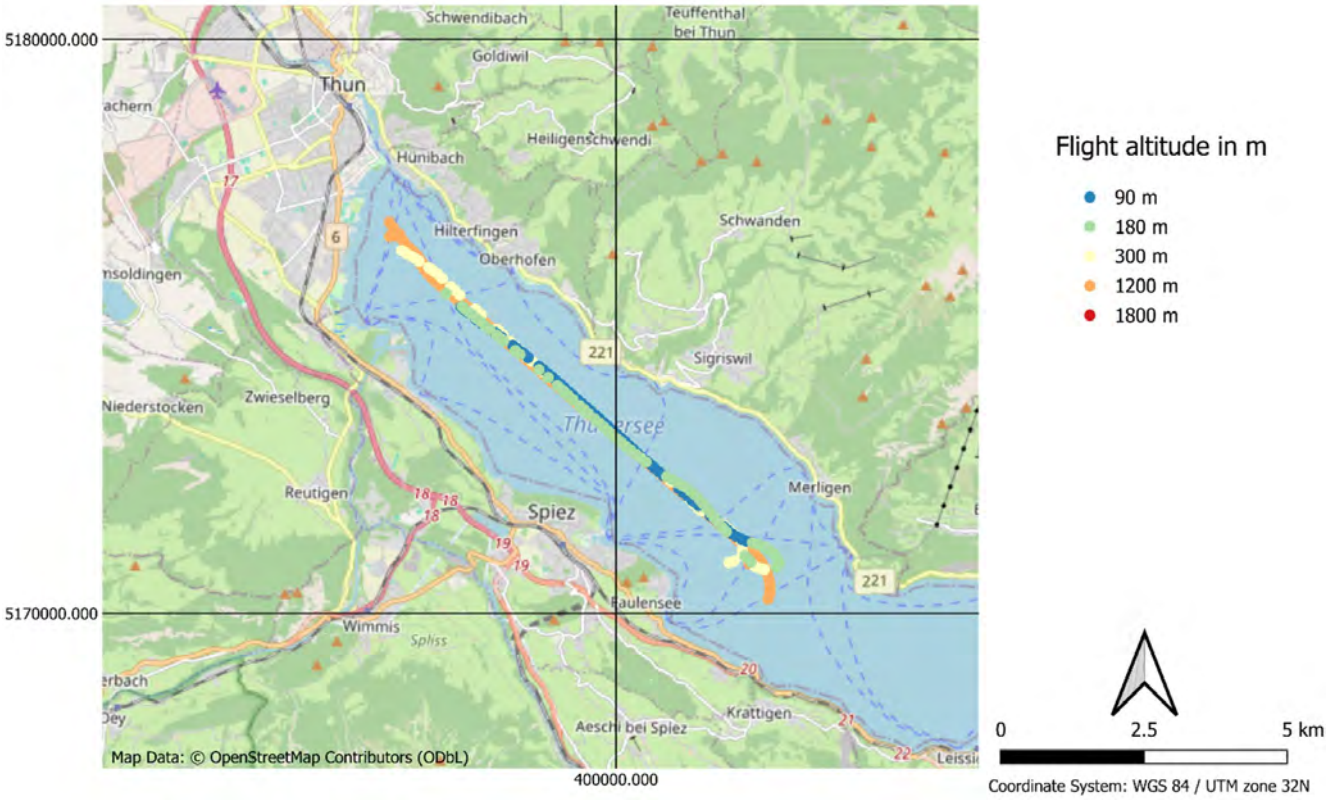

Figure 8.63: Flight path of the background measurements over Lake Thun (Team DEU).

Table 8.2: Background counts for the measurement system during the ACG25 exercise (Team DEU).

Nuclide	^{137}Cs	^{40}K	^{238}U	^{232}Th
Energy (keV)	662	1461	1765	2614
Count rate (cps)	13.6	5.03	2.64	1.15

8.3.4 FRA

For the French team, an issue with one detector meant that only a $12\,\mathrm{L}$ system was available during the measurements. In the subsequent analysis, the window counts from the background

measurement over Lake Thun were corrected to represent a four-detector system. The 2025 Thun results have been integrated with the French team's previous work on lake and sea flights.

The acquired spectra at increasing altitudes, presented in Figure 8.64, exhibit the same features observed in the spectra of the Swiss team CHE1, described in Section 8.3.1. Figure 8.65 shows the increase in count rates associated with the total window, ^{238}U, and ^{232}Th as a function of flight altitude over Lake Thun. The corresponding Thun data were also included in the correlation graphs in Figure 8.66: between the total window and dose rate, the ^{40}K and ^{238}U windows, and the total window and the ^{238}U window. These comparisons allow assessment of the relationship between window counts and cosmic contributions, as well as the linearity across the different energy windows for the French system.

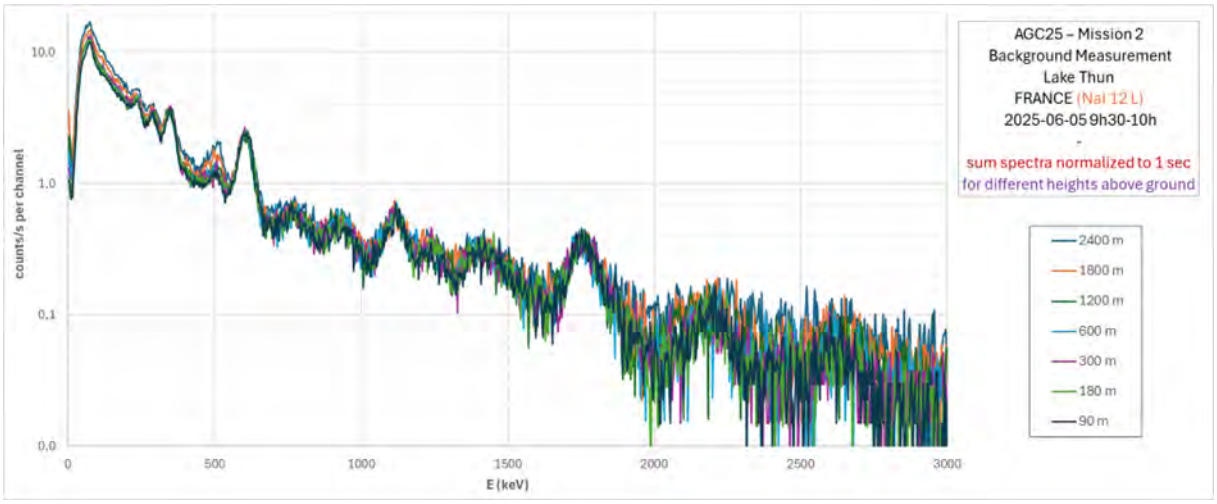

Figure 8.64: Acquired spectra at different altitudes over Lake Thun (team FRA).

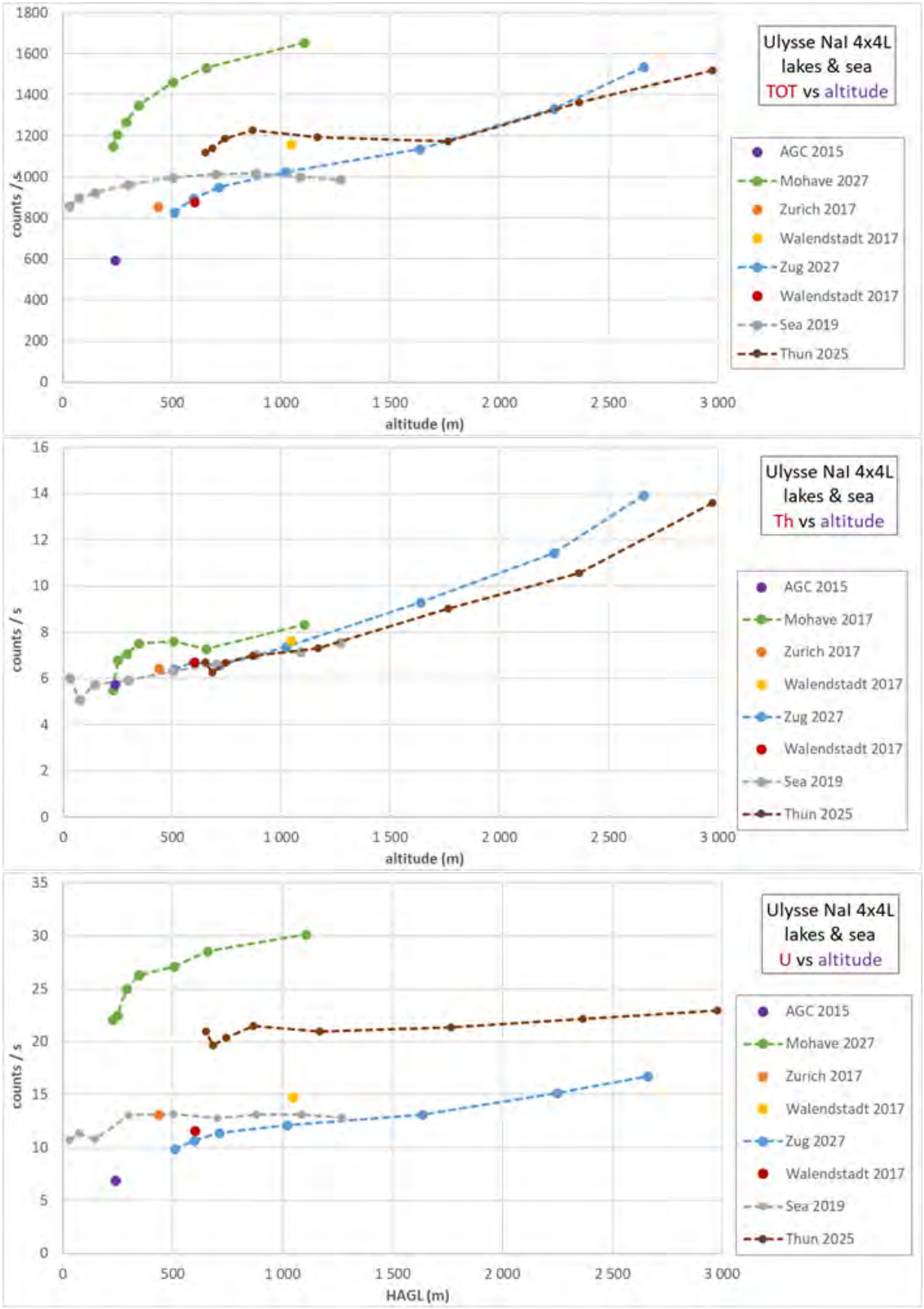

Figure 8.65: Count rates in specific windows measured by team FRA during altitude profiles, including Lake Thun 2025.The panels show the total window, ^{232}Th, and ^{238}U, respectively.

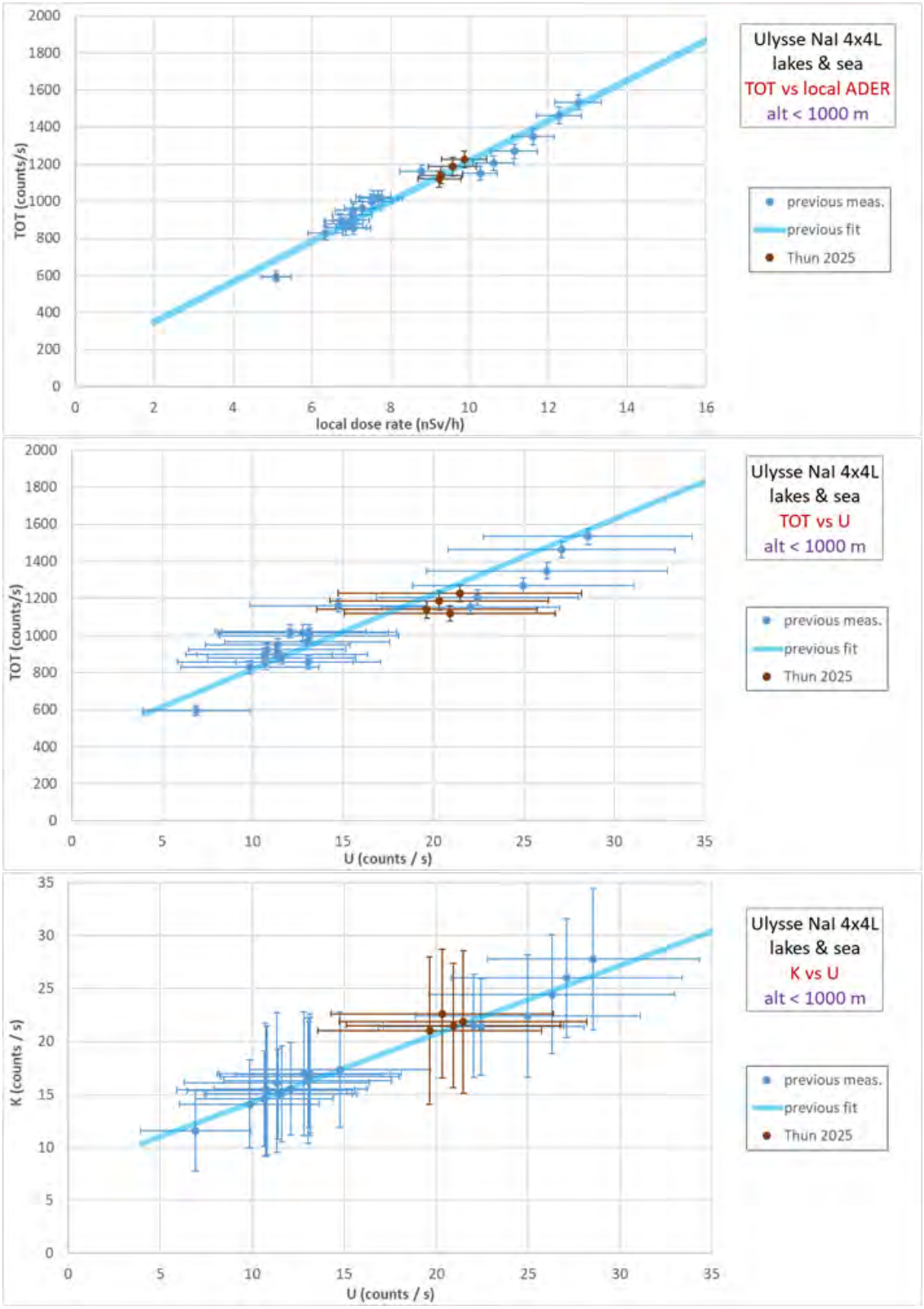

Figure 8.66: Comparison of count rates in selected energy windows measured by team FRA during altitude profiles, including the 2025 Lake Thun survey. From top to bottom, the images show: total window versus DHSR, total window versus ^{238}U, and ^{40}K versus ^{238}U.

8.3.5 LTU

To estimate the influence of cosmic radiation on the aerial survey data, the LTU team conducted flights over Lake Thun at seven different altitudes: $90\,\mathrm{m}$, $180\,\mathrm{m}$, $300\,\mathrm{m}$, $600\,\mathrm{m}$, $1200\,\mathrm{m}$, $1800\,\mathrm{m}$ and $2400\,\mathrm{m}$. The contribution of cosmic radiation was assessed using the count rate within the window corresponding to photon energies between $3\,\mathrm{MeV}$ and $3.6\,\mathrm{MeV}$. The corresponding spectra, averaged over the respective flight lines, are presented in Figure 8.67, where an altitude-dependent increase in count rates across the entire spectrum can be observed, along with a pronounced annihilation peak at $511\,\mathrm{keV}$, reflecting the growing impact of cosmic radiation. Figures 8.68–8.71 show the increase in count rates associated with ^{40}K, ^{238}U, ^{232}Th, cosmic contributions, and dose rate as a function of flight altitude over Lake Thun.

These comparisons enable the assessment of the relationship between window counts, dose rate, and cosmic contributions, confirming that cosmic radiation contributes increasingly to all measurements with rising altitude.

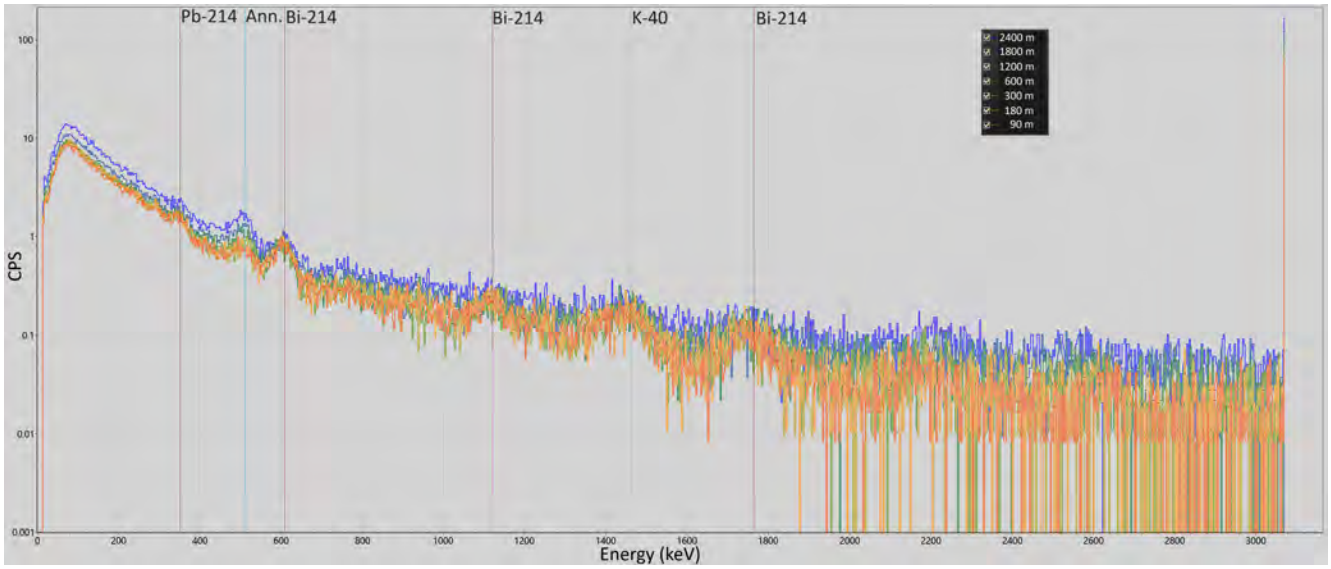

Figure 8.67: Spectra vs. altitude measured during mission 2 by the LTU team.

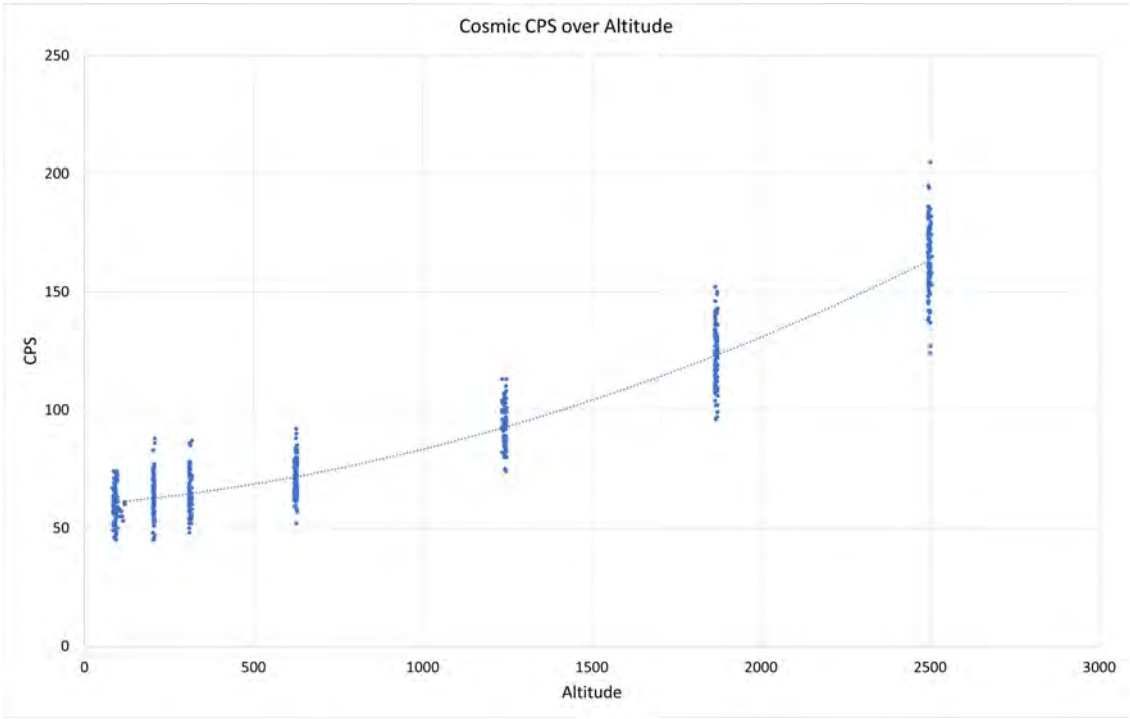

Figure 8.68: Cosmic count rate vs. altitude measured during mission 2 by the LTU team.

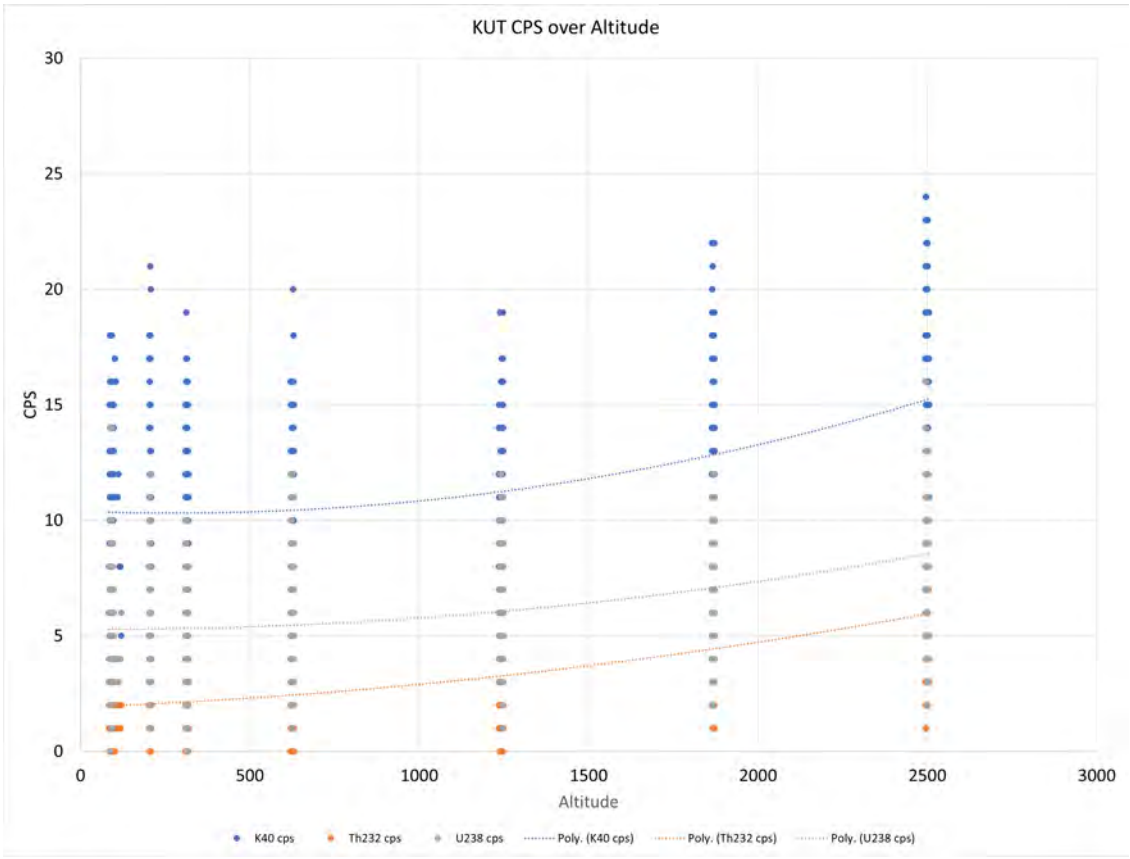

Figure 8.69: Relationship between each window count rate ^{40}K (blue), ^{238}U (gray), ^{232}Th (dark orange) vs. altitude measured during mission 2 by the LTU team.

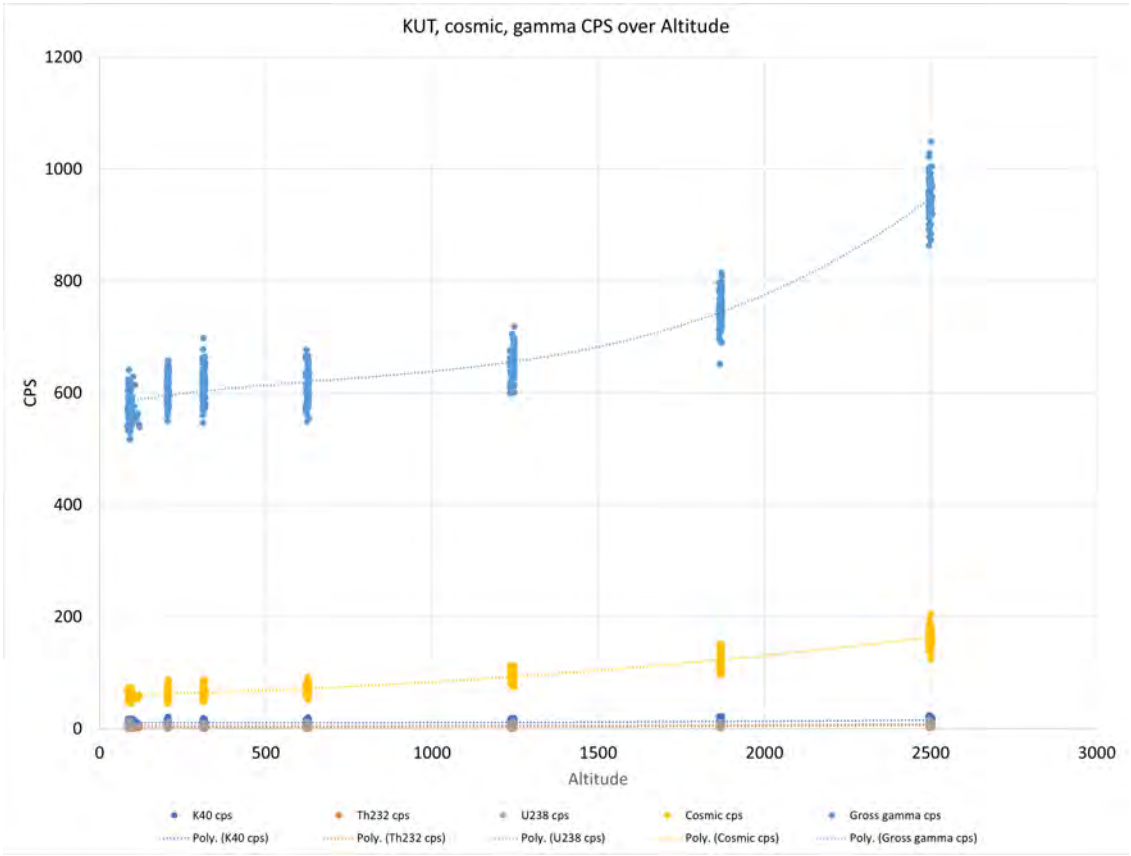

Figure 8.70: Relationship between each window count rate ^{40}K (blue), ^{238}U (gray), ^{232}Th (dark orange), cosmic count rate (orange) total count rate (light blue) vs. altitude measured during mission 2 by the LTU team.

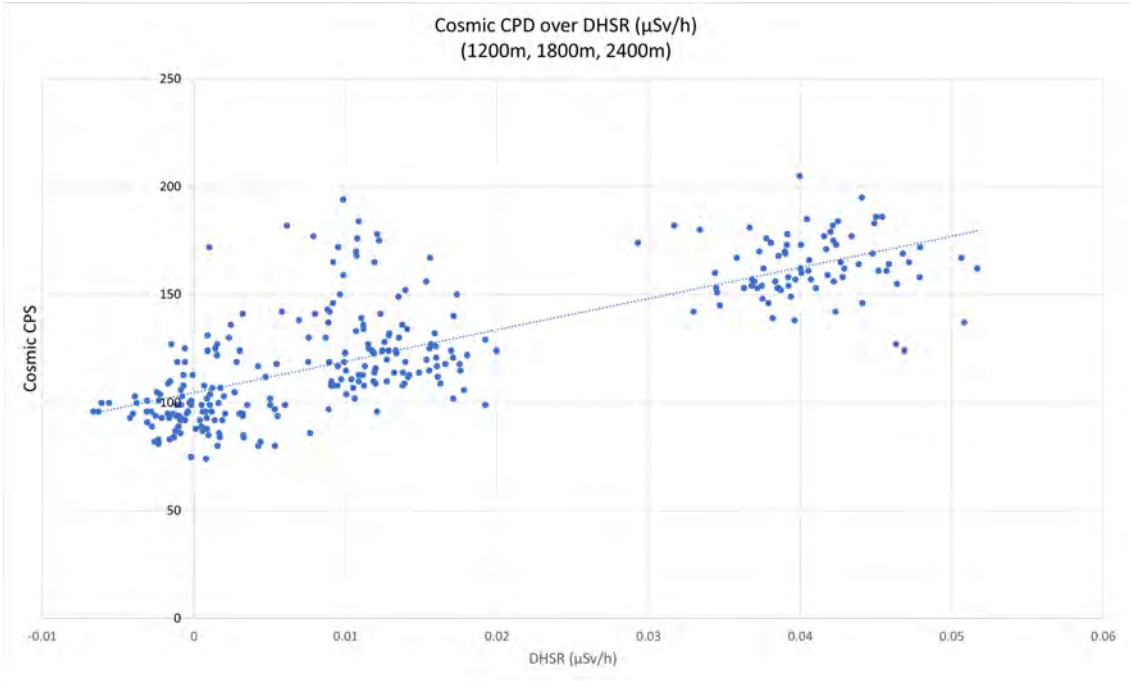

Figure 8.71: Relationship between dose rate and the cosmic count rate measured during mission 2 by the LTU team.

8.3.6 Radon presence in the air during background measurements

Some participants reported deviations from the linear models used to estimate the background and cosmic contributions. This effect can be attributed to the presence of radon in the air above the lake, particularly at lower flight altitudes.

Over large water bodies only cosmic radiation and radiation originating from the measuring system or helicopter should contribute to the observed counts, as emissions from ground radionuclides are shielded by the water. In practice, however, if the water body is not sufficiently large, radon emanating from the surrounding area may be transported or diffuse to the measurement point above the water, affecting the measurements.

For this reason, measurements over the sea or very large lakes are preferred, as sufficient distance can be put between the measurement point and the shoreline to exclude any influence from radon. Switzerland has no access to the sea and its lakes, despite many, are relatively small or elongated, making it difficult to ensure an adequate distance from the shore that would, under any weather circumstance, eliminate the influence of radon.

8.4 Mission 3 – CM

8.4.1 Coordination of composite mapping

The Mission commenced with planning on Monday, 2nd June, when a dedicated group, comprising members from all teams and guided by the host nation, was tasked with devising the survey strategy and subdividing and assigning areas to each team.

Based on the preliminary information provided in the Mission sheet

- Target survey area $2200\,\mathrm{km}^2$
- Unknown number of sources
- Minimum activity of $350\,\mathrm{MBq}$ of ^{137}Cs

the group established the following survey parameters: ground clearance $90\,\mathrm{m}$, flight speed $150\,\mathrm{km\,h^{-1}}$, and line spacing of $350\,\mathrm{m}$. The defined flight lines are shown in Figure 8.72, and the area assignments per team, optimised according to the flight endurance of the various helicopters, are illustrated in Figure 8.73. It was decided that all teams fly a common line at the beginning of the measurements, for subsequent data comparison. The plan envisaged two measurement flights per team – one in the morning and one in the afternoon – with refuelling at the LSMD base in Dübendorf over the lunch break.

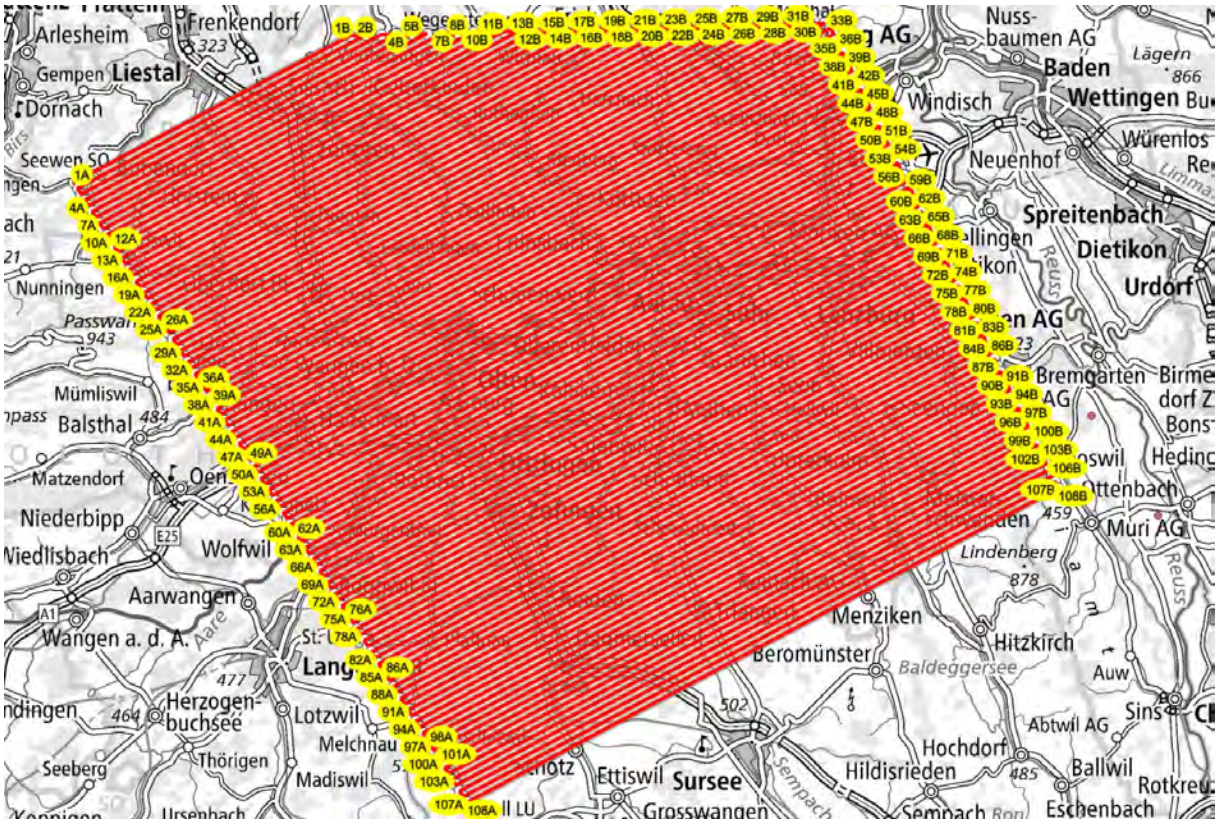

Figure 8.72: Flight lines planned for the composite mapping of Mission 3 (CM). Geodata©swisstopo.

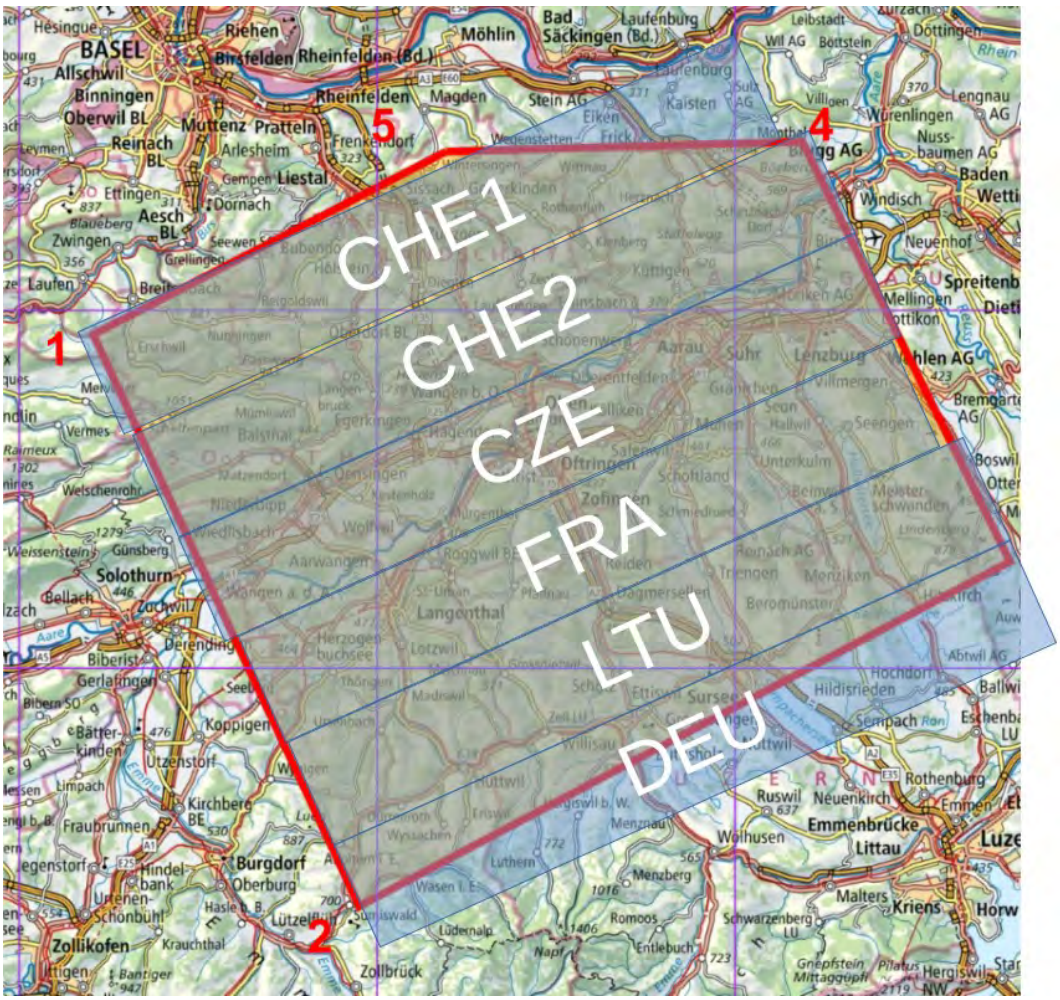

Figure 8.73: Planned area assignments for the composite mapping of Mission 3 (CM). Geodata©swisstopo.

On Tuesday, 3rd June, the day scheduled for the composite mapping, flights were suspended due to adverse weather affecting visibility. With forecasts indicating an improvement later in the afternoon, the group responsible for planning the composite mapping reconvened to devise a revised survey strategy covering a reduced portion of the originally planned area. As the exercise lead informed the group that two locations with radioactive sources lay outside the boundaries of the reduced survey area, an ad-hoc Mission was assigned to the CHE1 team to investigate these two points of interest: Seerbru and Eichwald, listed in Table 7.4. The adapted flight plan for the composite mapping and the revised area assignments per team are shown in Figures 8.74 and 8.75, respectively. At the start of the mission, each team was required to fly the common line, extending from PN 47.322788 / PE 8.340204 to PN 47.276412 / PE 8.384684, covering a distance of $6\,\mathrm{km}$.

The take-off sequence began at 13:30, with helicopters departing in succession. During the take-off procedures, the German team encountered an issue with one of the helicopter's instruments and decided to cancel the planned flight. This change was promptly communicated to all other teams, both in the air and on the ground. The Swiss team CHE1, engaged in measuring the two points of interest in the northern area, had the capacity to take over the task originally assigned to the German team, surveying their area after completing the initial measurements. Meanwhile, the German team identified the instrument fault, procured the necessary spare part, and installed it by Wednesday morning, restoring full operational capability. Team DEU was hence able to survey the assigned area during the afternoon of Wednesday the 4th of June.

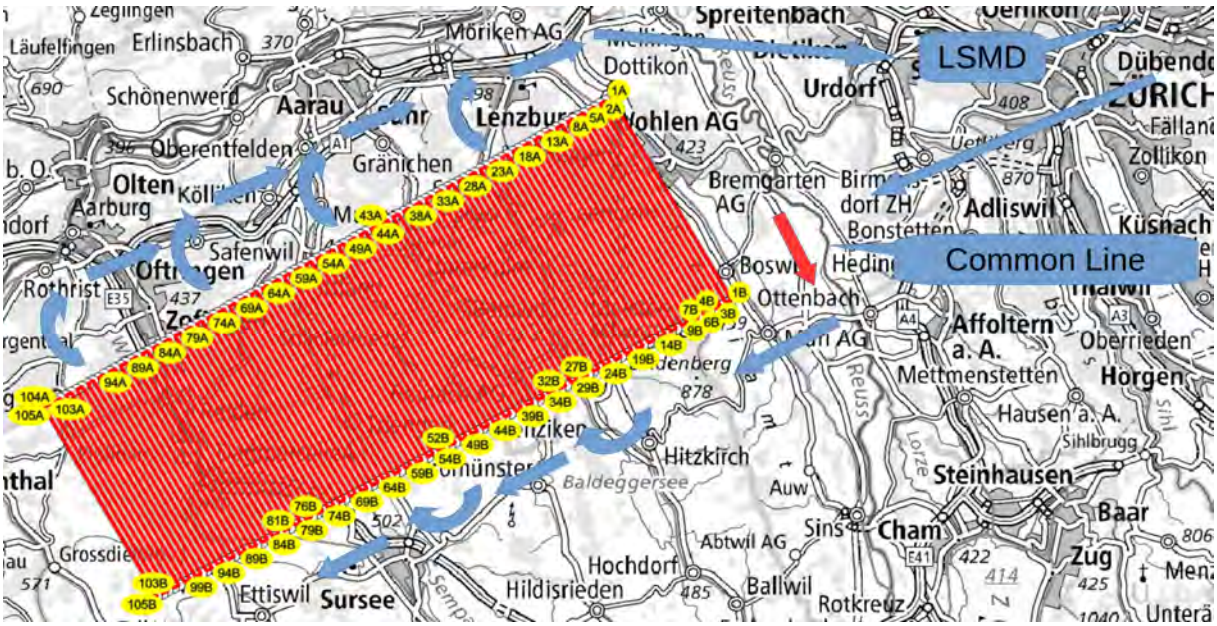

Figure 8.74: Flight lines after re-planning for the composite mapping of Mission 3 (CM). Geodata©swisstopo.

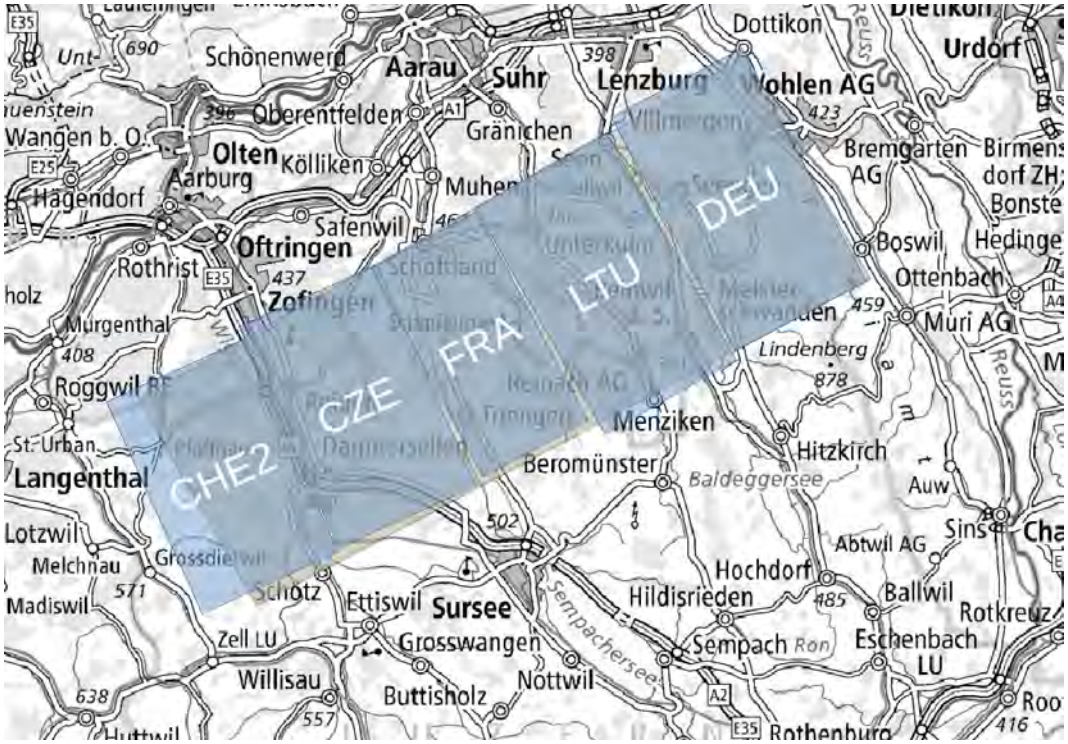

Figure 8.75: Area assignments after re-planning for the composite mapping of Mission 3 (CM). Geodata©swisstopo.

8.4.2 Source search

At Seebru (Table 8.3) ^{137}Cs was detected, already during flight (Figure 8.77), suggesting the presence of multiple sources that could not be individually located due to limited spatial resolution. A surface contamination is also possible; therefore, only the maximum activity of a single source was estimated.

At Eichwald (Table 8.4), several radionuclides were identified within a radius of about 50 metres (Figure 8.83). Terrain and vegetation caused considerable variability in activity estimates, particularly for ^{137}Cs. ^{241}Am was detected only during the reanalysis, appearing weakly and slightly displaced to the north.

The maps of Figures 8.77 – 8.87 provide sufficient evidence to support targeted ground searches and the secure recovery of sources, in the case of a real event.

In the region of Dagmersellen, no elevated ambient dose equivalent rate values were observed (Figures 8.89 and 8.90). Only in the subsequent detailed evaluation a point with a slightly increased anthropogenic dose rate and MMGC ratio was identified between Dagmersellen and Nebikon (Figures 8.88, 8.91 and 8.92), corresponding to a ^{137}Cs source that had inadvertently remained partially shielded, making it difficult to detect during aerial measurements. An estimation of the activity of the source was thus not possible.

Table 8.3: Estimated source activity at Seebru, evaluated by the CHE1 team in Mission 3.

Parameter	Preliminary evaluation	Final evaluation
Mirion Software (SPIR)		
Location	PN 47.464440	PE 7.701369
Identification/activity	^{137}Cs $464\,\mathrm{MBq}$	^{137}Cs $0.47 \pm 0.10\,\mathrm{GBq}$
AGS_CH		
Location	PN 47.464442	PE 7.701674
Identification/activity	^{137}Cs $120\,\mathrm{MBq}$	

Table 8.4: Estimated source activity at Eichwald, evaluated by the CHE1 team in Mission 3

Parameter	Preliminary evaluation	Final evaluation
Mirion Software (SPIR)		
Location	PN 47.466965	PE 8.097499
Identification/activity	^{137}Cs $1.25\,\mathrm{GBq}$	^{137}Cs $0.85\pm\ 0.1\,\mathrm{GBq}$
Identification/activity	^{60}Co $150\,\mathrm{MBq}$	^{60}Co $130\pm\ 70\,\mathrm{MBq}$
Identification/activity	^{133}Ba $950\,\mathrm{MBq}$	^{133}Ba $350\pm\ 100\,\mathrm{MBq}$
Identification/activity	^{241}Am n.a.	^{241}Am $1.2\pm\ 0.2\,\mathrm{GBq}$
AGS_CH		
Location	PN 47.46676	PE 8.097439
Identification/activity	^{137}Cs 310 MBq	
Identification/activity	^{60}Co 160 MBq	

Source search maps at Seebru

The maps were generated using a gridding procedure, with each grid cell measuring 75 metres, enabling consistent spatial interpolation and visualisation of the measurement results across the surveyed area.

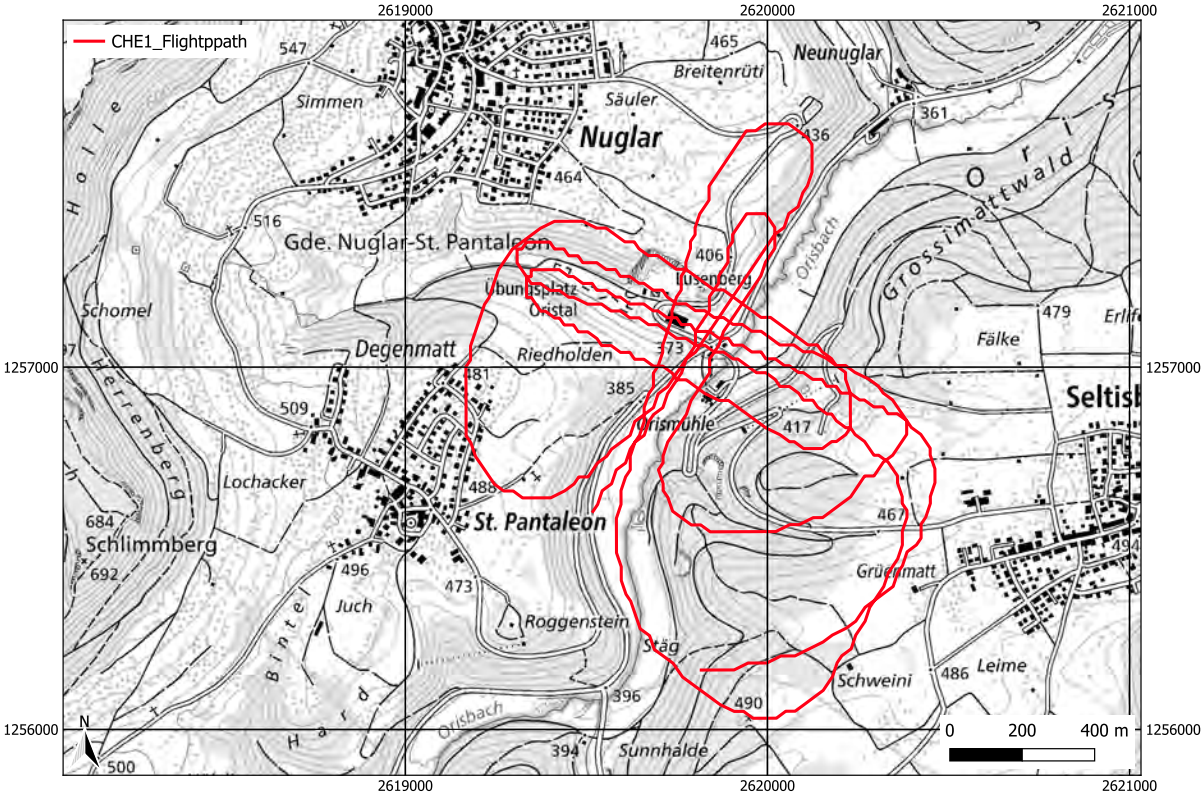

Figure 8.76: Flight path during Mission 3 at Seebru by CHE1 team. Geodaten©swisstopo.

Figure 8.77: Live detection data for ^{137}Cs recorded during Mission 3 at Seebru by CHE1 team.

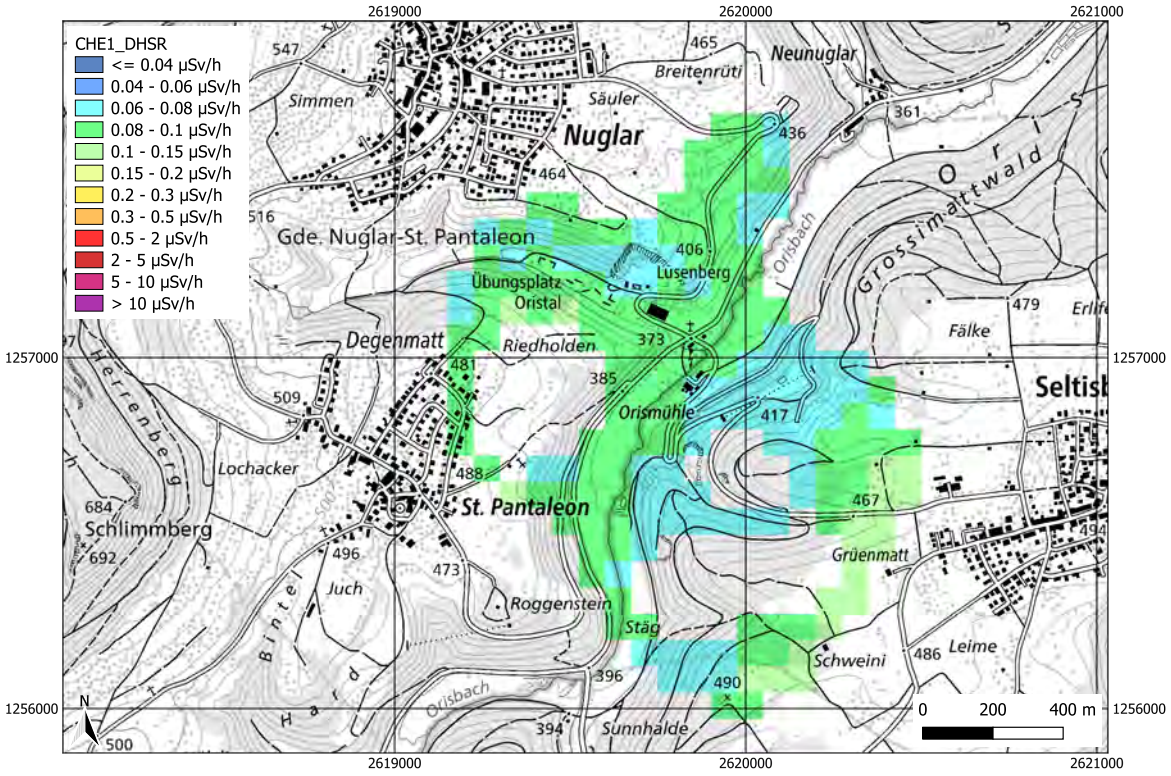

Figure 8.78: Ambient dose equivalent rate (DHSR) measured at Seebru by CHE1 team. Geodaten©swisstopo.

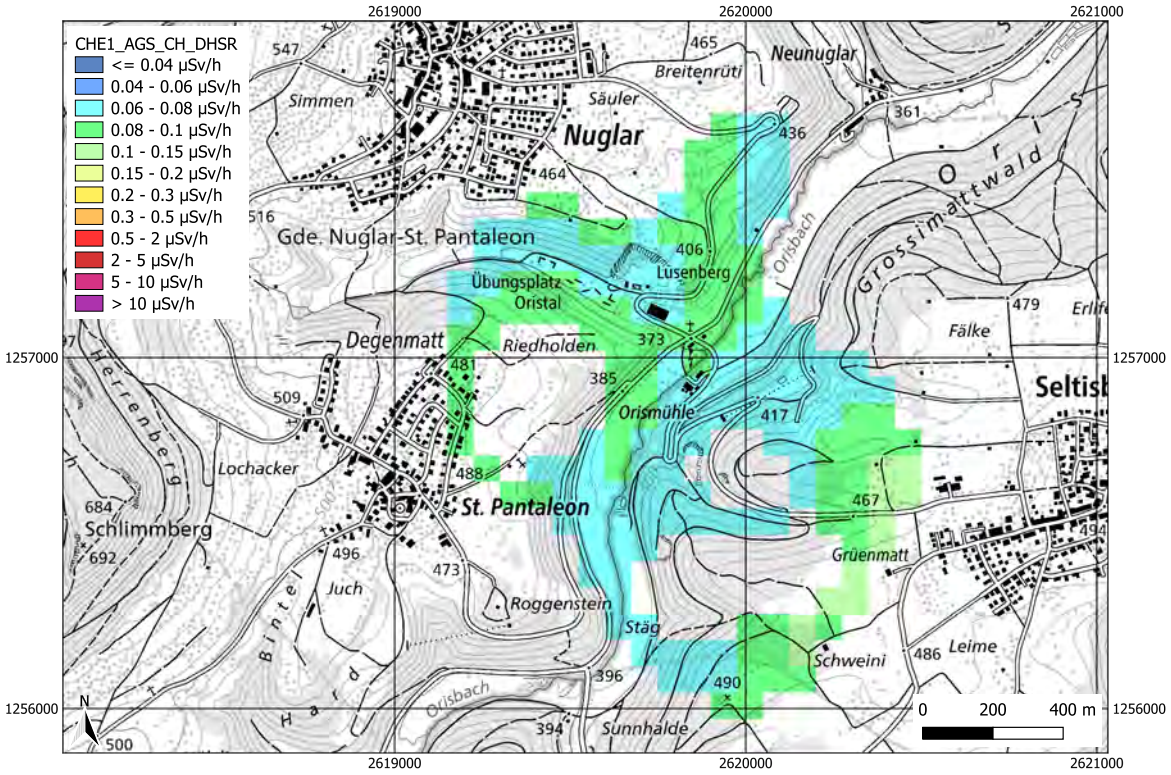

Figure 8.79: DHSR measured at Seebru by CHE1 team, analysed with AGS_CH. Geodaten©swisstopo.

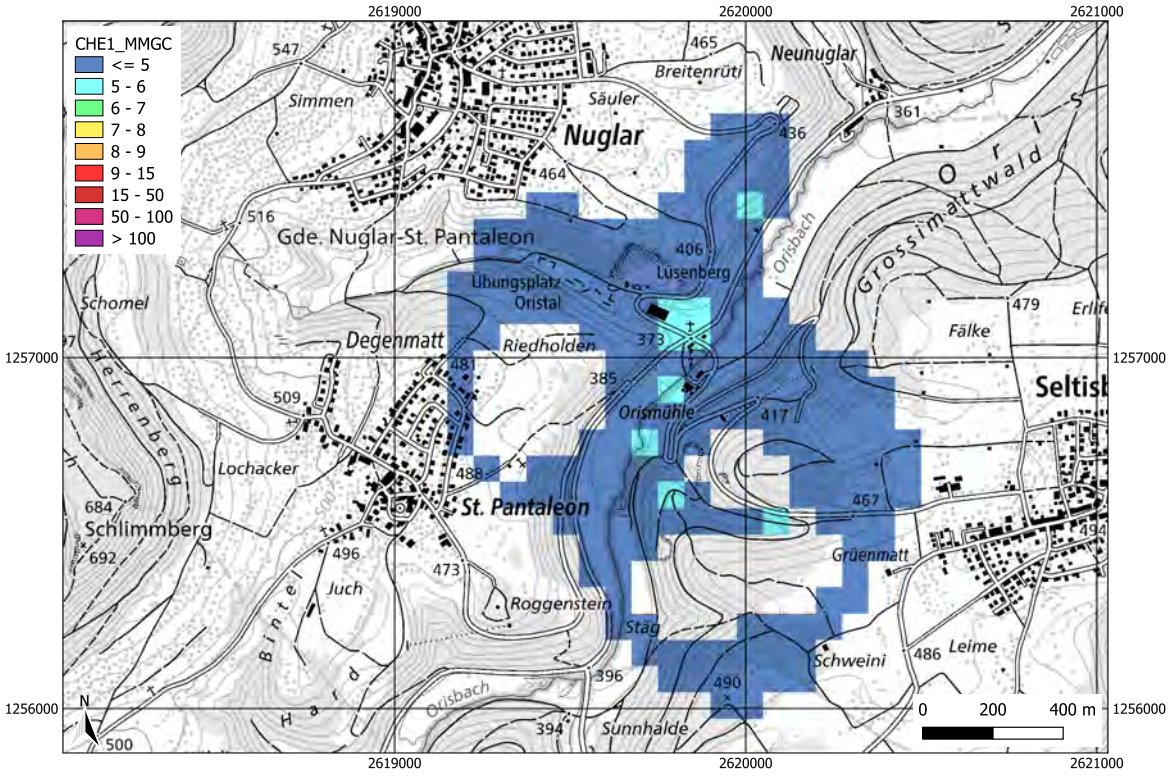

Figure 8.80: Man made gross count (MMGC) measured at Seebru by CHE1 team. Geodaten©swisstopo.

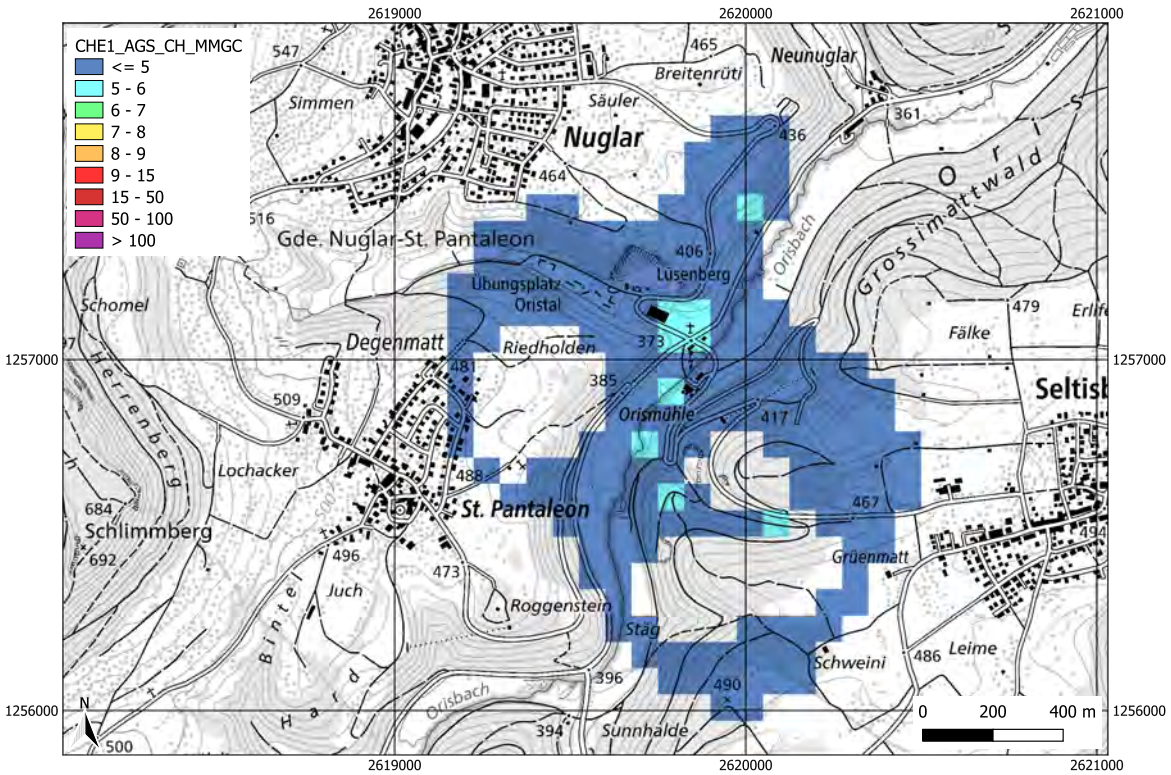

Figure 8.81: Man made gross count (MMGC) measured at Seebru by CHE1 team, analysed with AGS_CH. Geodaten©swisstopo.

Source search maps at Eichwald

The maps were generated using a gridding approach, with a cell size of 75 metres, providing a structured spatial representation of the measurement data.

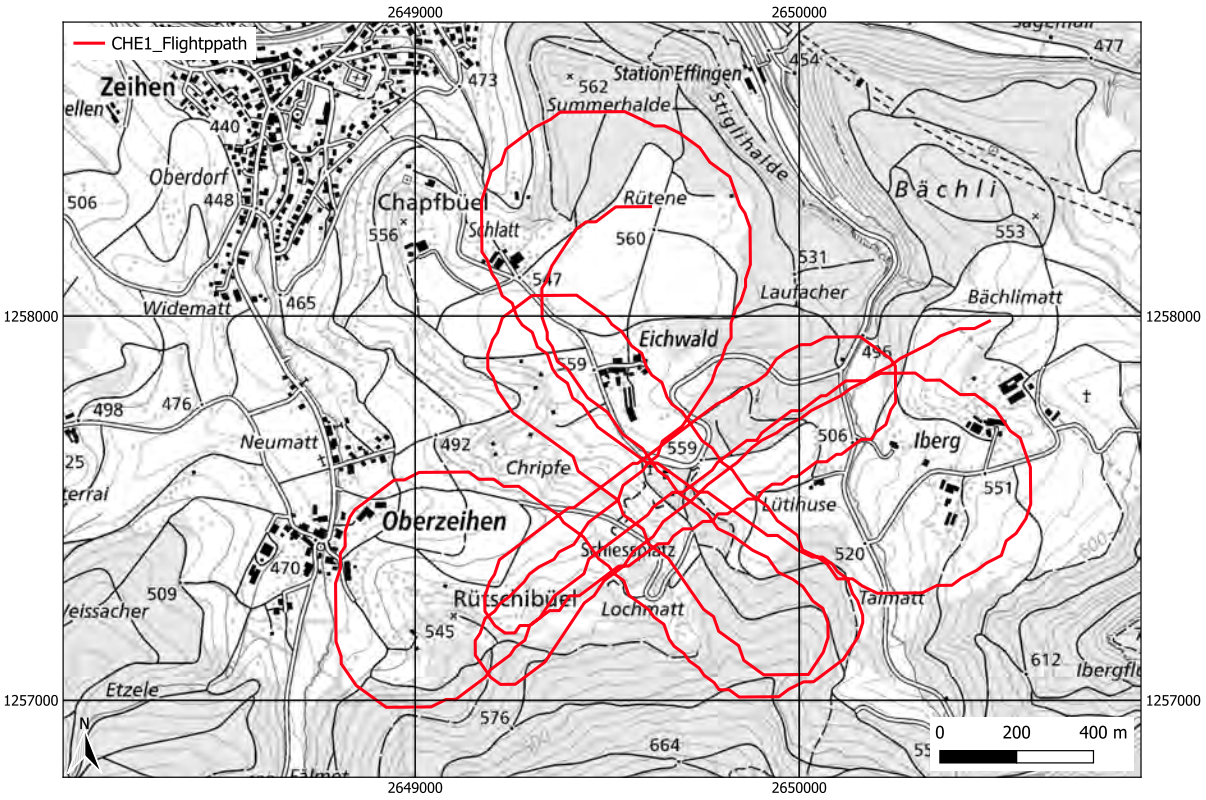

Figure 8.82: Flight path during Mission 3 at Eichwald by CHE1 team. Geodaten©swisstopo.

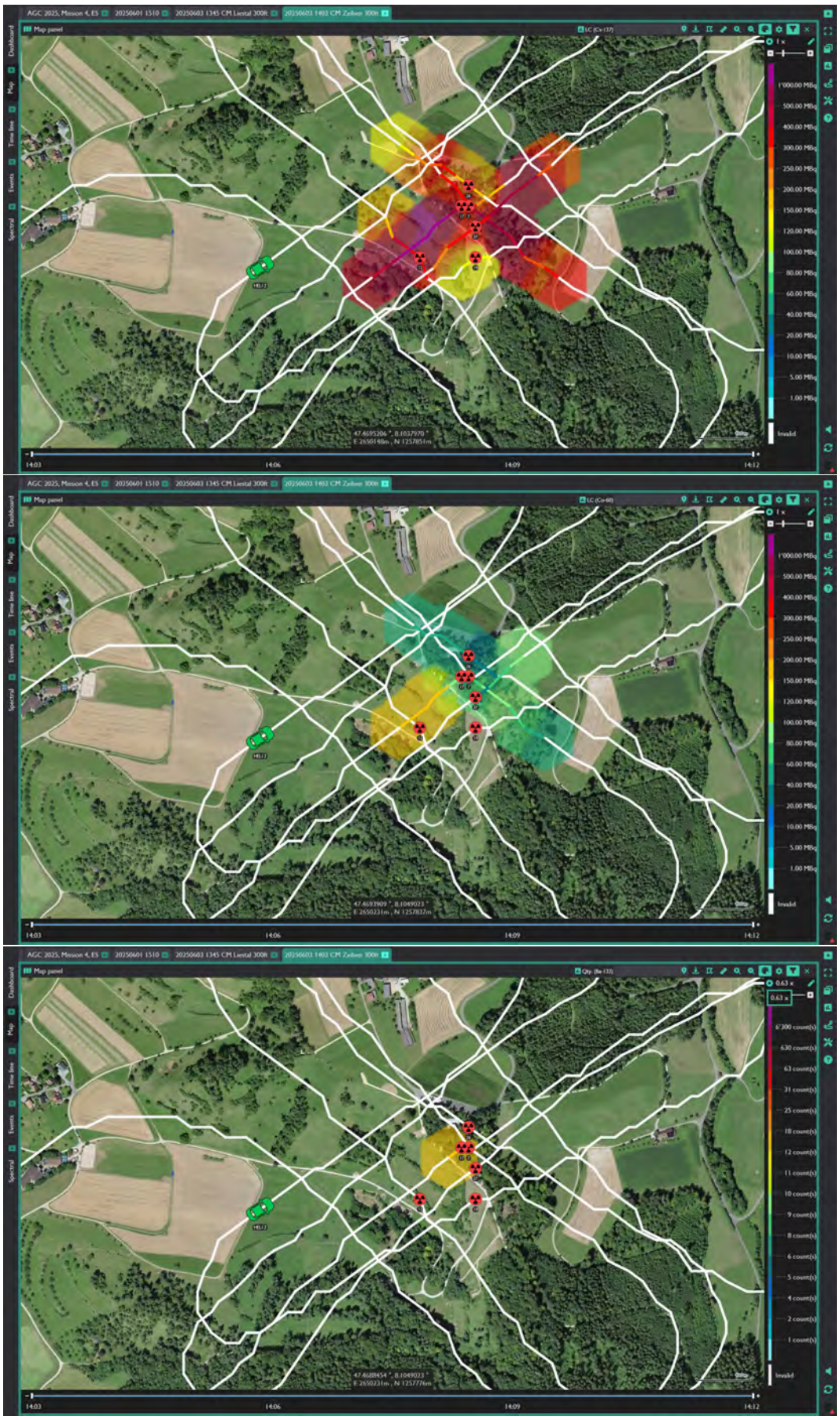

Figure 8.83: Live detection data for ^{137}Cs (top), ^{60}Co (centre), and ^{133}Ba (bottom) recorded during Mission 3 at Eichwald by the CHE1 team.

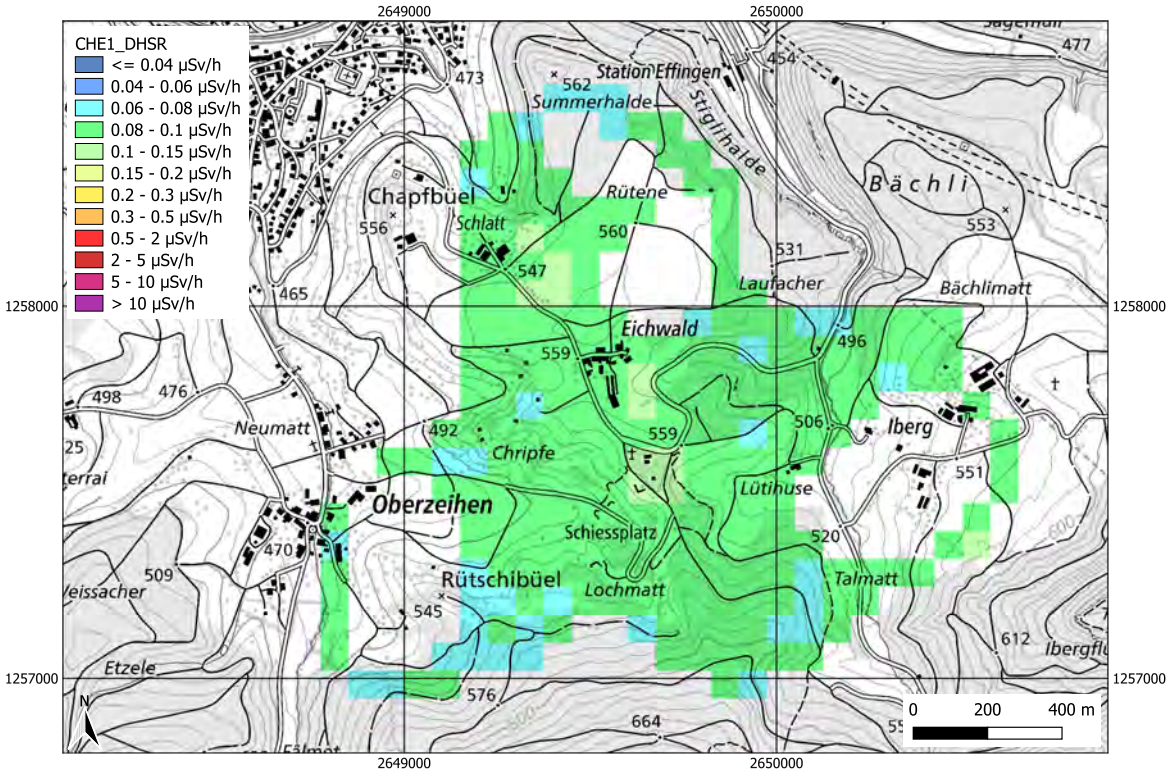

Figure 8.84: Ambient dose equivalent rate (DHSR) measured at Eichwald by CHE1. Geodaten©swisstopo.

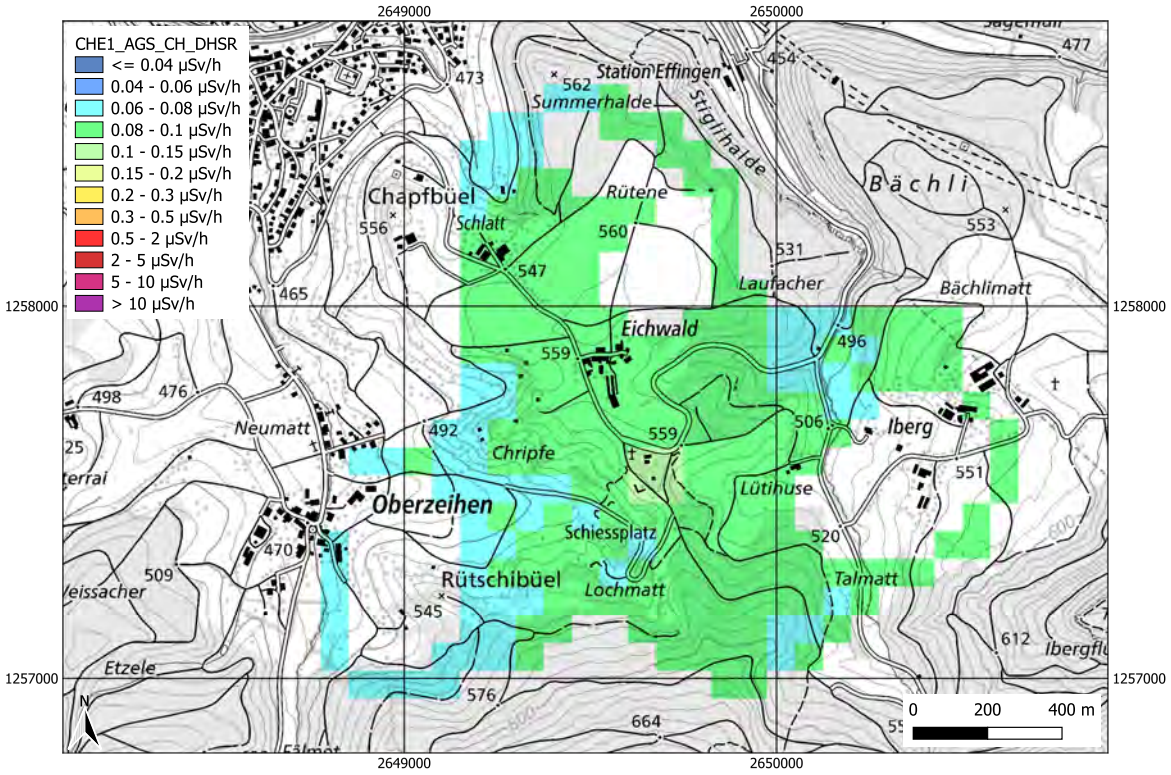

Figure 8.85: Ambient dose equivalent rate (DHSR) measured at Eichwald by CHE1, analysed with AGS_CH. Geodaten©swisstopo.

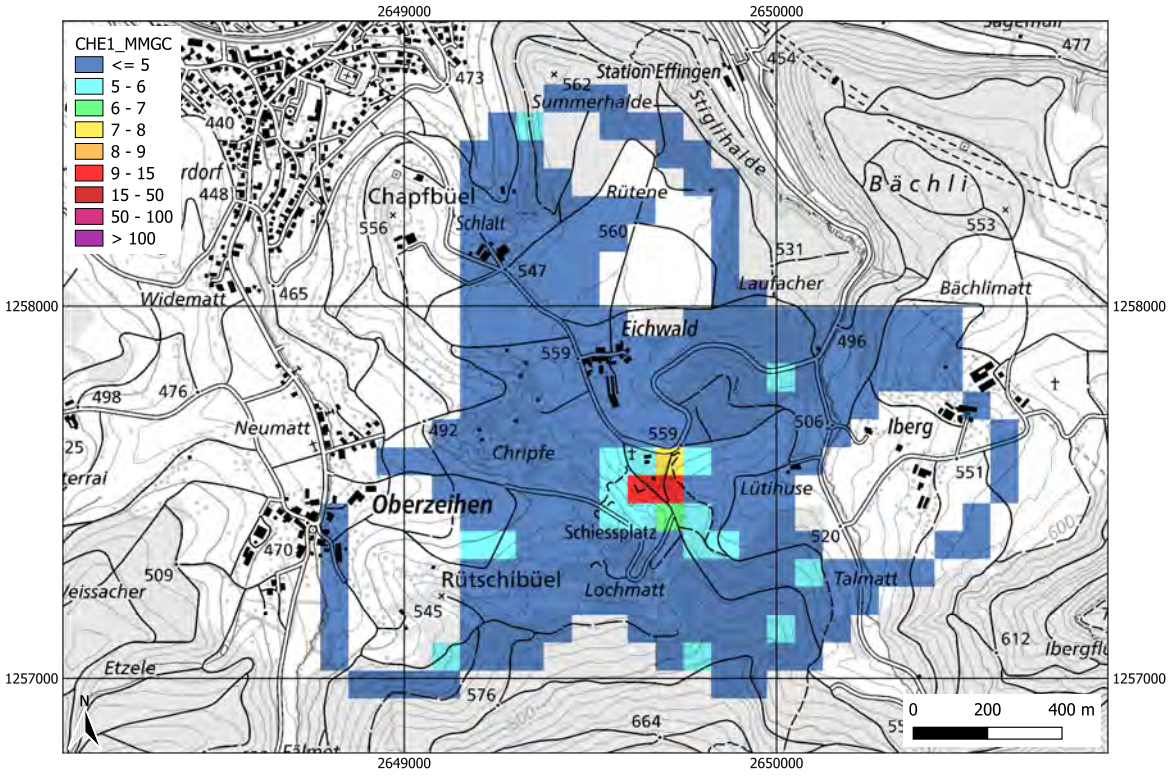

Figure 8.86: Man made gross count (MMGC) measured at Eichwald by CHE1 team. Geodaten©swisstopo.

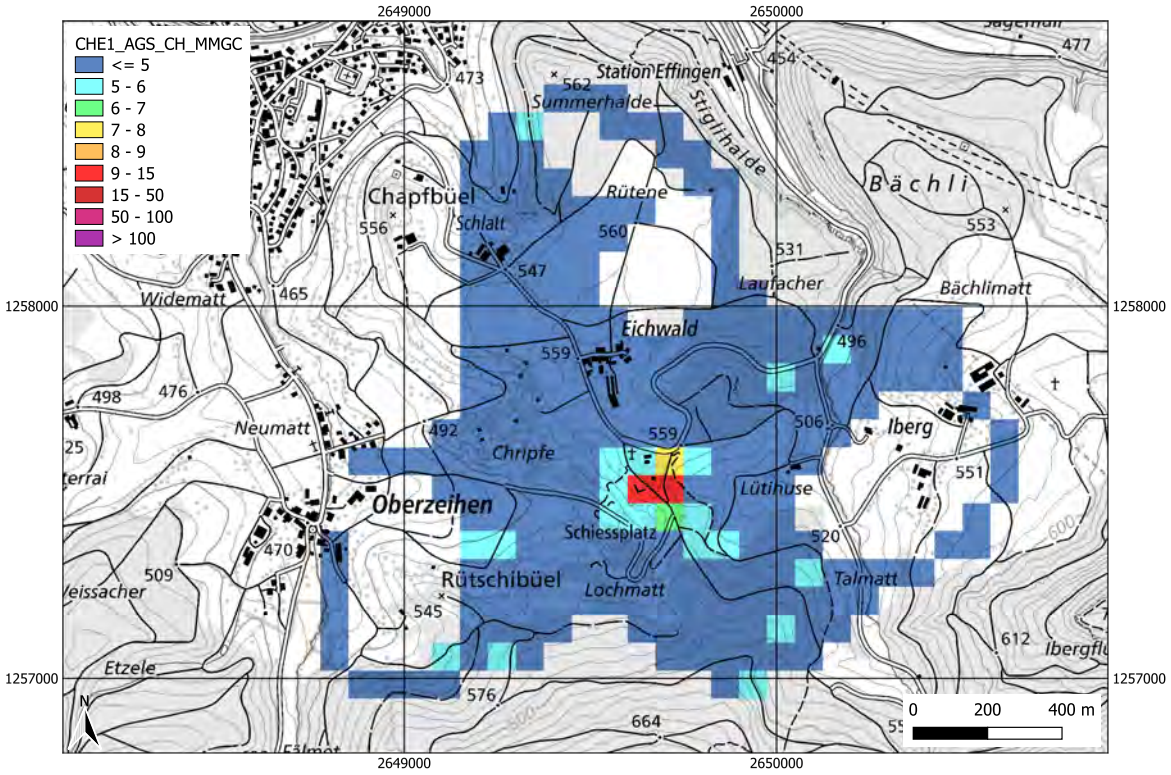

Figure 8.87: Man made gross count (MMGC) measured at Eichwald by CHE1 team, analysed with AGS_CH. Geodaten©swisstopo.

Source search maps at Dargmersellen

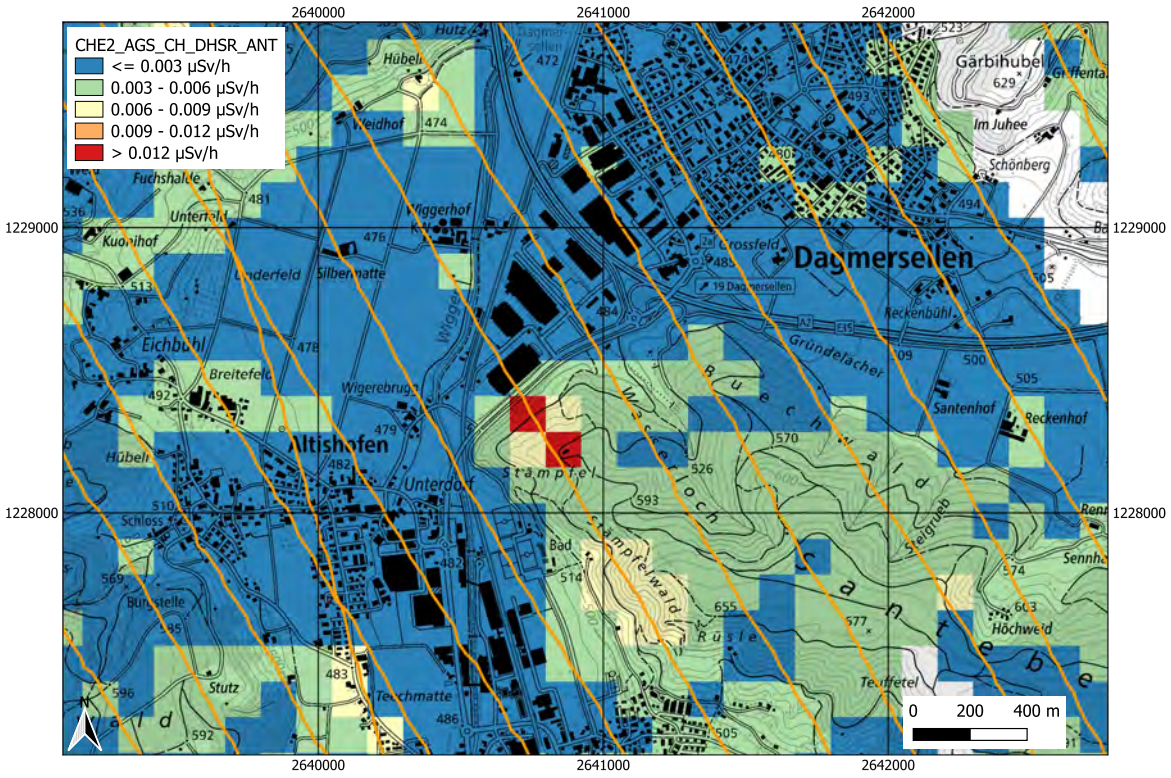

Figure 8.88: Flight path and anthropogenic ambient dose equivalent rate during Mission 3 at Dagmersellen by CHE2 team. The colour scale has been adapted to highlight variations. Geodaten©swisstopo.

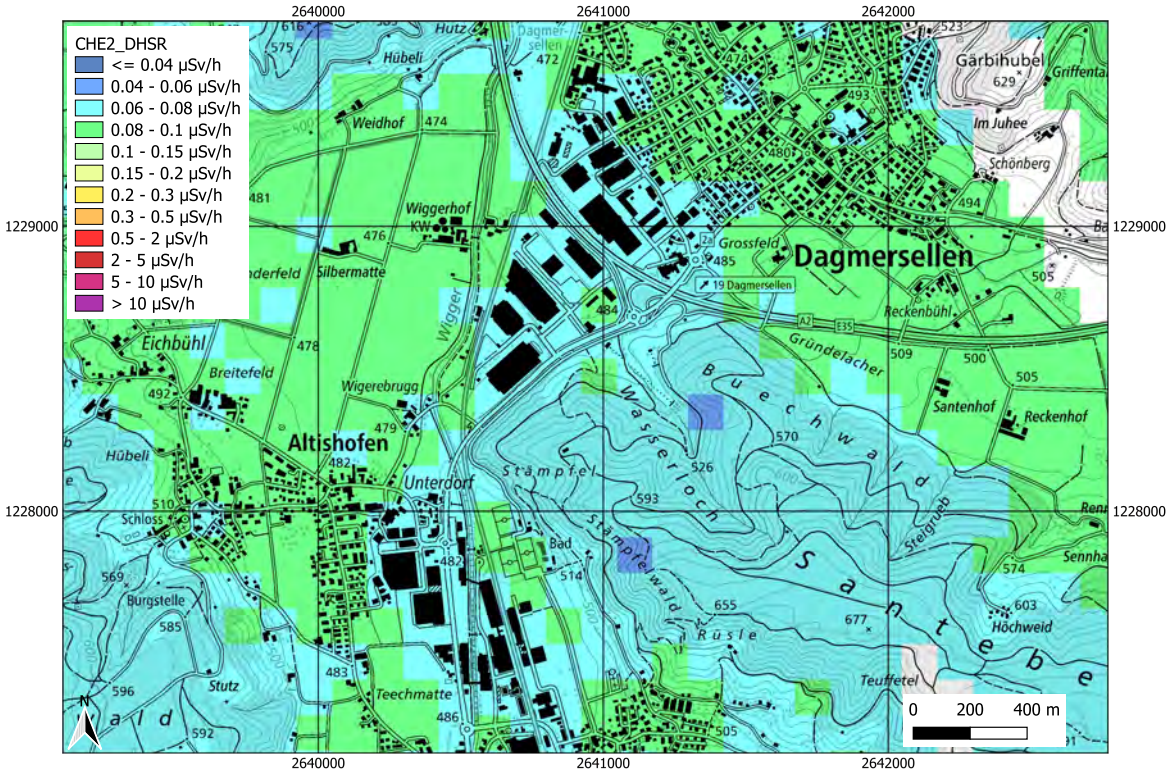

Figure 8.89: Ambient dose equivalent rate (DHSR) measured at Dagmersellen by CHE2. Geodaten©swisstopo.

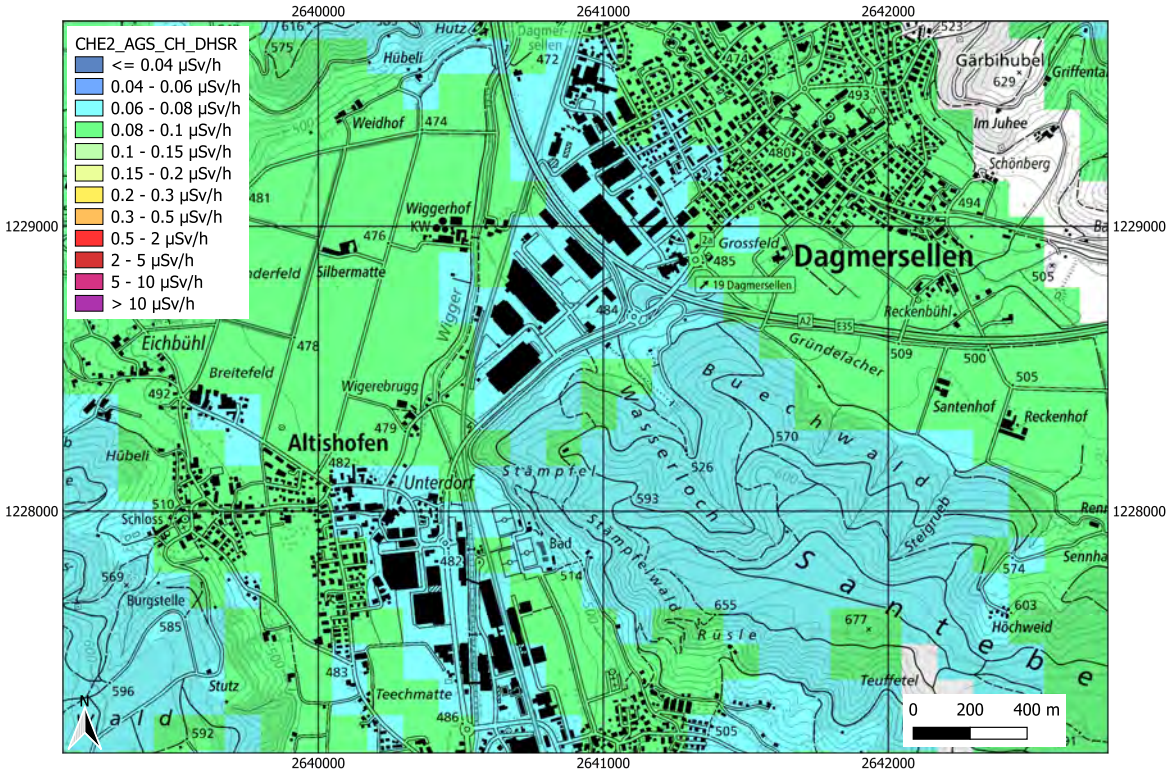

Figure 8.90: Ambient dose equivalent rate (DHSR) at Dagmersellen measured by CHE2, analysed with AGS_CH. Geodaten©swisstopo.

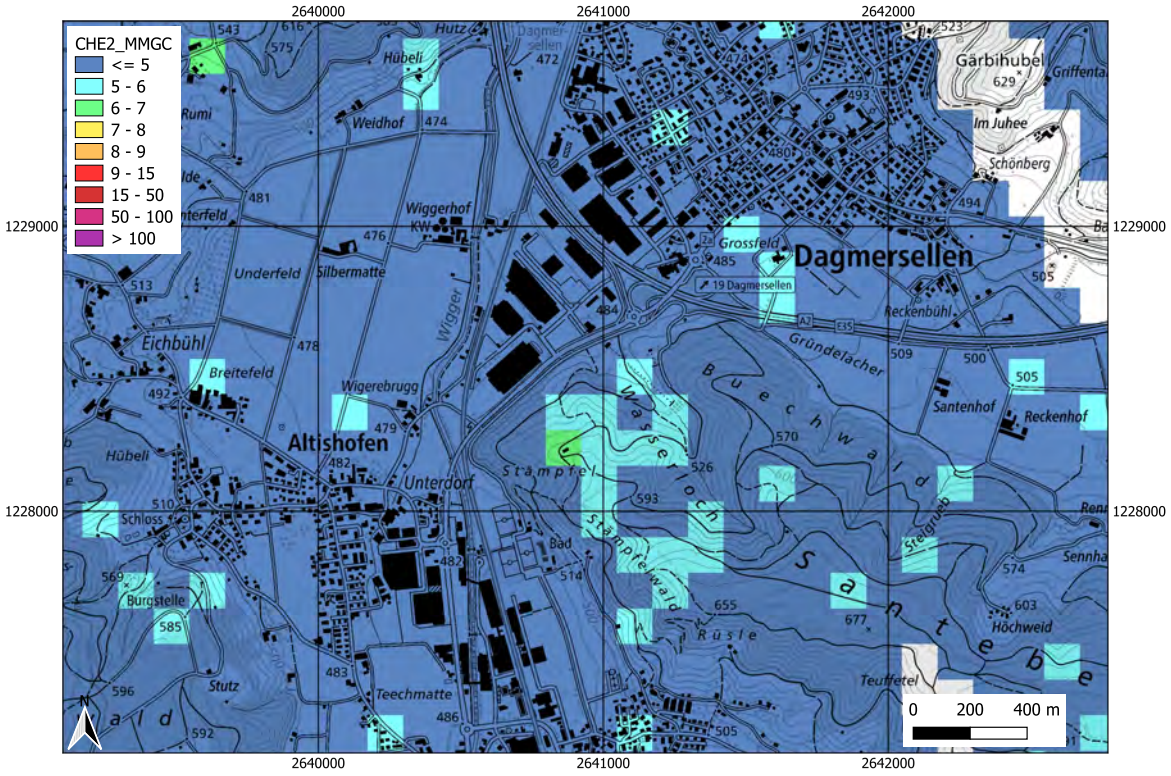

Figure 8.91: Man made gross count (MMGC) measured at Dagmersellen by CHE2 team. Geodaten©swisstopo.

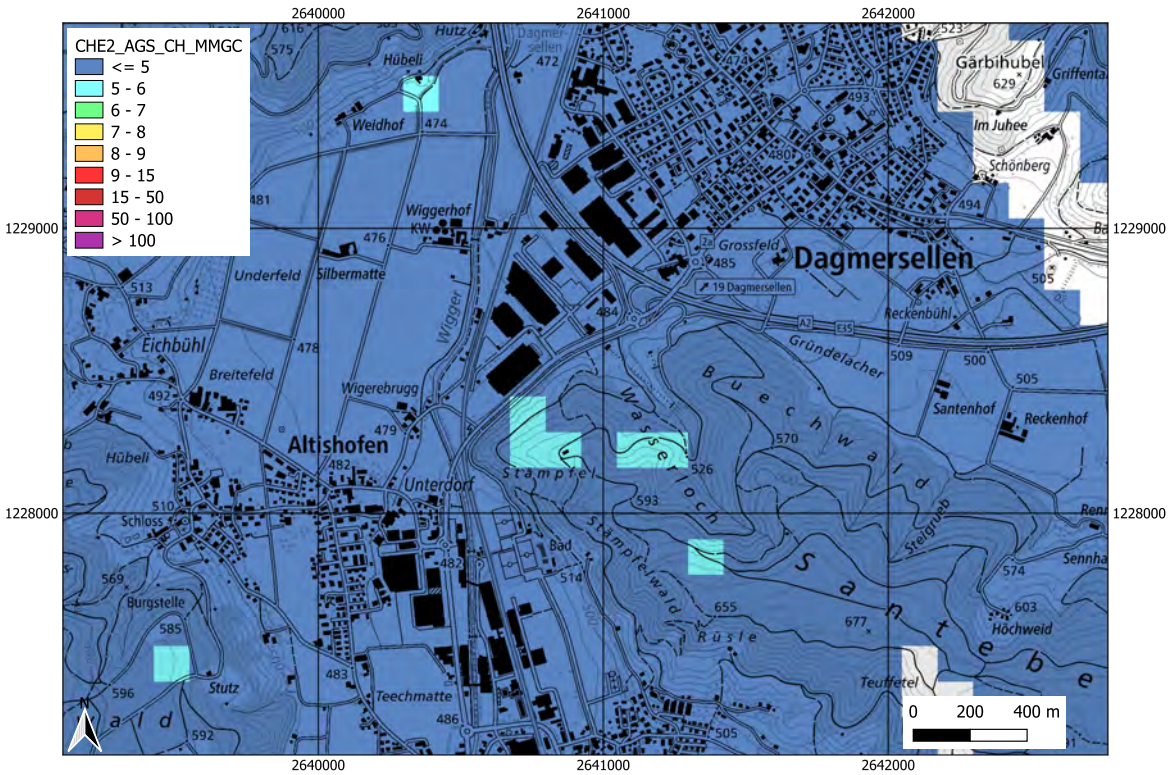

Figure 8.92: Man made gross count (MMGC) measured at Dagmersellen by CHE2 team, analysed with AGS_CH. Geodaten©swisstopo.

8.4.3 Composite mapping – preliminary evaluation

Maps

Maps of the target area of the composite mapping created during the AGC25 using the preliminary evaluation are reported in this section. Since the region assigned to the DEU team was flown by the CHE1 team as well, two maps are presented for each quantity, respectively displaying the measurements of each team.

The surveyed area is characterised by hilly terrain, with altitudes varying between $350\,\mathrm{m}$ and $850\,\mathrm{m}$ over the sea level, as illustrated in Figure 8.93. The flight lines flown by the different teams are shown in Figure 8.94. All teams except CHE2 did not have any radioactive sources placed in their assigned measurement areas. Figures 8.95 and 8.96 presents a composite map of the ambient dose equivalent rates reported by the measurement teams during the exercise (preliminary evaluation). Notably, team LTU reported lower values than the other teams, consistently with the discrepancies noted in the reference measurements of Mission 1, which can be clearly distinguished in the map. Further differences between teams' results can be seen in the maps of the natural radionuclides ^{40}K and ^{232}Th and ^{238}U (Figures 8.97 – 8.102). Although the observed deviations are not large, understanding their origin, likely associated with differences in cosmic rays, background and altitude correction treatment, is important, and a methodological harmonisation according to current best practice remains a key objective. Nevertheless, the differences observed among the teams even in the preliminary evaluation, would not impede the production of a reliable composite map in the event of a real emergency. In such circumstances, decisions would be guided by the order of magnitude of the detected dose rate and activity.

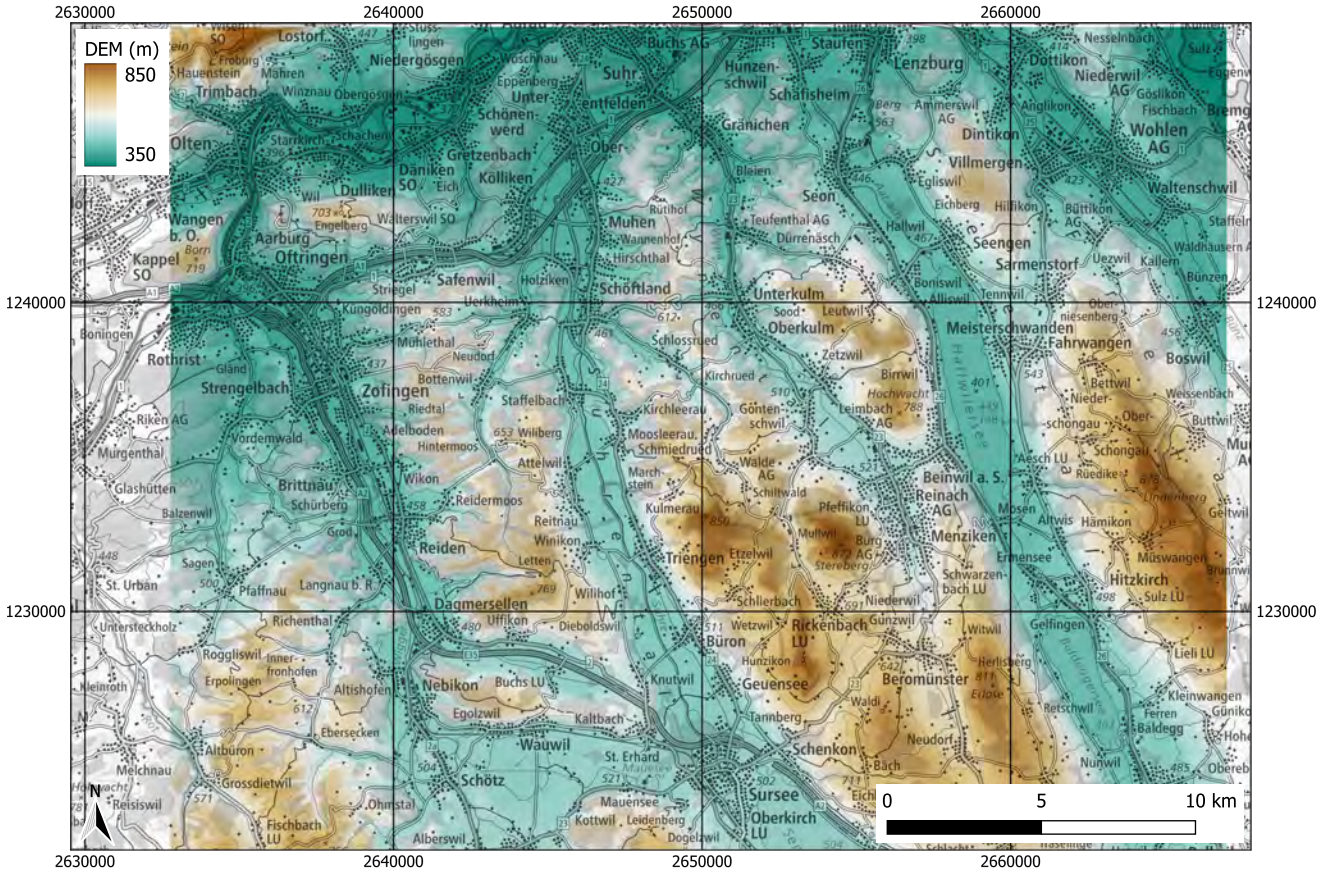

Figure 8.93: Digital Elevation Model of the region surveyed during Mission 3 (CM). Geodaten©swisstopo.

Flight paths

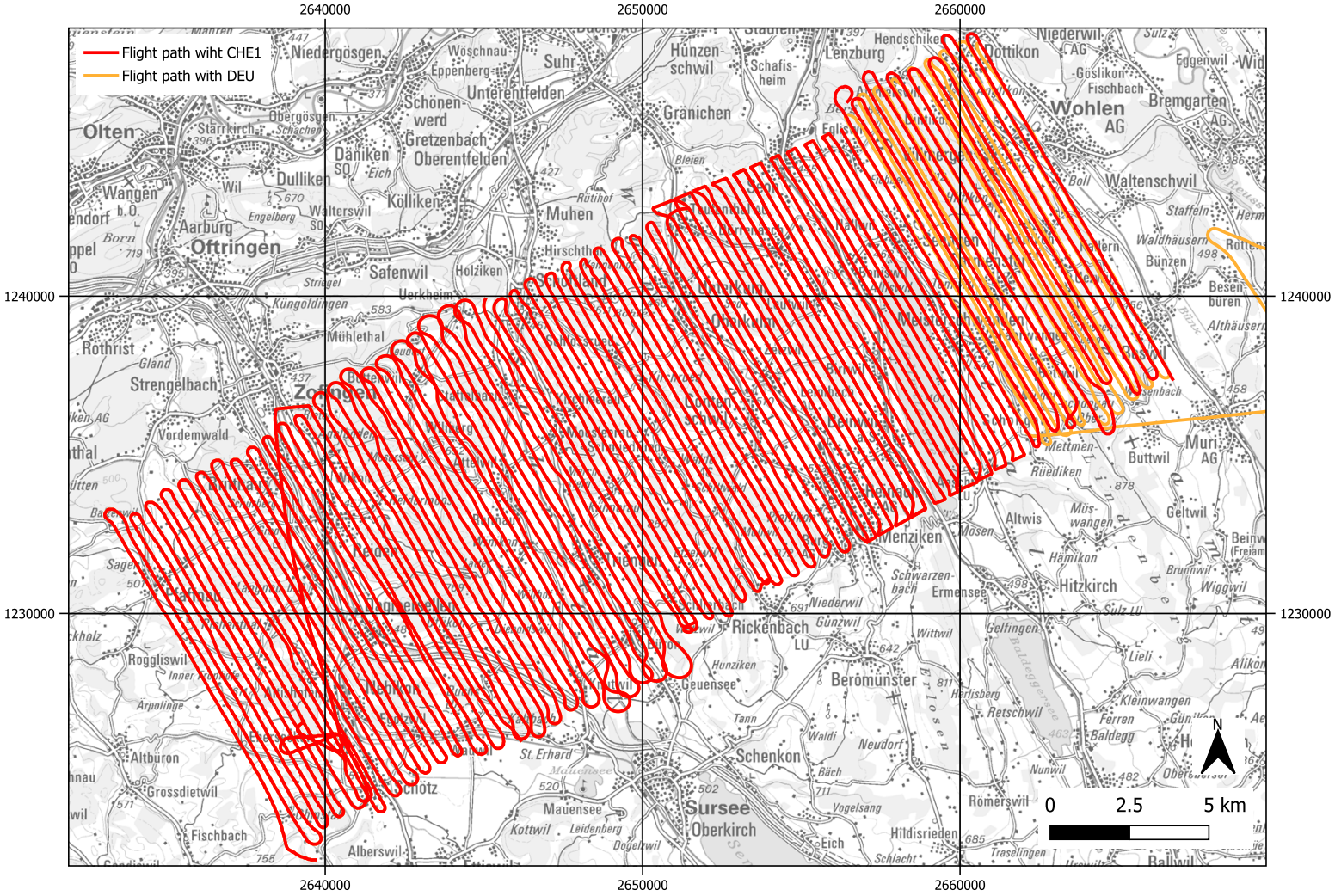

Figure 8.94: The flight paths of all teams combined are shown for Mission 3 (CM). Preliminary evaluation during the AGC25 week. Geodaten©swisstopo.

Ambient dose equivalent rate

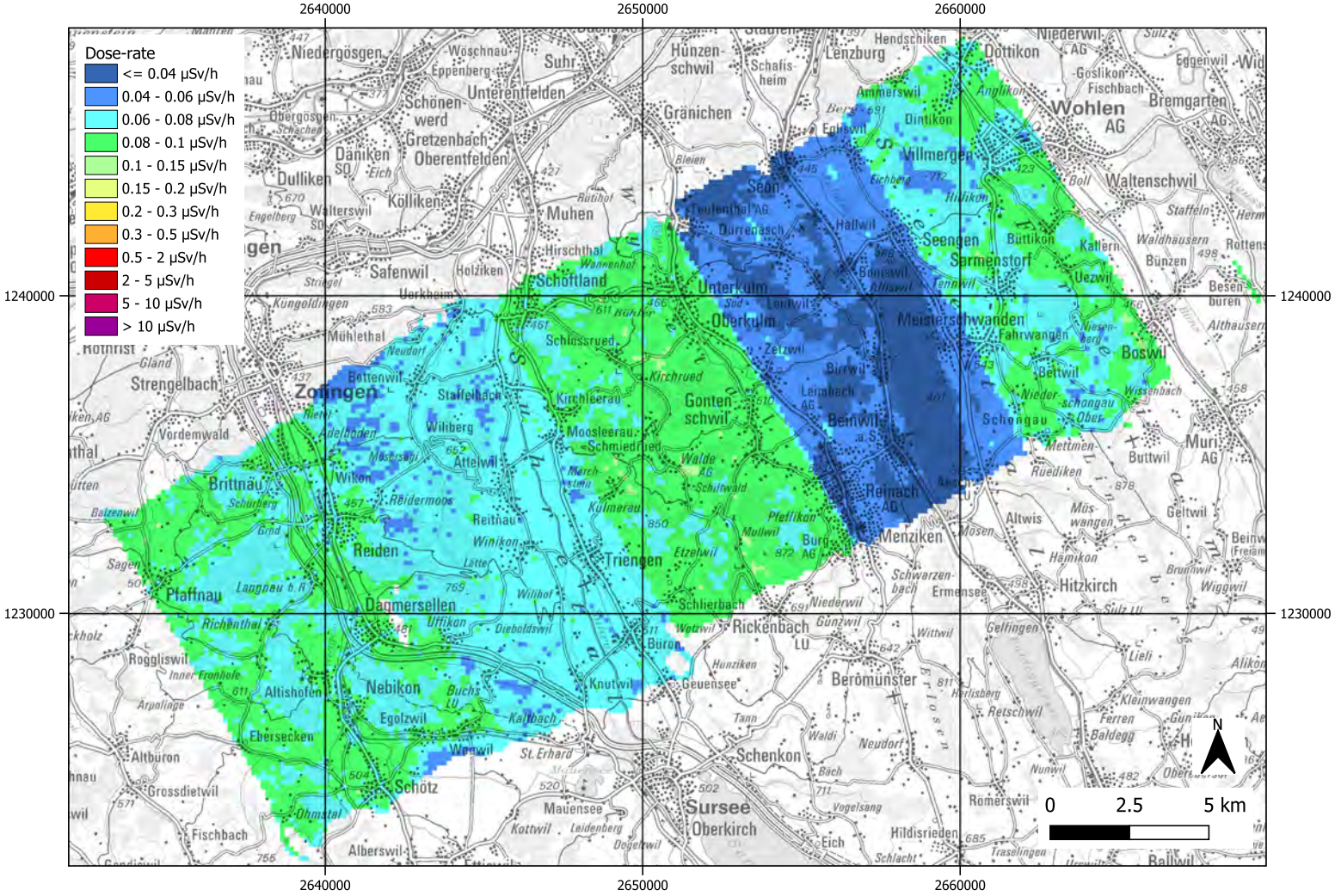

Figure 8.95: Ambient dose equivalent rate distribution (DHSR) measured during Mission 3 (CM) with DEU team. Preliminary results. Geodaten©swisstopo.

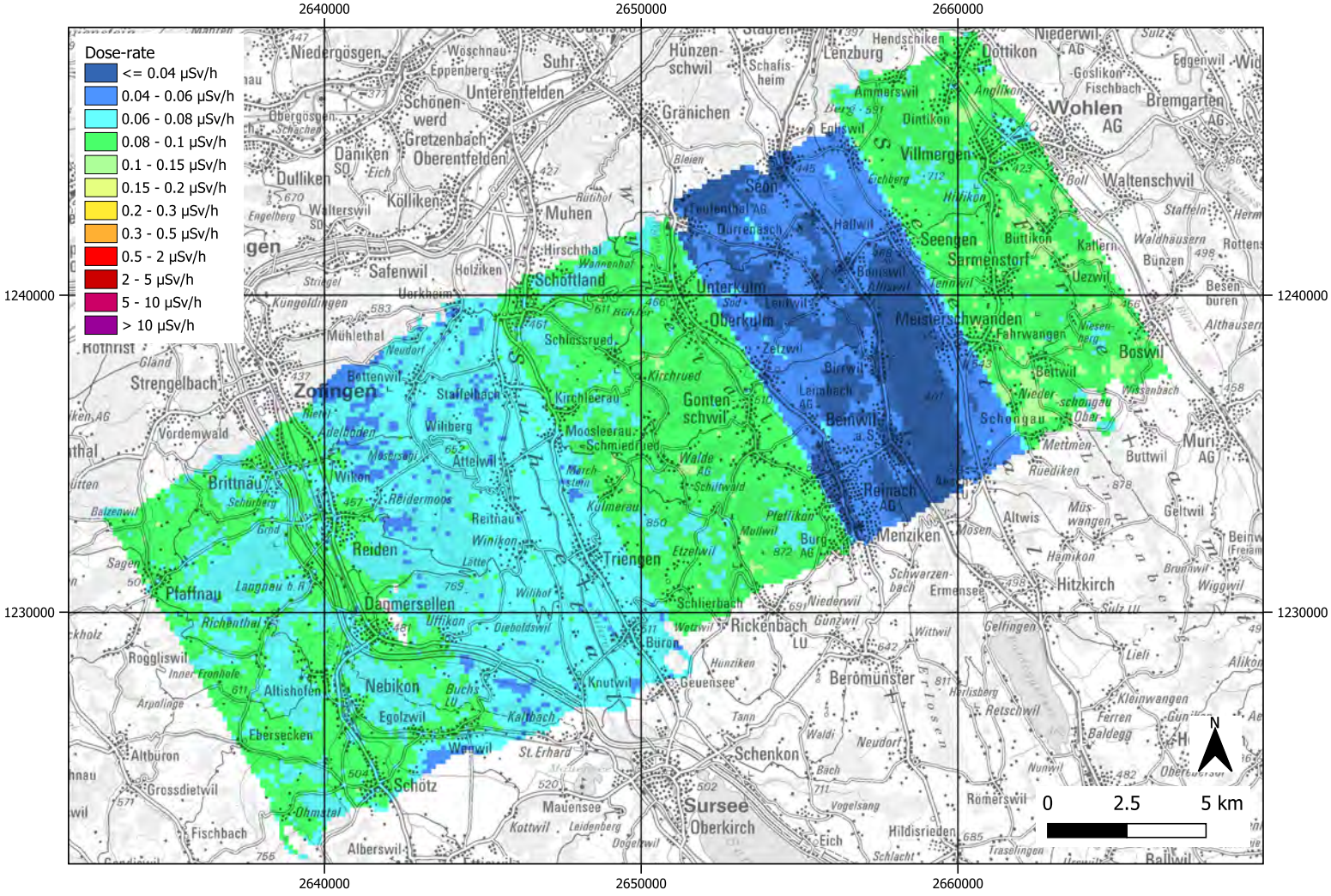

Figure 8.96: Ambient dose equivalent rate distribution (DHSR) measured during Mission 3 (CM) with CHE1 team. Preliminary results. Geodaten©swisstopo.

Activity concentration distribution of ^{232}Th

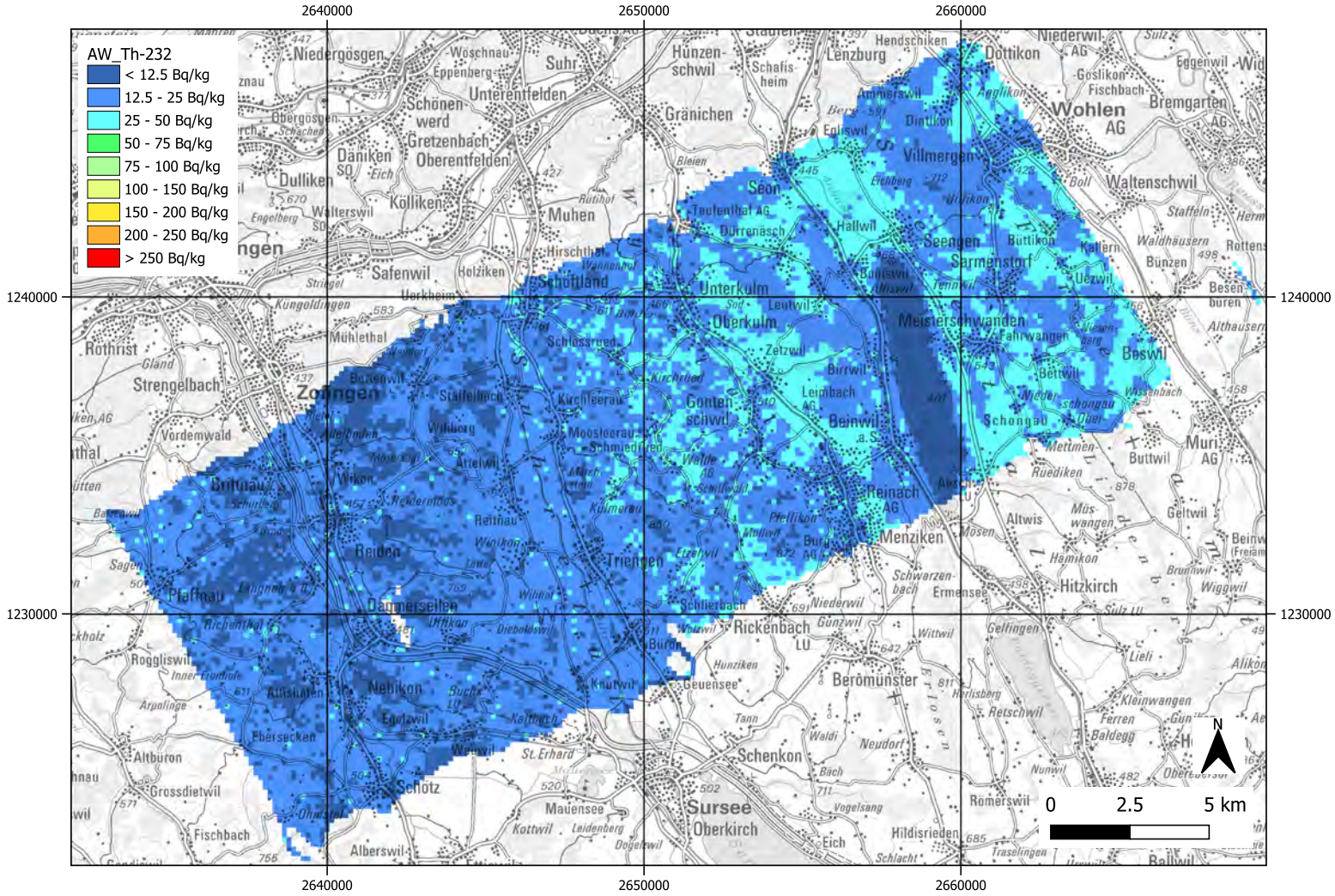

Figure 8.97: Activity concentration of ^{232}Th measured during Mission 3 (CM) with DEU team. Preliminary Results. Geodaten©swisstopo.

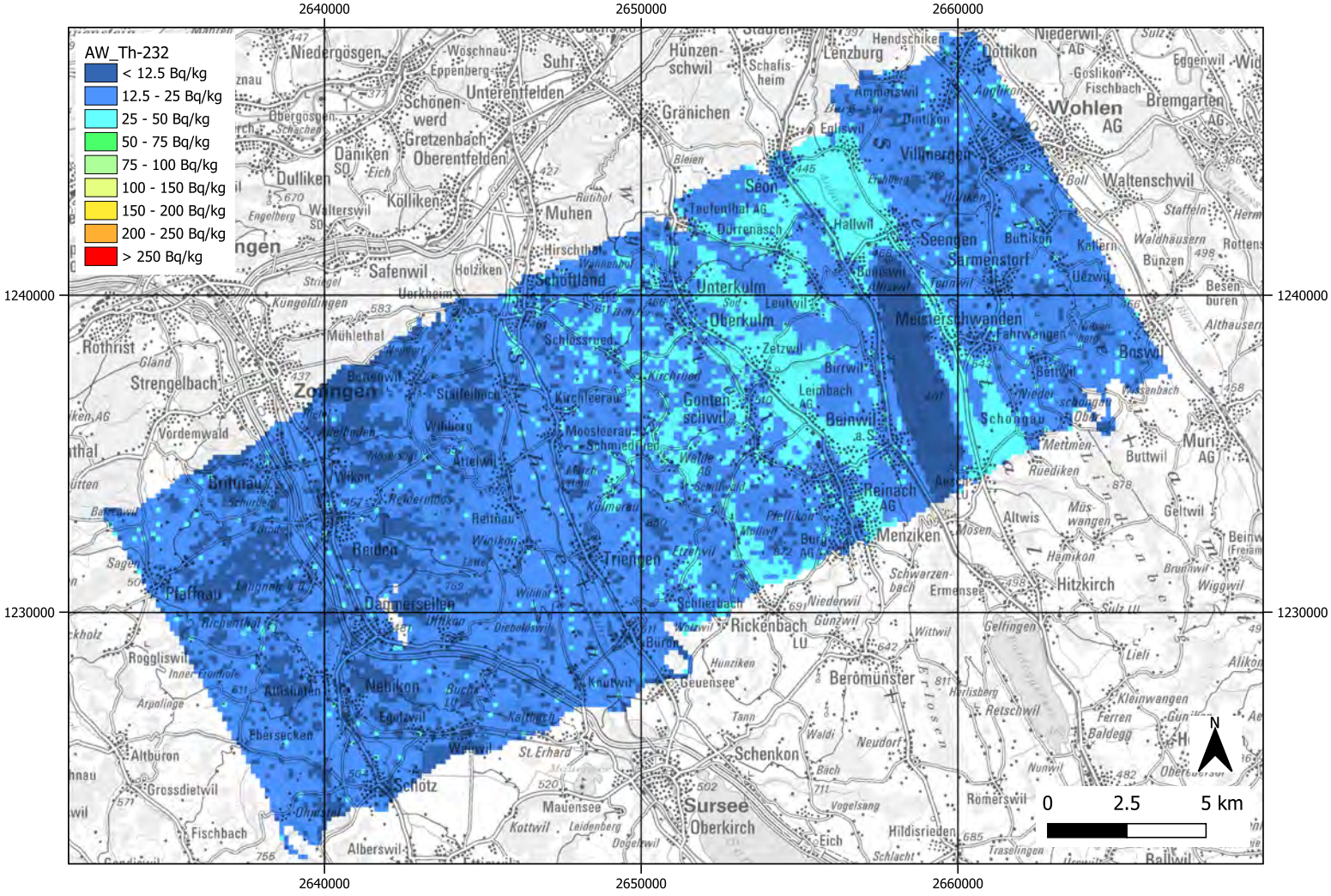

Figure 8.98: Activity concentration of ^{232}Th measured during Mission 3 (CM) with CHE1 team. Preliminary Results. Geodaten©swisstopo.

Activity concentration distribution of ^{238}U

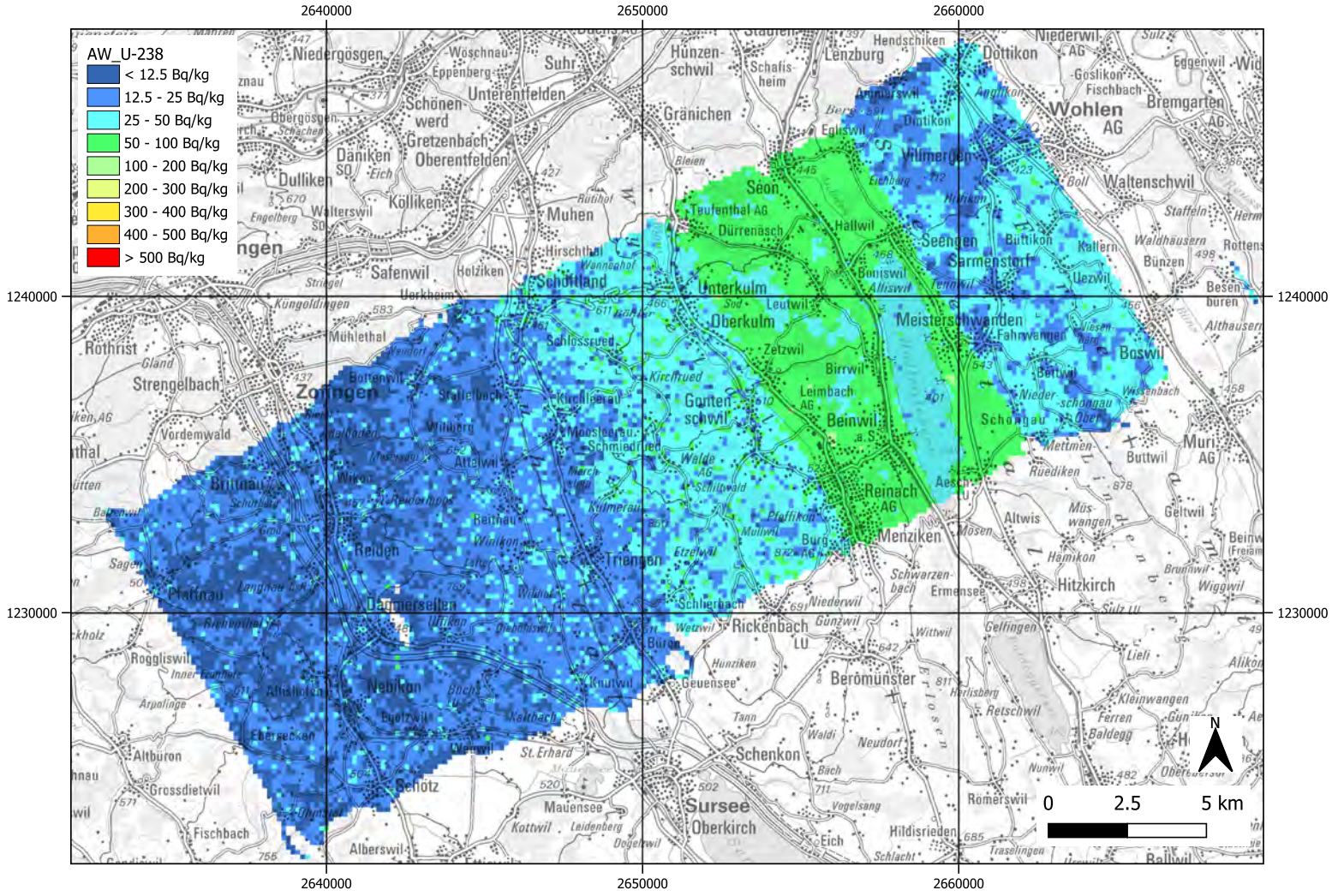

Figure 8.99: Activity concentration of ^{238}U measured during Mission 3 (CM) with DEU team. Preliminary Results. Geodaten©swisstopo.

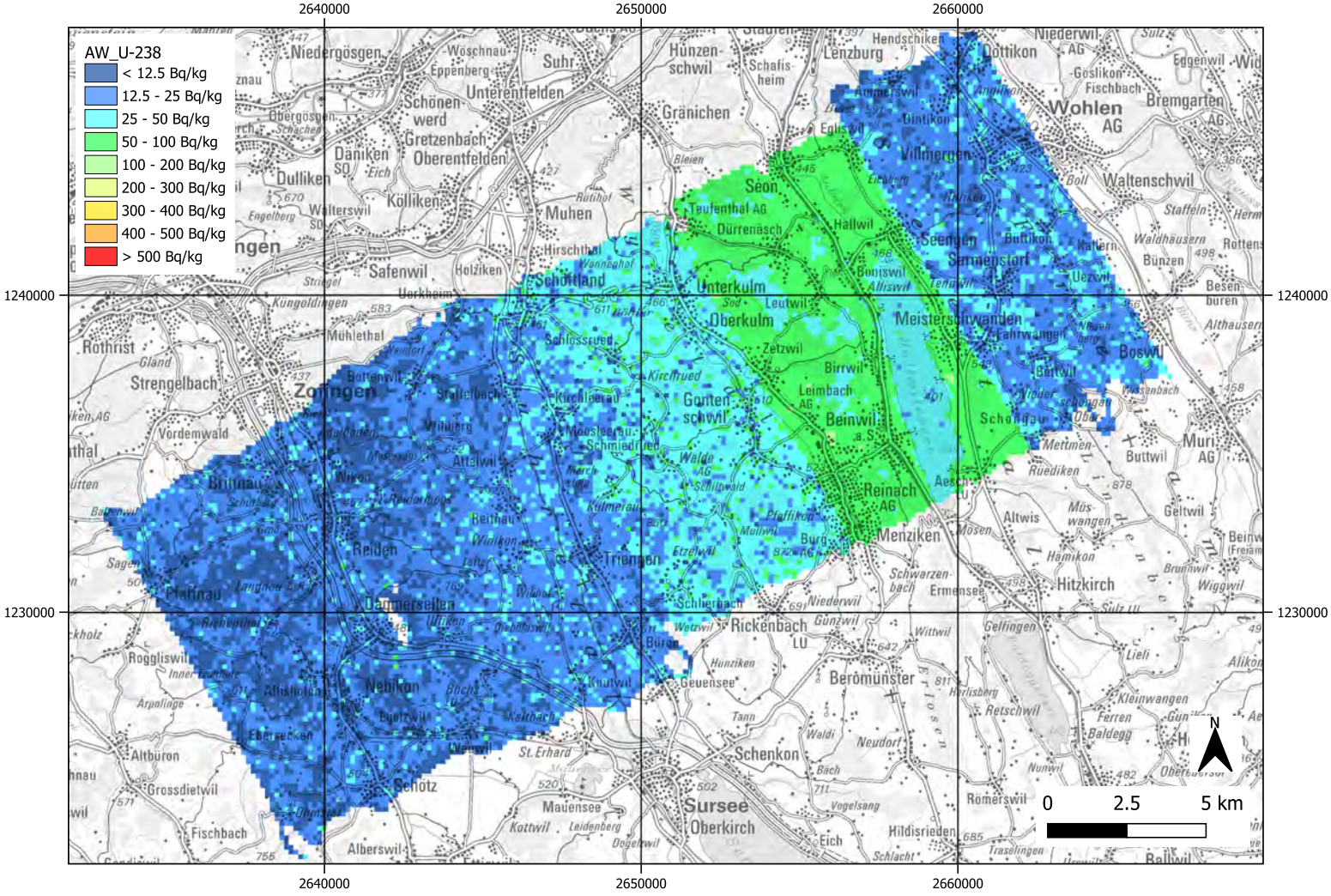

Figure 8.100: Activity concentration of ^{238}U measured during Mission 3 (CM) with CHE1 team. Preliminary Results. Geodaten©swisstopo.

Activity concentration distribution of ^{40}K

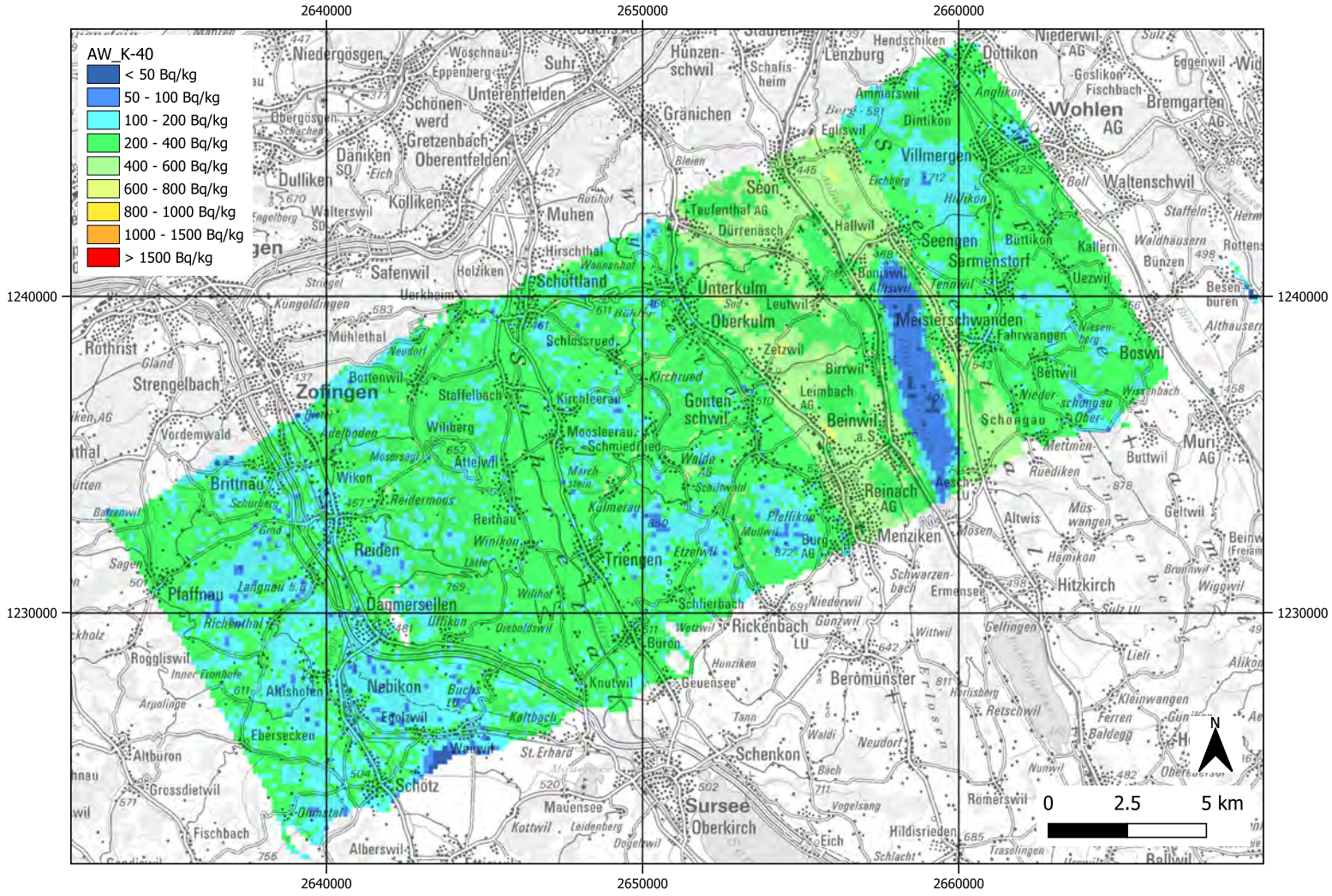

Figure 8.101: Activity concentration of ^{40}K measured during Mission 3 (CM) with DEU team. Preliminary Results. Geodaten©swisstopo.

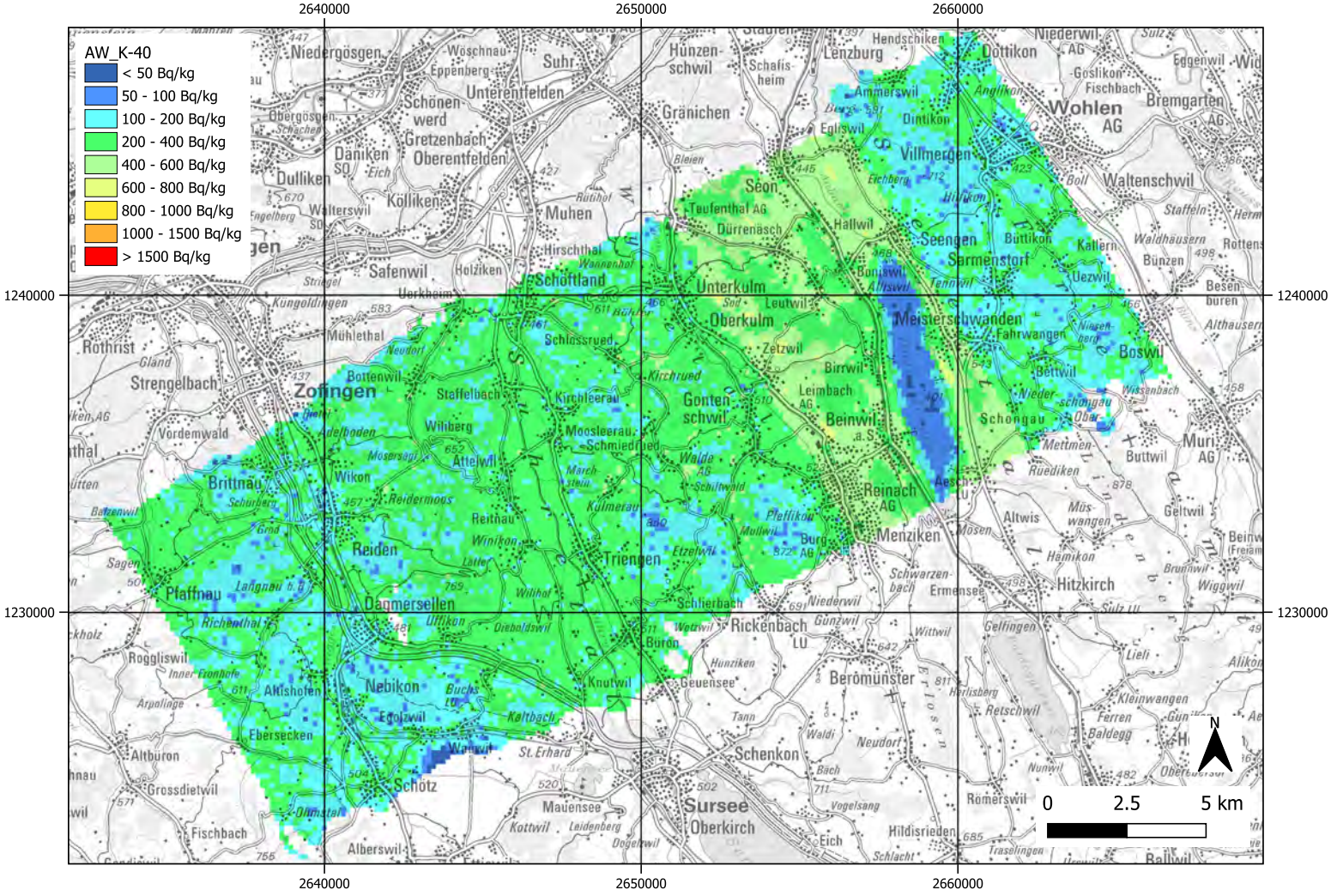

Figure 8.102: Activity concentration of ^{40}K measured during Mission 3 (CM) with CHE1 team. Preliminary Results. Geodaten©swisstopo.

8.4.4 Composite mapping – final evaluation

Owing to the overlap of the flight areas covered by the CHE1 and DEU teams in Mission 3 and accounting for the two analysis methods applied to the Swiss datasets (CHE1/CHE2 evaluation using Spir (Mirion) or CHE1_AGS_CH/CHE2_AGS_CH using the AGS_CH software), the results are presented for a notional total of eight teams.

Common line

As described in Section 8.4.1, before flying their assigned regions of the composite mapping area, all teams first surveyed a common reference line. This procedure, introduced during the coordination and planning of the composite mapping mission, was implemented for the first time. It offers several advantages over the previously used method, in which teams extended their survey areas into those of neighbouring teams. The new approach reduces overall flight time – since the common line can be positioned along the transit route to the measurement area – and enables a comparison across all participating teams rather than only bilateral comparisons between adjacent teams. Consequently, the method also provides a robust basis for adjusting the results of individual teams in cases where their calibration differs from the collective response.

The sampled data (coordinates and results) along the common line are shown in Figures 8.103 – 8.105. With the exception of DEU, whose system recorded data every two seconds, all teams sampled at $1\,\mathrm{Hz}$. The DEU dataset was therefore adapted to align with the acquisition points of the other teams along the common line. Mean values and standard deviations for the common-line measurements are summarised in Table 8.5.

All teams adhered to the assigned coordinates (PE and PN) for the common line (Figure 8.103) within normal flight-navigation tolerances. The intended ground clearance of $90\,\mathrm{m}$ was maintained by CHE1, CHE2, CZE, and FRA. DEU and LTU flew the common line at average clearances of $221\,\mathrm{m}$ and $479\,\mathrm{m}$, respectively.

The averaged values of the ambient dose equivalent rate (DHSR) summarised in Table 8.5 show good agreement, with a standard deviation of only about $7\,\%$ from the mean across all teams. The pointwise DHSR estimates from the LTU team, however, exhibit substantially larger variability than those of the other teams, as visible in Figure 8.104. This is to be expected, considering the much larger ground clearance compared with the other teams: at almost $500\,\mathrm{m}$ above ground, very little signal from the ground can be detected, and the measurements are therefore affected by significant statistical noise. The DHSR values recorded by the DEU team align well with the results of the other teams along the first section of the common line but begin to diverge slightly in the final segment. This trend is more visible in Figure 8.105, which presents the dataset without the LTU measurements, hence a restricted range of values on the ordinates. It may also be noted that this deviation correlates with an increase in ground clearance (PH), as visible in Figure 8.103.

Good agreement among all teams is also observed in the comparison of the average activity concentrations of ^{40}K, ^{232}Th, and ^{238}U. As shown in Figure 8.104 and reflected in the standard deviations listed in Table 8.5, the LTU results exhibit substantially larger point-to-point variations along the common line compared with the other teams. In addition, the LTU average activity concentrations for ^{232}Th and ^{238}U deviate noticeably from the values obtained by the rest of the teams. Although to a much lesser extent than the variations observed for LTU, Figure 8.105 shows that the DEU pointwise values occasionally fall below the general trend of the other teams, resulting in lower estimated activity concentrations. Nevertheless, overall agreement remains satisfactory when considering the relative standard deviation of the team-averaged values. When including the LTU dataset, the relative standard deviations for ^{40}K, ^{232}Th, and ^{238}U are 22%, 27%, and 59%, respectively. When excluding LTU from this calculation, the relative standard deviations for ^{232}Th and ^{238}U improve to 13% and 33%, respectively.

Team	PZ [m]		PH [m]	
	Average	St. dev.	Average	St. dev.
CHE1	507	34	93	8
CHE1_AGS_CH	507	34	93	8
CHE2	514	39	94	12
CHE2_AGS_CH	514	39	94	12
CZE	510	41	97	10
DEU	623	16	221	26
FRA	520	37	101	12
LTU	924	27	497	18

Team	DHSR [$\mu\mathrm{Sv\,h^{-1}}$]		AW_K-40 [$\mathrm{Bq\,kg^{-1}}$]	
	Average	St. dev.	Average	St. dev.
CHE1	0.097	0.007	230	53
CHE1_AGS_CH	0.091	0.004	325	37
CHE2	0.086	0.007	201	54
CHE2_AGS_CH	0.088	0.005	280	71
CZE	0.083	0.007	303	61
DEU	0.103	0.008	141	130
FRA	0.090	0.003	281	70
LTU	0.090	0.022	257	304

Team	AW_Th-232 [$\mathrm{Bq\,kg^{-1}}$]		AW_U-238 [$\mathrm{Bq\,kg^{-1}}$]	
	Average	St. dev.	Average	St. dev.
CHE1	21.5	6.9	19.5	12.5
CHE1_AGS_CH	27.4	4.7	22.2	8.1
CHE2	20.1	6.4	16.7	13.2
CHE2_AGS_CH	25.3	7.6	17.3	16.9
CZE	20.3	6.0	22.3	12.9
DEU	24.2	5.9	7.1	27.9
FRA	26.4	8.5	37.2	17.9
LTU	7.6	18.0	58.2	92.3

Table 8.5: Summary of measurements along the common line for different teams.

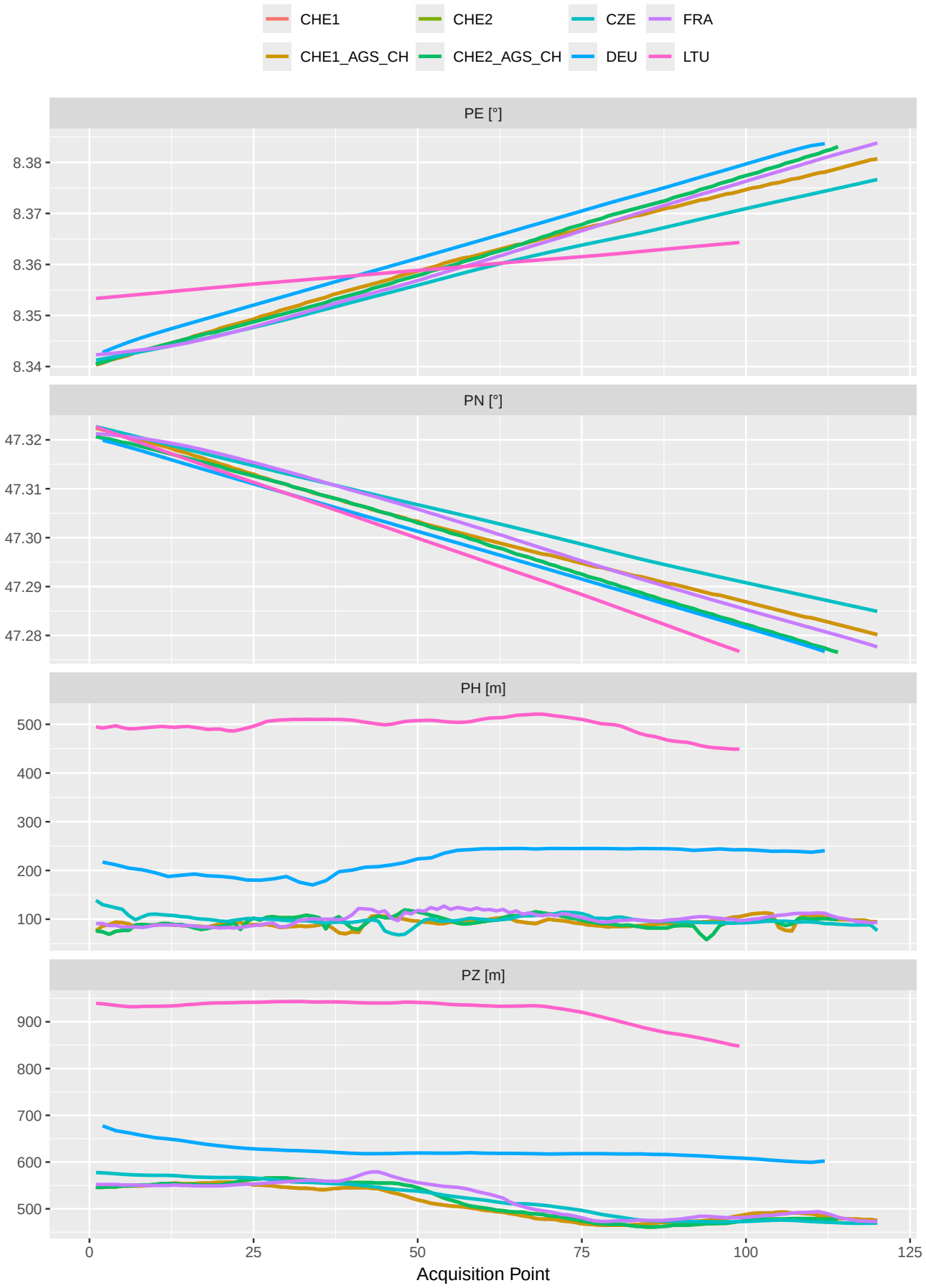

Figure 8.103: Geodata of the common line flown by all teams during the composite mapping.

Figure 8.104: Results obtained along the common flight line flown by all teams during the composite mapping.

Figure 8.105: Results obtained along the common flight line flown by all teams during the composite mapping. LTU results are not displayed.

Maps

Maps of the target area of the composite mapping based on the final data delivered by each team are reported in this section. For each quantity, maps are organised and displayed as follows:

- CHE2 – CZE – FRA – LTU – DEU. The CHE2 dataset was evaluated using the Spir software from Mirion.
- CHE2 – CZE – FRA – LTU – CHE1. The Swiss datasets CHE1 and CHE2 were evaluated using the Spir software from Mirion.
- CHE2_AGS_CH – CZE – FRA – LTU – CHE1_AGS_CH. The Swiss datasets CHE1 and CHE2 were evaluated by using the AGS_CH software.

With reference to the preliminary results of the composite mapping shown in Section 8.4.3, only the CZE, LTU, and FRA teams provided adjusted results following the AGC25 exercise. The CHE1, CHE2, and DEU teams considered their initial results sufficiently accurate, so no re-evaluation or adjustment was required. Consequently, the final results presented in the following maps for these teams are equivalent to their preliminary data. The evaluation of the CHE1 and CHE2 datasets using the AGS_CH software was carried out only after the AGC25 exercise, therefore it does not appear in the preliminary results.

Compared with the preliminary evaluation, only minor changes are observed in the ambient dose equivalent rate (DHSR) for the areas surveyed by CZE and FRA, as shown in Figures 8.107–8.108. In contrast, the LTU team shows more substantial changes, with their final results shifting from a slight underestimation in the preliminary data to a slight overestimation in the final evaluation. Discrepancies between Figures 8.108 and 8.109, which reflect the use of different evaluation software (Spir or AGS_CH) for the Swiss teams, are marginal and are attributed to minimal differences in evaluation procedures, corrections, and calibration factors. These differences are consistent with the reference measurements of Mission 1, discussed in Section 8.2 (Figures 8.179 - 8.182).

Figures 8.110 – 8.118 show the final activity concentration maps for ^{40}K, ^{232}Th, and ^{238}U. Compared with the preliminary evaluation, adjustments for CZE and FRA are generally minor. A slightly larger adjustment towards lower ^{238}U concentrations is observed for the FRA team, likely due to their assumption of a higher radon concentration relative to other teams, which may have led to an overcorrection in the ^{238}U window. The DEU team recorded slightly higher ^{238}U activity concentrations than other teams, a discrepancy likely resulting from changes in weather and environmental conditions, as their survey was conducted on the following day.

The LTU team's final activity concentration estimates for ^{40}K, ^{232}Th, and ^{238}U consistently reflect the calibration adjustments identified in Mission 1 and are now much closer to the results reported by the other teams. Similarly to DHSR, the minor differences in activity concentrations observed in the regions surveyed by the Swiss teams in Figures 8.111 and 8.112, 8.114 and 8.115, 8.117 and 8.118 evaluated using two different software packages, are marginal and can be attributed to slight variations in evaluation approaches, corrections, and calibration factors, consistent with the reference measurements from Mission 1.

Flight paths

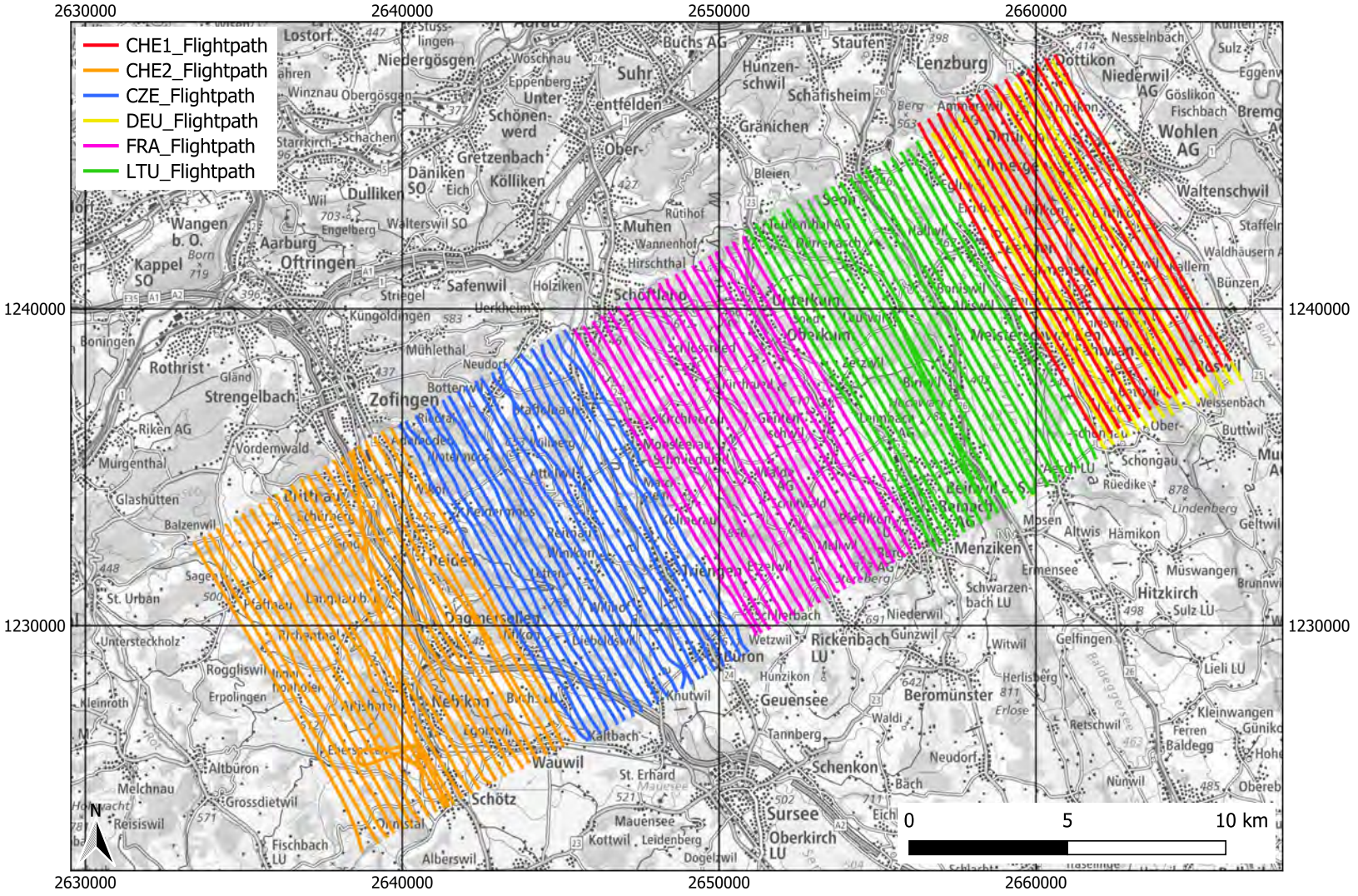

Figure 8.106: The flight paths of all teams combined are shown for Mission 3 (CM). Geodaten©swisstopo.

Ambient dose equivalent rate

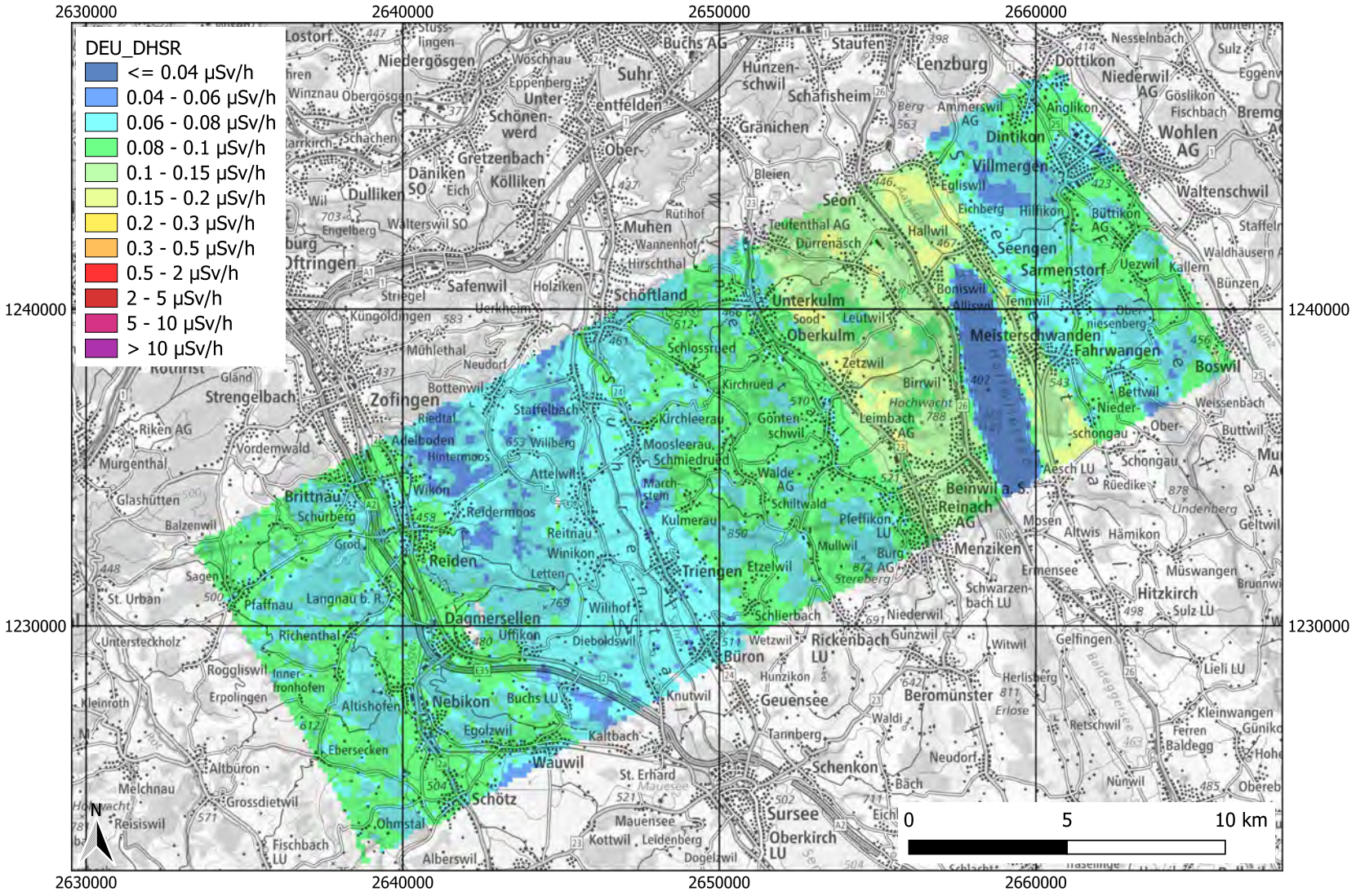

Figure 8.107: Ambient dose equivalent rate distribution (DHSR) measured during Mission 3 (CM) with DEU team. Final results. Geodaten©swisstopo.

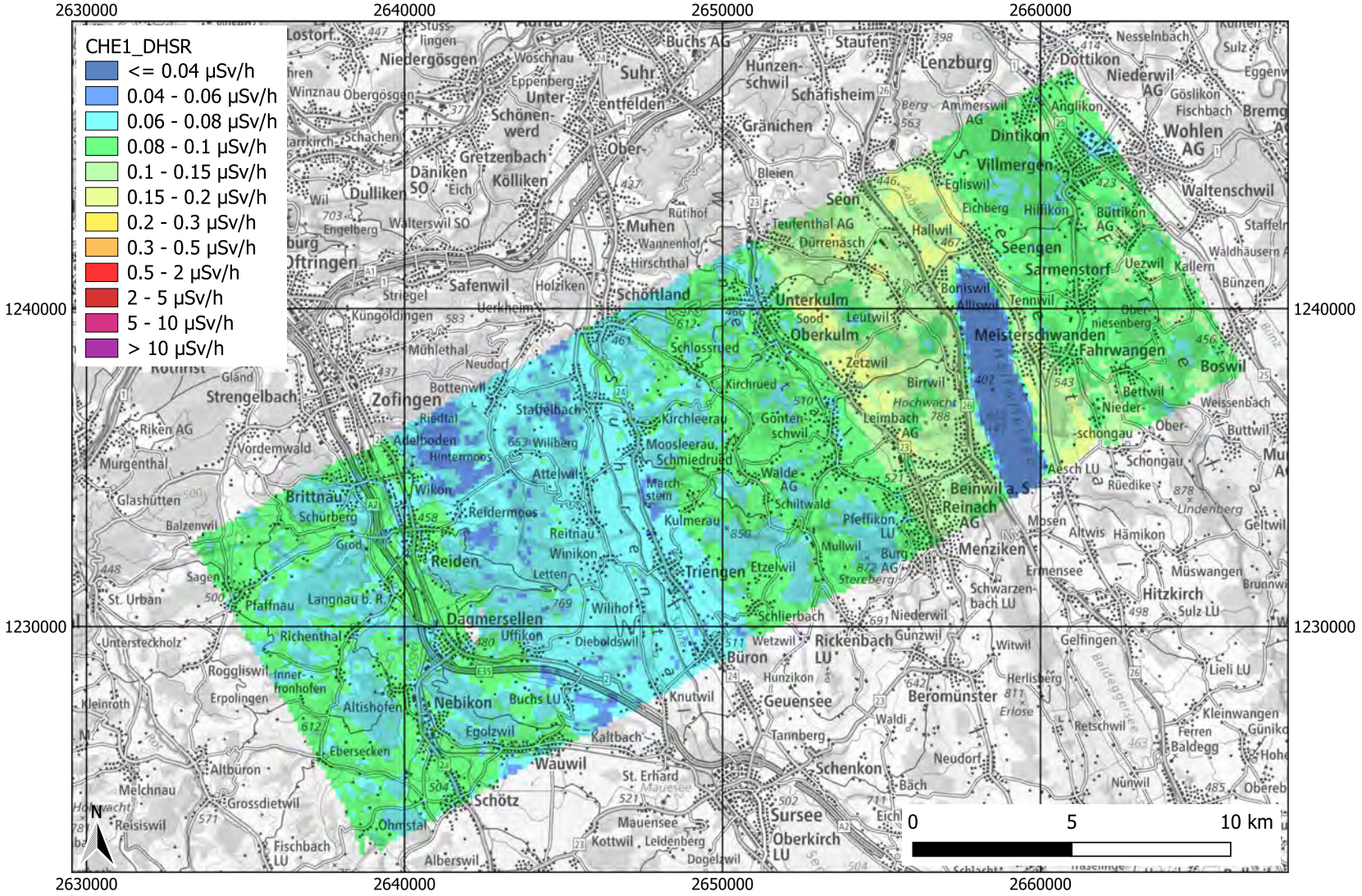

Figure 8.108: Ambient dose equivalent rate distribution (DHSR) measured during Mission 3 (CM) with CHE1 team. Final results. Geodaten©swisstopo.

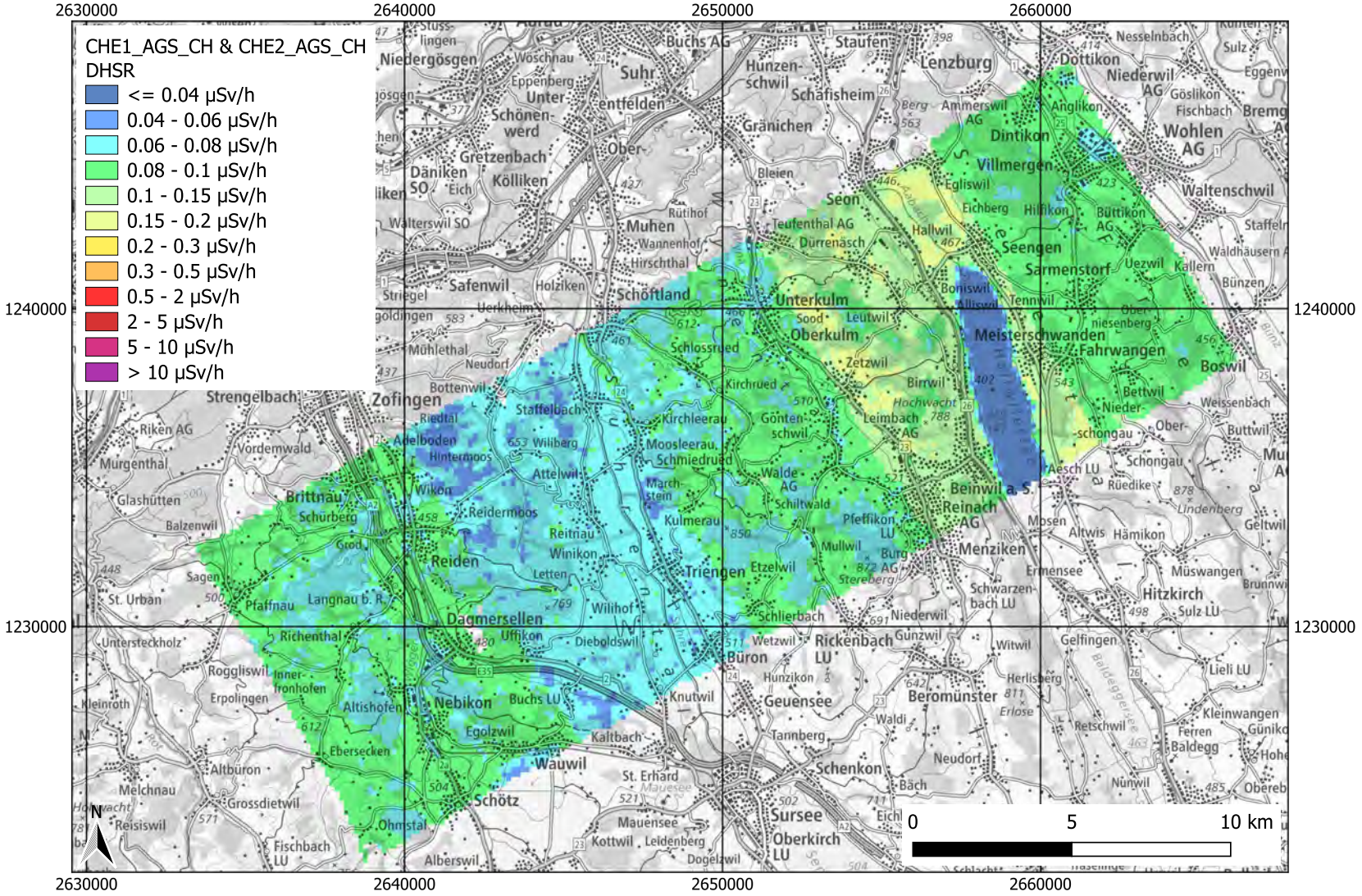

Figure 8.109: Ambient dose equivalent rate distribution (DHSR) measured during Mission 3 (CM) with CHE1 team, CHE1 and CHE2 data evaluated with AGS_CH. Final results. Geodaten©swisstopo.

Activity concentration distribution of ^{232}Th

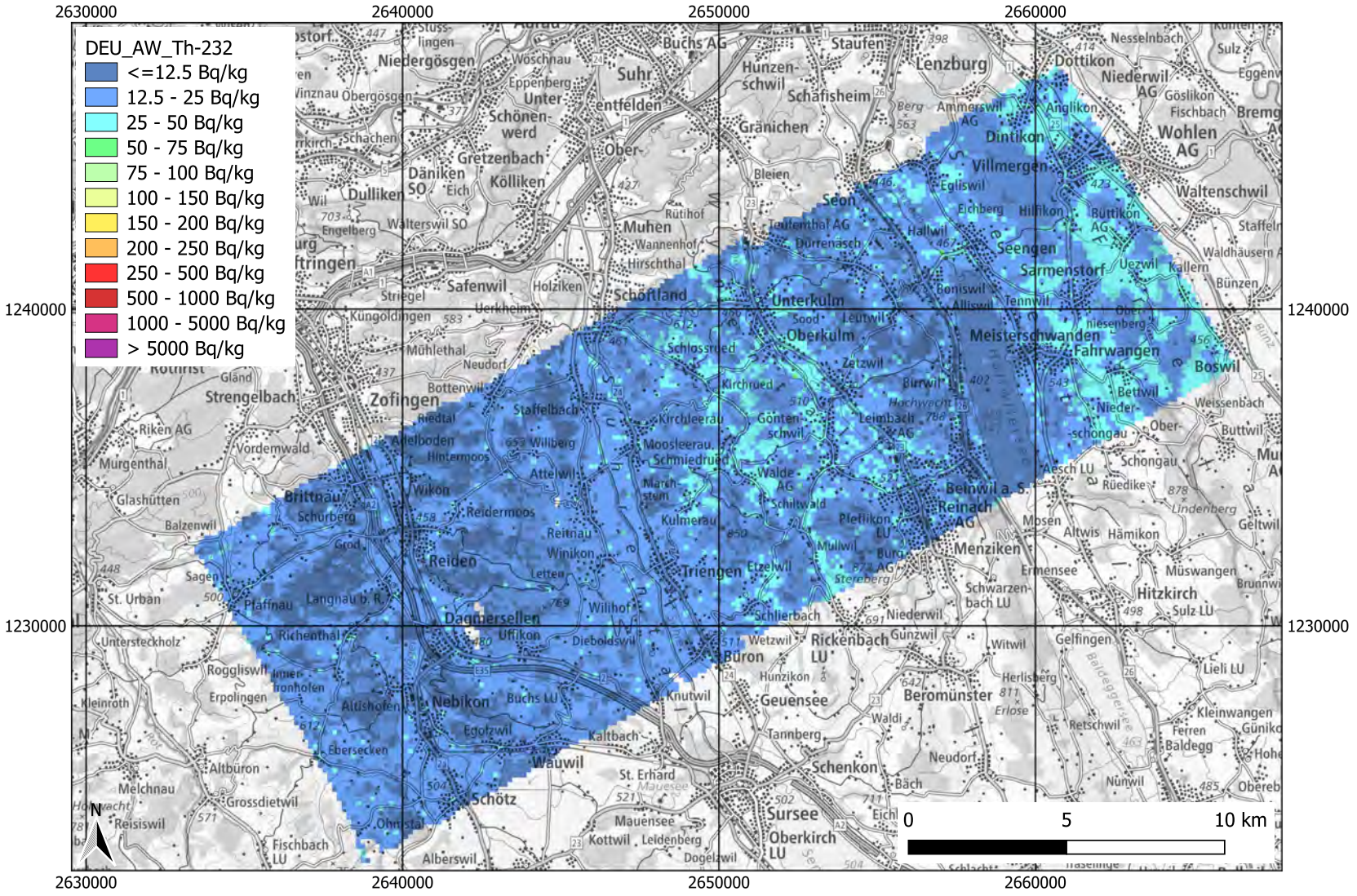

Figure 8.110: Activity concentration of ^{232}Th measured during Mission 3 (CM) with DEU team. Final Results. Geodaten©swisstopo.

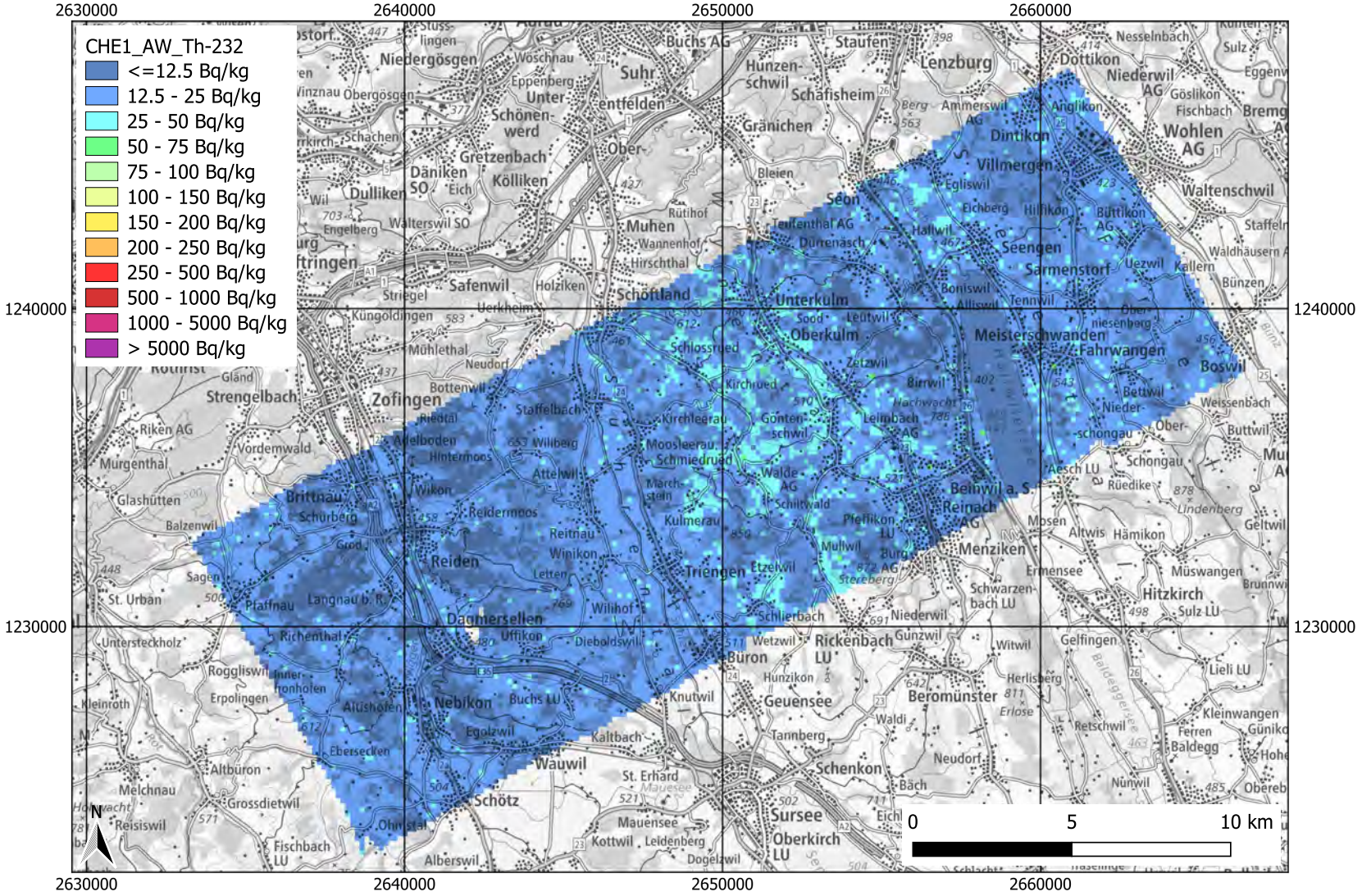

Figure 8.111: Activity concentration of ^{232}Th measured during Mission 3 (CM) with CHE1 team. Final Results. Geodaten©swisstopo.

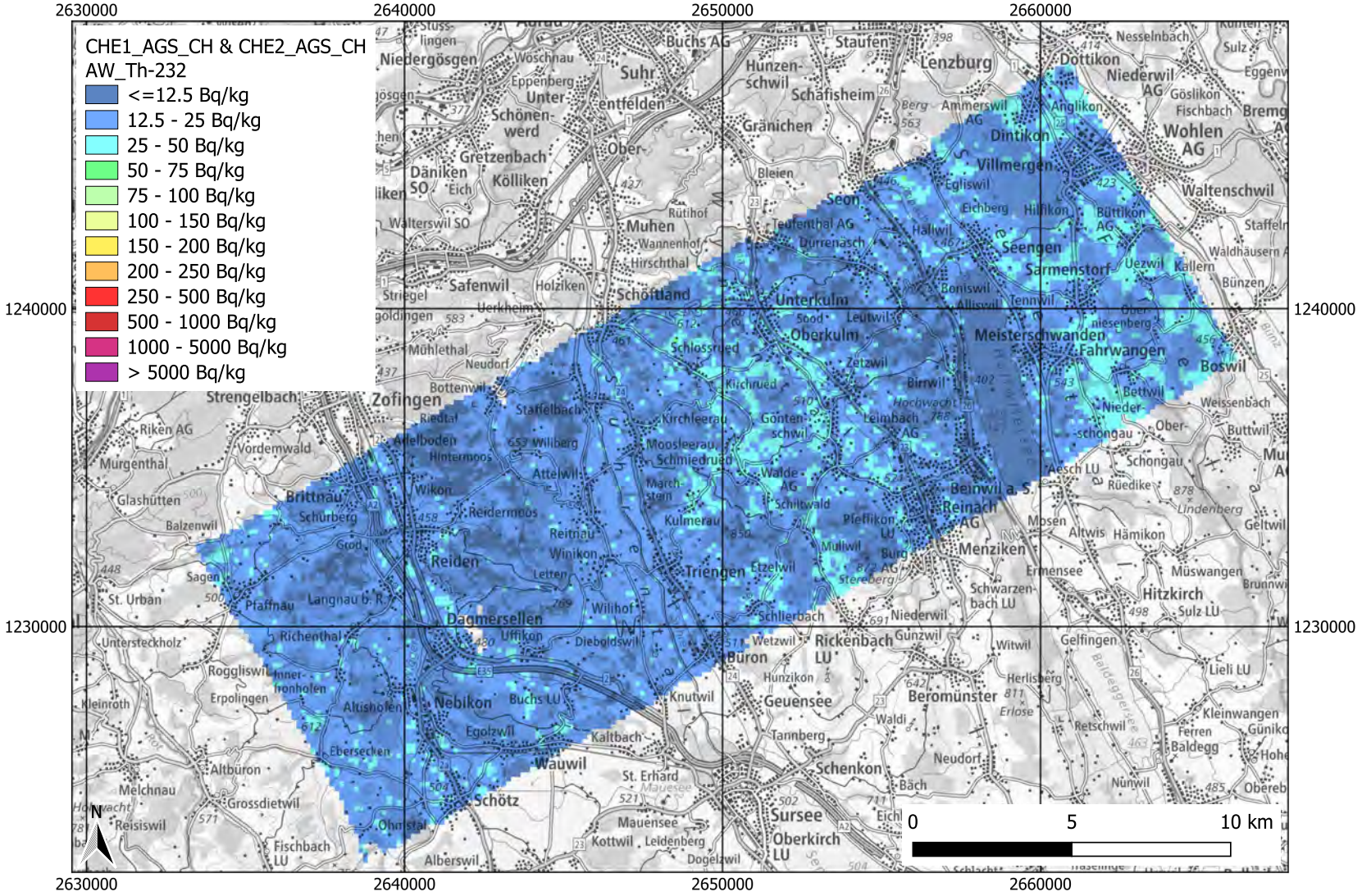

Figure 8.112: Activity concentration of ^{232}Th measured during Mission 3 (CM) with CHE1 team, CHE1 and CHE2 data evaluated with AGS_CH. Final Results. Geodaten©swisstopo.

Activity concentration distribution of ^{238}U

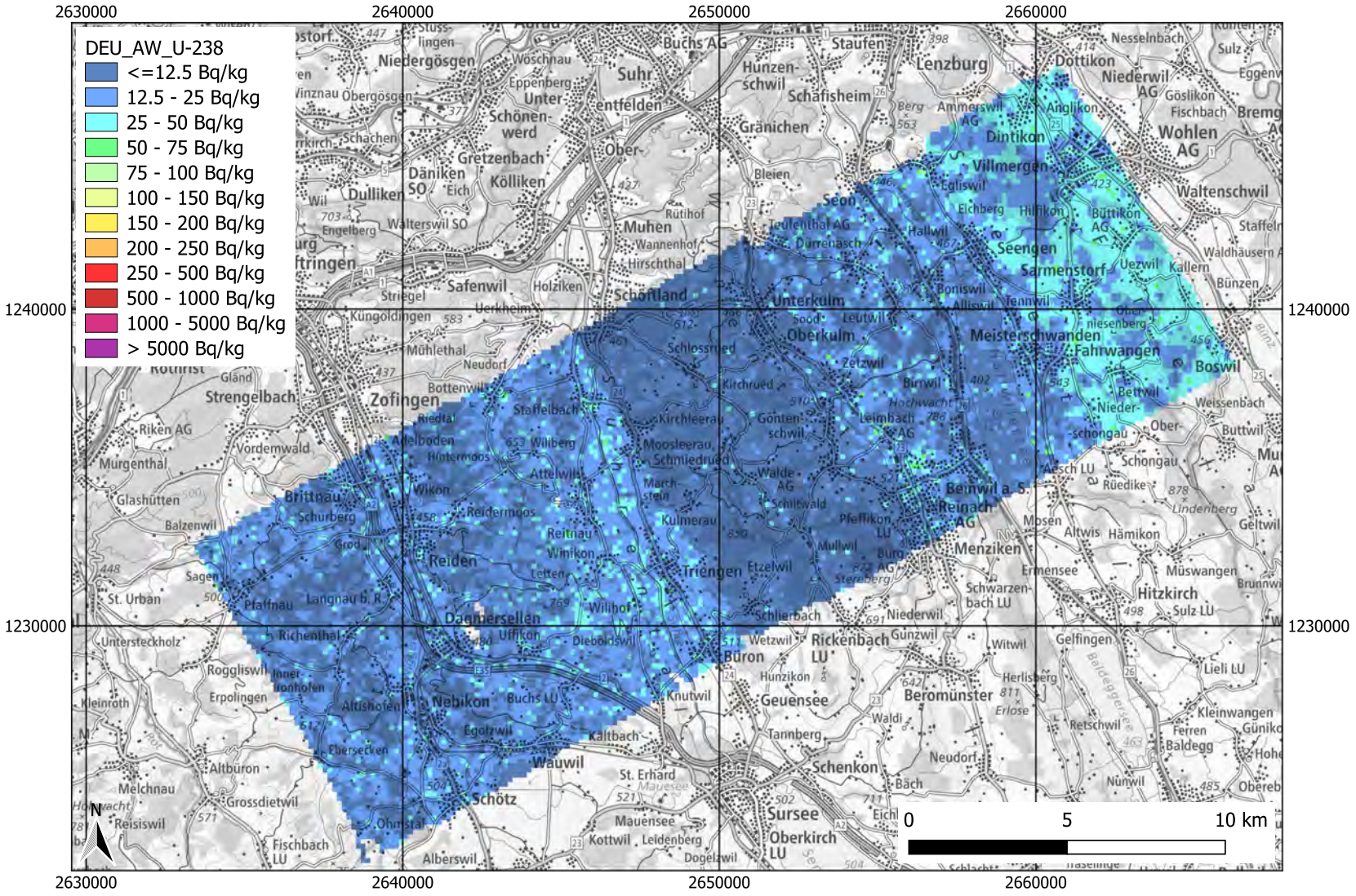

Figure 8.113: Activity concentration of ^{238}U measured during Mission 3 (CM) with DEU team. Final Results. Geodaten©swisstopo.

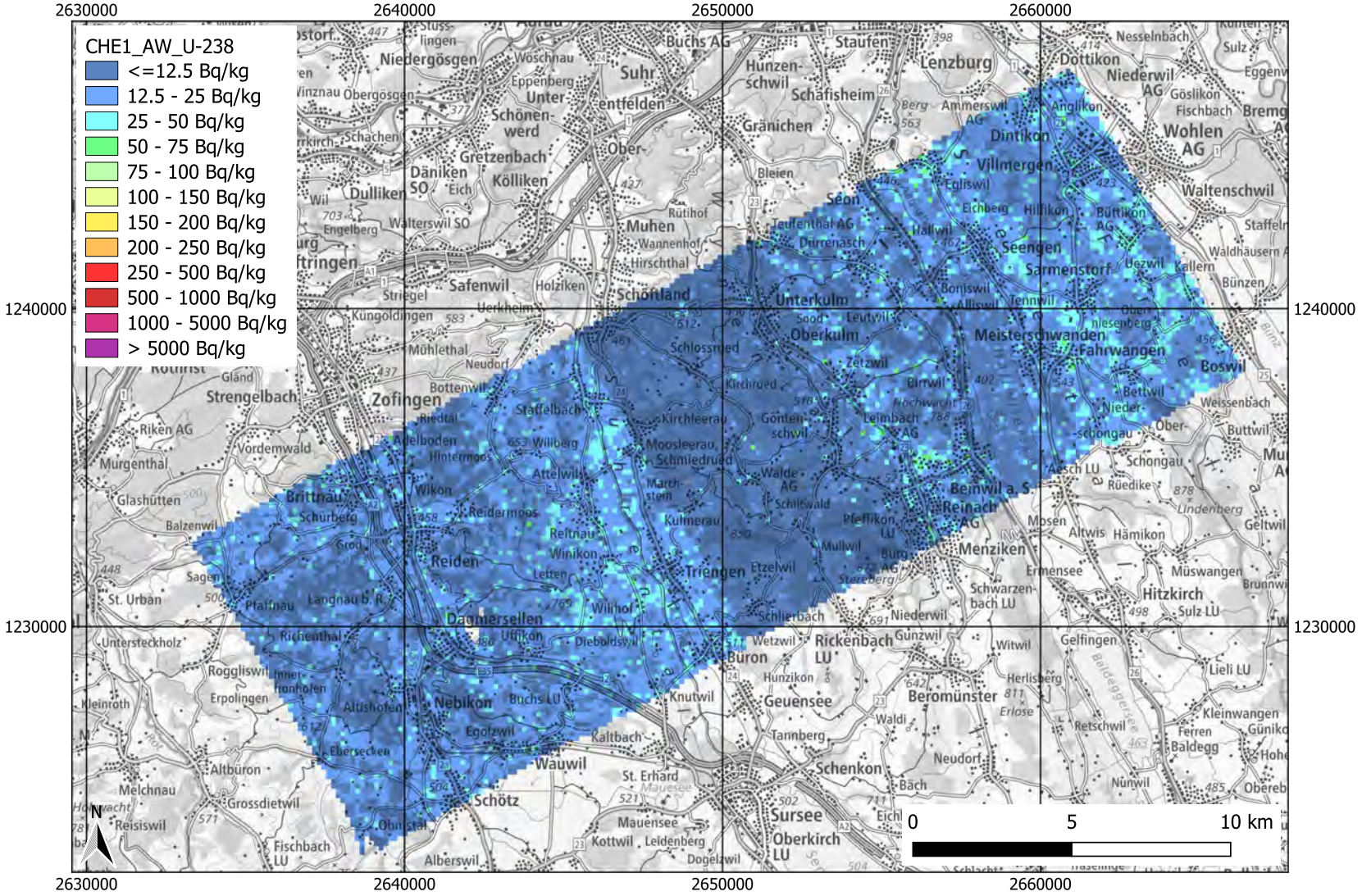

Figure 8.114: Activity concentration of ^{238}U measured during Mission 3 (CM) with CHE1 team. Final Results. Geodaten©swisstopo.

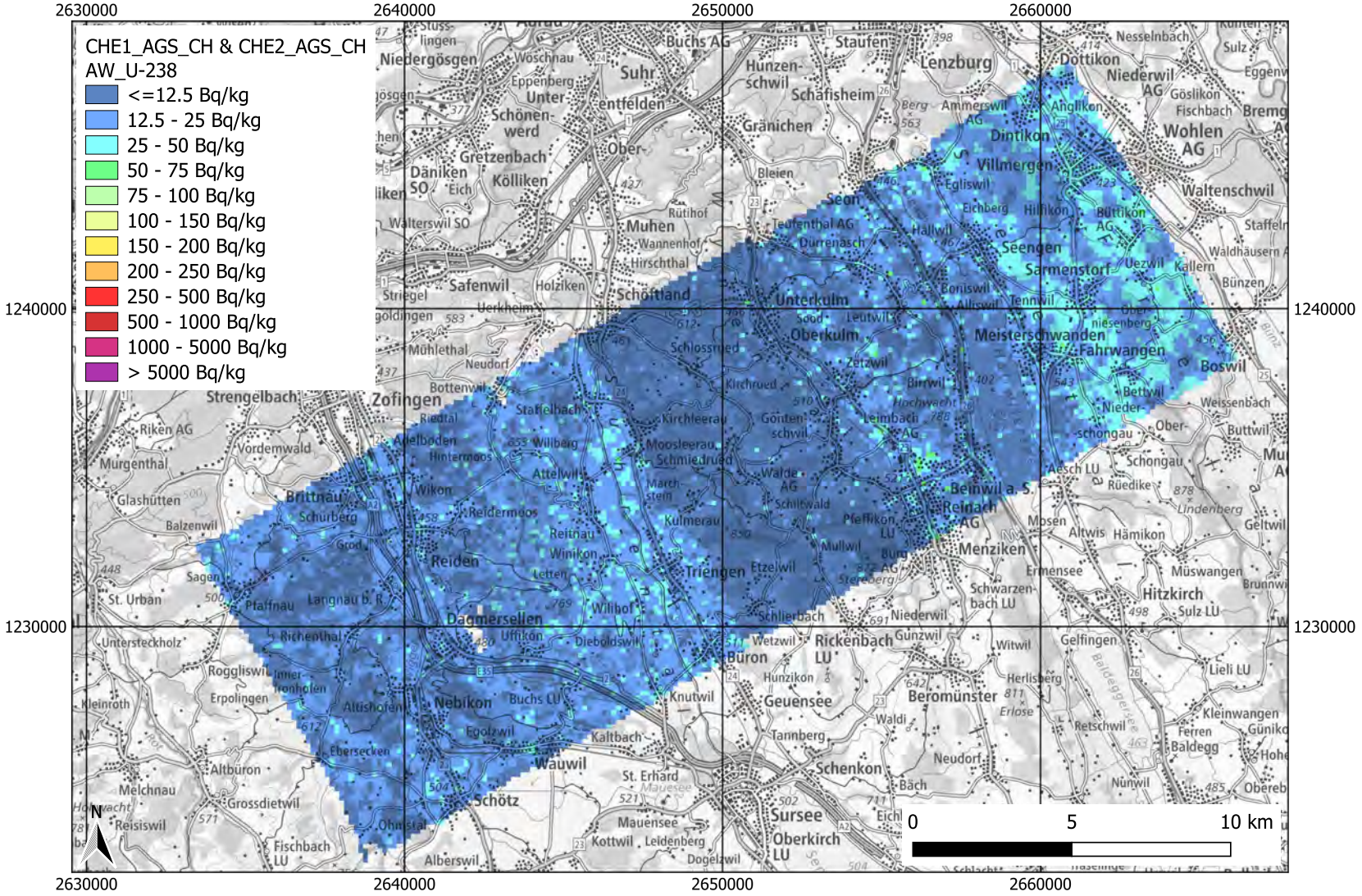

Figure 8.115: Activity concentration of ^{238}U measured during Mission 3 (CM) with CHE1 team, CHE1 and CHE2 data evaluated with AGS_CH. Final Results. Geodaten©swisstopo.

Activity concentration distribution of ^{40}K

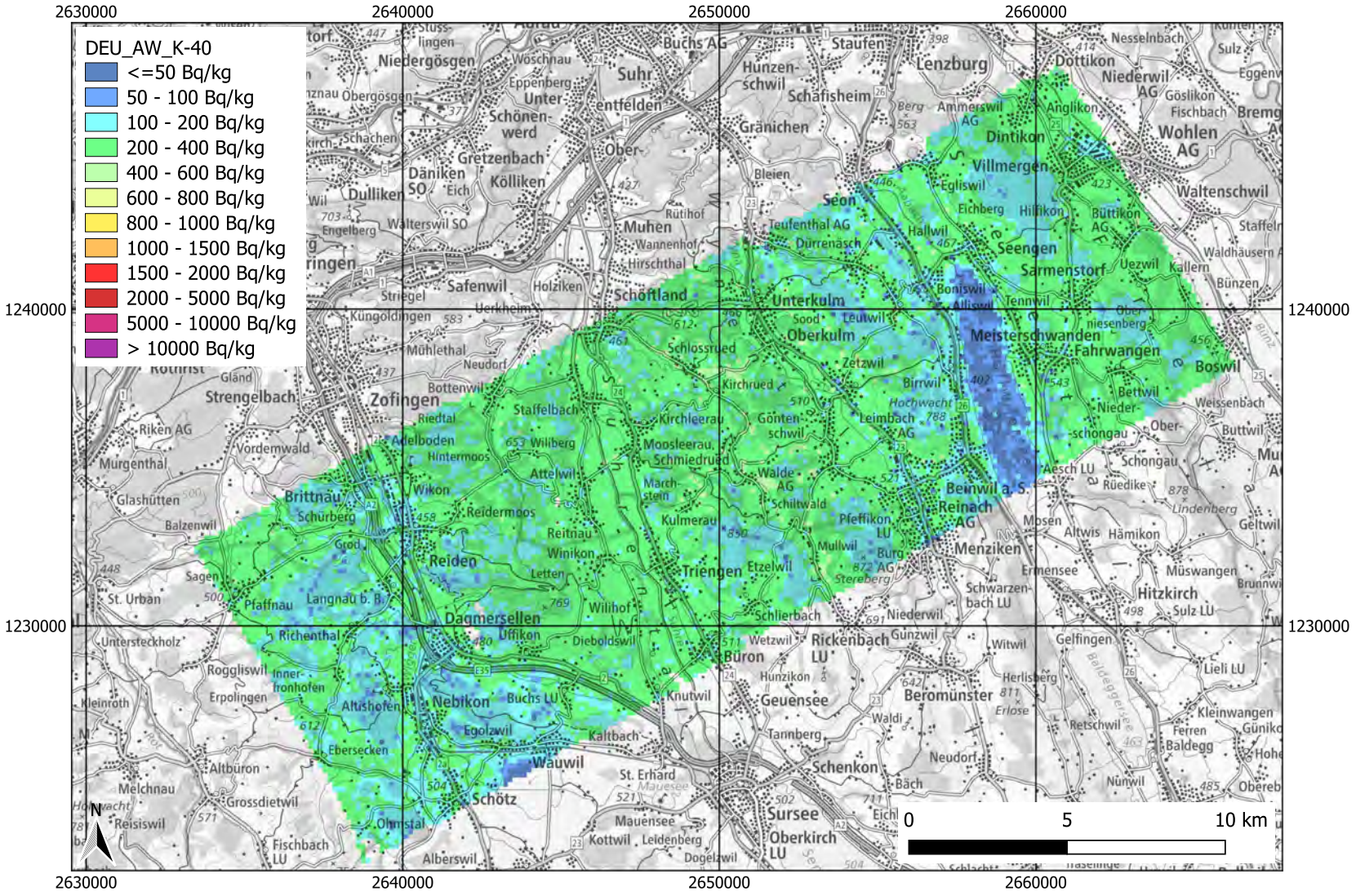

Figure 8.116: Activity concentration of ^{40}K measured during Mission 3 (CM) with DEU team. Final Results. Geodaten©swisstopo.

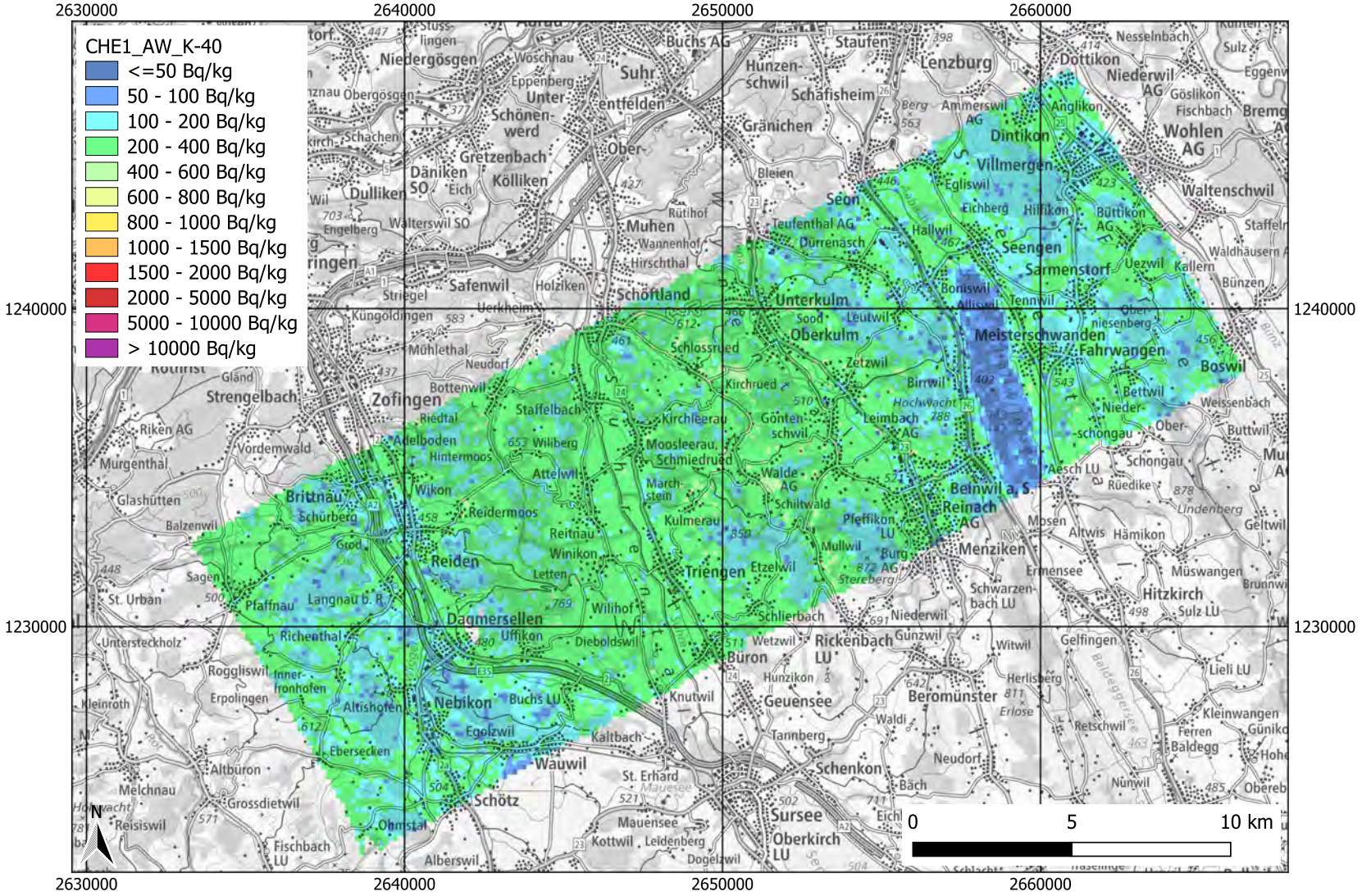

Figure 8.117: Activity concentration of ^{40}K measured during Mission 3 (CM) with CHE1 team. Final Results. Geodaten©swisstopo.

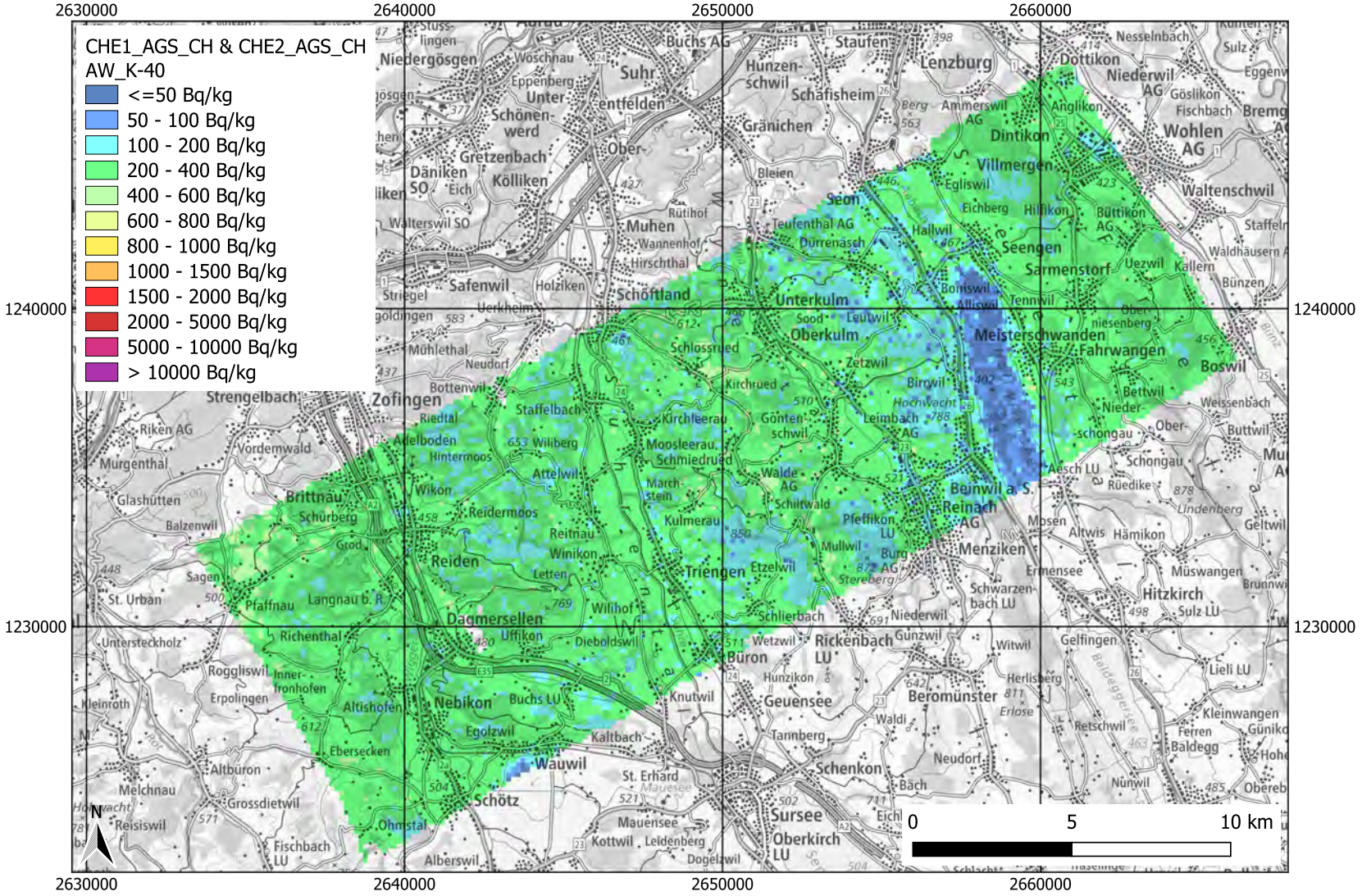

Figure 8.118: Activity concentration of ^{40}K measured during Mission 3 (CM) with CHE1 team, CHE1 and CHE2 data evaluated with AGS_CH. Final Results. Geodaten©swisstopo.

8.5 Mission 4 – ES – Frauenfeld military training area

8.5.1 Comparison

For the source search within a limited area, all teams adopted a similar strategy, albeit with some variations. Each team initially flew a raster pattern of parallel lines along the longest extension of the area, which allowed the preliminary localisation and identification of the radioactive sources (Figures 8.119 – 8.124). The LTU team flew the raster pattern in a shifted sequence (1 – 3 followed by 2 – 4) to achieve a dense grid of lines without sharp turns or additional time required for realignment (Figure 8.124). The Swiss teams adopted a coarser line spacing (Figures 8.119 and 8.120), i.e. more lines at a higher flight speed, whereas other teams preferred lower speeds to enhance the counting statistics of each acquisition. Team CHE1 flew using standard sampling settings, acquiring a spectrum every second, whereas team CHE2 operated in source search mode, recording each second a spectrum averaged over the preceding five seconds. The French team flew at an even higher speed in order to repeat the entire raster twice, applying a shift, to achieve denser coverage of the target area (Figure 8.123).

After completing the first parallel raster, most teams flew over the identified hotspots in a direction orthogonal to the previous flight pattern to enhance location accuracy and counting statistics to allow the activity quantification.

All teams successfully identified the two westernmost hotspots (Points 1 and 2). Both ^{137}Cs sources at these points were detected and quantified by all teams. The ^{60}Co source at Point 2, however, was not identified by the CHE1 team when using the Mirion software, either during the flight or in the offline evaluation. Nonetheless, identification and activity estimation were achieved by analysing the raw data with AGS_CH. The ^{133}Ba source posed a greater challenge, being identified and quantified by only three teams: CHE1, CHE2, and LTU. None of the teams detected, identified, or quantified the ^{241}Am source placed at the easternmost point (Point 3). The results of the source detection and activity estimations are summarised in Table 8.6.

Table 8.6: Estimated sources' activity and relative activity at points 1, 2, and 3 of Mission 4

	Point 1			Point 2		Point 3	
	PN	PE		PN	PE	PN	PE
Ref. Coordinates	47.577701	8.894868		47.581038	8.908427	47.584396	8.915952
Nuclide	^{137}Cs	^{133}Ba	^{60}Co	^{137}Cs		^{241}Am	
Ref. Activity [GBq]	0.7	0.4	0.16	0.4		1.8	
Activity estimation [GBq]							
CHE1	0.85	0.93	n.a.	0.4		n.a.	
CHE1_AGS_CH	0.27	n.a.	0.16	0.22		n.a.	
CHE2	0.93	0.49	0.19	0.6		n.a.	
CHE2_AGS_CH	0.42	n.a.	0.19	0.21		n.a.	
CZE	0.5	n.a.	0.10	0.2		n.a.	
DEU	0.45	n.a.	0.13	0.25		n.a.	
FRA	0.53	n.a.	0.06	0.35		n.a.	
LTU	0.57	0.28	0.15	0.57		n.a.	
Activity estimation relative to reference							
CHE1	21 %	133 %	n.a.	0 %		n.a.	
CHE1_AGS_CH	−61 %	n.a.	0 %	−45 %		n.a.	
CHE2	33 %	23 %	19 %	50 %		n.a.	
CHE2_AGS_CH	−40 %	n.a.	19 %	−48 %		n.a.	
CZE	−29 %	n.a.	−38 %	−50 %		n.a.	
DEU	−36 %	n.a.	−19 %	−38 %		n.a.	
FRA	−24 %	n.a.	−63 %	−13 %		n.a.	
LTU	−19 %	−30 %	−6 %	43 %		n.a.	

8.5.2 Maps

In this section, the flight paths, the spatial distributions of the ambient dose equivalent rate, and Man Made Gross Count Ratio where available, are presented for the Frauenfeld military training area, based on the analysis of the Mission 4 dataset. The variation in dose rate estimates among the teams reflects the calibration offsets discussed in the results of Mission 1 (Section 8.2).

Flight paths

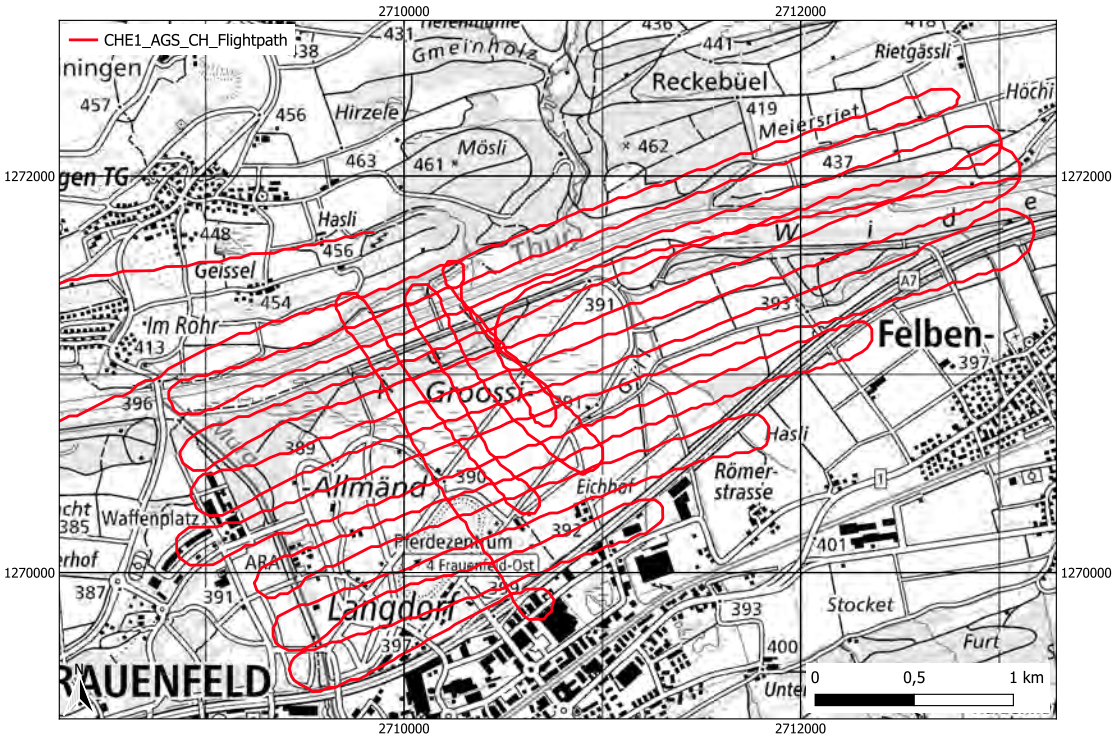

Figure 8.119: The flight path taken at the Mission 4 (ES) area by the CHE1 team. The flight paths are identical for the CHE1 and CHE1_AGS_CH datasets. Geodaten©swisstopo.

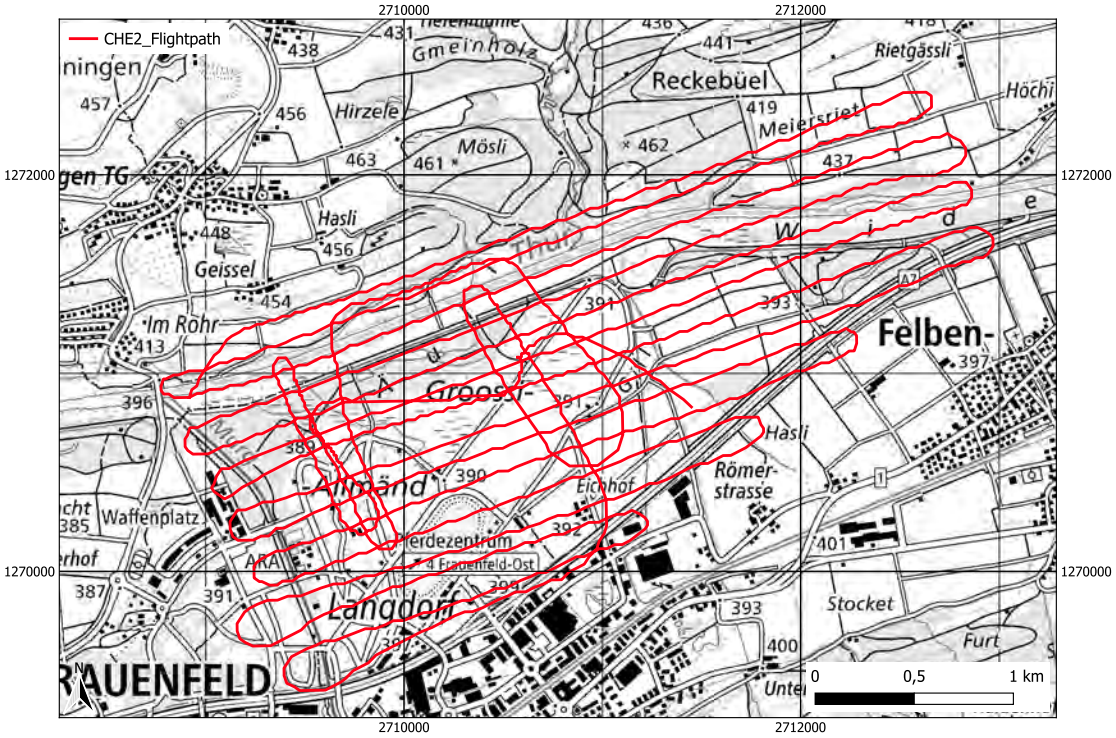

Figure 8.120: The flight path taken at the Mission 4 (ES) area by the CHE2 team. The flight paths are identical for the CHE2 and CHE2_AGS_CH datasets. Geodaten©swisstopo.

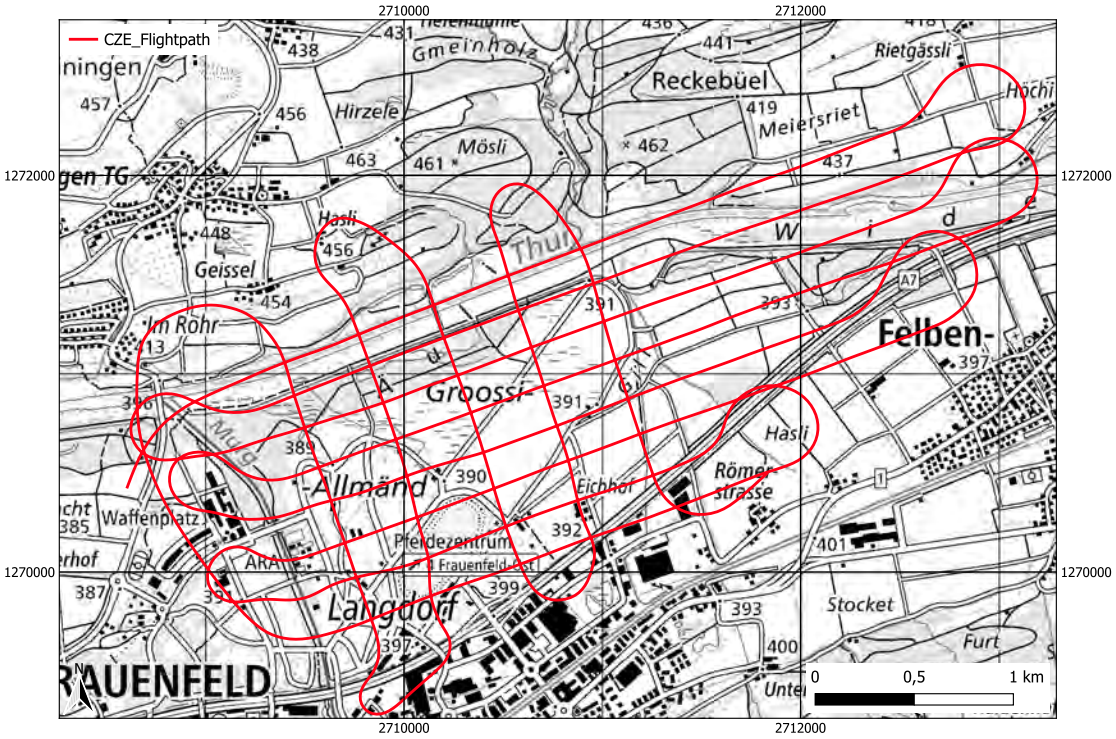

Figure 8.121: The flight path taken at the Mission 4 (ES) area by the CZE team. Geodaten©swisstopo.

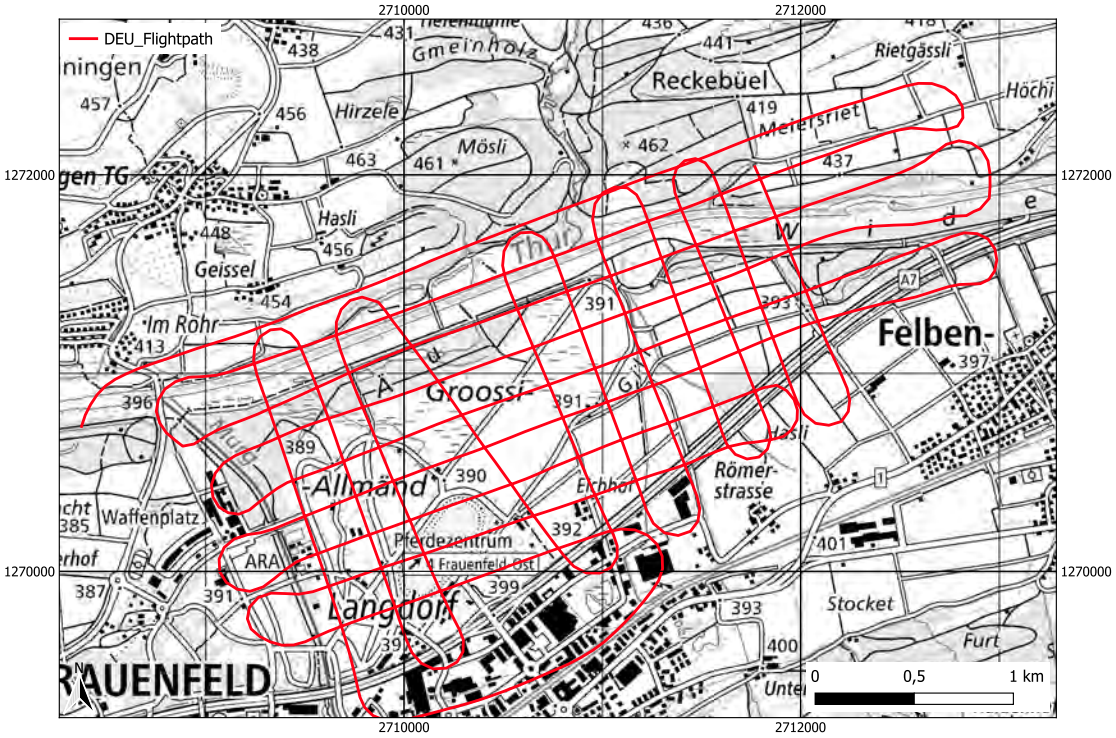

Figure 8.122: The flight path taken at the Mission 4 (ES) area by the DEU team. Geodaten©swisstopo.

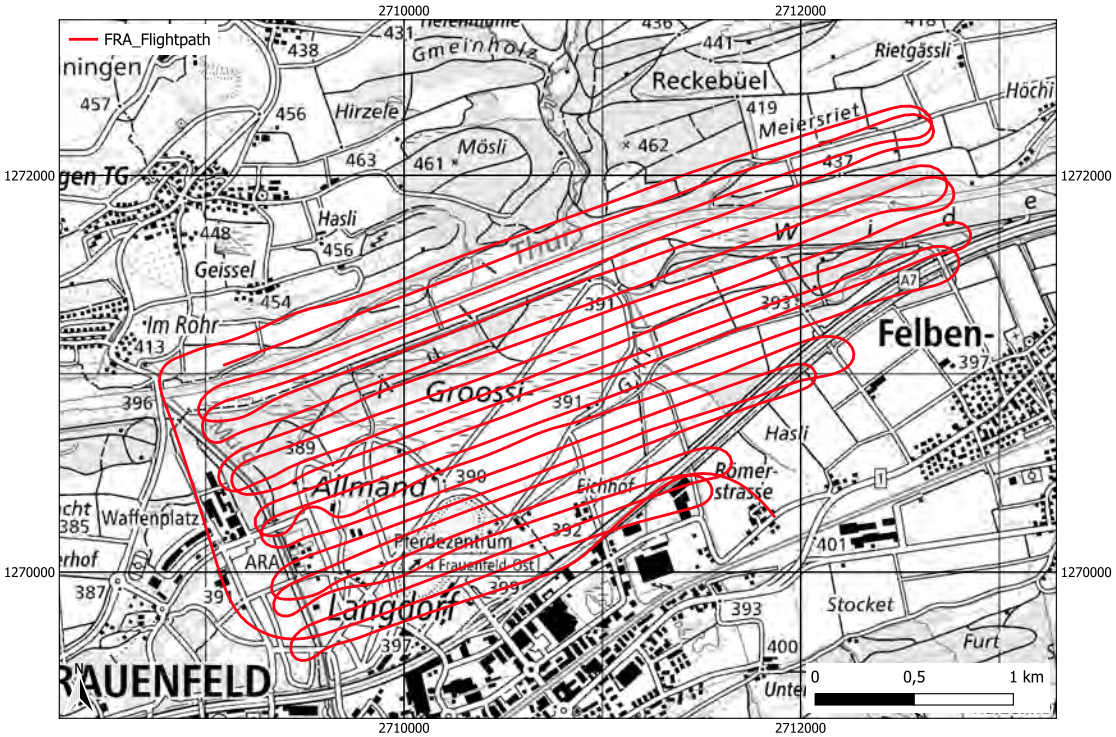

Figure 8.123: The flight path taken at the Mission 4 (ES) area by the FRA team. Geodaten©swisstopo.

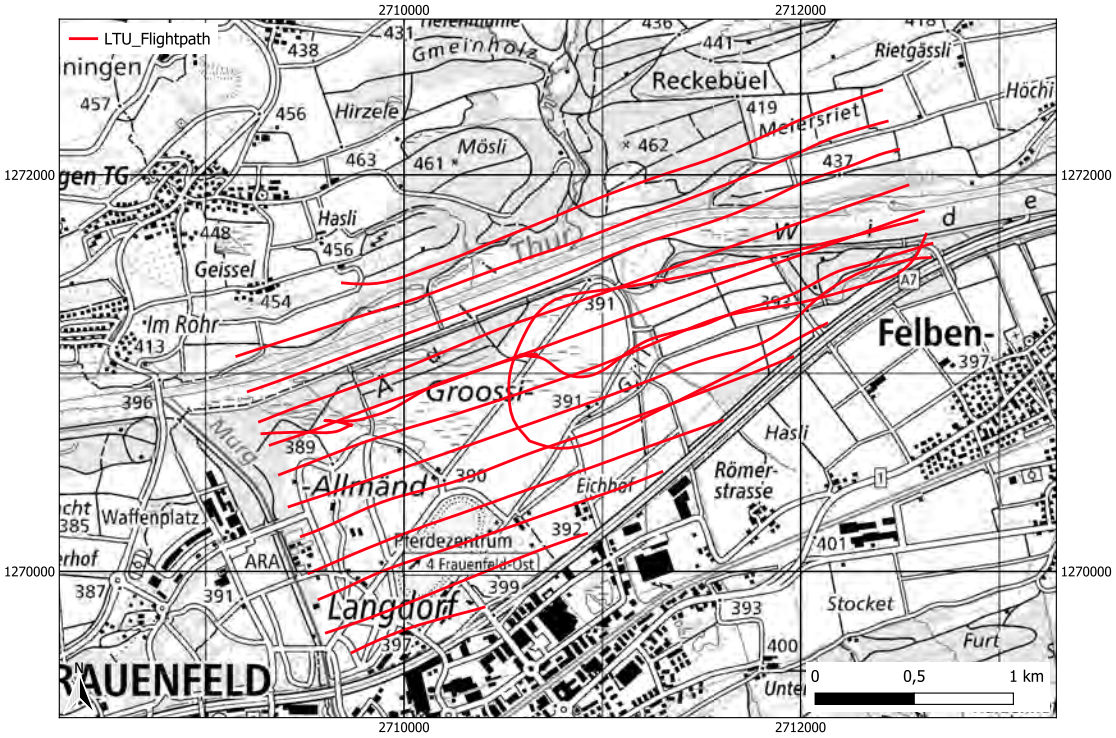

Figure 8.124: The flight path taken at the Mission 4 (ES) area by the LTU team. Geodaten©swisstopo.

Ambient dose equivalent rate

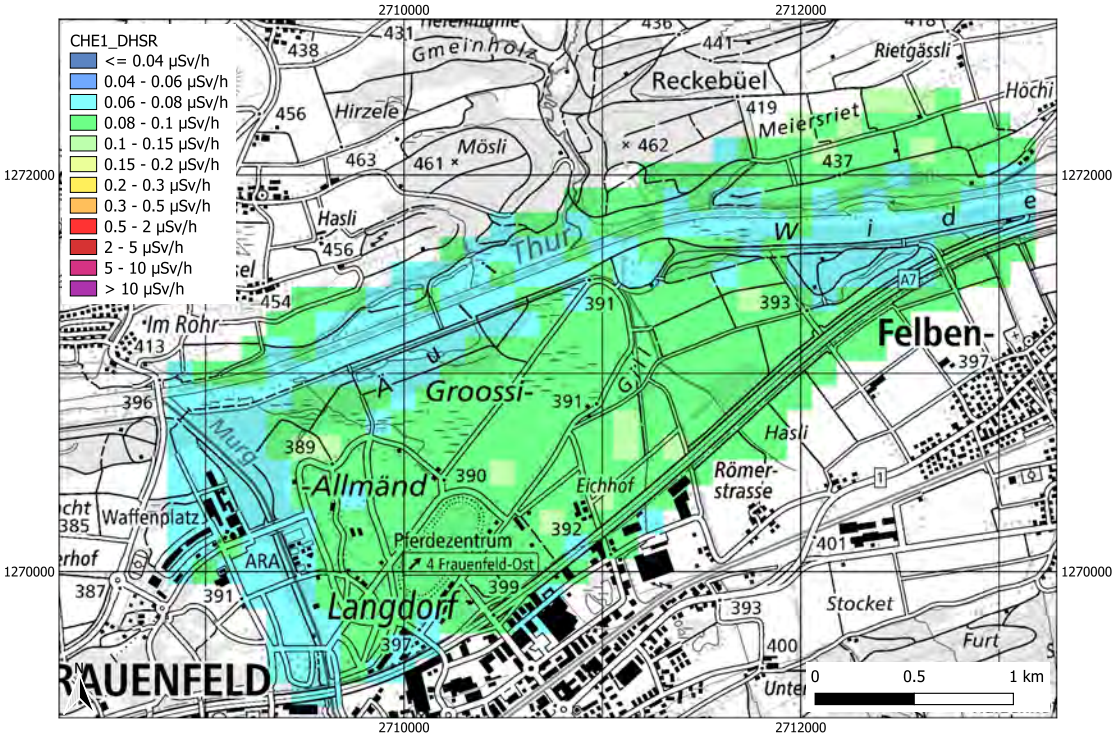

Figure 8.125: Ambient dose equivalent rate distribution (DHSR) measured at the Mission 4 (ES) area by the CHE1 team. Geodaten©swisstopo.

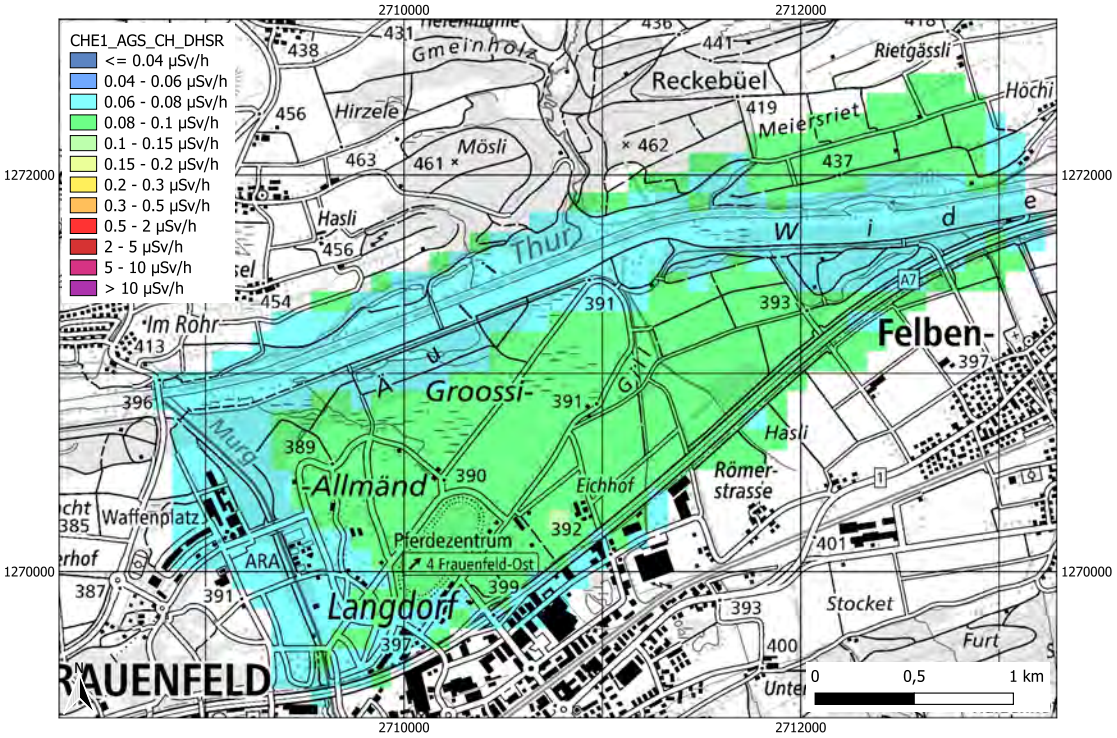

Figure 8.126: Ambient dose equivalent rate distribution (DHSR) measured at the Mission 4 (ES) area by the CHE1 team. Dataset is analysed with AGS_CH. Geodaten©swisstopo.

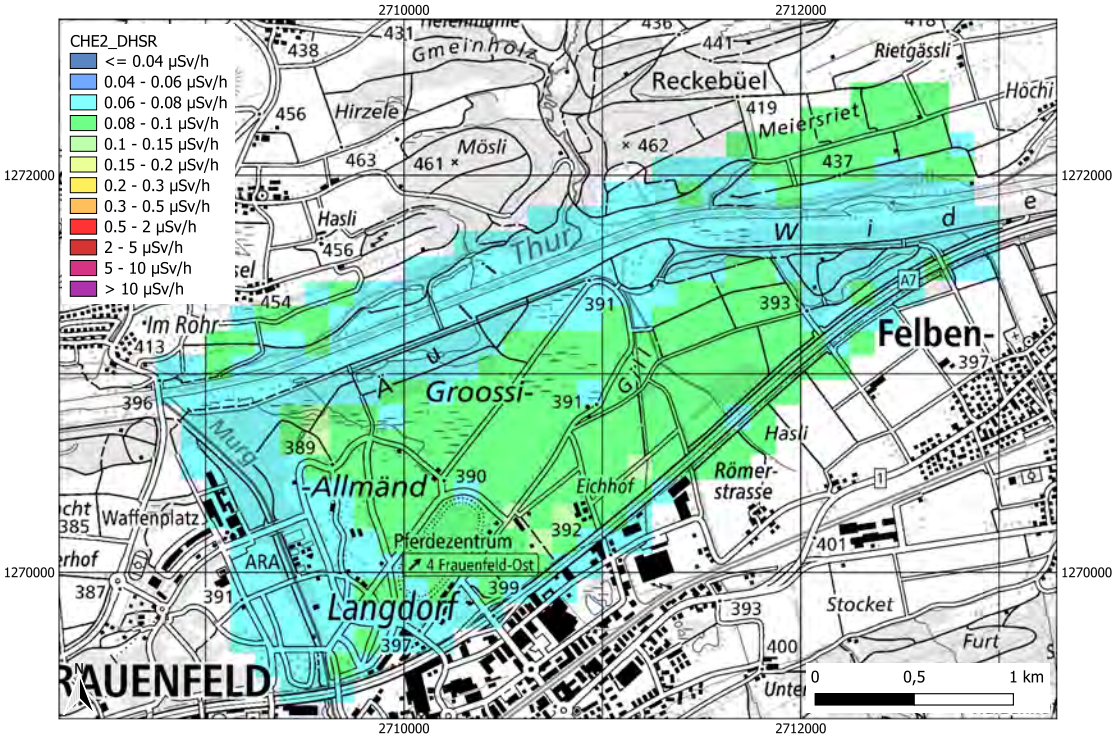

Figure 8.127: Ambient dose equivalent rate distribution (DHSR) measured at the Mission 4 (ES) area by the CHE2 team. Geodaten©swisstopo.

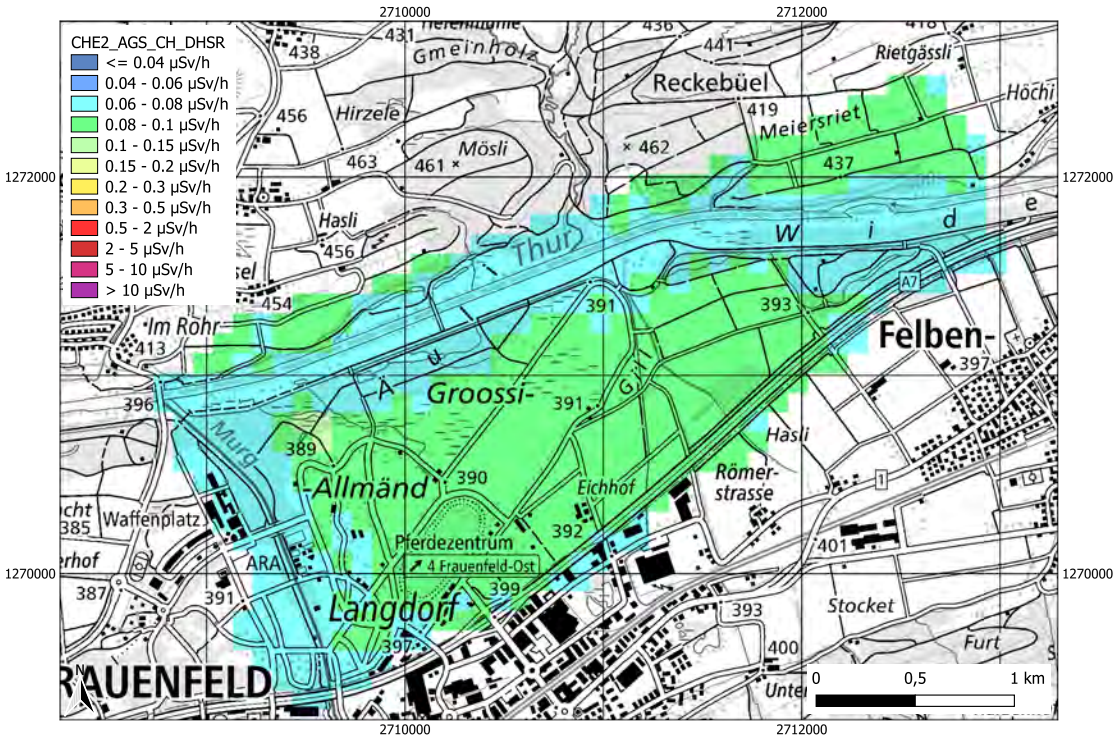

Figure 8.128: Ambient dose equivalent rate distribution (DHSR) measured at the Mission 4 (ES) area by the CHE2 team. Dataset is analysed with AGS_CH. Geodaten©swisstopo.

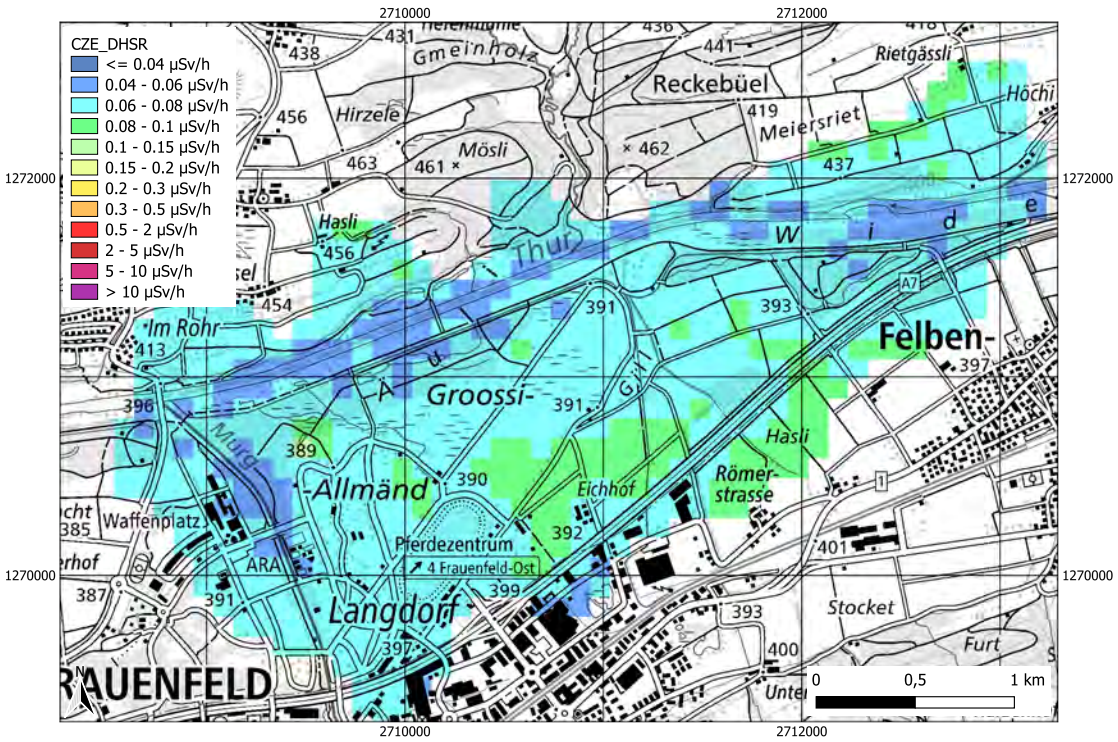

Figure 8.129: Ambient dose equivalent rate distribution (DHSR) measured at the Mission 4 (ES) area by the CZE team. Geodaten©swisstopo.

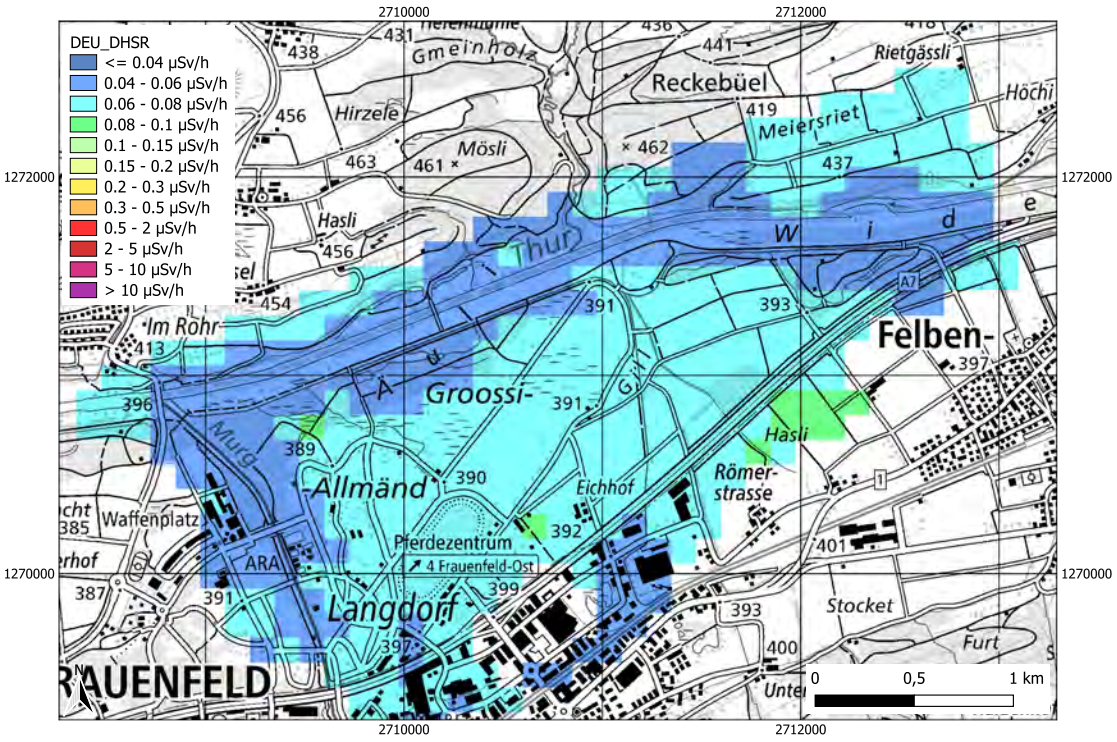

Figure 8.130: Ambient dose equivalent rate distribution (DHSR) measured at the Mission 4 (ES) area by the DEU team. Geodaten©swisstopo.

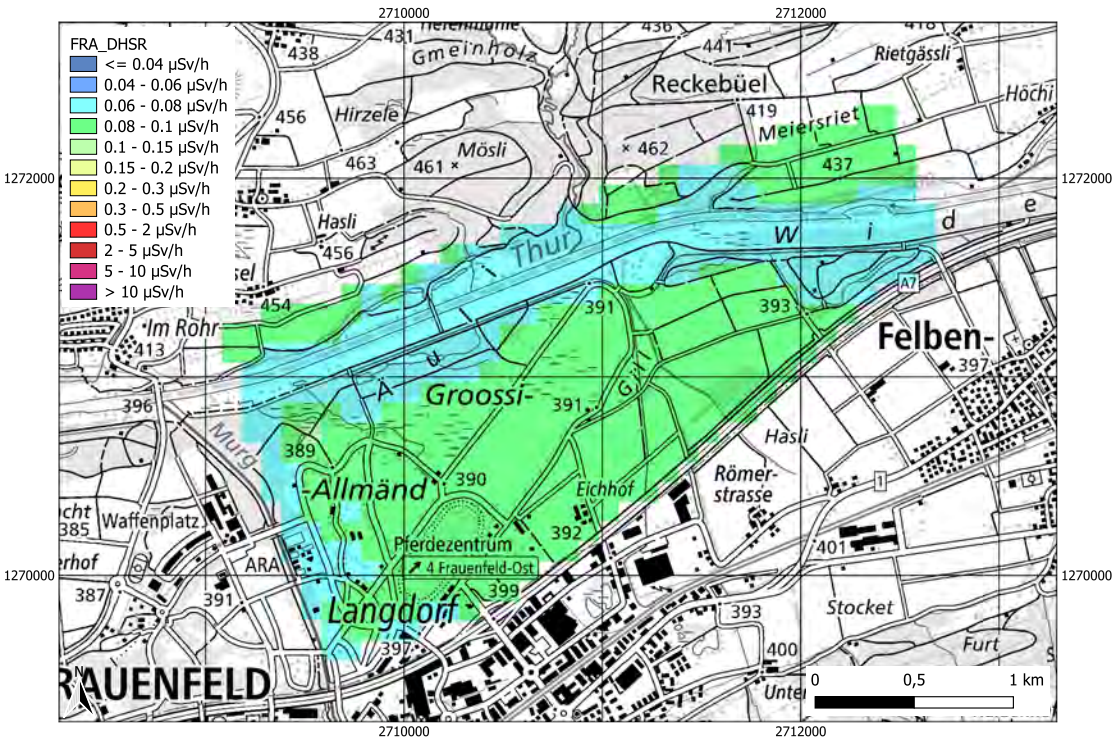

Figure 8.131: Ambient dose equivalent rate distribution (DHSR) measured at the Mission 4 (ES) area by the FRA team. Geodaten©swisstopo.

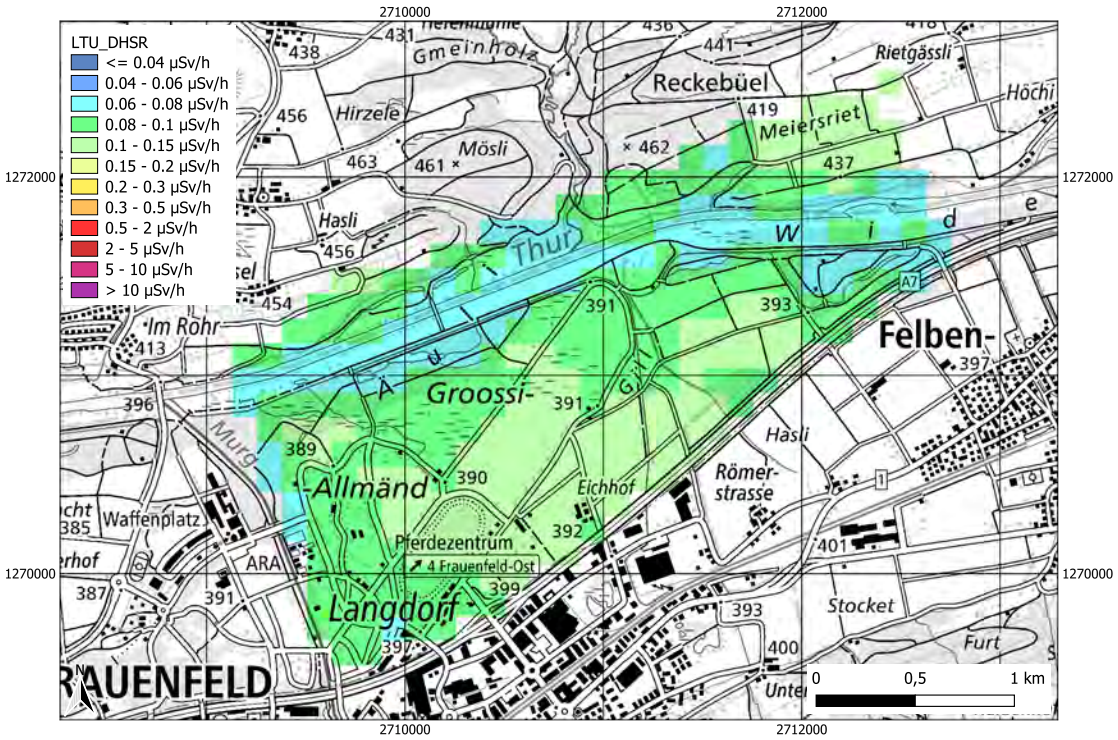

Figure 8.132: Ambient dose equivalent rate distribution (DHSR) measured at the Mission 4 (ES) area by the LTU team. Geodaten©swisstopo.

Man Made Gross Count Ration (MMGC)

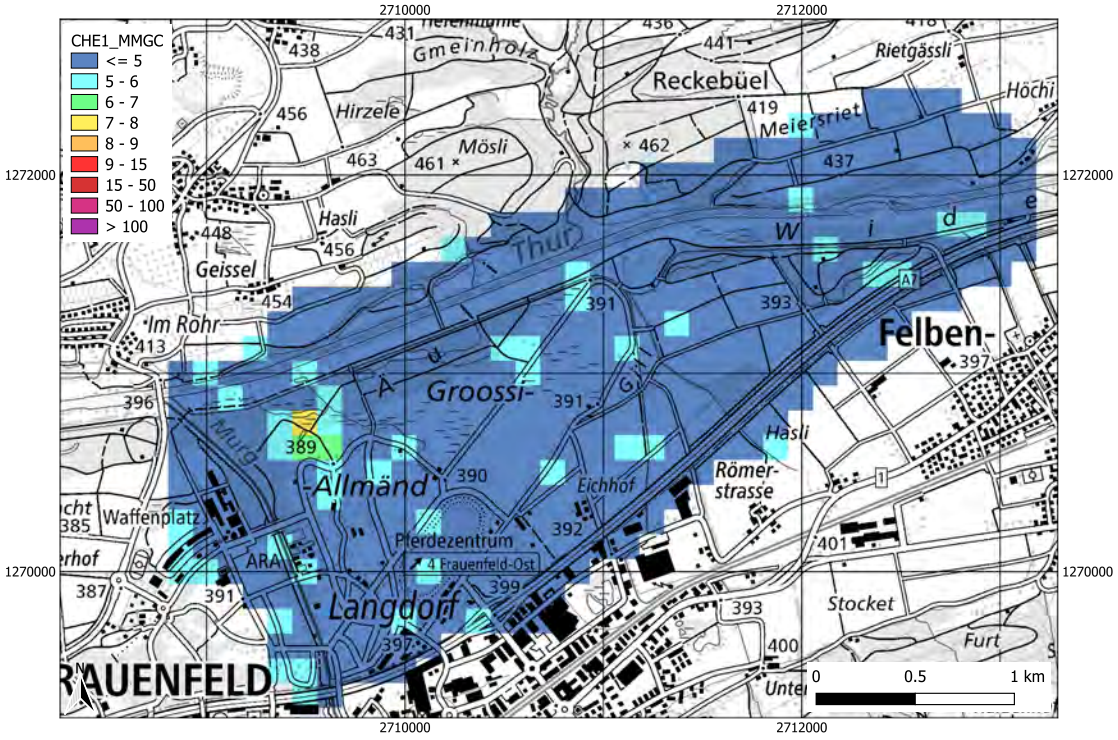

Figure 8.133: Man Made Gross Count Ratio measured at the Mission 4 (ES) area by the CHE1 team. Geodaten©swisstopo.

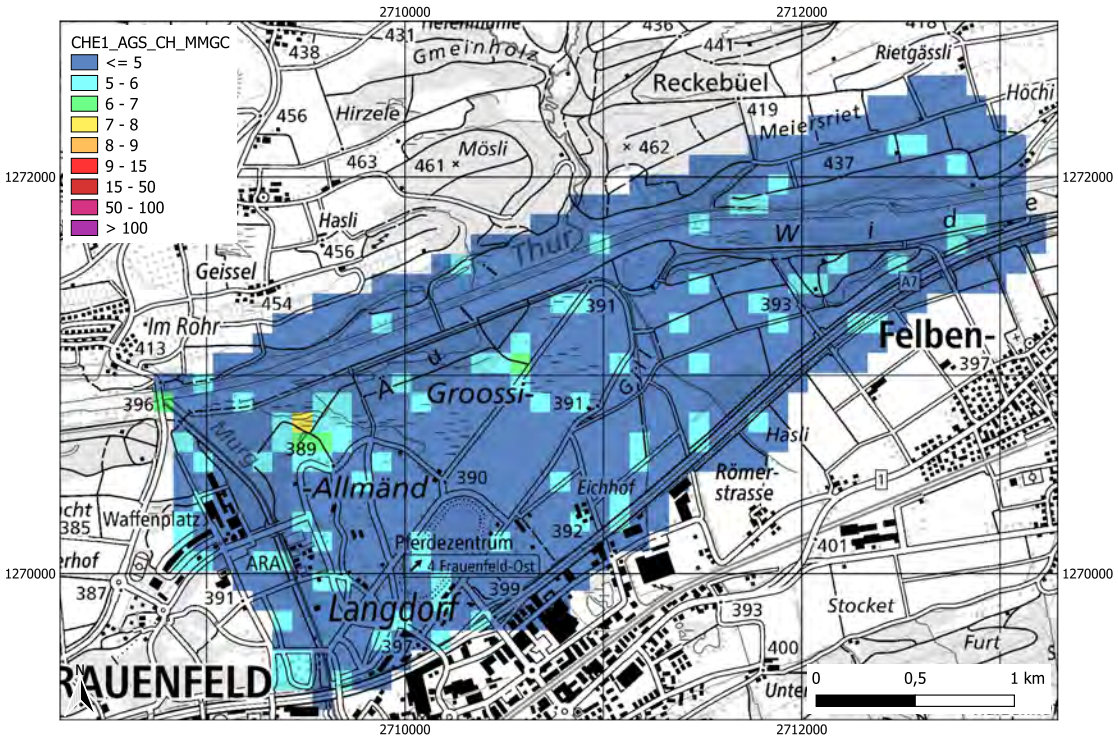

Figure 8.134: Man Made Gross Count Ratio measured at the Mission 4 (ES) area by the CHE1 team. Dataset is analysed with AGS_CH. Geodaten©swisstopo.

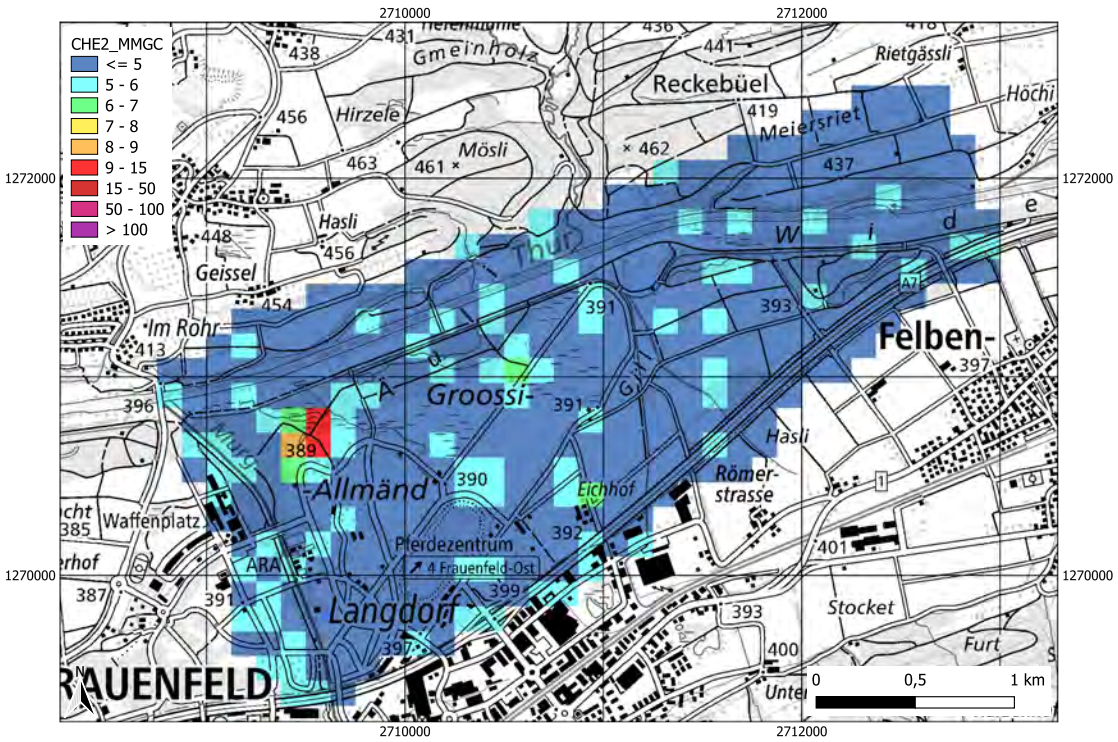

Figure 8.135: Man Made Gross Count Ratio measured at the Mission 4 (ES) area by the CHE2 team. Geodaten©swisstopo.

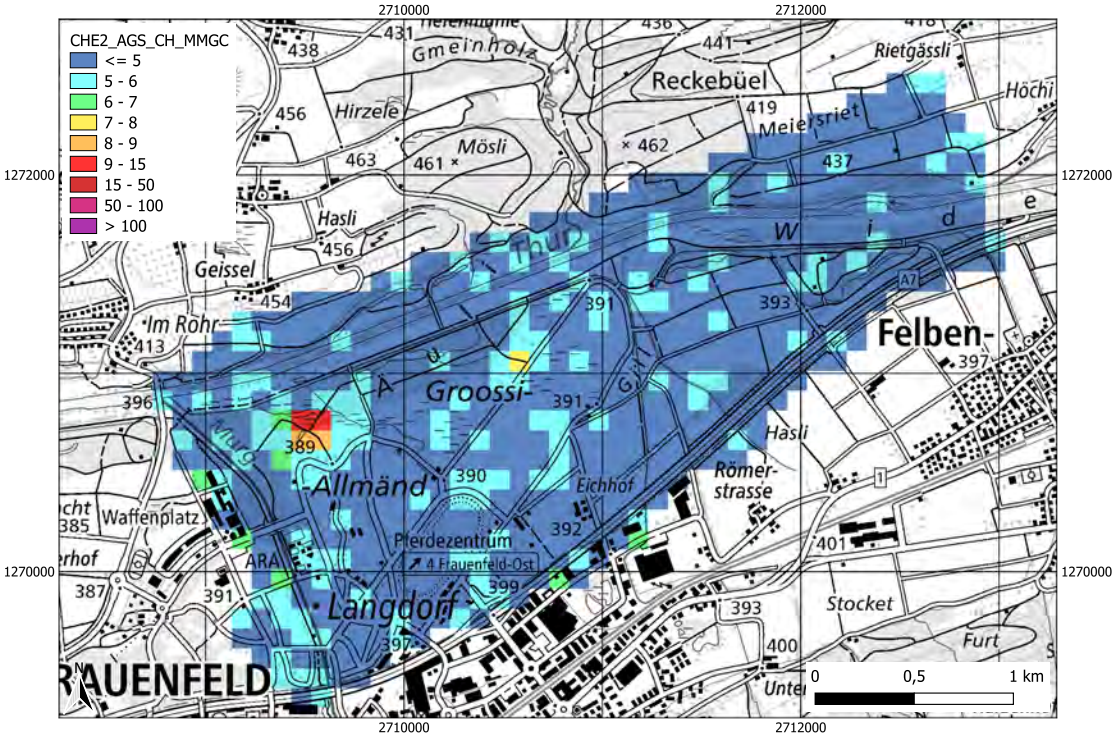

Figure 8.136: Man Made Gross Count Ratio measured at the Mission 4 (ES) area by the CHE2 team. Dataset is analysed with AGS_CH. Geodaten©swisstopo.

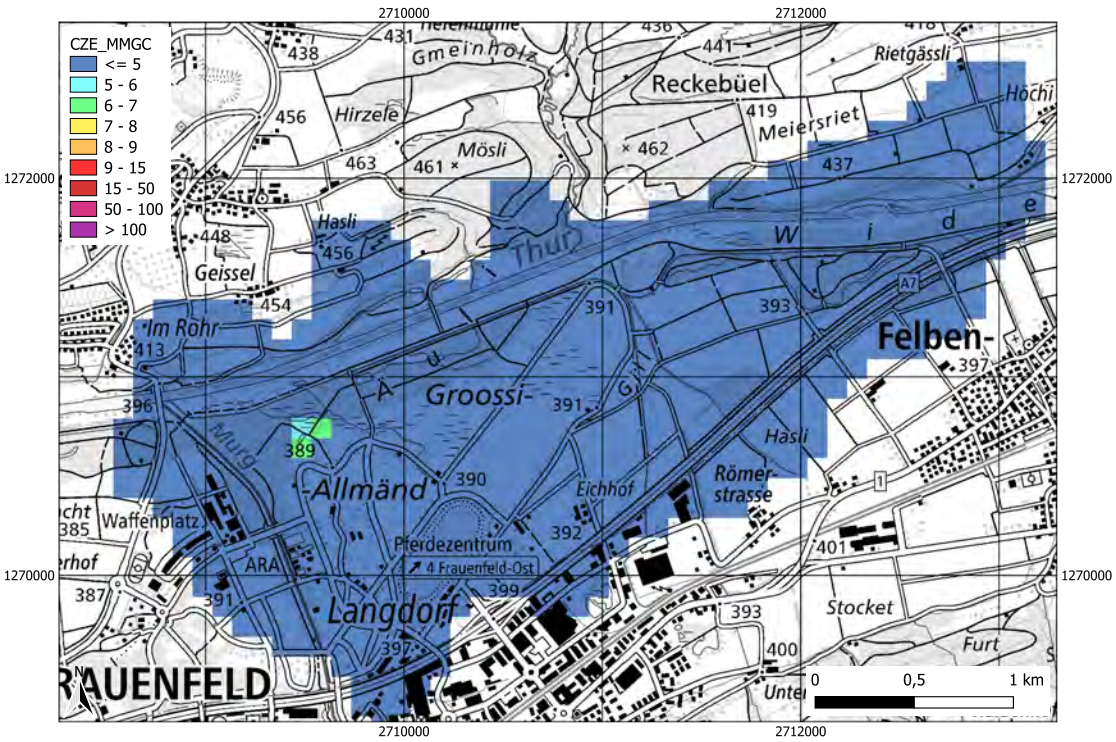

Figure 8.137: Man Made Gross Count Ratio measured at the Mission 4 (ES) area by the CZE team. Geodaten©swisstopo.

Figure 8.138: Live data of sources detection during Mission 4 by the CHE2 team

8.6 Mission 5 – MM – Paul Scherrer Institute

8.6.1 Comparison

The accelerator complex at PSI was operational on both days scheduled for Mission 5, allowing all teams the opportunity to detect the short-lived β^+ radionuclides emitted from the PSI stack of the experimental hall. Although the release of these radionuclides, authorised by the relevant authorities and continuously monitored, has long been documented in Swiss aeroradiometric reports, it was of particular interest to the foreign teams, who had the opportunity to measure it using their own equipment. Another area of notable interest within this region is the so-called "thorium anomaly" near Rotbergegg, where naturally elevated activity concentrations of ^{232}Th are present.

All teams adopted a similar survey flightpath strategy for Mission 5A, as illustrated in Figures 8.141 to 8.146. The detection of the characteristic signals by all teams in this region is documented in Figure 8.139. For each team, the figure shows in red the average spectra acquired over the PSI-West experimental hall, featuring the annihilation peak; in green, the background-averaged spectra recorded over the north-western part of the survey area; and in blue, the averaged spectra from the thorium-rich region near Rotbergegg.

The regions yielding the most interesting measurements are also evident in the ambient dose equivalent maps (Figures 8.147 – 8.154), which display increased values over the area surrounding Rotbergegg and above the accelerator hall at PSI-West. The thorium anomaly is likewise clearly visible in the ^{232}Th distribution maps (Figures 8.155 – 8.162). Available maps of the MMGC-ratio also clearly locate the emission of the short-lived β^+ emitters above the experimental hall. The variability observed among teams across all maps is consistent with the differences in calibration and data evaluation procedures already noted in the reference area measurements from Mission 1, described in Section 8.2.

Concerning Mission 5B, which involved the detection, identification, and quantification of a $2.7\,\mathrm{TBq}$ ^{75}Se source, all teams flew the prescribed line. A few teams had sufficient time remaining to perform an additional pass, or in some cases, a hover flight. Many teams experienced saturation of their spectrometric systems, which made the estimation of the source activity more difficult and, in certain cases, even prevented it altogether.

The average spectra acquired over the source by each team are illustrated in Figure 8.140, all showing peaks corresponding to the ^{75}Se emission lines. Significant pile-up can be observed in all spectra at energies $>400\,\mathrm{keV}$, indicating the high activity of the source. The activity estimations performed by each team, together with their discrepancies from the reference value, are reported in Table 8.7.

It should be noted that the source was shielded not only by its collimator but also by a lead well, designed to ensure the safety of the personnel on the ground responsible for handling and exposing the source. Due to this shielding, the unattenuated field produced by the source was available only within a relatively narrow cone of approximately $30°$. Consequently, the estimated activity could be strongly influenced by the actual flight trajectory of the helicopter over the source, the system's sampling rate, and the start and end points of data acquisition.

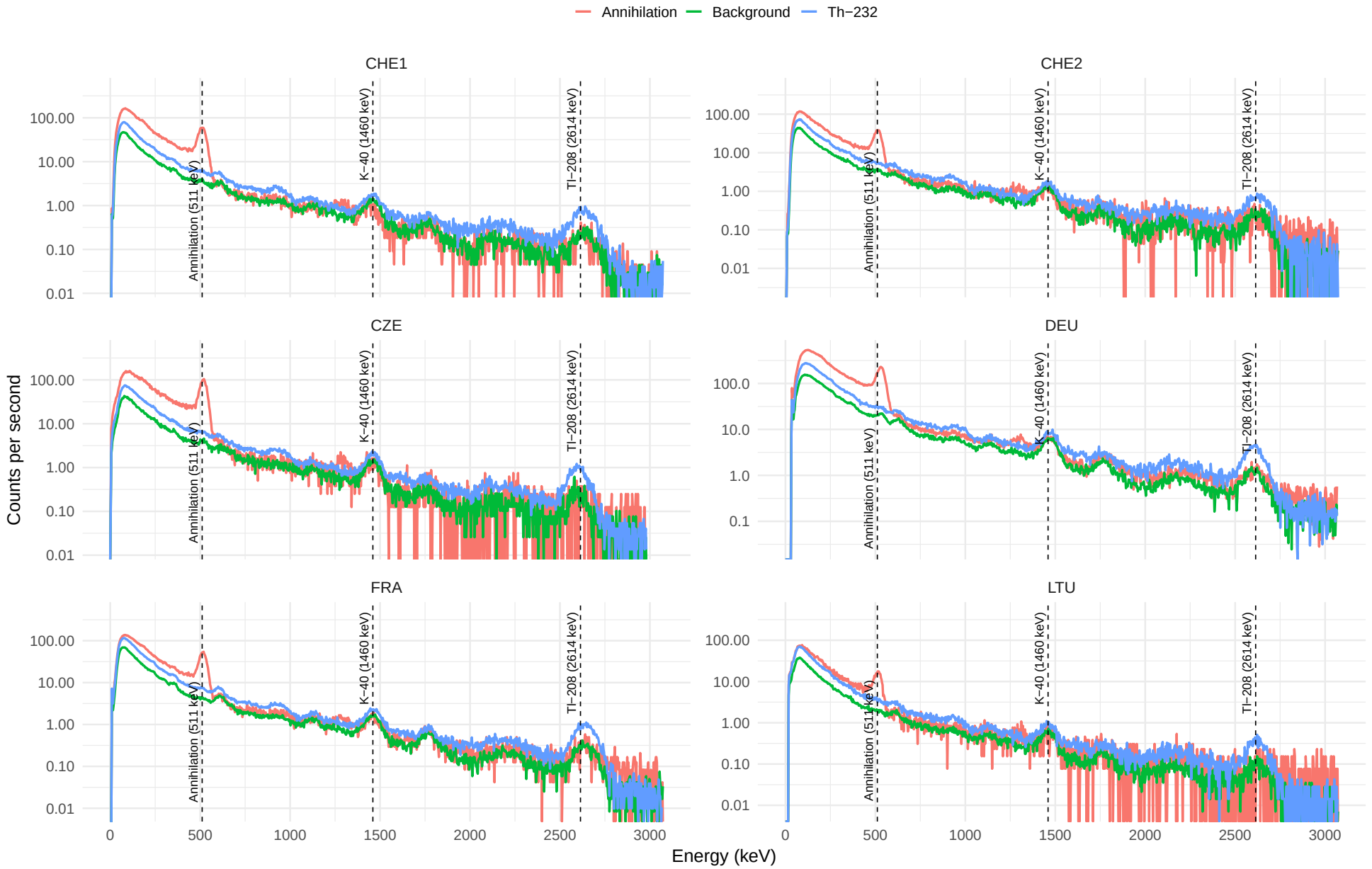

Figure 8.139: Background, annihilation and ^{232}Th spectra of Mission 5A.

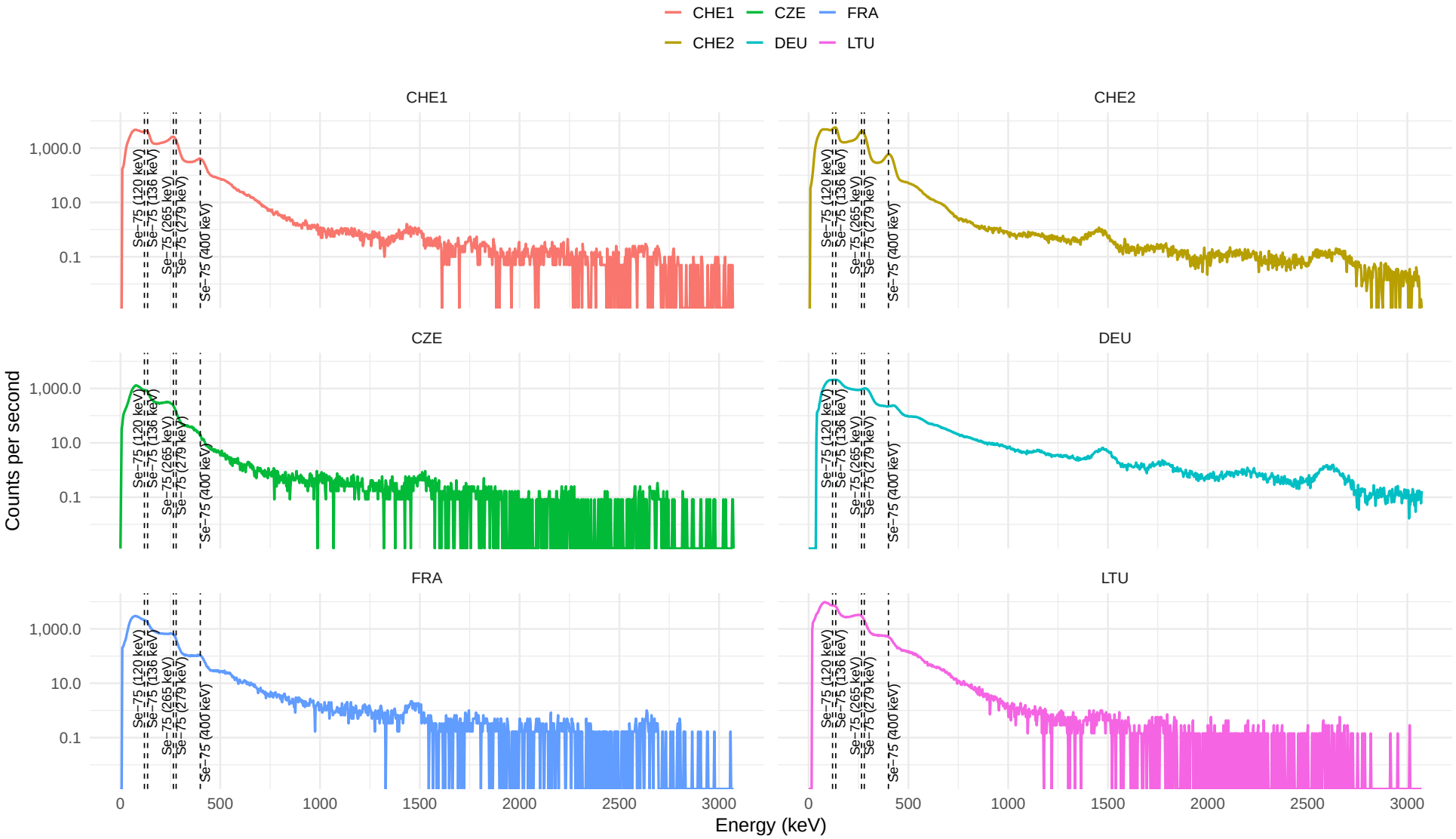

Figure 8.140: Spectra of Mission 5B acquired over the 2.7 TBq ^{75}Se source.

Table 8.7: Activity estimations of ^{75}Se source in Mission 5 B.

Reference Activity [GBq]	2700	
Coordinates	PN 47.528907, PE 8.231452	
	Activity [GBq]	Relative to Reference
CHE1	400	−85 %
CHE1 AGS_CH	n.a.	n.a.
CHE2	2670	−1 %
CHE2 AGS_CH	n.a.	n.a.
CZE	n.a.	n.a.
DEU	3000	11 %
FRA	1000	−63 %
LTU	1800	−33 %

8.6.2 Maps

In this section, the flight paths, the spatial distributions of dose rates and radionuclide activities are presented for the area of the Paul Scherrer Institute, based on the analysis of the Mission 5 dataset. First, the flight paths taken by each team are illustrated. Then, the total ambient dose equivalent rate distribution (DHSR) measured by each team are introduced. Last, the activity maps are presented for ^{238}U, ^{232}Th, and ^{40}K, respectively.

Flight paths

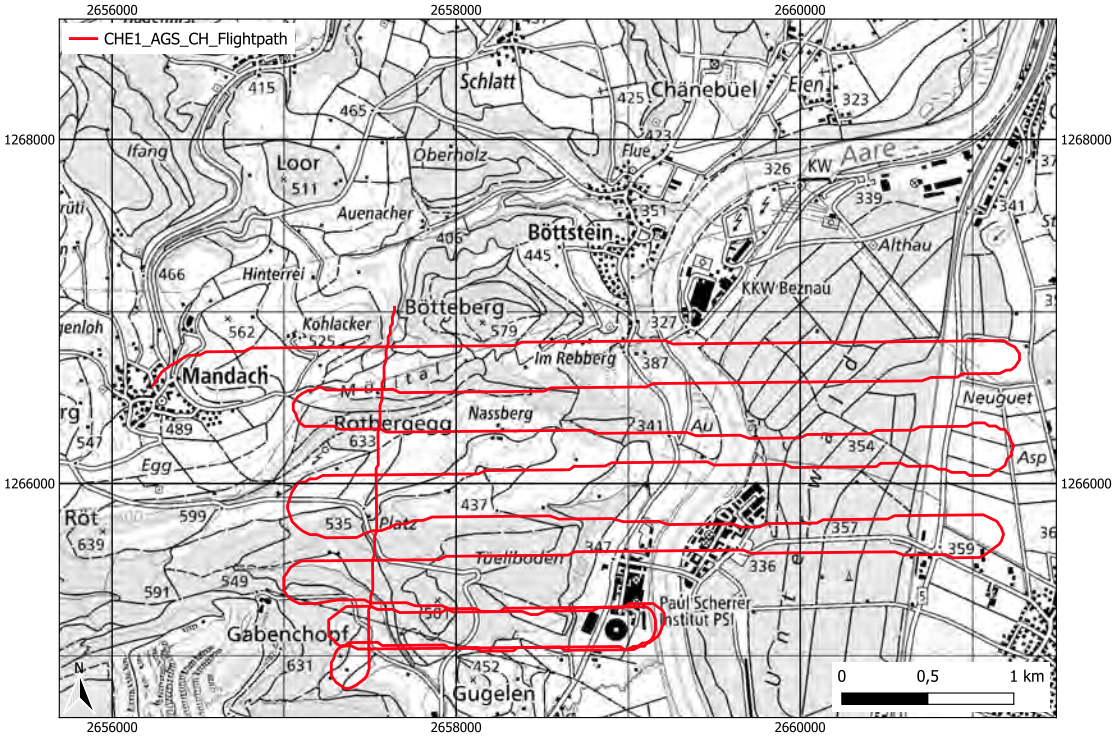

Figure 8.141: The flight path taken at the Mission 5 (MM) area by the CHE1 team. The flight paths are identical for the CHE1 and CHE1_AGS_CH datasets. Geodaten©swisstopo.

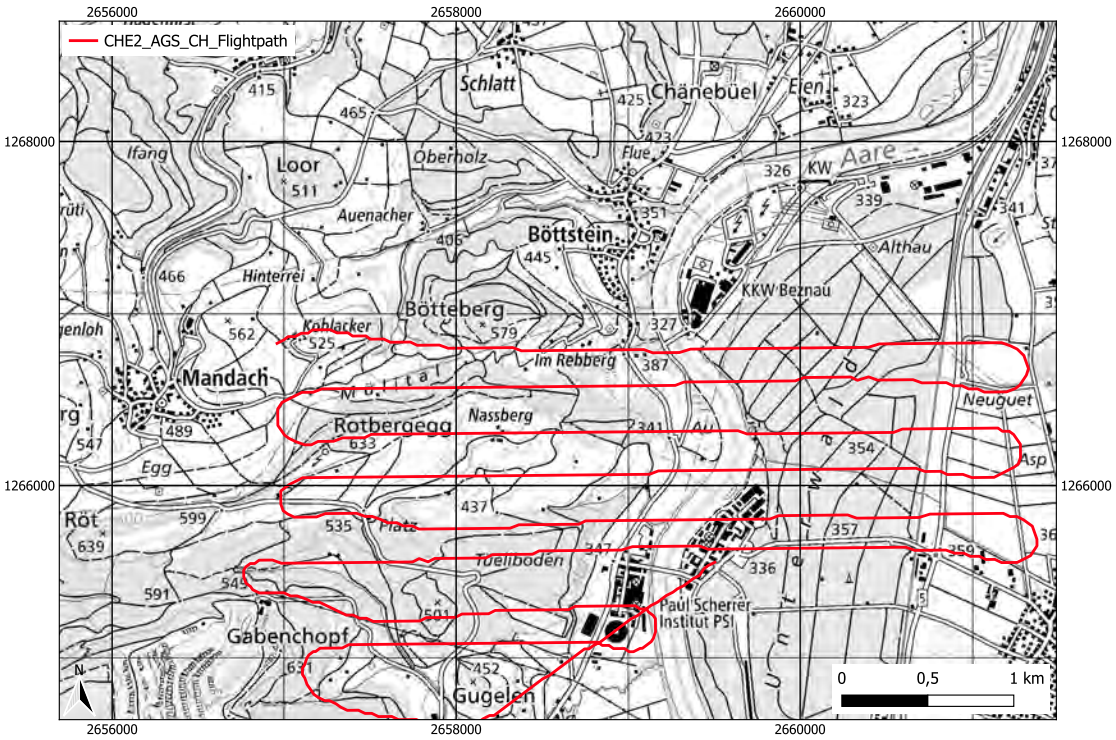

Figure 8.142: The flight path taken at the Mission 5 (MM) area by the CHE2 team. The flight paths are identical for the CHE1 and CHE1_AGS_CH datasets. Geodaten©swisstopo.

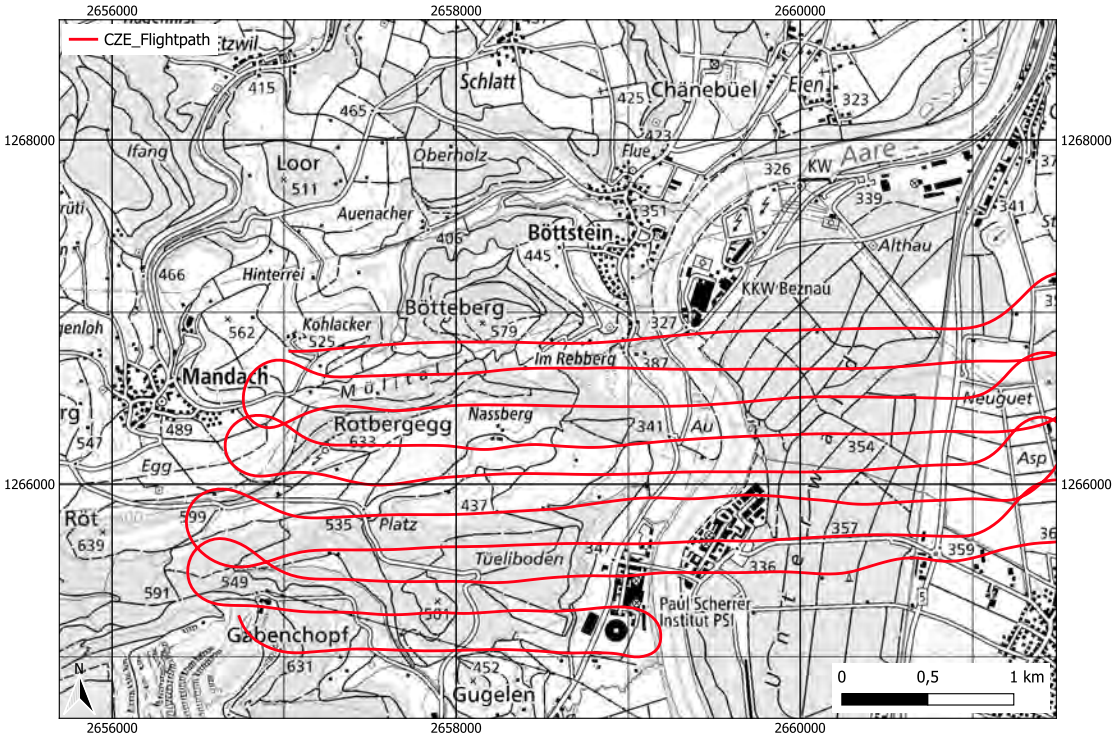

Figure 8.143: The flight path taken at the Mission 5 (MM) area by the CZE team. Geodaten©swisstopo.

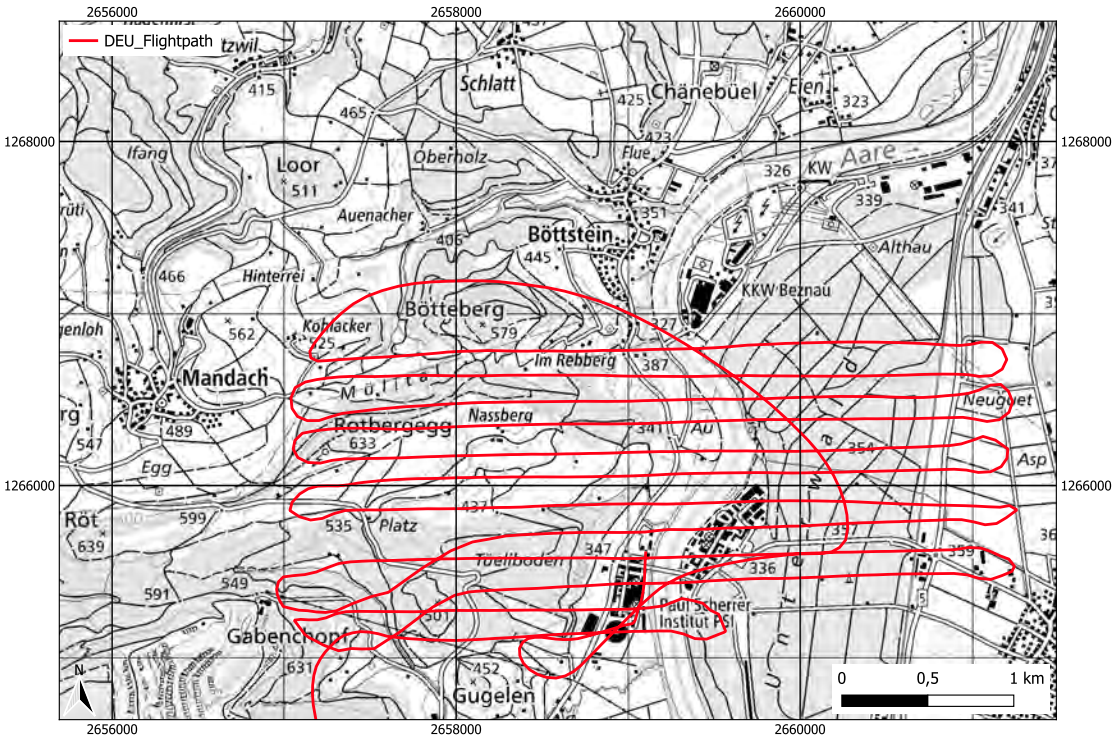

Figure 8.144: The flight path taken at the Mission 5 (MM) area by the DEU team. Geodaten©swisstopo.

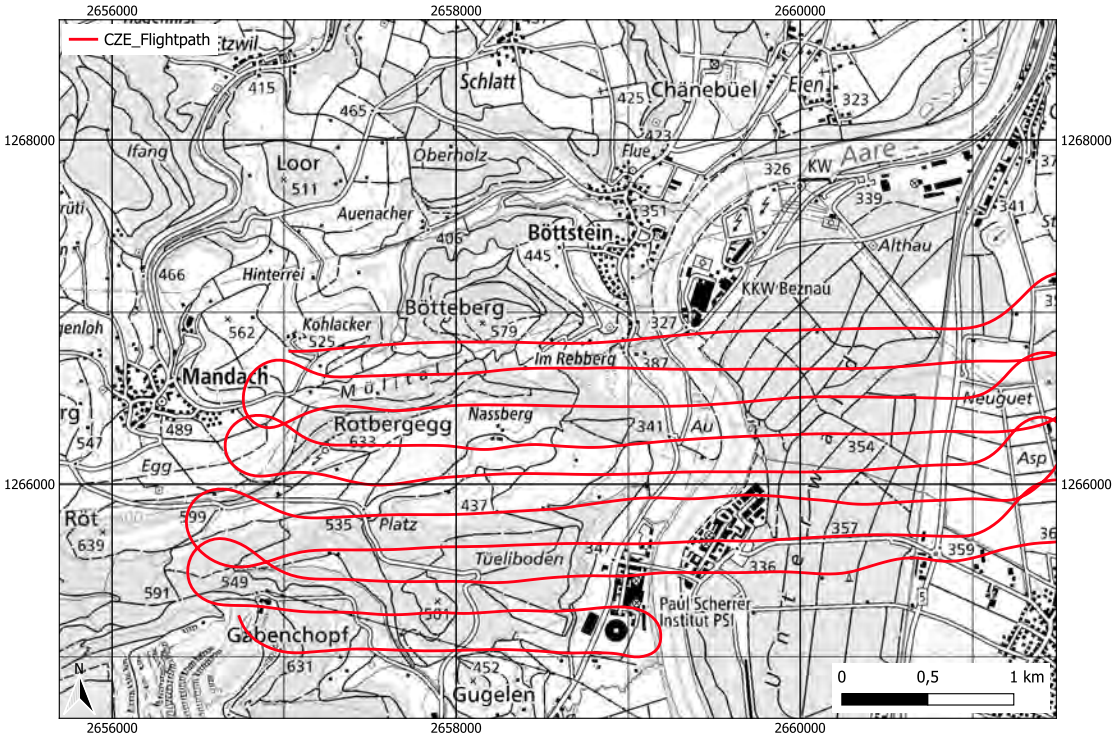

Figure 8.145: The flight path taken at the Mission 5 (MM) area by the FRA team. Geodaten©swisstopo.

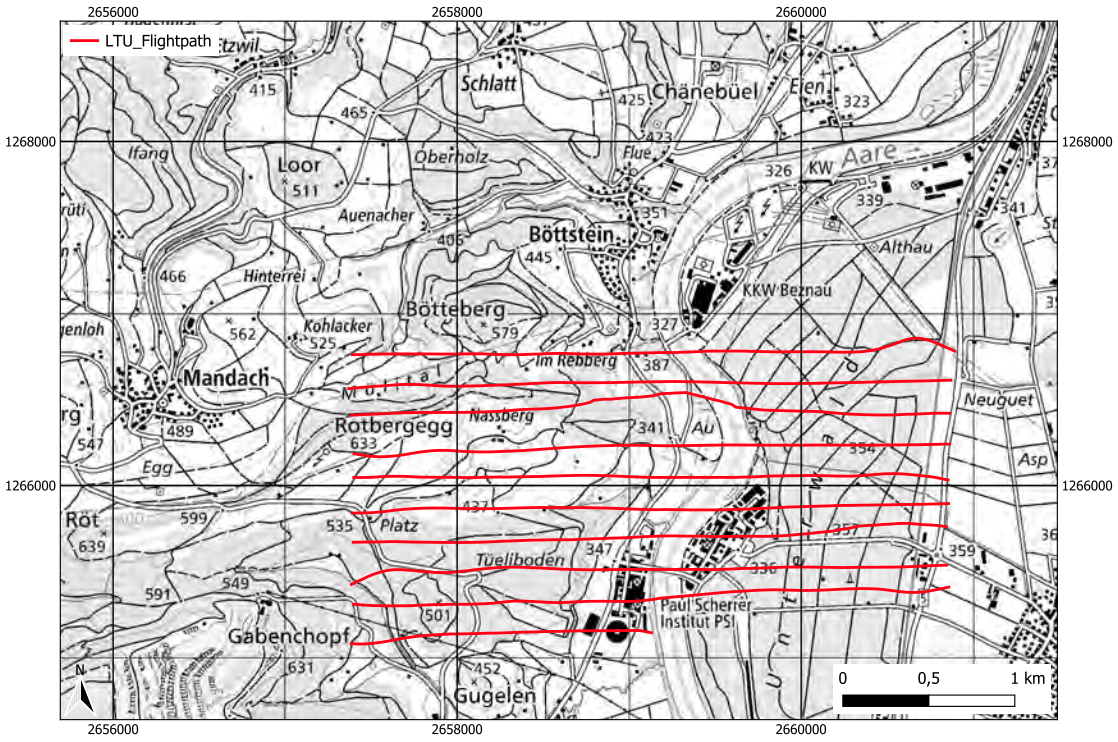

Figure 8.146: The flight path taken at the Mission 5 (MM) area by the LTU team. Geodaten©swisstopo.

Ambient dose equivalent rate

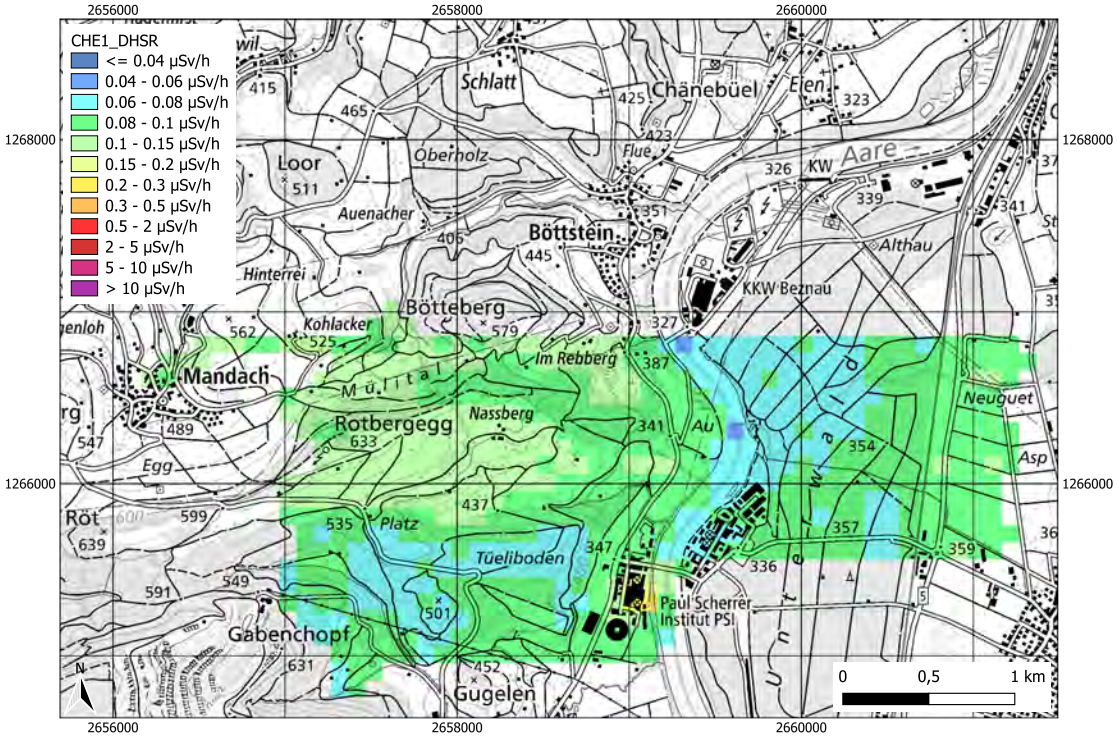

Figure 8.147: Ambient dose equivalent rate distribution (DHSR) measured at the Mission 5 (MM) area by the CHE1 team. Geodaten©swisstopo.

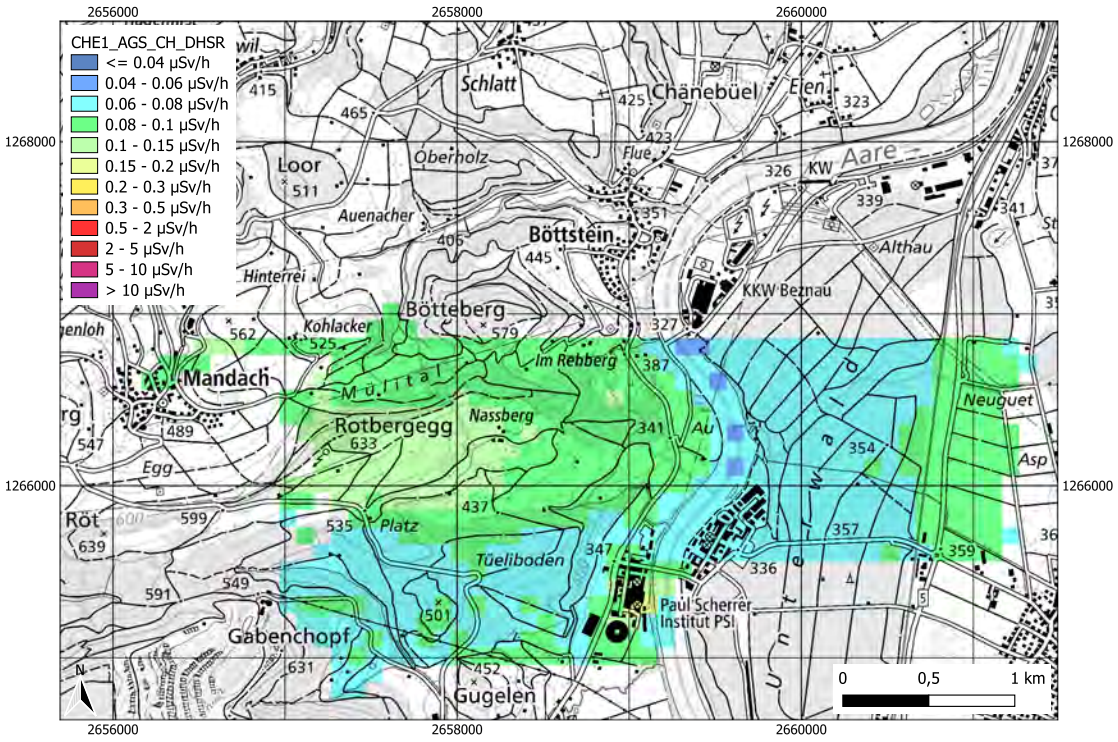

Figure 8.148: Ambient dose equivalent rate distribution (DHSR) measured at the Mission 5 (MM) area by the CHE1 team. Dataset is analysed with AGS_CH. Geodaten©swisstopo.

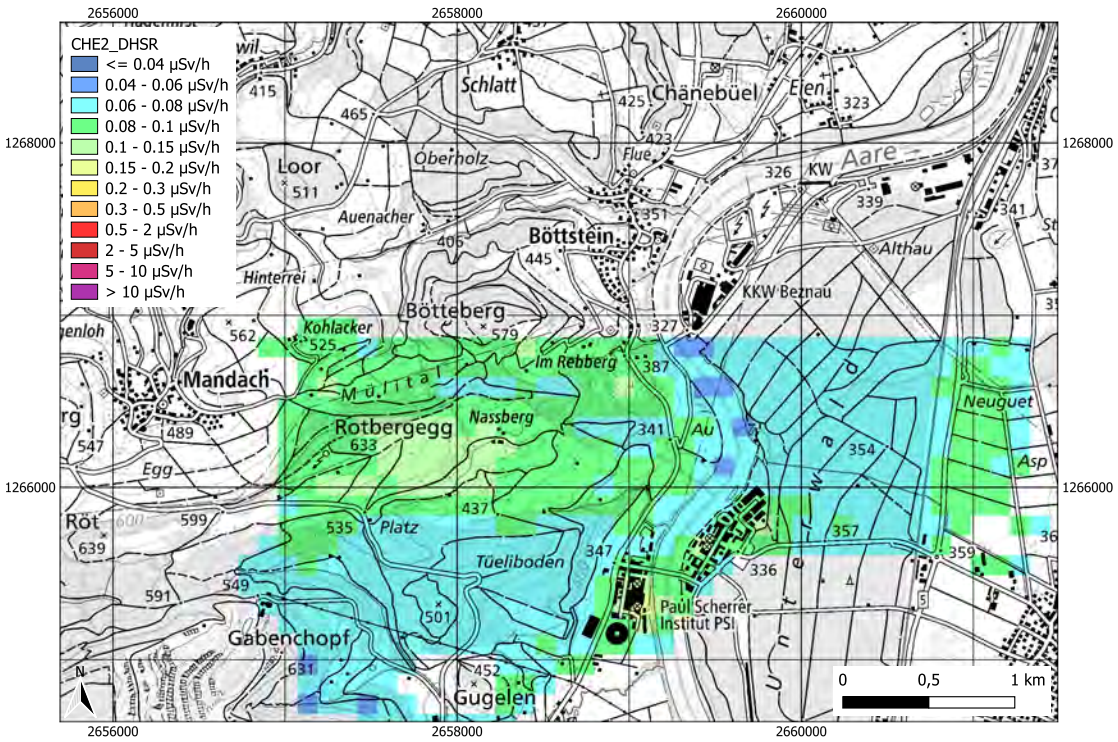

Figure 8.149: Ambient dose equivalent rate distribution (DHSR) measured at the Mission 5 (MM) area by the CHE2 team. Geodaten©swisstopo.

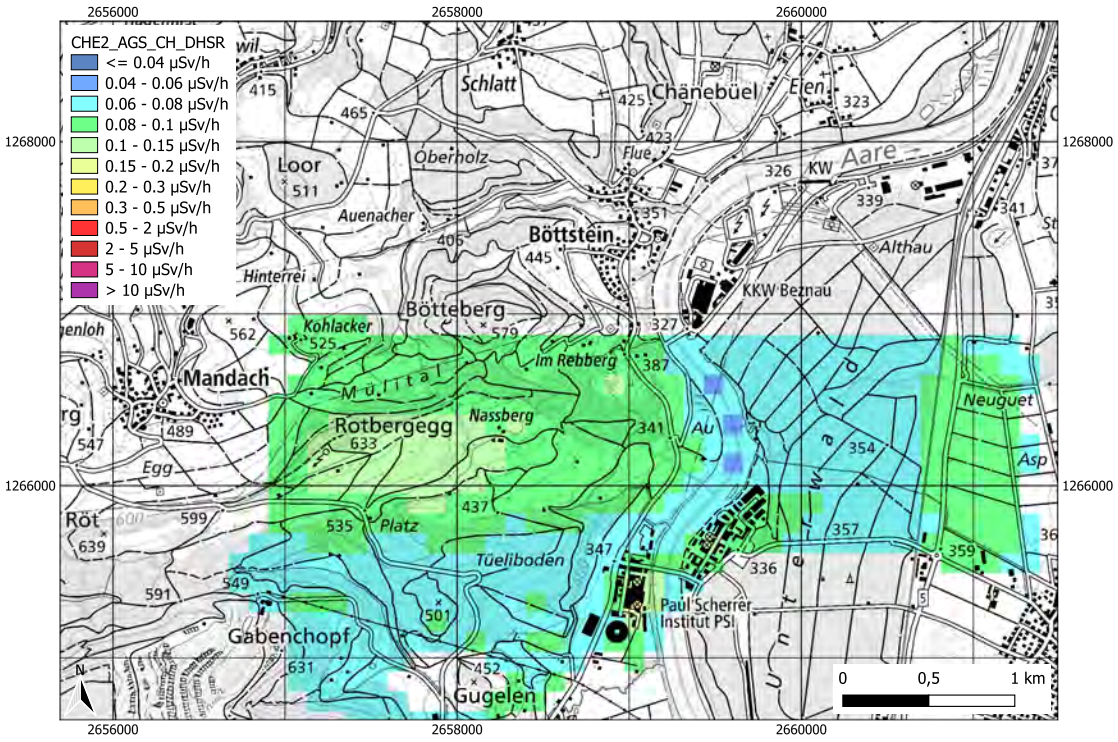

Figure 8.150: Ambient dose equivalent rate distribution (DHSR) measured at the Mission 5 (MM) area by the CHE2 team. Dataset is analysed with AGS_CH. Geodaten©swisstopo.

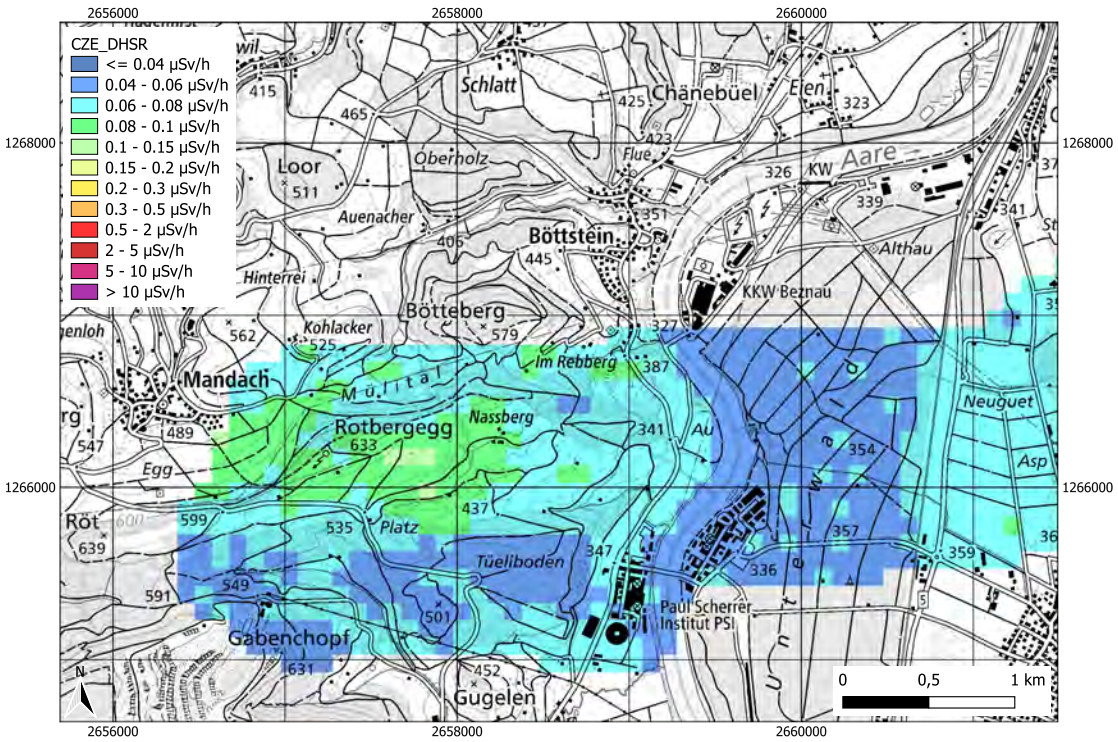

Figure 8.151: Ambient dose equivalent rate distribution (DHSR) measured at the Mission 5 (MM) area by the CZE team. Geodaten©swisstopo.

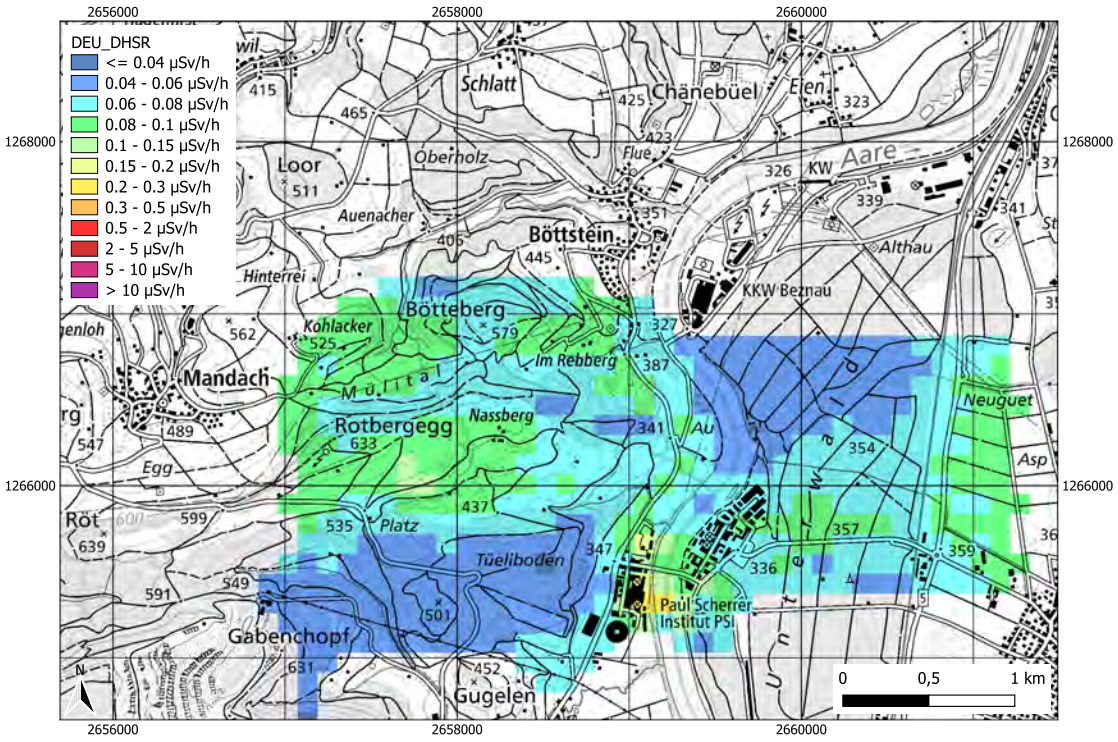

Figure 8.152: Ambient dose equivalent rate distribution (DHSR) measured at the Mission 5 (MM) area by the DEU team. Geodaten©swisstopo.

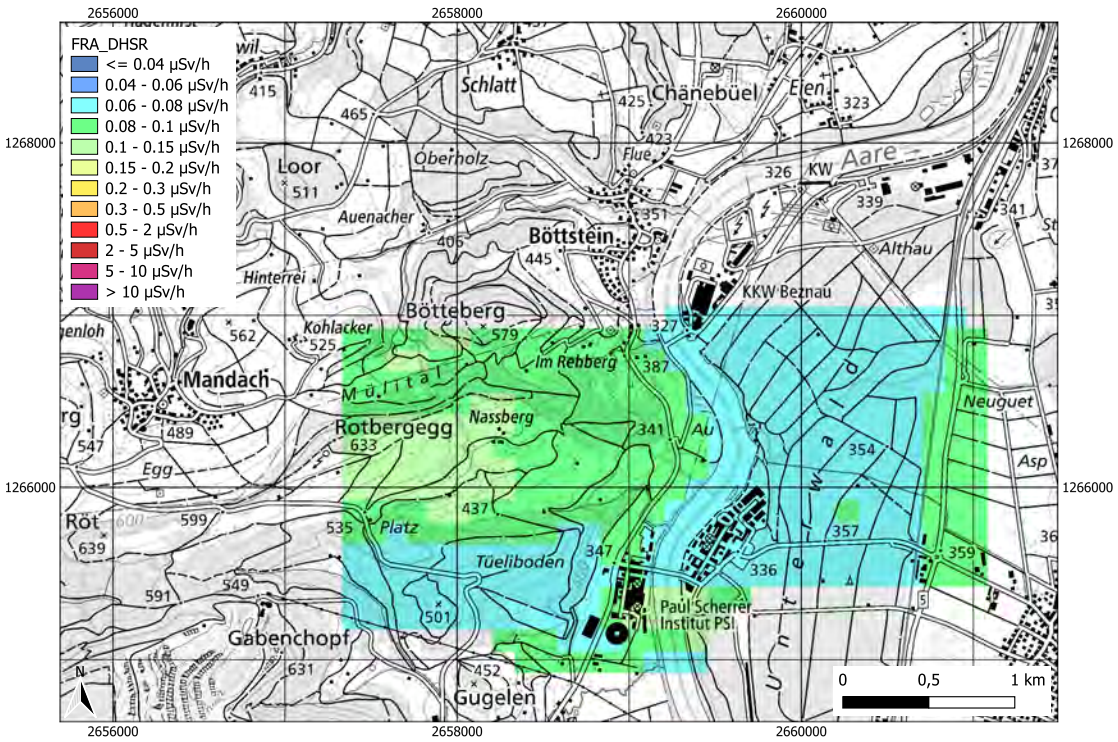

Figure 8.153: Ambient dose equivalent rate distribution (DHSR) measured at the Mission 5 (MM) area by the FRA team. Geodaten©swisstopo.

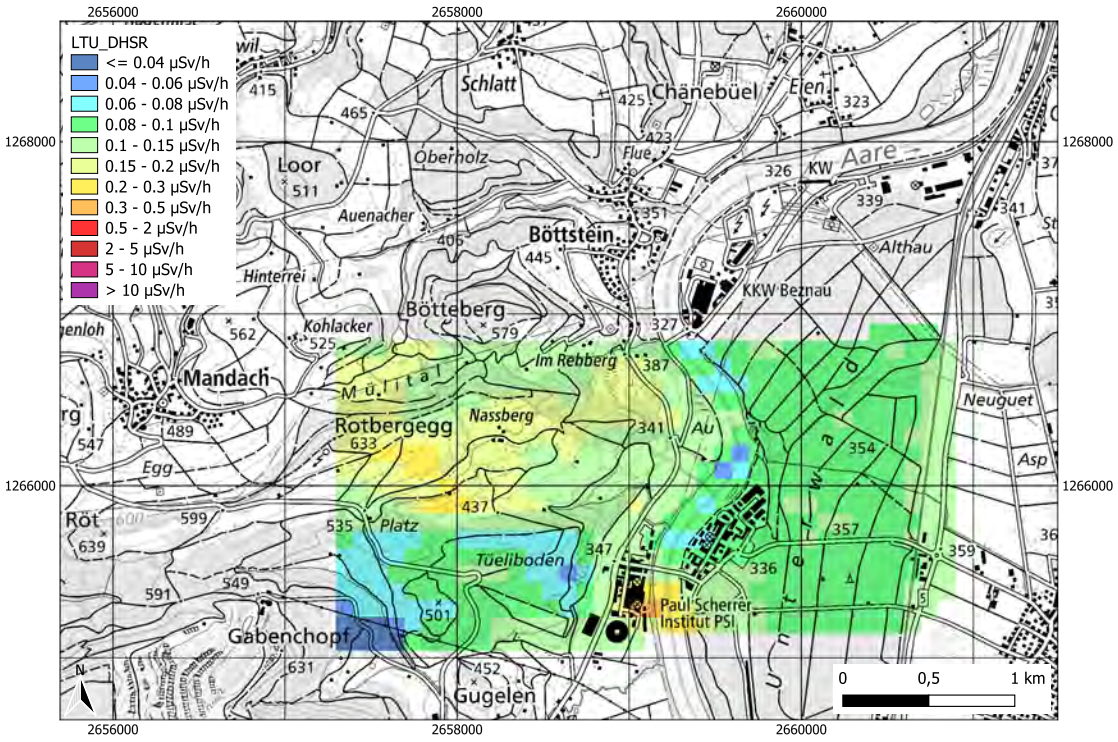

Figure 8.154: Ambient dose equivalent rate distribution (DHSR) measured at the Mission 5 (MM) area by the LTU team. Geodaten©swisstopo.

Activity concentration distribution of ^{232}Th

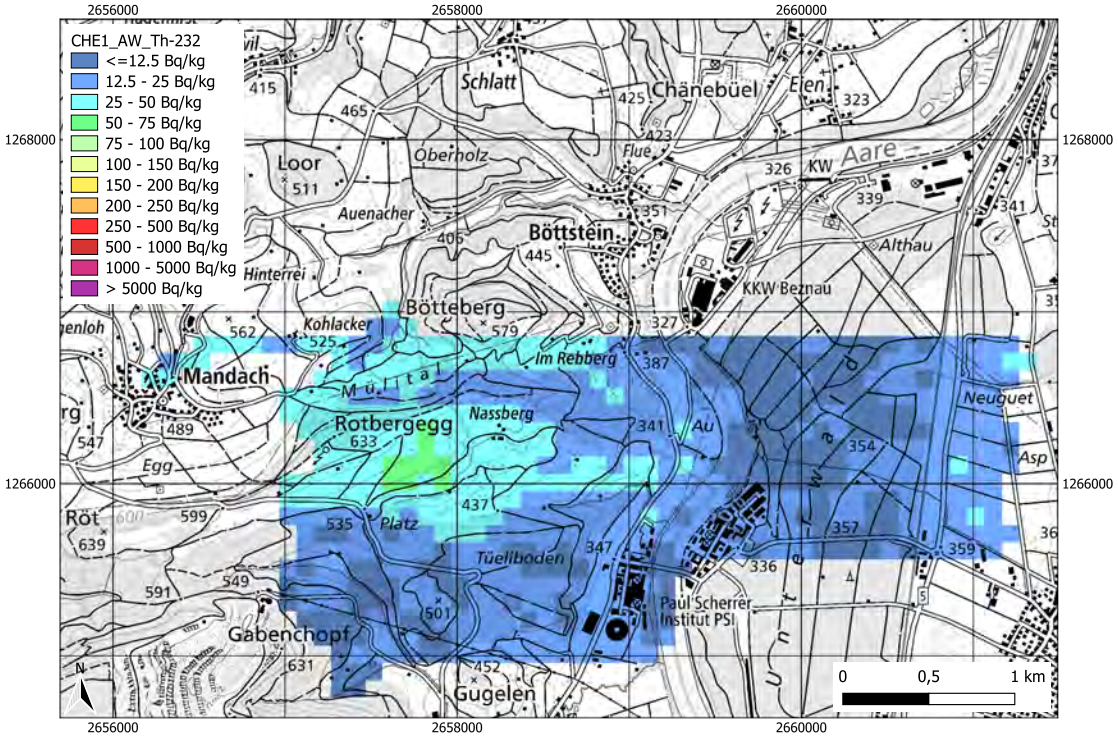

Figure 8.155: Activity concentration of ^{232}Th measured at the Mission 5 (MM) area by the CHE1 team. Geodaten©swisstopo.

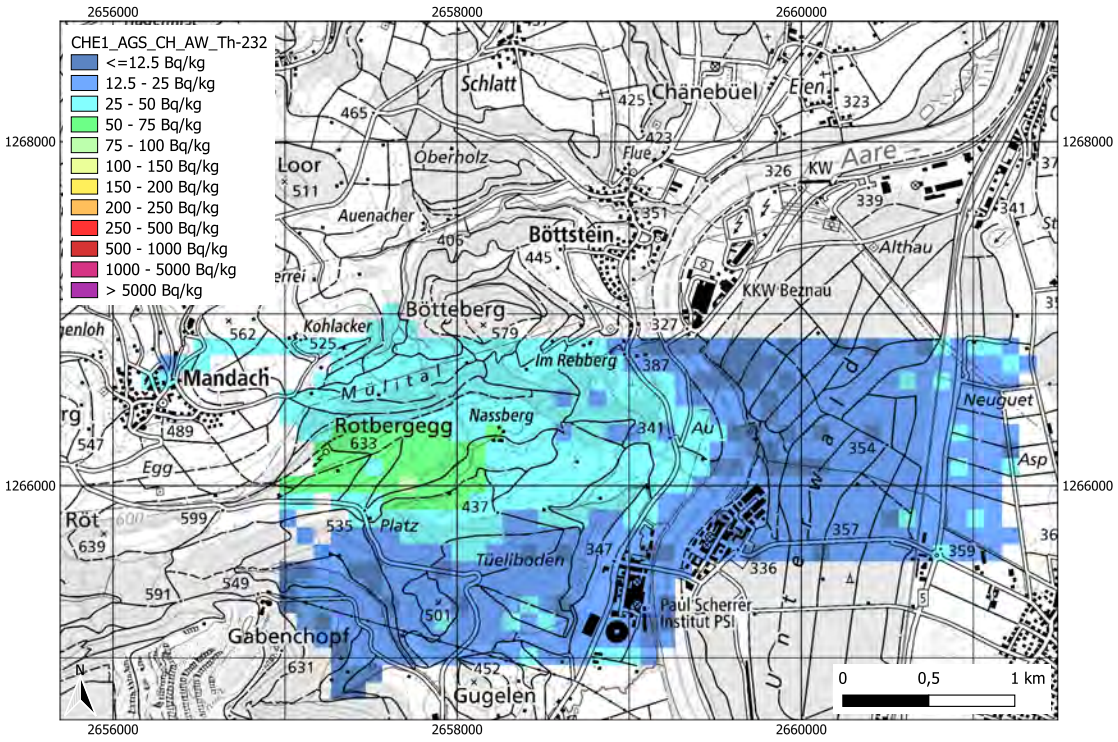

Figure 8.156: Activity concentration of ^{232}Th measured at the Mission 5 (MM) area by the CHE1 team. Dataset is analysed with AGS_CH. Geodaten©swisstopo.

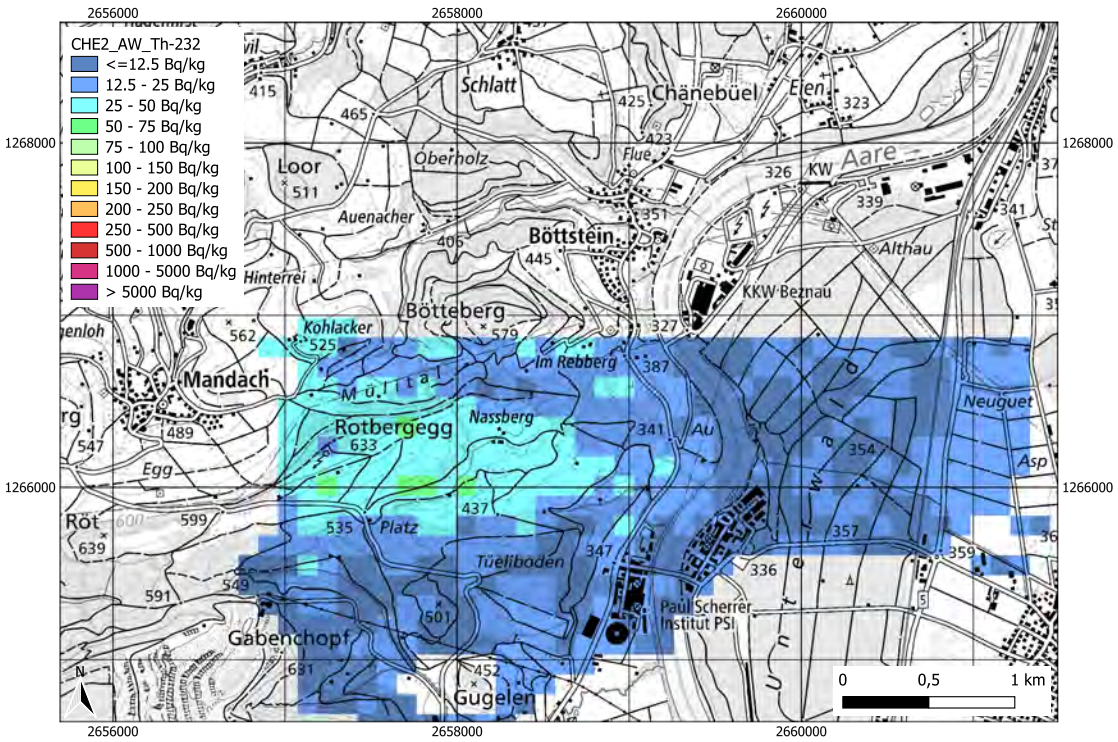

Figure 8.157: Activity concentration of ^{232}Th measured at the Mission 5 (MM) area by the CHE2 team. Geodaten©swisstopo.

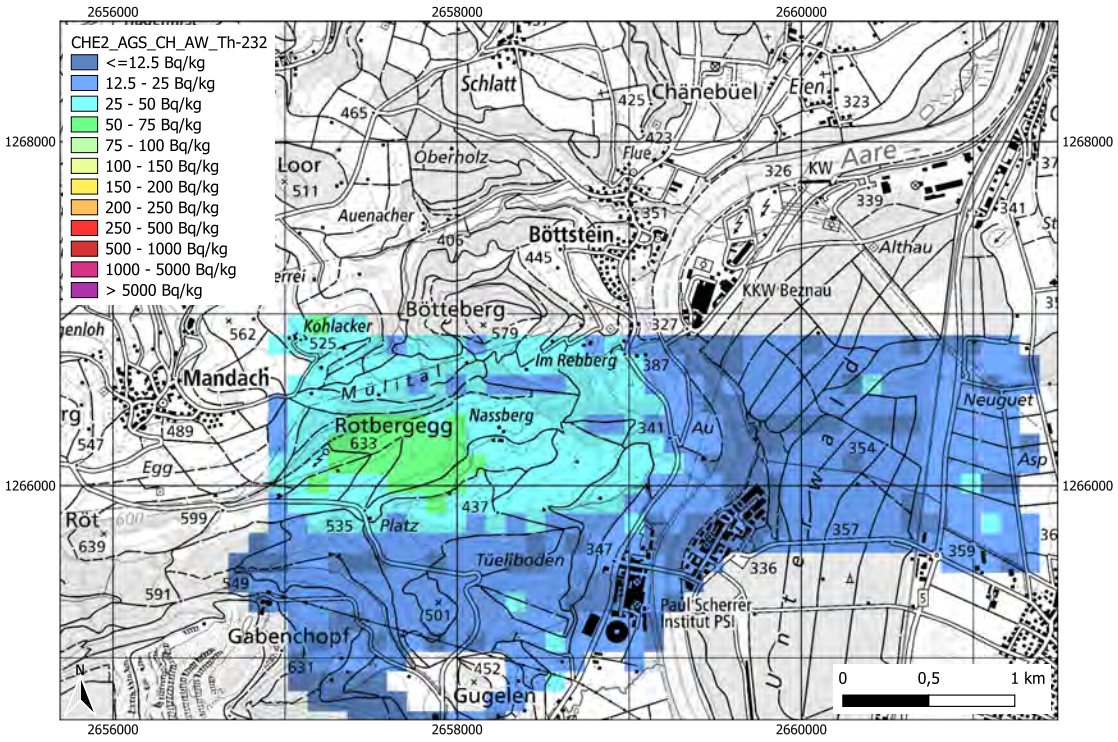

Figure 8.158: Activity concentration of ^{232}Th measured at the Mission 5 (MM) area by the CHE2 team. Dataset is analysed with AGS_CH. Geodaten©swisstopo.

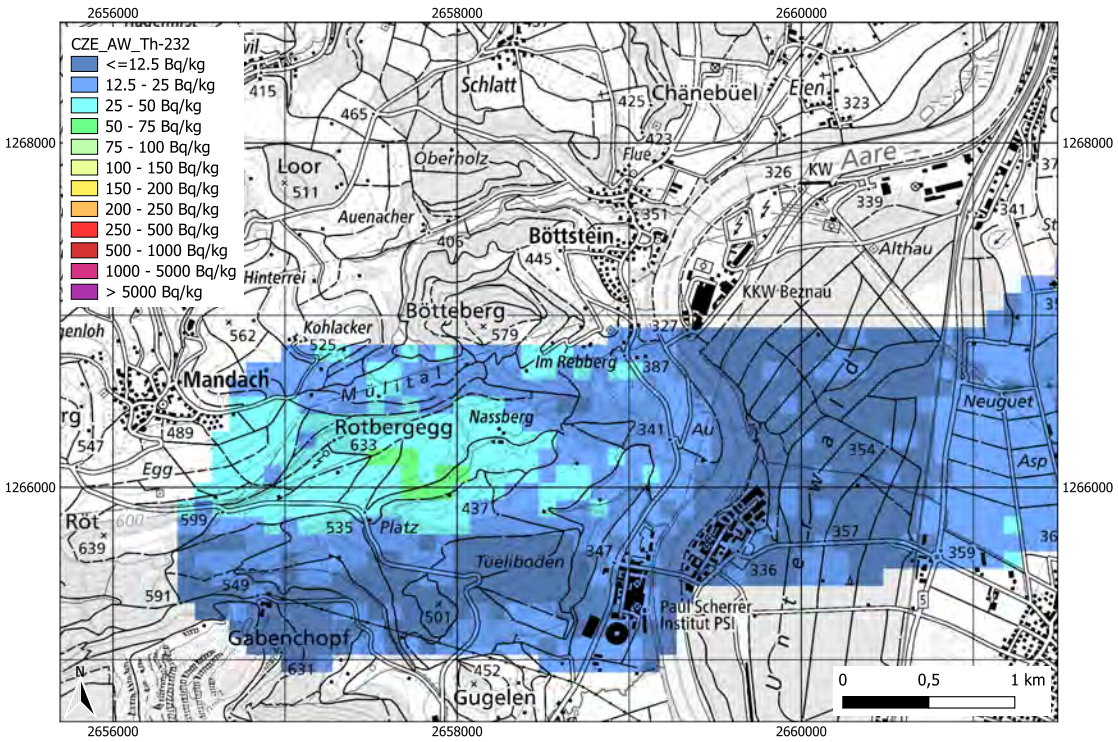

Figure 8.159: Activity concentration of ^{232}Th measured at the Mission 5 (MM) area by the CZE team. Geodaten©swisstopo.

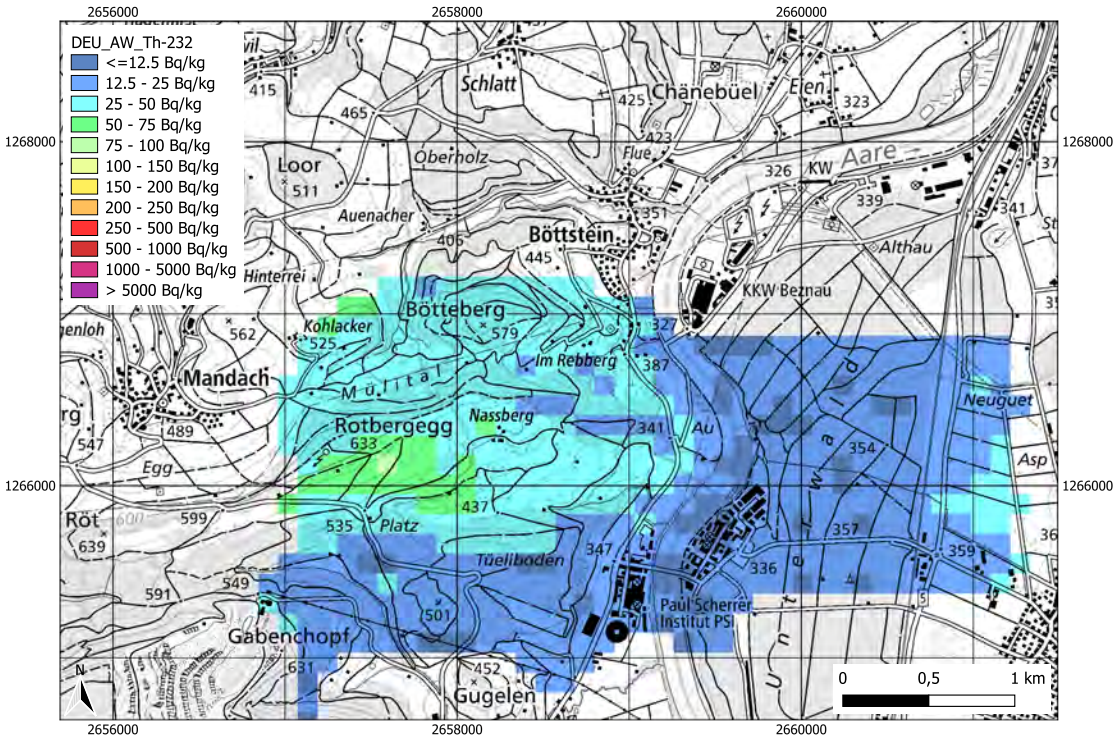

Figure 8.160: Activity concentration of ^{232}Th measured at the Mission 5 (MM) area by the DEU team. Geodaten©swisstopo.

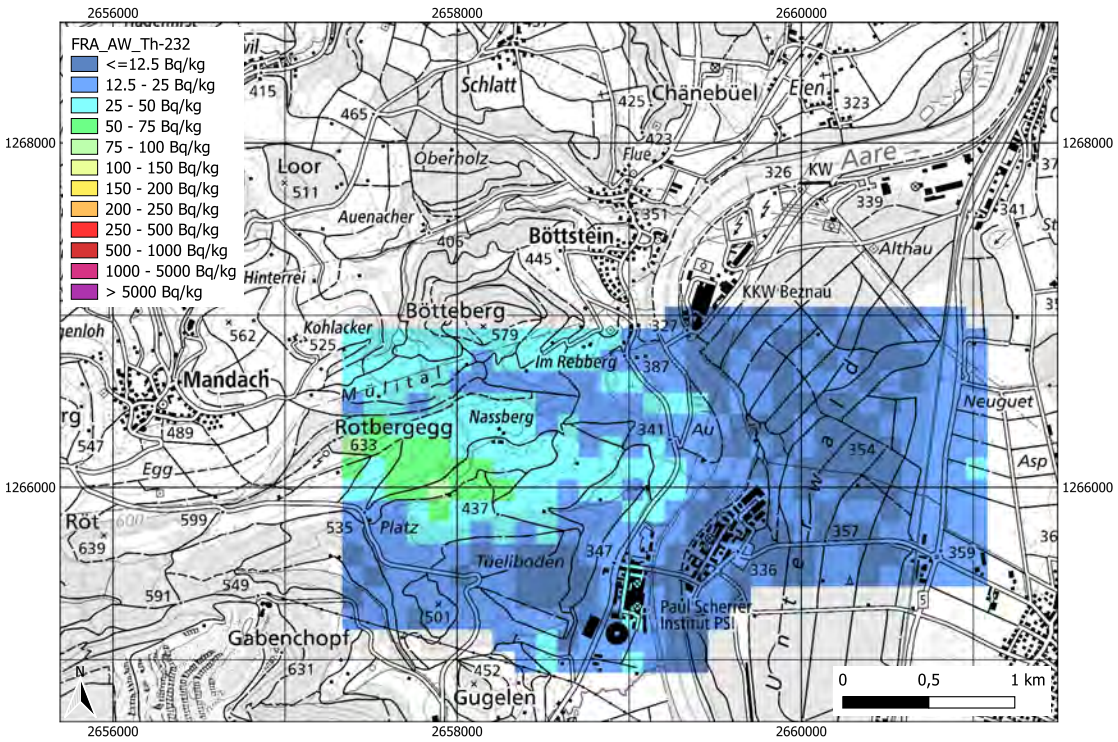

Figure 8.161: Activity concentration of ^{232}Th measured at the Mission 5 (MM) area by the FRA team. Geodaten©swisstopo.

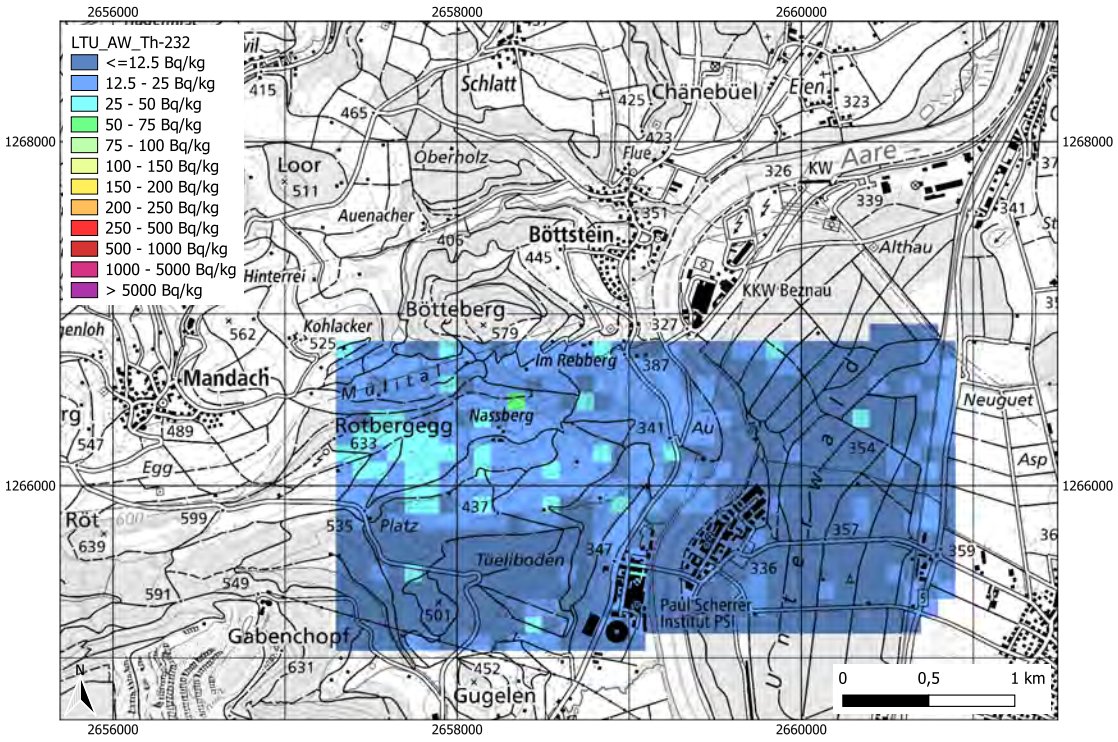

Figure 8.162: Activity concentration of ^{232}Th measured at the Mission 5 (MM) area by the LTU team. Geodaten©swisstopo.

Activity concentration distribution of ^{238}U

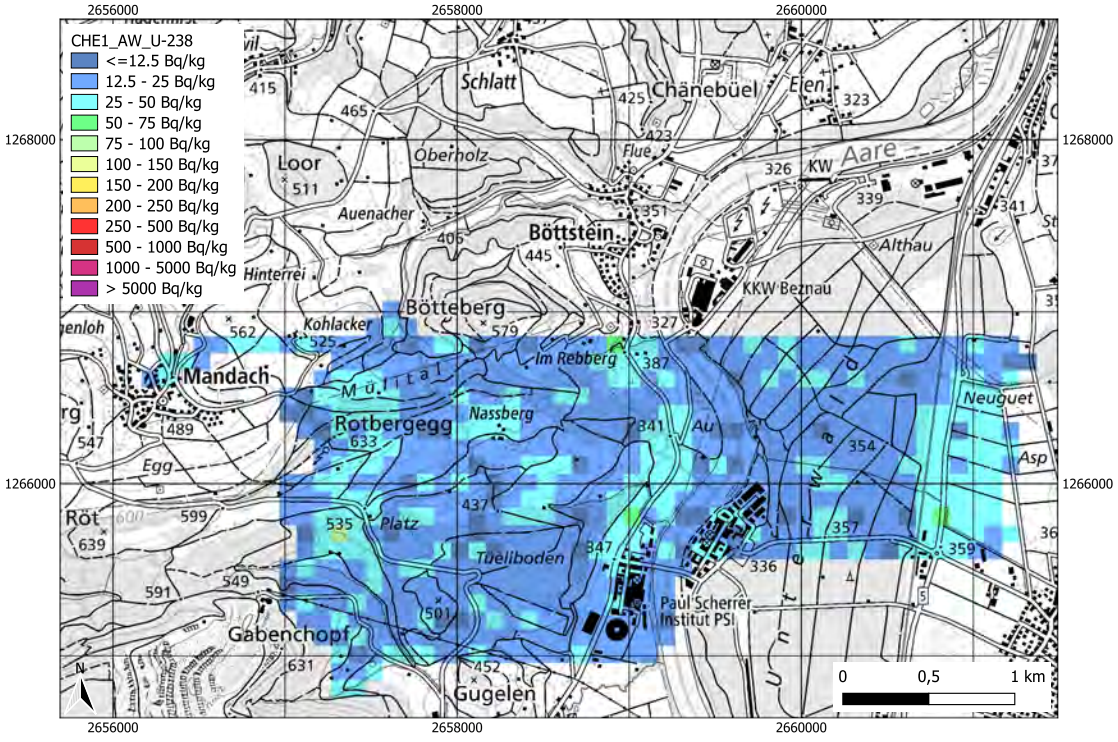

Figure 8.163: Activity concentration of ^{238}U measured at the Mission 5 (MM) area by the CHE1 team. Geodaten©swisstopo.

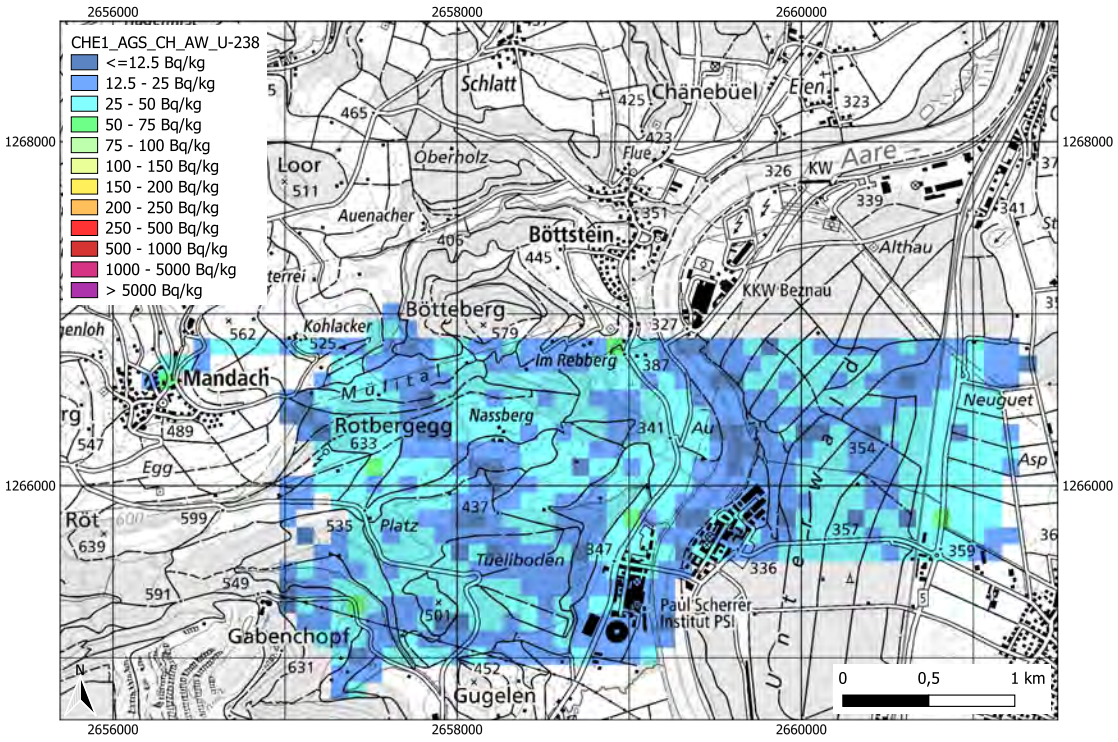

Figure 8.164: Activity concentration of ^{238}U measured at the Mission 5 (MM) area by the CHE1 team. Dataset is analysed with AGS_CH. Geodaten©swisstopo.

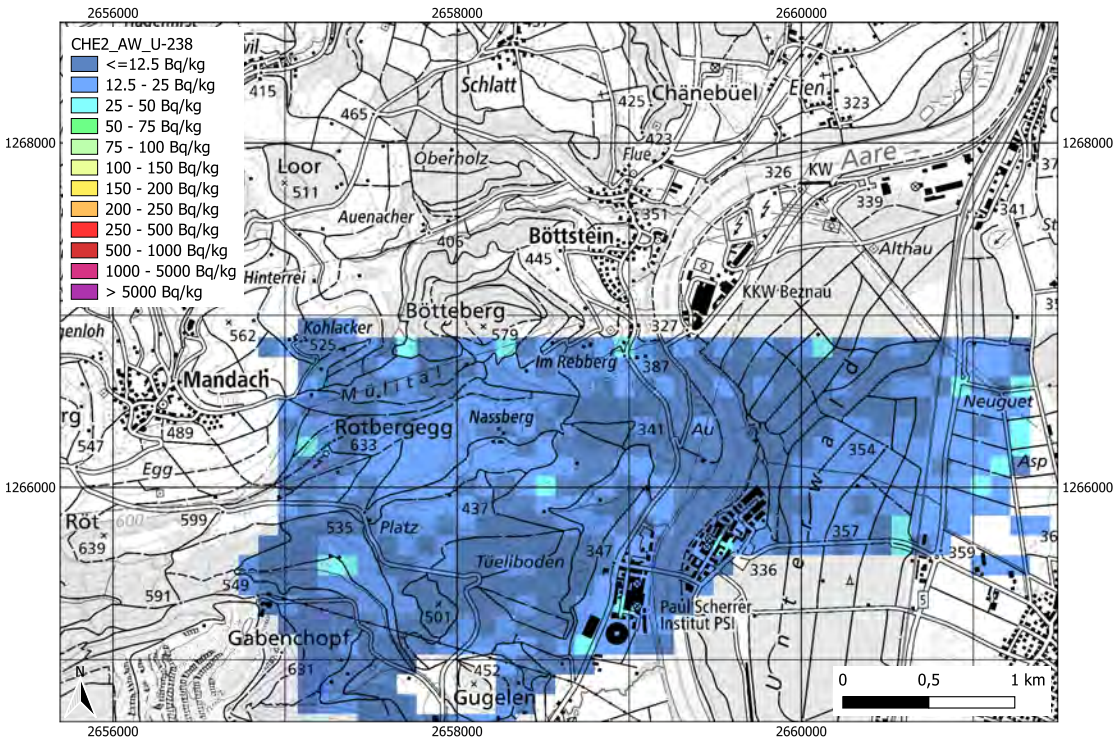

Figure 8.165: Activity concentration of ^{238}U measured at the Mission 5 (MM) area by the CHE2 team. Geodaten©swisstopo.

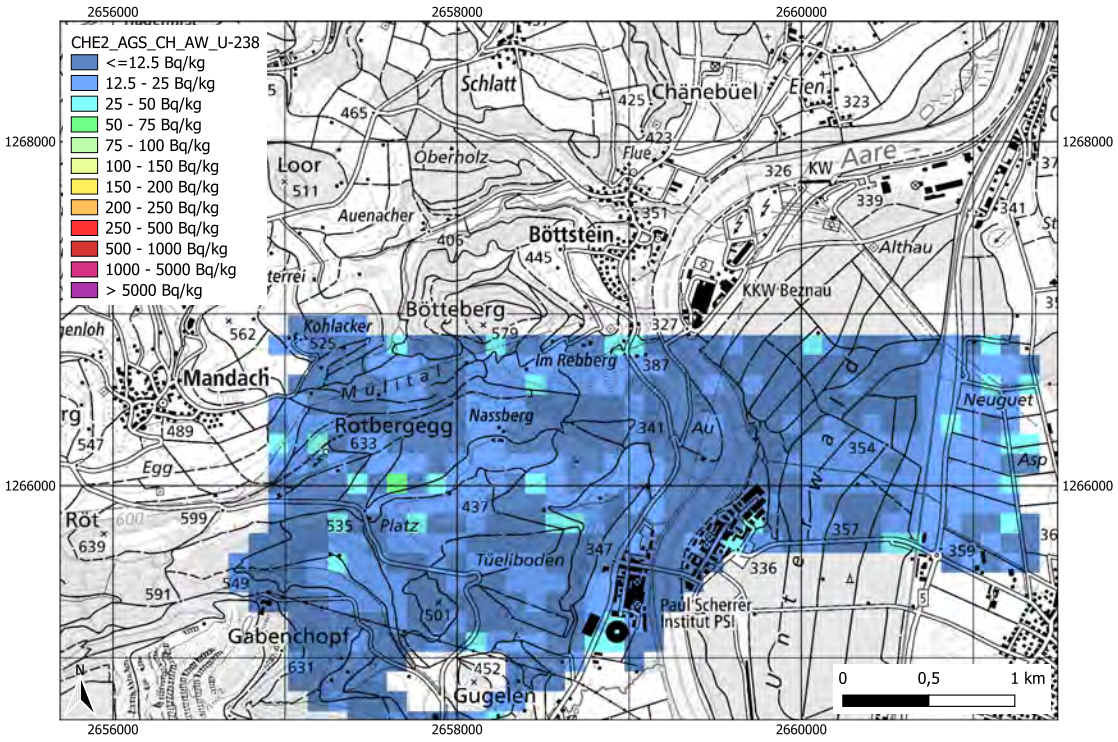

Figure 8.166: Activity concentration of ^{238}U measured at the Mission 5 (MM) area by the CHE2 team. Dataset is analysed with AGS_CH. Geodaten©swisstopo.

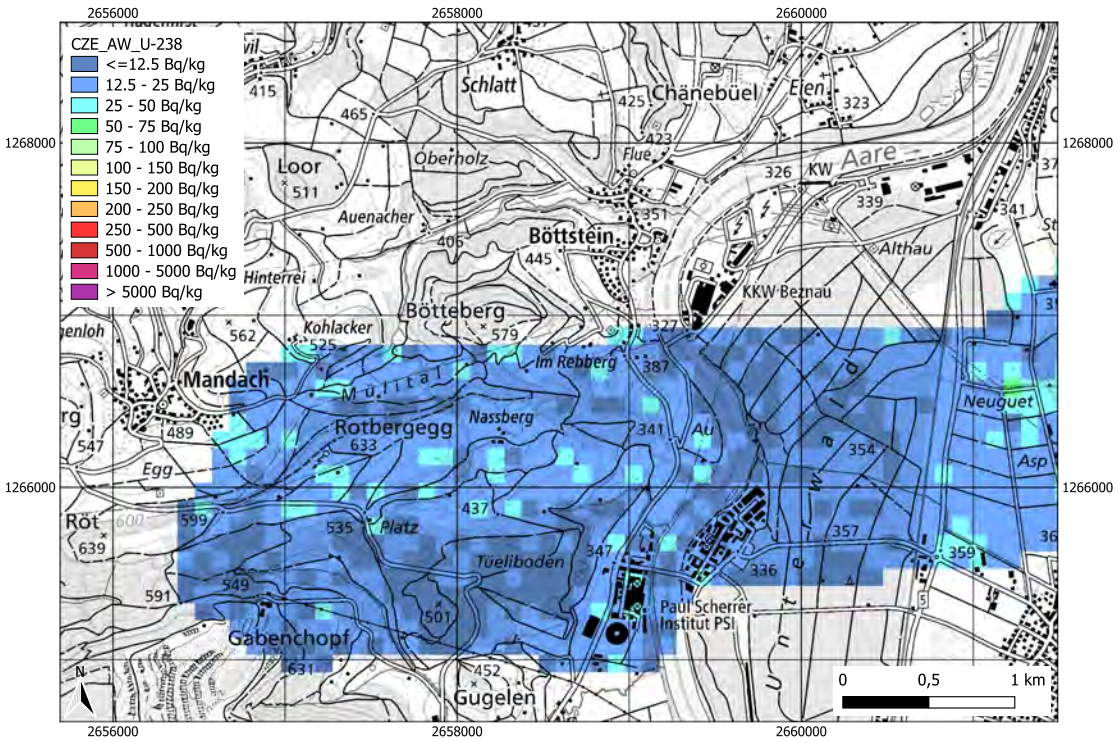

Figure 8.167: Activity concentration of ^{238}U measured at the Mission 5 (MM) area by the CZE team. Geodaten©swisstopo.

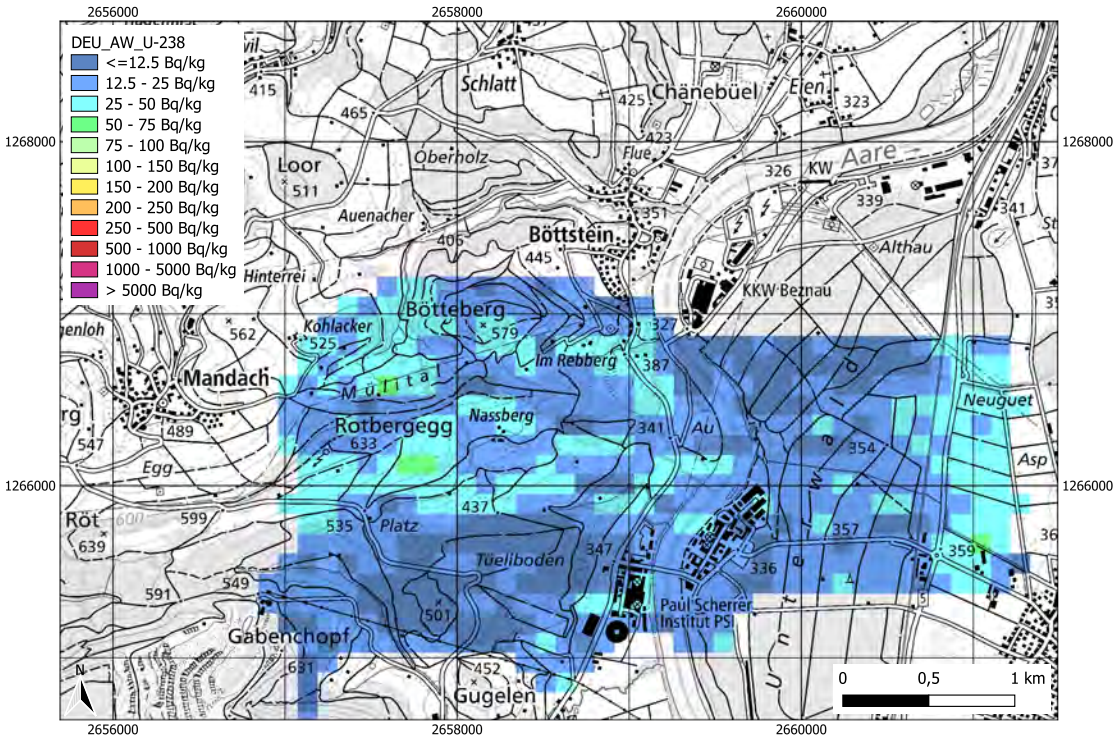

Figure 8.168: Activity concentration of ^{238}U measured at the Mission 5 (MM) area by the DEU team. Geodaten©swisstopo.

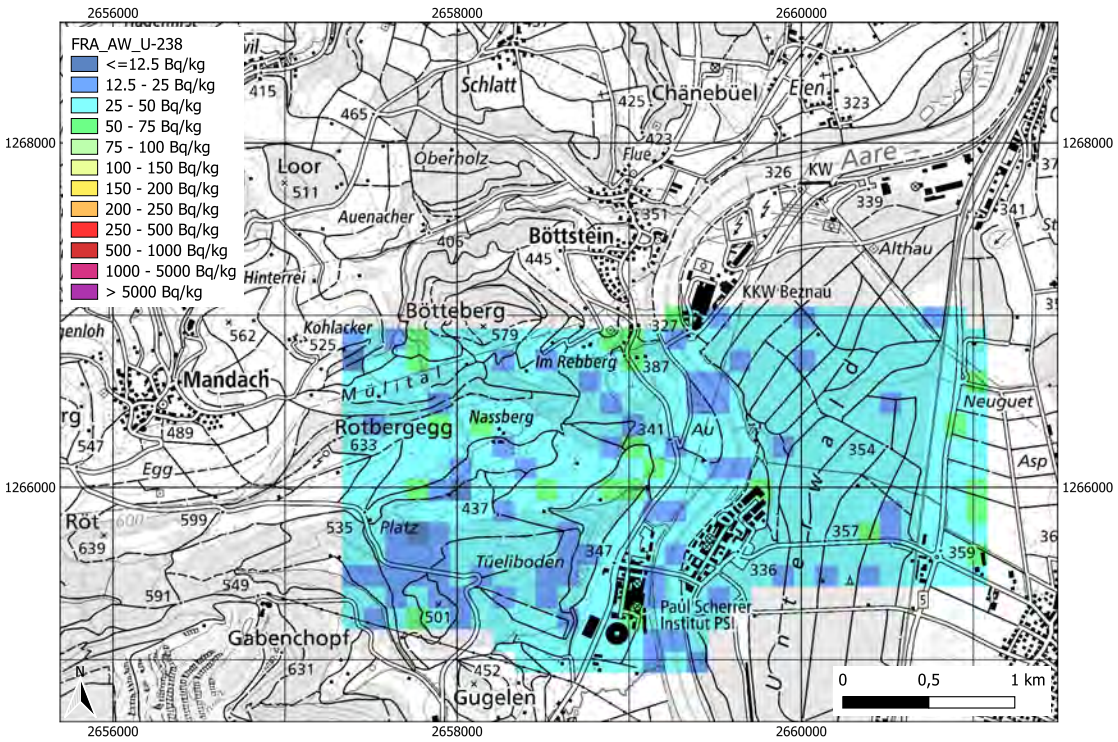

Figure 8.169: Activity concentration of ^{238}U measured at the Mission 5 (MM) area by the FRA team. Geodaten©swisstopo.

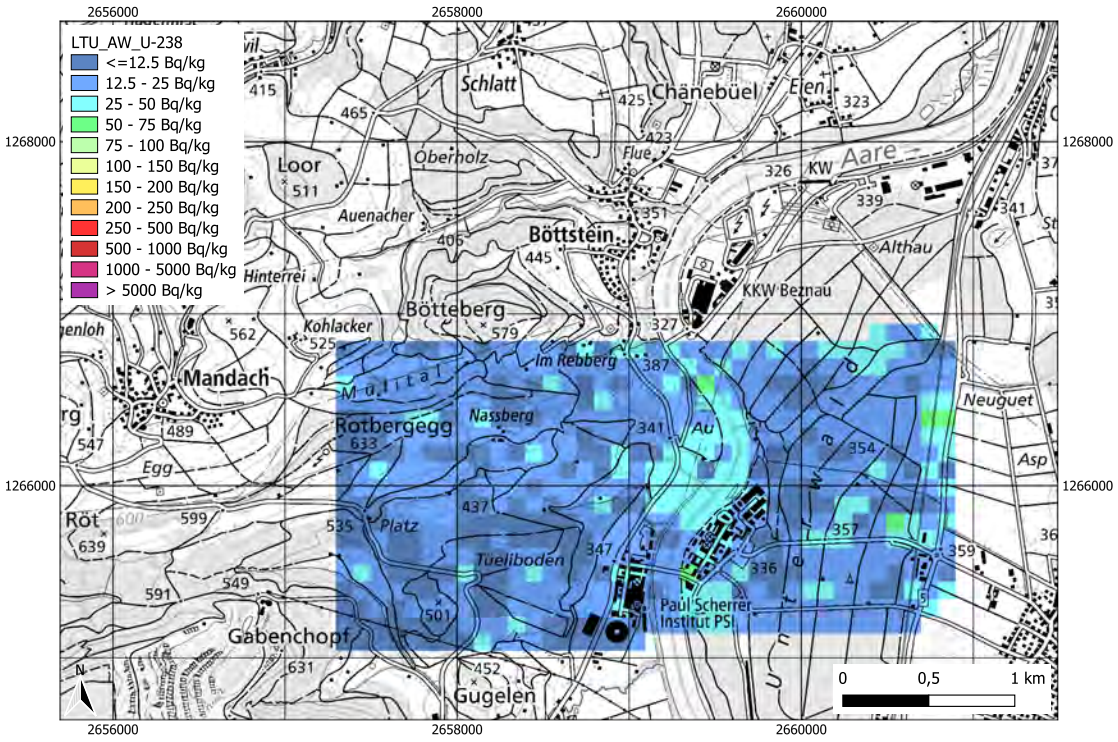

Figure 8.170: Activity concentration of ^{238}U measured at the Mission 5 (MM) area by the LTU team. Geodaten©swisstopo.

Activity concentration distribution of ^{40}K

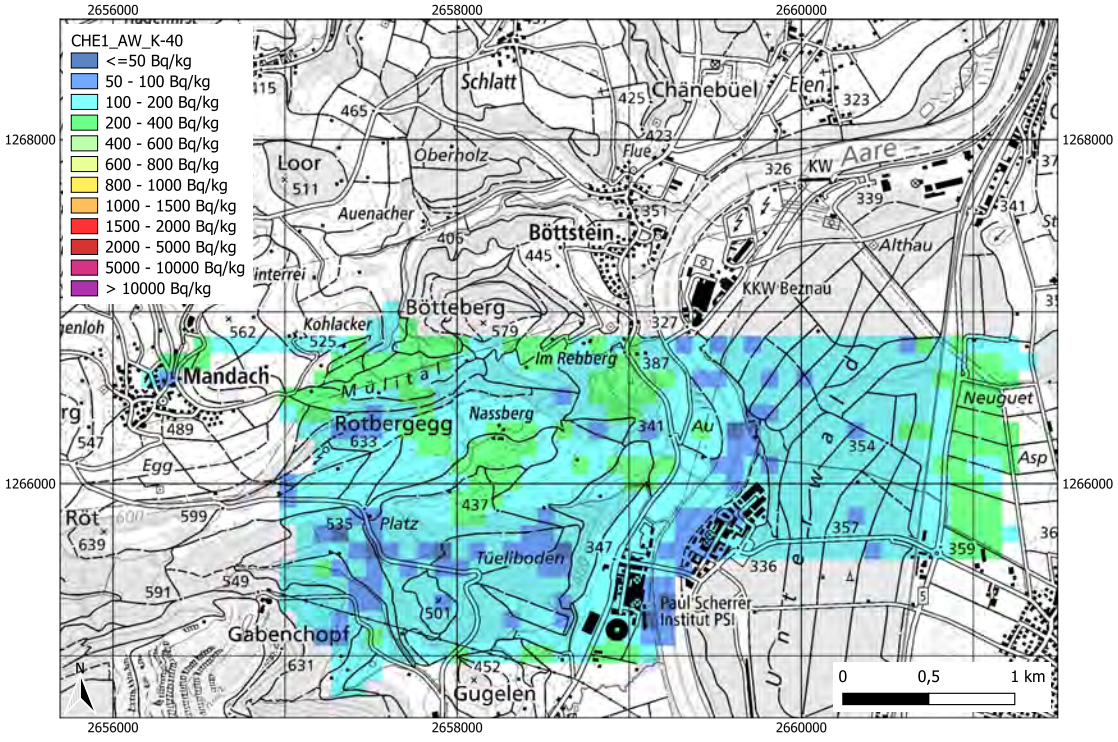

Figure 8.171: Activity concentration of ^{40}K measured at the Mission 5 (MM) area by the CHE1 team. Geodaten©swisstopo.

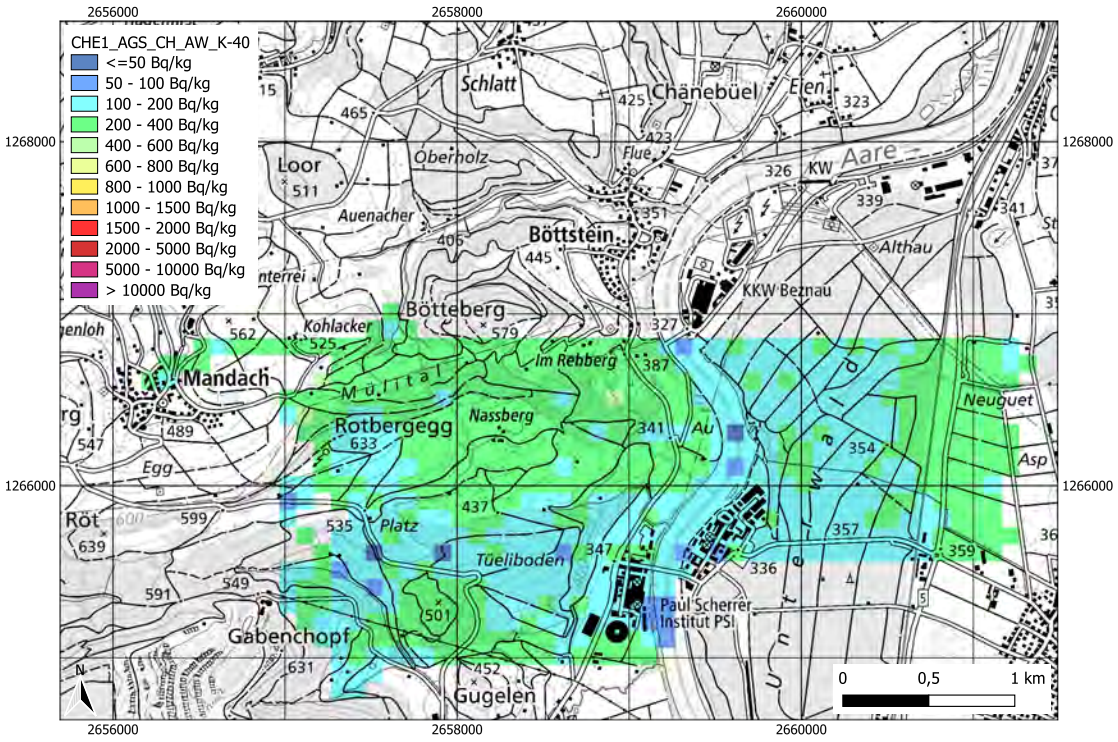

Figure 8.172: Activity concentration of ^{40}K measured at the Mission 5 (MM) area by the CHE1 team. Dataset is analysed with AGS_CH. Geodaten©swisstopo.

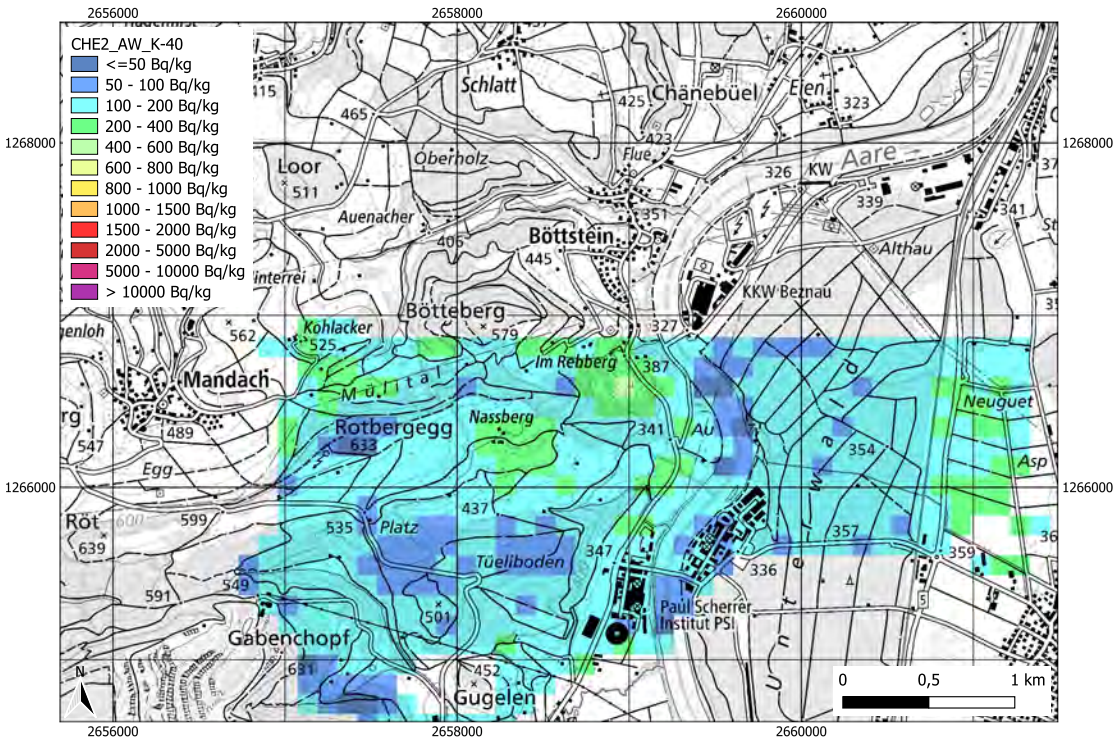

Figure 8.173: Activity concentration of ^{40}K measured at the Mission 5 (MM) area by the CHE2 team. Geodaten©swisstopo.

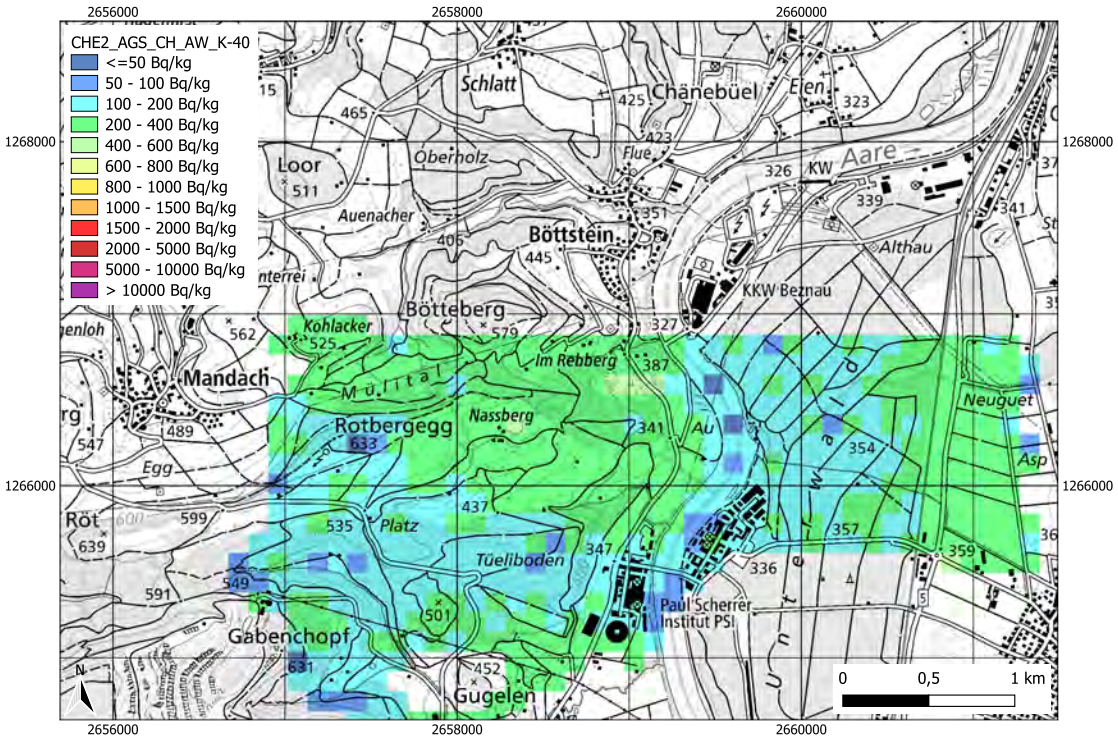

Figure 8.174: Activity concentration of ^{40}K measured at the Mission 5 (MM) area by the CHE2 team. Dataset is analysed with AGS_CH. Geodaten©swisstopo.

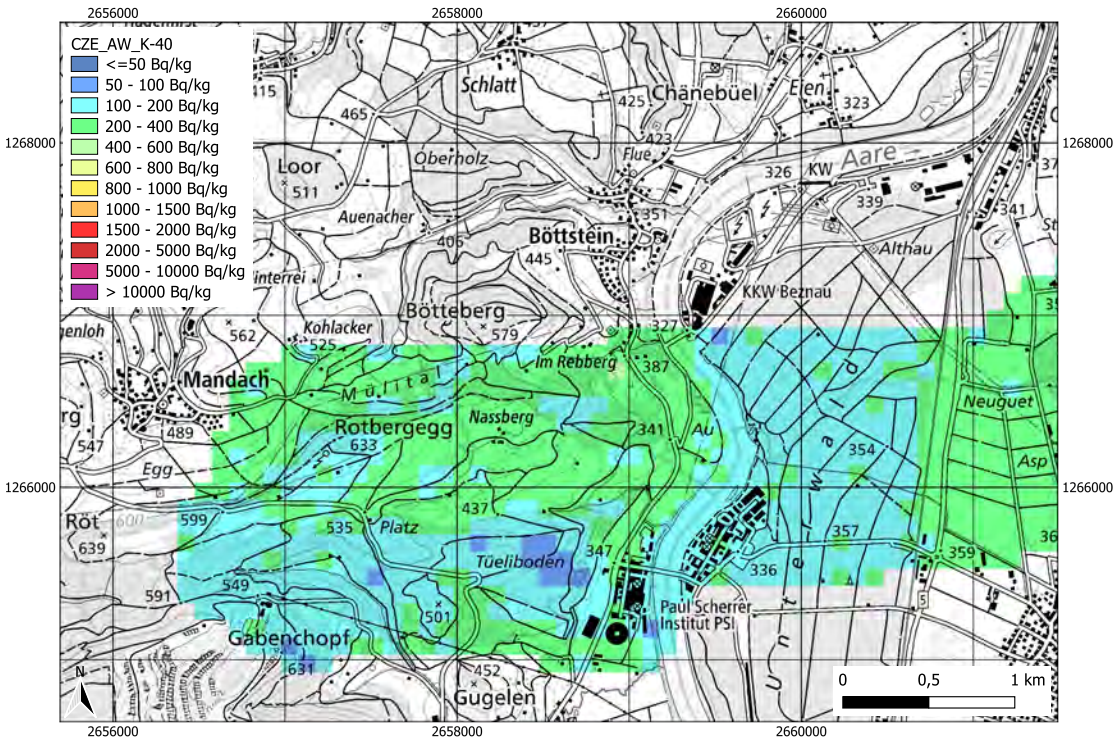

Figure 8.175: Activity concentration of ^{40}K measured at the Mission 5 (MM) area by the CZE team. Geodaten©swisstopo.

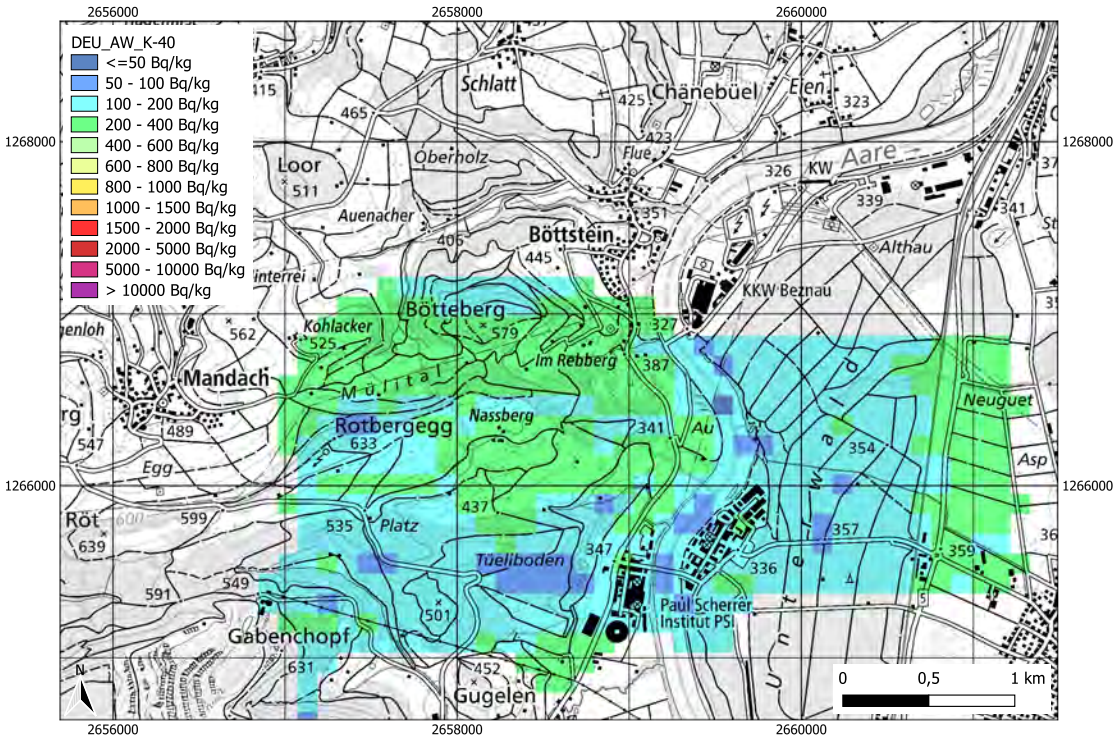

Figure 8.176: Activity concentration of ^{40}K measured at the Mission 5 (MM) area by the DEU team. Geodaten©swisstopo.

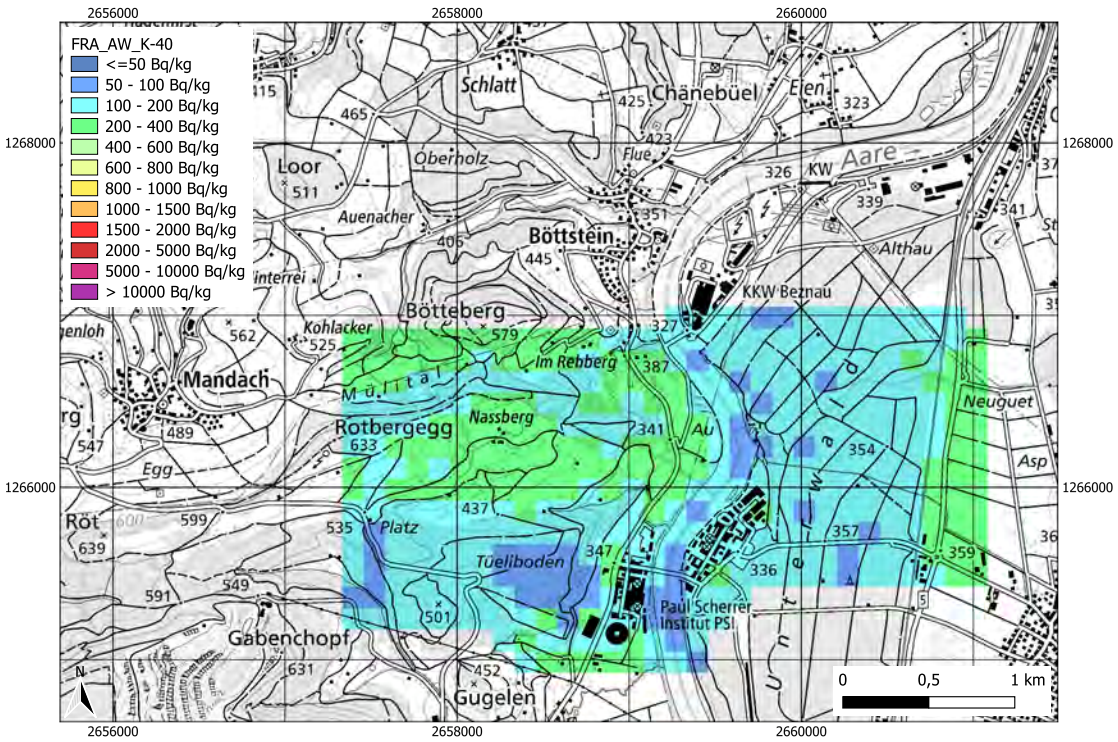

Figure 8.177: Activity concentration of ^{40}K measured at the Mission 5 (MM) area by the FRA team. Geodaten©swisstopo.

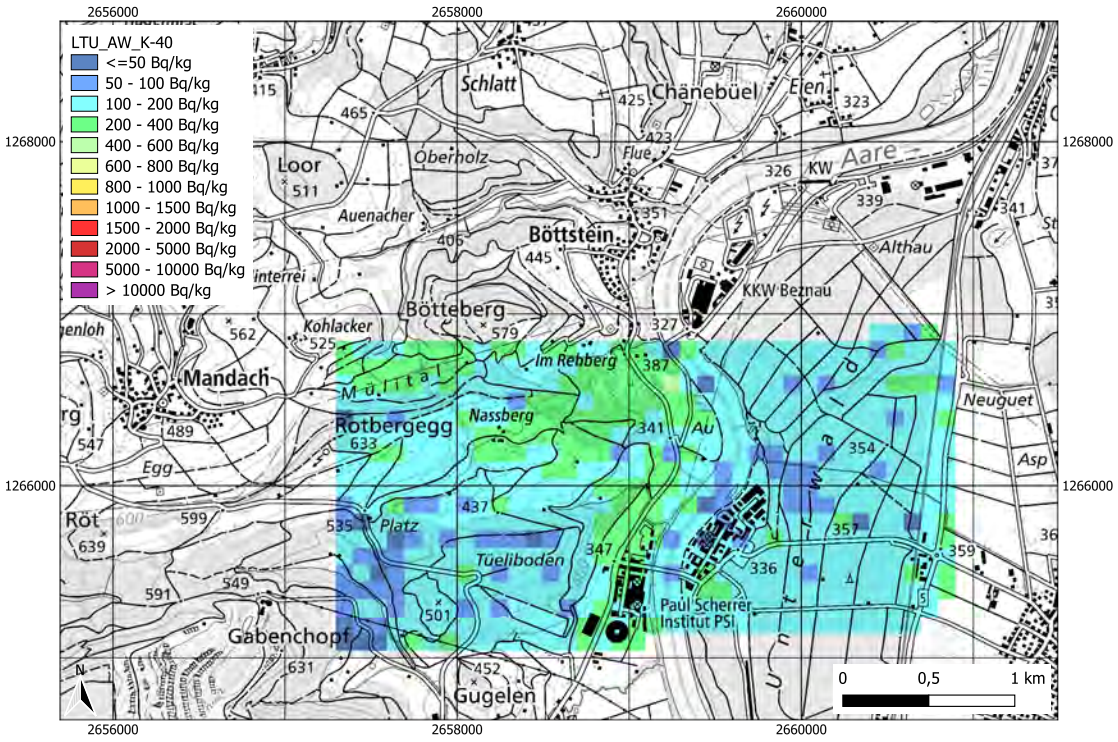

Figure 8.178: Activity concentration of ^{40}K measured at the Mission 5 (MM) area by the LTU team. Geodaten©swisstopo.

Man Made Gross Count Ratio (MMGC)

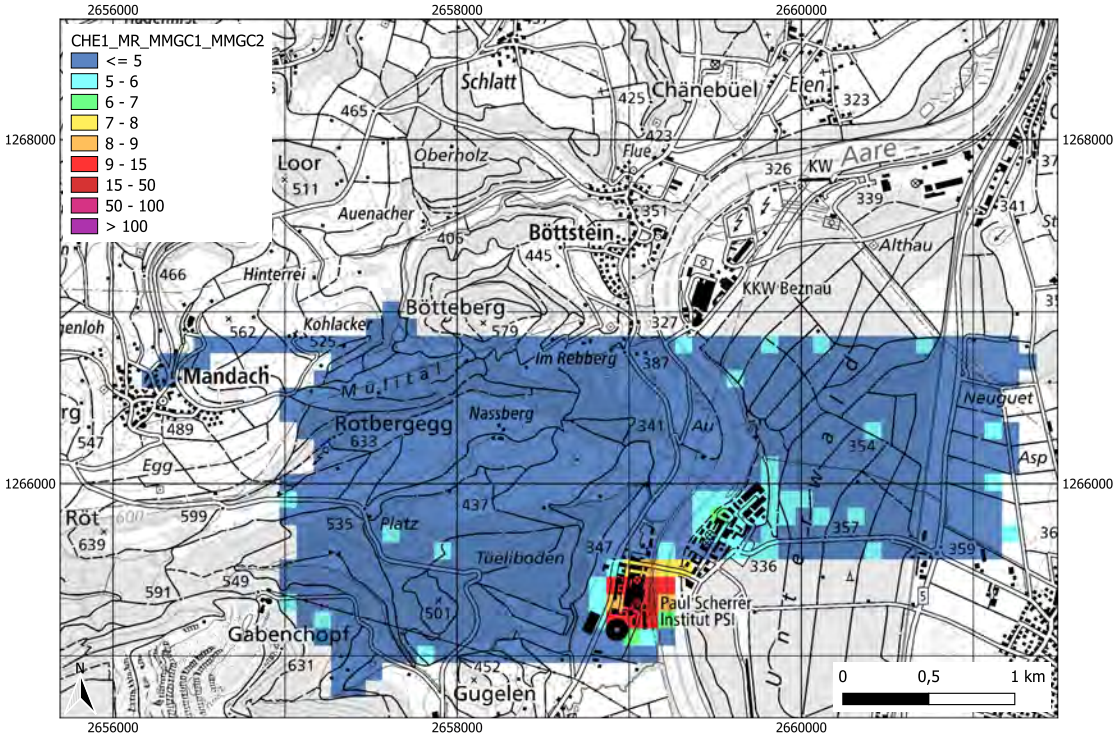

Figure 8.179: Man Made Gross Count Ratio measured at the Mission 5 (MM) area by the CHE1 team. Geodaten©swisstopo.

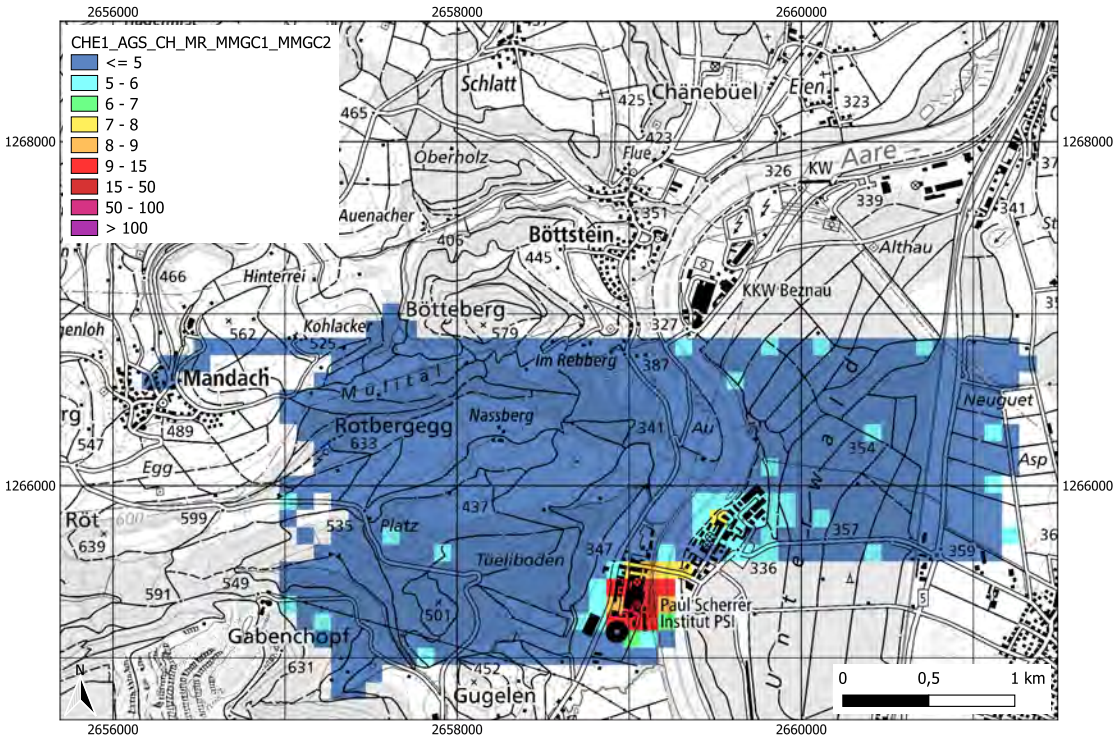

Figure 8.180: Man Made Gross Count Ratio measured at the Mission 5 (MM) area by the CHE1 team. Dataset is analysed with AGS_CH Geodaten©swisstopo.

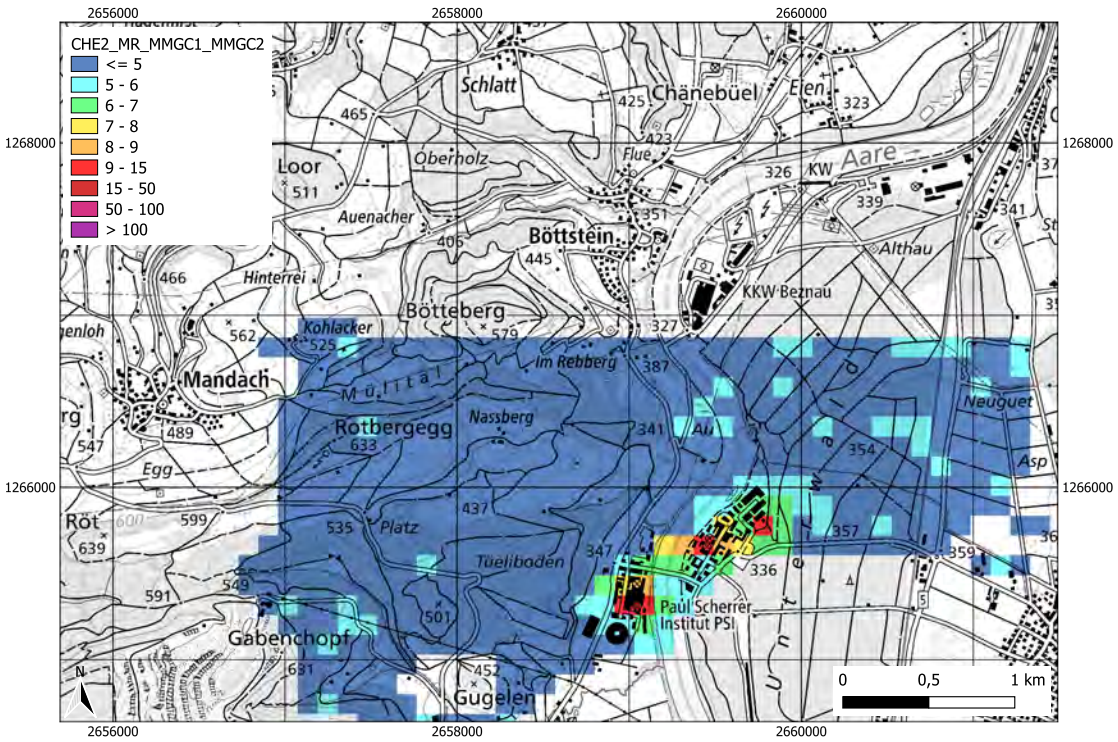

Figure 8.181: Man Made Gross Count Ratio measured at the Mission 5 (MM) area by the CHE2 team. Geodaten©swisstopo.

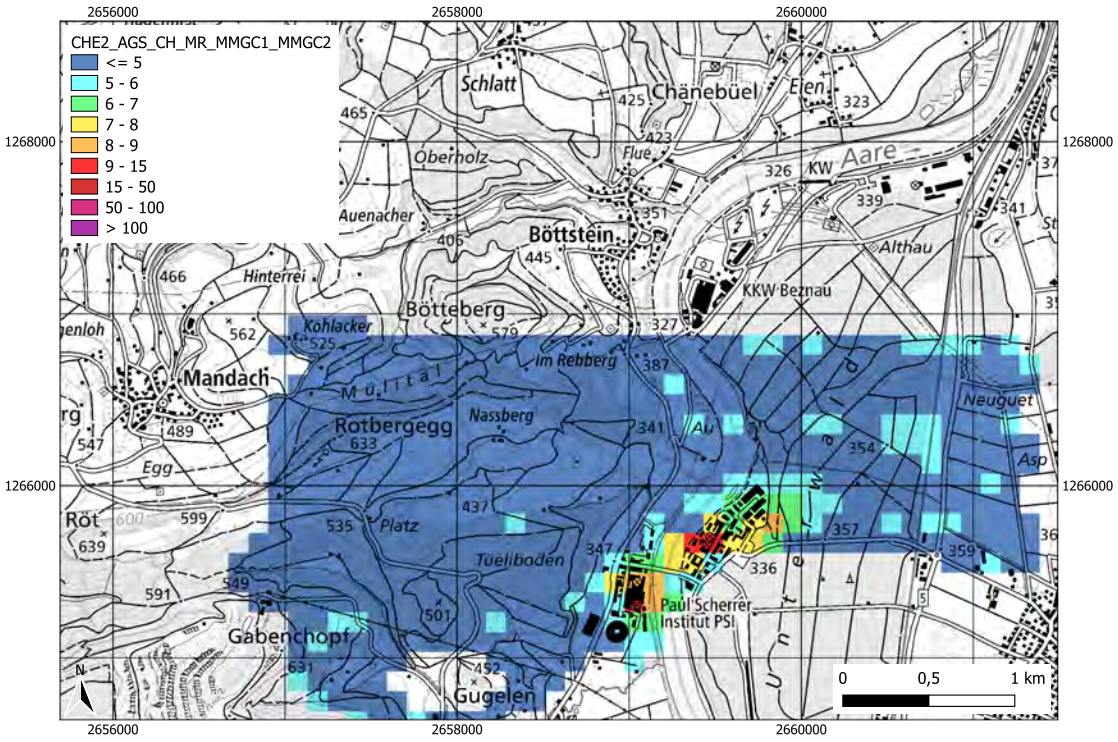

Figure 8.182: Man Made Gross Count Ratio measured at the Mission 5 (MM) area by the CHE2 team. Dataset is analysed with AGS_CH Geodaten©swisstopo.

8.7 Mission with drones

8.7.1 Comparison

All participating teams adopted a broadly similar strategy for locating the sources. Each team first conducted a grid flight over the defined area. The choice of parameters was left to the individual teams, resulting in variations in flight altitude, speed, and line spacing. Some flights were conducted automatically, by defining the perimeter and the flight parameters, while others were flown manually.

The flight altitudes for the grid surveys ranged from $5\,\mathrm{m}$ to $40\,\mathrm{m}$, depending on whether the team was flying over open fields or wooded areas. Flight speeds also varied considerably, between $2\,\mathrm{m\,s^{-1}}$ and $5\,\mathrm{m\,s^{-1}}$, and line spacing ranged from $5\,\mathrm{m}$ to $10\,\mathrm{m}$.

Following the initial grid flight, teams employed different approaches depending on the remaining time still available. In all cases, however, at least one additional static flight was conducted over each area of interest to determine the precise position and source activity. In some instances, an additional grid flight was carried out at a different altitude.

In Mission Drones Area 1, the ^{137}Cs sources were detected by all teams. Activity estimates varied, with underestimations of up to $50\,\%$ and overestimations of up to $30\,\%$. The ^{133}Ba source was detected by all teams except CHE; however, CZE and DEU were unable to estimate its activity. FRA and LTU were able to provide estimates, with deviations of approximately $30\,\%$ from the reference value. Such discrepancies may arise from the close proximity of the sources, which can lead to over or underestimation depending on the corrections applied during evaluation.

The ^{60}Co source was detected only by DEU and LTU, with activity deviations respectively of $40\,\%$ and $11\,\%$. Since the ^{60}Co source was located in a wooded area (Figure 7.12), all teams initially overflew the area at a high altitude ($40\,\mathrm{m}$). This, combined with a small detector volume, likely prevented other teams from detecting it effectively.

Table 8.8: Comparison of source detection and activity estimation in Area 1 (Mission Drones, Area 1).

	^{137}Cs	^{133}Ba	^{60}Co
Source Number	2	1	3
Ref. Activity [GBq]	0.74	0.40	0.167
Activity estimation [GBq]			
CHE	0.6–0.9	n.a.	n.a.
CZE	0.4–0.5	Detected, no Activity	n.a.
DEU	0.95	Detected, no Activity	0.23
FRA	0.6	0.55	n.a.
LTU	0.84	0.283	0.15

In Mission Drones Area 2, a total of six ^{137}Cs sources, each with an activity of $0.067\,\mathrm{GBq}$, were distributed along a footpath (see in Figure 7.13). The sources were spaced approximately $10\,\mathrm{m}$ apart. All teams detected ^{137}Cs; however, in each case, it was reported only as a single point source. Activity estimates varied considerably between teams, ranging from 0.15 to $0.57\,\mathrm{GBq}$. Variations in flight altitude and positioning when determining the activity can lead to such large discrepancies.

The ^{241}Am source was not detected by DEU or LTU. CZE located the source but could not estimate its activity. FRA and CHE were able to both locate the ^{241}Am source and estimate its activity; however, the measured values were up to three times lower than the reference value. This underestimation is attributed to the low detection efficiency of the system in the low-energy range.

Table 8.9: Comparison of source detection and activity estimation in Area 2 (Mission Drones, Area 2).

	^{137}Cs	^{241}Am
Source Number	$1-6$	7
Ref. Activity $[\mathrm{GBq}]$	6×0.067	1.8
Activity estimation $[\mathrm{GBq}]$		
CHE	0.22	$0.68-0.85$
CZE	$0.15-0.20$	Detected, no Activity
DEU	0.48	n.a.
FRA	0.14	0.87
LTU	0.57	n.a.

8.7.2 Maps

This section summarises the maps produced by the teams based on the drone measurements in Area 1 and Area 2. Since the CZE and DEU teams additionally provided the data of their drone missions in the standard format ERS 2.0, their data could be readily gridded in AGS_CH using a cell size of $10\,\mathrm{m}$, according to the specifications and the formatting defined for the helicopter flights. The corresponding dose rate maps are presented for the CZE team in Figures 8.183, 8.185 and for the DEU team in Figures 8.189, 8.190, 8.191, 8.192. This also underlines the importance of adopting a common format for data sharing. In a real event, the CZE and DEU drone teams would have had a clear advantage in terms of cooperation and the rapid production of collective datasets.

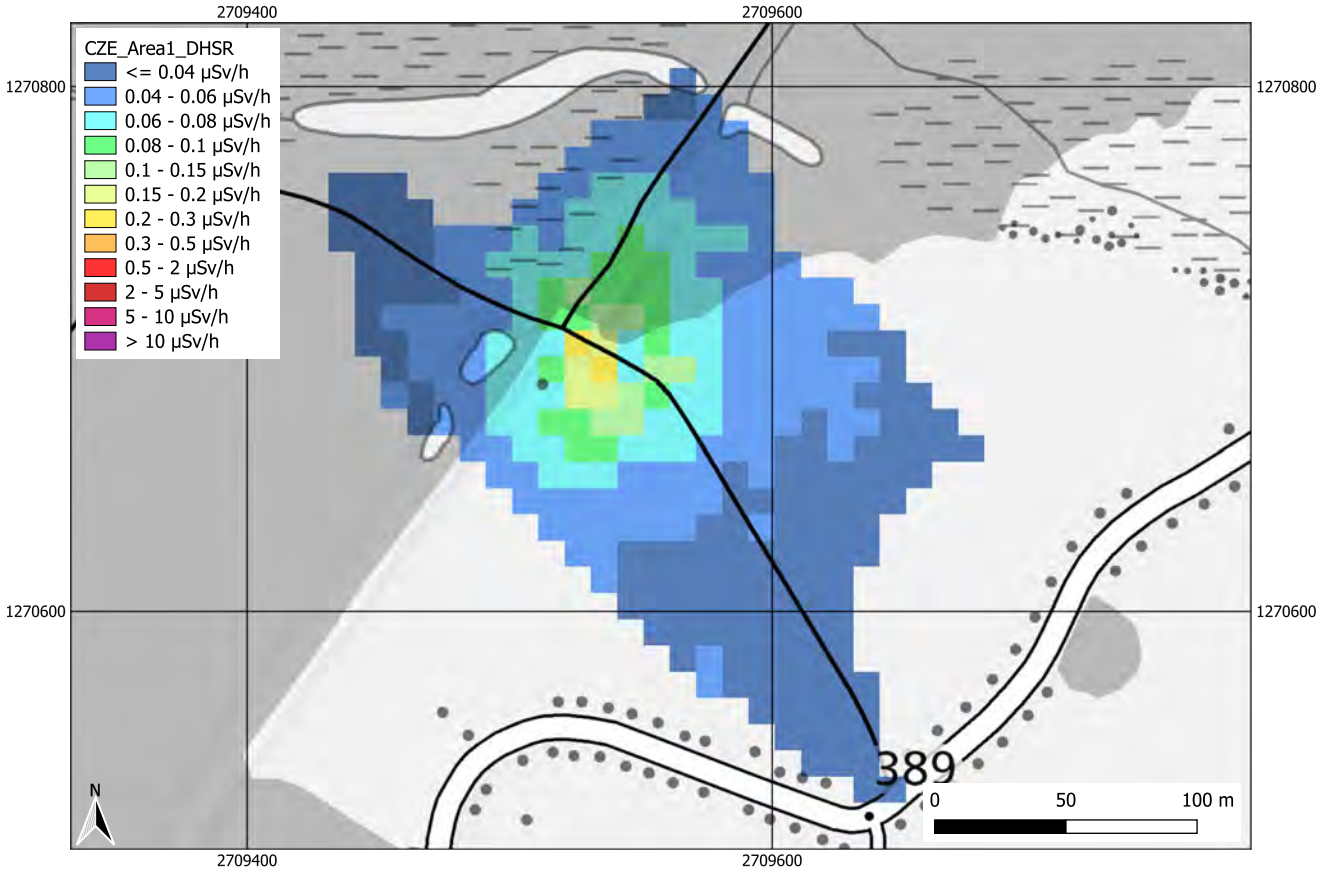

Figure 8.183: Ambient dose equivalent rate at the detector (DHSR_loc) during the drone mission, measured in Area 1 by the CZE team, results gridded from ERS 2.0 file.

Figure 8.184: Ambient dose equivalent rate at the detector (DHSR_loc) during the drone mission, measured in Area 1 by the CZE team.

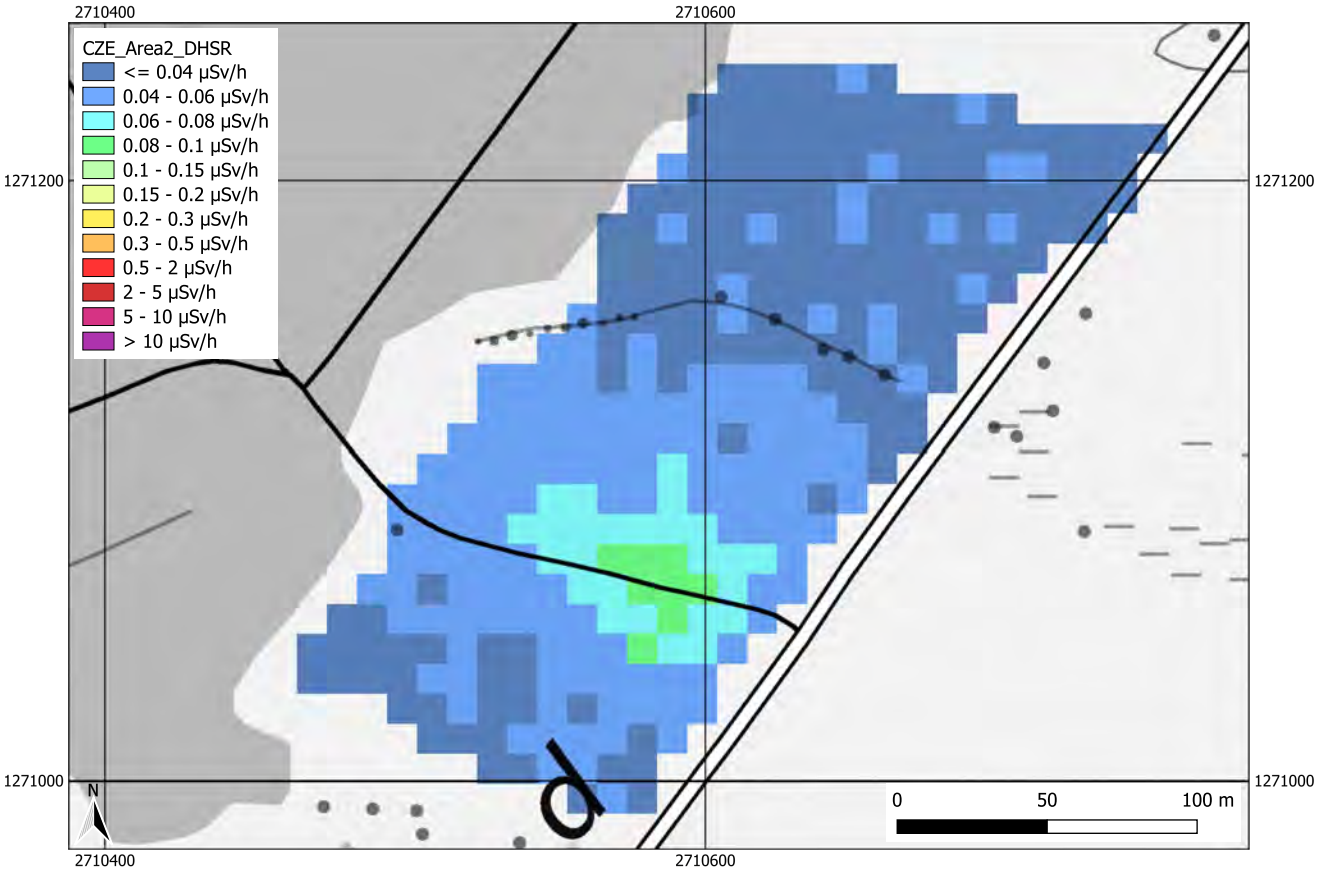

Figure 8.185: Ambient dose equivalent rate at the detector (DHSR_loc) during the drone mission, measured in Area 2 by the CZE team, results gridded from ERS 2.0 file.

Figure 8.186: Ambient dose equivalent rate at the detector (DHSR_loc) during the drone mission, measured in Area 2 by the CZE team.

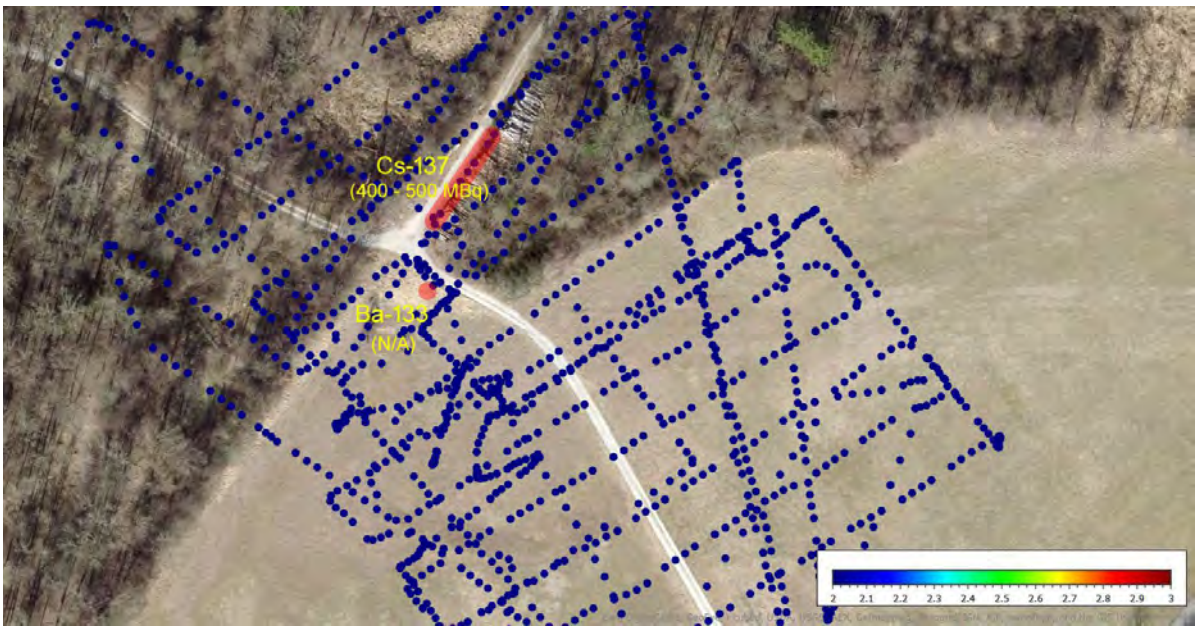

Figure 8.187: Estimation of the sources during the drone mission, measured in Area 1 by the CZE team.

Figure 8.188: Estimation of the sources during the drone mission, measured in Area 2 by the CZE team.

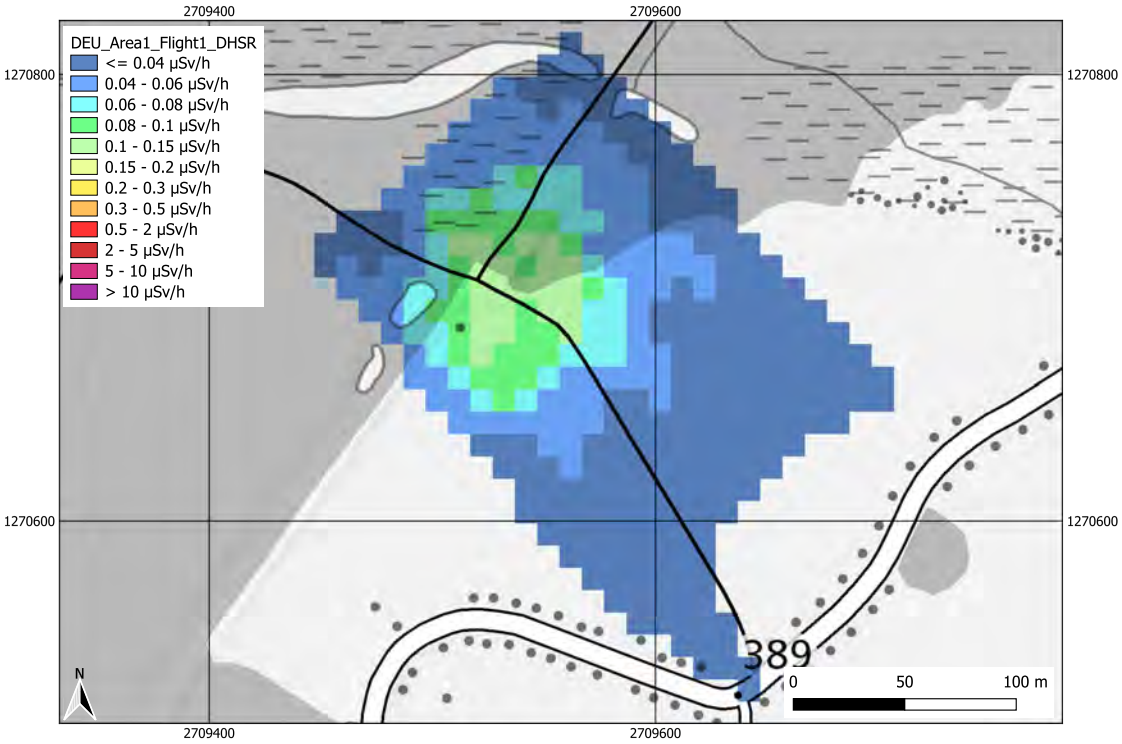

Figure 8.189: Ambient dose equivalent rate (DHSR) during the drone mission (Flight 1), measured in Area 1 by the DEU team, results gridded from ERS 2.0 file.

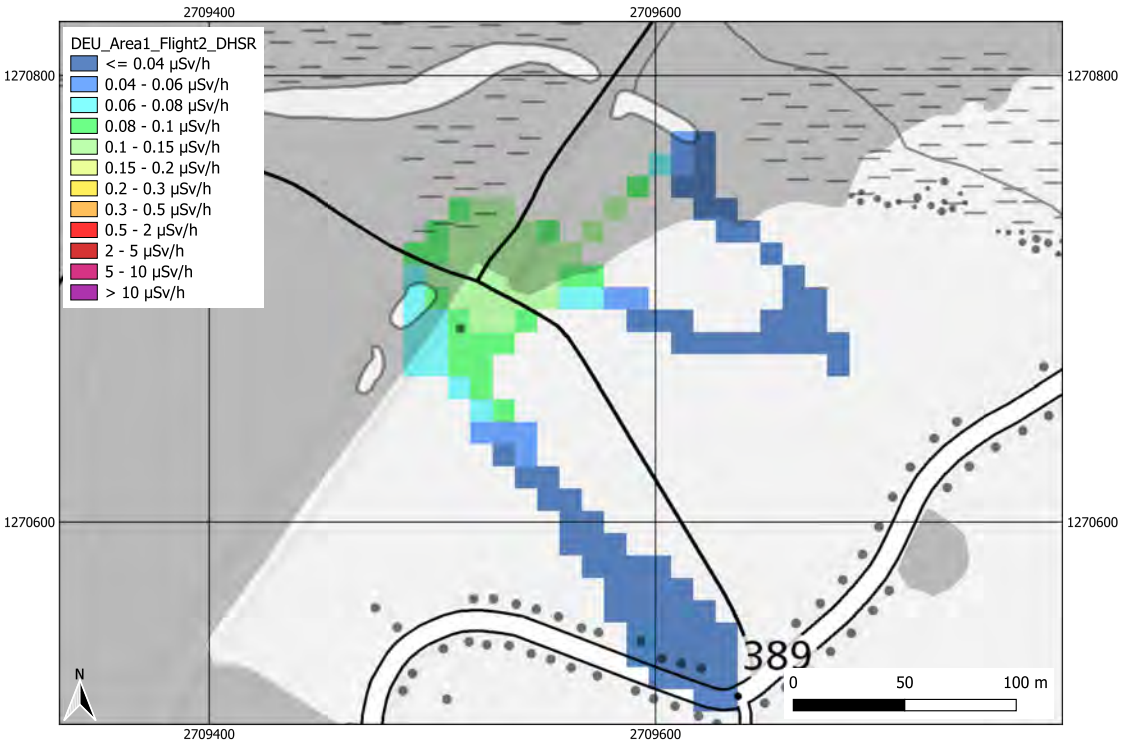

Figure 8.190: Ambient dose equivalent rate (DHSR) during the drone mission (Flight 2), measured in Area 1 by the DEU team, results gridded from ERS 2.0 file.

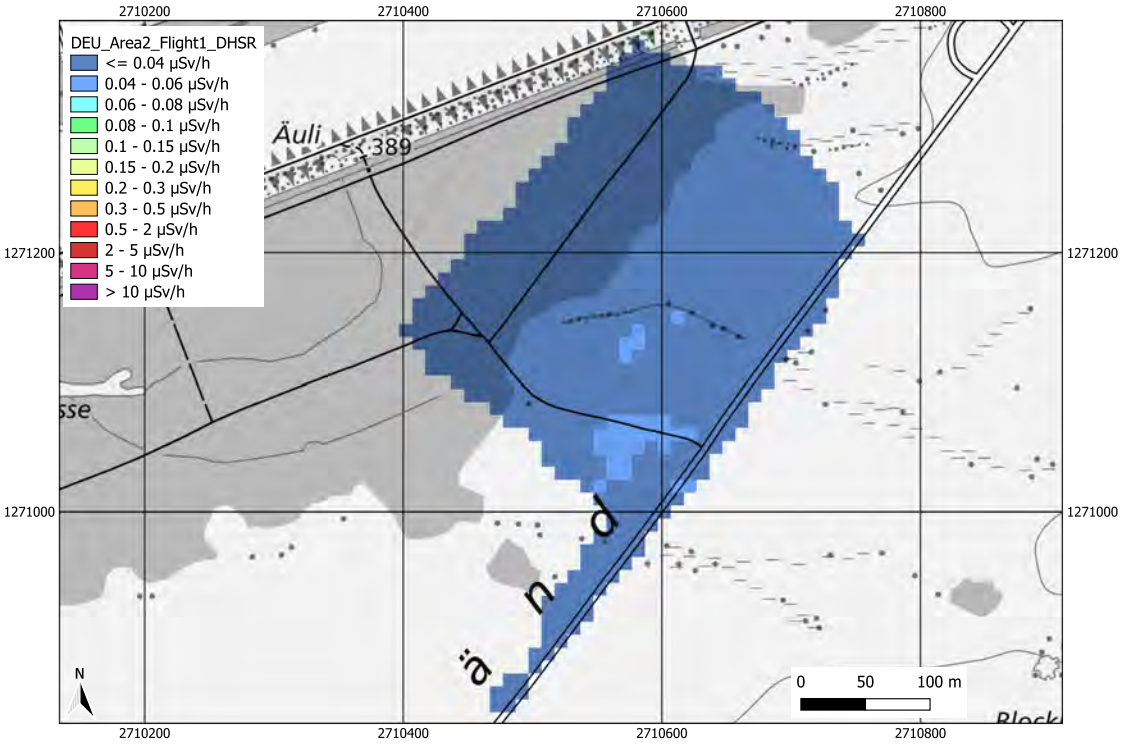

Figure 8.191: Ambient dose equivalent rate (DHSR) during the drone mission (Flight 1), measured in Area 2 by the DEU team, results gridded from ERS 2.0 file.

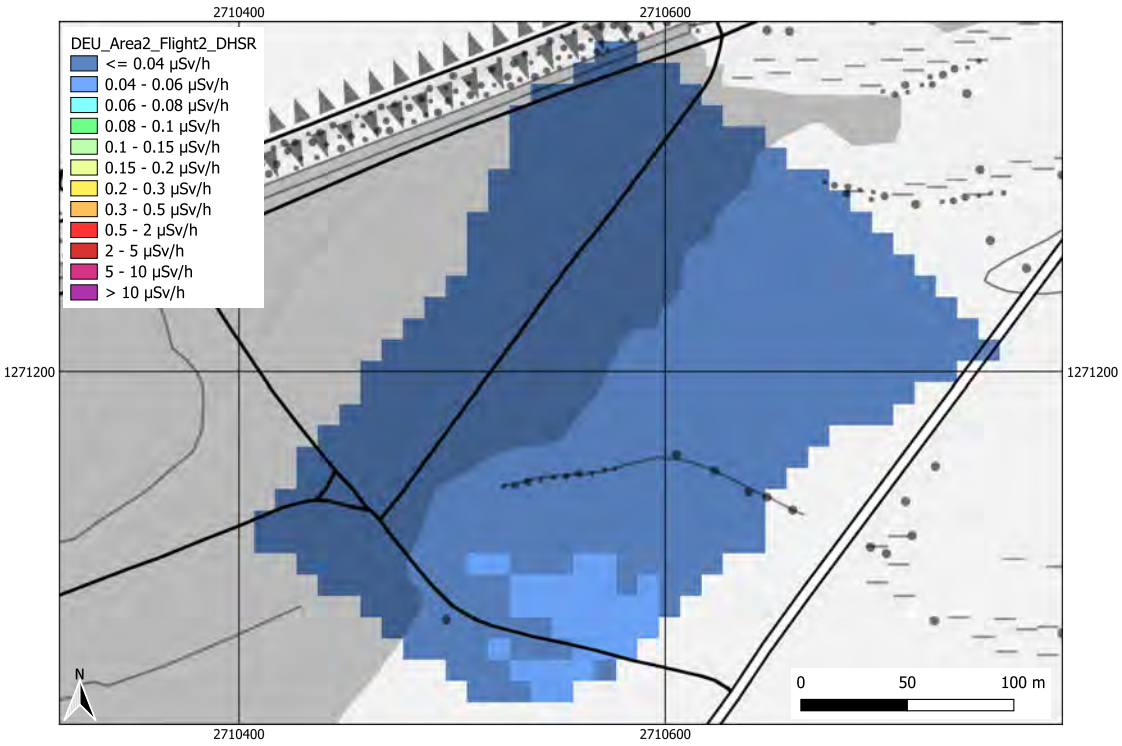

Figure 8.192: Ambient dose equivalent rate (DHSR) during the drone mission (Flight 2), measured in Area 2 by the DEU team, results gridded from ERS 2.0 file.

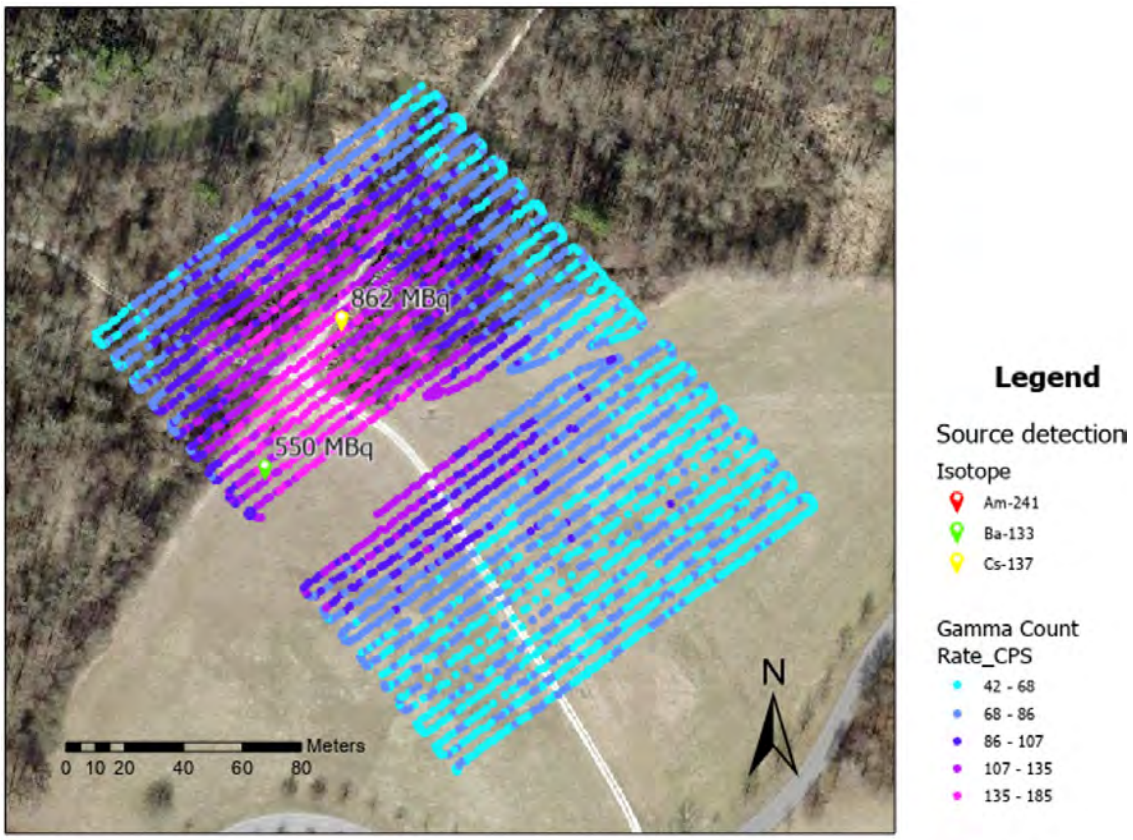

Figure 8.193: Count rate map and estimation of the sources during the drone mission, measured in Area 1 by the FRA team.

Figure 8.194: Count rate map and estimation of the sources during the drone mission, measured in Area 2 by the FRA team.

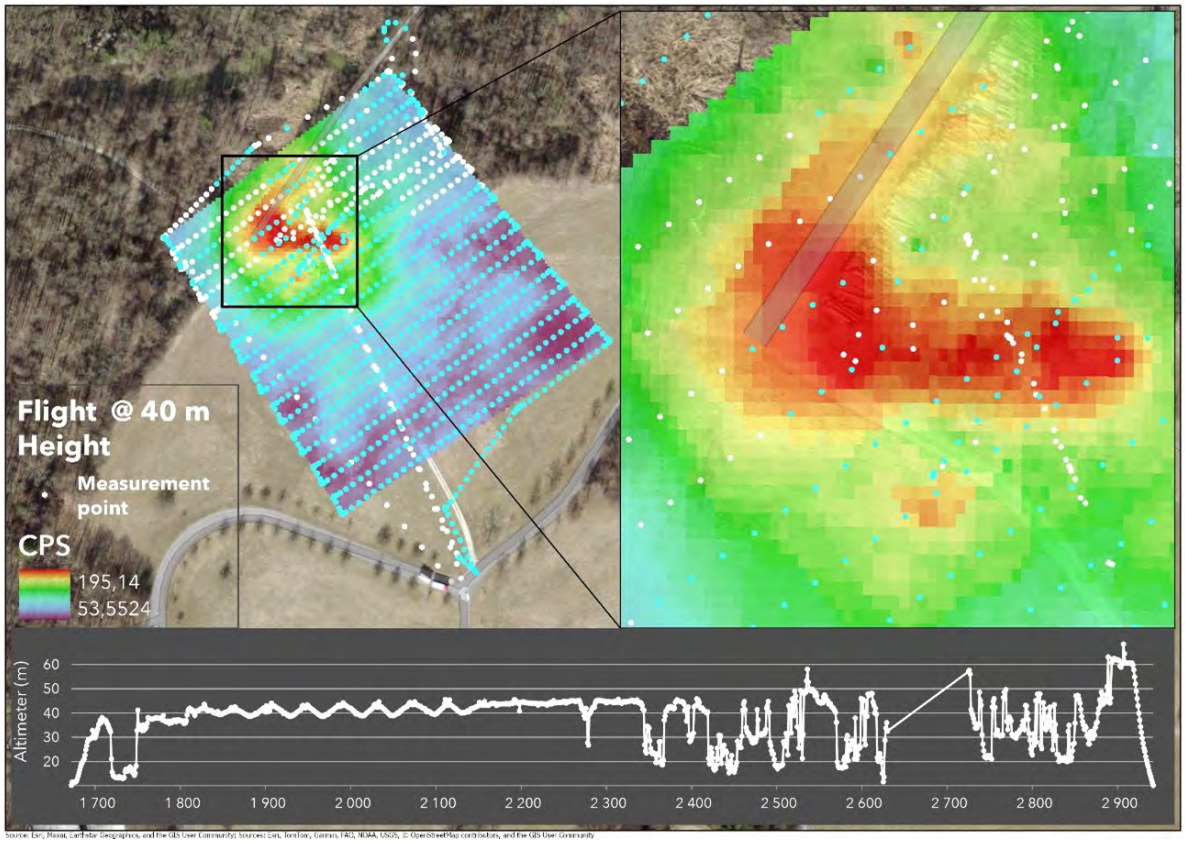

Figure 8.195: Count rate during the drone mission, measured in Area 1 by the LTU team.

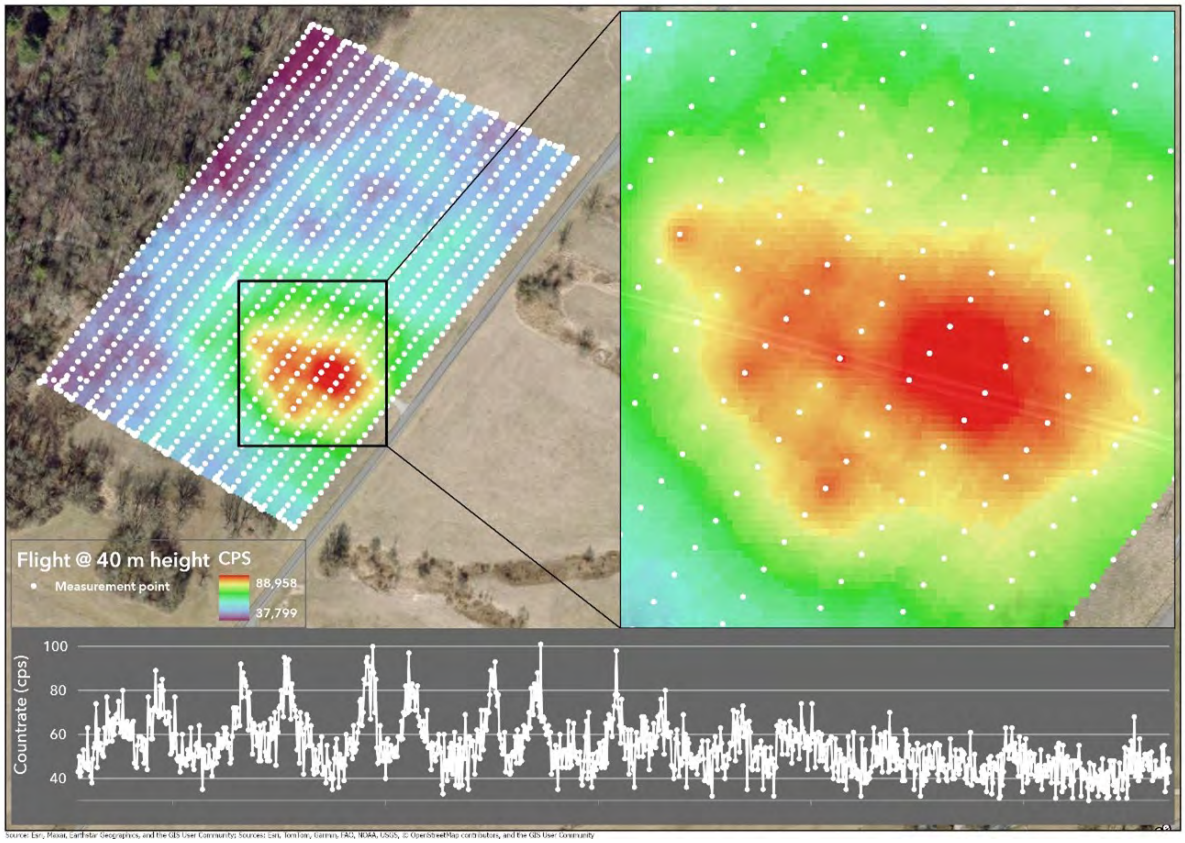

Figure 8.196: Count rate during the drone mission, measured in Area 2 by the LTU team.

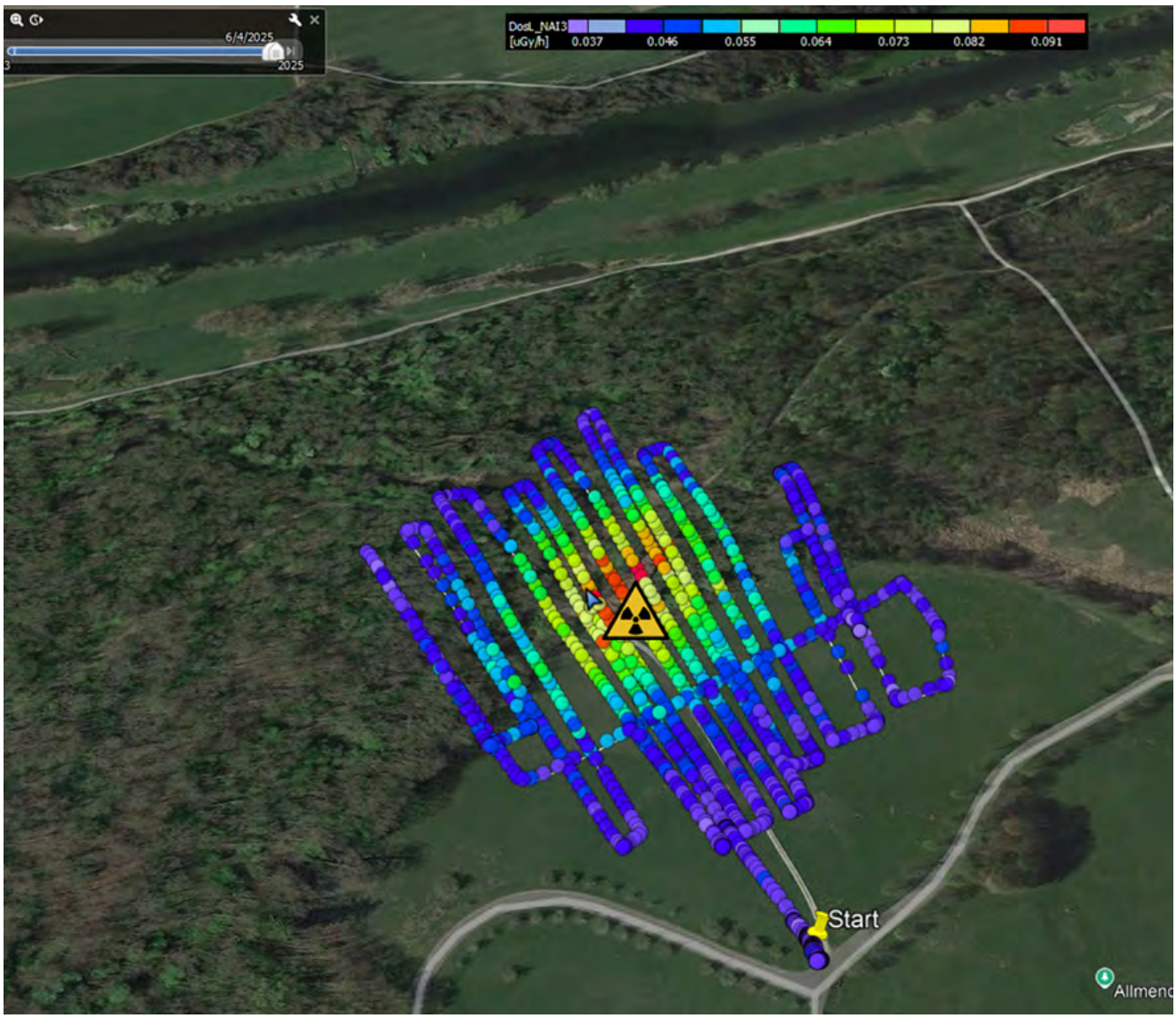

Figure 8.197: Ambient dose equivalent rate (DHSR) and localisation of the sources during the drone mission, measured in Area 1 by the CHE team.

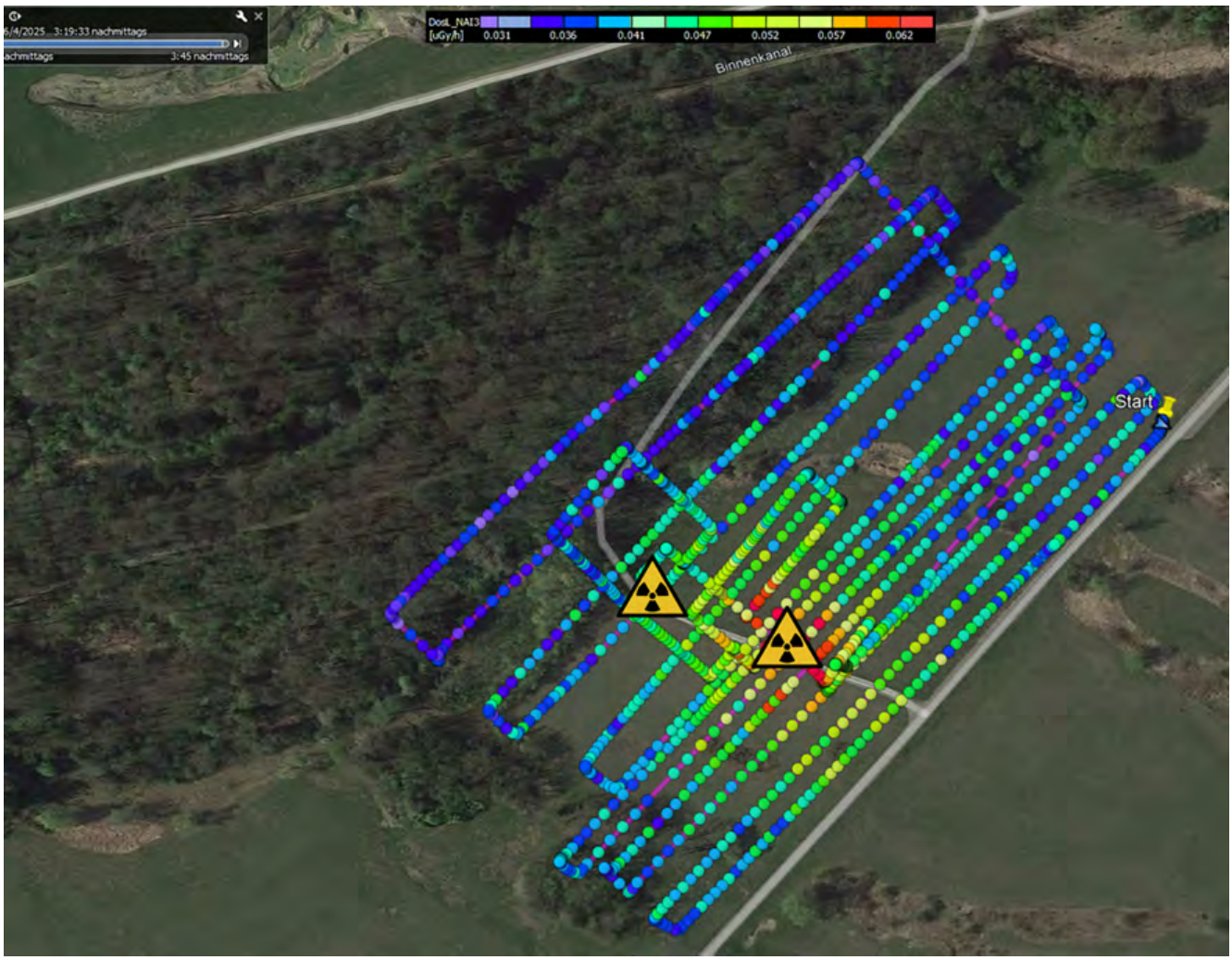

Figure 8.198: Ambient dose equivalent rate (DHSR) and localisation of the sources during the drone mission, measured in Area 2 by the CHE team

8.8 Ground-based measurements

As described in Section 7.7, in agreement with the organisers, the Swedish team performed car-borne and backpack surveys.

Mission i SWE

The SSM conducted three large-scale surveys during the week, covering a total distance of approximately $550\,\mathrm{km}$ and collecting over $10\,000$ measurements (each with a 5 second integration time). Results from the dose rate survey are shown in Figure 8.199. The only anomaly detected was a source located at the PSI (see results from Mission iii SWE).

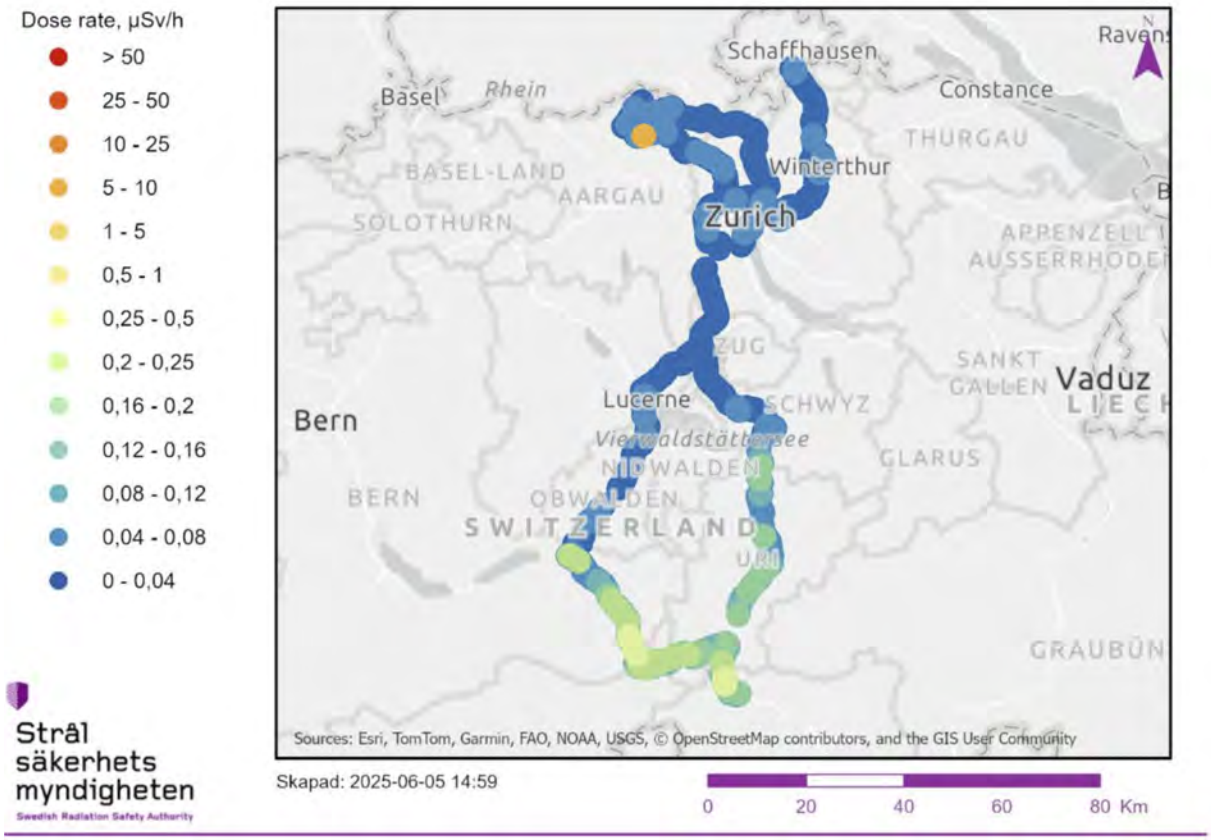

Figure 8.199: Ground-based dose rate survey in Switzerland during the AGC25 exercise performed by the SWE team.

Mission ii SWE

A total of nine sources were located and identified: two in Area 1 and seven in Area 2 (see Figures 8.200 and 8.201). Details of the source locations and estimated activities are summarised in Table 8.10. For Sources 3 – 8, the activity estimates are based on the average dose rate measured across all these sources, as they appear to be of the same type.

Table 8.10: List of identified sources during Mission ii SWE.

ID	Nuclide	Coordinates	Dose rate @ 1 m [µSv h^{-1}]	Estimated Activity	Relative to reference
1	^{60}Co	47.578218, 8.894846	63	200 MBq	25%
2	^{137}Cs	47.578009, 8.894568	79	800 MBq	14%
3	^{137}Cs	47.580928, 8.908832	9.0	90 MBq	34%
4	^{137}Cs	47.580948, 8.908682	9.2	90 MBq	34%
5	^{137}Cs	47.580969, 8.908593	8.2	90 MBq	34%
6	^{137}Cs	47.581003, 8.908379	8.8	90 MBq	34%
7	^{137}Cs	47.581010, 8.908281	7.7	90 MBq	34%
8	^{137}Cs	47.581069, 8.908048	7.9	90 MBq	34%
9	^{241}Am	47.581151, 8.907570	0.99	240 MBq	−87%

Figure 8.200: Ground-based survey results from Area 1, performed in Frauenfeld by the SWE team.

Figure 8.201: Ground-based survey results from Area 2, performed in Frauenfeld by the SWE team.

Mission iii SWE

One source was located near the end of the linear accelerator (see Figure 8.202). Access to the area where the source was situated was restricted, but the exact location could be estimated by visual inspection. The source was heavily shielded and collimated upwards towards the sky, making activity estimation difficult. The nuclide was identified as ^{75}Se (Table 8.11). Furthermore, while driving along *Forschungsstrasse* beside PSI West, a distinct annihilation peak at $511\,\mathrm{keV}$ was observed, although no significant increase in dose rate was detected.

Table 8.11: List of identified sources during Mission iii SWE.

ID	Nuclide	Coordinates	Dose rate @ $25\,\mathrm{m}$ [$\mu\mathrm{Sv\,h^{-1}}$]
10	^{75}Se	47.52884, 8.23146	7

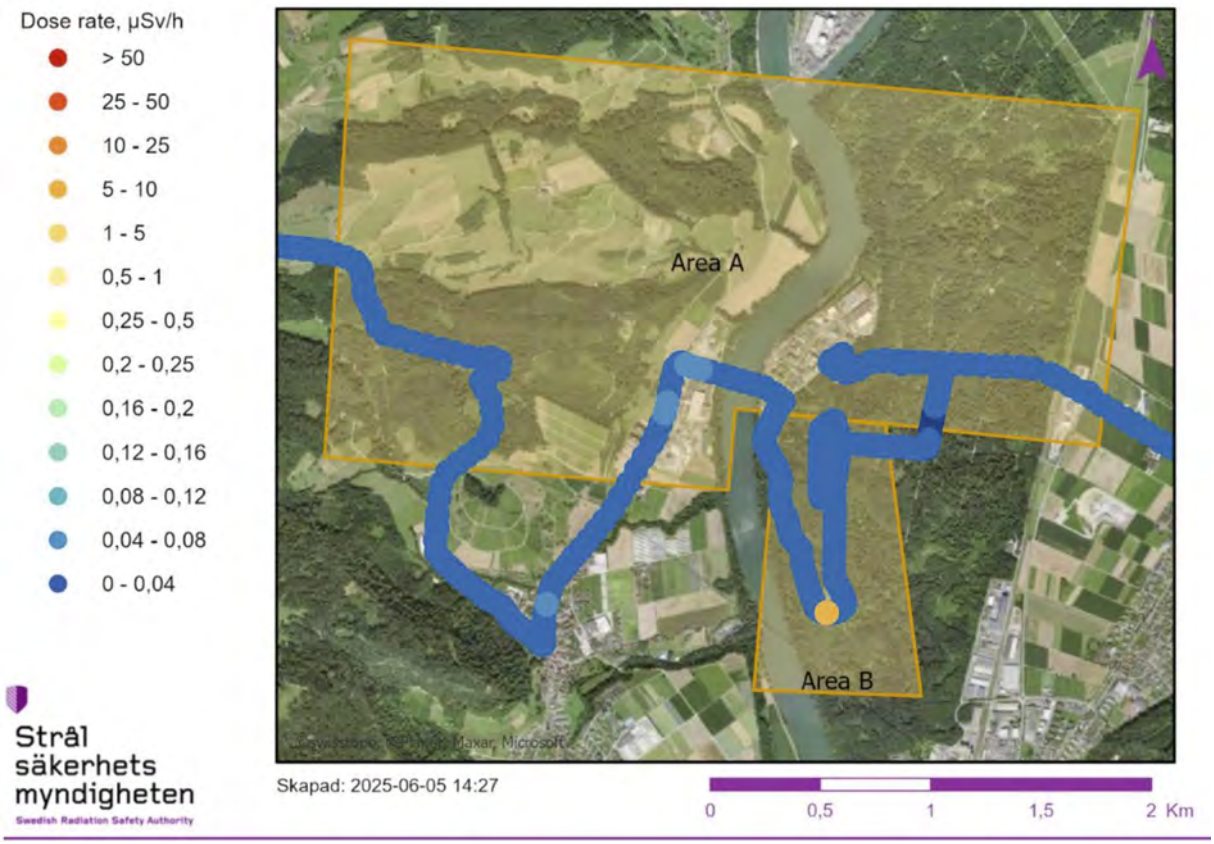

Figure 8.202: Ground-based survey results from Areas A and B, performed at the Paul Scherrer Institute by the SWE team.

Chapter 9

Overview of Swiss Measurements

Parameters describing the measurement flights conducted in 2025 by the Swiss teams CHE1 and CHE2 during the ARM25 and AGC25 campaigns and analysed with the AGS_CH software are listed in Table 9.1 and an overview of the corresponding flight lines, ARM25 in red and AGC25 in black, is shown in Figure 9.1. In addition, an overview is given of all Swiss measurements within Switzerland up to 2025 in Figure 9.2.

Table 9.1: Flight data of Swiss teams CHE1 and CHE2 of ARM25 and AGC25 measurements.

Location	Flight identification	Measuring time [s]	Length of run [km]	Area [km^2]
	Altitude profile			
Lake Thun	Heli 2_20250605 0846	876	40.4	
(Mission 2)	Heli 2_20250605 0850			
	Heli 2_20250605 0852			
	Heli 2_20250605 0855			
	Heli 2_20250605 0900			
	Heli 2_20250605 0902			
	Heli 2_20250605 0906			
	Heli 4_20250601 1530	993	53.3	
	Recurrent measuring areas over nuclear installations (ARM25)			
Region KKG	Heli 2_20250528 0813	7704	370.7	89.8
Region KKM	Heli 2_20250527 1400	7480	381.4	92.0
	AGC25 International campaign			
Thun military ground	Heli 2_20250605 0832	449	23.0	2.3
(Mission 1)	Heli 4_20250601 1510	465	23.8	2.5
Composite Mapping	Heli 2_20250603 1345	528	15.2	1.6
(Mission 3)	Heli 2_20250603 1402	550	18.0	2.0
	Heli 2_20250603 1533	151	7.1	
	Heli 2_20250603 CM DEU	3502	170.0	44.3
	Heli 4_20250603 1327	140	7.4	
	Heli 4_20250603 1348	6079	302.6	79.2
Frauenfeld military ground	Heli 2_20250602 0755	1775	73.5	7.1
(Mission 4)	Heli 4_ES_CHE2	1773	65.2	6.7
Region PSI	Heli 2_20250602 1358	1032	38.2	7.3
(Mission 5)	Heli 2_20250602 1416	499	19.1	2.4
	Heli 4_AGC25_MM_A_B	1335	55.6	10.4
	Heli 4_AGC25 MM hovering	157	2.1	0.3

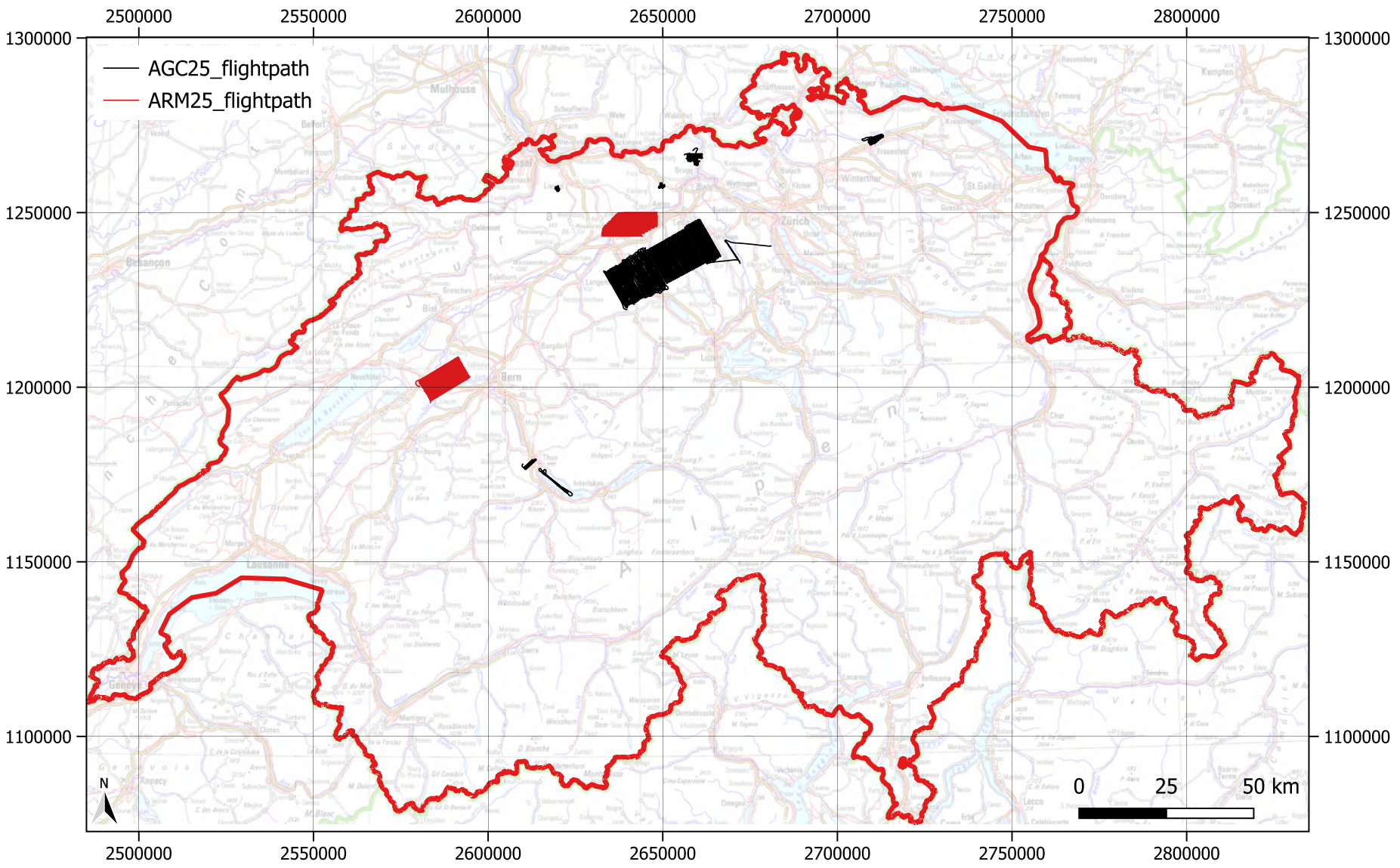

Figure 9.1: Overview of the measurement areas of ARM25 (red) and AGC25 (black). Geodata© swisstopo.

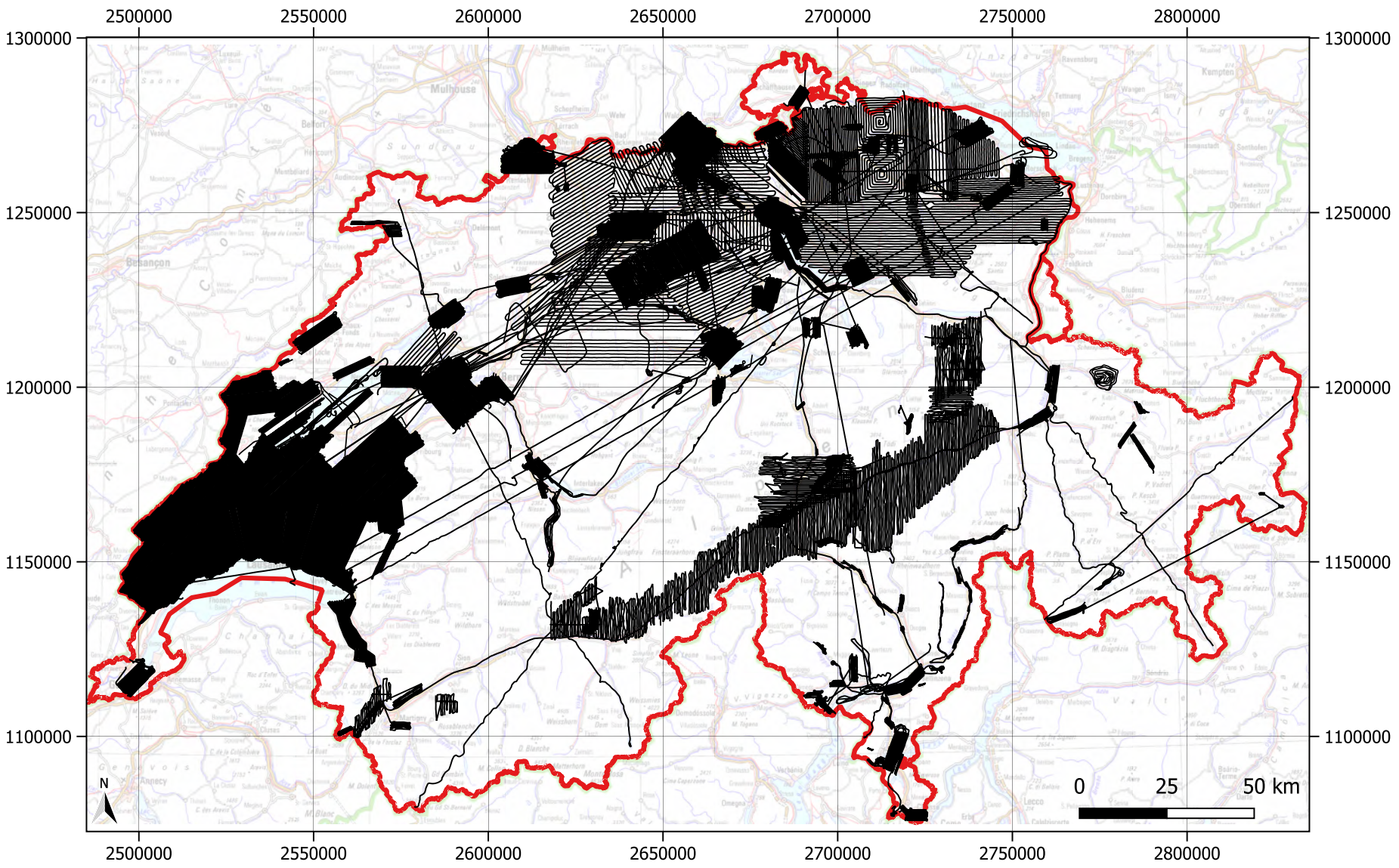

Figure 9.2: Overview of the areas in Switzerland surveyed up to 2025. Geodata© swisstopo.

Chapter 10

Conclusions

The recurrent inspection of the vicinity of Swiss nuclear power plants Gösgen (KKG) and Mühleberg (KKM) performed during the ARM25, prior to the international exercise AGC25, showed no artificial radionuclides outside the plant premises. As measured in previous years, ionising radiation emitted from activated reactor components, temporarily stored within KKM premises during the dismantling phase of the power plant, could be detected when flying over the restricted perimeter of KKM. Such activities are allowed and closely monitored by the competent authorities.

The international exercise AGC25, like the previous AGCs, clearly demonstrated the merits of cooperation at an international level. Switzerland, the Czech Republic, France, Germany and Lithuania, supported by the USA, participated in AGC25. The exercise comprised five different missions for the six helicopter teams, ground measurements performed by the Swedish team, invited as observers, and for the first time a mission dedicated to drones, which included two measurement flights.

Regarding helicopter measurements, the data exchange among participants, based on the ERS 2.0 format in use for several years, performed very well. The importance of a common data format was emphasised by the drone data exchange, for which no specific format had been defined. Consequently, each team produced maps independently, preventing seamless integration into a single composite map. The CZE and DEU teams distinguished themselves by implementing the ERS 2.0 format for drone measurements as well, demonstrating a significant advantage in emergency scenarios where pooled data from multiple teams is needed to produce radiological maps. More generally, using common standards and data formats, having clear task assignments, and maintaining familiarity among teams can save crucial time during an emergency.

The helicopter missions encompassed several tasks, namely: reference measurement, background measurement, composite mapping, source search and mixed measurement, with the aim of testing and comparing the different systems used and practising realistic scenarios involving international support and cooperation. Among other things, the exercise leadership aimed to test the system limits employing on the one hand very weak sources, to assess the lower detection thresholds, and on the other hand very strong sources, to assess the upper limit of the systems before saturation occurs.

The results summarised in this report show that, despite differences in the systems, survey strategies and evaluation algorithms employed, results among all teams are comparable and would be sufficient to produce an accurate radiological overview in the event of an accident, which could guide first responders and emergency organisations in their decisions and planning during a radiological crisis. Aeroradiometric measurements also provide critical information for planning and prioritising further ground-based measurements.

At the same time, the exercise highlighted several key considerations for harmonising airborne radiometric measurements across teams and platforms:

- A consistent treatment of the cosmic contribution and background correction, particularly prior to applying ground clearance corrections, is crucial for comparable dose rate and activity concentration estimates. Even small differences in these corrections can lead to systematic deviations that, although not large, are important to understand and address.
- The implementation of a common line in composite mapping should become a standard procedure. Flying this line under the same parameters and configuration as the primary mission allows for a direct and immediate comparison of measurements across teams, facilitates quality control, helps identify potential sources of variability, and enables quick recalibration if necessary. Incorporating this step into standard operating procedures ensures a more robust and reproducible approach to composite mapping.
- Measurements conducted with drones shall follow the same principles as those with helicopters. While drones typically carry smaller detectors, the underlying data evaluation routines and data exchange formats should ideally remain identical. This uniformity ensures that data from different platforms are directly comparable and simplifies joint analyses. Any necessary deviations from these standards should be explicitly justified based on operational constraints or technical limitations.

Taken together, these harmonisation steps not only improve the reliability and comparability of airborne radiometric measurements but also provide a framework for systematically understanding and reducing the remaining differences between teams. Implementing them represents best practice in line with current scientific and technical standards.

The collaboration of the teams was a pleasant experience, and the organisers thank all participants for their excellent work, looking forward to the next occasion for working together.

Acknowledgments

This exercise would not have been possible without the valuable contribution of numerous national and international partners and all participants. The exercise management, represented by the National Emergency Operations Centre (NEOC) and the Paul Scherrer Institute (PSI), shall like to express their sincere appreciation to:

- Swiss Air Force (SAF)
- NBC-EOD Centre of Excellence (NBC-EOD CoE)
- Spiez Laboratory (LS)
- NEOC military staff (Stab BR NAZ)
- Swiss Federal Nuclear Safety Inspectorate (ENSI)
- Czech team: National Radiation Protection Institute (SÚRO), Czech Armed Forces (ACR), Army Radiation Monitoring Network (ARMS)
- French team: Autorité de sûreté nucléaire et de radioprotection (ASNR)
- German team: Bundesamt für Strahlenschutz (BfS) and Bundespolizei-Flugdienst (BPOLFLD)
- Lithuanian team: Radiation Protection Centre (RSC) and State border guard police (SBGS), supported by Nevada National Security Site NNSS (USA)
- Swedish team: Swedish Radiation Safety Authority (SSM)
- Swiss regulatory authorities: Federal Office of Public Health (FOPH) and Swiss National Accident Insurance Fund (SUVA)
- Hazmat Partners
- Swiss Army: Military bases of Frauenfeld, Liestal, Brugg, Dagmersellen, Thun, and Army Logistics Center Othmarsingen
- Swiss Welding Society (SVS)
- SAR-Transport
- Federal Office for Customs and Border Security (BAZG)
- Federal Office of Civil Aviation (FOCA / BAZL)
- Cantonal Police Forces and CBRN Coordinators from the cantons of AG, BE, BL, LU, TG, SO.

The exercise management would also like to thank Dr. Gernot Butterweck (PSI) for his support and expertise during the conception and early organisational stages of AGC25, as well as for his outstanding contributions to the research field of AGS systems.

Bibliography

[1] Marcel Ohera, Lubomír Gryc, Jan Helebrant, Irena Češpírová, Martina Nováková, Cristina Poretti, Adrian Hess, Gerald Scharding, Alberto Stabilini, Martial Chevreuil, Céline Couvez, and Erwan Manach. Agc24 - international campaign of airborne emergency radiation monitoring teams. Report, STOREDB, 2025.

[2] G. F. Schwarz. Methodische Entwicklungen zur Aerogammaspektrometrie. Technical Report 23, Schweizerische Geophysikalische Kommission, Switzerland, 1991.

[3] Lukáš Kotík and Marcel Ohera. Full spectrum estimation of helicopter background and cosmic gamma-ray contribution for airborne measurements. *Nuclear Engineering and Technology*, 55(3):1052–1060, 2023.

[4] Marcel Ohera, Lubomír Gryc, Irena Češpírová, Jan Helebrant, and Lukáš Skála. Airborne hpge spectrometer for monitoring of air dose rates and surface activities. *Nuclear Engineering and Technology*, 55(11):4039–4047, 2023.

[5] IAEA. Guidelines for radioelement mapping using gamma-ray spectrometry data. TECDOC 1363, International Atomic Energy Agency (IAEA), Vienna, Austria, 2003.

[6] H. L. Beck, J. De Campo, and C. Gogolak. In situ ge(li) and nai(tl) gamma-ray spectrometry. Technical report, United States Department of Energy, 1974.

[7] ICRU. Gamma-ray spectrometry in the environment. Report 53, International Commission on Radiation Units and Measurements, Bethesda, MD, USA, 1994.

[8] State Institute of Radiation Protection (SÚRO), Czech Republic. Basic principles of AGAMA software package. Report no. 6/2023, SÚRO, 2023. In Czech.

[9] M. Ohera, D. Sas, and P. Sladek. Calibration of spectrometric detectors for air kerma rate. *Nuclear Technology & Radiation Protection*, 35(4):323–330, 2020.

[10] L. A. Currie. Limits for quantitative detection and qualitative determination. *Analytical Chemistry*, 40:586–593, 1968.

[11] Airborne gamma ray spectrometer surveying. Technical Reports Series 323, International Atomic Energy Agency, Vienna, 1991.

[12] Performance criteria for spectroscopy-based portal monitors used for homeland security. ANSI Standard N42.38, American National Standards Institute, Washington, DC, 2006.

[13] Radiation protection instrumentation – spectroscopy-based portal monitors used for the detection and identification of illicit trafficking of radioactive material. IEC Standard 62484, International Electrotechnical Commission, Geneva, 2010.

[14] R. Schütz, R. Mameghani, R. Stuchels, and L. Hummel. Weiterentwicklung der aero-gammaspektrometrischen Messsysteme des BfS und Anpassung der Mess- und Auswerteverfahren an die Anforderungen des Notfallschutzes. Forschungsvorhaben 3611S60013, http://nbn-resolving.de/urn:nbn:de:0221-2015080713158, 2015.

[15] ICRP. Conversion Coefficients for Use in Radiological Protection against External Radiation. ICRP Publication 74. Ann. ICRP 26 (3-4), 1996.

[16] Piotr T. Wasiolek. Ams ground truth measurements: Calibration and test lines. Technical Report DOE/NV/25946–2697, National Security Technologies, LLC; Remote Sensing Laboratory, Mercury, NV, USA, December 2015.

[17] B. Bucher. *Methodische Weiterentwicklungen in der Aeroradiometrie*. PhD thesis, ETH Zürich, 2001. Dissertation.

[18] G. F. Schwarz, L. Rybach, and E. E. Klingele. Design, calibration, and application of an airborne gamma spectrometer system in switzerland. *Geophysics*, 62(5):1369–1378, 1997.

[19] W. Edwards Deming. *Statistical Adjustment of Data*. John Wiley & Sons, New York, 1943. Dover Publications edition, 1985. ISBN 0-486-64685-8.

[20] A. Bouville and W. M. Lowder. Human population exposure to cosmic radiation. *Radiation Protection Dosimetry*, 24(1–4):293–299, 1988.

[21] UNSCEAR. Sources and effects of ionizing radiation. Scientific annex b: Exposures of the public and workers from various sources of radiation, United Nations Scientific Committee on the Effects of Atomic Radiation, New York, 2008.

[22] Sato Tatsuhiko. Analytical model for estimating terrestrial cosmic ray fluxes nearly anytime and anywhere in the world: Extension of PARMA/EXPACS. *PLOS ONE*, 10(12):1–33, 12 2015.

[23] David Breitenmoser. *Towards Monte Carlo based Full Spectrum Modeling of Airborne Gamma-Ray Spectrometry Systems*. Doctoral thesis, ETH Zürich, 2024. Open Access, ETH Bibliography.

[24] Cristina Poretti, Adrian Hess, and Gerald Scharding. Aeroradiometrie-Messkampagne 2025: Kurzbericht „AGC25“. Technical Report Ident-Nr./Vers. 10015129048/01, Eidgenössisches Departement für Verteidigung, Bevölkerungsschutz und Sport (VBS), Bundesamt für Bevölkerungsschutz (BABS), Nationale Alarmzentrale (NAZ), 2025. Messkampagne 27 Mai – 06 Juni 2025.

[25] Federal Office of Meteorology and Climatology MeteoSwiss. MeteoSwiss – Official Website. https://www.meteoswiss.admin.ch. Accessed: 2025-07-10.

[26] Naoto Fujinami. Observational study of the scavenging of radon daughters by precipitation from the atmosphere. *Environment International*, 22:181–185, 1996.

[27] Hatakka J. Paatero J. Wet deposition efficiency of short-lived radon-222 progeny in central Finland. *Boreal Environment Research*, 4:285–293, 1999.

[28] National Nuclear Data Center, Brookhaven National Laboratory. Nudat (nuclear structure and decay data). Accessed: July 10, 2025.

Appendix A

Previous reports

Reports since 1989 can be found and downloaded from the FAR website https://far.ensi.ch under Publications. Reports between 1989 – 2006 are available only in German.

- Schwarz, G. F., Klingelé, E. E., Rybach, L.: Aeroradiometrische Messungen in der Umgebung der schweizerischen Kernanlagen. Bericht für das Jahr 1989 zuhanden der Hauptabteilung für die Sicherheit der Kernanlagen (HSK). Interner Bericht, Institut für Geophysik, ETH Zürich, 1990.
- Schwarz, G. F., Klingelé, E. E., Rybach, L.: Aeroradiometrische Messungen in der Umgebung der schweizerischen Kernanlagen. Bericht für das Jahr 1990 zuhanden der Hauptabteilung für die Sicherheit der Kernanlagen (HSK). Interner Bericht, Institut für Geophysik, ETH Zürich, 1991.
- Schwarz, G. F., Klingelé, E. E., Rybach, L.: Aeroradiometrische Messungen in der Umgebung der schweizerischen Kernanlagen. Bericht für das Jahr 1991 zuhanden der Hauptabteilung für die Sicherheit der Kernanlagen (HSK). Interner Bericht, Institut für Geophysik, ETH Zürich, 1992.
- Schwarz, G. F., Klingelé, E. E., Rybach, L.: Aeroradiometrische Messungen in der Umgebung der schweizerischen Kernanlagen. Bericht für das Jahr 1992 zuhanden der Hauptabteilung für die Sicherheit der Kernanlagen (HSK). Interner Bericht, Institut für Geophysik, ETH Zürich, 1993.
- Schwarz, G. F., Klingelé, E. E., Rybach, L.: Aeroradiometrische Messungen in der Umgebung der schweizerischen Kernanlagen. Bericht für das Jahr 1993 zuhanden der Hauptabteilung für die Sicherheit der Kernanlagen (HSK). Interner Bericht, Institut für Geophysik, ETH Zürich, 1994.
- Schwarz, G. F., Rybach, L.: Aeroradiometrische Messungen im Rahmen der Übung ARM94. Bericht für das Jahr 1994 zuhanden der Fachgruppe Aeroradiometrie (FAR). Interner Bericht, Institut für Geophysik, ETH Zürich, 1995.
- Schwarz, G. F., Rybach, L.: Aeroradiometrische Messungen im Rahmen der Übung ARM95. Bericht für das Jahr 1995 zuhanden der Fachgruppe Aeroradiometrie (FAR). Interner Bericht, Institut für Geophysik, ETH Zürich, 1996.
- Schwarz, G. F., Rybach, L., Bärlocher, C.: Aeroradiometrische Messungen im Rahmen der Übung ARM96. Bericht für das Jahr 1996 zuhanden der Fachgruppe Aeroradiometrie (FAR). Interner Bericht, Institut für Geophysik, ETH Zürich, 1997.

- Bucher, B., Rybach, L., Schwarz, G., Bärlocher, C.: Aeroradiometrische Messungen im Rahmen der Übung ARM97. Bericht für das Jahr 1997 zuhanden der Fachgruppe Aeroradiometrie (FAR). Interner Bericht, Institut für Geophysik, ETH Zürich, 1998.
- Bucher, B., Rybach, L., Schwarz, G., Bärlocher, C.: Aeroradiometrische Messungen im Rahmen der Übung ARM98. Bericht für das Jahr 1998 zuhanden der Fachgruppe Aeroradiometrie (FAR). Interner Bericht, Institut für Geophysik, ETH Zürich, 1999.
- Bucher, B., Rybach, L., Schwarz, G., Bärlocher, C.: Aeroradiometrische Messungen im Rahmen der Übung ARM99. Bericht für das Jahr 1999 zuhanden der Fachgruppe Aeroradiometrie (FAR). Interner Bericht, Institut für Geophysik, ETH Zürich, 2000.
- Bucher, B., Rybach, L., Schwarz, G., Bärlocher, C.: Aeroradiometrische Messungen im Rahmen der Übung ARM00. Bericht für das Jahr 2000 zuhanden der Fachgruppe Aeroradiometrie (FAR). Interner Bericht, Institut für Geophysik, ETH Zürich, 2001.
- Bucher, B., Rybach, L., Schwarz, G., Bärlocher, C.: Aeroradiometrische Messungen im Rahmen der Übung ARM01. Bericht für das Jahr 2001 zuhanden der Fachgruppe Aeroradiometrie (FAR). Interner Bericht, Paul Scherrer Institut, Villigen, Schweiz, 2002.
- Bucher, B., Rybach, L., Schwarz, G., Bärlocher, C.: Aeroradiometrische Messungen im Rahmen der Übung ARM02. Bericht für das Jahr 2002 zuhanden der Fachgruppe Aeroradiometrie (FAR). Interner Bericht, Paul Scherrer Institut, Villigen, Schweiz, 2003.
- Bucher, B., Rybach, L., Schwarz, G.: Aeroradiometrische Messungen im Rahmen der Übung ARM03. PSI-Bericht 04-14, ISSN 1019-0643, Paul Scherrer Institut, Villigen, Schweiz, 2004.
- Bucher, B., Butterweck, G., Rybach, L., Schwarz, G.: Aeroradiometrische Messungen im Rahmen der Übung ARM04. PSI-Bericht 05-10, ISSN 1019-0643, Paul Scherrer Institut, Villigen, Schweiz, 2005.
  DOI https://doi.org/10.55402/psi:41689
- Bucher, B., Butterweck, G., Rybach, L., Schwarz, G.: Aeroradiometrische Messungen im Rahmen der Übung ARM05. PSI-Bericht 06-06, ISSN 1019-0643,Paul Scherrer Institut, Villigen, Schweiz, 2006.
  DOI https://doi.org/10.55402/psi:41685
- Bucher, B., Butterweck, G., Rybach, L., Schwarz, G.: Aeroradiometrische Messungen im Rahmen der Übung ARM06. PSI-Bericht 07-02, ISSN 1019-0643, Paul Scherrer Institut, Villigen, Schweiz, 2007.
  DOI https://doi.org/10.55402/psi:41681
- Bucher, B., Guillot, L., Strobl, C., Butterweck, G., Gutierrez, S., Thomas, M., Hohmann, C., Krol, I., Rybach, L., Schwarz, G.: International Intercomparison Exercise of Airborne Gammaspectrometric Systems of Germany, France and Switzerland in the Framework of the Swiss Exercise ARM07. PSI-Bericht Nr. 09-07, ISSN 1019-0643, Paul Scherrer Institut, Villigen, Schweiz, 2009.
  DOI https://doi.org/10.55402/psi:35550
- Bucher, B., Butterweck, G., Rybach, L., Schwarz, G.: Aeroradiometrische Messungen im Rahmen der Übung ARM08. PSI-Bericht Nr. 09-02, ISSN 1019-0643, Paul Scherrer Institut, Villigen, Schweiz, 2009.
  DOI https://doi.org/10.55402/psi:35581

- Bucher, B., Butterweck, G., Rybach, L., Schwarz, G., Strobl, C.: Aeroradiometrische Messungen im Rahmen der Übung ARM09. PSI-Bericht Nr. 10-01, ISSN 1019-0643, Paul Scherrer Institut, Villigen, Schweiz, 2010.
  DOI https://doi.org/10.55402/psi:35541

- Bucher, B., Butterweck, G., Rybach, L., Schwarz, G., Mayer, S.: Aeroradiometrische Messungen im Rahmen der Übung ARM10. PSI-Bericht Nr. 11-02, ISSN 1019-0643, Paul Scherrer Institut, Villigen, Schweiz, 2011.
  DOI https://doi.org/10.55402/psi:35201

- Bucher, B., Butterweck, G., Rybach, L., Schwarz, G., Mayer, S.: Aeroradiometric Measurements in the Framework of the Swiss Exercise ARM11. PSI-Report No. 12-04, ISSN 1019-0643, Paul Scherrer Institut, Villigen, Switzerland, 2012.
  DOI https://doi.org/10.55402/psi:35137

- Butterweck, G., Bucher, B., Rybach, L., Schwarz, G., Hödlmoser, H., Mayer, S., Danzi, C. Scharding, G.: Aeroradiometric Measurements in the Framework of the Swiss Exercise ARM12. PSI-Report No. 13-01, ISSN 1019-0643, Paul Scherrer Institut, Villigen, Switzerland, 2013.
  DOI https://doi.org/10.55402/psi:35134

- Butterweck, G., Bucher, B., Rybach, L., Schwarz, G., Hohmann, E., Mayer, S., Danzi, C. Scharding, G.: Aeroradiometric Measurements in the Framework of the Swiss Exercise ARM13. PSI-Report No. 15-01, ISSN 1019-0643, Paul Scherrer Institut, Villigen, Switzerland, 2015.
  DOI https://doi.org/10.55402/psi:35064

- Butterweck, G., Bucher, B., Rybach, L., Schwarz, G., Hohmann, E., Mayer, S., Danzi, C. Scharding, G.: Aeroradiometric Measurements in the Framework of the Swiss Exercises ARM14 and FTX14. PSI-Report No. 15-02, ISSN 1019-0643, Paul Scherrer Institut, Villigen, Switzerland, 2015.
  DOI https://doi.org/10.55402/psi:35062

- Butterweck, G., Bucher, B., Rybach, L., Schwarz, G., Hofstetter-Boillat, B., Hohmann, E., Mayer, S., Danzi, C. Scharding, G.: Aeroradiometric Measurements in the Framework of the Swiss Exercises ARM15, GNU15 and the International Exercise AGC15. PSI-Report No. 15-04, ISSN 1019-0643, Paul Scherrer Institut, Villigen, Switzerland, 2015.
  DOI https://doi.org/10.55402/psi:35047

- Butterweck, G., Bucher, B., Rybach, L., Poretti, C., Maillard, S., Schwarz, G., Hofstetter-Boillat, B., Hohmann, E., Mayer, S., Scharding, G.: Aeroradiometric Measurements in the Framework of the Swiss Exercises ARM16 and LAURA. PSI-Report No. 17-01, ISSN 1019-0643, Paul Scherrer Institut, Villigen, Switzerland, 2017.
  DOI https://doi.org/10.55402/psi:34988

- Butterweck, G., Bucher, B., Gryc, L., Debayle, C., Strobl, C., Maillard, S., Thomas, M., Helbig, A., Krol, I., Chuzel, S., Couvez, C., Ohera, M., Rybach, L., Poretti, C., Hofstetter-Boillat, B., Mayer, S., Scharding, G.: International Intercomparison Exercise of Airborne Gamma-Spectrometric Systems of the Czech Republic, France, Germany and Switzerland in the Framework of the Swiss Exercise ARM17. PSI-Report No. 18-04, ISSN 1019-0643, Paul Scherrer Institut, Villigen, Switzerland, 2018.
  DOI https://doi.org/10.55402/psi:34959,

- Butterweck, G., Bucher, B., Rybach, L., Poretti, C., Maillard, S., Schindler, M., Hofstetter-Boillat, B., Mayer, S., Scharding, G.: Aeroradiometric Measurements in the Framework of the Swiss Exercises ARM18 and the International Exercise CONTEX 2018. PSI-Report No. 19-01, ISSN 1019-0643, Paul Scherrer Institut, Villigen, Switzerland, 2019.
  DOI https://doi.org/10.55402/psi:34957,
- Butterweck, G., Bucher, B., Rybach, L., Poretti, C., Maillard, S., Schindler, M., Hofstetter-Boillat, B., Mayer, S., Scharding, G.: Aeroradiometric Measurements in the Framework of the Swiss Exercise ARM19. PSI-Report No. 20-01, ISSN 1019-0643, Paul Scherrer Institut, Villigen, Switzerland, 2020.
  DOI https://doi.org/10.55402/psi:44919
- Butterweck, G., Bucher, B., Breitenmoser, D., Rybach, L., Poretti, C., Maillard, S., Kasprzak, M., Ferreri, G., Gurtner, A., Astner, M., Hauenstein, F., Straub, M., Bucher, M., Harm, C., Scharding, G., Mayer, S.: Aeroradiometric Measurements in the Framework of the Swiss Exercise ARM20. PSI-Report No. 21-01, ISSN 1019-0643, Paul Scherrer Institut, Villigen, Switzerland, 2021.
  DOI https://doi.org/10.13140/RG.2.2.15326.51526
- Butterweck, G., Bucher, B., Breitenmoser, D., Rybach, L., Poretti, C., Maillard, S., Hess, A., Kasprzak, M., Scharding, G., Mayer, S.: Aeroradiometric Measurements in the Framework of the Swiss Exercise ARM21. PSI-Report No. 22-02, ISSN 1019-0643, Paul Scherrer Institut, Villigen, Switzerland, 2022.
  DOI https://doi.org/10.55402/psi:44921
- Butterweck, G., Stabilini, A., Bucher, B., Breitenmoser, D., Rybach, L., Poretti, C., Maillard, S., Hess, A., Kasprzak, M., Scharding, G., Mayer, S.: Aeroradiometric Measurements in the Framework of the Swiss Exercise ARM22. PSI-Report No. 23-01, ISSN 1019-0643, Paul Scherrer Institut, Villigen, Switzerland, 2023.
  DOI https://doi.org/10.55402/psi:51194
- Butterweck, G., Stabilini, A., Bucher, B., Breitenmoser, D., Rybach, L., Poretti, C., Maillard, S., Hess, A., Hauenstein, F., Gendotti, U., Kasprzak, M., Scharding, G., Mayer, S.: Aeroradiometric Measurements in the Framework of the Swiss Exercise ARM23. PSI-Report No. 24-02, ISSN 1019-0643, Paul Scherrer Institut, Villigen, Switzerland, 2023.
  DOI https://doi.org/10.55402/psi:60054
- Stabilini, A., Breitenmoser, D., Geser, F., Bucher, B., Rybach, L., Poretti, C., Maillard, S., Hess, A., Kasprzak, M., Scharding, G., Mayer, S.: Aeroradiometric measurements in the framework of the Swiss ARM24 and international AGC24 exercises. PSI-Report No.: 25-01, Paul Scherrer Institut, Villigen, Switzerland,2025.
  DOI https://doi.org/10.55402/psi:68900

Appendix B

Summary of spectrometers used in AGC25

A summary of the spectrometric systems used in the AGC25 is provided in Table B.1.

Table B.1: Summary of spectrometric systems used in AGC25.

	CZE	FRA	DEU	LTU	CHE1 & CHE2
Detection system	RadPatrol2 $4 \times 4\,\mathrm{L}$ NaI(Tl) AIRIS $4 \times 4\,\mathrm{L}$ NaI(Tl)	$4 \times 4\,\mathrm{L}$ NaI(Tl)	$4 \times 4\,\mathrm{L}$ NaI(Tl) HPGe Detector	$4 \times 2\,\mathrm{L}$ NaI(Tl)	$4 \times 4\,\mathrm{L}$ NaI(Tl)
Manufacturer	NUVIA Pico Envirotec	Mirion Technologies	Saint Gobain, Ortec Ortec	Radiation solutions	Mirion Technologies
Sampling time	$1\,\mathrm{s}$	$1\,\mathrm{s}$	$2\,\mathrm{s}$	$1\,\mathrm{s}$	$1\,\mathrm{s}$ ($5\,\mathrm{s}$ moving avg.)
Energy range	$35\,\mathrm{keV} - 3000\,\mathrm{keV}$	$30\,\mathrm{keV} - 3000\,\mathrm{keV}$	$40\,\mathrm{keV} - 3000\,\mathrm{keV}$ $20\,\mathrm{keV} - 3000\,\mathrm{keV}$	$15\,\mathrm{keV} - 3072\,\mathrm{keV}$	$30\,\mathrm{keV} - 3000\,\mathrm{keV}$
Number of channels	1024 512	1024	1024 2048	1024	1024
Installation position	Cabin	Basket	Cabin	Cabin	Fuselage
Positioning system	GPS	GPS	GPS	GPS	Military GPS
Altimetry system	Radar	GPS	Radar	GPS	Radar, GPS and barometer
Secondary Detector	Geiger-Müller Tube	Geiger-Müller Tube	Geiger-Müller Tube	$2 \times 4\,\mathrm{L}$ NaI(Tl) (Envinet) Geiger-Müller Tube	Geiger-Müller Tube

Appendix C

Evaluation parameters

The parameters used for data evaluation are stored in the header section of each generated ERS 2.0 file. The header section used in the current exercise are listed below.

C.1 Team CHE1, Detector RLL 002

These evaluation parameters were used in the Mirion software for the evaluation of the measurements in Switzerland and the international exercise AGC25, with detector RLL 002.

```
V 2.0
HCTRY CH;HORG ARM NAZ;HTEAM ;HMODE REAL
HFILE HELI 2_20250605 0832 Mission 1 CHE1
HSURVEY 20250605 0832 Mission 1 CHE1
HSW SpirReplay_4.7.2.0
ICA  HELI 2
IPR ARINC;IPG Radar altimeter;IPC WGS84;IPU deg;IPP m;IPP HDOP
IAP Detector:Mirion - NaI - 16l - Spectrometer:ASM - 1024 Channels - automatic gain control
ISW Cesium;ISWE1_Cesium 630;ISWE2_Cesium 700
ISW Cobalt;ISWE1_Cobalt 1100;ISWE2_Cobalt 1390
ISW Global;ISWE1_Global 30;ISWE2_Global 3000
ISW Low Energy;ISWE1_Low Energy 400;ISWE2_Low Energy 1400
ISW MMGC1;ISWE1_MMGC1 400;ISWE2_MMGC1 1400
ISW MMGC2;ISWE1_MMGC2 1400;ISWE2_MMGC2 3000
```

```
ISW High Energy;ISWE1_High Energy 1400;ISWE2_High Energy 3000
ISW K40;ISWE1_K40 1370;ISWE2_K40 1570
ISW U;ISWE1_U 1660;ISWE2_U 1860
ISW Th;ISWE1_Th 2410;ISWE2_Th 2810
ISW Global;ISWE1_Global 30;ISWE2_Global 3000
/* Energy calibration;ISC 1024;ISE0 0;ISE1 3;ISE2 0
```

These evaluation parameters were used in the AGS_CH software for the evaluation of the measurements in Switzerland and the international exercise AGC25, with detector RLL 002.

```
V 2.0
HSW AGS_CH V0.0
HORG Nationale Alarmzentrale NAZ
HCTRY Switzerland
IAP Mirion 16l Container System RLL 002
ICA Superpuma
IPC WGS84
IPG From ARINC bus of helicopter
/* Parameters used for data evaluation-----------------------------------------------------------
/* No data value;MND -999
/* Energy windows-------------------------------------------------------------------------------
ISW Total;ISWE1_Total 401;ISWE2_Total 2997;ISWB_Total 80.4;ISWC_Total 5.53;ISWT_Total 0.006;ISWRA_Total 0;ISWRB_Total 0
ISW K-40;ISWE1_K-40 1369;ISWE2_K-40 1558;ISWB_K-40 6.4;ISWC_K-40 0.32;ISWT_K-40 0.008;ISWRA_K-40 0;ISWRB_K-40 0
ISW U-238;ISWE1_U-238 1664;ISWE2_U-238 1853;ISWB_U-238 3.7;ISWC_U-238 0.23;ISWT_U-238 0.0055;ISWRA_U-238 0;ISWRB_U-238 0
ISW Th-232;ISWE1_Th-232 2407;ISWE2_Th-232 2797;ISWB_Th-232 0;ISWC_Th-232 0.27;ISWT_Th-232 0.006;ISWRA_Th-232 0;ISWRB_Th-232 0
ISW Cs-137;ISWE1_Cs-137 600;ISWE2_Cs-137 720;ISWB_Cs-137 13;ISWC_Cs-137 0.59;ISWT_Cs-137 0.01;ISWRA_Cs-137 0;ISWRB_Cs-137 0
ISW Co-60;ISWE1_Co-60 1100;ISWE2_Co-60 1400;ISWB_Co-60 7;ISWC_Co-60 0.66;ISWT_Co-60 0.008;ISWRA_Co-60 0;ISWRB_Co-60 0
ISW MMGC1;ISWE1_MMGC1 400;ISWE2_MMGC1 1400;ISWB_MMGC1 0;ISWC_MMGC1 0;ISWT_MMGC1 0.006;ISWRA_MMGC1 0;ISWRB_MMGC1 0
ISW MMGC2;ISWE1_MMGC2 1400;ISWE2_MMGC2 2997;ISWB_MMGC2 0;ISWC_MMGC2 0;ISWT_MMGC2 0.0065;ISWRA_MMGC2 0;ISWRB_MMGC2 0
ISW LOW;ISWE1_LOW 100;ISWE2_LOW 400;ISWB_LOW 0;ISWC_LOW 0;ISWT_LOW 0.02;ISWRA_LOW 0;ISWRB_LOW 0
ISW MID;ISWE1_MID 720;ISWE2_MID 2997;ISWB_MID 0;ISWC_MID 0;ISWT_MID 0.015;ISWRA_MID 0;ISWRB_MID 0
ISW SDI;ISWE1_SDI 240;ISWE2_SDI 2997;ISWB_SDI 53.3;ISWC_SDI 4.14;ISWT_SDI 0.0053;ISWRA_SDI 0;ISWRB_SDI 0
/* Stripping factors----------------------------------------------------------------------------
ISWS_U-238_K-40 0.955
ISWS_Th-232_K-40 0.462
ISWS_Co-60_K-40 0.062
```

```
ISWS_Th-232_U-238 0.334
ISWS_U-238_Th-232 0.057
ISWS_K-40_Cs-137 0.442
ISWS_U-238_Cs-137 3.213
ISWS_Th-232_Cs-137 1.589
ISWS_Co-60_Cs-137 0.134
ISWS_K-40_Co-60 0.755
ISWS_U-238_Co-60 2.347
ISWS_Th-232_Co-60 0.661
/* Conversion factors----------------------------------------------------------------------------
ISWA_AW_K-40 6.37
ISWA_AW_U-238 2.87
ISWA_AW_Th-232 1.42
ISWA_AW_Cs-137 1.13
ISWA_AA_Cs-137 222
ISWA_AP_Cs-137 837414
ISWA_AP_Co-60 867605
ISD_SDI 5.96E-08
ISWD_K-40 0.000329
ISWD_U-238 0.00159
ISWD_Th-232 0.00113
ISWD_Cs-137 0.000212
/* ---------------------------------------------------------------------------------------------
/* Corrections-----------------------------------------------------------------------------------
/* Factor for the calculation of synthetic cosmic counts;&Factor_COS 14.35
/* Topographic correction;MTC Y
/* Radon correction;MRC N
/* Definition of additional Identifiers for corrected altitude and ground clearance,
/* an indicator for a new flight and the factor for calculation of synthetic cosmic counts
DEFINE&PZ_korr Corrected altitude im m
DEFINE&PH_korr Corrected ground clearance in m
DEFINE&New_Flight Switch for data composed of several flights
DEFINE&Factor_COS Factor for calculation of synthetic cosmic counts
/* ---------------------------------------------------------------------------------------------
```

C.2 Team CHE2, Detector RLL 003

These evaluation parameters were used in the Mirion software for the evaluation of the measurements in Switzerland and the international exercise AGC25, with detector RLL 003.

```
V 2.0
HCTRY CHE;HORG NBC-EOD;HTEAM CHE2;HMODE REAL
HFILE Heli 4_AGC25_Mission1_RM_CHE2
HSURVEY AGC25_Mission1_RM_CHE2 - AGC25, Mission 1, RM, CHE2
HSW SpirReplay_4.7.4.0
ICA HELI 4 Heli 4
IPR ARINC;IPG Radar altimeter;IPC WGS84;IPU deg;IPP m;IPP HDOP
IAP Detector:Mirion - NaI - 16l - Spectrometer:ASM - 1024 Channels - automatic gain control
ISW Roi 1;ISWE1_Roi 1 30;ISWE2_Roi 1 300
ISW Roi 2;ISWE1_Roi 2 300;ISWE2_Roi 2 800
ISW Roi 3;ISWE1_Roi 3 800;ISWE2_Roi 3 3000
ISW Low Energy;ISWE1_Low Energy 400;ISWE2_Low Energy 1400
ISW MMGC1;ISWE1_MMGC1 400;ISWE2_MMGC1 1400
ISW MMGC2;ISWE1_MMGC2 1400;ISWE2_MMGC2 3000
ISW High Energy;ISWE1_High Energy 1400;ISWE2_High Energy 3000
ISW K40;ISWE1_K40 1370;ISWE2_K40 1570
ISW U;ISWE1_U 1660;ISWE2_U 1860
ISW Th;ISWE1_Th 2410;ISWE2_Th 2810
ISW Global;ISWE1_Global 30;ISWE2_Global 3000
/* Energy calibration;ISC 1024;ISE0 0;ISE1 3;ISE2 0
```


These evaluation parameters were used in the AGS_CH software for the evaluation of the measurements in the international exercise AGC25, with detector RLL 003.

```
V 2.0
HSW AGS_CH V0.0
HORG ABC-Kamir
HCTRY Switzerland
IAP Mirion 16l Container System RLL 003
ICA Superpuma
IPC WGS84
```

```
IPG From ARINC bus of helicopter
/* Parameters used for data evaluation-----------------------------------------------------------
/* No data value;MND -999
/* Energy windows-------------------------------------------------------------------------------
ISW Total;ISWE1_Total 401;ISWE2_Total 2997;ISWB_Total 77.1;ISWC_Total 5.51;ISWT_Total 0.006;ISWRA_Total 0;ISWRB_Total 0
ISW K-40;ISWE1_K-40 1369;ISWE2_K-40 1558;ISWB_K-40 5.2;ISWC_K-40 0.32;ISWT_K-40 0.008;ISWRA_K-40 0;ISWRB_K-40 0
ISW U-238;ISWE1_U-238 1664;ISWE2_U-238 1853;ISWB_U-238 3.8;ISWC_U-238 0.23;ISWT_U-238 0.0055;ISWRA_U-238 0;ISWRB_U-238 0
ISW Th-232;ISWE1_Th-232 2407;ISWE2_Th-232 2797;ISWB_Th-232 0;ISWC_Th-232 0.27;ISWT_Th-232 0.006;ISWRA_Th-232 0;ISWRB_Th-232 0
ISW Cs-137;ISWE1_Cs-137 600;ISWE2_Cs-137 720;ISWB_Cs-137 13.2;ISWC_Cs-137 0.59;ISWT_Cs-137 0.01;ISWRA_Cs-137 0;ISWRB_Cs-137 0
ISW Co-60;ISWE1_Co-60 1100;ISWE2_Co-60 1400;ISWB_Co-60 6.8;ISWC_Co-60 0.66;ISWT_Co-60 0.008;ISWRA_Co-60 0;ISWRB_Co-60 0
ISW MMGC1;ISWE1_MMGC1 400;ISWE2_MMGC1 1400;ISWB_MMGC1 0;ISWC_MMGC1 0;ISWT_MMGC1 0.006;ISWRA_MMGC1 0;ISWRB_MMGC1 0
ISW MMGC2;ISWE1_MMGC2 1400;ISWE2_MMGC2 2997;ISWB_MMGC2 0;ISWC_MMGC2 0;ISWT_MMGC2 0.0065;ISWRA_MMGC2 0;ISWRB_MMGC2 0
ISW LOW;ISWE1_LOW 100;ISWE2_LOW 400;ISWB_LOW 0;ISWC_LOW 0;ISWT_LOW 0.02;ISWRA_LOW 0;ISWRB_LOW 0
ISW MID;ISWE1_MID 720;ISWE2_MID 2997;ISWB_MID 0;ISWC_MID 0;ISWT_MID 0.015;ISWRA_MID 0;ISWRB_MID 0
ISW SDI;ISWE1_SDI 240;ISWE2_SDI 2997;ISWB_SDI 49.9;ISWC_SDI 4.13;ISWT_SDI 0.0053;ISWRA_SDI 0;ISWRB_SDI 0
/* Stripping factors----------------------------------------------------------------------------
ISWS_U-238_K-40 0.980
ISWS_Th-232_K-40 0.503
ISWS_Co-60_K-40 0.052
ISWS_Th-232_U-238 0.344
ISWS_U-238_Th-232 0.061
ISWS_K-40_Cs-137 0.476
ISWS_U-238_Cs-137 3.184
ISWS_Th-232_Cs-137 1.639
ISWS_Co-60_Cs-137 0.133
ISWS_K-40_Co-60 0.788
ISWS_U-238_Co-60 2.320
ISWS_Th-232_Co-60 0.629
/* Conversion factors---------------------------------------------------------------------------
ISWA_AW_K-40 6.37
ISWA_AW_U-238 2.87
ISWA_AW_Th-232 1.42
ISWA_AW_Cs-137 1.13
ISWA_AA_Cs-137 222
ISWA_AP_Cs-137 837414
ISWA_AP_Co-60 867605
```

```
ISD_SDI 5.96E-08
ISWD_K-40 0.000329
ISWD_U-238 0.00159
ISWD_Th-232 0.00113
ISWD_Cs-137 0.000212
/* ------------------------------------------------------------------------------------------
/* Corrections-------------------------------------------------------------------------------
/* Factor for the calculation of synthetic cosmic counts;&Factor_COS 14.35
/* Topographic correction;MTC Y
/* Radon correction;MRC N
/* Definition of additional Identifiers for corrected altitude and ground clearance,
/* an indicator for a new flight and the factor for calculation of synthetic cosmic counts
DEFINE&PZ_korr Corrected altitude im m
DEFINE&PH_korr Corrected ground clearance in m
DEFINE&New_Flight Switch for data composed of several flights
DEFINE&Factor_COS Factor for calculation of synthetic cosmic counts
/* ------------------------------------------------------------------------------------------
```

C.3 Team CZE

These evaluation parameters were used by the CZE team in the AGMA software for the evaluation of the measurements in the international exercise AGC25.

```
V 2.0
HSW AGAMA
/*
/* header data
/*
V 2.0
HCTRY Czech Republic
HORG SURO
HTEAM CZE
HSURVEY  MISSION 1
HSITE THUN MILITARY PLATZ
/*
/* measuring equipment
/*
IAP Rad-Patrol2 - NaI(Tl)-16L
ICA Mi-17
IPR Garmin
IPC WGS84
IPU deg
IPP m
IPG radar altimeter - TRA-3000
/*
/* detection limit
AA_LD 7000 Bq/m2 - for Cs-137: window method
/*
/* measuring methods and parameters
/*
ISW windows integrals with stripping
ISWT exp(-mueh*h)
/* used windows lower and upper energy
ISWE1_Kalium 1370.00
ISWE2_Kalium 1570.00
```

```
ISWE1_Uran_2 1660.00
ISWE2_Uran_2 1860.00
ISWE1_Thorium 2410.00
ISWE2_Thorium 2810.00
ISWE1_TOT 400.00
ISWE2_TOT 2810.00
/* ------------------------------------------------------------------------------------------
```

C.4 Team FRA

These evaluation parameters were used by the FRA team for the evaluation of the measurements in the international exercise AGC25.

```
/*
/* header data
/*
V 2.0
HCTRY Switzerland
HORG ASNR
HMODE EXERCISE
HSITE MISSION 1 Reference Measurement
HFILE IRSN_M5
HSURVEY line spacing: 130 m, flight altitude 90 m, speed 120 km/h
HTZ 0
/*
/* measuring equipment
/*
IAP MIRION NaI(Tl)-4x4L
ICA Ecureuil AS350
IPR 3GRT SOLUTIONS - TG-X5
IPC WGS84
IPU deg
IPG MNT SRTM 90m
/*
/* measuring methods and parameters
/*
ISW K-40
ISWE1_K-40 1370.00
ISWE2_K-40 1570.00
ISWB_K-40 16.10
ISW_U-238
ISWE1_U-238 1660.00
ISWE2_U-238 1860.00
ISWB_U-238 15.8
ISW_TH-232
ISWE1_TH-232 2410.00
```

```
ISWE2_TH-232 2810.00
ISWB_TH-232 5.0
/* ------------------------------------------------------------------------------------------
```

C.5 Team DEU

These evaluation parameters were used by the DEU team in the *Rohflug* software for the evaluation of the measurements in the international exercise AGC25.

```
/*
/* original filename RM_DEU.ERS
/*
/* ERS-export Rf2Win32 V.00.90.06  02.06.2025 16:38:35 by AERO-Admin@AEROGAMMA-1A
/*
/* header data
/*
V 2.0
HTEAM "BfS-ARME-02"
HCTRY "Germany"
HORG "Bundesamt für Strahlenschutz (BfS)"
HMODE "TRAINING"
HSURVEY "999-PROJEKT"
HSURVEY_+ "emergency exercise"
HSITE "TEST TEST TEST"
/*
/* measuring equipment
/*
IAQ_D01 "HPGe"
IAP_D02 "NaI(Tl)-4L"
IAP_D03 "NaI(Tl)-4L"
IAP_D04 "NaI(Tl)-4L"
IAP_D05 "NaI(Tl)-4L"
ICA "Eurocopter EC-135 T2i D-HVxx"
IPR "UBlox-Mouse"
IPC "WGS84"
IPU "deg"
IPP "m"
IPG "radio altimeter - ARINC 552"
/*
/* measuring methods and parameters
/* (< in front of a measured value means that this measured value is below the dynamically calculated detection limit)
```

```
/*
ISW "windows integrals with stripping"
ISWT "exp(-mueh*h)"
/* used windows lower and upper energy
ISWE1_Th-232 2415.00
ISWE2_Th-232 2815.00
ISWE1_Bi-214 1665.00
ISWE2_Bi-214 1885.00
ISWE1_K-40 1347.00
ISWE2_K-40 1580.00
ISWE1_Cs-137OFL 600.00
ISWE2_Cs-137OFL 720.00
ISWE1_TOT 250.00
ISWE2_TOT 3000.00
/* used windows backgrounds
ISWB_Th-232 1.150
ISWB_Bi-214 2.640
ISWB_K-40 5.030
ISWB_Cs-137OFL 13.600
ISWB_TOT 0.000
/* used windows calibration factors
ISWA_AW_Th-232 7.7000
ISWA_AW_Bi-214 15.0000
ISWA_AW_K-40 34.0000
ISWA_AA_Cs-137OFL 472.0000
ISDT 0.0003
/* used windows stripping coefficients
ISWS_K-40_Cs-137OFL 0.57000
ISWS_Bi-214_Cs-137OFL 2.65000
ISWS_Bi-214_K-40 0.99000
ISWS_Bi-214_Th-232 0.09000
ISWS_Th-232_Cs-137OFL 1.68000
ISWS_Th-232_K-40 0.57000
ISWS_Th-232_Bi-214 0.33000
/* used windows assumed distribution
SGM_Th-232 "for all measurement tasks - assumed uniform distribution [Bq/kg]"
```

```
SGM_Bi-214 "for all measurement tasks - assumed uniform distribution [Bq/kg]"
SGM_K-40 "for all measurement tasks - assumed uniform distribution [Bq/kg]"
SGM_Cs-137OFL "for all measurement tasks - assumed surface [Bq/m^2]"
SGM_TOT "for all measurement tasks - Danish method [mueSv/h]"
/* used detectors
/* DETECTOR 6 -  6=2+3+4+5 -s2 -g3
/* MCA-TYPE process
/* SPECTRUM_LENGTH 1024
/*
/* export use datafile & start  - P250602C.DAT             02.06.25 12:25:38
/*            parameterfile     - NAT_ODLers.RFP           02.06.25 16:17:26
/*            ERS scriptfile    - NAT_ODLers.ERS           02.06.25 16:38:06
/* export reduced data   - one position per spectrum
/* ------------------------------------------------------------------------------------------
```

C.6 Team LTU

Reported parameters by the LTU team for the evaluation of the measurements in the international exercise AGC25.

```
V 2.0
/* HSURVEY "Survey20250605065948"
/* HCTRY "Lithuania"
/* HORG "Radiation Protection Center"
/* IPC "WGS84"
/* IPU "deg"
/* IPP "m"
/* No data value;MND -999
/* Energy calibration;ISE0_D01 1.8081;ISE1_D01 2.9994;ISE2_D01 0;ISC_D01 1024;
/* ----------------------------------------------------------------------------------------
```

Appendix D

Pictures

This appendix provides a collection of pictures taken during the AGC25 exercise.


CZECH AIR FORCE


EC135
AIRBUS


MONT BLANC
HELICOPTERES


NEOC
NEOC
NEOC


Gerald Scharding
Head of National Emergency
Operations Centre (NEOC)


NAZ
T-319
RSI


RSI


SRF
RSI


Swiss Air Forc


BfS


BUNDE


BUNDESPOLIZEI


T-318
NAZ


ASS
NUR VERBINDUNGEN


nobo
Barracuda
Endurance in Mission area
FIN 2 h
CZE 2 h 40 min
LTU 2 h
DEU 100 min
CHE 1 3 h
CHE 2 3 h
height GND
Spacing
PET
Ziliukas


DVCI Sàrl


Robodrone


Du bist für uns Alle


10

Published by:

Paul Scherrer Institute PSI
Forschungsstrasse 111
5232 Villigen PSI
Switzerland
www.psi.ch